

Berichterstatter (Gutachter):

Prof. Dr. Andreas Eckart

Prof. Dr. J. Anton Zensus

Tag der mündlichen Prüfung:

12. Oktober 2017



Zusammenfassung

Untersuchungen der Wechselwirkung zwischen dem interstellaren Medium und der Umgebung des zentralen Schwarzen Loches auf Parsec-Skalen sind von großer Wichtigkeit für das volle Verständnis der Galaxienevolution. Das Galaktische Zentrum als nächstes Galaxienzentrum bietet uns die einmalige Möglichkeit die Dynamik von einzelnen Sternen und des nuklearen Sternhaufens als Ganzen zu beobachten.

Diese Dissertation behandelt den Übergangsbereich, in dem das komplexe interstellare Medium im Galaktischen Zentrum auf ein verhältnismäßig einfacheres Objekt trifft, aller Wahrscheinlichkeit nach ein Schwarzes Loch mit einer Masse von $\sim 4 \times 10^6$ Sonnenmassen, das nur durch drei klassische Parameter charakterisiert wird: seine Masse, seiner Spin und seine elektrische Ladung. Vor wenigen Jahren wurde dort das Objekt DSO/G2 entdeckt, das sich auf einem Orbit mit sehr hoher Exzentrizität bewegt und seine Periaps-Position 2014 mit einer Periapsdistanz von 2000 Schwarzschildradien durchlaufen hat. Der Orbit, das Nahinfrarot-Spektrum und deren Vergleich mit Modellen haben es ermöglicht, bisher unbekannte Eigenschaften der Umgebung von Sgr A* sowie der Beschaffenheit dieser rätselhaften Quelle zu bestimmen.

In einer Artikelserie haben wir die Dynamik verschiedener Szenarios für DSO/G2, seine Wechselwirkung mit dem interstellaren Medium nahe des Galaktischen Zentrums und seiner Nahinfrarot-Kontinuums-Strahlungseigenschaften untersucht. Ein wichtiges Resultat ist die Asymmetrie in der stellaren Bowshock Entwicklung in Gegenwart eines Ausflusses vom Galaktischen Zentrum. Weiterhin konnten wir mit polarimetrischen Messungen und 3D Monte Carlo Strahlungstransport-Simulationen ein Modell eines jungen Sterns mit nicht-sphärischer Staubhülle entwickeln, das seine Kompaktheit, seine hohe Nahinfrarot Emission und seine linear polarisierte Strahlung erklärt. Außerdem haben wir die Möglichkeit untersucht, dass das DSO und ähnliche Objekte Kandidaten für junge Neutronensterne sind, die mit heutigen und zukünftigen Observatorien zu beobachten sein sollten und helfen könnten, das „fehlende Pulsar Paradox“ zu lösen.

Indem wir uns der innersten Region des Galaktischen Zentrums nähern, stoßen wir auf das Problem der elektrischen Ladung von Sgr A*, die meistens als neutral angenommen wird. Wir stellen fest, dass eine stabile elektrische Ladung durch mehrere Mechanismen aufrechterhalten werden kann. Am Vielversprechendsten ist die Aufladung durch ein rotierendes Schwarzes Loch, das sich in einem homogenen Magnetfeld aufhält. Von uns berechnete realistische Werte

für die elektrische Ladung würden die Raumzeit-Metrik nicht beeinflussen, aber durchaus die Dynamik von Plasma im Galaktischen Zentrum. Darüberhinaus schlagen wir einen neuartigen Test vor, mit dem die Charakteristik der elektrischen Ladung durch eine Helligkeitsverteilung der Bremsstrahlung bestimmt werden kann.



Abstract

Studying the interaction between the interstellar medium and the black hole environment on the parsec scale is of crucial importance in the full understanding of galaxy evolution. Since the Galactic Centre is the closest galactic nucleus, it offers us the unique possibility to observationally study the dynamics of individual stars as well as the properties of the Nuclear Star Cluster as a whole.

This thesis deals with the transition region where the complex interstellar medium in the Galactic Centre meets a rather simple object at the very centre – most probably a black hole of 4×10^6 Solar masses characterized by only three classical parameters: mass, spin, and electric charge. Recently, a NIR-excess object named DSO/G2 was detected that is moving on a highly eccentric orbit, with the pericentre reached in 2014 at ~ 2000 Schwarzschild radii. The monitoring, the analysis of NIR data, and the comparison with models have provided an unprecedented opportunity to constrain the properties of previously unexplored region around Sgr A* as well as to determine the nature of this enigmatic source.

In a series of papers, we explored the dynamics of different scenarios for DSO/G2, its interaction with the ambient medium close to the Galactic centre, and the radiative properties of its NIR continuum emission. The main findings include the asymmetry of the stellar bow-shock evolution along the orbit when the outflow from the Galactic centre is present. Subsequently, using polarimetry measurements and 3D Monte Carlo radiative transfer, we were able to set up a model of a young star with a non-spherical dusty envelope that can explain its compactness, NIR-excess as well as its linearly polarized emission. Finally, we explore a possibility that the DSO and objects with similar characteristics could be candidates for young neutron stars that should be observable in NIR bands with current and future facilities, which can help to resolve the “missing pulsar paradox”.

Approaching the innermost region of the Galactic Centre, we explore the problem of an electric charge associated with Sgr A*, which is assumed to be zero in most studies. We found that a stable charge can be maintained by several mechanisms. One of the most promising ones is the charging due to the rotating black hole that is immersed in a uniform magnetic field. Realistic values of the charge that we calculated do not influence space-time metric, but can significantly influence the dynamics of plasma in the vicinity of the Galactic centre. Furthermore, we also propose a novel observational test for detecting the signature of the charge using a bremsstrahlung brightness distribution.



Contents

Zusammenfassung	iii
Abstract	v
Contents	vii
1 Introduction	1
1.1 Historical overview: from first compact objects to the Galactic centre black hole	1
1.1.1 Discovery of first white dwarfs and development of fundamental theories	2
1.1.2 Observational breakthroughs and the birth of relativistic astrophysics	5
1.1.3 Brief history of the observations of the Galactic centre	9
1.2 The Galactic centre environment – potential for star formation	12
1.2.1 Jeans instability criterion in the Galactic centre	15
1.2.2 Estimate of the number of dust-enshrouded stars near the Galactic centre	18
1.2.3 Formation of neutron stars and pulsar wind nebulae	20
1.3 Goals and outline of this thesis	23
2 Paper 1: Dynamics of a dust-enshrouded star	27
3 Paper 2: A young accreting star close to the SMBH	43
4 Paper 3: Bow-shock evolution close to the SMBH	65
5 Paper 4: A NIR source with a polarized emission	85
6 Paper 5: Nature of NIR-excess sources	99
7 Paper 6: A short review on the DSO	121
8 Paper 7: Interaction modes of neutron stars	127
9 Paper 8: Charge of the Galactic centre black hole	141

10 Conclusions and Outlook	159
10.1 Summary and discussion	159
10.1.1 NIR-excess sources: Nature of Dusty S-cluster Object (G2)	159
10.1.2 Interaction modes of neutron stars	161
10.1.3 Charge of Sgr A*	163
10.2 Future prospects	164
10.2.1 More dusty sources: DSO/G2, G1 and their friends	164
10.2.2 Neutron star dynamics	165
10.2.3 Dynamics of binary black hole systems: OJ287 as a special case	166
10.2.4 Analysis of JWST observations	168
Bibliography	169
Acknowledgements	179
Declaration	183
Curriculum Vitae	193

Introduction

Studying the black hole environment is of crucial importance for the current view of the Universe and the evolution of galaxies. Showing that black holes are not only entities within the General Theory of Relativity but also real astrophysical objects may be considered as one of the greatest achievements of astrophysics in the second half of the twentieth century and the beginning of the twenty-first century. In particular, the observations of the Galactic centre, starting towards the end of 1960s and the beginning of 1970s, largely contributed to the current theory that there is, beyond reasonable doubt, one supermassive black hole (SMBH) at the centre of the Milky Way and supposedly at least one SMBH in nuclei of most other galaxies.

1.1 Historical overview: from first compact objects to the Galactic centre black hole

Historically, black holes¹ were for a long time only theoretical and mathematical entities. The concept of very compact objects, from which light or light particles cannot escape, was first introduced by John Michell (1783) and Pierre-Simon Laplace (1796) in the 18th century (see [Israel 1987](#), for a historical review). One can consider these to be early theoretical speculations. It was not until Einstein's General Theory of Relativity ([Einstein 1915](#)), when the theoretical concept of singularities and event horizons emerged. In general, it was necessary to solve the set of Einstein's field equations (EFE), a system of ten non-linear, partial differential equations, which is significantly simplified given the symmetry of the problem as well as assuming vacuum. In 1916, the German astronomer Karl Schwarzschild found the solution of EFE for a non-rotating body in vacuum ([Schwarzschild 1916](#)). Shortly after that, [Reissner \(1916\)](#) found the solution for a stationary charged point mass, which was extended by [Nordström \(1918\)](#) for a spherically symmetric charged body. These solutions are spherically symmetric solutions to vacuum EFE and hence Birkhoff's theorem applies ([Birkhoff & Langer 1923](#)), according to which these solutions are static and asymptotically flat and cannot be sources of gravitational waves. During the whole first half of 20th century, black holes were considered as mathematical curiosities, not really having real astrophysical applications. They were

¹Not called like that at the time; they were usually referred to as dark stars, frozen stars or *corps obscurs*.

usually referred to as “frozen stars” and relativists often used the term Schwarzschild’s sphere, discontinuity, sphere catastrophique, frontier, barrier or even a magic circle to describe a singularity surrounded by an event horizon (see [Bartusiak 2015](#), for a historical account). The connection of singularities found by solving EFE with astrophysical objects was not clear at the beginning. Albert Einstein himself proposed that a collapsing star cannot form singularities in nature or in other words a stellar internal pressure should prevent it from further collapsing and forming a singularity ([Einstein 1939](#)). Black holes simply seemed too exotic to be associated with real objects or as Kip Thorne put it, “Like unicorns and gargoyles, black holes seem more at home in the realms of science fiction and ancient myth than in the real Universe,” ([Thorne 1994](#)).

1.1.1 Discovery of first white dwarfs and development of fundamental theories

Towards the end of 19th century and the beginning of 20th century, there were several observational implications that the Universe is not only populated by main-sequence stars² similar to the Sun, but more exotic objects seemed to exist even in our close cosmic vicinity. An important breakthrough was the discovery of a companion star of Sirius (the “Dog Star”), which is the brightest star in the night sky in the constellation of Canis Major. Friedrich Wilhelm Bessel working at the Königsberg observatory tracked the position of Sirius and Procyon and discovered their wobbling motion in 1844, which implied the presence of a darker companion ([Bessel 1844](#)). The companion – Sirius B – was discovered by Alvan Graham Clark on January 31, 1862 in Cambridgeport, Massachusetts, which was reported to George Bond, the director of Harvard College observatory who detected the companion as well ([Bond 1862](#)). Sirius B soon appeared to be rather exotic. The spectrum revealed that its effective temperature is significantly larger than that of the Sun, $T_{\text{Sirius B}} \approx 25\,000\text{ K}$, yet it was a dim object in comparison with Sirius A ([Adams 1914, 1915](#)). Given the spectral type of A0 and the luminosity of $L_{\text{Sirius B}} \approx 10^{-2} L_{\odot}$, we get the radius of $R_{\text{Sirius B}} \approx 4000\text{ km}$, which is comparable to the Earth’s size.

An object with the diameter of $\sim 10^4\text{ km}$ but the comparable mass to that of the Sun implied a significantly larger mean density, directly pointing to the existence of more compact and dense states than those of Sun-like stars. At the beginning of 20th century, in total three stars with similar parameters, namely the mass of $\sim 1 M_{\odot}$, the radius of $\sim 5000\text{ km}$, and the mean density of $\sim 10^6\text{ g cm}^{-3}$, were detected and studied (40 Eridani B, Syrius B, and Van Maanen’s star), which directly led to an intense theoretical analysis of how such compact, hot stars – *white dwarfs* – can be formed and supported ([Eddington 1926](#)). Although Arthur Eddington proposed that the classical gas laws break down at such large densities, the solution appeared with the onset of quantum mechanics. Ralph H. Fowler was the first to

²At the core of main-sequence stars, the thermonuclear fusion of hydrogen atoms into helium atoms occurs, which generates thermal energy. At this stage, the star is approximately in the hydrostatic equilibrium, where the outward force due to the pressure gradient is balanced by an inward gravitational force due to the outer layers: $\frac{dP}{dr} = -\frac{Gm(r)\rho}{r^2}$. The position of the star along the main sequence is determined primarily by its mass, where lower-mass stars are located towards the lower right corner of the colour-brightness diagram, also known as the Hertzsprung-Russel (HR) diagram, whereas the more massive stars occupy the upper left corner of the HR diagram. On the main sequence, the luminosity is proportional to the mass $L_{\star} \sim M_{\star}^{3.5}$, which is approximately valid for the mass range of $0.1\text{--}50 M_{\odot}$, and more massive stars have a shorter life-time due to the faster burning of the nuclear fuel.

apply quantum mechanics in astrophysics in 1926 (Fowler 1926). He used recently developed *Fermi-Dirac* statistics to introduce the pressure of degenerate electron gas that can support white dwarfs against the gravitational collapse. A more complete theory was developed by Chandrasekhar in 1930s (Chandrasekhar 1931a,b), who included special relativistic effects into the equation of state of degenerate electron gas. Stars that have exhausted all its fuel will continue to contract until the electrons occupy the volume in the phase-space equal to $(\Delta q_e \Delta p_e)^3 \sim h^3$, when the contraction is stopped by the pressure of degenerate electron gas. During his boat trip from India to Cambridge, Chandrasekhar derived the maximum mass a white dwarf can have. The maximum mass – now named *Chandrasekhar limit* – can be expressed entirely as a function of fundamental constants and the chemical composition of the star,

$$M_{\text{Ch}} \sim N_{\text{max}} m_{\text{B}} = \left(\frac{\hbar c}{G m_{\text{B}}^2} \right)^{3/2} m_{\text{B}} \simeq 1.5 M_{\odot}. \quad (1.1)$$

The limit automatically implied that after the thermonuclear fuel is exhausted inside the stars, they will shrink and end up as a white dwarf under the condition that their final mass is $M_{\star} \leq M_{\text{Ch}} \approx 1.4 M_{\odot}$. The question arose what happens if *the terminal mass of the star at the end of its stellar evolution is more than the Chandrasekhar limit?* Subrahmanyan Chandrasekhar realized that heavier remnants could not be supported by the pressure of degenerate electron gas anymore. Will the star then continue collapsing into a singularity? Or is there another degenerate stage? Chandrasekhar, often called Chandra, explored the possibility of the stellar collapse into a singularity in his early years at the Cambridge University. However, his endeavour was halted by Arthur Eddington, who after Chandra’s presentation of the theory of the gravitational collapse for stars heavier than the maximum mass at the meeting of the Royal Astronomical Society on 11 January 1935 opposed him and said, “There should be a law of Nature to prevent a star from behaving in this absurd way!” (Bartusiak 2015). At a meeting at Harvard University in 1936, he even called the Chandrasekhar limit for white dwarfs “stellar buffoonery” (Miller 2005; Bartusiak 2015). Despite protests from Eddington, Chandra’s analysis and the maximum mass for white dwarfs encouraged others to investigate the gravitational collapse of stars in a more detail, which in the end led to the study of neutron stars and black holes, which are even more compact stages of matter than white dwarfs.

In 1932 James Chadwick discovered a new particle – neutron – in Great Britain. At the same time Lev Landau, a Soviet scientist who independently of Chandra discovered the maximum mass for white dwarfs, introduced a neutronic core, the concept of how stars can obtain energy via the formation of a very dense and compact core that consists of neutrons. The basic formation set-up was that in dense stellar cores, atomic nuclei combine with electrons to form neutrons. In essence, the neutronic core forms one giant atomic nucleus (Landau 1938), with the mass density of $\sim 10^{14} \text{ g cm}^{-3}$ comparable to nuclear densities. The equilibrium radius associated with the star of the mass approaching the maximum mass M_{max} is given by the emergency of the relativistic degeneracy, in which case the Fermi energy is $E_{\text{F}} \geq m_{\text{f}} c^2$, where m_{f} is the fermion mass, i.e. the mass of electrons for white dwarfs and the mass of the neutron for neutron stars. Hence, the equilibrium radius for white dwarfs and neutron stars is quite different,

$$R_{\text{WD}} \lesssim \frac{\hbar}{m_e c} \left(\frac{\hbar c}{G m_{\text{B}}^2} \right)^{1/2} \approx 5 \times 10^8 \text{ cm}, \quad (1.2)$$

$$R_{\text{NS}} \lesssim \frac{\hbar}{m_n c} \left(\frac{\hbar c}{G m_{\text{B}}^2} \right)^{1/2} \approx 3 \times 10^5 \text{ cm}, \quad (1.3)$$

where R_{WD} and R_{NS} is the typical radius for white dwarfs and neutron stars, respectively. Hence it was first theoretically found that neutron stars are expected to be three orders of magnitude smaller and thus more compact than white dwarfs. It was Fritz Zwicky who gave the real astrophysical meaning to neutron stars together with Walter Baade in 1933. They linked supernova explosions to the formation of neutron stars (Baade & Zwicky 1934), but they lacked an observational evidence for this connection and most of the astronomers ignored it until 1960s. In the meantime, Richard C. Tolman studied the static structure of spherically symmetric spacetimes filled with fluids in the years between 1934 and 1939 (Tolman 1939). In 1939, J. Robert Oppenheimer and George Volkoff derived the equation for the structure of the spherically symmetric, static spacetime filled with fluid, now known as Tolman-Oppenheimer-Volkoff (TOV) equation in the form,

$$\frac{dP}{dr} = -\frac{G [\rho(r) + P(r)/c^2][M(r) + 4\pi r^3 P(r)/c^2]}{r^2 \left(1 - \frac{2GM(r)}{c^2 r} \right)} \quad (1.4)$$

where r is a radial coordinate, $\rho(r)$, $P(r)$, and $M(r)$ are the density, pressure, and the mass at the distance r , respectively. In non-relativistic cases, when the terms with $1/c^2$ can be neglected, TOV equation turns into the Newtonian equation of hydrostatic equilibrium, $\frac{dP}{dr} = -\frac{GM(r)\rho(r)}{r^2}$.

Using this equation and Tolman's results, Oppenheimer and Volkoff calculated that neutron stars have a maximum mass limit, so-called TOV limit, in a similar way as white dwarfs do (Oppenheimer & Volkoff 1939). They derived an upper mass limit of only 0.7 Solar masses based on TOV equation, see Eq. 1.4. However, since the TOV equation is not quite applicable to neutron stars (it does not include the short-range nuclear repulsive force among neutrons), modern estimates are larger by at least a factor of 2, yielding about $M_{\text{TOV}} \approx 1.5 M_{\odot}$ up to $3 M_{\odot}$ (Shapiro & Teukolsky 1983). The maximum mass for neutron stars implied three different types of stellar end-products: those below the Chandrasekhar limit – white dwarfs, those between the Chandrasekhar limit and the Oppenheimer-Volkoff limit – neutron stars, and *what happens for even larger masses?* This problem was grasped again by Oppenheimer and Hartland Snyder who found out that essentially the end-product for the mass larger than the Oppenheimer-Volkoff limit is a singularity or in other words, the gravitational contraction cannot be anymore stopped by degenerate pressure and continues till the singularity is formed or essentially a *black hole* (Oppenheimer & Snyder 1939). At that time, however, a general mindset among the physicists was that nature must prevent forming singularities. The fact that the singularity surrounded by an event horizon was the part of the basic solutions of EFEs (Schwarzschild, Reissner-Nordström) was explained either by its incompleteness, i.e. a new law would prevent forming them, or an astrophysical explanation was that strong stellar winds of massive stars would lead to such a large mass loss that the Chandrasekhar limit is never reached and the final stage is thus a white dwarf, which had been observed at that time (Bartusiak 2015). Even Einstein, the father of general relativity, did not consider singularities to be realistic. He published a paper one month after Oppenheimer's and Snyder's paper on the continuing gravitational collapse, in which he set up stars in such a way so that they

consist of circularly orbiting gravitating bodies like a stellar cluster (Einstein 1939). In this model, the centrifugal force acting on each particle prevents the system from collapsing. However, it was clear that the model cannot represent a star in a realistic manner and some historians even consider this study as Einstein's "worst scientific paper", which totally ignored the Oppenheimer-Snyder model already published at that time (Bartusiak 2015).

Simultaneously, the problem of how stars are powered was solved mainly by Hans Bethe at the Cornell University and his collaborators, who found out the chain of precise thermonuclear reactions that take place at the temperature several millions of Kelvin at the core of stars (Bethe 1939). Before that George Gamow and Carl Friedrich von Weizsäcker put forward the theory of proton-proton (pp) reactions that occur in the cores of Sun-like stars. Remaining questions were discussed at the fourth annual Washington Conference of Theoretical Physics at Carnegie Institute in Washington (Miller 2005), where other notable physicists were invited, namely Chandra, Strömberg, Bethe, and Edward Teller among others. By the end of the meeting, Hans Bethe with his collaborator Charles Critchfield, a graduate student of George Gamow, found the full series of nuclear reactions of the pp cycle that could also explain the presence of heavier elements (Li, Be) in the solar atmosphere. Later Bethe also solved the problem of thermonuclear reactions in heavier stars than the Sun, leading to the carbon-nitrogen-oxygen (CNO) cycle. For his cumulative contribution to the problem of stellar energy, Bethe received the Nobel Prize in 1967. The fundamental theory of stellar nucleosynthesis was later completed by Margaret and Geoffrey Burbidge, William Fowler, and Fred Hoyle and summarized in the study "Synthesis of the Elements in Stars" (Burbidge et al. 1957), which is also known as B²FH paper named using the initials of all authors. The stellar nucleosynthesis complemented the theory of *Big Bang* nucleosynthesis published earlier in *Alpher-Bethe-Gamow* paper (Alpher et al. 1948) having a title "The Origin of Chemical Elements", also known as $\alpha\beta\gamma$ paper.

1.1.2 Observational breakthroughs and the birth of relativistic astrophysics

The success in the discovery and the monitoring of compact objects in the second half of the 20th century was directly connected with the development of tools and novel techniques beyond the visible spectrum, mainly in the radio, infrared, and X-ray parts of the electromagnetic spectrum. In parallel, several attempts were taken to detect gravitational waves, especially suited for the physics of binary black holes and neutron stars, which was successful in 2015, one hundred years after the general theory of relativity was published.

In 1932, Karl G. Jansky founded the new discipline of radioastronomy, since he accidentally detected first radio waves at 20 MHz emanating from the central parts of the Galaxy while working at the Bell Telephone Laboratories (Jansky 1933). Subsequently, Grote Reber followed Jansky's radio observations with his nine-meter dish and extended them, confirming radio emission along the Galactic plane peaking towards the centre of the Milky Way (Reber 1944). Radio techniques were significantly improved during WWII when the radar techniques were developed. During this time, the radio emission of the Sun was first detected by James S. Hey and George C. Southworth (Hey 1975; Southworth 1982). One of the most intriguing findings of the newly-born field of radioastronomy were bright radio galaxies with bipolar lobes, such as the radio source Cygnus A. These lobes were only visible in the radio domain, not in the optical. The estimated combined magnetic and kinetic (particle) energy associated

with the radio-emitting lobes was equivalent to $\sim 10^7 \times M_{\odot}c^2 = 10^{60} \text{ erg s}^{-1}$ (Burbidge 1958, 1959). It was impossible to explain such an enormous energetic process with known chemical, nuclear, or matter-antimatter reactions. A radio-astronomy group at the University of Cambridge made systematic observations of radio sources across the sky at 159 MHz and created the Third Cambridge catalogue (Edge et al. 1959), where object names start with 3C and their order number. The first radio source, for which an optical counterpart was found by Allan Sandage and Thomas A. Matthews using the 5.1-meter Hale Telescope atop Mount Palomar, was 3C48 (Matthews & Sandage 1963). The source 3C48 was point-like, resembling a star with an unusual spectrum. At the beginning of 1960s, the astronomical community wondered about these *quasi-stellar* objects with a strong radio emission and enigmatic optical spectra with unknown emission lines. Using the method of lunar occultations, Australian radioastronomers pinpointed the position of the radio source 3C273 and identified its two components (Hazard et al. 1963). Based on their results, Caltech astronomer Maarten Schmidt solved the puzzle of quasistellar radio sources while taking the visible spectrum of the optical counterpart of the source 3C273 using the Palomar telescope (Schmidt 1963). He recognized the Balmer lines of hydrogen, which were, however, strongly redshifted, corresponding to the redshift of 0.158. Although the redshift was large in comparison with typical radial velocities measured for stars at that time, 3C273 is one of the closest quasars (as these objects started to be called) and the most luminous one at visible wavelengths (with an apparent magnitude of $m_V \approx 12.9$). The optical luminosity of the source corresponds to $\sim 4 \times 10^{12} L_{\odot}$ and the energetic output is located inside one light year as inferred from the short variability of the source ranging from days to weeks. The luminous nucleus thus outshines the whole host galaxy by about two orders of magnitude.

After Oppenheimer and Snyder's study of the gravitational collapse in 1939 (Oppenheimer & Snyder 1939), the interest in gravitational physics declined during WWII and shortly after it. While the best physicists were involved in nuclear, particle, and quantum physics, which was partially motivated by the Manhattan project and the development of nuclear and hydrogen bombs during and immediately after WWII, only a few physicists considered the career in gravitational physics. The majority viewed the General Theory of Relativity as too theoretical and many considered it to be more a mathematical discipline than a branch of physics, since experimental tests of general relativity were missing or practically not possible at that time (Bartusiak 2015). However, the development of classical celestial mechanics and related numerical methods continued, namely the Roche problem in the context of close binary systems (Kopal 1959). In parallel with the breakthrough observational discoveries in the 1950s and 1960s, the motivation to continue studying gravitational physics was partially encouraged by the establishment of the Gravity Research Foundation in 1948 by Roger Babson, an American stock market economist interested in physics and engineering. Originally, the Gravity Research Foundation was aimed at finding shielding against gravity (anti-gravitational technologies), but later it supported general studies of gravity by establishing an essay prize for the best essay on gravity (Stephen Hawking and Roger Penrose were among prize winners) as well as by organizing conferences and meetings on gravity. Babson's foundation partially supported, alongside the rich industrialist Agnew Bahnsen, the foundation of an institute for gravitational studies at the University of North Carolina, which was headed by Bryce DeWitt. In 1957 the new institute organized a conference at Chapel Hill, which is generally considered as a breakthrough meeting in terms of reviving an interest in gravitational studies. At the same time, John Archibald Wheeler, a professor at Princeton University, initiated the first university course in relativity and restarted the analysis of the gravitational collapse at the end of the

life of massive stars, initially to show that singularities cannot be avoided. Wheeler with his Princeton group used the first generation of digital computers – MANIAC (Mathematical Analyzer, Numerical Integrator, and Computer) – to revisit and extend the previous study of Oppenheimer and Snyder (Oppenheimer & Snyder 1939) on the continued gravitational collapse. At the international conference in Belgium in 1958, Wheeler presented that the singularity is avoided during the collapse since there is an efficient mechanism transforming the particles at the stellar core into electromagnetic, gravitational radiation or neutrinos, thus always avoiding the TOV limit and the star ends up its life either as a neutron star or a white dwarf. Oppenheimer was in the audience at the same conference and politely disagreed, claiming that the problem was solved already in their paper (Oppenheimer & Snyder 1939) and no new, exotic physics laws are needed to save the star from the complete collapse (Bartusiak 2015). Shortly afterwards Wheeler with his students found out that beyond a certain mass limit, nothing can indeed stop the star from collapsing into a singularity (Harrison et al. 1965), in particular no forces (nuclear, electrostatic), rotation, pulsations, and non-spherical geometry could prevent the star from the continuing collapse. This was further supported by the numerical simulations in the early 1960s by Stirling Colgate and Richard White, using the computer at the Livermore National Laboratories. The Colgate-White numerical model (Colgate & White 1966) of the stellar collapse properly included an equation of state and nuclear reactions and finally showed that when the stellar core is sufficiently massive, nothing can indeed stop it from the collapse and forming a singularity. Along the way, they also solved the problem of supernova explosions which are driven by the degenerate pressure of neutrino gas formed during the collapse. Their simulations convinced Wheeler and others that black holes are real entities in the Universe. Essentially the same results were independently reached by the Soviet relativist group around Yakov B. Zel’dovich (Zel’dovich 1964; Zeldovich & Guseynov 1966; Zel’dovich & Novikov 1972), which strengthened the necessity of a singularity formation during the collapse. The fact that black holes – or hidden singularities – are inevitable was also mathematically proved by Roger Penrose, who applied topology to black holes (Penrose 1969): “Deviations from spherical symmetry cannot prevent space-time singularities from arising.” In the end, the complete gravitational collapse leads to the formation of black holes that are fully characterized by three, externally observable classical parameters: mass, spin, and electric charge. As John Wheeler put it: “A black hole has no hair”, which became known as a *no-hair* theorem that is applicable to all black-hole solutions of the Einstein-Maxwell equations in general relativity (Misner et al. 1973).

The discovery of quasars as extremely distant, luminous sources and the renewed interest in gravitational physics started to fully intertwine in 1963, which marks the birth of relativistic astrophysics. From an observational point of view, the identification of the quasar by Maarten Schmidt was a crucial point (Schmidt 1963). On the theory side, Fred Hoyle and William Fowler put forward an idea that the enormous energy in extragalactic radio sources could be obtained by large concentrations of the mass in the nuclei of these sources (Hoyle & Fowler 1963). It was clear from the first principles that a sudden contraction of the matter to relativistic scales could generate enough energy to power these sources, which was also proposed by Vitaly L. Ginzburg earlier, but in combination with the formation of protostars (Ginzburg 1961). These and other scenarios were discussed at the First Texas Symposium on Relativistic Astrophysics in Dallas in December 1963, which was a crucial event for bringing together observers and theoreticians. The symposium did not provide final answers to the quasar energetics, but triggered new action and enthusiasm and is usually considered as the “landmark” event for the birth of relativistic astrophysics. The first proposal of the accretion of

gas and dust onto a collapsed object, in which the gravitational potential energy of matter is converted into the thermal energy and radiation, was published by Yakov Zel'dovich and Igor Novikov (Zel'dovich & Novikov 1972). Independently, the same set-up was proposed in 1964 by Edwin Salpeter at the Cornell University (Salpeter 1964). The theory of accretion as an efficient and a long-lasting source of energy that can explain the enormous energies of quasars was a vital model, which was studied and improved over upcoming years (Lynden-Bell 1969; Lynden-Bell & Rees 1971; Shakura & Sunyaev 1973).

In the same year as the First Texas Symposium took place, Roy Kerr was successful in finding the axially symmetric solution to EFE, which fully incorporates rotating uncharged bodies, including compact objects (Kerr 1963). Soon afterwards, the generalization to charged rotating bodies was found by Ezra Ted Newman (Newman et al. 1965). The overview of all black hole solutions is summarized in Table 1.1.

	Non-rotating ($J = 0$)	Rotating ($J \neq 0$)
Uncharged ($Q = 0$)	Schwarzschild (1916)	Kerr (1963)
Charged ($Q \neq 0$)	Reissner-Nordström (1916,1918)	Kerr-Newman (1965)

Table 1.1: Summary of all black hole solutions with the corresponding years of discovery.

Finally, the discovery of the first pulsar on August 6, 1967 by Jocelyn Bell (Hewish et al. 1968) was another significant milestone. The periodicity of 1.33730 seconds could have only been explained by a very compact, spinning neutron star, which also made the existence of black holes more convincing for the astronomical community.

Below we briefly summarize the introduction of two wide-spread words in the black hole astrophysics – *event horizon* and *black hole* – which were both introduced during the era of the revival of gravitational physics ($\sim 1960 - 1975$).

Origin of the *event horizon* terminology. The term *event horizon* was first used by Wolfgang Rindler, who was affiliated with the Cornell University at that time and graduated from the University of London. He used it in the cosmological context in 1956 to divide “events” in an expanding universe that can be still detected by us and those that are outside the visible Universe (Rindler 1956). In the 1960s, relativist physicists started to use the term for a completely collapsed objects – black holes – that cut themselves from the Universe in a similar sense, i.e. objects falling through the event horizon cannot be detected anymore (Bartusiak 2015).

First appearance of the *black hole*. The term *black hole* was first published on January 18, 1964 in the Science News Letter titled “Black Holes in Space” by Ann Ewing (Ewing 1964), who reported on the astrophysical session on degenerate stars at the annual conference of the American Association for the Advancement of Science (AAAS). The term was probably borrowed from Robert Dicke by Hong-Yee Chiu, the chair of the session, who suggested that the Universe was “peppered” with black holes (Bartusiak 2015). John A. Wheeler used the term again at the annual meeting of AAAS three years afterwards (1967) and after the publication of his keynote lecture in 1968 the term became popular.

1.1.3 Brief history of the observations of the Galactic centre

Historically, the Galactic centre was associated with different objects on the sky. Before the Copernican revolution the centre of the Universe was associated with the Earth. After the fall of the geocentric system the centre switched to the Sun. At the beginning of the 17th century, Galileo Galilei was able to resolve individual stars of the Milky Way. Based on these observations Thomas Wright proposed a model of the Milky Way in mid-18th century, in which observed stars form a disc that is gravitationally bound together. Towards the end of the 18th century, William Herschel (1792-1871) made a map of the Milky Way, depicting its shape based on the stellar counts in different directions. He was the first to notice that globular clusters are accumulated more towards the constellation of Sagittarius. This fact did not change even at the beginning of 20th century in 1922 when Jacobus Kapteyn presented the model of a lens-shaped island universe with the diameter of ~ 15 kpc in which the density decreased from its centre. The Sun was located relatively close to the centre. The model of the Galaxy, also known as the *Kapteyn Universe*, worked at higher galactic latitudes, but failed close to the Galactic plane, mainly because of the unknown absorption. Later Robert J. Trumpler showed that the interstellar reddening is much larger than previously estimated, which enlarged the island universe to 100 000 light years, with the Sun approximately at the distance of as much as 30 000 light years from the Galactic centre (Trumpler 1930). The current model of the Milky Way started to emerge at that time. In addition, the Great Debate between Harlow Shapley and Heber Curtis, which was held on April 26, 1920 at the Smithsonian Museum of Natural History in Washington D.C., contributed to the understanding that the Milky Way is one of billions of other similar galaxies (Shapley & Curtis 1921), which was the claim of Curtis in the debate, later confirmed by the discovery of the redshift of galaxies and the expansion of the Universe by Edwin Hubble (Hubble 1929). On the other hand, Harlow Shapley had a more precise model of the Galaxy, with the Sun at its outskirts. He estimated correctly that the higher concentration of globular clusters points towards the Galactic centre. Subsequently, he used the period-luminosity relations for variable stars to set the distance of ~ 13 kpc for the Sun from the Galactic centre (Shapley 1918). The reason for Shapley's overestimation of the distance of the Galactic centre was that he had mistaken RR Lyrae variables for Cepheids as *standard candles*. Over the years, the period-luminosity calibration of standard candles improved and the recent estimate based on Mira variables in clusters gives 7.9 ± 0.3 kpc (McNamara et al. 2000), which yields the angular-linear scale conversion, $1 \text{ arcsec} \approx 0.04 \text{ pc}$. The schematic image of the position of the Sun with respect to the Galactic centre and the spiral arms is in Fig. 1.1.

Other methods of the distance determination to the Galactic centre were developed and they may be summarized in the following way (for more details, see Genzel et al. 2010; Zajacek 2014):

- **direct:** 3D stellar orbits, trigonometric orbital parallax, statistical parallax,
- **indirect:** globular clusters, RR Lyrae stars, Cepheids, Mira variables, red giants, stellar populations in HR diagram,
- **model-based:** cluster parallax distance, Jeans modelling.

The observations of the Galactic centre may be divided into four main electromagnetic domains – radio, infrared, X-ray, and gamma wavelengths. Optical and ultraviolet observations

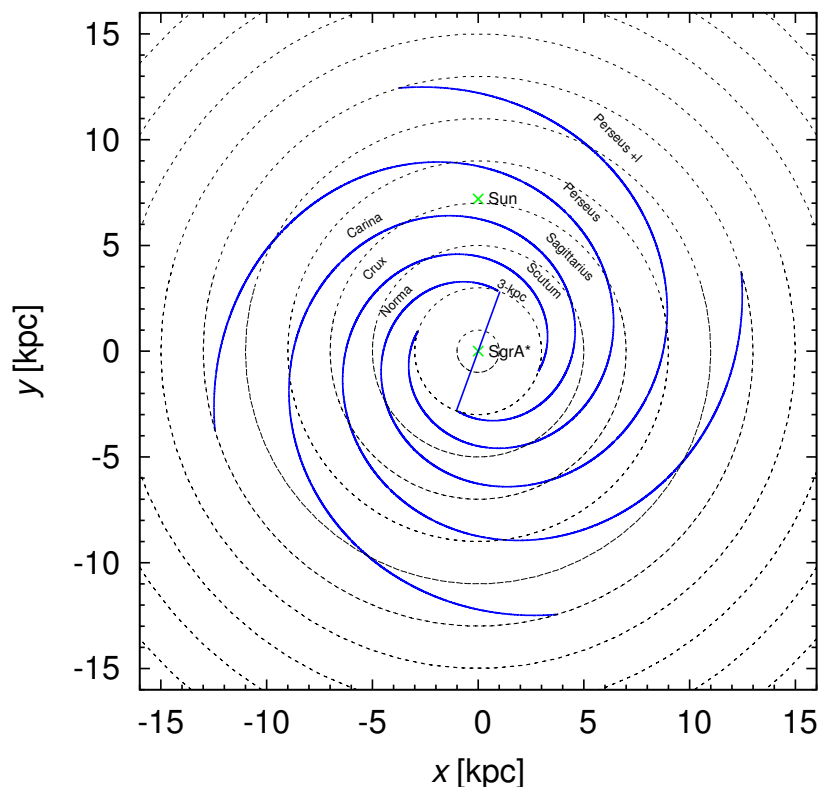


Figure 1.1: The Milky Way galaxy as viewed from the Galactic North Pole. The model is created using the logarithmic curve model with the pitch angle of 12° inwards and four spiral arms. The Galactic Bar is inclined by 20° with respect to the Sun-Centre line. The concentric circles start at 1 kpc with an increment of 2 kpc. The model was adopted from Vallée (2005).

are largely limited by the large gas and dust extinction, which amounts to the extinction coefficient of $A_V \sim 30^m$.

Overview of observations. The first detection of the Galactic centre at radio wavelengths was achieved by Karl Jansky in 1932 with the resolution of $24^\circ \times 35^\circ$ and at the frequency 20.5 MHz. Grote Reber continued in this effort between 1938 and 1948 and built his own radiotelescope and receivers. He detected the emission from the plane of the Milky Way at 1.9 m (160 MHz). In 1951 Jack H. Piddington and Harry C. Minnett detected a strong source of radio emission towards the Galactic centre at 1.2 and 3 GHz (Piddington & Minnett 1951). They also constrained the spectrum, which appeared to be flat between 100 and 1210 MHz similar to Taurus A. They speculated that optically thin thermal gas could be responsible for the observed emission. The strong source of radio emission became known as Sagittarius A. More than 10 years later Barry Clark and Dave Hogg used the Green Bank two-element interferometer in West Virginia to investigate the small-scale structure of radio-emission sources with $10''$ angular resolution. They were able to detect a compact structure in Sgr A with the flux density of 0.3 Jy at 11 cm (~ 2.8 GHz). The source was, however, strongly contaminated and confused with the thermal emission of Sgr A West (Clark & Hogg 1966). In 1971 Donald Lynden-Bell and Martin Rees made a prescient prediction that the Galactic centre could harbour a supermassive black hole and proposed Very Long Baseline Interferometry

(VLBI) to pinpoint its flux density and the position (Lynden-Bell & Rees 1971). The compact radio source Sgr A* was discovered on February 13 and 15, 1974 by Bruce Balick and Robert Brown (Balick & Brown 1974), who reported that its brightness temperature was in excess of 10^7 K and it was unresolved at $\sim 0.1''$. Resolving such a point-like object among an extended radio emission in the central $20''$ was possible thanks to the newly commissioned 35-km baseline interferometer Green Bank – Huntersville of the National Radio Astronomy Observatory (NRAO), which consisted of three 26-meter telescopes that were separated by $\lesssim 2.7$ kilometer baselines and the new 14-meter telescope installed on a mountaintop in Huntersville, which was separated ~ 35 kilometres from Green Bank.

The compactness, the large brightness temperature and the positional association of Sgr A* with the Galactic centre was in agreement with the black-hole hypothesis of Lynden-Bell and Rees. The basic properties were confirmed by Very Long Baseline Interferometry (VLBI) observations of the Galactic centre by Lo et al. (1975), who were able to resolve out the source up to $0.02''$ at 3.7 cm using a 242-km baseline. They also found an indication for the variability of the source.

The attempts to detect the Galactic centre in the NIR domains started as early as 1945, but due to the combination of the lack of sensitivity and a coarse sampling these observations were not successful (Stebbins & Whitford 1947; Moroz 1961). The first successful observations of the Galactic centre in the infrared were achieved by Eric Becklin and Gerry Neugebauer at the wavelength of $2.2 \mu\text{m}$ (Becklin & Neugebauer 1968). They performed single-pixel scans with $0.25'$ and $0.08'$ apertures that correspond to a linear scale of 0.62 pc and 0.2 pc, respectively. They were successful in resolving the compact Nuclear Star Cluster, which was further resolved out into individual complexes with higher-resolution single-detector scans. Later maps of NeII fine-structure lines were obtained at $12.8 \mu\text{m}$ (Wollman et al. 1976, 1977; Lacy et al. 1979, 1980) that revealed that the ionized gas moves supersonically and is highly-ordered in a sense that preferentially redshifted motions could be separated clearly from blueshifted ones. Using the Very Large Array (VLA), it was possible to make a radio map at 5 GHz with the similar angular resolution to that of infrared images (Brown et al. 1981). By comparing the radio maps with the infrared ones, it was possible to place the unresolved radio emitter in the thermal region of Sgr A West at the centre of the dynamical motion of thermal streamers. In the paper by Brown (1982), they introduce the notation Sgr A* for the first time to denote the radio point source that is distinct from the extended radio emission previously denoted as Sgr A. The analysis of the $^3P_1 - ^3P_2$ fine-structure line-emission of neutral oxygen at $63 \mu\text{m}$ in combination with the NeII line-emission revealed that the emitting gas is in rotation around a concentrated dynamical mass of $\sim 3 \times 10^6 M_\odot$ (Lacy et al. 1982; Townes et al. 1983; Genzel et al. 1984). The dual-frequency observations during 25 epochs over three years revealed flux density fluctuations of the centimeter emission of Sgr A* (Brown & Lo 1982). The light curve of the source varied by $\sim 20 - 40\%$ from short timescales (days) up to years. The variability of Sgr A* was soon connected to a down-scaled quasar activity and the source became one of prime candidates for a supermassive black hole. However, more significant indications for a relativistic compact object came with the detection of Keplerian stellar motions in NIR (Eckart & Genzel 1996, 1997; Ghez et al. 1998; Schödel et al. 2002; Gillessen et al. 2009a, 2017; Parsa et al. 2017) and the combined X-ray–NIR–submm–mm–radio light curves (Eckart et al. 2004a; Meyer et al. 2006b,a, 2007, 2009; Dovčiak et al. 2008; Zamaninasab et al. 2008; Eckart et al. 2008a,b, 2009; Zamaninasab et al. 2010; Kunneriath et al. 2010; Sabha et al. 2010; Witzel et al. 2012; Borkar et al. 2016).

1.2 The Galactic centre environment – potential for star formation

It has been shown that the Galactic centre, the closest galactic nucleus, hosts populations of both old and young stars (Genzel et al. 2010; Eckart et al. 2005; Schödel et al. 2014). The compact radio source Sgr A* at the very centre of the Galaxy associated with the supermassive black hole (hereafter SMBH) of $\sim 4 \times 10^6 M_{\odot}$, whose mass was constrained based on stellar proper motions and the orbital analysis of the motion of stars in its vicinity (Eckart & Genzel 1996, 1997; Ghez et al. 2003; Gillessen et al. 2009a), is embedded in this dense stellar cluster. In fact, nuclear star clusters are the densest stellar systems in the Universe, with the surface stellar densities of the order of $\sim 10^5 M_{\odot} \text{pc}^{-2}$ up to $\sim 10^7 M_{\odot} \text{pc}^{-2}$ (Schödel et al. 2014). Hence the nuclear cluster of the Milky Way (hereafter NSC or MWNSC) offers a unique possibility to study dynamical processes and test hypotheses in the very dense stellar environment around the SMBH (Schödel et al. 2014). The near-infrared observations revealed a large number of young, massive stars as close as $\sim 0.1 \text{pc}$ to the SMBH (Bartko et al. 2010). According to the decomposition of the populations of late-type and early-type stars by Buchholz et al. (2009), the early-type stars are found to be concentrated towards the SMBH, forming an unrelaxed cusp-like cluster. On the other hand, the density of late-type stars is not increasing towards Sgr A*. It seems that late-type stars have a rather core-like or hole-like distribution towards the centre, or at least a flat cusp (Do et al. 2009; Genzel et al. 2010). We illustrate the basic composition of the Nuclear Star Cluster in Fig. 1.2, where we also depict the denser streamers and clumps forming the three Minispiral streamers (Kunneriath et al. 2010; Moser et al. 2017).

The Minispiral by itself is a region of denser warm gas and dust, mostly ionized by UV emission of bright OB stars. Further away, the hydrogen atoms recombine and form mostly neutral and molecular Circum-Nuclear Disc (CND). Stars can effectively interact with the denser gas in the Minispiral and those with stronger winds and mass-loss rates form distinct bow-shock structures that are especially visible at longer NIR wavelengths and in MIR bands (Tanner et al. 2005; Mužić et al. 2010; Rauch et al. 2013; Sanchez-Bermudez et al. 2014; Zajaček et al. 2016). The bow-shock sources, which are also illustrated in Fig. 1.2, can be used as test probes to constrain either the density of the ambient medium or the stellar parameters, mainly a mass-loss rate or a stellar-wind velocity.

The presence of a large population of young stars and hence their efficient *in-situ* star formation, especially of low-mass stars, has been difficult to explain in this environment, since tidal forces are expected to be strong close to the Galactic centre due to the presence of the massive black hole and the dense stellar field around it (Morris 1993; Krabbe et al. 1995; Ghez et al. 2003; Levin & Beloborodov 2003). The main problem of *in situ* star formation in previous theories was the tidal disruption of infalling self-gravitating clouds, making their collapse into stellar cores difficult. However, Milosavljević & Loeb (2004) showed that the black-hole-assisted accumulation of molecular gas can make clouds temporarily self-gravitating and prone to fragmentation that leads to pre-stellar cores.

Recently, numerical Smooth Particle Hydrodynamics (SPH) simulations have confirmed that the tidal field may indeed catalyse the formation of stars very close to the SMBH (Jalali et al. 2014) due to the compression of infalling molecular gas. Thus the rapid dynamical friction bringing massive young stellar clusters (Gerhard 2001; Kim & Morris 2003; Portegies Zwart et al. 2003) close to the Galactic centre is not needed to explain the abundance of young

Nuclear Star Cluster around Sgr A* (inner 10 pc)

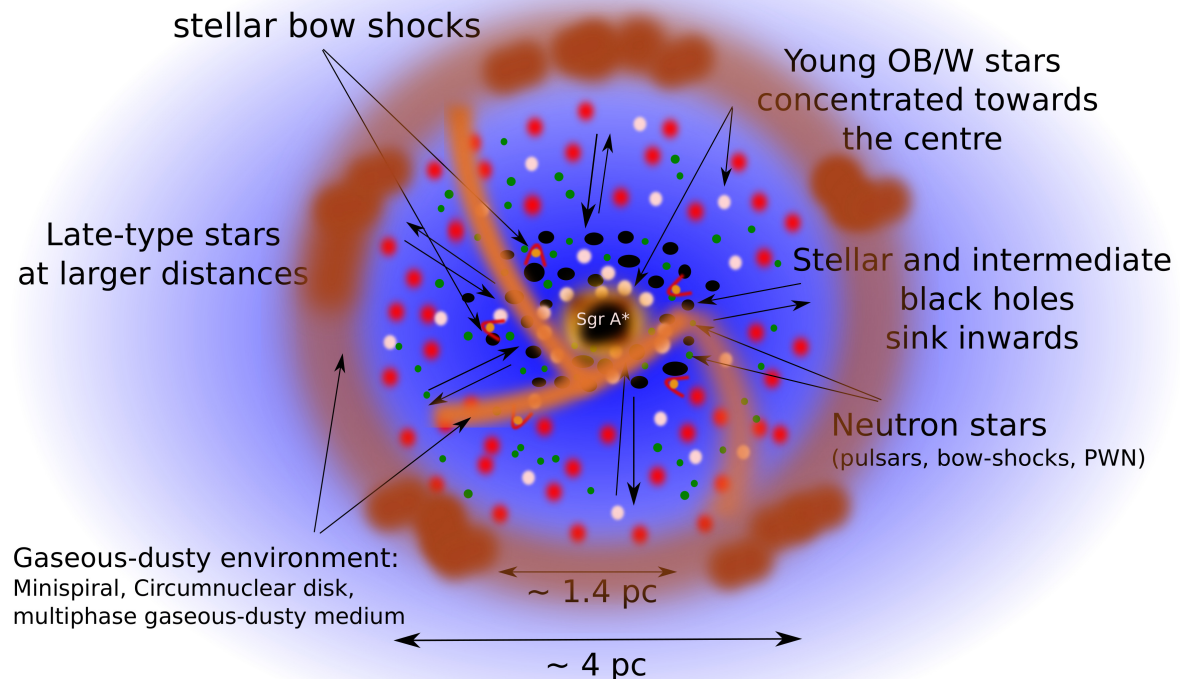


Figure 1.2: Illustration of the composition of the Nuclear Star Cluster, including late-type stars, early-type stars, compact remnants which can interact with the gaseous-dusty medium that forms denser filaments known as the Minispiral. When a star moves supersonically with respect to the denser streamers and clumps, the interaction can be detected in the form of bow shocks. The process of mass segregation in the cluster is depicted by arrows.

stars in the sphere of influence of the SMBH, whose radius $r_{\text{SI}} \approx 2$ pc for MWNSC can be estimated simply from (Merritt 2013)

$$r_{\text{SI}} \approx 1.7 \left(\frac{M_{\bullet}}{4.0 \times 10^6 M_{\odot}} \right) \left(\frac{\sigma}{100 \text{ km s}^{-1}} \right)^{-2}, \quad (1.5)$$

where M_{\bullet} is the central black hole mass and σ is the stellar velocity dispersion.

It seems, however, plausible that both processes – the infall of gas clouds that yield stars *in-situ* and mass segregation of stellar clusters – contributed to the overall structure of the MWNSC (Neumayer et al. 2011; Hartmann et al. 2011) since the MWNSC is located deep in the potential well of the Galaxy with gas clouds and stellar clusters easily descending to its bottom (Schödel et al. 2014). Imprints of these events could be detected through rotational and anisotropic patterns in stellar kinematics (Schödel et al. 2014), since two-body relaxation time-scale is of the order of Gyrs throughout the MWNSC (Merritt 2013).

Several objects in the Galactic centre region are detected as infrared-excess sources (Eckart et al. 2004b; Viehmann et al. 2006; Fritz et al. 2010; Meyer et al. 2014), for instance in the Northern arm of the Minispiral or in the IRS 13N and IRS 13E associations within the projected distance of 0.12 pc ($3''$). The spectral properties of these objects can be explained by the presence of a circumstellar envelope of gas and dust, possibly forming an accretion

disc closer to the stellar surface (Valencia-S. et al. 2015), in which case they are young, pre-main-sequence objects ($\lesssim 10^5$ yr). Recently the most monitored of them is Dusty S-cluster object named G2 (DSO/G2), whose nature is not firmly established yet, but stays compact up to now, which hints at a stellar nature rather than a core-less cloudy character. Some of the infrared excess sources could also be stellar systems with debris asteroid and planetesimal discs and rings whose tidal perturbations might trigger some of the flare activity of Sgr A* (Zubovas et al. 2012).

The abundance of stars with disc structures (gaseous accretion discs of pre-main-sequence stars, planetesimal discs, debris discs) close to the SMBH is given by the *in situ* star-formation rate near the Galactic centre. If the dominant mechanism of bringing stars close to the Galactic centre were the infall of stellar clusters, the likelihood of disc structures around stars would be quite low since the discs would be either accreted or destroyed in their mother clusters after the initial $\sim 10^5$ – 10^6 years (see Olczak et al. 2006, for the study of disc destruction in the Orion Nebula cluster).

The *in situ* star formation becomes only possible when clouds or their parts moving in the potential of the SMBH and that of the NSC with the total mass $M(r)$ meet the Roche criterion for self-gravitation. An infalling cloud does not disintegrate if its self-gravitation field exceeds the tidal field of the SMBH and that of the centrifugal force while moving with quasi-Keplerian angular velocity $\Omega_K^2 \simeq (GM(r))/r^3$ around the Galactic centre, where r is the distance from the SMBH and $M(r)$ is the mass content inside the radius r . We assume that the mass content can be approximated by the sum of the mass of the SMBH and that of the integrated density profile of the NSC, $M(r) = M_\bullet + M_{\text{NSC}}$. We take $M_\bullet = 4 \times 10^6 M_\odot$ and the mass of the NSC is given by

$$M_{\text{NSC}} = 4\pi \int_0^r \rho_{\text{NSC}}(r') r'^2 dr', \quad (1.6)$$

where the radial density profile can be approximated as

$$\rho_{\text{NSC}} = \rho_0 \left(\frac{r}{r_b} \right)^{-\gamma} \left[1 + \left(\frac{r}{r_b} \right)^\delta \right]^{\frac{(\gamma-\gamma_0)}{\delta}} \quad (1.7)$$

where we set $\rho_0 = 5.2 \times 10^5 M_\odot \text{pc}^{-3}$, $r_b = 0.5$ pc, $\gamma = 0.5$, $\gamma_0 = 1.8d$, $\delta = 2$ in accordance with Schödel et al. (2009a).

Hence, the estimate for the condition for the density ρ_{cl} of a self-gravitating cloud moving in the potential of SMBH is:

$$\rho_{\text{cl}} \gtrsim \frac{9M(r)}{4\pi r^3} = 1.94 \times 10^{-13} \left(\frac{M(r)}{4 \times 10^6 M_\odot} \right) \left(\frac{r}{0.1 \text{ pc}} \right)^{-3} \text{ g cm}^{-3}, \quad (1.8)$$

which yields number densities of $n_{\text{H}} \gtrsim 10^{11} [M(r)/(4 \times 10^6 M_\odot)] [r/(0.1 \text{ pc})]^{-3} \text{ cm}^{-3}$. Taking into account the distribution of the NSC, one gets the decreasing profile of the critical density with the distance.

Such high densities can be reached through shocks and compression of infalling clouds that pass near the SMBH. The tidal focusing of material by the SMBH and subsequent compression may result in volume decrease at the pericentre by at least a factor of 2 for highly-eccentric orbits (Jalali et al. 2014),

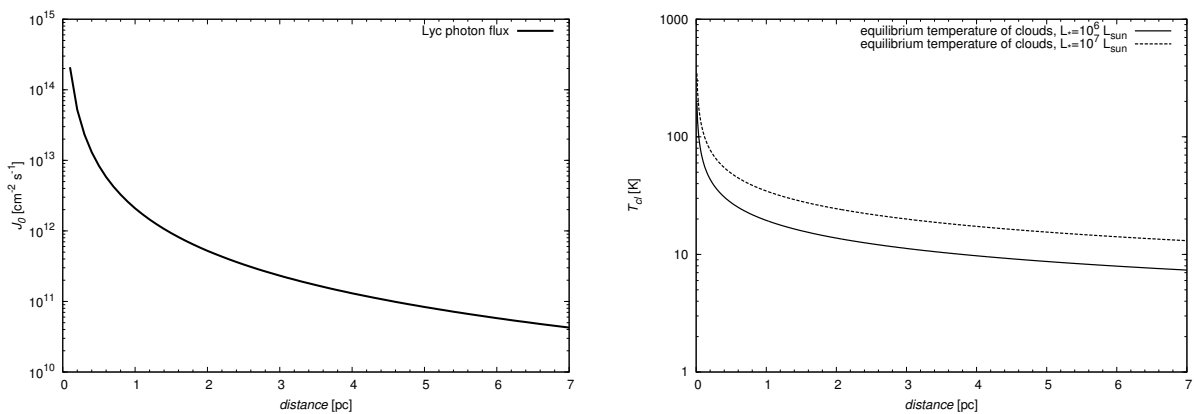


Figure 1.3: Left: Radial profile of Lyman continuum photon flux inferred from the inferred luminosity of the central ionizing source in the innermost parsec. Right: Equilibrium temperature of infalling clumps assuming the Lyman continuum production rate.

$$\frac{V_{\text{per}}}{V} \lesssim \frac{1}{1+e} \leq \frac{1}{2}, \quad (1.9)$$

which can help in overcoming the critical density limit given by Eq. 1.8.

Similarly, the pressure of stellar winds as well as that of the strong UV radiation field of the stars in the NSC could significantly contribute to the compression of gas clouds (Yusef-Zadeh et al. 2013).

The infalling clumps consisting of molecular and atomic hydrogen move through the HII region Sgr A West. Their typical radius r_{cl} is approximately given by the equilibrium condition between ionization and recombination (Dyson 1968; Vollmer & Duschl 2001a,b),

$$r_{\text{cl}} \approx \xi^2 J_0 n_i^{-2}, \quad (1.10)$$

where J_0 is the Lyman continuum photon flux in $\text{cm}^{-2}\text{s}^{-1}$, which originates mainly from the population of young, massive stars in the innermost parsec, n_i is the number density of the ionized medium in the ionization front, and $\xi \approx 4.87 \times 10^6 \text{ cm}^{-3/2}\text{s}^{1/2}$.

We assume the radial profile of Lyman continuum photon flux in the simple form $J_0 = N_{\text{LyC}}/(4\pi r^2)$, where $N_{\text{LyC}} \approx 10^{50}\text{s}^{-1}$ is the Lyman continuum production rate (Serabyn & Lacy 1985), see Fig. 1.3 (left). The equilibrium temperature T_{cl} of clumps may be estimated from $T_{\text{cl}} \approx (F_{\text{LyC}}(r)/(4\sigma))^{1/4}$, which for the flux profile $F_{\text{LyC}} \approx (L_{\text{LyC}}/4\pi)r^{-2}$ scales as $T_{\text{cl}} \propto r^{-1/2}$ from the Galactic centre, see Fig. 1.3(right) for two plausible luminosity values $L_{\text{LyC}} \approx 10^6 L_{\odot}$ (smooth dust distribution) and $L_{\text{LyC}} \approx 10^7 L_{\odot}$ (clumpy dust distribution) (Davidson et al. 1992).

1.2.1 Jeans instability criterion in the Galactic centre

The classical Jeans instability criterion is derived for infinite homogeneous medium from linearised equations of continuity, motion, and gravitational perturbation. The dispersion relation $\omega^2 = k^2 c_s^2 - 4\pi G \rho_0$ indicates the growth of instability for $\omega^2 < 0$, which gives the simple relation for the minimal length-scale over which instability develops,

$$\lambda_{\text{instab}} \geq \left(\frac{\pi c_s^2}{G \rho_0} \right)^{1/2}, \quad (1.11)$$

where c_s is the local sound speed and ρ_0 is the unperturbed density. By considering $r_{\text{cl}} \approx \frac{1}{2}\lambda_{\text{instab}}$ for the clump radius, we easily get the relation for the critical density of the medium under the assumption of the equation of state for an ideal isothermal cloud with temperature T_{cl} :

$$\rho_{\text{cl}} \gtrsim \frac{\pi k_{\text{B}} T_{\text{cl}}}{4G\mu m_{\text{u}} r_{\text{cl}}^2}, \quad (1.12)$$

where T_{cl} is given by the simple scaling $T_{\text{cl}} \propto r^{-1/2}$ at radiation equilibrium. The clump radius r_{cl} can be estimated from Eq. 1.10, which determines the distance from the clump core to the ionization front. [Vollmer & Duschl \(2001b\)](#) derived the clump radius as a function of sound speed of the neutral gas c_s , the sound speed of the ionization front c_i , and of the Lyman continuum photon flux J_0 ,

$$r_{\text{cl}} \approx \chi c_s^{8/3} c_i^{-4/3} J_0^{-1/3} \quad (1.13)$$

where $\chi = (9/64(\xi m_{\text{p}} \pi G)^{-2})^{1/3} \approx 3.64 \times 10^{15} \text{ cm}^{-1} \text{ s}$. Expressing the sound speed of neutral gas in the form,

$$c_s = \left(\frac{k_{\text{B}}}{\mu m_{\text{u}}} \right)^{1/2} \left(\frac{J_0 E_{\text{ion}}}{4\sigma} \right)^{1/8} \quad (1.14)$$

where E_{ion} is the ionization energy of hydrogen, $E_{\text{ion}} \approx 13.6 \text{ eV} \approx 2.179 \times 10^{-11} \text{ erg}$, the clump radius finally becomes,

$$r_{\text{cl}} \approx 8.72 \times 10^{15} \left(\frac{c_i}{7.6 \times 10^5 \text{ cm s}^{-1}} \right)^{-4/3} \text{ cm}, \quad (1.15)$$

where the sound in the ionization front corresponds to the electron temperature of 7000 K of the sparse ionized medium ([Roberts & Goss 1993](#)) typical of other HII regions. The typical length-scale of infalling compact clumps is thus $10^{16} \text{ cm} \approx 10^{-2} \text{ pc}$, i.e. the clumps can be of a stellar size and stay approximately constant unless the sound speed in the ionized medium changes or external factors become significant (radiation and wind pressure, tidal effects).

A similar order of magnitude for the clump length-scale one gets from the stability analysis. The warm molecular discs are typically susceptible to instability, since the Toomre criterion ([Toomre 1964](#)), $Q = c_s \Omega / (\pi G \Sigma)$, is typically less than 1 ([Milosavljević & Loeb 2004](#)). Assuming the quasi-Keplerian rotation around the SMBH, $\Omega = (GM_{\bullet}/r^3)^{1/2}$ and an isothermal ideal gas of $\sim 100 \text{ K}$, we get a condition for the surface density Σ_{Toomre} for which the disc undergoes instability:

$$\Sigma_{\text{Toomre}} > 1.84 \left(\frac{T}{100 \text{ K}} \right)^{1/2} \left(\frac{M_{\bullet}}{4 \times 10^6 M_{\odot}} \right)^{1/2} \left(\frac{r}{1 \text{ pc}} \right)^{-3/2} \text{ g cm}^{-2}. \quad (1.16)$$

For the typical parameters of the CND, the number density $n_{\text{CND}} \approx 10^7 \text{ cm}^{-3}$ and a height-scale of $h \approx 1 \text{ pc}$, the surface density is $\Sigma_{\text{CND}} \approx n_{\text{CND}} m_{\text{H}} h \approx 50 \text{ g cm}^{-2} > \Sigma_{\text{Toomre}}$. Hence assuming that the Circum-nuclear disc was originally a smooth structure, it fragmented into clumps whose size is given by the Jeans length-scale, Eq. 1.11, $\lambda_{\text{cl}} \approx 0.05 \text{ pc}$.

By combining the Jeans instability criterion given by Eq. 1.12 with the criterion for tidal stability, Eq 1.8, we get the radius range where instability is expected to occur and clouds can collapse to form stars, see Fig. 1.4. The region of stability where clumps are gravitationally

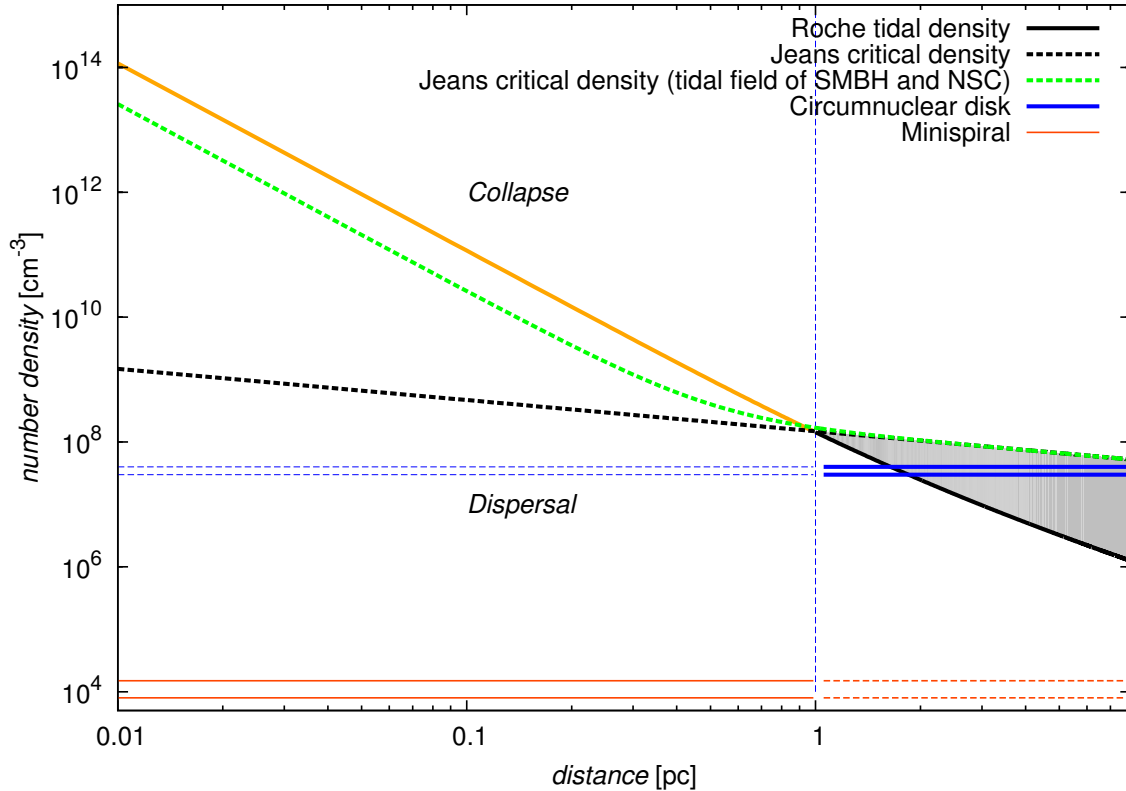


Figure 1.4: The Roche critical density (solid), eq. 1.8, above which clouds are gravitationally supported against tidal disruption. The density corresponding to the Jeans instability criterion (dashed), eq. 1.12, above which clumps are expected to collapse and form stars. The region where clumps falling towards the Galactic centre are expected to be stable is shaded. The parameter region where collapse and dispersal of clumps close to the Galactic centre are expected are also labelled. The horizontal lines mark the lower and upper density limits of Circumnuclear disc (blue lines, $(3-4)\times 10^7 \text{ cm}^{-3}$, [Christopher et al., 2005](#)) and the Minispiral (red lines, $(0.8-1.5)\times 10^4 \text{ cm}^{-3}$, [Kunneriath et al., 2012](#)).

supported against tidal disruption and do not collapse is shaded. In general, the clumps are prone to instability below ~ 1 pc from the Galactic centre which is consistent with the observations of the ‘central cavity’ region, which is sparse and ionized in comparison with the CND region. Two modes are possible in the innermost parsec: for densities larger than the Roche critical density, Eq. 1.8, the clumps are expected to collapse and are likely to form stars. Below this density limit clouds are prone to be dispersed by the tidal field.

However, the original derivation of the Jeans instability neglects the potential gradient of external tidal field, as is the general case of the environment in galactic nuclei. Specifically, the derivation of the Jeans minimal length-scale over which instability develops, Eq. 1.11, considers the unperturbed potential to be constant in space, $\nabla\Phi_0 = 0$ (so-called Jeans “swindle”).

The derivation of the dispersion relation for the external tidal field was provided by [Jog \(2013\)](#). The dispersion relation changes due to the external potential Φ_{ext} to the form $\omega^2 = k^2 c_s^2 - 4\pi G\rho_0 + T_0$ where the tidal term is given by $T_0 = -\nabla^2\Phi_{\text{ext}}$. The external potential in the Galactic centre may be considered to be the sum of the SMBH approximated as a point

mass and the potential of the NSC $\Phi_{\text{ext}} = -GM_{\bullet}/r + \Phi_{\text{NSC}}$. The tidal term then becomes $T_0 = 2GM_{\bullet}/r^3 - 4\pi G\rho_{\text{NSC}}(r)$, where the mass density of the NSC is taken from Eq. 1.7. Depending on the distribution of matter in the NSC, the tidal term can be both positive and negative, which causes the Jeans length-scale to prolong or shorten, respectively. The relation derived from the modified dispersion relation is as follows,

$$\lambda'_{\text{instab}} \geq \frac{\lambda_{\text{instab}}}{\sqrt{1 - \frac{T_0}{4\pi G\rho_0}}}. \quad (1.17)$$

For a given cloud radius r_{cl} , $\lambda'_{\text{instab}} \approx 2r_{\text{cl}}$. The critical Jeans density of a clump changes by the tidal field correspondingly,

$$\rho'_{\text{cl}} \geq \frac{1}{4\pi G} \left(\frac{\pi^2 c^2}{r_{\text{cl}}^2} + T_0 \right). \quad (1.18)$$

The qualitative change can be seen in Fig. 1.4, where the tidal field of the SMBH and the NSC causes the critical Jeans density to increase, especially in the innermost 1 pc (green line). Further away it comes back to the original critical density profile. It seems that the tidal forces of the SMBH and the NSC make it more difficult to form stars unless there are factors that compress the clump.

1.2.2 Estimate of the number of dust-enshrouded stars near the Galactic centre

The probability of detecting a pre-main sequence star surrounded by a primordial disc (gaseous or debris disc) in the Galactic centre ($r \lesssim 2$ pc) may be approximately determined from the estimate of the star-formation rate in this environment and consequently by using the corresponding time-scales related to disc dynamics.

The dense clumps necessary for star-formation to proceed are assumed to originate in the neutral and molecular circum-nuclear disc (CND), which consists of denser clumps (e.g. [Christopher et al. 2005](#), and references therein) that can collide inelastically and consequently lose angular momentum and descend towards the SMBH ([Vollmer & Duschl 2001a,b](#); [Jalali et al. 2014](#)). The CND has a sharp inner edge at ~ 2 pc, which coincides with the radius of the sphere of influence of the SMBH, see eq. 1.5.

The rate of clump collisions is approximately given by $\Gamma_{\text{col}} \approx n_{\text{cl}}\Sigma_{\text{col}}\sigma_{\text{vel}}$, where n_{cl} is the number volume density of dense clumps, Σ_{col} is the clump-clump collisional cross-section, and σ_{vel} is the velocity dispersion of clumps in CND. Using the volume filling factor Φ_{V} and the radius of the cloud r_{cl} one can express the number density as $n_{\text{cl}} = \Phi_{\text{V}}/(4/3\pi r_{\text{cl}}^3)$. The effective cross-section of clump-clump collisions is approximately given by $\Sigma_{\text{col}} \approx 2\pi r_{\text{cl}}^2$. Hence we get a simple relation for the estimate of the rate of collisions $\Gamma_{\text{col}} \approx 3\phi_{\text{V}}\sigma_{\text{vel}}/(2r_{\text{cl}})$. According to [Christopher et al. \(2005\)](#) the mean radius of clumps is $r_{\text{cl}} \approx 0.1$ pc, the velocity dispersion of clouds $\sigma_{\text{vel}} \approx 20$ km s $^{-1}$, and the volume filling factor is $\Phi_{\text{V}} \approx 0.01$ ([Jackson et al. 1993](#)). Inserting these values leads to the collisional rate of

$$\Gamma_{\text{col}} \approx 3 \times 10^{-6} \left(\frac{\Phi_{\text{V}}}{0.01} \right) \left(\frac{\sigma_{\text{vel}}}{20 \text{ km s}^{-1}} \right) \left(\frac{r_{\text{cl}}}{0.1 \text{ pc}} \right)^{-1} \text{ yr}^{-1}. \quad (1.19)$$

To obtain the rate of infalling clouds Γ_{in} the collisional rate has to be divided by two to select two out of four possible directions (along/opposite disc rotation and inwards/outwards the

centre) and multiplied by ~ 0.3 to select the colliding clumps that have the velocity dispersion larger than the average by 1σ (hence those that efficiently remove angular momentum). Thus we get $\Gamma_{\text{in}} \approx 5 \times 10^{-7} \text{ yr}^{-1}$ for the inward flux of clumps and nominal values of parameters.

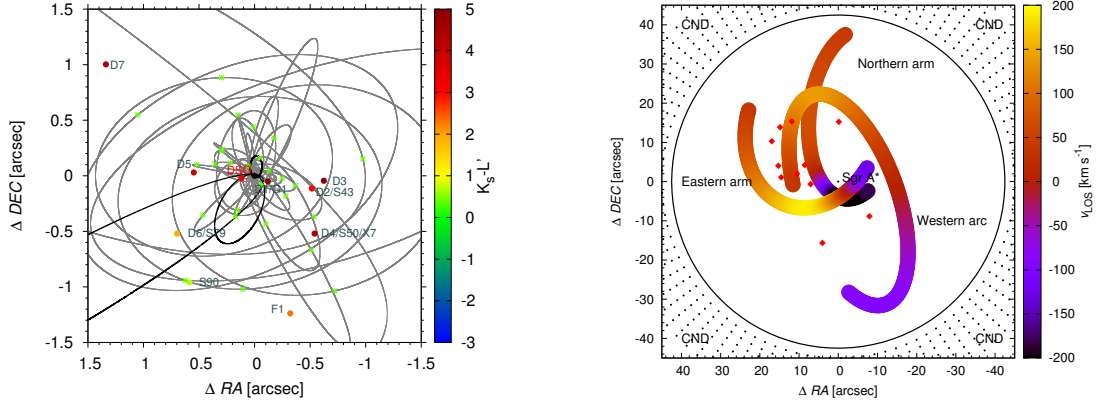


Figure 1.5: Candidates for young stellar sources near the Galactic centre. **Left panel:** Positions of NIR-excess sources and S stars in the innermost $3' \times 3'$, i.e. the close vicinity of Sgr A*. The colours denote the infrared excess $K_s - L'$ adopted from Eckart et al. (2013). The orbits and positions were calculated according to orbital solutions by Gillessen et al. (2009b), Valencia-S. et al. (2015), and Witzel et al. (2017). The thick black ellipses represent the orbits of DSO/G2, G1, and S2. **Right panel:** A schematic image of the Circumnuclear Disc and the Minispiral with the corresponding radial velocities according to Zhao et al. (2009) (see the colour bar). The red points mark the sites of SiO emission possibly associated with the outflows from young stellar objects (according to ALMA observations by Yusef-Zadeh et al. 2013).

Assuming a mass of infalling clouds $M_c \approx 100 M_\odot$ and the star-formation efficiency factor $f_{\text{ef}} \approx 0.3$ (Jalali et al. 2014), the total stellar mass after the star-formation epoch for a single infall is $M_{\text{stars}} \approx 30 M_\odot$. The number of stars that meet the luminosity constraint for DSO ($\lesssim 10L_\odot$) and thus must have a mass in the range of $(m_1, m_2) = (0.1, 2.5) M_\odot$ can be estimated from the Salpeter IMF:

$$N_\star = \frac{2 - \alpha}{1 - \alpha} \frac{m_2^{1-\alpha} - m_1^{1-\alpha}}{m_{\text{max}}^{2-\alpha} - m_{\text{min}}^{2-\alpha}} M_{\text{stars}} \quad (1.20)$$

where we set the index $\alpha = 2.35$ and the minimum and the maximum mass of stars to $(m_{\text{min}}, m_{\text{max}}) = (0.1, 100.0) M_\odot$. We obtain $N_\star \approx 80$ and thus the expected number of embedded young stellar objects may be calculated as $N_{\text{YSO}} = N_\star \Gamma_{\text{in}} \tau_{\text{YSO}} \approx 80 \times (1.5 \times 10^{-6} \text{ yr}^{-1}) \times 10^5 \text{ yr} \approx 10$. The time-scale τ_{YSO} corresponds to the duration of the phase when the star is surrounded by the dusty-gaseous envelope and/or an accretion disc. This order of magnitude is consistent with the detected number of infrared-excess sources (5 sources including DSO/G2 shown in Fig. 2 of Meyer et al., 2014) taking into account that the lightest, least luminous objects are beyond the detection limit. A similar number of NIR-excess sources was also reported in the continuum study by Eckart et al. (2013). Those NIR-excess sources that are located in the innermost S-cluster ($\lesssim 1'' = 0.04 \text{ pc}$) are schematically depicted in Fig. 1.5. In the right panel of Fig. 1.5, we also included the positions for SiO(5-4) emission possibly associated with the outflows of high-mass young stellar objects (see Yusef-Zadeh

et al. 2013). Hence, there are several indications for very recent star-formation activity ($10^5 - 10^6$ yr) in the innermost parsec of the Galactic centre. However, more observations are needed with a larger sensitivity and angular resolution to associate these objects with pre-main-sequence stars.

1.2.3 Formation of neutron stars and pulsar wind nebulae

Many massive stars that formed in situ in the Galactic centre have ended up their life as neutron stars, which are characterized by strong magnetic fields, rapid rotation, and extremely compact sizes. The population of neutron stars in the Galactic centre region is currently unexplored due to a lack of detections. However, it is certainly worth attempting to find the members of such a population since monitoring of neutron stars will help to shed more light on the following astrophysical problems of the vicinity of Sgr A*:

1. constraining the star-formation history, in particular the massive star formation, via the age and the spatial distribution of the detected neutron stars (Wharton et al. 2012), e.g. an over-abundance of magnetars over normal pulsars would imply a top-heavy Initial Mass Function (IMF Dexter & O’Leary 2014),
2. testing the gravitational potential around the supermassive black hole using their period derivatives, with the aim to probe the metric of the central massive black hole (Paczynski & Trimble 1979; Wex & Kopeikin 1999; Pfahl & Loeb 2004; Angéilil et al. 2010),
3. improvement of the knowledge about the magnetohydrodynamical conditions in the Galactic centre (Wharton et al. 2012; Eatough et al. 2013b), especially thanks to the *electron density* along the line of sight $n_e(l)$ as inferred from the distribution of pulsar dispersion measures,

$$DM = \int_0^D n_e dl, \quad (1.21)$$

where D is the distance of the source, and the inference of the line-of-sight *magnetic field* $B(l)$ via the Faraday rotation, i.e. the rotation of the polarization vector of the emission at wavelength λ in an external magnetic field by the angle $\Delta\Phi = RM \lambda^2$, where the rotation measure

$$RM = \frac{e^3}{2\pi m_e^2 c^4} \int_0^D B(l) n_e(l) dl, \quad (1.22)$$

depends on the line-of-sight magnetic field component $B(l)$, free-electron density $n_e(l)$, distance D of the source, and the electron charge e , mass m_e , and the speed of light c .

Previously, the attempts to detect neutron stars via radio timing observations failed to detect a substantial number of neutron stars, except for one magnetar in the innermost parsec (Mori et al. 2013; Rea et al. 2013; Spitler et al. 2014). It is, however, worth considering other wavebands for the search of neutron stars. In particular, infrared observations with a high sensitivity and angular resolution may detect young neutron stars whose spectral properties are expected to be similar to the enigmatic DSO object, as we argued in Zajaček et al. (2017). Here we estimate how many young neutron stars and pulsar wind nebulae (PWN) can be realistically present and detected in the Nuclear Star Cluster.

Following Wharton et al. (2012), the number of neutron stars N_{NS} in the innermost parsec may be estimated from an extended mass of $M_{ext} \approx 10^6 M_\odot$ (Schödel et al. 2009b) using

the initial mass function, $dN/dm \propto m^{-\alpha_{IMF}}$, which after the integration leads to the formula for N_{NS} in the form of Eq. 1.20 with $M_{stars} \equiv M_{ext}$. In Table 1.2, we include estimates of the number of neutron stars for two possible values of the IMF, standard Salpeter-Kroupa $\alpha_{IMF} = 2.35$ and the top-heavy IMF $\alpha_{IMF} = 0.45$. In addition, two different mass ranges (m_1, m_2) are considered for the stars that turn into neutron stars: $(m_1, m_2) = (9, 25) M_{\odot}$ and $(9, 40) M_{\odot}$, see also Wharton et al. (2012) for the discussion. The minimum and the maximum mass of stars are fixed to $(m_{min}, m_{max}) = (0.1, 100) M_{\odot}$.

Neutron star number	M_{ext}	α_{IMF}	(m_1, m_2)
4900	$10^6 M_{\odot}$	2.35	$(9, 25) M_{\odot}$
5700	$10^6 M_{\odot}$	2.35	$(9, 40) M_{\odot}$
5700	$10^6 M_{\odot}$	0.45	$(9, 25) M_{\odot}$
9500	$10^6 M_{\odot}$	0.45	$(9, 40) M_{\odot}$

Table 1.2: An estimated number of neutron stars for a nuclear star cluster with an extended mass of $10^6 M_{\odot}$ in the innermost parsec. Different values of parameters are considered.

It turns out that even different values of the IMF slope do not significantly affect the order of magnitude of the number of neutron stars. Based on the estimates in Table 1.2, we set the number of neutron stars to $N_{NS} = 10^4$ for further calculations. Given the overall extended mass of $10^6 M_{\odot}$, we may estimate the formation of neutron stars per stellar mass as $\beta_{NS} = N_{NS}/M_{ext} \approx 10^4/10^6 M_{\odot}^{-1} = 10^{-2} M_{\odot}^{-1}$.

In the further estimates, we focus on neutron stars that are energetic and radiatively efficient enough to be detected in NIR bands. Given the K_s -band flux density of the DSO, an estimated spin-down energy would be $\dot{E} \approx 1.4 \times 10^{38} \text{ erg s}^{-1}$. In the ATNF pulsar catalogue (Manchester et al. 2005), the number of pulsars with spin-down power exceeding $10^{38} \text{ erg s}^{-1}$ is of the order of unity: there is just one pulsar among 854 pulsars with distances $\leq 3 \text{ kpc}$ and 3 pulsars among all 2573 pulsars. Therefore, the fraction of highly energetic pulsars can be estimated as $f(\geq 10^{38}) \approx 10^{-3}$. It is highly questionable if the distribution of spin-down energies in the Galactic centre neutron star population is comparable to the Galactic plane population. If we extrapolate the statistics to the Galactic centre region, we get $N(\geq 10^{38}) = f(\geq 10^{38})N_{NS} \approx 10^{-3} \times 10^4 = 10$.

Another estimate is based on pulsar wind nebulae as powerful sources of magnetospheric synchrotron emission. The energetic winds also collide with the ambient medium producing termination shocks that contribute to the non-thermal emission. To estimate the number of PWN from the overall population of neutron stars, we use a heuristic relation,

$$N_{PWN} = f_{\tau} f_v f_{PWN} f_{PSR} N_{NS} = f_{\tau} f_v f_{PWN} f_{PSR} \beta_{NS} M_{\star}, \quad (1.23)$$

where f_{PSR} is a fraction of neutron stars that become pulsars (which we assume to be unity, $f_{PSR} \simeq 1$), and f_{PWN} is a fraction of pulsars that power wind nebulae at a certain stage for the time-scale of τ_{PWN} . In addition, Eq. 1.23 contains the retention fraction f_v , the number of neutron stars that are retained within the stellar cluster, and f_{τ} is an actual fraction of pulsars that power a PWN. In the estimate above, we are interested in the non-pulsed, continuum emission, so we do not consider a beaming fraction, which is about 20% (Wharton et al. 2012). Finally, M_{\star} is the mass of the stellar population considered in the calculation.

The fraction of pulsars that power PWN for a certain period τ_{PWN} is assumed to be unity.

It is more complicated to determine the retention fraction f_v of neutron stars in the central parsec. In theory, the natal kick velocities due to binary dissociation or asymmetric supernova explosions, whose mean value is $\langle v_{birth} \rangle = 380 \text{ km s}^{-1}$ (Faucher-Giguère & Kaspi 2006), have to exceed the local escape velocity in the potential of the central black hole (Wharton et al. 2012),

$$v_{esc} \simeq 185 \left(\frac{M_\bullet}{4 \times 10^6 M_\odot} \right)^{1/2} \left(\frac{r}{1 \text{ pc}} \right)^{-1/2} \text{ km s}^{-1}. \quad (1.24)$$

Using the Maxwellian distribution of kick velocities according to Faucher-Giguère & Kaspi (2006), Wharton et al. (2012) compute the retention fractions of $f_v \approx 0.1$ and $f_v \approx 0.25$ for 1 pc and 0.5 pc, respectively. For other possible distributions, they get the retention factors of $0.1 \lesssim f_v \lesssim 0.5$. However, similar distributions typically underestimate the retention factors in globular clusters by an order of magnitude, which can be due to neglecting neutron stars bound in multiple systems. Since the Galactic centre has even higher stellar densities than what is typical in globular clusters, we may set $f_v \approx 1$ following Wharton et al. (2012).

Clearly, to estimate the number of PWN, one needs to consider a typical PWN lifetime: $\tau_{\text{PWN}} \sim 10^5 \text{ yr}$ based on the PWN catalogue (Roberts 2005). The fraction of pulsars that power PWN depends on the star-formation history of the considered population (Wharton et al. 2012). For a continuous star formation, the fraction may be estimated as follows, $f_\tau \sim \tau_{\text{PWN}}/t_{\text{SF}}$, where t_{SF} is the time elapsed since the star formation started.

The estimates for the number of PWN may be derived for different stellar populations observed in the innermost parsec (Buchholz et al. 2009) that can be a result of either a continuous star formation or an episodic starburst. First, we take into account the overall stellar population with the mass of $M_\star \approx 10^6 M_\odot$, for which we consider the star formation to be approximately continuous with the start $t_{\text{SF}} \approx 10^{10} \text{ yr}$ ago. Then the fraction of pulsars powering PWN is $f_\tau \approx 10^5/10^{10} = 10^{-5}$, which leads to

$$N_{\text{PWN}}^{\text{cont1}} = 0.1 \left(\frac{f_\tau}{10^{-5}} \right) \left(\frac{\beta_{\text{NS}}}{10^{-2} M_\odot^{-1}} \right) \left(\frac{M_\star}{10^6 M_\odot} \right). \quad (1.25)$$

Second, a promising source of young pulsars is the population of about 200 young, massive OB stars that were formed in a starbursts episode a few million years ago (Paumard et al. 2006; Bartko et al. 2010). Some of these stars are a part of a coherent kinematic structure, so-called clockwise disc. A total mass of this OB population is of the order of $M_\star = 10^4 M_\odot$ (Paumard et al. 2006; Bartko et al. 2010). Given the life-time of this population, $t_{\text{SF}} \leq 10^7 \text{ yr}$, the fraction of pulsars powering PWN is in the range of $f_\tau \approx 0.01$ – 0.1 . Then, the estimated number of PWN resulting from this episodic star-formation is

$$N_{\text{PWN}}^{\text{ep1}} = 1.0 \left(\frac{f_\tau}{0.01} \right) \left(\frac{\beta_{\text{NS}}}{10^{-2} M_\odot^{-1}} \right) \left(\frac{M_\star}{10^4 M_\odot} \right). \quad (1.26)$$

An insight into the star-formation history of the nuclear star cluster was obtained by comparing simulated stellar populations with the population of cool giant stars observed in the central parsec. Blum et al. (2003) and Pfuhl et al. (2011) consistently found that the bulk of the mass of the NSC ($\geq 80\%$) was formed $\geq 5 \text{ Gyr}$ ago. The star formation rate dropped to the minimum around 1–2 Gyr ago and then started to increase again during the last $\sim 100 \text{ Myr}$. Pfuhl et al. (2011) infer the star-formation rate of $10^{-3} M_\odot \text{ yr}^{-1}$ within 1 pc of Sgr A*, which is consistent with the stellar mass of $10^5 M_\odot$ formed during the last 10^8 yr .

Assuming the continuing star-formation history during this time-scale, the fraction of pulsars associated with PWN is then $f_\tau \approx 10^5/10^8 = 10^{-3}$. By combining the terms, we get the following estimate of the PWN population,

$$N_{\text{PWN}}^{\text{cont}2} = 1.0 \left(\frac{f_\tau}{10^{-3}} \right) \left(\frac{\beta_{\text{NS}}}{10^{-2} M_\odot^{-1}} \right) \left(\frac{M_\star(t < 10^8 \text{ yr})}{10^5 M_\odot} \right). \quad (1.27)$$

Finally, an observational support for the presence of PWN in the Galactic centre was given by [Muno et al. \(2008\)](#) using 1 Ms Chandra X-ray observations (ACIS-I). They identified 34 diffuse X-ray features, out of which ~ 20 in the central 20 pc (in projection) meet the spectral characteristics of PWN. Four of these sources lie within the projected distance of 1 pc of Sgr A*.

In summary, based on the analytical estimates as well as X-ray observations, we would expect ~ 1 – 10 of PWN in the innermost parsec. Hence, it is not unlikely that at least one of the sources previously identified in NIR as excess sources (with a positive slope towards longer wavelengths) is actually a PWN. However, a confirmation of such a nature will require multiwavelength observations (X-ray–IR–radio) primarily with a new generation of instruments (E-ELT, SKA).

1.3 Goals and outline of this thesis

In the previous sections, we discussed the key components of the Galactic centre that interact with each other inside the sphere of the gravitational influence of the supermassive black hole. We paid a special attention to young stars and compact remnants – neutron stars. In my work during the PhD, I focused on these two extreme stellar populations, which belong to unsolved problems of the Nuclear Star Cluster. In particular, the following topics were relevant:

- (a) dynamics of young stars near the compact radio source Sgr A*, in particular those formed *in situ*,
- (b) interactions of stars with the environment, with the focus on dynamics of stellar bow-shocks,
- (c) fate of stellar remnants in the Nuclear Star Cluster, with the focus on magnetized remnants – neutron stars,
- (d) evidence for Sgr A* being a black hole in an astrophysical and philosophical context.

For Topic (a), we focused on the dynamics of envelopes of dust-enshrouded, young stars that approach the supermassive black holes with pericentre distances larger than the the tidal radius $r_t = R_\star(3M_\bullet/M_\star)^{1/3} \approx 13(R_\star/R_\odot)(M_\star/M_\odot)^{-1/3} r_s$, where R_\star is the stellar radius and r_s is the Schwarzschild radius, $r_s \equiv 2GM_\bullet/c^2 \approx 2.95 \times 10^5 M_\bullet/M_\odot$ cm. Although the star itself is not tidally disrupted for this distance range, its extended envelope can be effected both via tidal interaction as well as hydrodynamical effects, such as (magneto)hydrodynamical drag and instabilities. The main goal was to determine the stability and dynamics of circumstellar dusty envelopes of dust-enshrouded stars. The study was observationally motivated by the results of [Gillessen et al. \(2012a, 2013a,b\)](#), who discovered the fast-moving, dusty source DSO (G2), and later by [Witzel et al. \(2014\)](#) and [Valencia-S. et al. \(2015\)](#), who obtained further information about the continuum and line emission of the DSO. The star-formation potential of

the Galactic centre region was confirmed by the discovery of young, dusty sources in IRS13N association (Mužić et al. 2008) and the formation of such associations was modelled by Jalali et al. (2014) by infalling molecular clumps that get tidally stretched and compressed and the self-gravitating gaseous clumps can overcome the Jeans limit and form young associations.

Projects in Topic (b) deal with stars that move supersonically through the environment, forming bow shocks – shells with larger gas and dust densities than the surrounding medium that are approximately given by the Rankine-Hugoniot jump conditions. Several bow shock sources were detected and studied (Mužić et al. 2010; Rauch et al. 2013; Sanchez-Bermudez et al. 2014) and their importance lies in the fact that the distribution and properties of bow shocks can be used to constrain the density of the ambient medium if the 3D velocity of the star is known as well as the characteristics of its stellar wind, namely the mass-loss rate, \dot{m}_w , and the terminal wind velocity, v_w . On the other hand, if the ambient density is well-constrained, the bow-shock stagnation radius R_{bs} can be used to estimate stellar parameters. These statements are valid under the assumption that the observed stellar bow shock forms at the ram-pressure and the stellar-wind pressure equilibrium, $P_{ram} = P_{sw}$ and the thermal pressure may be neglected. Then the bow-shock stagnation radius is given by,

$$R_{bs} = \sqrt{\frac{\dot{m}_w v_w}{4\pi\rho_a v_\star^2}}, \quad (1.28)$$

where ρ_a is the ambient density and v_\star is the relative velocity with respect to the ambient medium. Eq. (1.28) thus gives the basic length-scale for the bow-shock and other important quantities, such as the surface density profile of the bow shock as well as the velocity profile, are scaled by it. In my project, I am interested how the bow-shock properties are influenced by the outflow from the Galactic centre (or the inflow). *Can one use the star as a test probe of the accretion flow close to Sgr A*?*

Within Topic (c), I focused on the interaction of magnetized stellar end-products, specifically neutron stars, with the ambient gaseous medium in the Galactic centre region. Although the observations show that the Nuclear Star Cluster is one of the densest stellar clusters in the Galaxy, astronomers have detected only one neutron star – magnetar (soft gamma repeater, SGR J1745-2900) – in the innermost parsec (Mori et al. 2013; Kennea et al. 2013; Rea et al. 2013; Eatough et al. 2013a; Spitler et al. 2014). The predictions based on the continuing star formation over the age of the bulge, $\sim 10^{10}$ yr, yield $\sim 10^4$ neutron stars of various ages. The angular broadening and temporal scattering of the magnetar put limits on the scattering screen, which is located between us and the Galactic centre, specifically the estimated distance for the thin scattering screen is $\Delta_{scat} = 5.8 \pm 0.3$ kpc, consistent with the gas and dust located in the Scutum spiral arm (Bower et al. 2014). Therefore it should be possible to detect millisecond pulsars at frequencies $\nu \gtrsim 10$ GHz and normal pulsars at even smaller frequencies. The fact that only one pulsar has been detected so far in spite of optimistic predictions was named also as “missing pulsar paradox” (Dexter & O’Leary 2014). In my project, I aim at analysing interaction modes of the Galactic centre neutron star population, in particular the abundance of ejectors, accretors, and propellers (Lipunov 1992) as a function of environmental characteristics (density and temperature). Subsequently, we look at alternative ways to detect neutron stars, mainly based on their interaction with the ambient medium. I also look at other wavelengths, in particular the infrared domain, where young pulsars could be detected.

The work in the thematic Topic (d) focused in particular on the philosophical and astrophysical aspects of Sgr A* being a supermassive black hole. Despite an ever mounting evidence that the Galactic centre harbours a massive black hole, the final proof is missing and some alternatives, such as a boson star or a gravastar cannot be completely ruled out, especially as their new theories still emerge. *At what point can we be sure that the massive black hole is located at the Galactic centre? Is the Galactic centre black hole fully described by only three parameters according to the no-hair theorem?* We created a framework within the philosophy of science, through which we can address this fundamental question (Eckart et al. 2017). In this project, I aimed at tests of the black hole theory using the gravitational-wave emission and pulsars. Furthermore, I also looked into the question of the charge of Sgr A* as well as the motion of charged particles close to the Galactic centre black hole.

In the following Chapters 2–9, I present the peer-reviewed studies which were published in high-impact international journals. These are namely:

- **Dynamics of a dust-enshrouded star close to the SMBH:** Chapter 2 – Research topics: (a) and (b), paper: [Zajaček et al. \(2014\)](#).
- **A young accreting star close to the SMBH:** Chapter 3 – Research topics: (a) and (b), paper: [Valencia-S. et al. \(2015\)](#)
- **Bow-shock evolution close to the SMBH:** Chapter 4 – Research topics: (b), paper: [Zajaček et al. \(2016\)](#)
- **A NIR source with a polarized emission:** Chapter 5 – Research topics: (a) and (b), paper: [Shahzamanian et al. \(2016\)](#)
- **Nature of NIR-excess sources close to the Galactic centre:** Chapter 6 – Research topics: (a), (b), and (c), paper: [Zajaček et al. \(2017\)](#)
- **A short review on the DSO:** Chapter 7 – Research topics: (a) and (b), paper: [Zajacek et al. \(2017\)](#)
- **Interaction modes of neutron stars:** Chapter 8 – Research topics: (c), paper: [Zajacek et al. \(2015\)](#)
- **Charge of the Galactic centre black hole:** Chapter 9 – Research topics: (d), paper: [Zajaček et al. \(2018\)](#)

Dynamics of a dust-enshrouded star close to the SMBH

The discovery of a fast, reddened, NIR-excess source named DSO/G2 in 2011 ([Gillessen et al. 2012a](#)) triggered a lot of attention since there was a possibility that part of the dusty envelope could be detached from the object before and during its pericentre passage.

We followed this discovery and suggested three possible scenarios for the character of the source: a core-less cloud, a dust-enshrouded star, and a binary. It was clear that these three scenarios have different dynamical consequences. While a star stays compact and continues orbiting the SMBH along the original orbit, a core-less cloud undergoes stretching and strong interaction with the ambient medium, resulting in the formation of a filamentary structure and its continuous inspiral towards the SMBH. A dynamical evolution of a binary system depends on the semi-major axis and the mass ratio of its components. We showed that if a binary is originally on a nearly parabolic orbit, it can be disrupted during the pericentre fly-by, with one component escaping on a hyperbolic orbit and the other becoming more bound to the SMBH.

This work was a part of my master thesis and I include it here since it fits into the overall framework of young stars and NIR-excess objects in the Galactic centre.

The following peer-reviewed paper summarizes the dynamical analysis of these three scenarios.

Credit: Zajaček et al., A&A 565, A17 (2014). Reproduced with permission ©ESO.

Dust-enshrouded star near supermassive black hole: predictions for high-eccentricity passages near low-luminosity galactic nuclei

Michal Zajaček^{1,2}, Vladimír Karas¹, and Andreas Eckart^{3,4}

¹ Astronomical Institute, Academy of Sciences, Boční II 1401, 14100 Prague, Czech Republic
 e-mail: mi.chal_zajacek@yahoo.com

² Charles University in Prague, Faculty of Mathematics and Physics, V Holešovičkách 2, 18000 Prague, Czech Republic

³ I. Physikalisches Institut der Universität zu Köln, Zùlpicher Strasse 77, 50937 Köln, Germany

⁴ Max-Planck-Institut für Radioastronomie (MPIfR), Auf dem Hügel 69, 53121 Bonn, Germany

Received 19 September 2013 / Accepted 18 March 2014

ABSTRACT

Context. Supermassive black holes reside in cores of galaxies, where they are often surrounded by a nuclear cluster and a clumpy torus of gas and dust. Mutual interactions can set some stars on a plunging trajectory towards the black hole.

Aims. We model the pericentre passage of a dust-enshrouded star during which the dusty envelope becomes stretched by tidal forces and is affected by the interaction with the surrounding medium. In particular, we explore under which conditions these encounters can lead to periods of enhanced accretion activity.

Methods. We discuss different scenarios for such a dusty source. To this end, we employed a modification of the *Swift* integration package. Elements of the cloud were modelled as numerical particles that represent the dust component that interacts with the optically thin gaseous environment.

Results. We determine the fraction of the total mass of the dust component that is diverted from the original path during the passages through the pericentre at $\approx 10^3$ Schwarzschild radii and find that the main part of the dust ($\geq 90\%$ of its mass) is significantly affected upon the first crossing. The fraction of mass captured at the second passage generally decreases to very low values.

Conclusions. As an example, we show predictions for the dusty source evolution assuming the current orbital parameters of the G2 cloud (also known as Dusty S-Cluster Object, DSO) in our Galactic centre. Encounter of a core-less cloud with a supermassive black hole is, most likely, a non-repeating event: the cloud is destroyed. However, in the case of a dust-enshrouded star, part of the envelope survives the pericentre passage. We discuss an offset of $\lesssim 0.3$ arcsec between the centre of mass of the diverted part and the star along the eccentric orbit. Finally, we examine an interesting possibility of a binary star embedded within a common wind envelope that becomes dispersed at the pericentre passage.

Key words. black hole physics – Galaxy: center – galaxies: individual: Sgr A*

1. Introduction

Most galaxies host supermassive black holes (SMBH; $10^6 M_\odot \lesssim M_\bullet \lesssim 10^9 M_\odot$) in their cores, where these accrete gas and dust in the form of an accretion flow from their immediate neighbourhood (Krolik 1999; Meier 2012). The example nearest to us is the compact radio source Sgr A*, which contains a black hole of mass $M_\bullet = 4.4 \times 10^6 M_\odot$ at distance 8.2 kpc in the centre of the Milky Way (Eckart et al. 2005; Melia 2007; Genzel et al. 2010).

The character of accretion and the corresponding accretion rate vary greatly over different galaxy types. It appears that the availability of mass supply and the accretion mode that is established in the course of evolution of the system are the main agents that determine the power output and the spectral energy distribution of supermassive black holes (Frank et al. 2002). In several ways, the Galactic centre can serve as a paradigm for low-luminosity nuclei.

Active galactic nuclei (AGN) and quasars host radiatively efficient types of disc accretion (i.e., the standard scheme of geometrically thin accretion discs, or slim discs; Shakura & Sunyaev 1973; Abramowicz et al. 1988) with accretion rates reaching and even exceeding the Eddington limit of $\dot{M}_{\text{Edd}} \approx L_{\text{Edd}}/(0.1c^2)$, where

$$L_{\text{Edd}} = \frac{4\pi GM_\bullet m_p c}{\sigma_T} \approx 1.3 \times 10^{44} \frac{M_\bullet}{10^6 M_\odot} \quad [\text{erg/s}], \quad (1)$$

with m_p proton mass, σ_T Thomson cross-section.

Low-luminosity nuclei exhibit significantly lower accretion rates, $\dot{M}_\bullet \ll \dot{M}_{\text{Edd}}$ (Eckart et al. 2013a). This can be explained as a combination of a diminishing supply of material falling onto the black hole and the radiatively inefficient mode of accretion at certain stages. In this context, the present state of the Galactic centre represents an extreme example of an inactive nucleus: $\dot{M}_\bullet \approx 10^{-8} M_\odot$ per year, which can be understood in terms of advection-dominated flow (Narayan & McClintock 2008)¹.

The temperature of the accreted material grows in the course of its infall in the gravitational field of the central black hole because the potential energy is converted into heat and is only partially released in the form of emerging radiation (e.g. Frank et al. 2002; Krolik 1999). While at the distance of several tens to hundreds Schwarzschild radii ($r_s \equiv 2GM_\bullet/c^2 \approx 2.95 \times 10^5 M_\bullet/M_\odot$ cm) the medium consists of ionised gas of the accretion disc and hot, diluted corona, farther out the temperature drops below the critical value for dust sublimation, $T_{\text{sub}} \approx 1.5 \times 10^3$ K (Barvainis 1987; Krishna Swamy 2005). Therefore,

¹ For the supermassive black hole of Sgr A* in the Galactic centre, the quiescent bolometric luminosity is $L_{\text{bol}} = \eta \dot{M}_\bullet c^2 \approx 10^{36}$ erg s⁻¹. This corresponds to the dimensionless efficiency parameter for the conversion of accreted mass into radiation of about $\eta \approx 10^{-3}$, although it can be as low as 10^{-5} at the present stage of the source. The accretion outflow of Sgr A* is radiatively inefficient compared with predictions from the standard accretion disc theory, where $\eta \approx 0.06$ – 0.42 is the predicted range.

at larger distances a clumpy torus can persist with a fraction of its mass in the form of dust (Krolik & Begelman 1988; Hönig & Kishimoto 2010).

An equilibrium can be reached through processes of dust sublimation (by strong irradiation from the central source and stars of the nuclear cluster), in competition with the replenishment of dust by stellar winds and the infall of clouds from the outer regions, where the circumnuclear torus is present (Antonucci 1993; Urry & Padovani 1995). The co-evolution of gas and dust phases within clouds falling onto a supermassive black hole is relevant for our understanding of mass transport in the innermost regions of galactic nuclei.

Recently, an infrared-excess source named G2/DSO has been discovered (Gillessen et al. 2012) and subsequently detected in L - and K -bands (Gillessen et al. 2013a; Phifer et al. 2013; Eckart et al. 2013b). It may indeed be a manifestation of a common mechanism of material transport in low-luminosity nuclei. We analyse the scenario of an infrared-excess, dusty stellar source. As indicated in Shcherbakov (2014), the cloud component of the source is optically thin and diluted and not thick and dense. Therefore, it is valid to assume that the cloud component is mainly constituted by the gaseous wind driven by the radiation pressure of central star and the dust that is located and formed in such a wind. This is the reason that in the following analysis we assume the dust to be in contact only with stellar wind and the ambient atmosphere around Sgr A* through which G2/DSO travels.

The adopted scenario is not necessarily only connected to this single event. It may be applied to other observed infrared-excess stellar sources that have been shown to move through the gaseous medium near the Galactic centre (e.g., Moutaka et al. 2005; Mužić et al. 2010). Moreover, it may be relevant for modelling the environment in other low-luminosity active galactic nuclei.

In this paper we adopt a simplified (toy) model: dust grains are treated as numerical particles under the influence of gravity of SMBH ($M = M_\bullet$) and the embedded star ($M = M_\star$), or the components of a binary ($M_\star^{(1)}, M_\star^{(2)}$), and the effect of an outflowing wind of gas. We focus on dust-enshrouded stars with different distributions of dust bound to the central star, and we explore the amount of material that is lost from the cloud to the black hole. Effects arise from the ambient pressure of a central wind, the wind pressure from the star, and a bow-shock forming at the interface of winds. The star moves at transonic speed near the pericentre.

In this way we address the question whether and how dust particles embedded in the wind envelope are affected by close passages near the SMBH. For most model parameters, most of the dusty material is stripped from the envelope already on the first transit. For low accretion rates, the dust component can survive down to quite small radii, especially in regions shielded by obscuration. Furthermore, if the Field criterion (Field 1965; Barai et al. 2012) is fulfilled for the thermal stability of a two-temperature medium, the dust may co-exist with the hot medium at the same radius. The dust component by itself would be unimportant, but it contributes significantly to the radiation in NIR and tracing it helps to understand the observed emission. Similar treatment of dust dynamics is often employed in other astrophysical systems (mainly protoplanetary discs and stellar atmospheres, see e.g., van Marle et al. 2011).

We model the encounters over a broad span of parameters. To present specific examples we use orbital parameters relevant for the Galactic centre G2/DSO infrared source (Gillessen et al. 2013b), and we also attempt to distinguish among different

outcomes of the passages through the pericentre (Eckart et al. 2013c; Phifer et al. 2013).

Furthermore, we point out to the possibility that the stellar core may actually consist of two components of a binary star. This idea is suggested by models of the origin of S-stars in the Galactic centre as a product of three-body interaction during the pericentre passage of a binary star on a highly eccentric trajectory (Gould & Quillen 2003; Perets et al. 2007). Although the presence of a stellar core and its putative binary nature within the G2 cloud are on a purely hypothetical level, this scenario can connect, in a natural way, two apparently different aspects: the high eccentricity of the plunging trajectory, and the origin of the population of stars near the supermassive black hole. If there is indeed a star enshrouded by a dusty atmosphere, it was proposed that high eccentricity can be achieved by the Kozai mechanism (Šubr & Karas 2005) or by resonant relaxation (Hopman & Alexander 2006).

The geometrical setup and the main ingredients of our model are illustrated in Fig. 1. Three different flavours of the basic scenario were considered: a core-less cloud infalling onto the SMBH, a star embedded within the dusty envelope, and an embedded binary that becomes disrupted near the SMBH. We focus on the latter two scenarios. Our simplified approach is complementary to purely hydrodynamical situations that neglect the dust component (Anninos et al. 2012; Burkert et al. 2012; Ballone et al. 2013; Shcherbakov 2014), which is consistent with an optically thick, dense medium where the dust is dragged along with the gas. However, for optically thin atmospheres, dust dynamics needs to be treated separately.

In the following analysis, we do not treat Br γ production or the radiation processes in the bow-shock region (Sądowski et al. 2013). We do see, however, that the dusty envelope is stretched by the gravitational and drag forces (depending on the initial distribution of particles in phase space and the parameters of the wind outflow), which leads to the gradual offset between the dust component and the stellar core. We note that observationally any difference between the cloud location in L -band with respect to the location of K (Br γ) in the orbit is most likely due to uncertainties in the determination of the orbital positions; it may be heavily affected by different systematics in the two bands.

The paper is organized as follows: in Sect. 2 we set up the model and describe the numerical procedure to explore the mutual interaction between the star and its environment. We discuss the dependence of the dust temperature on the distance and the luminosity of the central source. Then we consider the effect of the star enshrouded by an initially spherical dusty envelope and a remnant disc. In Sect. 3, we present the results of the simulations including the wind blowing from the centre and the effect of the bow-shock region. We compare the difference between a disc-like Keplerian distribution and a Gaussian distribution of particles in the phase space. Finally, we determine the fraction of dust mass affected at subsequent encounters, and we show the offset that develops gradually between the centre of mass of the cloud and the nominal position of the star in the orbit. In Sect. 4 we summarize and discuss our results, and we conclude in Sect. 5.

2. Model setup, numerical scheme, and tests

2.1. Clouds infalling onto SMBH – test runs

Accretion tori are not smooth, instead, they often form individual clouds with a mixed composition of gas and dust phases (e.g., Cox 2005; Vladimirov et al. 2005). The patchy structure evolves

Michal Zajačák et al.: Dust-enshrouded star near supermassive black hole

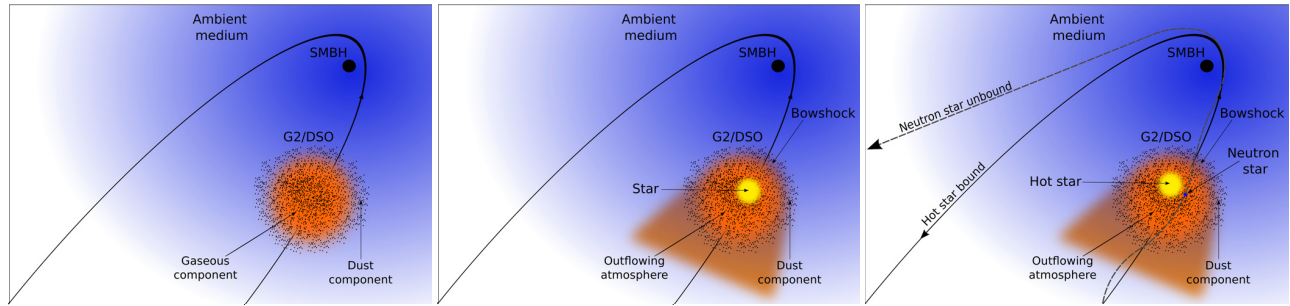


Fig. 1. Three variants of the model setup for which the predictions are qualitatively different especially at the post-pericentre phase. The model ingredients include the central supermassive black hole (black circle), an infalling cloud made of gas and dust (red), an embedded star (yellow), and a hot diluted flow (blue). We consider the pericentre at about 10^3 Schwarzschild radii, so that the star is not expected to be tidally disrupted. However, the gaseous/dusty envelope is affected significantly. *Left panel:* a core-less cloud on an eccentric trajectory, interacting with the diluted ambient medium near the SMBH. *Middle panel:* the cloud enshrouds an embedded star. A radial wind of the outflowing gaseous atmosphere occurs and a bow-shock forms ahead of the stellar body. *Right panel:* binary system enclosed by a common envelope that becomes largely dispersed at the first pericentre passage. At the same time, the three-body interaction with the central SMBH causes the binary components to separate from the nominal trajectory.

by collisions, and some of the clumps can be set on a highly eccentric trajectory with the pericentre close to the central black hole. Interaction with the surrounding environment leads to the drift and gradual separation of different constituents of the cloud and deformation of its shape – dust and gas components of the cloud move with respect to each other, and with respect to the star (if embedded in the cloud core).

A bow shock develops around an embedded star and different species are transported across discontinuities in a different manner (smaller grains tend to be bound to the gas component, while the large grains are capable of penetrating into the interstellar medium; cf. MacGregor & Stencel 1992; van Marle et al. 2011; Keppens et al. 2012). If large portions of the medium are neutral, viscous forces play an important role, while in a fully ionised plasma the efficient mechanism of dust grain charging operates. Then the main parameter that defines the coupling between dust and gas is the Coulomb coupling parameter, which is the ratio of the Coulomb potential energy of the particle interaction to the kinetic energy of the thermal motion. Depending on the system parameters, both weak coupling and strong coupling have been observed in dusty plasmas.

The grain size is a dominant factor for the forces acting on the gas/dust mixture. The mutual coupling between these two components of the complex plasma (including the viscous forces) is thought to just increase the effective dust grain mass by the amount of gas that is dragged along in the coupling. The particle mass is not relevant within the strong gravitational field of the SMBH and/or the star, instead, it may only be relevant for the wind force acting on the dust. For a gas-to-dust ratio of 100:1, the effective increase of the grain mass load by two orders of magnitude would then correspond to the grain size variation by factor of about 5. This is well contained in the factor of a hundred in the grain sizes that we considered here. The relation between size and mass is uncertain because grains are most likely fluffy and not solid. Moreover, other factors are also connected with the grain size, for example, the typical electric charge that can develop by the interaction with the surrounding plasma and by photoionisation.

An infalling cloud passes through the external environment with physical properties spanning a wide range of values. We modelled the passages of stars with dusty envelopes through the pericentre by numerically integrating the trajectories of star(s) and that of dust particles that represent one of elementary constituents of the cloud. These are followed in the gravitational

field of the SMBH, taking into account the hydrodynamical interaction with the diluted ambient wind. Gravitational effects need to be taken into account, but nonetheless, the Newtonian description is adequate for the gravitational field because we considered the motion with the pericentre at $\approx 10^3 r_s$, so not in the immediate vicinity of the black hole horizon, where the relativistic effects on the orbit evolution become important. The variety of factors listed above underline a potentially important influence of the grain properties for the gas/dust coupling and hence support our simulation approach.

We employed the integration package Swift (Levison & Duncan 1994), which has been designed to evolve a set of mutually gravitationally interacting bodies together with a group of test particles that are influenced by gravity of the massive bodies, but do not affect each other (or the massive bodies). In the numerical scheme we included the effect of radial wind outflow and that of ambient gaseous wind and employed a sufficiently accurate Bulirsch-Stoer integrator with an adjustable time-step.

The adopted procedure allowed us to follow a large number of numerical particles in the gravitational field, namely, a superposed gravitational field of the central SMBH and the embedded star. The gravity of the black hole plays a role in the motion of parcels because their mass is relatively large (like dust grains compared to gas atoms), but we modified the integration routine to also include the hydrodynamic drag that acts through the interaction of particles with the gaseous ISM as well as an outflowing stellar wind. The dust grain mass is a parameter that allowed us to study different cases, including a toy model where the grains represent super-particles of mass exceeding that of realistic cosmic dust.

2.2. Non-gravitational forces acting on dust

Although the stellar atmosphere consists largely of outflowing gas, here we concentrated mainly on the dust component. Both species interact with each other, but they can separate to a certain extent during the evolution. Observationally, the gas is expected to be revealed by Bry spectral line emission, while the dust grains will contribute to the thermal continuum and can be detected by polarisation. This provides information about in situ conditions of the surrounding environment, but the predictions are currently uncertain due to incomplete knowledge about the nature and composition of G2/DSO.

In a galactic nucleus all objects interact with the hot plasma that is supplied by stellar winds, in particular, of hot, massive OB stars. The effects of this interaction depend on temperature and density profiles of the ISM. For the purpose of this work, we used semi-analytical relations for electron density $n_e(r)$ and electron temperature $T_e(r)$ radial profiles based on the models of radiatively inefficient accretion flows (Broderick & Loeb 2006; Broderick et al. 2011),

$$n_e(r) = n_e^0 \left(\frac{r}{r_s} \right)^{-1.1}, \quad T_e(r) = T_e^0 \left(\frac{r}{r_s} \right)^{-0.84}. \quad (2)$$

In these dependencies, we considered quantities n_e and T_e to adopt averaged values, $n_e^0 = 3.5 \times 10^7 \text{ cm}^{-3}$ and $T_e^0 = 9.5 \times 10^{10} \text{ K}$. Electrons are decoupled from ions at small distances from the SMBH; ion temperatures are ~ 1 to 5 times higher than electron temperatures resulting from MHD simulations (e.g., Dexter et al. 2010). The density profile (2) is used in Eq. (7) to estimate the ambient density $\rho_a = m_H n_H$ (with $n_H \approx n_e$).

The profiles in eq. (2) were originally derived for the accretion flows up to $\sim 100 r_s$, whereas we considered the pericentre passages at a typical distance one order of magnitude larger, $r \sim 10^3 r_s$. However, the densities inferred from the one-dimensional model (used to fit Chandra X-ray data farther away from the Galactic centre; Quataert 2004) do not differ much when extrapolated from the inner flow to the region of our interest (factor of ~ 3 ; see Psaltis 2012, for comparisons).

In general, the equation describing the motion of dust particles in the gaseous environment (optically thin stellar atmospheres, protoplanetary discs) is

$$\frac{d\mathbf{v}}{dt} = \mathbf{a}_{\text{grav}} + \mathbf{a}_{\text{drag}} + \mathbf{a}_{\text{rad}}, \quad (3)$$

where \mathbf{a}_{grav} represents gravitational interactions, \mathbf{a}_{drag} stands for the wind drag acceleration, and \mathbf{a}_{rad} is the acceleration due to radiation pressure.

The radiation pressure acceleration acting on a grain that is located at distance r_* from the star with flux $\Phi_* = L_*/(4\pi r_*^2)$ may be expressed by (e.g., Bertotti et al. 2003)

$$\mathbf{a}_{\text{rad}} = Q \frac{\Phi_* \sigma_{\text{eff}}}{mc} \left[\left(1 - \frac{\mathbf{r}_* \cdot \mathbf{v}_*}{r_* c} \right) \frac{\mathbf{r}_*}{r_*} - \frac{\mathbf{v}_*}{c} \right] + O\left(\frac{v_*^2}{c^2}\right), \quad (4)$$

where the factor Q reflects the way the particle absorbs or reflects light, m denotes the dust mass, σ_{eff} its effective cross-section, \mathbf{v}_* is the velocity vector in the frame of the star, and c is the speed of light. The terms in the brackets represent the direct pressure, the change of radiation energy due to the Doppler effect, and the Poynting-Robertson drag, respectively. Equation (4) is valid in a Newtonian approximation that is consistent with the pericentre passage of a star at the distance of $\sim 1000 r_s$ at most. However, in the immediate vicinity of the SMBH, it would be necessary to include the second and higher powers of (v_*/c) as well.

The first two radial terms in Eq. (4) effectively change the mass of the star, which itself is a free parameter in our model, and the non-radial Poynting-Robertson term causes the decrease in the semimajor axis and eccentricity of the orbit and contributes to the inspiral of dust towards the star on the Poynting-Robertson time scale τ_{pr} , which may be approximated using

Eq. (4) and setting the effective cross-section equal to the geometrical cross-section of the grain, $\sigma_{\text{eff}} = \pi R^2$:

$$\begin{aligned} \tau_{\text{pr}} &= \frac{16\pi c^2}{3Q} L_*^{-1} R \rho_d r^2 \\ &= 28 \times 10^2 \text{ yr} \frac{1}{Q} \left(\frac{L_*}{L_\odot} \right)^{-1} \left(\frac{R}{1 \mu\text{m}} \right) \left(\frac{\rho_d}{1 \text{ g cm}^{-3}} \right) \left(\frac{r}{1 \text{ AU}} \right)^2. \end{aligned} \quad (5)$$

In our model, we worked with time scales of 100 yr, which are shorter than τ_{pr} by one order of magnitude for distances of $\sim 1 \text{ AU}$. For more distant orbits, the time scale is significantly prolonged because of its quadratic dependence on the distance.

The radiation pressure from other S-stars in the background also contributes, but it is at least two orders of magnitude weaker. For an estimate, we took $\sim 500 \text{ mas} \approx 4125 \text{ AU}$ as an average distance of individual S-cluster members. The estimated number of $\sim 20 M_\odot$ stars is ~ 30 and we compared the effect of their radiation with a low-mass (LM) star of $2 M_\odot$. Hence, the ratio of accelerations due to radiation, Eq. (4), is

$$\begin{aligned} \frac{a_{\text{LM}}}{a_{\text{S}}} &\approx \frac{L_{\text{LM}}}{30 L_{\text{S}}} \left(\frac{r_{\text{S}}}{r_{\text{LM}}} \right)^2 \\ &\approx \frac{1}{30} \left(\frac{M_{\text{LM}}}{M_{\text{S}}} \right)^{3.5} \left(\frac{r_{\text{S}}}{r_{\text{LM}}} \right)^2 \\ &= \frac{1}{30} \left(\frac{2 M_\odot}{20 M_\odot} \right)^{3.5} \left(\frac{4125 \text{ AU}}{1 \text{ AU}} \right)^2 \approx 180. \end{aligned} \quad (6)$$

Similarly, the Poynting-Robertson time scale, Eq. (5), yields $\tau_{\text{pr}} \approx 10^5 \text{ yr}$ for the average distance of 500 mas and the luminosity of $\sim 30 \text{ } 20 M_\odot$ stars. Scoville & Burkert (2013) also estimated that although a production rate of Lyman continuum photons is high, very few of them are intercepted because of the small area of the bow shock formed ahead of the star. Hence, the effect of radiation pressure from background stars is weak on the time scale of $\sim 100 \text{ yr}$ considered here.

The radiation drag in the vicinity of a putative star will only slightly affect individual orbits of grains on the time scale of a few orbital periods. The ensemble of particles behaves similarly with and without the radiation term involved, which shows that gravitational forces and hydrodynamical drag are dominant for their dynamics. To reduce computation costs, we omitted this term in most of our numerical calculations.

The acceleration caused by the drag for both supersonic (Stokes law) and subsonic (Epstein law) modes may be written in a closed form (e.g., Kwok 1975; van Marle et al. 2011):

$$\mathbf{a}_{\text{drag}} = -\eta_{\text{drag}} \frac{\pi R^2}{m} \rho_a \sqrt{v_{\text{rel}}^2 + \bar{v}_i^2} \mathbf{v}_{\text{rel}}, \quad (7)$$

where $\mathbf{v}_{\text{rel}} = \mathbf{v} - \mathbf{v}_g$ is the relative velocity of grains with respect to the gas motion \mathbf{v}_g . The mean thermal velocity, assuming Maxwellian distribution, is $\bar{v}_i = (8/\pi)^{1/2} c_s$, which is proportional to the sound speed $c_s = \sqrt{kT/m_H}$ (for ideal gas). The factor η_{drag} acquires the value $4/3$ for the Epstein law and $1/2 C_d(Re)$ for the Stokes law, where the coefficient $C_d(Re)$ depends on the Reynolds number Re (for an in-depth discussion see Perets & Murray-Clay, 2011). As shown in Fig. 2, orbital velocities within the inner $\sim 10^6$ Schwarzschild radii are supersonic, $v_{\text{orb}} \approx \sqrt{GM_\bullet}/r > c_s$, so the Stokes law is approximately valid. This is also true for grains embedded in the outflowing wind atmosphere close to the star, see Fig. 3. If we assume an isothermal atmosphere with $T \approx 10\,000 \text{ K}$ that is in ionisation equilibrium with the environment, orbital velocities are approximately

Michal Zajačák et al.: Dust-enshrouded star near supermassive black hole

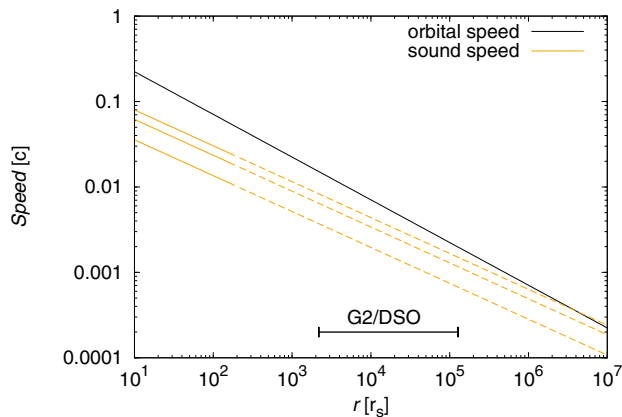


Fig. 2. Comparing the orbital (Keplerian) velocity with the sound speed at corresponding radius from the central black hole (units of Schwarzschild radii). The range of G2/DSO is labelled. On the vertical axis, the unit of speed is the speed of light, c .

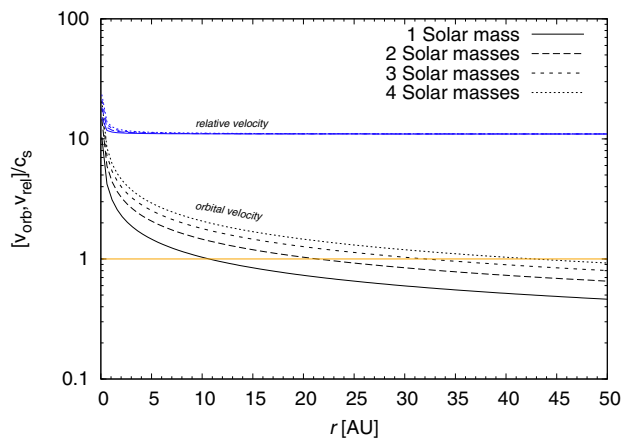


Fig. 3. Ratio of orbital velocities (black lines) and relative velocities (blue lines) to the speed of sound as a function of distance from the star. Relative velocities are typically higher than the sound speed by about one order of magnitude for wind velocities of the order of 100 km s^{-1} .

equal to the sound speed at distance $r_s \approx GM_\star m_H / (kT)$ and decrease. However, relative velocities with respect to radial outflow, in case of circular orbits of grains, are higher than the sound speed by about factor of 10 for typical terminal wind velocities of 100 km s^{-1} . Assuming that grains have a spherical shape with diameter d and substituting the dust grain volume times density for the mass, we obtain $a \approx -\frac{3}{4} C_d (Re) (\rho_a / \rho_d) d^{-1} v_{\text{rel}} v_{\text{rel}}$ and we set $C_d = 1^2$.

We note that the magnetic field frozen in the stellar wind and potentially that of the interstellar medium near the galactic nucleus as well may influence the motion of charged dust, mainly of a smaller size. This is mainly determined by the ratio of the charge of the grain q resulting from photo-charging and its mass m , q/m . When the main component of the field is radial, $\mathbf{B} = B_r \mathbf{r}$, and dust motion is azimuthal, $\mathbf{v} = v_\phi \hat{\phi}$, the Lorentz acceleration, $a_L = (q/m) v_\phi B_r$ causes the grain inclination to increase or decrease, depending on the mutual orientations of the magnetic field and velocity vectors. The field orientation may flip after some time and may lead to oscillations around the orbital plane. Because of the many uncertainties concerning the

² From subsonic to supersonic regimes, the drag coefficient changes typically by about a factor of two.

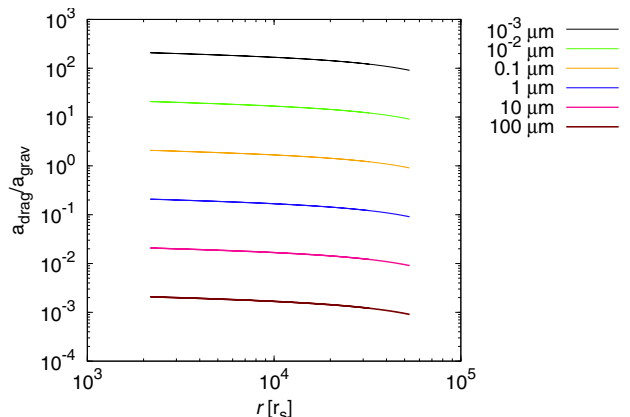


Fig. 4. Ratio of the hydrodynamical drag to the gravitational acceleration across the range of radii. The two effects can be of comparable magnitude and, therefore, both need to be taken into account in the model of the orbit evolution.

magnetic field strength and the efficiency of photo-charging, we did not consider the magnetic field in our analysis.

Despite the arguments for neglecting these terms and effects, this is just a crude model. Nonetheless, it allows us to reproduce the relevant trends in a semi-analytical way.

In Fig. 4 we plot the ratio of the magnitude of the acceleration due to the drag force (7) with respect to the gravitational acceleration across the range of radii. In this case we neglected the motion of ambient medium and set the relative velocity v_{rel} equal to the orbital speed. Although the ratio varies significantly (by six orders of magnitude), it is non-negligible for some typical particle sizes in the range $\sim 0.1 \mu\text{m} - 1 \mu\text{m}$ (for the smallest particles it exceeds the gravitational acceleration magnitude)³.

As the cloud approaches the central region, the dust absorbs the radiation mainly at shorter wavelengths and heats up. The dust temperature grows to the sublimation temperature T_{sub} and eventually leads to sublimation. When we take into account only the radiation of the central accretion flow, the sublimation radius is easily determined (e.g., Barvainis 1987):

$$r_{\text{sub}} = 567 T_{\text{sub}}^{-2.8} \left[\left(\frac{L_{\text{uv}}}{L_\odot} \right) \exp(-\tau_{\text{uv}}) \right]^{\frac{1}{2}} [\text{pc}], \quad (8)$$

where L_{uv} stands for the luminosity of the central source at ultraviolet wavelengths expressed in units of solar luminosity L_\odot . The optical depth, τ_{uv} , enables us to estimate the sublimation radius or inversely the temperature of dust at given r (again, realistic profiles must be more complicated; Kishimoto et al. 2011). Furthermore, in sources with radiatively efficient accretion, X-ray heating contributes significantly (Czerny & Hryniewicz 2011).

For the sublimation temperature $T_{\text{sub}} \approx 1500 \text{ K}$ (Barvainis 1987), low optical depth, and $L_{\text{uv}} \approx 10^3 L_\odot$, the relation (8) gives $r_{\text{sub}} \approx 2.3 \times 10^{-5} \text{ pc} \approx 56 r_s$ as a lower estimate (we did not consider hot OB stars present near the centre, whose radiation probably heats the dust further). When the stellar populations are taken into account, the central luminosity can be estimated to a few $\sim 10^6 L_\odot$ for the smooth distribution, and up to $10^7 L_\odot$ for the

³ The effect might be more significant in AGN, where the typical density of the environment is higher than in inactive nuclei, but in that case strong irradiation leads to dust heating and destruction in a relatively large volume around the central source.

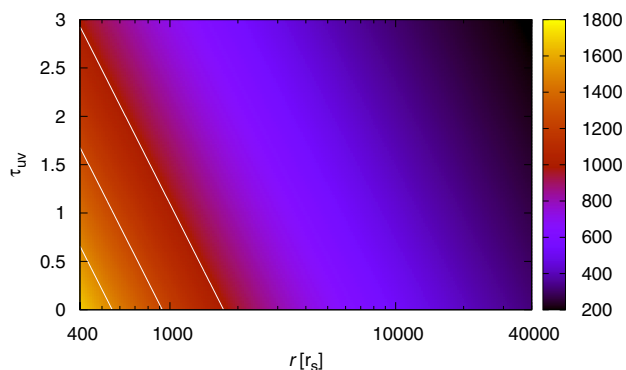


Fig. 5. Colour-coded profile of temperature $T \equiv T(r, \tau_{uv})$ of dust for the central source of luminosity $10^5 L_\odot$ near the central SMBH. From right to left, the three lines are isotherms corresponding to $T = 1000$ K, 1250 K, and 1500 K (dust sublimation temperature).

clumpy structure (Davidson et al. 1992), which leads to $r_{\text{sub}} \approx 2.3 \times 10^{-3} \text{ pc} \approx 5600 r_s$ as an upper limit for the sublimation radius.

Given the uncertainty, it is appropriate to refer to the sublimation zone extending from a few tens of Schwarzschild radii up to $\sim 5 \times 10^3 r_s$. To shorten the integration time of numerical experiments, we safely set the inner sublimation radius to $300 r_s$ in our test runs. Using the inverse relation $T = T(r, \tau_{uv})$ in Eq. (8), we estimate the temperature profile of dust near the source of central luminosity $10^5 L_\odot$, which is intermediate between the limits of 10^3 and $10^7 L_\odot$ (see Fig. 5).

The passages with pericentre above $\approx 1 \times 10^3 r_s$ (the case of G2/DSO, the Dusty S-cluster Object in the Galactic centre)⁴ probably does not heat the dust to the sublimation temperature, which would only be reached at $\approx 600 r_s$. However, the mechanism of heating is more complicated not only because of the presence of stars, but also because of the shock heating that may contribute in case of transonic motion.

2.3. Role of central star

It has often been advocated (e.g., Gillessen et al. 2013b) that the infalling DSO/G2 source may represent a core-less clump that has originated farther out at greater distance, $\gtrsim 10^4 r_s$, and now is on the way toward the pericentre, where it will largely disintegrate and undergo accretion onto the SMBH. However, it may be also a dusty envelope that enshrouds a star. Extended shells surrounding stars near Sgr A* have been reported, see for example Moultaqa et al. (2005).

Before the pericentre passage, the two cases are expected to produce a similar image and the corresponding spectrum to contain a thermal component from the dust. On the other hand, a transit through the pericentre must reveal the nature in a clearer way. Because we considered a pericentre distance of the order of $10^3 r_s$, the star itself is not destroyed by tidal forces of the SMBH, instead, it continues to follow the eccentric ellipse. The diluted atmosphere is more visibly affected by its interaction with the ambient medium.

First, we compared the temporal evolution of the spatial distance and velocity with/without the hydrodynamical drag for the high-eccentricity orbits of a single particle. As a specific

⁴ The S-cluster is the 1'' diameter star cluster of high-velocity stars surrounding Sgr A* (Eckart & Genzel 1996; Ghez et al. 1998; Eckart et al. 2005; Melia 2007; Genzel et al. 2010).

example, we used the L' -band based nominal orbital elements of G2/DSO (Gillessen et al. 2013a). The resulting evolution is plotted in Fig. 6; it appears to be consistent with eccentricities and semi-major axes of dust grains gradually decreasing, as they move in the ambient medium.

Next, we considered a cloud of particles with a certain initial distribution of positions and velocities and included different effects acting on the motion. Gillessen et al. (2012, 2013a) studied the evolution of such a cloud of particles in the field of the Sgr A* SMBH. We revisited their simulations by including the interaction with different prescriptions for the ambient wind. In our simulations, for example, 2000 particles were initially distributed according to a spherically symmetric Gaussian distribution in the position-velocity phase space. We used the same L' -band-based orbital elements for the G2/DSO cloud as above.

The evolution in the orbital plane and in the velocity-distance plane are plotted in Fig. 7 (left panels) for selected epochs since the start of the simulation. The initial FWHM of the phase-space distribution was set to be 25 mas for positions (the value adopted from Gillessen et al. 2013b), and 5 km s^{-1} as a typical turbulent velocity within the cloud. These simulations reveal that because of the drag of the ambient ISM and gravity of the SMBH, most particles continue to spiral in towards the centre. The cloud as a whole becomes progressively stretched by the tidal forces, and the velocity dispersion rises abruptly as particles approach the SMBH.

Secondly, we examined the evolution with an embedded star, whose mass has been set to $M_\star = 2 M_\odot$. Dust grains ($d = 5 \mu\text{m}$) initially obey a uniform distribution of semi-major axes in the range (0.1, 50) AU, eccentricities in the range (0, 0.1), and inclinations within $(0^\circ, 180^\circ)$ ⁵. The distribution of velocities is Keplerian. Figure 7 also shows the evolution of such a stellar source (right panels).

The particles start to trail behind the star because of the drag. In combination with the tidal effects, the position and the velocity dispersion gradually increase up to the pericentre. During the post-pericentre phase the velocity dispersion first decreases, then increases again while particles spiral inwards to the SMBH. In Fig. 7 we clearly see how the attraction of the star influences some of the particles (cp. the epoch 15.05). A small fraction of particles remain bound to the star; specifically for this run, about 5% particles remained bound to the star; this number did not change after the second pericentre passage.

2.4. Dust truncation radius

To estimate the dust mass diverted from the initial nominal trajectory of the cloud at its pericentre passages, it is useful to consider the Hill radius of the binary system star-SMBH. At the pericentre,

$$r_H = a(1 - e) \left(\frac{M_\star}{3 M_\bullet} \right)^{1/3}, \quad (9)$$

which for the mass $M_\star = 2 M_\odot$ and the position at the pericentre yields ~ 1 AU; inside this sphere of influence the particles remain bound to the star, while outside it the particles are captured by the SMBH.

The sphere of influence increases after each pericentre passage, as illustrated in Fig. 8, where we plot the Hill radius evolution over an interval of time. We varied the eccentricity, but

⁵ Inclination values lower than 90° correspond to a prograde (direct) orbit, values exceeding 90° are reserved for the retrograde sense of motion.

Michal Zajaček et al.: Dust-enshrouded star near supermassive black hole

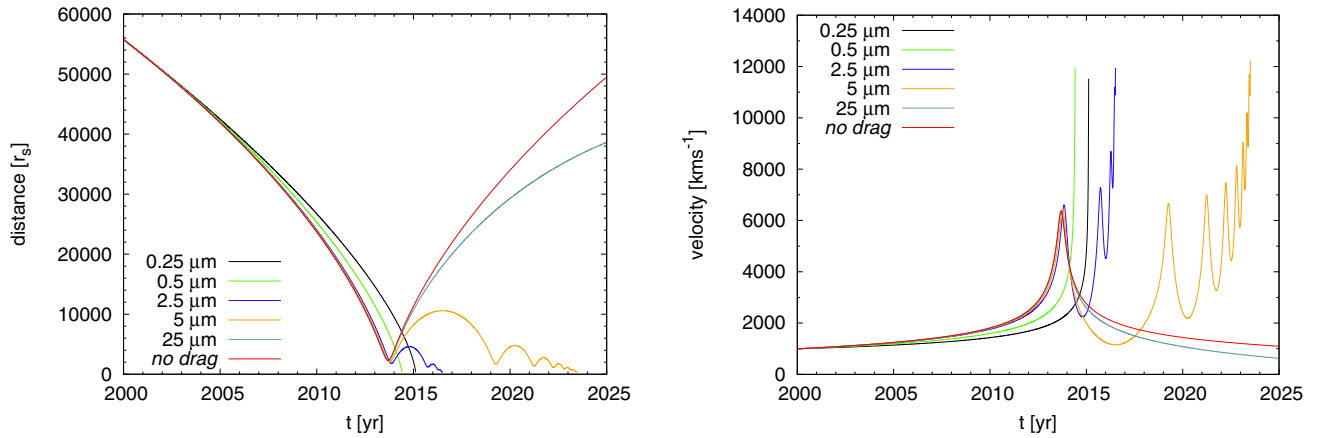


Fig. 6. Single-particle approximation. *Left panel:* the temporal evolution of 3D distance (in Schwarzschild radii); the orbital parameters are set consistent with the G2/DSO in Galactic centre. Different particle (dust grain) sizes are considered, taking into account the effect of gravity and the hydrodynamical drag exerted by the ambient medium. *Right panel:* the corresponding velocity as a function of time. Hydrodynamical drag acts more efficiently on particles of larger size, causing their rapid in-spiralling and accretion onto the central black hole.

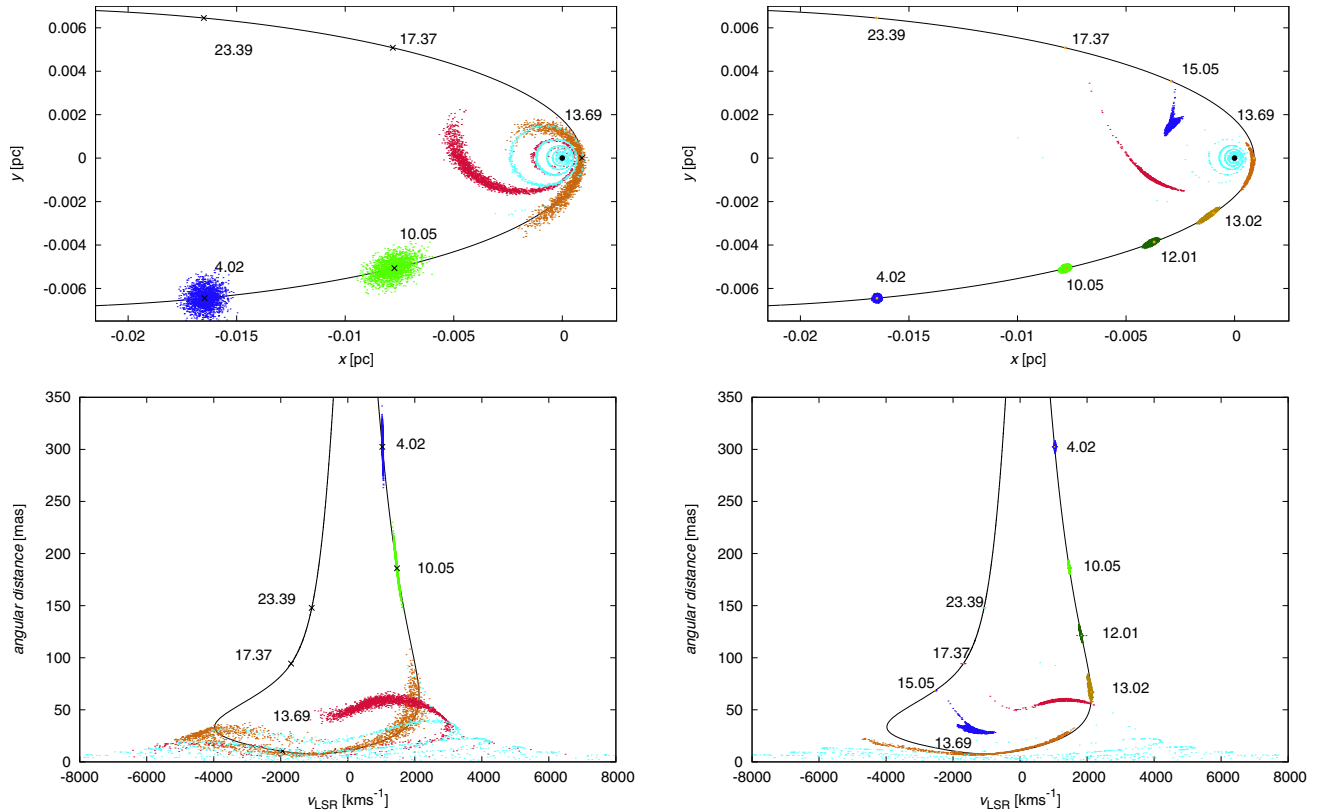


Fig. 7. Numerical representation of the dust/gas cloud in terms of elementary parcels, trajectories of which are integrated in the gravitational field and influenced by the hydrodynamical drag. *Top left:* the evolution of the cloud in the orbital plane for selected epochs since the start of the simulation. Snapshots of the cloud are distinguished by different colours and shown at several moments of time (time marks correspond to years since the initial moment of integration). The cloud particles are characterised by the Gaussian dispersion around the nominal trajectory in the phase space (the black curve). *Bottom left:* representation of the evolution from the *top-left panel* is shown in the velocity-distance plane. The velocity is transformed into the local standard of rest. The angular distance is expressed in milliarcseconds. *Top right:* the evolution as in the *top-left panel*, but for a cloud with an embedded star in the core. *Bottom right:* the track in the velocity-position plane corresponding to the trajectory from the *top-right panel*.

other orbital parameters remained fixed ($M_{\bullet} = 4.4 \times 10^6 M_{\odot}$ for Sgr A* SMBH). Highly eccentric trajectories ($e \gtrsim 0.9$) are prone to a significant mass loss when the atmosphere of the star undergoes the Roche-lobe overflow onto the black hole.

The Hill radius expressed by Eq. (9) employs only tidal shearing. However, in our case the motion of dust is influenced by drag from the wind outflow, and this may indeed decrease the critical radius at which orbits of grains become unstable and

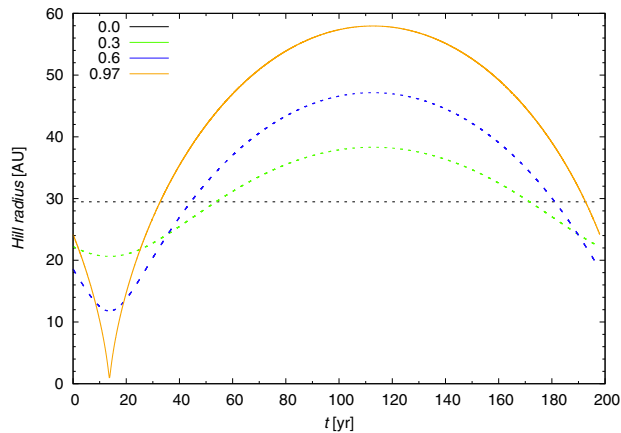


Fig. 8. Critical Hill radius $r_H(t)$ for four different eccentricities: $e = 0.0$, 0.3 , 0.6 , and 0.97 . Enhanced accretion occurs when some of the dust particles move beyond r_H .

consequently leave the circumstellar environment. Following the analysis of [Perets & Murray-Clay \(2011\)](#), we define the wind-truncation radius at which the gravitational acceleration acting on the grain GM_\star/r_\star^2 is equal to the acceleration a_{drag} resulting from the wind drag:

$$r_w = \left(\frac{GM_\star}{a_{\text{drag}}} \right)^{1/2}. \quad (10)$$

After inserting the drag term (7) into (10), we obtain

$$r_w = \left(\frac{GM_\star m}{\eta_{\text{drag}} \pi R^2 \rho_\star (v_{\text{rel}}^2 + \bar{v}_t^2)^{1/2} v_{\text{rel}}} \right)^{1/2}. \quad (11)$$

To derive an estimate, we assumed the Stokes law and rewrote Eq. (11) as a function of grain diameter d and distance from the star r_\star ,

$$r_w(d, r_\star) = \left(\frac{4}{3} \frac{GM_\star}{C_d} \rho_d \right)^{1/2} \left(\frac{d}{\rho_\star v_{\text{rel}}^2} \right)^{1/2}, \quad (12)$$

where both the stellar wind density ρ_\star and the relative velocity of grains with respect to the wind v_{rel} are functions of the distance from the star. We rewrote Eq. (12) into a convenient form, taking $\rho_d = 2260 \text{ kg m}^{-3}$ for the density of dust (e.g., [Barvainis 1987](#)) and assuming the density of spherical wind outflow $\rho_\star = \dot{m}_\star / (4\pi r_\star^2 v_w)$,

$$r_w = 0.28 \left(\frac{M_\star}{M_\odot} \right)^{1/2} \left(\frac{d}{\mu\text{m}} \right)^{1/2} \left(\frac{v_{\text{rel}}}{100 \text{ km s}^{-1}} \right)^{-1} \left(\frac{v_w}{100 \text{ km s}^{-1}} \right)^{1/2} \times \left(\frac{\dot{m}_\star}{10^{-8} M_\odot \text{ yr}^{-1}} \right)^{-1/2} \left(\frac{r_\star}{\text{AU}} \right) \text{ AU}. \quad (13)$$

In Fig. 9, we plot the wind-truncation radius as a function of both the grain diameter (in μm) and the distance from $2 M_\odot$ -star (in AU) with the typical mass-loss rate of $10^{-8} M_\odot \text{ yr}^{-1}$ and the terminal wind speed of 100 km s^{-1} . The wind drag generally causes the stability region to shrink below the Hill radius (in our case $\sim 1 \text{ AU}$ at the pericentre), mainly affecting small grains $\lesssim 1 \mu\text{m}$.

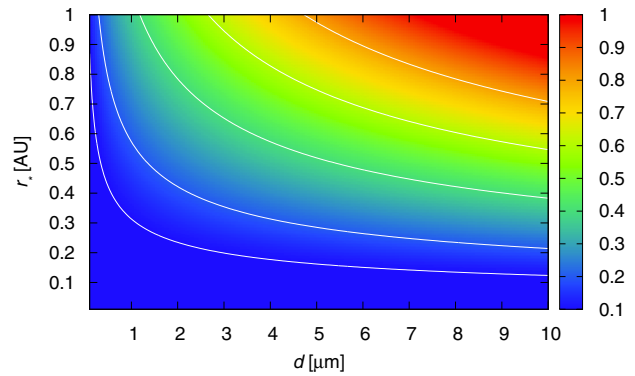


Fig. 9. Colour-coded plot of the wind-truncation radius (colour bar units in AU). Each point in the graph estimates the truncation radius from the equilibrium between gravitational and drag forces for a given distance from the star and a grain diameter. The contours stand for values 0.1 , 0.2 , 0.4 , 0.6 , and 0.8 AU .

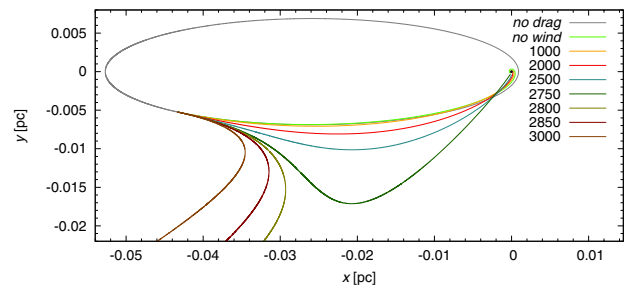


Fig. 10. Trajectory of a single dust grain ($d = 1 \mu\text{m}$) for different cases of the central wind outflow velocity. The grey ellipse corresponds to the nominal trajectory, neglecting the drag by the wind. The values of the outflow velocity are expressed in km s^{-1} in the legend.

3. Results of simulations

3.1. Effects of wind and a bow shock – the case of G2/DSO

Comet-shaped features have been observed near the Galactic centre that point to the role of the radial outflow in the form of a wind from the central region ([Mužić et al. 2010](#)). The source of the wind can be hot stars and/or the accretion flow in the vicinity of the SMBH. A similar effect is expected to occur in our model as well. One of the differences that distinguishes the core-less cloud from a dust-enshrouded star is the size of the bow shock (e.g., [van Marle et al. 2011](#); [Araudo et al. 2013](#)). In the case of a star, the bow shock is formed by the wind interaction; a powerful wind outflow (as in the case of massive stars) develops the stagnation point radius at a much larger radius than the size of the star. On the other hand, in the case of a core-less cloud the bow shock is only slightly larger than the size of the cloud.

We included the radial wind outflow by setting $\mathbf{v}_{\text{rel}} = \mathbf{v} - \mathbf{v}_w$ in Eq. (7), where \mathbf{v} stands for the velocity of numerical particles with respect to the SMBH, and \mathbf{v}_w is the wind velocity (we assumed a spherical outflow at $r \lesssim 1''$). The particles feel the wind drag; the computed trajectories for particles of $d = 1 \mu\text{m}$ are shown in Fig. 10. The initial conditions were the same for all cases and were computed according to the nominal orbital elements of the G2/DSO object. For small and moderate wind velocities ($\lesssim 1000 \text{ km s}^{-1}$), the trajectory is only slightly affected. The time of pericentre passage is delayed and the rate of spiralling inwards increases because there is an additional

Michal Zajačec et al.: Dust-enshrouded star near supermassive black hole

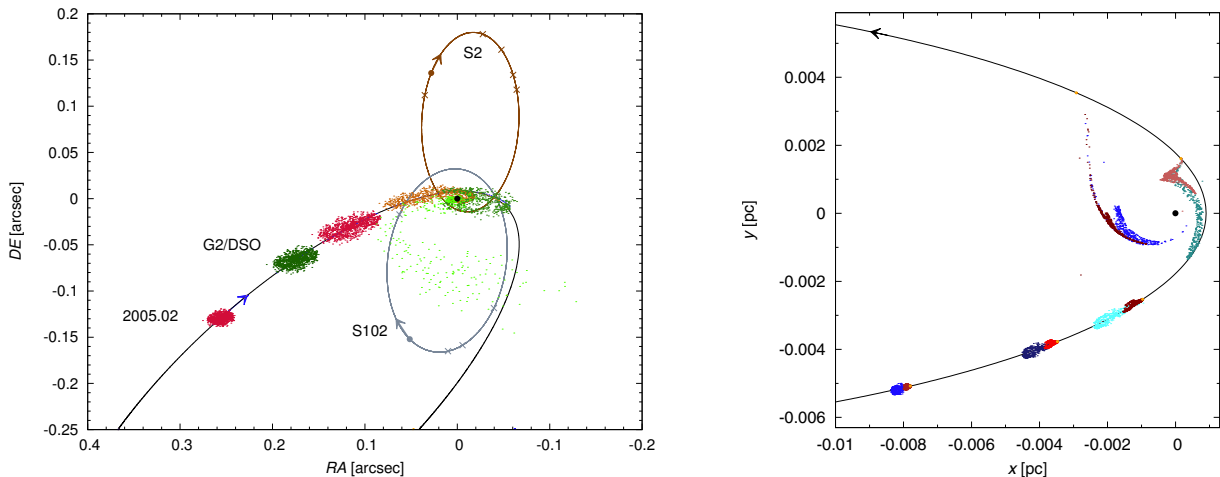


Fig. 11. *Left panel:* a sketch of the orbit orientation on the sky, consistent with the current nominal trajectory of the G2/DSO (i.e., arriving from the south-east direction and going into pericentre from the north, then leaving towards the south-east, showing the offset from the SMBH position in the origin). Two eccentric orbits of the S-stars are also indicated. *Right panel:* two cases of the possible evolution a gaseous/dusty stellar envelope, initially bound to the star: (i) with a radial wind blowing from the centre ($v_w = 1000 \text{ km s}^{-1}$; bluish colours); and (ii) without the outflowing wind (reddish colours). Here the same nominal trajectory as in the left panel is plotted, now with respect to the (x, y) orbital plane. See the text for details.

non-radial term (due to the aberration). For $v_w \gtrsim 2800 \text{ km s}^{-1}$ the particles are blown away with the wind. Mužić et al. (2010) found evidence of the presence of wind speed from the centre that are of this order of magnitude.

Consequently, we compared the evolution of a bound star-gas-dust system with and without the effect of a spherical wind from the centre. Particles ($d = 2.5 \mu\text{m}$) were initially distributed uniformly around the star ($M_\star = 3 M_\odot$ in this example). The range of inclination was set from 0° to 180° , semi-major axes spanned the interval $(0.001, 10) \text{ AU}$, and eccentricities varied from 0 to 0.1. The resulting evolution is plotted in Fig. 11. The wind slows the particles down and the initial shape of the shell is more stretched than in the no-wind case.

If a wind-blowing star moves supersonically through ISM, a bow shock is formed. The effect has also been confirmed at 0.2 pc distance from the Galactic centre (Mužić et al. 2010). Here we employed a two-dimensional model of the bow shock,

$$R(\theta) = R_0 \csc \theta \sqrt{3(1 - \theta \cot \theta)}, \quad (14)$$

which we rotated around the symmetry axis to obtain the correct orientation of the shock in 3D. In Eq. (14), R_0 stands for the stand-off distance, where the ram pressures of the ambient medium and the stellar wind are at balance (Wilkin 1996),

$$R_0 = \left(\frac{\dot{m}_w v_w^\star}{4\pi \rho_a v_{\text{rel}}^2} \right)^{1/2}, \quad (15)$$

where \dot{m}_w is the stellar mass-loss rate, v_w^\star is the terminal velocity of the stellar wind. We used Eq. (2) to find ρ_a , and $v_{\text{rel}} = |\mathbf{v} - \mathbf{v}_w|$ at a specific point on the orbit. The symmetry axis of the bow shock is aligned with the direction of the relative velocity, \mathbf{v}_{rel} , as expected.

We assumed that the wind-blowing star has a spherical wind with the constant magnitude equal to its terminal velocity. In our numerical scheme, particles outside the bow shock feel the drag and wind from the ambient medium near the nucleus. Inside the bow shock, the drag is approximately proportional to the second power of the relative velocity with respect to the circumstellar environment with the radial outflow, and to the

circumstellar density ρ_\star , $\rho_\star = \dot{m}_w / (4\pi r_\star^2 v_w^\star)$. In further examples we used the parameters relevant for a young, low-mass (T Tauri) star (Scoville & Burkert 2013): $\dot{m}_w = 10^{-8} M_\odot \text{ yr}^{-1}$, $v_w^\star = 200 \text{ km s}^{-1}$, but the procedure may be also applied to more evolved stellar types.

Now we also included the effect of the bow shock on the cloud evolution. In our example we set the mass of an embedded star to $M_\star = 2 M_\odot$ and compared two cases (Fig. 12): first, the wind blowing from the centre at velocity of 500 km s^{-1} , and, second, the other case with 1000 km s^{-1} wind. In each, case particles have a uniform distribution of semi-major axes in the interval $(0.1, 50) \text{ AU}$, inclination $(0^\circ, 180^\circ)$, and eccentricity $(0, 0.1)$. We note that the character and orientation of the bow-shock sources can in principle be tested observationally via polarimetry (Buchholz et al. 2013; Valencia-S et al. 2012), although we did not attempt this here.

The evolution is similar in the two cases – the material outside the bow shock spirals towards the SMBH because of the drag, while inside the bow shock the cloud elements continue to move through the circumstellar environment. Figure 12 shows a very narrow shape of the bow shock near the pericentre. At this stage, many particles are torn away from the star, which is enhanced by both stellar wind and the outflow from the centre (see Sect. 2.4). However, a fraction that occupies the bow-shock region continues to orbit. In the case of strong wind from the centre, the particles are dragged more efficiently, so that a long tail forms behind the star. As mentioned above, only a diminishing part of the initial material survives the repeating passages through pericentre. The cloud is progressively stretched and accreted, and its centre drifts away from the position of the embedded star.

We also plot the changing division between the predicted position of the star and the centre of mass of the cloud (Fig. 12, bottom row). The mutual separation tends to grow with time (apart from fluctuations) till the pericentre passage, then decreases again as the fraction of the cloud unbound to the star sublimates or becomes accreted onto the black hole. This offset is expected to be detectable in the NIR band if sufficient resolution is reached to resolve the cloud structure.

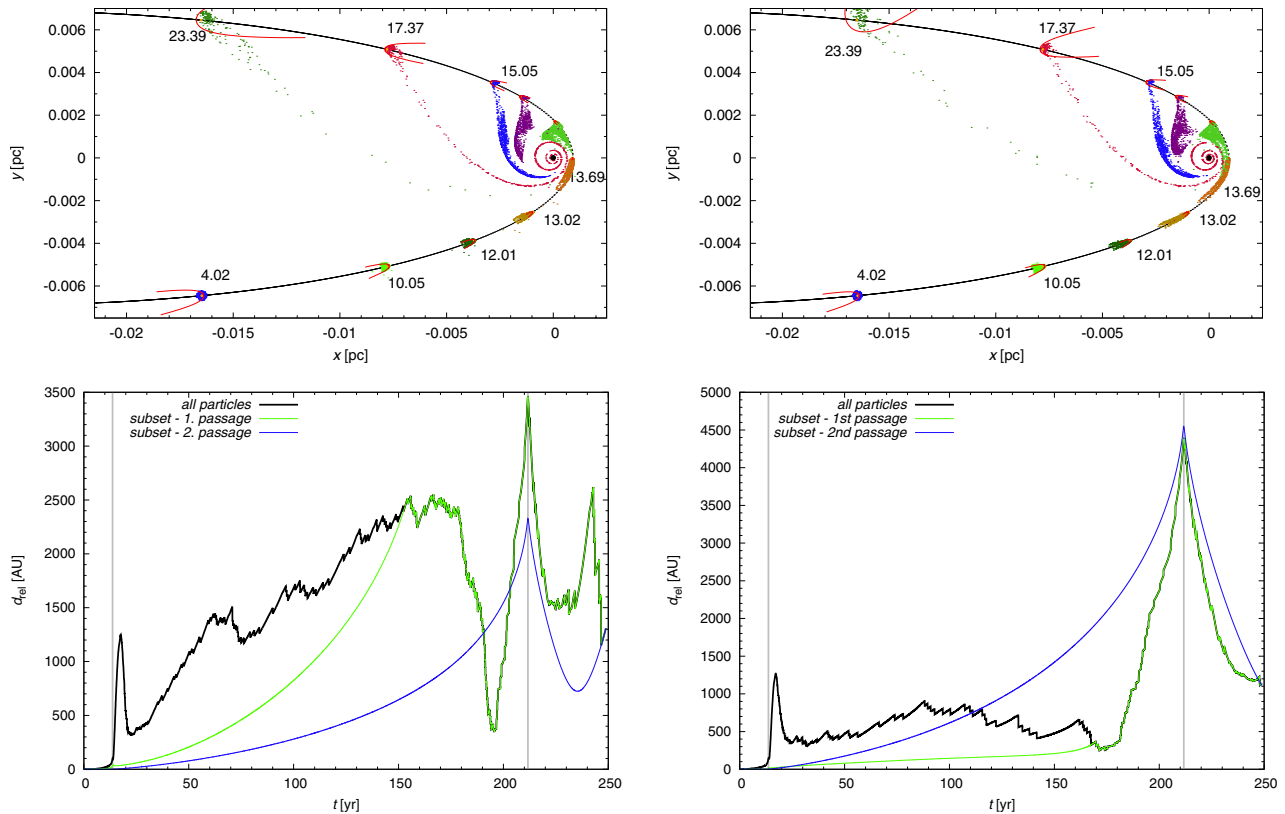


Fig. 12. Evolution of the star with a dusty envelope together with an instantaneous orientation of the bow shock (*top panels*). *Top left*: star mass $M_* = 2 M_\odot$. The velocity of the wind from the centre is $v_w = 500 \text{ km s}^{-1}$. *Top right*: same parameters as in the left panel except for $v_w = 1000 \text{ km s}^{-1}$, showing the change of orientation of the bow shock. In both cases, the mass transfer peaks with a slight delay after the pericentre passage. Corresponding to the two panels in the top row, an offset is shown between the star position along its nominal orbit from the centre of mass of the cloud in the bottom panels. Different curves show the offset computed for all particles forming the cloud (black curve), a subset of particles in the cloud that survive the first passage through the pericentre (green curve), and a subset of those that also survive the second passage. Moments of pericentre passages are indicated by vertical lines. The separation of 1000 AU corresponds to ≈ 0.12 arcsec at the distance to Sgr A*^{*}. *Bottom left*: $v_w = 500 \text{ km s}^{-1}$. *Bottom right*: $v_w = 1000 \text{ km s}^{-1}$.

3.2. Spherical cloud vs. disc-like structure

Near a protostar or T Tauri star, two types of dust/gas environment can be considered: a spherical cloud with an approximately Gaussian distribution in the position-velocity phase space, and a disc-like configuration with a Keplerian distribution of bulk velocity. The latter case represents a protoplanetary or a debris disc. Murray-Clay & Loeb (2012) proposed such a disc as the origin of the cloud near SMBH. We compared the evolution of the two geometries.

In both cases, dust grains are distributed around a $2 M_\odot$ star with the parameters from the previous section. For the Gaussian velocity dispersion cloud, the initial FWHM was taken to be equal to 100 AU (≈ 12 mas) and 5 km s^{-1} , respectively. Particles in the disc were distributed uniformly, with semi-major axes in the range (0.1, 50) AU, low eccentricity in the range (0, 0.1), and inclinations in the range (0, 30°) and (150, 180°) (taking into account both direct and retrograde orbits with respect to the orbit of the star).

In Fig. 13 we plot a typical evolution in the orbital plane for the chosen epochs (*top panels*) as well as the distribution in the position-velocity diagrams (*bottom panels*). These simulations indicate that a Gaussian cloud is not as much affected by the star as the particles in the disc. It is also evident that in case of the disc structure, more particles survive the pericentre passage and continue to orbit the star.

3.3. Fraction of mass influenced at subsequent encounters

High-eccentricity passages are more likely to be non-repeating events if the cloud does not host a body inside its volume (see Fig. 7). The material of the cloud becomes dispersed and largely accreted onto the SMBH at the first pericentre passage. However, in the scenario with a shell surrounding a stellar object, a fraction of material remains bound to the star while only the rest is rerouted towards the black hole. In Table 1, we summarise the typical results of computations of the percentage of the captured material for the first and the subsequent pericentre passages.

As soon as the star/cloud on its trajectory reaches the critical radius for the mass overflow, the percentage of captured mass is high ($\geq 90\%$ at the first pericentre passage). For the Gaussian distribution in the position-velocity phase space, it is near or equal to 100% in both the bow-shock and no-bow-shock cases. When the bow shock is included and particles follow the bulk Keplerian distribution in a disc, more particles remain bound after the first pericentre crossing than the no-bow-shock scheme predicts (the bow-shock region protects some particles from being diverted from the cloud orbit near the pericentre). This is connected with the character of the drag forces on both sides of the bow shock in our model and also agrees with previous results concerning the fate of a pressure supported gas cloud, which appears to be particularly prone to complete destruction near the pericentre. However, one should bear in mind that we work with

Michal Zajaček et al.: Dust-enshrouded star near supermassive black hole

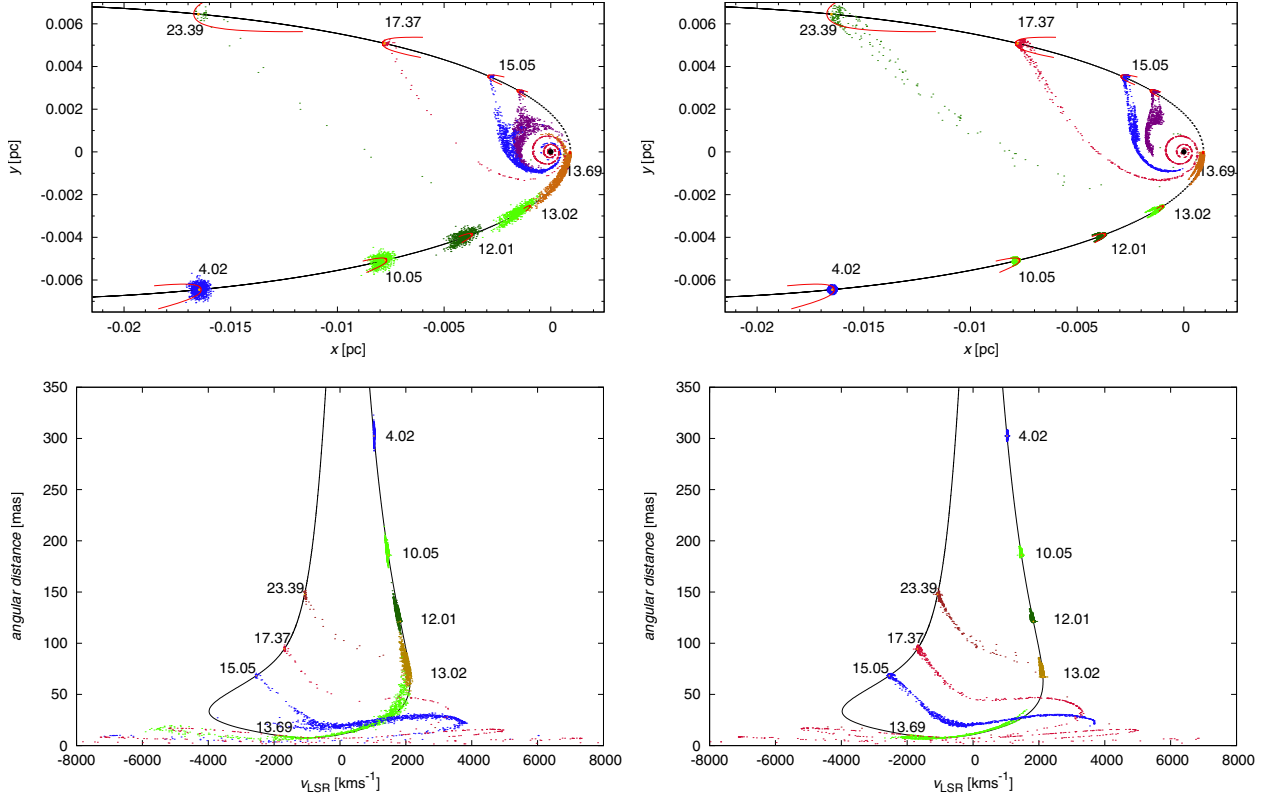


Fig. 13. Analogy to Fig. 7 for the case with the bow-shock. *Top left:* the evolution of an initially spherical Gaussian envelope in the presence of a star for chosen epochs since the start of the simulation. *Bottom left:* representation of the evolution from the *top-left panel* is shown in the velocity-distance plane. The angular distance is expressed in milliarcseconds. *Top right:* as in the *top-left panel*, but for a star-disc system. *Bottom right:* the track in the velocity-position plane corresponds to the trajectory from the *top-right panel*.

Table 1. Typical examples from different runs for the fraction of material deflected from the original trajectory during the first and second pericentre passages (evaluated with respect to the total number of particles in the cloud at the corresponding stage).

Run	Model characteristics				Note	Mass capture [%]	
	Initial distribution	Bow shock	M_*/M_\odot	Grain size [μm]		1st passage	2nd passage
1	disc-like (dr)	no	3	2.5	–	99.2	0.0
2	spherical	no	3	2.5	–	100.0	0.0
3	disc-like (dr)	no	3	2.5	–	99.4	0.0
4	disc-like (dr)	no	3	5	–	99.6	0.0
5	disc-like (dr)	no	2	5	–	99.6	50.0
6	disc-like (dr)	no	2	5	–	99.5	0.0
7	disc-like (dr)	no	3	2.5	(i)	95.2	12.5
8	disc-like (dr)	no	3	2.5	(i), (ii) 1000 km s ⁻¹	94.4	14.3
9	disc-like (dr)	yes	2	2.5	(ii) 500 km s ⁻¹	86.6	83.6
10	disc-like (dr)	yes	2	2.5	(ii) 1000 km s ⁻¹	88.6	58.8
11	spherical	yes	2	2.5	(ii) 500 km s ⁻¹	99.2	100.0
12	disc-like (dr)	yes	2	2.5	(ii) 500 km s ⁻¹	91.3	65.5
13	disc-like (dr)	yes	2	0.6	(ii) 500 km s ⁻¹	91.3	71.3
14	disc-like (dr)	yes	2	0.1	(ii) 500 km s ⁻¹	98.1	100.0
15	disc-like (dr)	yes	2	2.5	(ii) 500 km s ⁻¹	87.3	90.6
16	sphere+disc (dr)	yes	3	2.5	(ii), 1000 km s ⁻¹ , rad	93.3	68.7
17	disc-like (d)	yes	2	2.5	(ii), 1000 km s ⁻¹ , rad	88.6	74.8
18	disc-like (r)	yes	2	2.5	(ii), 1000 km s ⁻¹ , rad	90.6	89.8

Notes. Columns of model characteristics specify the initial distribution of particle positions and velocities (disc-like Keplerian vs. spherical Gaussian), presence or absence of the bow-shock effect and wind, assumed mass of the star in the cloud core, and size of the dust grains. (i) dust region extending from $r = 0.001$ AU; (ii) central outflow wind v_w included; “rad” denotes radiation pressure from the star; (d, r, dr) denotes only direct orbits, only retrograde orbits, and both, respectively. Additional (non-essential) parameter is the number of numerical particles in each run (typically of the order of 10^3).

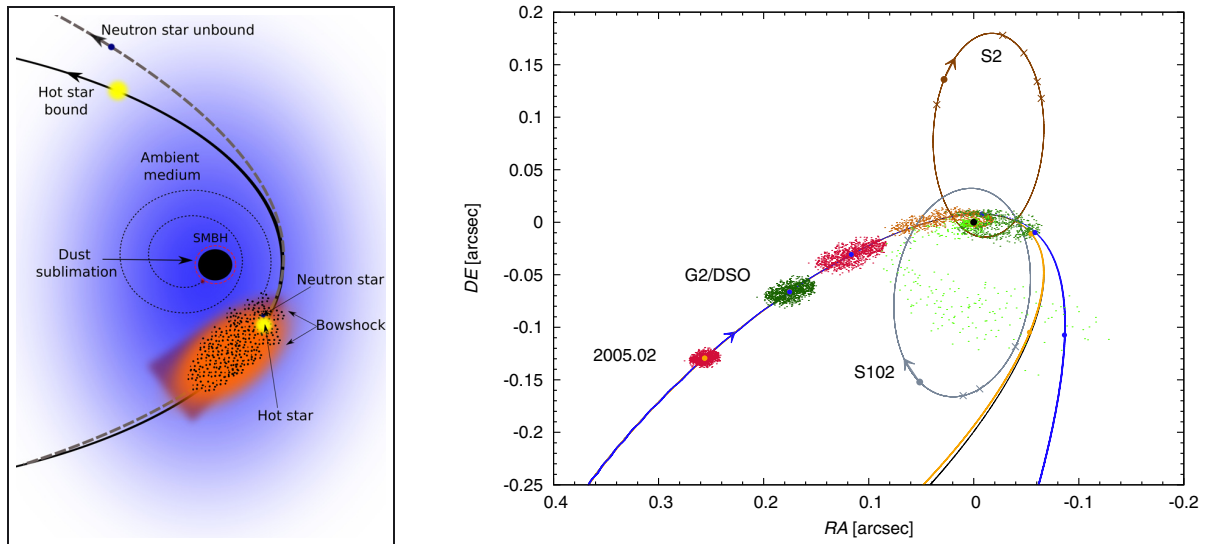


Fig. 14. Sketch of the model geometry for a binary with a common envelope (in the left panel) and the orientation consistent with the G2/DSO nominal trajectory on the sky (in the right panel). The two components (i.e., hot star+neutron star in this example) deviate from each other, the first one being bound and the other one unbound at the moment of pericentre passage. The cloud is then dispersed in the ambient medium and eventually accreted onto the SMBH.

a four-parametric model. At the second pericentre passage, the total amount of the captured material is generally much smaller than at the first passage, nevertheless, the percentage fluctuates significantly in terms of the immediate mass of the cloud.

We also tested a potential difference between the stability of direct (prograde) and retrograde discs. From the classical three-body theory, one can derive the difference between the critical Hill radii of direct and retrograde orbits, r_d and r_r , respectively, resulting from the Coriolis term (Innanen 1979):

$$\frac{r_r}{r_d} = \left[\frac{5 + e + 2(4 + e)^{1/2}}{3 + e} \right]^{2/3}, \quad (16)$$

which leads to the ratio of $r_r/r_p \approx 1.9$ for the eccentricity $e \approx 1$, which is our case. Hence, retrograde discs may not be as truncated as direct discs; the upper limit to the prolongation of their critical radius is the factor of ~ 1.9 . This is consistent with our test runs involving only gravity. A direct disc around a $2-M_\odot$ star with the semi-major axes in the range (0.05, 10) AU, low inclinations (0, 10) $^\circ$, and low eccentricities (0, 0.01) dissolves after one revolution after the first pericentre passage, forming families of orbits along the original trajectory and trajectories with smaller semi-major axes, with some particles escaping the system. A few of them remain in orbit of the star inside the Hill radius. A retrograde disc with the same distribution of orbital elements remains more compact and detached particles spread mostly along the original trajectory. However, when drag forces from both the stellar wind and the central outflow are involved, there is no difference in terms of stability between direct and retrograde discs (see runs 17 and 18 in Table 1). This is because the stability of discs is no longer determined by the gravitational Hill radius, but by the smaller wind-truncation radius (see Sect. 2.4).

These results demonstrate that in the most cases the stellar envelope is significantly affected around the pericentre, and the diverted part eventually becomes largely dispersed during the accretion event. The outcome is similar to the case of a gaseous cloud, treated in the hydrodynamical regime (Anninos et al. 2012; Burkert et al. 2012), although a small fraction of the dusty envelope can survive to the following revolution.

3.4. Binary embedded within common envelope

The high eccentricity of the G2/DSO trajectory suggests that it might be possible to connect this object with hypothetical events of the three-body interaction (Hills 1988) involving the SMBH as the origin of stars on bound orbits near SMBH (Gould & Quillen 2003, see Fig. 14). In this tentative scenario a binary system is disrupted during the pericentre passage. As a result of this interaction, one of the remnant bodies remains on a circularised orbit, whereas the other component gains orbital energy and is ejected (Löckmann et al. 2008; Bromley et al. 2012). For realistic estimates of disruption rates, see Perets et al. (2007).

Might the infalling cloud contain such a binary stellar system? The initial eccentric trajectory of the binary centre of mass was set in agreement with the infalling cloud within which it remain embedded. The orbital parameters of the binary system are expected to be disturbed at the moment of close encounter with the SMBH and the observational resolution about the nature of the object should emerge soon after the pericentre passage. We can illustrate two qualitatively different options for the possible outcome of the post-pericentre evolution: (i) both components remain bound to the SMBH; (ii) one component is ejected from the system on a hyperbolic trajectory at the expense of the orbital energy of the other component.

For each case we performed a number of simulations with a different setup of free parameters, namely, the masses $M_\star^{(i)}$ of the two components and the osculating elements of the embedded binary system. The primary component $M_\star^{(1)}$ represents a hot, wind-blowing star, the secondary $M_\star^{(2)}$ is thought to be a neutron star (for definiteness of the simulation). The gaseous-dusty envelope enshrouding the whole binary was modelled in the same way as in previous examples, that is, in terms of dust particles that experience the hot atmosphere of the SMBH, the stellar wind from the primary and the bow-shock effect. The initial conditions and parameters are summarised in Table 2. In general, the fraction of cloud initial mass that is retained after the pericentre passage is diminished by the presence of the binary star in the core compared with an otherwise similar set-up with a single stellar object embedded inside.

Michal Zajaček et al.: Dust-enshrouded star near supermassive black hole

Table 2. Two exemplary cases of an embedded binary evolution.

Parameter	Case A	Case B
Mass of the binary components [M_{\odot}]	4.0 1.4	3.0 1.4
True anomaly [$^{\circ}$]	120.0	80.0
Semi-major axis [AU]	3.0	2.0
Eccentricity	0.05	0.05
\dot{m}_w [$M_{\odot} \text{ yr}^{-1}$]		10^{-7}
v_c [km s^{-1}]		500
v_w^* [km s^{-1}]		700

Notes. The true anomaly is the initial value, \dot{m}_w stands for the mass-loss rate. Additional wind parameters v_c and v_w^* denote the terminal velocities of the assumed spherical wind from the centre and the star, respectively. In these examples we performed integration runs with 1000 numerical particles representing the material of an initially spherical cloud, whereas the circumbinary disc population consisted of 500 particles with semi-major axes uniformly distributed from 10 AU to 50 AU, inclinations up to 30° , and eccentricities ranging from 0.0 to 0.1. The spherical cloud population adopts a Gaussian distribution in the phase space with the initial FWHMs of 12.5 mas and 5 km s^{-1} . In both examples, the integration starts at the true anomaly of -167° for the barycentre position.

In Fig. 15 we show the distance-velocity plots, the temporal evolution of the binary semimajor axis a , and eccentricity e . At the pre-pericentre phase, the components orbit the common centre of mass, while at the pericentre they become unbound with respect to each other and start to move independently with different semi-major axes and eccentricities. We note, however, that this is a multi-parametric system where the outcome of the evolution depends on a mutual interplay of different parameters.

The disruption event occurs when the secondary is outside the tidal-shearing radius, which may be again estimated using the Hill radius of the primary, Eq. (9). For cases A and B, we derived $r_H \sim 1.3 \text{ AU}$ and $\sim 1.2 \text{ AU}$, respectively. Following the discussion in the previous subsection, the disruption radius for the binary orbiting the black hole approximated by Eq. (9) is effectively enlarged if the secondary orbits the primary in a retrograde sense.

The observation of a single event of the binary disruption while passing close to the SMBH is improbable and should be regarded only as a speculative scenario. However, other proposed scenarios for the G2/DSO infrared source, such as isothermal clouds or the disruption of a star, are also rare given the rate at which streams and winds collide or stars disrupt to produce such a cloud. Moreover, the nature of the binary content in the Galactic centre is still unclear (Antonini & Perets 2012). Hence, all the estimates of binary replenishment in the central region are crude. The binary scenario can be easily rejected/confirmed by observations based on the post-pericentre evolution of the trajectory of the G2/DSO infrared source.

4. Discussion

We examined the pericentre passages and gradual destruction of dusty envelopes of stars that move supersonically through the immediate vicinity of the SMBH. Motivation for this topic arises because stars are shown to interact with the ionised medium close to Sgr A*, forming bow-shock structures (e.g., Mužić et al. 2010, and references therein). Here we focused on stars with a significant dust content that interacts with an optically thin wind

outflow. Examples of such stars may also be found in the disc population of the Galaxy, specifically Herbig Ae/Be-type stars, see for instance Boersma et al. (2009).

The potential importance of the subject is heightened by the current passage of the infrared-excess G2/DSO source near Sgr A*. We focused on stellar-origin scenarios in which a star is enshrouded by a dusty shell. We revisited a simplified core-less scenario for comparisons of time scales and position-velocity distributions, although we did not perform detailed hydrodynamical simulations. The adopted approach is in several aspects complementary to hydrodynamical and MHD schemes, and it appears relevant for exploration of the dust component. We computed the evolution in the presence of the star and the SMBH and also included additional effects within an approximation:

- hydrodynamical drag due to the plasma environment in the SMBH inner accretion zone;
- radially directed wind outflowing from the centre;
- wind-shearing in the immediate circumstellar environment;
- bow-shock formation due to supersonic motion through the ISM.

We plotted the results showing the shape of a Keplerian disc-like system and a Gaussian envelope at different epochs. We computed the line-of-sight velocities (transformed to the local standard of rest) and the angular distance-velocity plots.

The idea of stars embedded in clouds of gas and dust does not have to be limited to our Galaxy. It has been explored by various authors (e.g., Zurek et al. 1994; Armitage et al. 1996; Šubr & Karas 1999; Vilkoviskij & Czerny 2002, and references therein) in the context of repetitive interactions of stars of the nuclear cluster with the material of the accretion disc or a dusty torus in AGN.

The mini-spiral of the Galactic centre is a potential source of matter for infalling clouds. This structure contains a mixture of hot, warm, and cold phases. Under such conditions the accreted medium consists of complex plasma with a non-negligible content of dust (Chan et al. 1997). Located at a distance about 0.1–0.2 pc (projected distance $\sim 0.06 \text{ pc}$) from the supermassive black hole, this feature can be understood as consisting of three independent clumpy streams of mainly gaseous material at roughly Keplerian motion around the centre (Zhao et al. 2010; Kunneriath et al. 2012). The streams collide, and their mutual interaction may cause the loss of angular momentum and an occasional inflow of the clumpy material towards the black hole (Paumard et al. 2005; Czerny et al. 2013a). In this scenario, the distribution of angular momentum determines the probability of setting the clouds on a plunging orbit (Czerny et al. 2013b).

One can thus expect that the current example of G2/DSO in the centre of the Milky Way may be a signature of a common mechanism that transports the gaseous clumpy medium and stars to the immediate vicinity of the central SMBH on sub-parsec scales.

5. Conclusions

We modelled the fate of an infalling star with an extended envelope near the SMBH. The complex medium was treated in terms of numerical particles with their mass and size as parameters, interacting with the ambient environment. The mass of dust particles is typically large enough so that the gravitational influence on the grains needs to be taken into account close to the SMBH and the mass-losing star.

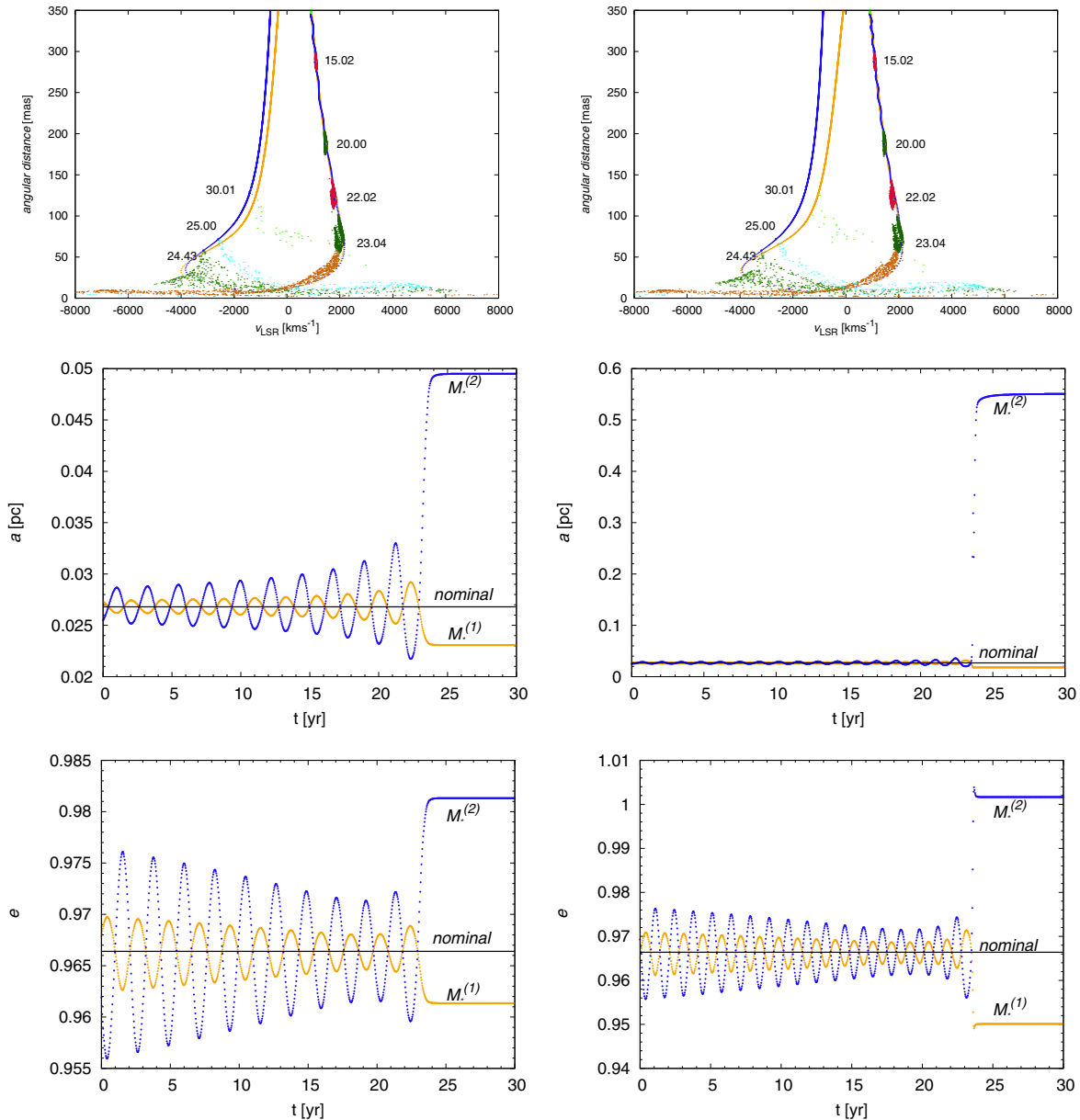


Fig. 15. Evolution of the cloud with an embedded binary, components of which become unbound via the three-body interaction at the pericentre passage near the central SMBH. The initial trajectory of the binary barycentre corresponds to the nominal trajectory of the G2/DSO (black solid line), whereas the post-pericentre stage depends strongly on the path of the individual components emerging from the system. Two exemplary cases are shown in different columns, corresponding to the choice of the component masses $M_\star^{(i)}$. *Left panel:* $M_\star^{(1)} = 4.0 M_\odot$, $M_\star^{(2)} = 1.4 M_\odot$. *Right panel:* $M_\star^{(1)} = 3.0 M_\odot$, $M_\star^{(2)} = 1.4 M_\odot$.

We assumed an orbit pericentre of the order of $10^3 r_s$, so that the star itself was not tidally disrupted. However, the surrounding cloud was affected very significantly (core-less clouds are influenced even more, and they are basically destroyed on the first encounter with the black hole). We noticed a significant mass-loss from the cloud at the first pericentre passage in all considered cases ($\geq 90\%$). During the second passage the mass loss fluctuates. In other words, if the star is enshrouded in a dusty shell before the first pericentre passage, it becomes stripped of most of the envelope, unless the material is continuously replenished. If a binary star is embedded within the envelope, there is a chance that the two components separate during the pericentre passage, revealing the nature of the cloud core.

During the pericentre passage, the centre of mass of the cloud separates from the stellar core inside the cloud, but then it returns to the star as the unbound particles are destroyed by sublimation or become accreted onto the black hole. The presence of the bow shock around a star somewhat diminishes the amount of captured particles (Table 1), and a greater fraction of the cloud can survive to the following pericentre passage. On the other hand, the presence of a binary tends to dissolve the cloud more efficiently at the moment of close encounter with the SMBH. The characteristics of motion across the bow shock depend strongly on parameters, mainly the mass-loss rate and the stellar-wind velocity, so the predictions are uncertain and the outcome of the simulations vary. In addition, there are still

Michal Zajaček et al.: Dust-enshrouded star near supermassive black hole

uncertainties in the density and temperature profiles of the flow near the Galactic centre. However, the comparison of our simulations with post-pericentre observations can help to set better constraints.

Acknowledgements. We thank Miroslav Brož for discussions and help with the Swift integration package. We are grateful to Hagai B. Perets and Ladislav Šubr for critical, constructive comments. The research leading to these results has received funding from the student grant of the Charles University in Prague (GAUK 879113), and the collaboration project of the Czech Science Foundation and Deutsche Forschungsgemeinschaft (GACR-DFG 13-00070J). The Astronomical Institute has been operated under the program RVO:67985815 in the Czech Republic.

References

- Abramowicz, M. A., Czerny, B., Lasota, J. P., & Szuszkiewicz, E. 1988, *ApJ*, 332, 646
- Anninos, P., Fragile, P. C., Wilson, J., & Murray, S. D. 2012, *ApJ*, 759, 132
- Antonini, F., & Perets, H. B. 2012, *ApJ*, 757, 27
- Antonucci, R. 1993, *ARA&A*, 31, 473
- Araudo, A. T., Bosch-Ramon, V., & Romero, G. E. 2013, *MNRAS*, 436, 3626
- Armitage, P. J., Zurek, W. H., & Davies, M. B. 1996, *ApJ*, 470, 237
- Ballone, A., Schartmann, M., Burkert, A., et al. 2013, *ApJ*, 776, 13
- Barai, P., Proga, D., & Nagamine, K. 2012, *MNRAS*, 424, 728
- Barvainis, R. 1987, *ApJ*, 320, 537
- Bertotti, B., Farinella, P., & Vokrouhlický, D. 2003, *Physics of the Solar System – Dynamics and Evolution, Space Physics, and Spacetime Structure, Astrophys. Space Sci. Lib.*, 293,
- Boersma, C., Peeters, E., Martín-Hernández, N. L., et al. 2009, *A&A*, 502, 175
- Broderick, A. E., & Loeb, A. 2006, *ApJ*, 636, L109
- Broderick, A. E., Fish, V. L., Doelman, S. S., & Loeb, A. 2011, *ApJ*, 738, 38
- Bromley, B. C., Kenyon, S. J., Geller, M. J., & Brown, W. R. 2012, *ApJ*, 749, L42
- Buchholz, R. M., Witzel, G., Schödel, R., & Eckart, A. 2013, *A&A*, 557, A82
- Burkert, A., Schartmann, M., Alig, C., et al. 2012, *ApJ*, 750, 58
- Chan, K.-W., Moseley, S. H., Casey, S., et al. 1997, *ApJ*, 483, 798
- Cox, D. P. 2005, *ARA&A*, 43, 337
- Czerny, B., & Hryniewicz, K. 2011, *A&A*, 525, L8
- Czerny, B., Karas, V., Kunneriath, D., & Das, T. K. 2013a, in *IAU Symp.*, eds. C. M. Zhang, T. Belloni, M. Méndez, & S. N. Zhang (Cambridge: Cambridge University Press), 290, 199
- Czerny, B., Kunneriath, D., Karas, V., & Das, T. K. 2013b, *A&A*, 555, A97
- Davidson, J. A., Werner, M. W., Wu, X., et al. 1992, *ApJ*, 387, 189
- Dexter, J., Agol, E., Fragile, P. C., & McKinney, J. C. 2010, *ApJ*, 717, 1092
- Eckart, A., & Genzel, R. 1996, *Nature*, 383, 415
- Eckart, A., Schödel, R., & Straubmeier, C. 2005, *The Black Hole at the Center of the Milky Way* (London: Imperial College Press)
- Eckart, A., Britzen, S., Horrobin, M., et al. 2013a, in *Nuclei of Seyfert Galaxies and QSOs, Proc. Sci.*, 004
- Eckart, A., Horrobin, M., Britzen, S., et al. 2013b [[arXiv:1311.2753](https://arxiv.org/abs/1311.2753)]
- Eckart, A., Mužić, K., Yazici, S., et al. 2013c, *A&A*, 551, A18
- Field, G. B. 1965, *ApJ*, 142, 531
- Frank, J., King, A., & Raine, D. J. 2002, *Accretion Power in Astrophysics: 3rd edn.* (Cambridge: Cambridge University Press)
- Genzel, R., Eisenhauer, F., & Gillessen, S. 2010, *Rev. Mod. Phys.*, 82, 3121
- Ghez, A. M., Klein, B. L., Morris, M., & Becklin, E. E. 1998, *ApJ*, 509, 678
- Gillessen, S., Genzel, R., Fritz, T. K., et al. 2012, *Nature*, 481, 51
- Gillessen, S., Genzel, R., Fritz, T. K., et al. 2013a, *ApJ*, 763, 78
- Gillessen, S., Genzel, R., Fritz, T. K., et al. 2013b, *ApJ*, 774, 44
- Gould, A., & Quillen, A. C. 2003, *ApJ*, 592, 935
- Hills, J. G. 1988, *Nature*, 331, 687
- Hönig, S. F., & Kishimoto, M. 2010, *A&A*, 523, A27
- Hopman, C., & Alexander, T. 2006, *ApJ*, 645, 1152
- Innanen, K. A. 1979, *AJ*, 84, 960
- Keppens, R., van Marle, A. J., & Meliani, Z. 2012, in *Numerical Modeling of Space Plasma Flows*, eds. N. V. Pogorelov, J. A. Font, E. Audit, & G. P. Zank, *ASP Conf. Ser.*, 459, 73
- Kishimoto, M., Hönig, S. F., Antonucci, R., et al. 2011, *A&A*, 536, A78
- Krishna Swamy, K. S. 2005, *Dust in the Universe: Similarities and Differences, World Scientific Series in Astronomy and Astrophysics*, 7 (Singapore: World Scientific Publishing)
- Krolik, J. H. 1999, *Active Galactic Nuclei: From the Central Black Hole to the Galactic Environment* (Princeton: Princeton University Press)
- Krolik, J. H., & Begelman, M. C. 1988, *ApJ*, 329, 702
- Kunneriath, D., Eckart, A., Vogel, S. N., et al. 2012, *A&A*, 538, A127
- Kwok, S. 1975, *ApJ*, 198, 583
- Levison, H. F., & Duncan, M. J. 1994, *Icarus*, 108, 18
- Löckmann, U., Baumgardt, H., & Kroupa, P. 2008, *ApJ*, 683, L151
- MacGregor, K. B., & Stencel, R. E. 1992, *ApJ*, 397, 644
- Meier, D. L. 2012, *Black Hole Astrophysics: The Engine Paradigm* (Berlin: Springer)
- Melia, F. 2007, *The Galactic Supermassive Black Hole* (Princeton: University Press)
- Moultaka, J., Eckart, A., Schödel, R., Viehmann, T., & Najarro, F. 2005, *A&A*, 443, 163
- Murray-Clay, R. A., & Loeb, A. 2012, *Nature Commun.*, 3
- Mužić, K., Eckart, A., Schödel, R., et al. 2010, *A&A*, 521, A13
- Narayan, R., & McClintock, J. E. 2008, *New Astron. Rev.*, 51, 733
- Paumard, T., Maillard, J.-P., & Morris, M. 2005, in *Growing Black Holes: Accretion in a Cosmological Context*, eds. A. Merloni, S. Nayakshin, & R. A. Sunyaev (Berlin: Springer), 197
- Perets, H. B., Hopman, C., & Alexander, T. 2007, *ApJ*, 656, 709
- Perets, H. B., & Murray-Clay, R. A. 2011, *ApJ*, 733, 56
- Phifer, K., Do, T., Meyer, L., et al. 2013, *ApJ*, 773, L13
- Psaltis, D. 2012, *ApJ*, 759, 130
- Quataert, E. 2004, *ApJ*, 613, 322
- Śądowski, A., Narayan, R., Sironi, L., & Özel, F. 2013, *MNRAS*, 433, 2165
- Scoville, N., & Burkert, A. 2013, *ApJ*, 768, 108
- Shakura, N. I., & Sunyaev, R. A. 1973, *A&A*, 24, 337
- Shcherbakov, R. V. 2014, *ApJ*, 783, 31
- Šubr, L., & Karas, V. 1999, *A&A*, 352, 452
- Šubr, L., & Karas, V. 2005, *A&A*, 433, 405
- Urry, C. M., & Padovani, P. 1995, *PASP*, 107, 803
- Valencia-S, M., Bursa, M., Karssen, G., et al. 2012, *J. Phys. Conf. Ser.*, 372, 012073
- van Marle, A. J., Meliani, Z., Keppens, R., & Decin, L. 2011, *ApJ*, 734, L26
- Vilkoviskij, E. Y., & Czerny, B. 2002, *A&A*, 387, 804
- Vladimirov, S. V., Ostriker, K., & Samarina, A. A. 2005, *Physics and Applications of Complex Plasmas* (London: Imperial College Press)
- Wilkin, F. P. 1996, *ApJ*, 459, L31
- Zhao, J.-H., Blundell, R., Moran, J. M., et al. 2010, *ApJ*, 723, 1097
- Zurek, W. H., Siemiginowska, A., & Colgate, S. A. 1994, *ApJ*, 434, 46

A young accreting star close to the SMBH

Continued monitoring of the DSO/G2 NIR-excess source has revealed recombination emission lines of helium and hydrogen, namely HeI and Bry line. In the paper by [Valencia-S. et al. \(2015\)](#), we detected a rather compact, single-peak Bry emission line at each epoch, both before and after the peribothron passage. This finding was in contradiction with the dynamical evolution of a core-less cloud, where both the red-shifted and blue-shifted component were expected to be detected simultaneously during the peribothron passage.

Given these findings, we proposed a model of young, accreting star embedded in an optically thick dusty envelope. I analysed several plausible sources of Bry emission, taking into account the spatial compactness and the inferred large line width of the order of several 100 km s^{-1} . A potential source that could explain both the inferred luminosity as well as the line width is the inner portion of a circumstellar accretion disc that is truncated by magnetic field lines. The gas is channeled along the lines of force and hits the stellar surface, gets shocked and emits the continuum that is revealed in UV/optical continuum excess. Since the accreted gas reaches nearly free-fall velocities of several 100 km s^{-1} , it can explain the width of observed Bry line. Other possible sources for Bry line within the framework of the magnetospheric accretion model are disc winds, a disc jet, or a shocked stellar wind.

In my model calculations, I focused on the poloidal velocity profile of gas that is channelled along the magnetic field lines and the associated emission measure of the Bry emission. My contribution to the paper by [Valencia-S. et al. \(2015\)](#) is mainly summarized in Section 4.5 “The DSO as a Young Accreting Star” and Section 5 “Possible origin, stability, and the fate of the DSO”.

Credit: Valencia-S., Eckart, Zajaček et al., ApJ 800, 125 (2015). Reproduced with permission ©American Astronomical Society.

MONITORING THE DUSTY S-CLUSTER OBJECT (DSO/G2) ON ITS ORBIT TOWARD
THE GALACTIC CENTER BLACK HOLE

M. VALENCIA-S.¹, A. ECKART^{1,2}, M. ZAJAČEK^{1,2,3}, F. PEISSKER¹, M. PARSA¹, N. GROSSO⁴, E. MOSSOUX⁴, D. PORQUET⁴,
B. JALALI¹, V. KARAS³, S. YAZICI¹, B. SHAHZAMANIAN¹, N. SABHA¹, R. SAALFELD¹, S. SMAJIC¹, R. GRELLMANN¹, L. MOSER¹,
M. HORROBIN¹, A. BORKAR¹, M. GARCÍA-MARÍN¹, M. DOVČIAK³, D. KUNNERIATH³, G. D. KARSEN¹, M. BURSA³,
C. STRAUBMEIER¹, AND H. BUSHOUSE⁵

¹ I. Physikalisches Institut der Universität zu Köln, Zùlpicher Strasse 77, D-50937 Köln, Germany; mvalencias@ph1.uni-koeln.de

² Max-Planck-Institut für Radioastronomie, Auf dem Hügel 69, D-53121 Bonn, Germany

³ Astronomical Institute of the Academy of Sciences Prague, Boční II 1401/1a, CZ-141 31 Praha 4, Czech Republic

⁴ Observatoire Astronomique de Strasbourg, Université de Strasbourg, CNRS, UMR 7550, 11 Rue de l'Université, F-67000 Strasbourg, France

⁵ Space Telescope Science Institute, Baltimore, MD 21218, USA

Received 2014 October 30; accepted 2014 December 27; published 2015 February 18

ABSTRACT

We analyze and report in detail new near-infrared (1.45–2.45 μm) observations of the Dusty S-cluster Object (DSO/G2) during its approach to the black hole at the center of the Galaxy that were carried out with the ESO Very Large Telescope/SINFONI between 2014 February and September. Before 2014 May we detect spatially compact Br γ and Pa α line emission from the DSO at about 40 mas east of Sgr A*. The velocity of the source, measured from the redshifted emission, is $2700 \pm 60 \text{ km s}^{-1}$. No blueshifted emission above the noise level is detected at the position of Sgr A* or upstream of the presumed orbit. After May we find spatially compact Br γ blueshifted line emission from the DSO at about 30 mas west of Sgr A* at a velocity of $-3320 \pm 60 \text{ km s}^{-1}$ and no indication for significant redshifted emission. We do not detect any significant extension of the velocity gradient across the source. We find a Br γ line FWHM of $50 \pm 10 \text{ \AA}$ before and $15 \pm 10 \text{ \AA}$ after the peribothron transit, i.e., no significant line broadening with respect to last year is observed. Br γ line maps show that the bulk of the line emission originates from a region of less than 20 mas diameter. This is consistent with a very compact source on an elliptical orbit with a peribothron time passage in 2014.39 ± 0.14 . For the moment, the flaring activity of the black hole in the near-infrared regime has not shown any statistically significant increment. Increased accretion activity of Sgr A* may still be upcoming. We discuss details of a source model according to which the DSO is a young accreting star rather than a coreless gas and dust cloud.

Key words: astrometry – black hole physics – Galaxy: center – line: identification – line: profiles – techniques: imaging spectroscopy

1. INTRODUCTION

Recently, the Galactic center region has attracted a lot of attention owing to the fact that a dusty object has been detected (Gillessen et al. 2012, 2013a; Eckart et al. 2013) that is approaching the central supermassive black hole (SMBH) associated with the radio source Sgr A*. As a result of its infrared (IR) excess and as indicated through nomenclature (G2) it has been speculated that the source consists of a dominant fraction of gas and dust (Gillessen et al. 2012, 2013a; Pfuhl et al. 2015). By now the object is expected to have passed through its peribothron and tidal disruption, and intense accretion events have been predicted. Eckart et al. (2013) show a possible spectral decomposition of this source using the *M*-band measurement by Gillessen et al. (2012). Depending on the relative stellar and dust flux density contributions, the *M*-band measurement is consistent with a dust temperature of 450 K and an integrated luminosity of up to $\sim 10 L_{\odot}$. This allows for a substantial stellar contribution in mass and reddened stellar luminosity. A stellar nature is also favored by many other authors (see also Murray-Clay & Loeb 2012; Scoville & Burkert 2013; Ballone et al. 2013; Phifer et al. 2013; Zajaček et al. 2014). We will therefore refer to it in the following as a Dusty S-cluster Object, or DSO (Eckart et al. 2013). Hence, although the Br γ line emission may be dominated by optically thin emission, a contribution from more compact optically thick regions cannot be excluded. Also, it is uncertain how large the extinction toward the center of the

gas cloud really is. Therefore, the total mass of the object is very uncertain but is presumably less than that of a typical member of the high-velocity S-star cluster (i.e., $\lesssim 20 M_{\odot}$; Ghez et al. 2003; Eisenhauer et al. 2005; Martins et al. 2006). The compactness of the DSO is also supported by the recent *L*-band detection close to peribothron (Ghez et al. 2014; Witzel et al. 2014).

Gillessen et al. (2013a, 2013b) and Pfuhl et al. (2015) report that the Br γ luminosity of the DSO has remained constant over the entire time range covered by spectroscopy from 2004 to 2013. Figures 1 and 5 in Pfuhl et al. (2015) show that in their 2014 April data set the blue line emission is approximately as spatially compact as the red side and has a significantly stronger peak emission than the red line emission. Their derived integrated Br γ luminosities for the blue side are about 1.14 times brighter than those for the red side (Section 3.2 in Pfuhl et al. 2015).

During the past year we have obtained a substantial, independent imaging spectroscopy data set using SINFONI at the ESO Very Large Telescope (VLT). In addition, we have re-reduced a large number of data sets available from the ESO archive and have used our own and published positional data to reestimate the orbit of the DSO. Here we present the results of this detailed investigation. The paper is organized in the following way: in Sections 2 and 3 we present the observations and data reduction, including the analysis of the spectral line properties of the DSO. In Section 4 we discuss the results, including the orbit (Section 4.1), the tidal interaction of the DSO with Sgr A*

(Section 4.2) and the ambient medium (Section 4.3), consequences for the flare activity (Section 4.4), and the interpretation of the DSO as a possible pre-main-sequence star (Section 4.5). After discussing the origin and fate of the DSO in Section 5, we summarize and conclude in Section 6.

2. OBSERVATIONS AND DATA REDUCTION

Here we present the data sets we are using in the study of the DSO. The procedures for data reduction and data quality selection are also described. We report mainly on the observations⁶ we conducted from 2014 February to September. We use earlier archive data to discuss general properties like the DSO orbit.

2.1. The 2014 Data Set

We performed near-IR (NIR) integral field observations of the Galactic center using SINFONI at the VLT in Chile (Eisenhauer et al. 2003; Bonnet et al. 2004). The instrument is an image-slicer integral field unit fed by an adaptive optics (AO) module. The AO system uses an optical wavefront sensor that was locked on a bright star 15'54 north and 8'85 east of Sgr A*. We employed H+K grating that covers the 1.45–2.45 μm range with a spectral resolution of $R \sim 1500$ (i.e., approximately 200 km s^{-1} at 2.16 μm). The 0'8 \times 0'8 field of view was jittered around the position of the star S2, in such a way that the star remained within the upper half zone of the detector. This was done in order to avoid a region with possible nonlinear behavior of the detector. Observations of different B- and G-type stars were taken to obtain independent telluric templates.

The Galactic center region was observed in intervals of 400 s or 600 s, followed or preceded by time slots of equal length on a dark cloud 5'36" north and 12'45" west of Sgr A*. The integration times were chosen of that length in order to be able to also monitor the flux density of Sgr A* for time intervals of typical flare lengths and to provide a higher flexibility in data selection to optimize the quality of the data. Although this observational strategy reduces the effective integration time on source to about a third when compared with parsed sky observations at a rate of about once per hour, it ensures better control of the noise in the frames. Because of the variable weather conditions, the point-spread function (PSF) changed along the observing nights. The quality of individual exposures was judged based on the PSF at the moment of the observation, as measured from the shape of the stars in the field of view. For the analysis presented here, we have created two final data cubes, one from the combination of the best-quality exposures, and another including also medium-quality data, as described below. Table 1 shows the list of the observing dates, including the number of exposures that fulfilled the selection criteria. Note that (for both pre- and post-peribothron) our observations are bracketing and preceding those presented by Pfuhl et al. (2015).

2.2. Calibration

In the data reduction process, we first followed the SINFONI reduction manually to correct for the bad lines created by the data processing at the detector level. We used the suggested IDL procedure, adjusting the identification threshold (two times the background noise $\sigma_{\text{background}}$) whenever necessary. A first cosmic-ray correction to the sky and target files was performed

using the algorithm developed by Pych (2004). The random pattern introduced by some detector amplifiers was detected and removed in science and calibration files following the algorithms proposed by Smajić et al. (2014). Then we used the SINFONI pipeline for the standard reduction steps (like flat-fielding and bad pixel corrections) and wavelength calibration. We obtained one data cube for each on-source exposure.

DPUSER routines (Thomas Ott, MPE Garching; see also Eckart & Duhoux 1991) were used to flag remaining bad pixels and cosmic rays on the plane of the slitlets in the detector (x - z , which corresponds to declination–wavelength), in each data cube. The combined effects of the atmospheric refraction were appreciable as a spatial displacement of the stars by a couple of pixels when going from short to long wavelengths. Fixing the position of the center of a bright source at a particular wavelength and making a spatial subpixel shift at all other wavelengths could correct the problem, but the shape of the resulting spectrum in each pixel would depend on the interpolation algorithm. Therefore, to preserve the integrity of the spectrum in the narrow spectral regions where emission lines are present, the spatial image shift was done in steps of 0.045 μm .

A two-dimensional Gaussian, fitted to the bright star S2, was taken as an indication of the PSF. Cubes where the FWHM of the fitted Gaussian is less than 83 mas (or 6.65 pixels) were categorized as best-quality cubes, while those with FWHM values between 83 and 96 mas (or 7.65 pixels) were classified as medium-quality cubes. The combination of the selected data cubes was done by averaging every spatial and spectral pixel after a proper alignment of the images. The combination of the 63 best-quality cubes produced a final data cube with a total of 7.2 hr of on-source integration time. When including the 30 medium-quality exposures, the resulting data cube covers a total of 10.8 hr of integration time on-source. This second data cube was used to evaluate the effects of the data quality in the signal-to-noise ratio (S/N) of the measured quantities, and unless it is specifically mentioned in the text, all measurements and plots are derived from the higher-quality data cube.

Flux calibration was done using aperture photometry on a deconvolved K -band image created from the final data cube. The deconvolution was performed using the Lucy–Richardson algorithm incorporated in DPUSER, while the PSF was estimated using the IDL-based StarFinder routine (Diolaiti et al. 2000). We used as calibration stars S2 ($K_s = 14.1$), S4 ($K_s = 14.6$), S10 ($K_s = 14.1$), and S12 ($K_s = 15.2$) and adopted the K -band extinction correction $m_{AK} = 2.46$ of Schödel et al. (2010); see also Witzel et al. (2012) for the flux estimation.

The NIR spectrum of the inner $\sim 0'5$ around Sgr A* is dominated by the stellar continuum of hundreds of stars fainter than $K_s = 18$ mag that are part of the central cluster and that are unresolved with the current instrumentation (Sabha et al. 2012). Several absorption features from the stellar atmospheres can be recognized in the HK -band data. Line emission of ionized species (hydrogen and helium) at the position of the S-stars and all across the field is also substantial. We refer to the aggregate of all these components as background, and we show how it affects the detection of the faint emission of the DSO.

3. RESULTS

In summary, we find that both the line shape and line intensity in 2014 are very similar to those of the previous years. Before 2014 May we find no blue line emission from hydrogen or helium above the noise level. The red line center has shifted to a

⁶ ESO programs 092.B-0009 (PI: A. Eckart), 093.B-0092 (PI: A. Eckart), and 092.B-0920 (PI: N. Grosso).

Table 1
Summary of the Galactic Center Observations

Date (YYYY.MM.DD)	Start Time (UT)	End Time (UT)	Number of On-source Exposures			Exp. Time (s)
			Total	Medium Quality	High Quality	
2014.02.28	08:34:58	09:54:37	7	0	0	400
2014.03.01	08:00:14	10:17:59	12	0	0	400
2014.03.02	07:49:06	08:18:54	3	0	0	400
2014.03.11	08:03:55	10:03:28	11	5	8	400
2014.03.12	07:44:35	10:07:45	13	5	9	400
2014.03.26	06:43:05	09:58:12	11	8	8	600
2014.03.27	06:32:50	10:04:12	18	1	7	400
2014.04.02	06:31:39	09:53:52	18	0	5	400
2014.04.03	06:20:46	09:45:02	18	14	17	400
2014.04.04	05:58:19	09:47:58	21	14	17	400
2014.04.06	07:51:42	08:43:15	5	4	1	400
2014.06.09	04:48:49	09:51:47	14	14	0	400
2014.06.10	04:54:21	09:49:49	5	5	0	400
2014.08.25	23:57:46	04:34:49	4	4	0	400
2014.09.07	00:11:08	04:20:07	2	2	0	400

Notes. List of start and end times and number and quality of exposures. ESO program 092.B-0009 for 2014.02.28, 2014.03.01, 2014.03.02, 2014.03.26, 2014.03.27, and 2014.04.06; ESO program 092.B-0920 for 2014.03.11, 2014.03.12, 2014.04.02, 2014.04.03, and 2014.04.04; and ESO program 093.B-0092 for 2014.06.09, 2014.06.10, 2014.08.25, and 2014.09.07. Pre- and post-peribothron measurements are separated by a horizontal line.

higher velocity of about $2700 \pm 60 \text{ km s}^{-1}$ about 40 mas east of Sgr A*. In addition, we measure the Pa α 1.875 μm line between atmospheric absorption bands but find that the sky-subtracted He I (2.05 μm) is very weak, i.e., less than a fifth of the Br γ line emission. In 2014 June our data do not allow us to detect the He I or Pa α line emission. Peribothron happened in 2014 May, and after that we see in 2014 June a blueshifted Br γ line about 16 mas west of Sgr A* at -3320 km s^{-1} and no red line emission. In 2014 June we find no blue line emission helium, Br γ , or Pa α above the noise level.

3.1. Redshifted Pre-peribothron Lines

In 2014, the Br γ line emission from the DSO shifted to a spectral region where the emission and absorption features of the surroundings are very prominent. Moreover, the Pa α and the possible He I lines lie in a wavelength range where the atmospheric absorption plays a main role. Therefore, a proper background estimation and subtraction, as well as an adequate fitting and correction of the tellurics, are critical to detect and measure any emission from the DSO. The latter is expected to change from one day to the next, and also during one observing night if the weather conditions are unstable, but it is approximately the same across the field of view. The former, on the other hand, varies strongly across the field and significantly in periods of about 6 months, because of the high stellar proper motions. This means that, while the telluric absorption can be, in principle, fitted and corrected using extra observations of stars or sources in the field, the exact shape of the background spectrum at the position of the DSO cannot be known, but only approximated by using apertures in the field. A carefully calculated approximation to the background leads to a reliable estimation of the spectral properties of the source's line emission, as well as the spatial position and extension of the DSO emission.

3.1.1. The Br γ Emission Line

Figure 1 shows the spectrum integrated over apertures of radius 0".05 at the position where the redshifted Br γ emission

from the DSO is strongest. It also shows the background spectra constructed from four different surrounding regions, as well as the resulting line emission after subtracting them from the source spectrum. In the left panels, the spatial pixels from which the spectra of the source and the background have been extracted are marked with blue crosses and pink filled squares, respectively. The Sgr A* position is marked with the big cross. The middle panels display the integrated spectrum at the DSO position (thick blue line) in comparison with the background spectra (thin pink line). The vertical dashed line at 2.166 μm marks the spectral position of the zero-velocity Br γ line. Arrows at 2.076 μm and 2.185 μm indicate the approximate location of the DSO redshifted He I and Br γ emission lines. The inset panel corresponds to the dashed-line box, which is a zoom-in to the spectra in the 2.18–2.20 μm range. The arrow in the inset panel marks again the position of the redshifted Br γ line and highlights the importance of the background subtraction to recover the spectral properties of the emission. Because of the change of the spectral slope across the field of view, the overall shape of the spectrum extracted from the background area has to be slightly modified to better fit the continuum in the DSO aperture. To do that, we divide it by a third-order polynomial fitted to the ratio between the source spectrum and the spectrum of the background aperture. This is done using only the spectral windows marked with (green) crosses in the top panel of the middle column. Then, the background was scaled to best match the continuum emission around the spectral location of the Br γ redshifted emission (i.e., at 2.173–2.183 μm and 2.195–2.220 μm). These spectra, with modified slope and scaled continuum, are used as an approximation of the background emission at the DSO position. They reproduce well most of the features in the source spectrum, as can be seen in the middle panels. Given that at wavelengths shorter than $\sim 2.08 \mu\text{m}$ the emission is highly absorbed by tellurics, we did not include this spectral region in the fit of the overall background spectral shape, but used only the selected spectral windows as described above. For this reason, the background continuum in the source aperture at $\lambda \lesssim 2.08 \mu\text{m}$ cannot be fitted properly and produces an excess of emission in the background-subtracted DSO spectra,

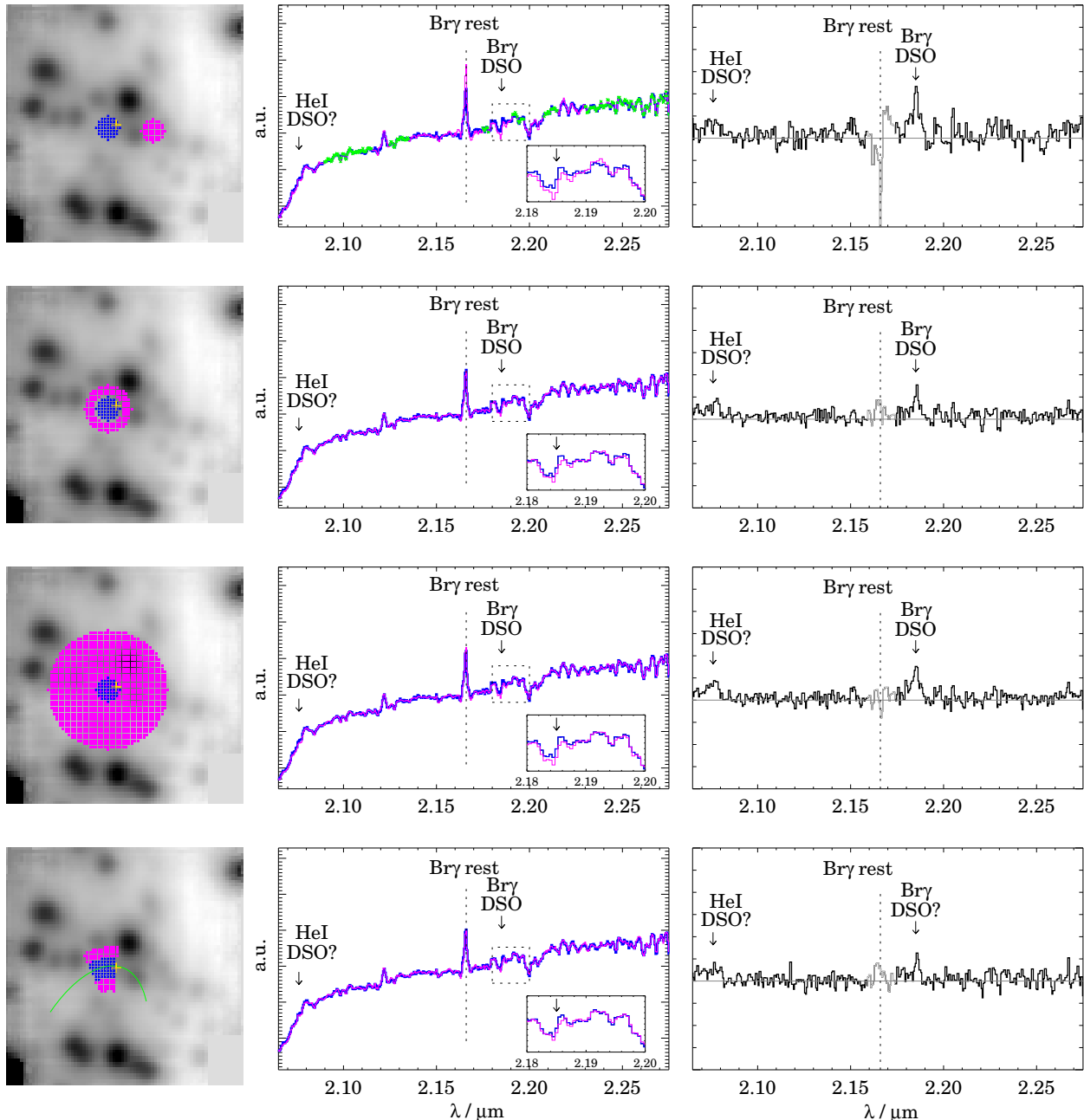


Figure 1. Br γ redshifted emission of the DSO before May at 43 mas east and 5 mas south of Sgr A*. Left panels: 1×1 arcsec² SINFONI mosaic of the Galactic center region in 2014 February to April. DSO (blue crosses) and background (pink squares) apertures are shown. Middle panels: comparison between the DSO (thick line) and the background (thin line) spectra. Arrows mark the expected location of the redshifted He I and Br γ lines. Right panels: results of the subtraction of the background from the DSO spectrum. The baseline is shown in gray. The vertical range of the plots corresponds to one unit in the middle panels; see details in the text.

which can be seen in the right panels. There, the large mismatch observed in the spectra in a range of $0.82 \mu\text{m}$ around the zero-velocity Br γ line is due to strong variations of the ionized hydrogen emission in the central $r \sim 1''$ region. Lines within the telluric absorption region are treated differently to improve their signal strength; see Section 3.1.3.

The four examples shown in Figure 1 correspond to the cases when (1) the background is created from an aperture of the same size and shape as that of the source, and it is located just

beside it. (2) Iris photometry is applied, i.e., the background aperture is a ring around the source aperture. In this case, the inner radius was chosen to be $0''.06$, and the outer radius, $0''.11$. (3) An averaged background is created from a region of radius $0''.25$ at the source position that includes the DSO aperture. (4) The source emission is integrated in a segment of $0''.075$ width taken along the best-fit elliptical orbit with a length of $\sim 0''.10$ (see Section 4.1). The background is integrated from the $0''.048$ width stripes above and below the source area. In all cases the

redshifted Br γ line is detected with S/Ns between 3.9 (in the second case) and 4.7 (in the third one).

Fitting a Gaussian to the line emission in each case, we find a rather robust determination of the line peak at $2.185 \mu\text{m}$, i.e., 2700 km s^{-1} on average with a variation of 60 km s^{-1} . However, as can be noticed from Figure 1, the line profile changes depending on the subtracted background. The FWHM of the Br γ line, corrected for instrumental broadening, is 730 km s^{-1} in the first and third cases, 560 km s^{-1} in the second one, and only 240 km s^{-1} in the fourth one. Averaging over a dozen background-subtracted source apertures, the $\text{FWHM}(\text{Br}\gamma) \approx 720 \pm 150 \text{ km s}^{-1}$, i.e., the line width is $50 \pm 10 \text{ \AA}$. The line flux changes, in general, by a factor of two owing to the background subtraction. In the first three examples shown in Figure 1, it is in the range $3.1\text{--}6.0 \times 10^{-16} \text{ erg s}^{-1} \text{ cm}^{-2}$, while in the last case it only reaches $1.7 \times 10^{-16} \text{ erg s}^{-1} \text{ cm}^{-2}$. For a distance of 8 kpc to the Galactic center, the average luminosity of the observed redshifted Br γ line is $1.0 \times 10^{-3} L_{\odot}$, and twice this value when integrating over a larger aperture of radius $r = 0''.075$.

In the last example in Figure 1 the recovered properties of the emission line are quite different from those of any other case, although the bulk of the source emission seems to be well within the aperture placed along the orbit, and it covers a very similar area to the circular aperture used in the first three cases: e.g., the line width in the last case is narrower and the line flux is only $\sim 35\%$ of that measured in any other background-subtracted spectrum. From this analysis, we call for precaution when measuring line properties along predetermined areas in the field of view.

3.1.2. Position of the DSO

To confirm the position of the Br γ emission, we removed the background emission in every pixel of the field of view following the procedure described above using the spectrum shown in the second example of Figure 1 as a background—as classical iris photometry makes unbiased and efficient use of the background in the immediate surrounding of the source. Then we integrated the residual flux in the range $2.181\text{--}2.193 \mu\text{m}$. The result, shown in the top left panel of Figure 2, is an image of the excess flux, compared to the continuum, emitted by the source in this wavelength range. Fitting a Gaussian to this emission in every spatial pixel allows us to mask the areas where the flux within the line is less than $2\times$ the noise level. When such a mask is applied (Figure 2, top right), the location of the DSO shown by its redshifted Br γ emission is clearly revealed. The position of the DSO as indicated by the position of the brightest Br γ peak in Figure 2 is 8.6 mas south and 41.5 mas east of Sgr A*.

3.1.3. The He I and Pa α Emission Lines

The detection of Pa α $1.875 \mu\text{m}$ and He I $2.058 \mu\text{m}$ emission requires modeling of the atmospheric absorption. Although we observed some standard stars during the different runs to use them for the telluric modeling, the sky variation throughout the nights was large and the corrections unsatisfactory. The alternative is to use a bright star in the field, or a combination of some of them, as tracers of the telluric absorption. Figure 3 shows the case where the star S2 is used for this purpose. In the top panel, a comparison between the DSO spectrum and that of S2 is shown. The absorption features in the source spectrum around $1.9 \mu\text{m}$ are well approximated, but the overall shapes of both spectra differ from each other, as expected from the earlier discussion.

Following the common telluric correction procedure, the DSO spectrum is divided by the normalized telluric spectrum (in the case of Figure 3, that of S2). The same correction is applied to the background spectrum. Here we selected without preference the background shown in the third example of Figure 1. The resulting DSO spectrum, after the background correction, is still very noisy around $1.9 \mu\text{m}$, but hints of the redshifted He I and Pa α are visible. The lines are observed with an S/N of about 2 in the case of helium and just above 1 in the case of Pa α . The fact that Pa α is not observed with the expected strength (approximately 12 times brighter than Br γ , after extinction correction) is probably due to the low elevation of the Galactic center region in February–April, which resulted in stronger telluric absorption in this region. We fit the redshifted He I with a Gaussian to obtain the line properties. It peaks at $2.076 \pm 0.078 \mu\text{m}$, i.e., $\sim 2650 \pm 100 \text{ km s}^{-1}$ within the uncertainties at the same receding velocity as indicated by the Br γ line. It also exhibits a similar width $\sim 750 \text{ km s}^{-1}$. After correcting for extinction assuming $A_V \approx 26.8 \text{ mag}$, we find $\text{He I}/\text{Br}\gamma \sim 0.6$, consistent with models in which the emission is dominated by optically thin material (Gillissen et al. 2013b; Shcherbakov 2014).

However, this value must be taken with caution, given the low S/N of the lines and the high influence of the tellurics and background corrections in the measured line fluxes.

3.2. Blueshifted Pre-peribothron Lines

The blue side of the line emission would be extremely diluted if we observed the source very close to its peribothron position, and the radial velocity range would span almost 6000 km s^{-1} , significantly broadening the emission line and making it virtually impossible to detect. Only if the time span for such an event were of the order of a week (depending on the exact orbit) would observations immediately after our measurements have picked up significant blue line emission.

3.2.1. No Detected Blue Br γ Emission

Using a variety of apertures, we conducted a systematic search of the DSO blueshifted Br γ emission along the portion of the orbit that lies upstream of the red emission. As we did not find blueshifted emission at the pre-peribothron position of the DSO, we extended our search to consecutive positioned apertures upstream of the 2014 April pre-peribothron position. Corresponding to the findings of Pfuhl et al. (2015), the blue line emission should have been the brightest line component in our data. If the blueshifted emission is compact, and at least half as bright as the redshifted one, we should be able to detect it with an S/N ~ 2.5 or higher.

Following the same approach presented in Section 3.1.1., i.e., subtracting background spectra created in different ways from the source spectrum, we aimed to find hints of the blueshifted component. The DSO spectrum was integrated from an aperture with the PSF size ($r = 0''.05$) that was placed several times in a grid mapping a squared area of $200 \text{ mas} \times 200 \text{ mas}$ with Sgr A* at the northeast corner.

In this way we covered the large area to the west and to the south of Sgr A* where the approaching side of the DSO is expected to be found. We also searched for the blueshifted emission using slightly larger apertures to account for a possibly more extended emission that could be expected in case the source was not as compact as before the peribothron passage.

Figures 4 and 5 show two attempts at finding the Br γ DSO emission in two different positions upstream of the best-fit

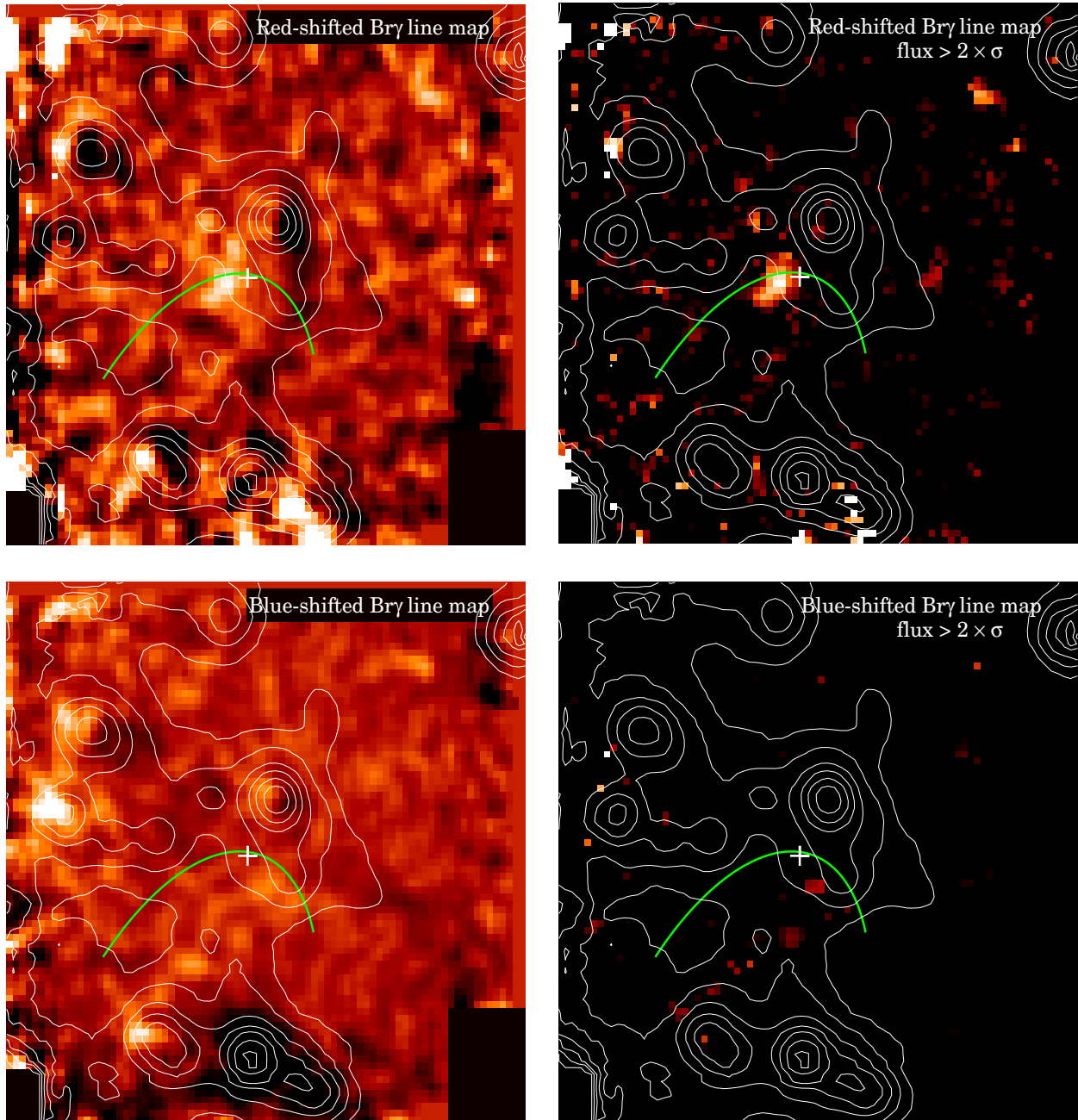


Figure 2. Bry line maps. Panels show $1.0 \times 1.0 \text{ arcsec}^2$ of the Galactic center region in 2014 February–April. The cross marks the position of Sgr A*. The thick green line corresponds to the best-fit elliptical orbit. The *K*-band continuum contours depict the brightest S-cluster members. Top panels: DSO redshifted Bry line map. Left: integrated emission in a range of 120 \AA around $2.185 \mu\text{m}$ after subtracting the background in every spatial pixel of the field of view. Right: same as left panel, but showing only emission that is brighter than $2\times$ the noise level. Bottom panels: blueshifted Bry line map. Left: integrated emission in a range of 120 \AA around $2.147 \mu\text{m}$, i.e., around the expected blueshifted Bry line emitted by a source approaching us at a speed of 2700 km s^{-1} . The background has been subtracted in every spatial pixel of the field of view. The color scale is the same as in the top panels. Right: same as left panel, but showing only emission brighter than $2\times$ the noise.

elliptical orbit. These are examples of the systematic search for the DSO Bry emission south/west of Sgr A*. The apertures are placed at the position (and one consecutive position) along the orbit at which Pfuhl et al. (2015) and earlier Gillessen et al. (2013b) had reported the detection of blueshifted line emission.

As in Figure 1, left panels show the size and position of the background and source apertures, middle panels compare the spectra extracted from them, and right panels present the

subtraction of the two. The expected spectral positions of the blueshifted Bry and He I are derived assuming the emitting source to approach us after peribothron with a similar speed as the still receding part. The vertical range in the right panels is the same as the one used in Figure 1 and therefore can be directly compared. In case there is a source emitting a blueshifted line at any of these two positions, the line should be clearly visible in all four rows displayed within one figure. This is because, in

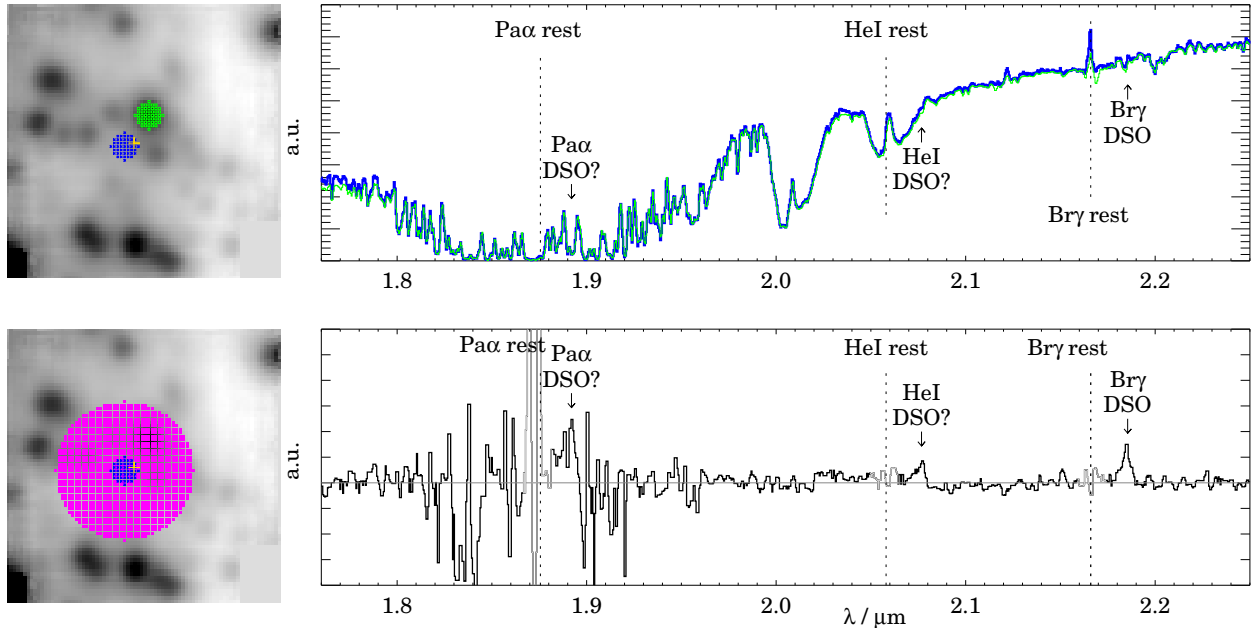


Figure 3. He I and Pa α redshifted emission of the DSO before May. Top left: 1×1 arcsec² SINFONI mosaic of the Galactic center region in 2014 February–April. The DSO aperture is marked with blue crosses. The spectrum extracted from the aperture placed on S2, marked with empty green squares, is used to model the telluric absorption. Top right: comparison between the DSO spectrum (thick blue line) and the telluric model (thin green line). The positions of the zero-velocity hydrogen and helium lines are signaled with vertical dashed lines, while the expected positions of the redshifted emission lines from the DSO are indicated with the arrows. Bottom left: same as in left panels of Figure 1. Bottom right: results of the subtraction of the background from the DSO spectrum, after correcting both spectra for tellurics. Dashed lines and arrows are the same as above.

these four examples, the source spectrum is extracted from the same region and the only difference must be the S/N of the line, which depends on the subtracted background (we come back to this point in Section 3.2.3). Hence, we can rule out that there is a blue line similar to that seen on the redshifted side, despite the fact that the source should be similarly compact (see Figures 1 and 5 in Pfuhl et al. 2015 and comments in our introduction section).

3.2.2. Upper Limit for the Blueshifted Br γ Line

Another strategy for searching a line emission is, as we did in previous sections, to subtract a background spectrum from the entire data cube and then integrate the remaining flux within narrow spectral windows around the expected wavelength. For this search we used different background spectra and integrated the residual flux in the range 2.143–2.151 μm . Figure 2 (bottom left) shows one example. We fitted a Gaussian to every spatial pixel to create a mask that selects those places where the flux is less than $2\times$ the noise level. In the right panel of Figure 2 (bottom right), such a mask has been applied. We see possible hints of a spatially compact source at 37.5 mas west and 68.8 mas south of Sgr A* that is not located on the expected DSO orbit. Looking at the line properties, we find that on average the emission is very broad, with FWHM > 2000 km s⁻¹ (i.e., larger than 0.015 μm) and centroid at ~ 2.149 μm . Assuming that the blueshifted Br γ line emission is as wide as the redshifted one, i.e., 720 km s⁻¹, and with a noise in that spectral range of $\sim 2.9 \times 10^{-14}$ erg s⁻¹ cm⁻² μm^{-1} , we obtain an upper limit for the line flux of $\sim 4.7 \times 10^{-16}$ erg s⁻¹ cm⁻², i.e., a luminosity $L(\text{Br}\gamma_{\text{blue}}) < 1.0 \times 10^{-3} L_{\odot}$. Whether this emission is real, considering the multiple sources of noise, and whether it has

some relation with the DSO is unknown. For the apertures placed along the orbit, the upper limit of a blueshifted Br γ line flux is $\sim 2.8 \times 10^{-16}$ erg s⁻¹ cm⁻², which is about half of that of the redshifted line.

3.2.3. Influence of the Selected Background

There is no doubt that the subtraction of the background emission plays an important role in the detection of faint line emission. The usage of different background spectra from regions close to the position of interest is an effective tool to discriminate between a source line emission and the unlikely presence of a background feature at the studied wavelength. In the first row of Figures 6(a) and (b) we present examples of background that produce a spurious blueshifted Br γ emission at positions far away from the expected orbit. The panels in the second row of each example show how, after selecting different background spectra, a very good overlap with the source spectrum is obtained and only noise remains after the subtraction. The aperture shown in Figure 6(a) is located at the position of the bright blob closest to Sgr A* in the bottom panels of Figure 2. The background-subtracted spectrum of this aperture was used above to estimate the upper limit for the blueshifted line. In this case, the S/N of the feature at ~ 2.15 μm depends strongly not only on the background selected but also on the way it is scaled and subtracted. As we were not able to produce spurious detections on the red side, we conclude that those in the blue may result from an enhanced local variation of the background in this particular spectral range. Based on this analysis, we call for caution when studying line emission properties of faint sources in crowded fields.

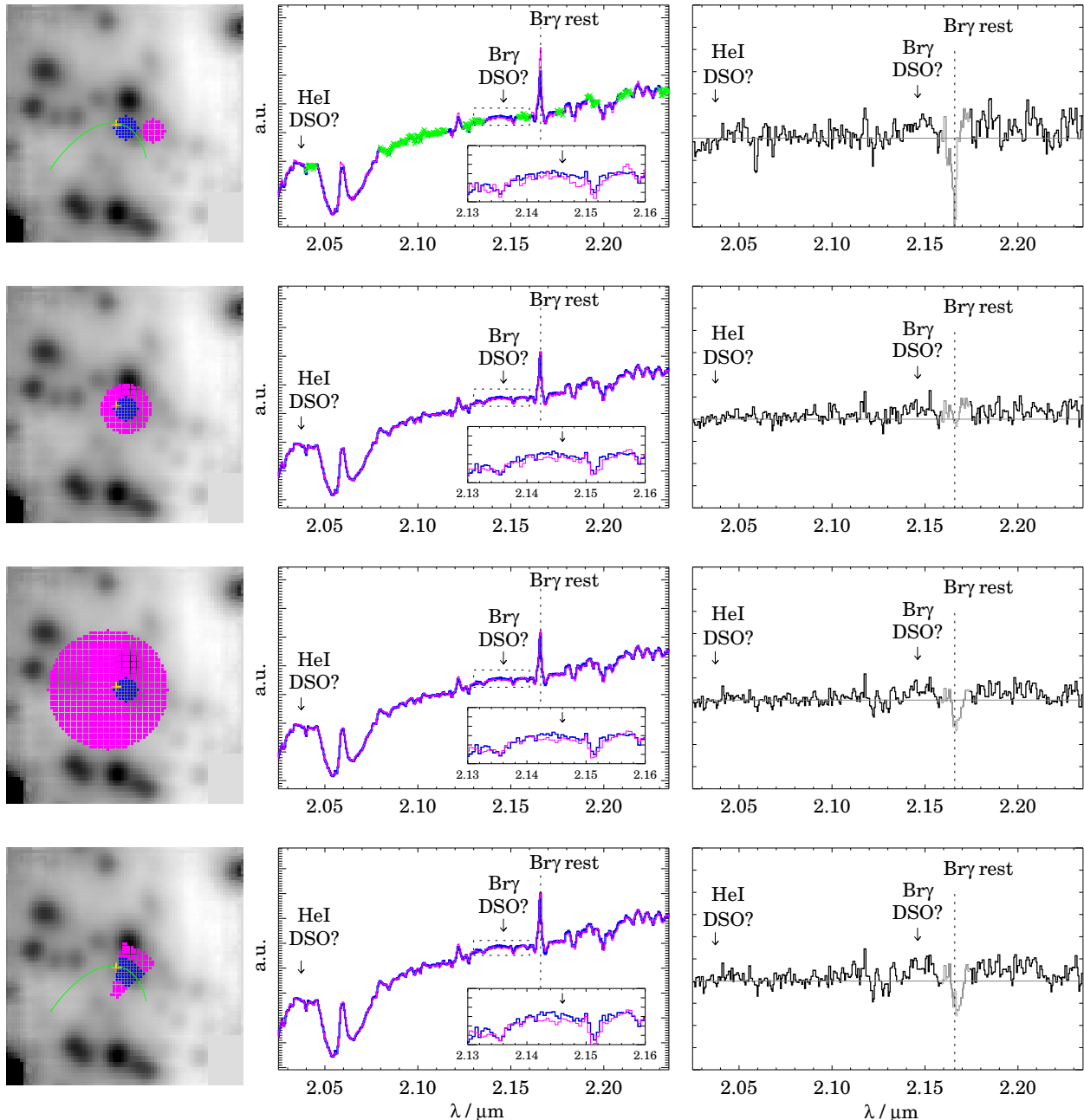


Figure 4. Nondetection of $\text{Br}\gamma$ blueshifted emission before May at a first upstream position at 43 mas east and about 11 mas south of Sgr A*. Left panels: same as Figure 1. Middle panels: comparison between the DSO (thick blue line) and the background (thin pink line) spectra. Arrows at $2.037\ \mu\text{m}$ and $2.146\ \mu\text{m}$ indicate the approximate location of the expected DSO blueshifted He I and $\text{Br}\gamma$ emission lines, in case the speed of the approaching component was the same as that of the receding one. The inset panel corresponds to the dashed-line box, which is a zoom-in to the spectra in the $2.13\text{--}2.16\ \mu\text{m}$ range. The arrow in the inset panel marks again the position of the blueshifted $\text{Br}\gamma$ line. The spectral windows marked with crosses in the top panel are used to fit the slope of the background spectrum to that of the DSO. Right panels: results of the subtraction of the background from the DSO spectrum. The vertical range of the plots corresponds to one unit in the middle panels and spans the same range as in the right panels of Figure 1. The zero line is shown in gray.

3.3. Blueshifted Post-peribothron $\text{Br}\gamma$

Figure 7 shows the spectrum integrated over an aperture of radius $0''.05$ at the post-peribothron in 2014 June at a position of 16 mas west and about 6 mas south of Sgr A* at an S/N of 2.5–3.1 depending on the background subtraction. The line has a blueshifted center velocity of $-3320 \pm 60\ \text{km s}^{-1}$ and, after correcting for spectral resolution, an FWHM of $15 \pm 10\ \text{\AA}$.

Line flux and width were derived using several background corrections similar to what is shown in Figure 1. The $\text{Br}\gamma$ line luminosity is about $0.4 \times 10^{-3} L_{\odot}$. The narrow line estimate could be a result of the weak line detection; it could also point to a stellar nature of the source (see below).

The excess line emission can clearly be seen even before background subtraction in the inset of the middle top plot in Figure 7. Based on the post-peribothron observing dates

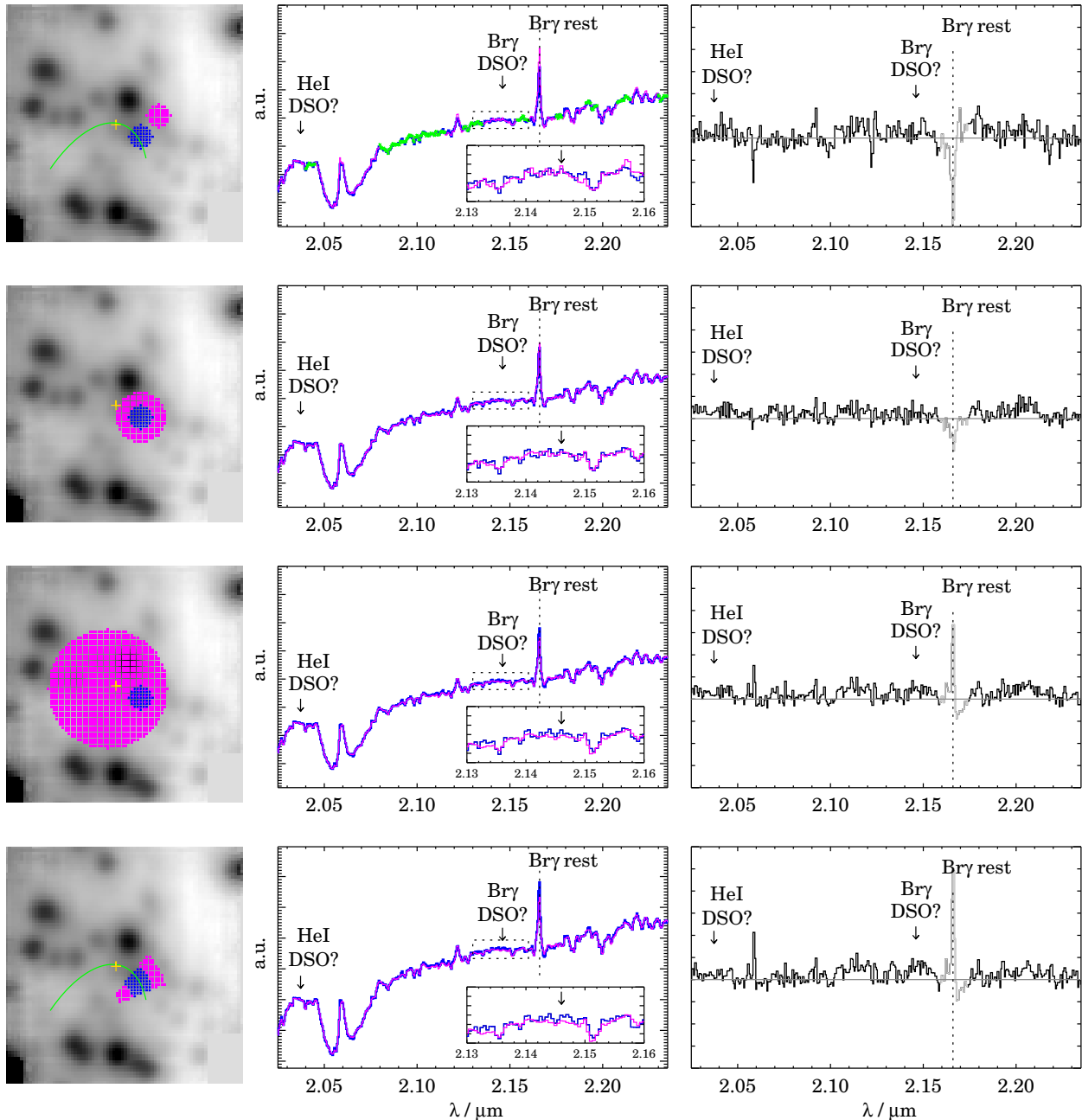


Figure 5. Nondetection of Br γ blueshifted emission before May at a second upstream position 103.8 mas west and 50 mas south of Sgr A*. Panels and symbols are the same as in Figure 4.

listed in Table 1, we assigned an integration time weights epoch of 2014.55 to this measurement. No red line emission can be claimed for this epoch at this position. In the lower plots of Figure 7 we show that at that epoch neither red- nor blueshifted Br γ line emission can be seen at our pre-peribothron position (see also the inset of the middle bottom plot). The excess line emission can clearly be seen even before background subtraction in the inset of the middle top plot. The baseline used for this spectrum excludes the region around blueshifted (2.138–2.146 μm) and redshifted Br γ and He line emission (2.175–2.190 μm and 2.070–2.080 μm) we used at the

pre-peribothron position. No redshifted emission was detected at the post-position. No redshifted line emission was detected at any position downstream of the post-peribothron position. In Figure 8 we show summary spectra at the pre- and post-peribothron positions for 2014. We obtained the spectra using a $0''.050$ radius source and a $0''.25$ radius background aperture centered on the DSO. We subtracted a high-pass-filtered version of the spectra that we obtained by replacing the range over which detectable line emission is present (indicated by the three lines at the bottom of the graph) by the mean in the neighboring spectral elements and smoothed the resulting spectrum with a

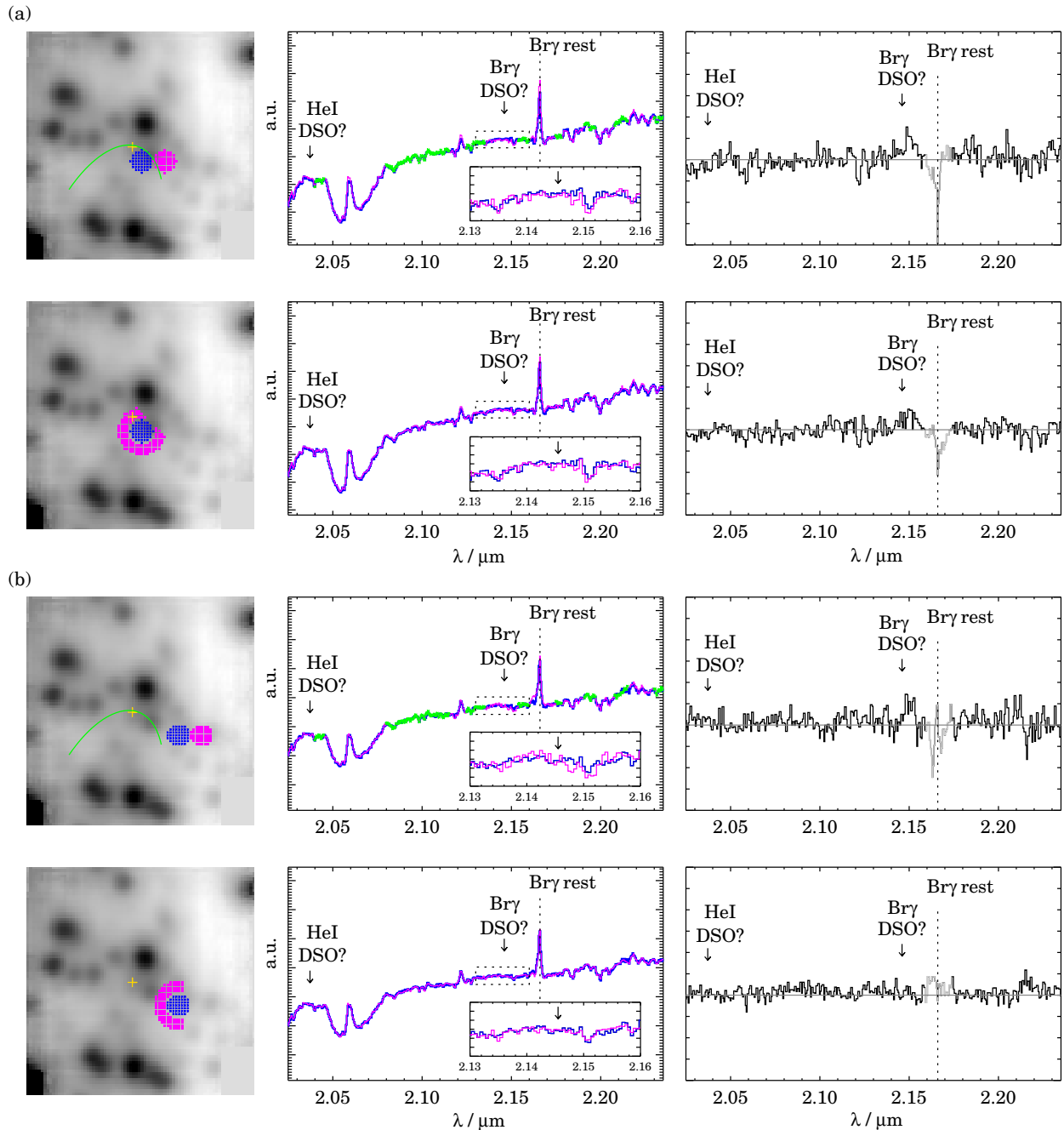


Figure 6. Spurious blueshifted $\text{Br}\gamma$ emission due to background selection. Panel descriptions are the same as in Figure 4. The two shown cases correspond to sources at (a) 37.5 mas west and 68.8 mas south of Sgr A*, and (b) 200 mas west and 100 mas south of Sgr A*.

Gaussian having an FWHM of 10 spectral resolution elements. The location of the $\text{Br}\gamma$ rest emission is indicated by a vertical dashed line.

An important question is that of the size of the line emission region and possible velocity gradients across the DSO. To investigate this, we obtained line maps of the $\text{Br}\gamma$ emission. In Figure 9 we show maps of the DSO in its $\text{Br}\gamma$ line emission for the times before (epoch 2010.45 May⁷ and 2014.32 April)

and after (epoch 2014.55) the peribothron. For the brightest and least confused $\text{Br}\gamma$ line maps for 2010 May (Figure 9) we find a geometrical mean FWHM of 6.5 pixels. For the star S2 we find an FWHM of 6.2 pixels. With 12.5 mas per pixel this gives an upper limit on the deconvolved FWHM source size of 24 mas. The centroid positions of the emission-line maps of the left half, right half, and full line in milliarcseconds relative to the position of the full line map centroid position are given in Table 2. Under the assumption that differences in the relative positions of the red and blue half of the single-line $\text{Br}\gamma$

⁷ SINFONI data from ESO program 183.B-100.

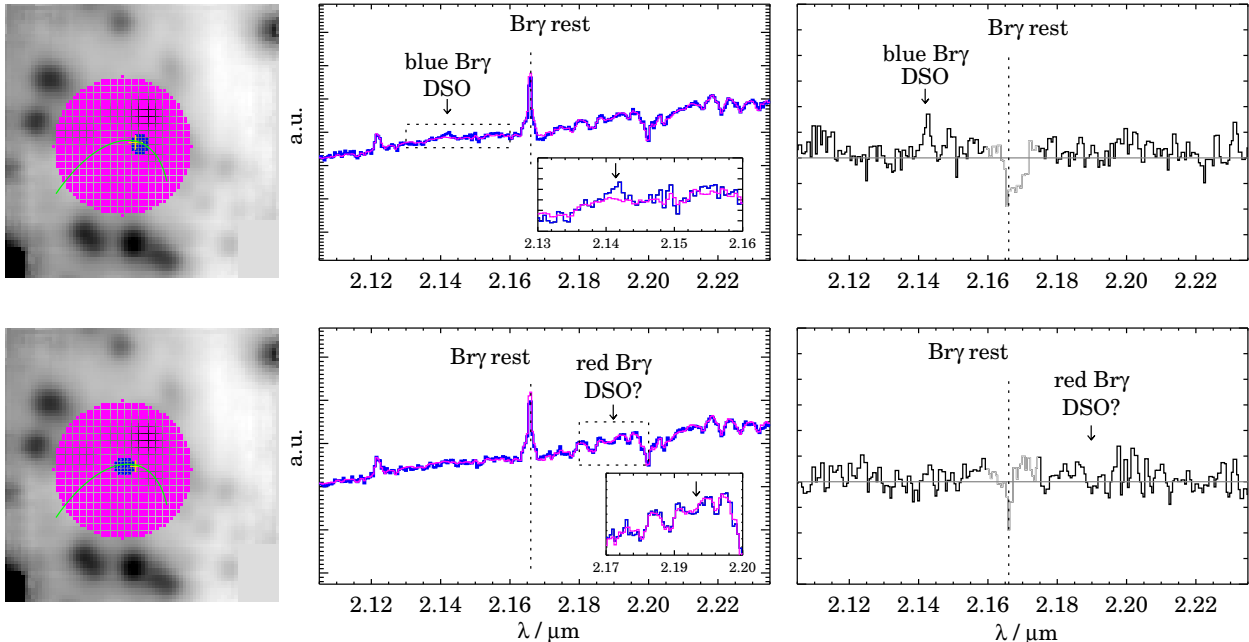


Figure 7. Br γ line emission after peribothron passage: Top: blueshifted Br γ emission detected at 12 mas west and about 5 mas north of Sgr A*. Bottom: no red- or blueshifted Br γ emission detected at our pre-peribothron position at 43 mas east and about 5 mas south of Sgr A*.

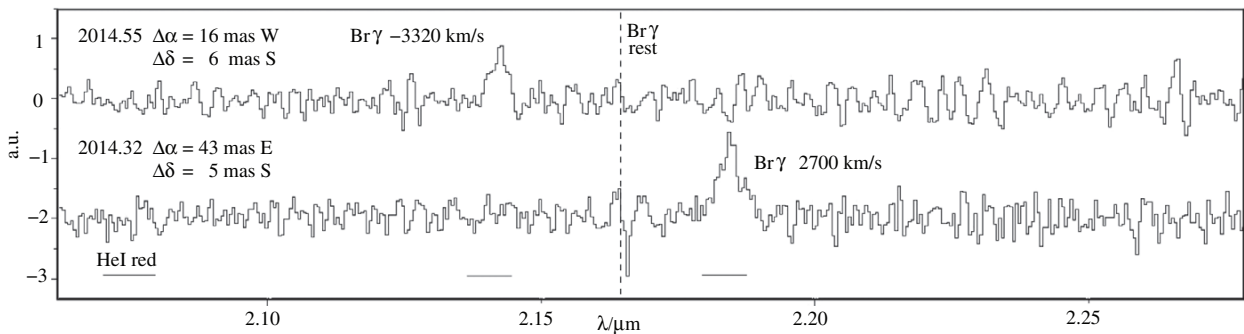


Figure 8. Summary spectra at the pre- and post-peribothron positions for the 2014 April and June epoch; see details in text.

Table 2
Centroids of DSO Line Maps

Epoch	Blue Half		Full Line		Red Half		Red-Blue Half	
	(mas)	(mas)	(mas)	(mas)	(mas)	(mas)	(mas)	(mas)
2014 Apr	-6.75	-7.63	0.0	0.0	+6.25	+6.00	+13.0	+13.6
2014 Jun	-0.25	+4.25	0.0	0.0	+4.50	-3.88	-4.75	-8.13
2010 May	-4.63	-6.00	0.0	0.0	+4.13	+4.63	+8.75	+10.63

Notes. For the single emission line we measured at both the 2014 and 2010 May epochs we list the line map right ascension and declination centroids for the blue and red half of the corresponding single line in milliarcseconds with respect to the full line position. In the last two columns we list the positional difference between the red- and blue-half centroid positions. One pixel corresponds to 12.5 mas.

emission-line map can be interpreted as being due to a velocity gradient of a tidally stretched source, we find for all epochs an upper limit of the corresponding source size of 15 mas. This implies that the source emitting the bulk of the Br γ line is very compact, and we adopt the value of 15 mas as an upper limit on the line-emitting FWHM source size. This is consistent with the analysis of L' -band continuum images by Eckart et al. (2013) showing that >90% of the DSO emission at 3.8 μm wavelength

is compact ($\text{FWHM} \leq 20$ mas) and only up to 10% of the flux density of the DSO can be extended on the scale size of the PSF. Our size limit is also consistent with the upper limit of 32 mas presented by Witzel et al. (2014). These size estimates are all smaller than or at the lower bound of the 2008–2013 size estimate of 42 ± 10 mas Gillessen et al. (2013b). Our adopted Br γ source size corresponds to 120 AU at a distance of 8 kpc, i.e., it is close to the peribothron distance of the source. However, it is still

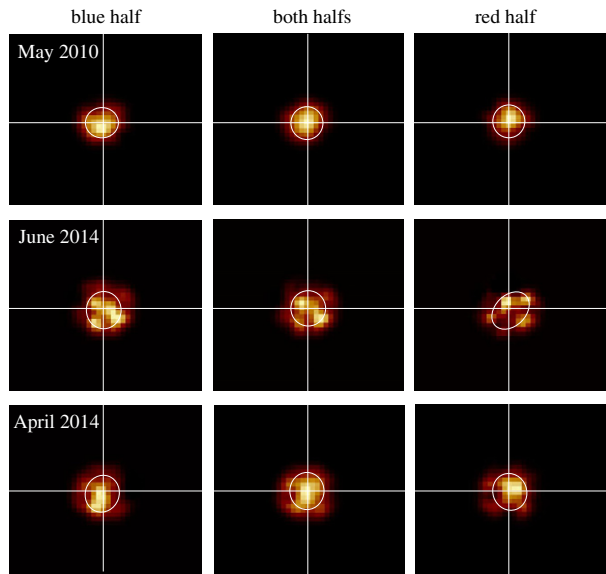


Figure 9. Maps of the DSO in its Br γ line emission for the 2014.32 April, 2014.55 June, and 2010.45 May epochs. The maps are 0.5×0.5 in size. The centroid data are given in Table 2.

about 50 times larger than the estimated size of an optically thick dust shell of a $2 M_{\odot}$ star of about 2.6 AU Witzel et al. (2014).

4. DISCUSSION

The fact that we found redshifted Br γ emission at the pre-peribothron position but did not detect any blueshifted emission upstream (in Sections 3.2.2 and 3.2.1 we only show two examples—we probed several positions along the orbit) and vice versa (Section 3.3) has implications on the orbit and on the DSO model.

4.1. The Orbit

Based on L -band imaging, an IR excess source within the central cluster of high-velocity S-stars was found to approach the immediate vicinity of Sgr A* (Gillessen et al. 2012). In addition, Br γ line emission was reported by Gillessen et al. (2013a) and Phifer et al. (2013). In Eckart et al. (2013) we report the identification of K -band emission from a source at the position of the L -band identifications. Gillessen et al. (2013b) report a marginally spatial extension of the Br γ line emission in their SINFONI data and find an intrinsic Gaussian FWHM size of 42 ± 10 mas (using 2008–2013 data). Given the peculiar orientation of the source estimated orbit, precise estimates of the source elongation along the orbit are difficult to obtain. Combining these observational facts indicated that a dusty object—possibly associated with a stellar object—is on an elliptical orbit around Sgr A*. The observational data were also used to derive the orbit of this object and to predict its peribothron transition. Owing to the presumably high ellipticity of the orbit, only very weakly curved sections of the orbit were available, and first predictions of the peribothron transition time in 2013 (Gillessen et al. 2012) proved to be incorrect. The inclusion of (or even restrictions to) the Br γ line emission resulted in new predictions for early 2014 (Gillessen et al. 2013a; Phifer et al. 2013). The fact that the telescope PSF in the L band is intrinsically larger and therefore more susceptible to

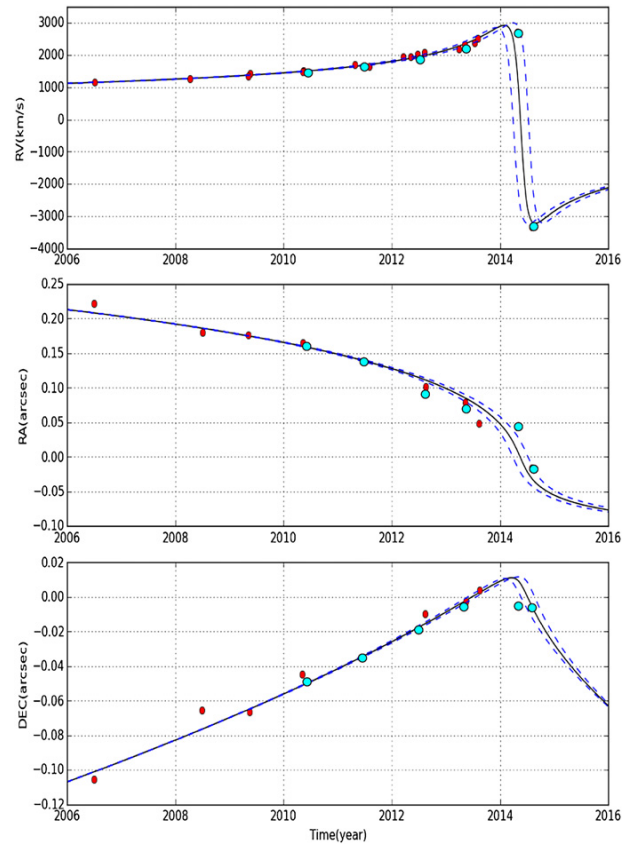


Figure 10. Right ascension, declination, and radial velocity of the DSO together with the best orbital fit we obtained; see details in text.

diffuse extended emission is probably the main reason for this discrepancy.

However, the predicted interactions of the gas and dust with the strong gravitational field of Sgr A* have shown that the gas itself may also not be a good probe of the exact orbital motion. This is supported by the spatial extent and the velocity gradient across the Br γ line emission. It is also highlighted by the expected interaction of the DSO with the ambient medium and the gravitational field. Therefore, even though the recently derived Br γ -based orbital solutions are in reasonable agreement (Meyer et al. 2014a, 2014b), the orbital elements may still be uncertain.

Using results from our measurements with SINFONI obtained between 2014 February and September, SINFONI archive data, and the published Keck data (Meyer et al. 2014a, 2014b), we revisited the determination of the DSO orbit. Given that the red emission is only about 40 mas east of Sgr A* and at a radial velocity of about 2700 ± 60 km s $^{-1}$ and blue emission about 30 mas west of Sgr A* at -3320 km s $^{-1}$, we obtained a new orbital solution that places the peribothron passage at 2014.39 ± 0.14 , a bit later than but close to 2014.2 as derived earlier (Meyer et al. 2014a, 2014b). Otherwise, the orbital elements are very similar to the ones derived earlier. In Figure 10 we show the fit to the data we used. The formal statistical uncertainties of the positional measurements are of the order of a few milliarcseconds. However, the systematic effects probably limit the uncertainties to a value closer to ± 10 mas (see Figure 9 in Eckart et al. 2012a). For the 2014 data presented here the exact

Table 3
Orbital Parameters for the DSO

e	a (mpc)	i (deg)	Ω (deg)	ω (deg)	T (yr)	P (yr)
0.976 ± 0.001	33.0 ± 3	113 ± 1	76 ± 8	94 ± 8	2014.39 ± 0.14	262 ± 38

Notes. The orbital parameters and their uncertainties have been derived on the basis of the UCLA measurements and the 2014 April data point we obtained using SINFONI at the VLT. We assume a distance of 8 kpc and a black hole mass of $4 \times 10^6 M_{\odot}$.

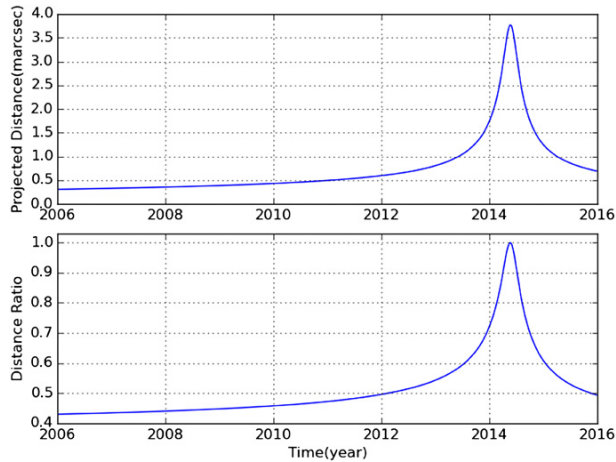


Figure 11. Orbital projection effects. Top: evolution of the projected separation between two neighboring points of arbitrary 0.5 units in 2011. Bottom: foreshortening factor of any structure along the orbital extent as a function of time.

positioning of the $\text{Br}\gamma$ line emission critically depends on the transfer of the Sgr A* position as obtained during a 3 mJy flare we observed in March to all the other 2014 epochs. This was done using the known position and velocity of the southward moving bright star S2 that is currently about $0'.11$ north and $0'.06$ west of Sgr A*. For the radial velocities we assume the value of 60 m s^{-1} we adopted for the SINFONI data. The light-blue filled circles indicate our per- and post-peribothron 2014 data points we obtained using SINFONI at the VLT. The other light-blue filled circles show the results from our re-reduction of earlier SINFONI VLT archive data. Red filled circles represent data as obtained with the Keck Telescope and published by Meyer et al. (2014a, 2014b). The dashed lines indicate the approximate 1σ uncertainty of the fit. The orbital elements are given in Table 3. With the ellipticity $e = 0.976$ and the half-axis length of 33 Mpc, we obtain a pericenter distance of about 163 AU, which is comparable to previous estimates (Pfuhl et al. 2015; Phifer et al. 2013; Meyer et al. 2014b) and indicates that even if the DSO is an embedded star, its outer shell may very well be subject to tidal disruption (see also Section 5 and Eckart et al. 2013; Witzel et al. 2014).

In Figure 11 we show the size evolution of structures along the orbit under the assumption of freely moving neighboring points. In the case of the DSO the shapes of the two graphs by chance look very similar. We verified that they are indeed very different for other orbital configurations, i.e., lower inclination or the apobothron pointing toward the observer. The top graph shows the evolution of the projected size of a source moving along the orbit. The bottom graph shows the same quantity divided by the actual three-dimensional size of the source, i.e., the amount of foreshortening that the observer needs to correct

for. Both graphs demonstrate that close in time to the peribothron passage the foreshortening correcting is close to unity and that the DSO can be seen close to its full extent along the orbit.

4.2. Tidal Interaction with Sgr A*

The way in which the gas cloud will get disrupted depends on the exact orbit and the nature of the DSO, i.e., whether there is a stellar core or not. If there is a central star, then higher-mass (typically 10 solar masses) objects may retain more of the gas and dust mass in their corresponding Roche lobe than low-mass objects (one solar mass and below). This is discussed in Eckart et al. (2013). Recent model calculations for cases with a stellar core or even a binary core have been published by Zajaček et al. (2014).

A tail that is physically connected to the DSO has been reported by Gillessen et al. (2012, 2013a, 2013b). Eckart et al. (2013, 2014b), Phifer et al. (2013), and Meyer et al. (2014b) have questioned this physical association of the DSO with the extended $\text{Br}\gamma$ and dust continuum emitting filament about $0'.3$ southeast of Sgr A*. The rather extended shape of this emission close to rest-frame velocities may very well be associated with the Galactic center fore/background features, which are numerous in this region. It also does not follow precisely the orbital track of the DSO. Especially at velocities close to rest-frame velocities, the general central cluster region is very crowded. Hence, despite an indication of very faint emission pointing toward this general region $0'.3$ southeast of Sgr A*, a physical association of the bright tail emission is still questionable.

If the DSO is a pure, very compact and solitary gas and dust cloud, then it formed through a special process at a very special place and time. As speculated by Pfuhl et al. (2015), it must have formed between 1990 and 2000. Unless one claims, as a further special feature of this source, that it has been formed at 100% efficiency, some relics and further similarly compact dust filaments or bullets must have been formed along that process. These have not been identified yet. It also must be noted that during the 1990–2000 time interval the entire Galactic center region was under detailed investigation in the entire NIR/mid-IR (MIR) and radio wavelength band with observing runs closely placed in time. No special event in the mini-spiral to the southeast of Sgr A* had been reported then.

It has been noted that the thermal instability can explain in a natural way the pressure equilibrium between the hot and the cold plasma in the mini-spiral region (Czerny et al. 2013; Róžańska et al. 2014).

Hence, this process is relevant for the possibility of survival of the infalling clouds in the region, and it also allows us to estimate the typical size of clouds. In fact, clouds as large as 10^{14} – 10^{15} cm (0.001–0.01 lt-yr) can persist. From the dominating optically thin DSO line emission a total mass of the clouds of $\simeq 10$ Earth masses can be derived, depending on the strength of the ambient radiation field. This agrees with recent results (Shcherbakov

2014) suggesting the mass of the DSO/G2 cloud to be within the range 4–20 M_{\oplus} . Naturally, this would be upon the assumption of a coreless cloud scenario, whereas the mass estimates do not apply if a star is embedded within the cloud. It turns out that clouds located a distance exceeding ~ 0.05 pc from Sgr A* can survive a few hundred years, which means that the cooling and evaporation time is shorter than the free-fall time onto the black hole.

Gillessen et al. (2013b) and Pfuhl et al. (2015) suggest that 13 years prior to the DSO peribothron passage the source G1 went through its peribothron on an orbit connected to the current DSO orbit. Dust heating of G1 would then explain the moderate IR excess of 0.3 K -band magnitudes of the star S2 in 2002 (Appendix in Pfuhl et al. 2015) as it passed close to Sgr A* and G1. However, with Sabha et al. (2012) we have shown that over timescales of a few months to a few years—especially close to the center—serendipitous sources can frequently be formed owing to density fluctuations of the background stars in the central arcsecond.

The DSO is supposed to be on a similar orbit to the G1 source (Pfuhl et al. 2015). However, up to this point, as it is approaching peribothron, the DSO has not shown any increase in K - or even L -band flux density that could be attributed to dust heating. In fact, while approaching Sgr A* in 2013, the L -band identification of the DSO was lost (Pfuhl et al. 2015). This can in part be attributed to confusion. To some extent diffusion or destruction of dust as the source entered the immediate surroundings of Sgr A* may be responsible as well, but certainly no brightening of the source in its K - or L -band emission has been observed.

Until now several models have placed a star at the center of the DSO (Murray-Clay & Loeb 2012; Eckart et al. 2013; Scoville & Burkert 2013; Ballone et al. 2013; Phifer et al. 2013; Zajaček et al. 2014). An at least partial tidal disruption is also expected if the DSO is an embedded star. A Roche description of the Sgr A*/DSO system (Eckart et al. 2013) suggests that a more massive central star will lose less of the gas and dust from the central few AU than a solar-mass-type star or a dwarf. Simulations of compact systems by Zajaček et al. (2014) support this finding as well (see also Section 4.5).

For source sizes that are much smaller than the peribothron distance with Jalali et al. (2014) we have shown that at the peribothron position the gaseous source volume is compressed by at least a factor of two owing to gravitational focusing. This results in the fact that before and after peribothron the source stays relatively compact despite the influence of possible turbulences and shocks that may be induced owing to shearing gas streams close to peribothron. Depending on the density of the overall environment, hydrodynamic interactions with the ambient material set in well past peribothron. This is consistent with all hydrodynamic and particle simulations that have been used to predict the future development of the DSO or similar sources (e.g., Zajaček et al. 2014; Burkert et al. 2012; Schartmann et al. 2012; Jalali et al. 2014).

4.3. Interactions with the Ambient Medium

If the DSO passes through an accretion wind from Sgr A*, it may develop a bow shock. In case it is indeed a dusty star, then one may expect to see cometary source structures quite similar to the sources X3 and X7, which are in the overall mini-cavity region just south of Sgr A* at a projected distance of $0''.8$ and $3''.4$ (Mužić et al. 2010). In mid-2014 the DSO is well within a sphere of hot gas surrounding Sgr A* out to approximately the Bondi radius ($\approx 10^5 R_S$). As a dusty source, the DSO can therefore

be regarded as an obvious probe for strong winds possibly associated with Sgr A*. However, there is no clearly resolved structure that can be considered as a bow shock, although the DSO is already closer to Sgr A* than X3 and X7. This may indicate that the wind from Sgr A* is highly non-isotropic, possibly directed toward the mini-cavity (Mužić et al. 2010), and that the DSO has not yet passed through that wind. However, the mass load of such a wind (due to the radiatively inefficient accretion mechanism) may not be high enough to allow for the formation of a prominent cometary tail structure. The detailed density profile for the central region of the radiatively inefficient accretion flow is difficult to obtain. Methods are rather indirect and accretion model dependent (Baganoff et al. 2003; Marrone et al. 2007; Wang et al. 2013). However, Eckart et al. (2014a) have pointed out that the smaller size compared to X3 and X7 may be due to the higher particle density within the accretion stream close to Sgr A* (e.g., Shcherbakov & Baganoff 2010).

4.4. Flare Activity

A possibly efficient probe of the interaction of the DSO with its ambient environment or with the black hole itself is monitoring the flux density originating from the central few tenths of an arcsecond. However, the results of these efforts have not been very revealing so far.

The NIR flare activity we observed through SINFONI during the peribothron approach in 2013/2014 is in full agreement with the statistical expectations as we described them with Witzel et al. (2012). There was no exceptional activity, with three flares of a few milli-Jansky strength.

If the DSO were to develop a bow shock while approaching the immediate environment of Sgr A*, then this event might lead to shock accelerations of electrons and to correspondingly strong excursions in the radio emission. However, the strength of these emission peaks depends critically on the size of the bow shock, and early estimates on the order of 1–20 Jy in the decimeter to short centimeter wavelength range had to be revised to values on the order of 0.01–0.2 Jy (Narayan et al. 2012; Sądowski et al. 2013; Crumley & Kumar 2013). Despite a dense monitoring program with the Very Large Array (Sjouwerman & Chandler 2014), strong radio flares have not yet been reported and the now-predicted strength of the variability would be in the normal range of the flux density variations observed toward Sgr A* (e.g., Markoff et al. 2001, 2007; Eckart et al. 2012b).

So far in the X-ray observable ≥ 2 keV band no elevated continuum flux density level or extraordinary X-ray variability has been reported (Haggard et al. 2014). Such an extra emission would have been expected to originate from the shock-heated gas (Gillessen et al. 2012).

Although Sgr A* is extremely faint in the X-ray bands, it is strongly variable in this domain of the electromagnetic spectrum (Baganoff et al. 2001, 2003; Porquet et al. 2003, 2008; Eckart et al. 2012b; Nowak et al. 2012; Degenaar et al. 2013; Barrière et al. 2014; Mossoux et al. 2015; Neilsen et al. 2013). The statistical investigation of the NIR variability by Witzel et al. (2012) suggests that the past strong X-ray variations are potentially linked with the origin of the observed X-ray echoes (Revnivtsev et al. 2004; Sunyaev & Churazov 1998; Terrier et al. 2010; Capelli et al. 2012). Assuming an underlying synchrotron self-Compton process, the NIR variability can in fact explain the required X-ray flare fluxes as a natural and nonexceptional phenomenon of the source. Therefore, Sgr A* is the ideal extremely low accretion rate target that allows us to study this particular phase, in which apparently most SMBHs

spend their lifetime. Phenomena like the passage of the DSO may dominate the variability of objects in this phase throughout the electromagnetic spectrum.

While the DSO is a very compact continuum and line-emitting source (see Section 3.3 and Eckart et al. 2013), its peribothron distance is rather small (see Section 4.1). Hence, it is still an open question whether and when some activity of Sgr A* is triggered by the DSO fly-by.

4.5. The DSO as a Young Accreting Star

Large line widths are common among pre-main-sequence stars, including both T Tauri stars (with an age of about 10^5 – 10^6 yr) and protostars (with an age of about 10^4 – 10^5 yr), with an infalling envelope that forms a disk close to the star. Bertout (1994) already pointed out that Doppler broadening from pre-main-sequence stars may range roughly from 50 to 500 km s^{-1} in the course of the accretion phase. As an example, hydrogen recombination and Na D line profiles of several hundred kilometers per second in a number of pre-main-sequence stars (e.g., T Tau, DG Tau, DR Tau, AS205, and SCrA) are shown. The M0V classical T Tauri star LkCa-8 (IP Tau) (Wolk & Walter 1996; Moto’oka & Itoh 2013) has a 600 – 700 km s^{-1} Br γ line width (Edwards et al. 2013), quite comparable to the width currently found for the DSO. Another case of a low-mass star with exceptionally large line widths is DK Tau A, with an 800 km s^{-1} wide line (Eisner et al. 2007). It is listed by Herczeg & Hillenbrand (2014) as a K8.5 star with a mass of $0.68 M_{\odot}$.

Without doubt the Br γ line traces high-excitation regions; however, in the case of young embedded protostars it is currently unclear whether these regions are associated with accretion funnel flows, the jet base (Davis et al. 2011), or less collimated ionized winds. All of these elements can contribute to the emission and the large observed line width. In the case of the DSO there are several mechanisms that can contribute to a large line width.

1. *Contribution from collisional ionization in a bow shock.* A possible origin of a broad wide Br γ emission line was discussed by Scoville & Burkert (2013) on the basis of the bow shock model that is relevant for the supersonic motion of the object through the hot ambient interstellar medium (ISM) emitting X-rays. They show that Br γ emission may arise from the collisional ionization and the gas cooling in the narrow but dense cold ($\sim 10^5$ – 10^6 K) and shocked layer of the stellar wind. The high densities ($\sim 10^8 \text{ cm}^{-3}$) in this layer can explain the observed emission measure.

2. *Contribution from wind drag in a bow shock.* The large increase in FWHM line width from 137 km s^{-1} in 2006 to 730 km s^{-1} in 2014 could also be related to the increase in orbital velocity from about 1200 km s^{-1} to almost 9000 km s^{-1} at peribothron. Discussing the emission from photoionized stellar wind bow shocks, Cantó et al. (2005) calculate the change of velocity in the thin shocked layer that develops while the source is moving through the ISM. In the context of the DSO this effect has not yet been discussed before. In their Equations (19) and (33) they approximate the dependence of that velocity as $v_{\text{sl}} \propto v_w \times f(v_a, R, \theta, \phi)$. Here v_{sl} is the velocity in the shock layer, v_w is the stellar wind velocity, and v_a is the velocity relative to the ISM. The radius R and the angles θ and ϕ describe the geometry of the shock front. It is the change of v_{sl} across the shock front that may contribute to the observed Br γ line width. The analytic solution of Wilkin (1996) for the thin

steady-state bow shock layer yields the estimate for the shock layer velocity $v_{\text{sl}} \approx 2v_a\theta/[3(1+v_a/v_w)]$ close to the symmetry axis, where the angle θ is small. The ratio of this velocity at the same θ , but different epochs, 2006 and the peribothron crossing, yields $v_{\text{sl}}^{\text{per}}/v_{\text{sl}}^{2006} \approx 1.07$ – 1.26 for the terminal wind velocities of 100 – 400 km s^{-1} , respectively. Thus, the increase in velocity by about 10% could be contributed by wind drag in a bow shock layer.

3. *Contribution from stellar or disk winds.* There can also be a contribution to Br γ emission from the gaseous inner disk, stellar wind, stellar-field-driven wind (X-wind), or disk wind (Lima et al. 2010) that can originate from the corotation radius to several astronomical units (see Kraus et al. 2008 for discussion and their Figure 1). Günther (2011) shows that for classical pre-main-sequence stars, wind velocities of a few hundred kilometers per second can occur.

4. *Tidal contribution.* The increase in FWHM of DSO would then be caused by the tidal stretching and perturbation of the accretion disk, especially close to the peribothron, which would consequently lead to larger velocity dispersions of inflow and outflow streams. Simple considerations analogous to the computation of tidal compression presented by Jalali et al. (2014) show the increase of velocity deviation. There are several ways to assess the importance of tidal stretching of the DSO along its orbit from our data:

α —if the total pre-peribothron line width of about 720 km s^{-1} was dominated by tidal stretching, then a minimum source size of about 65 mas is expected based on the mean slope of 1000 km s^{-1} over a projected orbital path of about 90 mas (i.e., $\sim 11 \text{ km s}^{-1} \text{ mas}^{-1}$) within the past 2 yr.

β —attributing the 2008–2013 size estimate of $42 \pm 10 \text{ mas}$ Gillessen et al. (2013b) to the year 2013 and assuming a free gas cloud subjected to orbital stretching along the orbit, we find that the source should be 5–8 times larger, i.e., 210 – 336 mas , close to peribothron. We cannot confirm such a large size from our Br γ line maps in Figure 9 (see also Table 2).

γ —the separation of apparently simultaneously observed extreme velocity components of G2 close to the peribothron passage (Figures 1 and 15 in Gillessen et al. (2013b); Pfuhl et al. (2015), which is consistent with a cut through their p v -diagram in Figure 1) implies a size between 90 mas and 150 mas along the orbit. With our data we only see a single-lined DSO either red- or blueshifted with a diameter of $<20 \text{ mas}$, and, given the low foreshortening (Section 4.1 and Figure 11), we cannot confirm the presence of multiple sources or a large source extent (see Section 3.3 and Figure 9).

δ —we measured very close to the points at which extreme orbital velocities in the red and blue can be observed. At these positions for an extended tidally stretched source the emission previously blue of the source center will become redshifted and blueshifted, respectively. Hence, a line width that can be up to a factor of two narrower is expected. However, the post-peribothron line width is about a third of the pre-peribothron value, and the small source sizes are in conflict with an extended tidally stretched source. In addition, the orbital compression expected for such a scenario would imply a larger line width and a higher line flux density owing to the increased density of the emitting gas volume. Instead, for a dust-enshrouded accreting stellar object line variability in integrated line flux density and line shape is expected.

5. *Contributions from accretion.* However, there can also be a contribution from the gas accretion of the circumstellar envelope onto the stellar surface if the DSO is a young stellar object as

has already been proposed and discussed (Murray-Clay & Loeb 2012; Eckart et al. 2013; Scoville & Burkert 2013; Zajačec et al. 2014; De Colle et al. 2014). In this framework an increase of the Br γ line width as a function of time could result from an increased perturbation of the envelope or disk that leads to an enhanced velocity dispersion in the accretion stream onto the central star as it gets closer to the peribothron.

In the following we investigate whether the infalling gas that is approximately in free fall and is being shocked upon reaching the stellar surface can explain the observed large line width of the DSO Br γ line, which evolved from FWHM(Br γ) \sim 200 km s $^{-1}$ in 2006 to FWHM(Br γ) \sim 700 km s $^{-1}$ in 2014, as laid out in Section 3.1.1 (see also Phifer et al. 2013; Gillessen et al. 2013b). This corresponds to radial velocities v_r of infalling material that range from about 100 km s $^{-1}$ to several hundred kilometers per second.

4.5.1. The Model Geometry

For simplicity, we consider an *axisymmetric magnetospheric accretion model* (see Bouvier et al. 2007 for review) for the accretion on pre-main-sequence stars where the gas moves ballistically along the magnetic field lines from the innermost orbit of the disk and gains large infall velocities of the order of \sim 100 km s $^{-1}$ (Hartmann et al. 1994). Unlike the boundary layer model, the magnetospheric accretion scenario can indeed explain observed redshifted absorption minima at free-fall velocity and blueward asymmetry in emission lines (Muzerolle et al. 1998a, and references therein).

The presence of a magnetic field around pre-main-sequence stars is justified by the observation of the Zeeman broadening of photospheric lines (Johns-Krull et al. 1999, 2001), as well as by the measurement of the electron cyclotron maser emission (Smith et al. 2003). The inferred field strength is \sim 1–3 kG. In the context of the dipole magneto-accretion model, in which the gas is in free fall, the truncation radius in terms of stellar radii is (e.g., Bouvier et al. 2007)

$$\frac{R_T}{R_*} \approx 6.5 B_3^{4/7} R_2^{5/7} \dot{M}_{-8}^{-2/7} M_1^{-1/7}, \quad (1)$$

where the strength of the dipole magnetic field at the equator B_3 is in kG, the stellar radius R_2 is in units of $2 R_\odot$, the accretion rate \dot{M}_{-8} is expressed in $10^{-8} M_\odot \text{ yr}^{-1}$, and the stellar mass M_1 is in units of $1 M_\odot$. The truncation radius in Equation (1) is derived for gas in free fall in the spherical symmetry. For disk accretion it may serve as an upper limit, since the ram gas pressure is higher in that case and the truncation radius is thus shifted inward.

For stable accretion to proceed, the truncation radius expressed by Equation (1) has to be smaller than the corotation radius R_{co} , $R_T \lesssim R_{\text{co}}$, at which the Keplerian angular velocity is equal to the rotational angular velocity of the star,

$$R_{\text{co}} \approx 4.2 M_1^{1/3} P_1^{2/3} R_\odot, \quad (2)$$

where M_1 is the stellar mass in units of $1 M_\odot$ and P_1 is the stellar rotation period in units of 1 day (see Bouvier et al. 2007, for discussion). The inner portion of the disk is purely made up of gas up to the dust sublimation radius, which, according to simulations by Whitney et al. (2004), may be expressed in terms of the dust sublimation temperature and the stellar effective temperature as

$$R_{\text{sub}} = R_* \left(\frac{T_{\text{sub}}}{T_*} \right)^{-2.085}, \quad (3)$$

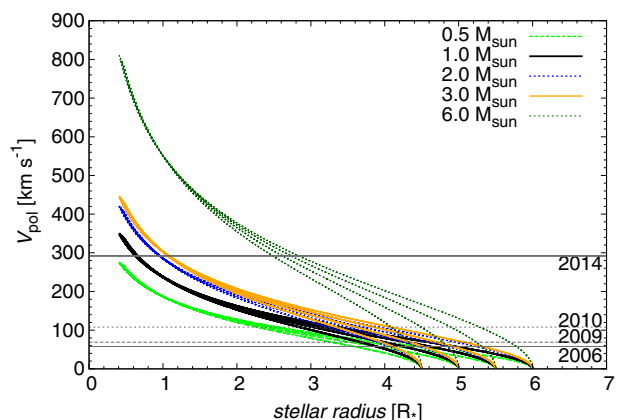


Figure 12. Poloidal velocity profile as a function of the distance from the pre-main-sequence star in a magnetospheric accretion model (Hartmann et al. 1994) for different masses of pre-main-sequence stars at \sim 1 Myr (Siess et al. 2000). The gray horizontal lines represent the observed radial velocity for years 2006, 2009, 2010, and 2014 with an increasing tendency (Phifer et al. 2013; Gillessen et al. 2013b; this work).

which for typical values of T_* (spectral types K, M: 3000–4500 K) and $T_{\text{sub}} \approx 1500$ K has values of \sim 4–10 R_* . Beyond the dust sublimation radius, dust can coexist with the gaseous phase. The emerging radiation from the accretion flow is reprocessed by the circumstellar dust, giving rise to the IR excess.

For the calculation of the velocity profiles of the accretion flow we assume the truncation radius to be at $R_T = 5 R_*$ (Gullbring et al. 1998; Alcalá et al. 2014), which is close to the estimate in Equation (1). We compute the poloidal velocity profiles in the framework of the magnetospheric accretion model (see Equations (1) and (3) of Hartmann et al. 1994) for 0.5, 1.0, 2.0, and 3.0 M_\odot pre-main-sequence stars with a stellar radius of 2.1, 2.6, 3.6, and 4.8 R_\odot , respectively, at 1 Myr (Siess et al. 2000) for solar metallicity and no overshooting; see Figure 12 for the comparison of the poloidal velocity for the observed radial velocity, which is observed to increase with the approach of the DSO to the peribothron. For earlier epochs the observed FWHM is consistent with the accretion onto a low-mass object of \sim 0.5–1 M_\odot . To explain the higher FWHM in 2014, a massive pre-main-sequence star of Herbig Ae/Be type is needed at the first glance, since for lower-mass stars only the upstream parts reach comparable velocities; see the poloidal velocity profile of the 6 M_\odot star with a radius of 2.9 R_\odot in Figure 12. However, such a massive stellar core having a luminosity of \gtrsim 100 L_\odot is inconsistent with the luminosity constraint on the DSO (\leq 10 L_\odot), and the pre-main-sequence stage is also very short (Siess et al. 2000).

The physics of circumstellar material of pre-main-sequence stars is generally more complex, especially close to the SMBH, where the disk surrounding the star is expected to be warped and perturbed by tidal effects. Although basic observational signatures of pre-main-sequence stars (strong stellar magnetic fields, truncation radius, accretion shocks observed mainly for classical pre-main-sequence stars) are in accordance with the magnetospheric accretion model (Bouvier et al. 2007) and suggest that Br γ originates in gas infall rather than outflow (Najita et al. 1996), it is plausible that there is a contribution to Br γ emission from stellar or disk winds.

We note that the line profile may be generally nonsymmetric and its width dependent on the inclination, at which the emerging

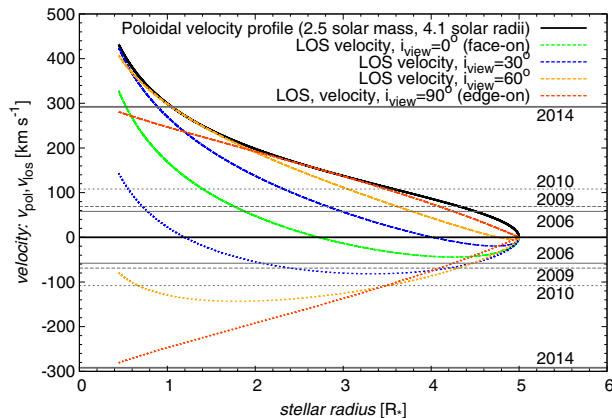


Figure 13. Profiles of maximum line-of-sight velocity as a function of the distance from the star in a magnetospheric accretion model (Hartmann et al. 1994) for a $2.5 M_{\odot}$ pre-main-sequence star for a different inclination of the view of emerging radiation. The receding flow (nearer to the observer, mostly redshifted, positive velocities) is labeled by dashes, while the approaching flow (farther away, mostly blueshifted, negative velocities) is represented by dots. The gray horizontal lines represent the observed radial velocity $v \sin i$ for years 2006, 2009, 2010, and 2014 with an increasing tendency (Phifer et al. 2013; Gillissen et al. 2013b, this work):

emission is viewed. This is demonstrated by the profiles of the maximum line-of-sight velocity in Figure 13, where we plot separately approaching (mostly blueshifted) and receding (mostly redshifted) accretion streams for $2.5 M_{\odot}$ pre-main-sequence stars (at ~ 1 Myr; Siess et al. 2000). The separation between the dashed and the dotted lines for each stellar radius and inclination is an approximate measure of the observed line width. The line broadening is generally bigger for a larger inclination (see also Muzerolle et al. 1998a, for detailed radiative transfer modeling). The results in Figure 13 clearly show that with a star of about $2 M_{\odot}$ the observed $\text{Br}\gamma$ line widths, covering the full range from about 200 km s^{-1} to 700 km s^{-1} , can be reproduced. From the range of maximum and minimum velocities it is also evident that the line profile can be asymmetric and skewed to one side.

4.5.2. Accretion Luminosity and Rate

In fact, the broad hydrogen $\text{Br}\gamma$ line with the FWHM of the order of $\sim 100 \text{ km s}^{-1}$ is frequently observed in the spectra of accreting pre-main-sequence stars (detection rate 70%–74%; Folha & Emerson 2001; Ilee et al. 2014) and appears to be a useful tracer of magnetospheric accretion on embedded pre-main-sequence stars (Muzerolle et al. 1998a, 1998b; Folha & Emerson 2001; Calvet et al. 2004). Here the star is assumed to accrete matter from its envelope or the inner edge of an accretion disk. Accretion from the surrounding ISM can be considered as insignificant.

The correlation between $\text{Br}\gamma$ emission-line luminosity and accretion luminosity is found to be tight (Muzerolle et al. 1998b; Calvet et al. 2004). The empirical relation between emission-line and accretion luminosities is based on various signatures of accretion luminosity ($H\alpha$ luminosity, optical, and UV excess). The recent fit is as follows (Alcalá et al. 2014):

$$\log(L_{\text{acc}}/L_{\odot}) = \zeta_1 \log[L(\text{Br}\gamma)/L_{\odot}] + \zeta_2, \quad (4)$$

with $\zeta_1 = 1.16 \pm 0.07$ and $\zeta_2 = 3.60 \pm 0.38$. This correlation may then be extended to heavily extinguished protostars that are enshrouded in a dusty envelope.

If we naively apply this relation to the DSO and its $\text{Br}\gamma$ emission-line luminosity of $L(\text{Br}\gamma) = f_{\text{acc}} \times 10^{-3} L_{\odot}$, where f_{acc} is a factor of the order of unity, we get a reasonable range for the accretion luminosity, $\log(L_{\text{acc}}/L_{\odot}) \approx 1.16 \log f_{\text{acc}} + 0.12$; $L_{\text{acc}} = 1.3 \times 14.5^{\log f_{\text{acc}}} L_{\odot}$, and for $f_{\text{acc}} = \{1, 2, 3, 4\}$ yielding $(1.3, 3.0, 4.7, 6.6) L_{\odot}$.

For the assumption of the innermost radius of $R_{\text{in}} = 5 R_{\star}$, the accretion rate is given by (Gullbring et al. 1998)

$$\dot{M}_{\text{acc}} \cong \frac{L_{\text{acc}} R_{\star}}{GM_{\star}} \left(1 - \frac{R_{\star}}{R_{\text{T}}}\right)^{-1}, \quad (5)$$

which can be written as

$$\dot{M}_{\text{acc}} \approx \xi \left(\frac{L_{\text{acc}}}{L_{\odot}}\right) \left(\frac{R_{\star}}{R_{\odot}}\right) \left(\frac{M_{\star}}{M_{\odot}}\right)^{-1} M_{\odot} \text{ yr}^{-1}, \quad (6)$$

with $\xi = 4.1 \times 10^{-8}$.

Inserting the estimated values for mass, radius, and the accretion luminosity, we obtain an accretion rate of the order of $\lesssim 10^{-7} M_{\odot} \text{ yr}^{-1}$, which is about 10 times larger than the median value observed for pre-main-sequence stars in the Taurus and Chameleon I regions (Hartmann et al. 1998). It is, however, consistent with the span of pre-main-sequence accretion rates, which seem to evolve with the age of the pre-main-sequence star as $\dot{M}_{\text{acc}} \propto t^{-2.1}$ (Baxter et al. 2008).

The gas outflow rate was shown to correlate with the accretion in pre-main-sequence systems. The ratio of rates was established approximately as $\dot{M}_{\text{w}}/\dot{M}_{\text{acc}} \sim 0.1$ (Edwards et al. 2006, and references therein), which corresponds to the order of $\dot{M}_{\text{w}} \lesssim 10^{-8} M_{\odot} \text{ yr}^{-1}$. This order of magnitude for the wind outflow rate was discussed by Scoville & Burkert (2013) for the wind–wind bow shock origin of $\text{Br}\gamma$ emission.

The estimates of accretion luminosity and accretion and mass-loss rates are upper limits since there may be contribution to $\text{Br}\gamma$ flux from sources other than accretion flows, namely, stellar wind or disk outflows (Kraus et al. 2008).

4.5.3. Density and Emission Measure

The radial density profile of the accretion flow may be inferred based on the estimated values of pre-main-sequence star mass, radius, mass accretion rate, and the assumed size of the magnetosphere. Assuming an axisymmetric steady flow of matter along the streamlines, the following relation holds for the hydrogen number density (Hartmann et al. 1994),

$$n_{\text{H}}(r) = \frac{\dot{M}_{\text{acc}}}{4\pi m_{\text{H}} \left(\frac{1}{r_{\text{mi}}} - \frac{1}{r_{\text{mo}}}\right)} \frac{r^{-5/2} (4-3y)^{1/2}}{(2GM_{\star})^{1/2} (1-y)^{1/2}}, \quad (7)$$

where the magnetic streamlines are described by $r = r_{\text{m}} \sin^2 \theta$, where θ denotes the angle between the magnetic dipole axis and the radius vector \mathbf{r} ; in Equation (7) $y = r/r_{\text{m}} = \sin^2 \theta$ and r_{mi} and r_{mo} stand for the radius of the innermost and the outermost streamline intersecting the accretion disk, respectively; we take $r_{\text{mi}} = 5 R_{\star}$ and $r_{\text{mo}} = 7 R_{\star}$ for definiteness. The mass accretion rate is held fixed at $\dot{M}_{\text{acc}} = 10^{-7} M_{\odot} \text{ yr}^{-1}$ in accordance with Equation (6). The density profiles for the same set of stars as in Figure 12 are plotted in Figure 14.

The density profile in Figure 14 enables us to estimate the emission measure, $\text{EM} \propto n_{\text{e}}^2 V$, under the assumption $n_{\text{e}} \approx n_{\text{H}}$; see Equation (7). The computation is performed for the distance range where the poloidal velocity, Figure 12, reaches the values

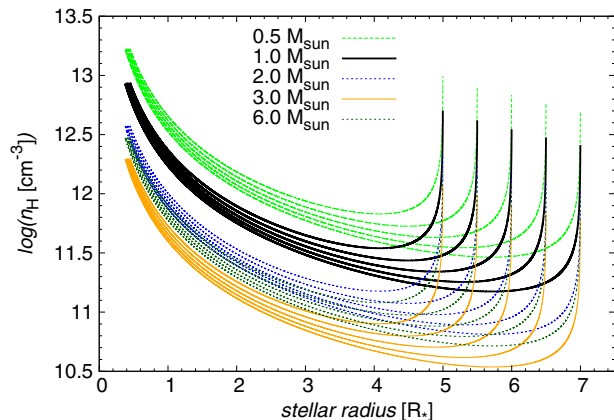


Figure 14. Radial number density profile as a function of the distance from the star in units of stellar radii. The computed profile is valid for the steady axisymmetric accretion on a pre-main-sequence star. Individual lines correspond to accretion flows along magnetic streamlines for a particular mass of a star (see the labels). The radius of a star is adopted from the evolutionary tracks of Siess et al. (2000) at ~ 1 Myr.

of $v_{\text{pol}} = 200 \pm 100 \text{ km s}^{-1}$, which roughly corresponds to the observed FWHM of the $\text{Br}\gamma$ line. Finally, we get the profiles of cumulative emission measure for a different mass of a pre-main-sequence star according to the evolutionary tracks by Siess et al. (2000) at ~ 1 Myr; see Figure 15. The emission measure is of the order of 10^{58} – 10^{61} cm^{-3} , being higher for lower-mass stars, and these values originate from close to the star, on the scale of ~ 1 – $3 R_*$. This implies that luminous line emission at the observed high velocities can originate from close to a few solar mass star.

One should consider these values highly estimative because of the uncertain values of mass accretion rate and the size and character of the magnetosphere. The temperature of the accretion flow was also not discussed. However, models of the accretion on pre-main-sequence stars show that the infalling gas is shock heated and the $\text{Br}\gamma$ line can be effectively produced close to the stellar surface (Bouvier et al. 2007). In principle, it is possible to reproduce the emission measure of $\sim 10^{57} \text{ cm}^{-3}$ that is obtained in the cold bow shock model by Scoville & Burkert (2013) and that corresponds to the observed flux of $\text{Br}\gamma$ emission. Thus, both mechanisms, wind–wind interaction and gas infall, can contribute in case the DSO is a young stellar object.

Given the accretion rate of $\lesssim 10^{-7} M_{\odot} \text{ yr}^{-1}$, the star associated with the DSO would be embedded within the hot accretion flow surrounding the star with a probably complex geometry. On the length scale of one stellar radius the density profiles in Figure 10 imply large IR K band and visible extinction of $A(K) \sim 0.1 \times A(V) \approx 0.1 \times (1.8 \times 10^{21})^{-1} \int n_e(l) dl$, which is ~ 59 , 37, 20, and 16 mag for a $0.5 M_{\odot}$, $1.0 M_{\odot}$, $2.0 M_{\odot}$, and $3.0 M_{\odot}$ star, respectively. Combined with the possible contribution of an extended outer dust shell and a warped or inflated outer disk, this is plenty of extinction to dim the light from the central star and produce the observed continuum characteristics of the DSO (Eckart et al. 2013, 2014a, 2014b; Phifer et al. 2013; Gillessen et al. 2012).

The material within the accretion flow is certainly not homogeneous. To first order we assume that it consists of cloudlets, sheets, or filaments that have a dense, optically thick core surrounded by a shell of optically thin material. Since the

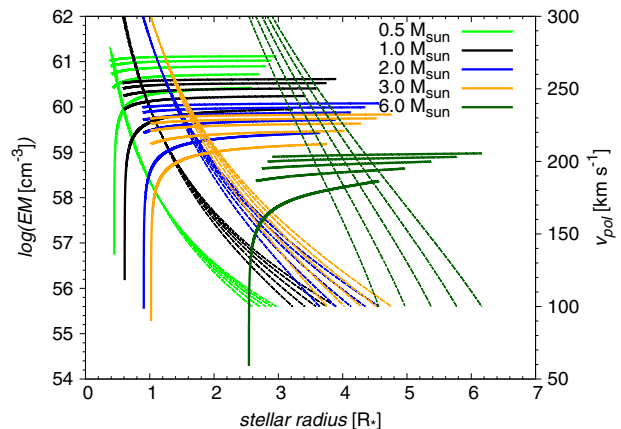


Figure 15. Logarithm of emission measure, EM (solid lines, with labels on the left vertical axis) and poloidal velocity profile v_{pol} (dot-dashed lines, with labels on the right vertical axis) as a function of the distance from the star in units of stellar radii. The computed profile is valid for the steady axisymmetric accretion on a pre-main-sequence star. Individual lines correspond to accretion flows along magnetic streamlines for a particular mass of a star (see the key). The radius of a star is adopted from the evolutionary tracks of Siess et al. (2000) at ~ 1 Myr.

overall line emission is dominated by optically thin material, and given the uncertainties in the $\text{Pa}\alpha/\text{Br}\gamma$ and $\text{He I}/\text{Br}\gamma$ line ratios, the maximum contribution of the optically thick material to the line fluxes can only be of the order of 0.05. Since the dense material is bright, the ratio η between the mean emission measure of the optically thin and thick material needs to be involved. Hence, a volume filling factor around $0.05 \times \eta$ will reproduce the optically thin line ratios and give a substantial contribution to the observed velocity profile. In addition, there will be a temperature gradient from the start of the accretion stream near the dust sublimation radius and the contact point on the stellar surface, leading to an enhanced contribution of the higher-velocity material.

The observed accreting pre-main-sequence stars generally have a lower accretion rate than the time-averaged infall rate (Audard et al. 2014). As a result, the gas from an infalling envelope is thought to be accumulated first in the quasi-Keplerian circumstellar disk. The accumulation of matter continues until the instability causes an increase in the mass transfer by about three to four orders of magnitude from the disk to the star, the so-called episodic accretion (Audard et al. 2014). If the DSO is indeed an embedded accreting pre-main-sequence star, the tidal effects from the SMBH lead to a gravitational instability that, combined with magnetorotational instability (Zhu et al. 2009), can cause a continual mass transfer from the disk, especially close to the peribothron, where the tidal radius shrinks to $\lesssim 1 \text{ AU}$ for a $1 M_{\odot}$ star; see also the tidal radius discussion related to Figure 16.

Let us sum up that the observed emission up to now is not in contradiction with the scenario of a pre-main-sequence star that is surrounded by a dusty envelope and accretes matter from an accretion disk inside the dust sublimation radius. Hot accretion flows as discussed here, possibly combined with disk winds (Günther 2011), can indeed produce emission lines with FWHM of several hundred kilometers per second. Hence, we find that for a 1 – $2 M_{\odot}$ embedded pre-main-sequence star these two effects can already fully account for the observed $\text{Br}\gamma$ line widths. However, in general the observed $\text{Br}\gamma$ line profile and flux may result from the combination of hydrogen recombination

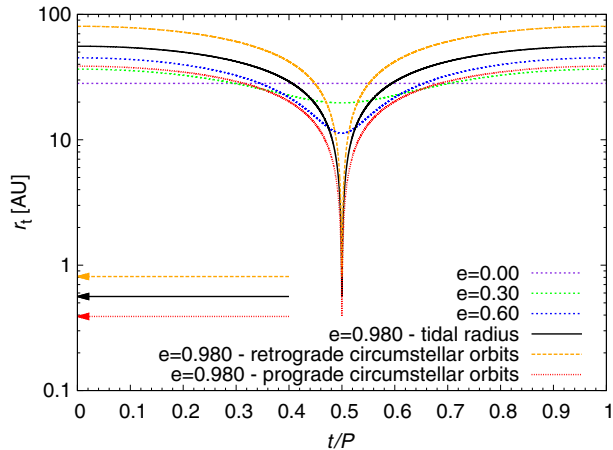


Figure 16. Temporal evolution of the tidal Hill radius for the orbits of a $1 M_{\odot}$ star around the SMBH with a different orbital eccentricity. At $t/P = 0.5$ the pericenter passage occurs. For the inferred orbit of the DSO, tidal radii for prograde as well as retrograde orbits are depicted. Actual values of the tidal radii at the peribothron are depicted by corresponding arrows. The current orbital solution implies a considerable tidal stripping for distances from the star $\gtrsim 1$ AU.

emission of the gaseous dusty envelope photoionized by nearby stars (Shcherbakov 2014), the collisionally ionized cold bow shock layer (Scoville & Burkert 2013), and the hot accretion flow on a pre-main-sequence star, as is discussed here. Whether and to what extent each of these processes contributes to the final emission will be constrained by further observations and modeling during the post-peribothron phase.

5. POSSIBLE ORIGIN, STABILITY, AND FATE OF THE DSO

There is evidence of both young and more evolved stars in the Galactic center (Genzel et al. 2010) that lie in the sphere of influence (~ 2 pc) of the SMBH. Mutual interactions among stars cause the oscillations of their orbital eccentricity via the mechanism of resonant relaxation (Hopman & Alexander 2006) or the Kozai oscillations (Karas & Šubr 2007; Chen & Amaro-Seoane 2014). These can set some stars on a plunging trajectory toward the SMBH (Zajaček et al. 2014). Similarly, with Jalali et al. (2014) we have shown that young stellar objects can efficiently be formed on plunging orbits in the vicinity of SMBHs as a consequence of orbital compressing of infalling gas clumps. An embedded young star/protostar is surrounded by an accretion disk whose orbit orientation can be any (direct, retrograde, or perpendicular) with respect to the orbit of the host star around the SMBH. These DSOs (Eckart et al. 2013) have an IR excess, and the currently observed DSO may indeed serve as a paradigm of these objects.

The restricted three-body problem may be used to obtain the approximations for critical stability (Hill) radii of disks. Using the restricted circular three-body problem, the equation of motion for a mass element in the rotating frame of star–SMBH becomes (i.e., Innanen 1979, 1980)

$$\frac{d^2 r}{dt^2} \simeq \left(\Omega^2 - \frac{d^2 V}{dR^2} - \frac{GM_{\star}}{r^3} \right) r \pm 2\Omega v_r, \quad (8)$$

where r is the distance of a mass element from the star and R labels the distance of the star from the SMBH, $r \ll R$.

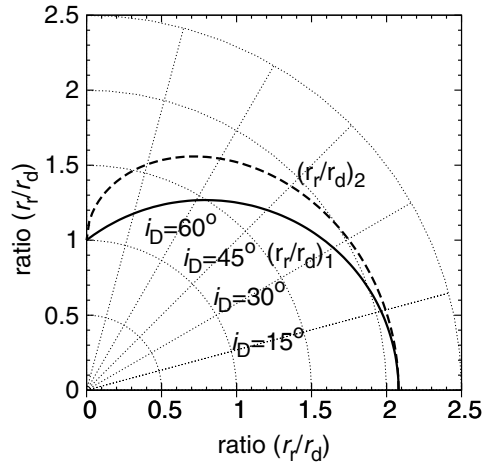


Figure 17. Polar plot of the dependence of the ratio of critical tidal radii of retrograde (r_r) and prograde (r_d) disks on the inclination of the accretion disk around a pre-main-sequence star with respect to the orbital plane of the star around the SMBH. In this plot the vertical and horizontal axes represent the same quantity—the ratio between retrograde and prograde tidal radii. The ratio dependence on the inclination was derived by Innanen (1980). The plotted relations have the form of $(r_r/r_d)_{1,2} = \{1 + f_{1,2}/2 + [f_{1,2} + (f_{1,2}/2)^2]^{1/2}\}^{2/3}$, where $f_1 = 4(\cos^2 i)/3$ and $f_2 = 4 \cos i/(2 + \cos i)$. The relation $(r_r/r_d)_1$ dominates the second one. The largest difference between the critical tidal radii of a factor of ~ 2 is for low-inclination orbits with respect to the orbital plane of DSO.

For $R \gg R_g$, the gravitational potential of the black hole is approximately equal to the Newtonian $V \equiv V(R)$, hence $-d^2 V/dR^2 = 2GM_{\bullet}/R^3$. The angular frequency of the circular motion for the star is $\Omega^2 = GM_{\bullet}/R^3$, and for the minor body $\omega^2 = GM_{\star}/r^3$. The difference between direct and retrograde orbits arises from the different signs of the Coriolis term $\pm 2\Omega v_r$, where $v_r = \omega r$.

When generalized for orbits with eccentricity e , one gets the following ratio of critical tidal radii for retrograde and direct disks, $r_{H,r}$ and $r_{H,d}$, respectively (Innanen 1979):

$$\frac{r_{H,r}}{r_{H,d}} = \left[\frac{5 + e + 2(4 + e)^{1/2}}{3 + e} \right]^{2/3}. \quad (9)$$

In terms of the critical tidal radius,

$$r_t = R(t)(M_{\star}/(3M_{\bullet}))^{1/3}, \quad (10)$$

the critical Hill radius for prograde orbits r_d and retrograde orbits r_r may be expressed as $r_r = 3^{1/3} r_t$ and $r_d = 3^{-1/3} r_t$. Since the mass of the SMBH M_{\bullet} is larger by at least five orders of magnitude than the mass of any star M_{\star} , the tidal Hill radius r_t expressed by Equation (10) extends up to Lagrangian points L1 and L2, beyond which the circumstellar matter is strongly tidally perturbed and may escape the Roche lobe of the star (see Figure 18 of Eckart et al. 2013). The temporal evolution of the tidal radii for the current orbital elements and the stellar mass of $m_{\star} = 1 M_{\odot}$ is shown in Figure 16.

The ratio $r_{H,r}/r_{H,d}$ acquires values of (1.9, 2.1) for eccentricities $e \in (1, 0)$. Therefore, retrograde orbits are expected to be stable for larger distances from the host star, approximately by a factor of two for low-inclination orbits; see Figure 17 for the polar plot of the dependence of the ratio of tidal Hill stability radii $r_{H,r}/r_{H,d}$ on the inclination i_D between a putative circumstellar accretion disk and the orbital plane of DSO.

6. CONCLUSIONS

In our sensitive imaging spectroscopy data set we measured prominent line emission from the DSO and determined new orbital parameters based on data from 2014 February to September. The source appeared to be single lined at all times. Before the peribothron, we detected redshifted Br γ line emission (at 2700 km s⁻¹) but no blueshifted emission above the noise level at the position of Sgr A* or upstream of the presumed orbit. After the peribothron, we detected blueshifted Br γ line emission (at -3320 km s⁻¹) but no redshifted emission above the noise level at the position of Sgr A* or downstream of the presumed orbit. We find a Br γ line FWHM of 50 ± 10 Å before and 15 ± 10 Å after the peribothron transit, i.e., no significant line broadening with respect to last year is observed. Such a broadening would be expected in the case of significant tidal interaction. This is a further indication for the fact that the DSO is spatially rather compact.

We show that for a 1–2 M_{\odot} embedded pre-main-sequence star hot accretion streams close to the star, possibly in combination with disk winds, can fully account for the luminous observed Br γ emission with line widths covering the full range from about 200 km s⁻¹ to 700 km s⁻¹. The accretion material and the surrounding shell/disk provide enough extinction to explain the IR colors of the DSO (Eckart et al. 2013). The resulting line profile can be asymmetric and skewed to one side, calling for precaution when using the line emission to derive orbital parameters. Following the pre-main-sequence evolutionary tracks of low- and intermediate-mass stars by Siess et al. (2000), we find that after an initial phase of a few × 10⁵ yr 1–2 M_{\odot} stars can stay for a major portion of their T Tauri stage with a luminosity of less than 10 L_{\odot} (see also Chen & Amaro-Seoane 2014). This is consistent with a dust temperature of 450 K and a possible spectral decomposition of the NIR/MIR spectrum (Eckart et al. 2013) of the DSO using the M -band measurement by Gillessen et al. (2012). Higher stellar masses would not comply with this luminosity limit and are not required to explain the Br γ line widths. An embedded pre-main-sequence star can also explain the increase of the Br γ line width assuming that tidal stretching and perturbation of the envelope lead to an enhancement of the velocity dispersion in the accretion stream onto the central star as the DSO approaches the peribothron. An identification of the DSO with a dust-embedded star also puts the interpretation of a common history of the DSO/G2 and G1 at risk (Pfuhl et al. 2015). Owing to the higher mass (1–2 M_{\odot} instead of 3 Earth masses), a much higher drag force than the one provided by the small source size would be required to connect the DSO orbit to that of G1.

We also find that the NIR flaring activity of Sgr A* has not shown any statistically significant increment. This points to the fact that the DSO had not yet reached its peribothron before 2014 May. Even if the source has a stellar core, a major part of the enshrouding cloud may be dissolved during the peribothron passage. Therefore, increased accretion activity of Sgr A* may still be upcoming. The Sgr A*/DSO system can be looked upon as a binary system, and the Roche lobe picture can be adopted in which the Lagrange point L1 between the two objects is of special importance if mass transfer between the two objects needs to be considered. If the central star has around one solar mass, the L1 will get very close (~1 AU) and may allow the dominant part of the gas and dust to transit into the Sgr A*-dominated Roche lobe. As a result, the low-mass stellar core may be even less luminous after the transit than the matter in its immediate vicinity (i.e., 1 AU) before the transit. This will,

however, be only for a very short time, and it is not clear whether the gas close to the star will remain in the Roche lobe of the star after peribothron or not. For higher-mass stellar cores that were heavily extinguished before peribothron, most of the material closer to the stars (i.e., a few AU) may be largely unaffected by the transition, and the stellar core may be even cleared from extinguishing material and brighter in the NIR bands than before the peribothron.

In the near future it will become increasingly difficult to measure the strength and spatial extent of the line emission on the blue side of the orbit. This is due to a high-velocity star that is moving into this field from the northwest. It will then be followed by S2 going through peribothron around 2017.9 ± 0.35 (Gillessen et al. 2009; Eisenhauer et al. 2003) and S0–102 around 2021.0 ± 0.3 (Meyer et al. 2014a, 2014b). Strong continuum contributions and residual line features in the stellar atmospheres may make sensitive observations very difficult and time-consuming.

The research leading to these results received funding from the European Union Seventh Framework Program (FP7/2007–2013) under grant agreement n312789. This work has been financially supported by the Programme National Hautes Energies (PNHE). This work was supported in part by the Deutsche Forschungsgemeinschaft (DFG) via the Cologne Bonn Graduate School (BCGS), the Max Planck Society through the International Max Planck Research School (IMPRS) for Astronomy and Astrophysics, as well as special funds through the University of Cologne. M.Z., B.S., S.S., and A.B. are members of the IMPRS. Part of this work was supported by fruitful discussions with members of the European Union funded COST Action MP0905: Black Holes in a Violent Universe and the Czech Science Foundation—DFG collaboration (No. 13-00070J). This work was co-funded under the Marie Curie Actions of the European Commission (FP7-COFUND). M.G.-M. is supported by the German federal department for education and research (BMBF) under project number 50OS1101. We are grateful to all members of the ESO PARANAL team.

REFERENCES

- Alcalá, J. M., Natta, A., Manara, C. F., et al. 2014, *A&A*, 561, A2
 Audard, M., Ábrahám, P., Dunham, M. M., et al. 2014, arXiv:1401.3368
 Baganoff, F. K., Bautz, M. W., Brandt, W. N., et al. 2001, *Natur*, 413, 45
 Baganoff, F. K., Maeda, Y., Morris, M., et al. 2003, *ApJ*, 591, 891
 Ballone, A., Schartmann, M., Burkert, A., et al. 2013, *ApJ*, 776, 13
 Barrière, N. M., Tomsick, J. A., Baganoff, F. K., et al. 2014, *ApJ*, 786, 46
 Baxter, E., Corrales, L., Yamada, R., & Esin, A. A. 2008, *ApJ*, 689, 308
 Bertout, C. 1994, *LNP*, 431, 49
 Bonnet, H., Abuter, R., Baker, A., et al. 2004, *Msngr*, 117, 17
 Bouvier, J., Alencar, S. H. P., Harries, T. J., Johns-Krull, C. M., & Romanova, M. M. 2007, in *Protostars and Planets V*, ed. B. Reipurth, D. Jewitt, & K. Keil (Tucson, AZ: Univ. Arizona Press), 479
 Burkert, A., Schartmann, M., Alig, C., et al. 2012, *ApJ*, 750, 58
 Calvet, N., Muzerolle, J., Briceño, C., et al. 2004, *AJ*, 128, 1294
 Cantó, J., Raga, A. C., & González, R. 2005, *RMxAA*, 41, 101
 Capelli, R., Warwick, R. S., Porquet, D., Gillessen, S., & Predehl, P. 2012, *A&A*, 545, A35
 Chen, X., & Amaro-Seoane, P. 2014, *ApJL*, 786, L14
 Crumley, P., & Kumar, P. 2013, *MNRAS*, 436, 1955
 Czerny, B., Kunneriath, D., Karas, V., & Das, T. K. 2013, *A&A*, 555, A97
 Davis, C. J., Cervantes, B., Nisini, B., et al. 2011, *A&A*, 528, A3
 De Colle, F., Raga, A. C., Contreras-Torres, F. F., & Toledo-Roy, J. C. 2014, *ApJL*, 789, L33
 Degenaar, N., Miller, J. M., Kennea, J., et al. 2013, *ApJ*, 769, 155
 Diolaiti, E., Bendinelli, O., Bonaccini, D., et al. 2000, *A&AS*, 147, 335
 Eckart, A., Britzen, S., Horrobin, M., et al. 2012a, <http://pos.sissa.it/cgi-bin/reader/conf.cgi?confid=169>, id.4

- Eckart, A., & Duhoux, P. R. M. 1991, in ASP Conf. Ser. 14, *Astrophysics with Infrared Arrays*, ed. R. Elston (San Francisco, CA: ASP), 336
- Eckart, A., García-Marín, M., Vogel, S. N., et al. 2012b, *A&A*, 537, A52
- Eckart, A., Horrobin, M., Britzen, S., et al. 2014a, in IAU Symp. 303, *The Galactic Center: Feeding and Feedback in a Normal Galactic Nucleus*, ed. L. O. Sjouwerman, C. C. Lang, & J. Ott (Cambridge: Cambridge Univ. Press), 269
- Eckart, A., Mužić, K., Yazici, S., et al. 2013, *A&A*, 551, A18
- Eckart, A., Valencia-S., M., Peissker, F., et al. 2014b, *ATel*, 6285, 1
- Edwards, S., Fischer, W., Hillenbrand, L., & Kwan, J. 2006, *ApJ*, 646, 319
- Edwards, S., Kwan, J., Fischer, W., et al. 2013, *ApJ*, 778, 148
- Eisenhauer, F., Abuter, R., Bickert, K., et al. 2003, *Proc. SPIE*, 4841, 1548
- Eisenhauer, F., Genzel, R., Alexander, T., et al. 2005, *ApJ*, 628, 246
- Eisner, J. A., Hillenbrand, L. A., White, R. J., et al. 2007, *ApJ*, 669, 1072
- Folha, D. F. M., & Emerson, J. P. 2001, *A&A*, 365, 90
- Genzel, R., Eisenhauer, F., & Gillessen, S. 2010, *RvMP*, 82, 3121
- Ghez, A. M., Duchêne, G., Matthews, K., et al. 2003, *ApJL*, 586, L127
- Ghez, A. M., Witzel, G., Sitarski, B., et al. 2014, *ATel*, 6110, 1
- Gillessen, S., Eisenhauer, F., Fritz, T. K., et al. 2009, *ApJL*, 707, L114
- Gillessen, S., Genzel, R., Fritz, T. K., et al. 2012, *Natur*, 481, 51
- Gillessen, S., Genzel, R., Fritz, T. K., et al. 2013a, *ApJ*, 763, 78
- Gillessen, S., Genzel, R., Fritz, T. K., et al. 2013b, *ApJ*, 774, 44
- Gullbring, E., Hartmann, L., Briceño, C., & Calvet, N. 1998, *ApJ*, 492, 323
- Günther, H. M. 2011, *AN*, 332, 448
- Haggard, D., Baganoff, F. K., Rea, N., et al. 2014, *ATel*, 6242, 1
- Hartmann, L., Calvet, N., Gullbring, E., & D'Alessio, P. 1998, *ApJ*, 495, 385
- Hartmann, L., Hewett, R., & Calvet, N. 1994, *ApJ*, 426, 669
- Herczeg, G. J., & Hillenbrand, L. A. 2014, *ApJ*, 786, 97
- Hopman, C., & Alexander, T. 2006, *ApJ*, 645, 1152
- Ilee, J. D., Fairlamb, J., Oudmaijer, R. D., et al. 2014, *MNRAS*, 445, 3723
- Innanen, K. A. 1979, *AJ*, 84, 960
- Innanen, K. A. 1980, *AJ*, 85, 81
- Jalali, B., Pelupessy, F. I., Eckart, A., et al. 2014, *MNRAS*, 444, 1205
- Johns-Krull, C. M., Valenti, J. A., & Koresko, C. 1999, *ApJ*, 516, 900
- Johns-Krull, C. M., Valenti, J. A., Piskunov, N. E., Saar, S. H., & Hatzes, A. P. 2001, in ASP Conf. Ser. 248, *Magnetic Fields Across the Hertzsprung–Russell Diagram*, ed. G. Mathys, S. K. Solanki, & D. T. Wickramasinghe (San Francisco, CA: ASP), 527
- Karas, V., & Šubr, L. 2007, *A&A*, 470, 11
- Kraus, S., Hofmann, K.-H., Benisty, M., et al. 2008, *A&A*, 489, 1157
- Lima, G. H. R. A., Alencar, S. H. P., Calvet, N., Hartmann, L., & Muzerolle, J. 2010, *A&A*, 522, A104
- Markoff, S., Bower, G. C., & Falcke, H. 2007, *MNRAS*, 379, 1519
- Markoff, S., Falcke, H., Yuan, F., & Biermann, P. L. 2001, *A&A*, 379, L13
- Marrone, D. P., Moran, J. M., Zhao, J.-H., & Rao, R. 2007, *ApJL*, 654, L57
- Martins, F., Trippe, S., Paumard, T., et al. 2006, *ApJL*, 649, L103
- Meyer, L., Ghez, A. M., Witzel, G., et al. 2014a, in IAU Symp. 303, *The Galactic Center: Feeding and Feedback in a Normal Galactic Nucleus*, ed. L. O. Sjouwerman, C. C. Lang, & J. Ott (Cambridge: Cambridge Univ. Press), 264
- Meyer, L., Witzel, G., Longstaff, F. A., & Ghez, A. M. 2014b, *ApJ*, 791, 24
- Mossoux, E., Grosso, N., Vincent, F. H., & Porquet, D. 2015, *A&A*, 573, 46
- Moto'oka, K., & Itoh, Y. 2013, *RAA*, 13, 1189
- Murray-Clay, R. A., & Loeb, A. 2012, *NatCo*, 3, 1049
- Muzerolle, J., Calvet, N., & Hartmann, L. 1998a, *ApJ*, 492, 743
- Muzerolle, J., Hartmann, L., & Calvet, N. 1998b, *AJ*, 116, 2965
- Mužić, K., Eckart, A., Schödel, R., et al. 2010, *A&A*, 521, A13
- Najita, J., Carr, J. S., & Tokunaga, A. T. 1996, *ApJ*, 456, 292
- Narayan, R., Özel, F., & Sironi, L. 2012, *ApJL*, 757, L20
- Neilsen, J., Nowak, M. A., Gammie, C., et al. 2013, *ApJ*, 774, 42
- Nowak, M. A., Neilsen, J., Markoff, S. B., et al. 2012, *ApJ*, 759, 95
- Pfuhl, O., Gillessen, S., Eisenhauer, F., et al. 2015, *ApJ*, 798, 111
- Phifer, K., Do, T., Meyer, L., et al. 2013, *ApJL*, 773, L13
- Porquet, D., Grosso, N., Predehl, P., et al. 2008, *A&A*, 488, 549
- Porquet, D., Predehl, P., Aschenbach, B., et al. 2003, *A&A*, 407, L17
- Pych, W. 2004, *PASP*, 116, 148
- Revnivtsev, M. G., Churazov, E. M., Sazonov, S. Y., et al. 2004, *A&A*, 425, L49
- Różańska, A., Czerny, B., Kunneriath, D., et al. 2014, *MNRAS*, 445, 4385
- Sabha, N., Eckart, A., Merritt, D., et al. 2012, *A&A*, 545, A70
- Sądowski, A., Sironi, L., Abarca, D., et al. 2013, *MNRAS*, 432, 478
- Schartmann, M., Burkert, A., Alig, C., et al. 2012, *ApJ*, 755, 155
- Schödel, R., Najarro, F., Muzic, K., & Eckart, A. 2010, *A&A*, 511, A18
- Scoville, N., & Burkert, A. 2013, *ApJ*, 768, 108
- Shcherbakov, R. V. 2014, *ApJ*, 783, 31
- Shcherbakov, R. V., & Baganoff, F. K. 2010, *ApJ*, 716, 504
- Siess, L., Dufour, E., & Forestini, M. 2000, *A&A*, 358, 593
- Sjouwerman, L. O., & Chandler, C. J. 2014, in IAU Symp. 303, *The Galactic Center: Feeding and Feedback in a Normal Galactic Nucleus*, ed. L. O. Sjouwerman, C. C. Lang, & J. Ott (Cambridge: Cambridge Univ. Press), 327
- Smajić, S., Moser, L., Eckart, A., et al. 2014, *A&A*, 567, A119
- Smith, K., Pestalozzi, M., Güdel, M., Conway, J., & Benz, A. O. 2003, *A&A*, 406, 957
- Sunyaev, R., & Churazov, E. 1998, *MNRAS*, 297, 1279
- Terrier, R., Ponti, G., Bélanger, G., et al. 2010, *ApJ*, 719, 143
- Wang, Q. D., Nowak, M. A., Markoff, S. B., et al. 2013, *Sci*, 341, 981
- Whitney, B. A., Indebetouw, R., Bjorkman, J. E., & Wood, K. 2004, *ApJ*, 617, 1177
- Wilkin, F. P. 1996, *ApJL*, 459, L31
- Witzel, G., Eckart, A., Bremer, M., et al. 2012, *ApJS*, 203, 18
- Witzel, G., Ghez, A. M., Morris, M. R., et al. 2014, *ApJ*, 796, L8
- Wolk, S. J., & Walter, F. M. 1996, *AJ*, 111, 2066
- Zajaček, M., Karas, V., & Eckart, A. 2014, *A&A*, 565, A17
- Zhu, Z., Hartmann, L., & Gammie, C. 2009, *ApJ*, 694, 1045

Bow-shock evolution close to the SMBH

Towards the Galactic centre, stars can move faster than the local speed of sound. Although the plasma emitting X-ray bremsstrahlung is hot, stars can still reach supersonic relative velocities with respect to the ambient medium. Moreover, there is an observational evidence of bow shocks, especially those interacting with minispiral arms ([Sanchez-Bermudez et al. 2014](#)) and with the central outflow ([Mužić et al. 2010](#)). Also, several candidates for photoevaporative proplyds were detected in radio continuum ([Yusef-Zadeh et al. 2015](#)).

When stars approach Sgr A*, dynamical timescales become short enough so that proper motions and in some cases radial velocities can be detected, therefore the stellar orbit around the SMBH can be determined. It is of theoretical but also observational interest to consider the evolution of a stellar bow shock along the orbit, especially when the ambient medium has a considerable velocity field with respect to the stellar orbital velocity. I focused on studying the effect of the asymmetry in the bow-shock evolution along the orbit with respect to the peribothron passage. This asymmetry is induced by either an ambient inflow, outflow, or by the combination of both.

The main results of this analysis are published in the following peer-reviewed paper published in the Monthly Notices of the Royal Astronomical Society.

Credit: Zajaček et al., MNRAS 455, 1257 (2016). Reproduced with permission ©Oxford University Press.



Effect of an isotropic outflow from the Galactic Centre on the bow-shock evolution along the orbit

M. Zajaček,^{1,2,3★†} A. Eckart,^{2,1} V. Karas,³ D. Kunneriath,³ B. Shahzamanian,^{2,1†}
N. Sabha,² K. Mužić^{4,5} and M. Valencia-S.²

¹Max-Planck-Institut für Radioastronomie (MPIfR), Auf dem Hügel 69, D-53121 Bonn, Germany

²I. Physikalisches Institut der Universität zu Köln, Zùlpicher Strasse 77, D-50937 Köln, Germany

³Astronomical Institute, Academy of Sciences, Boční II 1401, CZ-14131 Prague, Czech Republic

⁴European Southern Observatory, Alonso de Córdova 3107, Casilla 19001, Santiago 19, Chile

⁵Nucleo de Astronomía, Facultad de Ingeniería, Universidad Diego Portales, Av. Ejército 441, Santiago, Chile

Accepted 2015 October 7. Received 2015 October 7; in original form 2015 May 26

ABSTRACT

Motivated by the observations of several infrared-excess bow-shock sources and proplyd-like objects near the Galactic Centre, we analyse the effect of a potential outflow from the centre on bow-shock properties. We show that due to the non-negligible isotropic central outflow the bow-shock evolution along the orbit becomes asymmetric between the pre-peribothron and post-peribothron phases. This is demonstrated by the calculation of the bow-shock size evolution, the velocity along the shocked layer, the surface density of the bow shock, and by emission-measure maps close to the peribothron passage. Within the ambient velocity range of $\lesssim 2000 \text{ km s}^{-1}$ the asymmetry is profound and the changes are considerable for different outflow velocities. As a case study we perform model calculations for the Dusty S-cluster Object (DSO/G2) as a potential young stellar object that is currently being monitored and has passed the pericentre at ~ 2000 Schwarzschild radii from the supermassive black hole (Sgr A*) in 2014. We show that the velocity field of the shocked layer can contribute to the observed increasing line width of the DSO source up to the peribothron. Subsequently, supposing that the line emission originates in the bow shock, a decrease of the line width is expected. Furthermore, the decline of the bow-shock emission measure in the post-peribothron phase could help to reveal the emission of the putative star. The dominant contribution of circumstellar matter (either inflow or outflow) is consistent with the observed stable luminosity and compactness of the DSO/G2 source during its pericentre passage.

Key words: stars: pre-main-sequence – stars: winds, outflows – ISM: jets and outflows – Galaxy: centre.

1 INTRODUCTION

The centre of the Milky Way contains a large number of young stars (~ 10 – 100 Myr) that orbit the compact radio source Sgr A* associated with the supermassive black hole of $\sim 4 \times 10^6 M_{\odot}$ (hereafter denoted as SMBH; Ghez et al. 2003; Eckart, Schödel & Straubmeier 2005; Genzel, Eisenhauer & Gillessen 2010). These stars of spectral type O/B are concentrated partially in the coherent clockwise disc structure with a sharp inner edge at ~ 0.03 pc and extending out to 0.5 pc (Levin & Beloborodov 2003). High-velocity stars of spectral type B, which have orbital periods of $\lesssim 300$ yr, are located in the S-cluster in the innermost 0.05 pc with isotropic orientation of orbits (Eckart & Genzel 1996, 1997; Gillessen et al. 2009; Sabha et al.

2012) and high eccentricities approximately following the thermal distribution, $f(e)de \approx 2ede$. Some young stars of spectral type O/WR do not form any clear kinematic structure (Genzel et al. 2010) and they have rather random orbital orientations (Sanchez-Bermudez et al. 2014).

The radius of the sphere of the gravitational influence of the SMBH depends on the central black hole mass M_{\bullet} and the stellar velocity dispersion σ (Merritt 2013) in the following way:

$$r_{\text{SI}} \approx 1.7 \left(\frac{M_{\bullet}}{4.0 \times 10^6 M_{\odot}} \right) \left(\frac{\sigma}{100 \text{ km s}^{-1}} \right)^{-2} \text{ pc}. \quad (1)$$

This coincides approximately with the radius of the central cavity, which is filled with ionized hot and sparse gas mostly supplied by stellar winds of massive OB stars. The density and temperature profiles of this ambient corona are fitted by semi-analytical radial profiles based on the model of radiatively inefficient accretion flows (RIAF; Blandford & Begelman 1999; Broderick & Loeb 2006;

* E-mail: zajacek@ph1.uni-koeln.de

† IMPRS Member.

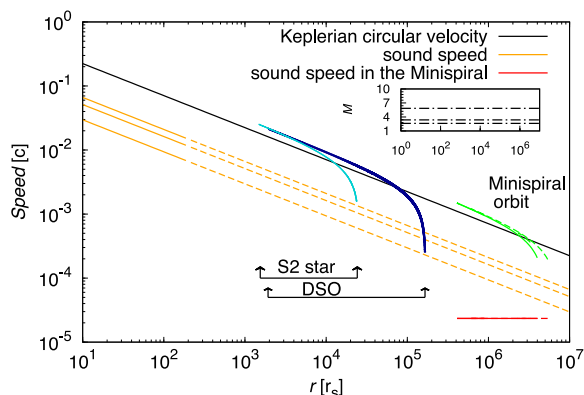


Figure 1. Comparison of Keplerian orbital speed and sound speed towards the Galactic Centre, both expressed in terms of the speed of light. Three lines for the sound speed (orange) stand for possible different temperatures of electron and ion components. The dashed lines mark the extrapolation of the original fit (solid lines). The distance–orbital speed plots for the DSO and S2 are also labelled and the arrows denote the distance range for both objects. The estimate of the sound speed for the gas phase of the mini-spiral region is marked by the red line. The set of green lines corresponds to the estimate of the orbital velocity for three prominent streams (arms) of the mini-spiral. The plot inset shows the estimates of the Mach number M , $M = v_{\text{orb}}/c_s$.

Broderick et al. 2011):

$$n_a \approx n_a^0 \left(\frac{r}{r_s} \right)^{-1}, \quad (2)$$

$$T_a \approx T_a^0 \left(\frac{r}{r_s} \right)^{-1}, \quad (3)$$

where r_s is the Schwarzschild radius ($r_s \equiv 2GM_\bullet/c^2 \doteq 2.95 \times 10^5 M_\bullet/M_\odot$ cm). The normalization parameters are set to $n_a^0 = 1.3 \times 10^7 \text{ cm}^{-3}$ and $T_a^0 = 9.5 \times 10^{10} \text{ K}$. At a small distance from the SMBH, electrons are expected to be decoupled from ions. The ion temperature T_i can be ~ 1 – 5 times higher than the electron temperature T_e as was found by comparing MHD simulations with VLBI millimetre data (Dexter et al. 2010). This is also expressed in Fig. 1 by three lines for the sound speed profile corresponding to the temperature of T_e , $3T_e$, and $5T_e$.

The profile for the sound speed in Fig. 1 is a simple extrapolation of the semi-analytic fits, equations (2) and (3), to VLBI millimetre measurements of the emission in the inner $\sim 100 r_s$, while the orbits of the observed S-stars lie at least an order of magnitude further from the SMBH. However, the extrapolation of the one-dimensional fit of *Chandra* X-ray measurements (Quataert 2004) towards smaller distances leads to similar values of density and temperature in the region of our interest (a factor of 3 difference; see Psaltis 2012 for discussion). In any case the density increase towards the centre naturally leads to higher ambient ram pressure, $P_a = \rho_a v_a^2$, acting on the outflows of propagating stars.

When the stellar motion with respect to the surrounding environment is supersonic, bow-shock structures are formed. The distance range, where the Keplerian orbital velocity $v_{\text{orb}}/c = \sqrt{2}/2(r/r_s)^{-1/2}$ is greater than the sound speed $c_s \approx \sqrt{k_B T_a / (\mu m_H)}$, calculated from profiles given by equations (2) and (3), may be inferred from the comparison in Fig. 1, where we plot both velocities (in units of speed of light c) as functions of the distance r

from the SMBH. The motion seems to be supersonic for a large span of distances, from $\sim 10 r_s$ up to $\sim 10^6 r_s$, where the orbits of the S-stars lie (see also Psaltis 2012). In fact, the radial profile of Mach number, $M \equiv v_{\text{orb}}/c_s$, is approximately flat, since both the orbital velocity and the sound speed fall off as $(r/r_s)^{-1/2}$ for the assumed ambient temperature profile adopted here, which leads to $M \approx (GM_\bullet \mu m_H / k_B T_a r_s)$ and approximate values of 2.6, 3.4, and 5.8 (see also the plot inset in Fig. 1).

Nowadays we have a great deal of observational information for the interaction of wind-blowing stars with their surroundings near the Galactic Centre (see e.g. Sanchez-Bermudez et al. 2014). The sources IRS 1W, IRS 3, IRS 5, IRS 8, IRS 10W, and IRS 21, which interact mainly with the warm ionized gas in the mini-spiral region (Tanner et al. 2002, 2005; Viehmann et al. 2005; Buchholz et al. 2013; Sanchez-Bermudez et al. 2014), are clear evidence of bow-shock formation in the near- and mid-infrared (NIR and MIR) parts of the spectrum. The mini-spiral region is in general colder and denser in comparison with the radial profiles (equations 2 and 3) of the ambient medium at the distance of $\sim 10^6 r_s$ corresponding to the mini-spiral region (Kunneriath et al. 2012). This can be understood in the framework of a multiphase environment where cool and hot phases co-exist (Róžańska et al. 2014). The ionized component of the high-density regions of the northern and eastern arm has the mean electron temperature of $\bar{T}_e \approx 6 \times 10^3 \text{ K}$, corresponding to a sound speed of $\sim 7 \text{ km s}^{-1}$, whereas the Keplerian circular velocity at this distance is of the order of a few 100 km s^{-1} . Hence, unless the sources are comoving with the mini-spiral streams, the relative velocities are typically supersonic.

Bow-shock sources appear to be extended and brighter at longer wavelengths, which is in agreement with the dust emission in the bow shocks. Viehmann et al. (2006) showed that the peak of the continuum emission of typical bow-shock sources lies in the wavelength range ~ 4 – $10 \mu\text{m}$, corresponding to the dust temperature of a few 100 K. Moreover, Buchholz et al. (2013) pointed out the strong polarization degree of IRS 1W and 21 in the NIR wavelengths that increases towards longer wavelengths, which highlights the importance of dust for explaining the emission properties of bow-shock sources in this region. Besides the continuum emission, bow-shock sources associated with young stellar objects in H II regions are observed in hydrogen recombination lines (Bally, O’Dell & McCaughrean 2000). Scoville & Burkert (2013) show that the dense, shocked layer typically associated with a young star of T Tauri type may significantly contribute to observed Br γ emission of the Dusty S-cluster Object (DSO/G2), which is intensively monitored.

The detection and analysis of the comet-shaped sources named X3 and X7 indicates that they interact with the outflowing medium from the direction of the Galactic Centre (Mužić et al. 2007, 2010). This outflow originates within the central $\sim 0.2 \text{ pc}$ from the direction of Sgr A* and its estimated terminal velocities are of the order of $\sim 1000 \text{ km s}^{-1}$. The discovery of a new MIR bow shock suggests the presence of this outflow at even larger distances, $\sim 0.68 \text{ pc}$ (Sabha et al. 2014).

The presence of an outflow from the Galactic Centre is consistent with the low-luminosity state of Sgr A* (Wang et al. 2013). The observed unabsorbed X-ray luminosity in the 2–10 keV range is $\sim 10^{33} \text{ erg s}^{-1}$, which is about eight orders of magnitude less than the X-ray luminosity expected from the accretion of stellar winds at the Bondi capture radius, $r_B \approx 4 \text{ arcsec} (T_a/10^7 \text{ K})^{-1}$. This has been often explained by the presence of RIAFs (Blandford & Begelman 1999), which involve a powerful wind that is responsible for the loss of mass, angular momentum, and energy from accreting

material (Yuan, Bu & Wu 2012; see also Yuan & Narayan 2014 for a review).

Besides the *RIAF* mechanism of accretion the outflow may be supported by stellar winds from ~ 100 hot, massive OB/WR stars that are known to be present at $\sim 1-10$ arcsec, or it may be launched by the activity of compact remnants indicated by diffuse hard X-ray emission (Perez et al. 2015). It is also not clear whether the outflow is isotropic or rather anisotropic. However, the recent analysis of radio interferometric observations showed that the closure phase remained zero within uncertainties, which indicates that the outflow is rather symmetric outside $\sim 100r_s$ from Sgr A* (Park et al. 2015).

In this paper we investigate the effect of an isotropic outflow from the Galactic Centre with different terminal velocities (v_a) on the stellar bow-shock properties. The fundamental feature studied here is the temporal asymmetry of a bow-shock evolution due to the outflow from the centre. Using an analytic solution of Wilkin (1996) we construct a semi-analytical toy model that can be used to investigate the bow-shock properties (equilibrium stand-off distance, shell velocity, surface density, emission measure maps) for different outflow velocities and a large span of distances from Sgr A*.

The basic qualitative properties of the asymmetry are general and are applicable to any wind-blowing source moving in the potential of the SMBH. To show specific results, we apply the model to the DSO (Eckart et al. 2013), also named G2 (Burkert et al. 2012; Gillessen et al. 2012), which is being monitored in detail and shows signs of being an infrared-excess dust-enshrouded star with the basic characteristics of a young T Tauri star (see Murray-Clay & Loeb 2012; Ballone et al. 2013; Eckart et al. 2013; Scoville & Burkert 2013; De Colle et al. 2014; Zajaček, Karas & Eckart 2014; Valencia-S. et al. 2015, for details). Our basic set-up is similar to the 2D hydrodynamic simulations of Ballone et al. (2013) and 3D hydrodynamic simulations of De Colle et al. (2014). We complement their work by analysing the effect of the outflow from the Galactic Centre on bow-shock properties. Although our semi-analytic approach does not allow us to trace microphysical processes along the shocked layer in detail, it can be easily used to track the evolutionary trends of the bow-shock source along the whole orbit and a large span of distances from the Galactic Centre, which would be computationally highly demanding using 3D hydrodynamical calculations. The qualitative results can be applied to any bow-shock source that is followed along the orbit and its bow-shock emission is at least partially resolved. Even if the orbit of the source is not determined, the internal properties of the bow shock depend not only on its distance from Sgr A*, but are also influenced by the sense of motion with respect to the source of the outflow in the Galactic Centre.

The structure of the paper is as follows. In Section 2 we describe the model set-up and the calculation of characteristics of stellar bow shocks. We continue with the description of the main results in Section 3, where we focus on the formation of asymmetry in the bow-shock evolution along the orbit (Section 3.1) and calculate the shell velocity (Section 3.2) and density profiles (Section 3.3) as functions of both the distance from the SMBH and the angle measured along the bow shock. We calculate the emission measure maps in Section 3.4. In Section 3.5 we compare the bow-shock emission measure to the other possible sources of emission – the stellar wind and pre-main-sequence accretion. The analysis of the Doppler contribution of the shell velocity field to the emission of bow-shock sources is presented in Section 3.6. In Section 3.7 we revisit the previous estimates of non-thermal emission for a stellar bow shock at the peribothron and compare it with the passage of a coreless gas cloud. We discuss the results in Section 4 and conclude in Section 5.

2 DESCRIPTION OF THE BOW-SHOCK MODEL SET-UP

In this section we describe the mathematical details of an adopted bow-shock model. We consider a momentum-supported bow-shock model originally proposed by Baranov, Krasnobaev & Kulikovskii (1971). The analytical solution and the formalism of the momentum-supported, geometrically thin bow shock were developed by Wilkin (1996, 2000), where the reader can find the full derivation. Here we extend the analytical scenario by a semi-analytical treatment of the bow-shock evolution along the orbit.

We consider a star on a nearly radial, highly eccentric orbit ($e \gtrsim 0.9$) around the SMBH. As a first approximation, the ambient medium is described by the spherically symmetric temperature and density profiles, equations (2) and (3). The outflow is assumed to be isotropic with the characteristic terminal outflow velocity v_a . The basic set-up is illustrated in Fig. 2.

Young, low-mass stars in the Galactic Centre region, which the DSO source may belong to, seem to have a proplyd-like, bow-shock appearance (Yusef-Zadeh et al. 2015a). Several sources exhibit strong NIR excess (Eckart et al. 2013), and the spectral decomposition implies that they are probably young stars surrounded by dust shells (Eckart et al. 2004). They are embedded within the photoionized H II region of the central cavity. The central region ionized by massive OB stars is similar to the expanding M42 region in the Orion nebula. Young, low-mass stars of LL Ori type (Bally et al. 2000; Bally & Reipurth 2001) have radiative winds that drive a shock into the ambient medium. In order to apply the exact solution of Wilkin (1996, 2000) to study the evolution and properties of stellar wind bow shocks near the Galactic Centre, we assume the following properties.

- (i) The bow shock is momentum-supported, i.e. the internal momentum is conserved within the shell.
- (ii) The post-shock cooling is efficient. Consequently, the shell of shocked gas becomes *geometrically* thin.¹ In other words, the cooling parameter $\chi = t_{\text{cool}}/t_{\text{dyn}}$, where t_{cool} is the cooling time-scale of the shocked gas and t_{dyn} is the dynamical time-scale of the system, is assumed to be smaller than 1. Especially slower winds ($v_w \lesssim 300 \text{ km s}^{-1}$) seem to be susceptible to radiative cooling in the high-pressure environment of Sgr A* (Cuadra et al. 2005).
- (iii) The stellar wind with the terminal velocity v_w is isotropic and stationary. The density profile of the circumstellar medium is then given simply by the relation $\rho_w = \dot{m}_w / (4\pi r_*^2 v_w)$, where \dot{m}_w is the stellar mass-loss rate and r_* is the distance from the star.
- (iv) At each point of the stellar orbit the equilibrium bow-shock structure is approximately reached; see Appendix A for estimates. The density of the ambient medium ρ_a is given by equation (2). We neglect the density gradient at a given position of the star from the centre as well as the velocity divergence of the ambient flow, which are small for a fixed distance and do not affect the main features of orbital asymmetry studied here. See Appendix B for details.

The star passing through the interstellar medium around the SMBH is characterized by the mass-loss rate \dot{m}_w and terminal stellar wind velocity v_w . An important variable is the relative velocity of the star with respect to the surrounding medium $\mathbf{v}_{\text{rel}} = \mathbf{v}_* - \mathbf{v}_a$. In general, the bow-shock geometry may be described by spherical coordinates (R, θ, ϕ) , where R is the distance of the shock

¹ This does not imply that the material is optically thin. The term thin bow shock is used to denote a bow shock with negligible geometrical thickness in comparison with the stagnation radius.

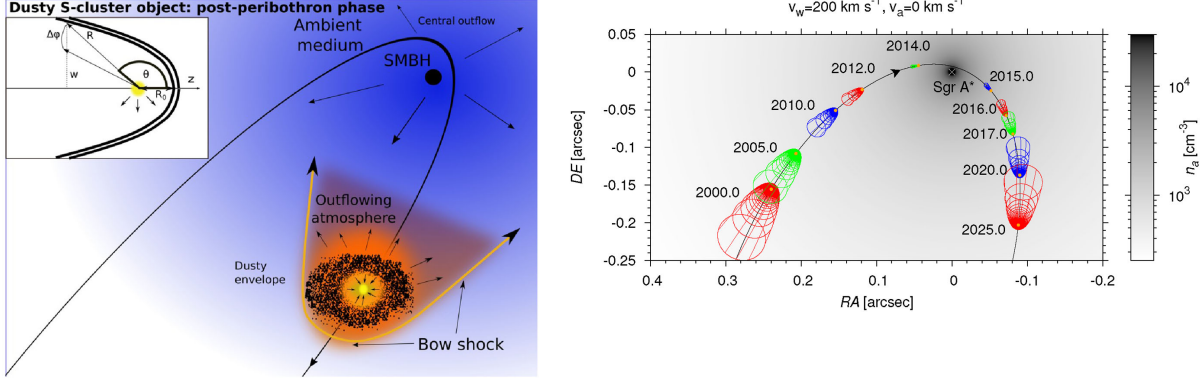


Figure 2. Left: illustration of the model set-up – wind-blowing Dusty S-cluster Object (DSO) on an eccentric trajectory around the SMBH in the post-peribothron phase. The figure inset depicts the geometry of the axisymmetric bow shock. The stand-off distance R_0 is labelled as well as the distance $R = R(\theta)$ of the bow shock at angle θ from the axis of symmetry. Right: the exemplary evolution of the bow-shock geometry along an eccentric trajectory. In this case the ambient flow is considered negligible with respect to the stellar motion. The colour axis shows the particle density per cm^3 according to the profile given by equation (2).

from the star, θ is the angle from the z -axis (the axis of symmetry for axisymmetric bow shocks; see Fig. 2), and ϕ is the polar angle in xy -plane. We also define the cylindrical radius $w = R \sin \theta$ and denote the velocity of the flow in the shell as v_t . The relative velocity of the star has the direction of the z -axis, $\mathbf{v}_{\text{rel}} = v_{\text{rel}} \mathbf{e}_z$.

The material within the shell of a stellar axisymmetric bow-shock flows along a slice with constant ϕ (Wilkin 1996). The flux of the mass along any slice of angle $\Delta\phi$ may be expressed as

$$\Delta \dot{m} = w v_t \sigma \Delta\phi, \quad (4)$$

where σ is the surface density within the shock. In an axisymmetric bow-shock model, the flux of the mass from the stellar wind and the ambient medium (along any slice) may be also expressed as

$$\Delta \dot{m} \equiv \frac{\dot{m}_w}{4\pi} f_m(\theta) \Delta\phi, \quad (5)$$

where the function $f_m(\theta)$ depends on an adopted axisymmetric bow-shock model.

The momentum flux in the shell resulting from the momentum imparted by the stellar wind and ambient medium may be expressed using model-dependent functions $f_w(\theta)$, $f_z(\theta)$ (separately in w and z directions):

$$\Delta \dot{\Pi}_z \equiv \frac{\dot{m}_w v_w}{4\pi} f_z(\theta) \Delta\phi, \quad (6)$$

$$\Delta \dot{\Pi}_w \equiv \frac{\dot{m}_w v_w}{4\pi} f_w(\theta) \Delta\phi. \quad (7)$$

Consequently, the velocity in the shell v_t may be expressed in terms of its components v_w and v_z :

$$v_w = v_w \frac{f_w(\theta)}{f_m(\theta)}, \quad (8)$$

$$v_z = v_w \frac{f_z(\theta)}{f_m(\theta)}, \quad (9)$$

as $v_t = \sqrt{v_w^2 + v_z^2}$, leading to

$$v_t = v_w \frac{\sqrt{f_w(\theta)^2 + f_z(\theta)^2}}{f_m(\theta)}. \quad (10)$$

Let us denote the coordinate across the shell of the bow shock by l and the total thickness of the shell by h . The flow in the

bow shock creates centrifugal pressure and the final shape of the shock is determined by the balance of the ram pressure of both the stellar wind and ambient medium flows on one hand and the centrifugal pressure on the other hand. Then, assuming that the flow is characterized by isothermal sound speed c_s , the surface density σ of the shell of the bow shock can be calculated as (Cantó, Raga & González 2005)

$$\sigma = \int_0^h \rho_l dl = \frac{H}{c_s^2} (P_a - P_w), \quad (11)$$

where $H \equiv c_s^2/g$ is the pressure scaleheight; g is the centrifugal acceleration of the flow. The pressure of the ambient flow, $P_a = \rho_a(r) v_{\text{rel},n}^2$, and the pressure of the stellar wind $P_w = \rho_w(R) v_{w,n}^2$, depend on normal components of corresponding velocities, which can be expressed in an axisymmetric form as (Cantó et al. 2005)

$$v_{\text{rel},n} = v_{\text{rel}}(r) \frac{\sin \theta [R \cos \theta + (\partial R / \partial \theta) \sin \theta]}{\sqrt{[R^2 + (\partial R / \partial \theta)^2] \sin^2 \theta}}, \quad (12)$$

$$v_{w,n} = v_w \frac{R \sin \theta}{\sqrt{[R^2 + (\partial R / \partial \theta)^2] \sin^2 \theta}}. \quad (13)$$

The surface density σ can be also calculated by combining the expressions for the mass flow and the velocity along the shell, equations (4) and (10), respectively.

In order to produce the emission maps of hydrogen line emission or free-free continuum emission we follow Cantó et al. (2005) who calculate the emission measure by integrating the square of the density profile across the shell in the following way:

$$\text{EM} = \int_0^h (\rho / \bar{m})^2 dl = \frac{\sigma (P_a + P_w)}{2 \bar{m}^2 c_s^2}, \quad (14)$$

where $\bar{m} \approx 1.4 m_h$ is the average mass per ionized hydrogen particle.

2.1 Application to a single axisymmetric bow shock around the SMBH

An exact solution for a thin shell bow shock was found by Wilkin (1996) for the case of an isotropic stellar wind and homogeneous ambient medium. We apply this model for every point of the stellar orbit around the SMBH and calculate the properties of the equilibrium stellar bow shock along the trajectory (a similar approach

was already used in Zajaček et al. 2014). In this way we create a semi-analytic toy model that can be used to easily investigate the changes of basic bow-shock characteristics along the orbit.

The bow-shock shape $R = R(\theta)$ in the axisymmetric thin shell model can be expressed analytically as follows (Wilkin 1996):

$$R = R_0 \csc \theta \sqrt{3(1 - \theta \cot \theta)}, \quad (15)$$

where R_0 is the stagnation radius given by the equilibrium of the ambient and the stellar wind ram pressure,

$$R_0 = \sqrt{\frac{\dot{m}_w v_w}{4\pi \rho_a v_{\text{rel}}^2}}. \quad (16)$$

The 3D model is generated by rotation around the z -axis:

$$R_{3D}(\theta, \phi) = \text{rot}\{R(\theta), \phi\}, \quad 0^\circ \leq \phi \leq 180^\circ. \quad (17)$$

In the following expressions we will use the dimensionless cylindrical radius $\bar{w} = w/R_0$. Let us define the ratio of relative velocity and stellar wind velocity, $\alpha \equiv v_{\text{rel}}/v_w$. Then, in the framework of the thin-shell axisymmetric model (Wilkin 1996), the model-dependent functions $f_m(\theta)$, $f_w(\theta)$, and $f_z(\theta)$ may be expressed in terms of the angle θ along the shocked layer, the cylindrical radius \bar{w} , and the ratio of the relative and stellar wind velocities α :

$$f_m(\theta) = (1 - \cos \theta) + \frac{\bar{w}^2}{2\alpha}, \quad (18)$$

$$f_w(\theta) = \frac{1}{2}(\theta - \sin \theta \cos \theta), \quad (19)$$

$$f_z(\theta) = \frac{1}{2}(\sin^2 \theta - \bar{w}^2). \quad (20)$$

Using equations (4), (10), and (14) and the functions for the axisymmetric thin bow-shock model, equations (18)–(20), we may calculate basic characteristics of stellar bow shocks that can be tested observationally.

Finally, the axisymmetric bow-shock model applied throughout the paper gives the following relations for the thin-shell velocity v_t and surface density σ (Wilkin 1996), respectively:

$$v_t = v_{\text{rel}} \frac{\sqrt{(\theta - \sin \theta \cos \theta)^2 - (\sin^2 \theta - \bar{w}^2)^2}}{2\alpha(1 - \cos \theta) + \bar{w}^2}, \quad (21)$$

$$\sigma = R_0 \rho_a \frac{[2\alpha(1 - \cos \theta) + \bar{w}^2]^2}{2\bar{w} \sqrt{(\theta - \sin \theta \cos \theta)^2 - (\sin^2 \theta - \bar{w}^2)^2}}. \quad (22)$$

For a given angle θ along the shocked layer, the emission measure in the axisymmetric case is computed using equation (14). The exact formula is as follows:

$$\text{EM}(\theta) = \frac{\sigma(\theta)}{2\bar{m}^2 c_s^2} \times \frac{\rho_a v_{\text{rel}}^2 [R \cos \theta + (dR/d\theta) \sin \theta]^2 + \rho_w v_w^2 R^2}{R^2 + (dR/d\theta)^2}, \quad (23)$$

where the radial distance R of the shock from the source is given by equation (15) and the derivative with respect to the angle θ may be expressed in the following way:

$$\frac{dR}{d\theta} = R_0 \csc \theta \left[\frac{3(\theta - \cos \theta \sin \theta)}{2\bar{w} \sin^2 \theta} - \bar{w} \cot \theta \right]. \quad (24)$$

The model is applied for the case of a single star on an eccentric trajectory around the SMBH. We set the mass-loss rate of the star, \dot{m}_w , to $10^{-8} M_\odot \text{ yr}^{-1}$ and the terminal stellar wind speed, v_w , to

200 km s^{-1} . These are based on a comparison of the observed emission of the DSO with the model of a pre-main-sequence accreting star (Valencia-S. et al. 2015); see also Scoville & Burkert (2013) for a discussion of the T Tauri star model of DSO.

An exemplary evolution of the bow-shock geometry along the trajectory of a stellar source is depicted in Fig. 2 (right-hand panel), where the ambient flow is negligible with respect to the motion of the star and the density distribution of the ambient medium is colour-coded. In our model calculations we assume the mass of the SMBH of $4 \times 10^6 M_\odot$ and its distance from the Sun is 8 kpc, which is in the range of values inferred by independent measurements (Genzel et al. 2010).

3 QUALITATIVE PROPERTIES OF TEMPORAL ASYMMETRY FOR AN EQUILIBRIUM BOW SHOCK: DUSTY S-CLUSTER OBJECT AS CASE STUDY

The NIR excess source DSO has been highly monitored during its passage around Sgr A* (Witzel et al. 2014; Pfuhl et al. 2015; Valencia-S. et al. 2015, and references therein) since its discovery (Gillen et al. 2012). The DSO shows several characteristics of a dust-enshrouded young star, namely emission lines with a large full width at half-maximum (FWHM) of the order of 1 nm (see Valencia-S. et al. 2015, for detailed discussion). Since the source has been reported to remain spatially compact during the pericentre passage² and immediate post-pericentre phase (Witzel et al. 2014; Valencia-S. et al. 2015; see also Bally 2015, for a recent review), it can serve as a probe of the properties of the ambient medium during the post-peribothron phase of its orbital evolution.

The estimate of accretion rate \dot{m}_{acc} is determined using the tight correlation between Bry emission-line luminosity and accretion luminosity for young stellar objects (see Valencia-S. et al. 2015, for details). The mass-loss rate is then estimated using the ratio $\dot{m}_w/\dot{m}_{\text{acc}} \approx 0.01-0.1$ that is verified both theoretically and observationally for several T Tauri stars (Edwards et al. 2006; Ferreira, Dougados & Cabrit 2006). The adopted terminal wind velocity of 200 km s^{-1} lies in the range $\sim 50-400 \text{ km s}^{-1}$ expected for supersonic outflows of T Tauri stars (extended disc winds, X-winds or stellar winds; see Ferreira et al. 2006, for a derived diagnostic diagram). A typical Mach number for the stellar wind is then $M_w \approx 8.52 v_2 T_4^{-1/2}$, where $v_2 = v_w/100 \text{ km s}^{-1}$ is the terminal wind velocity and $T_4 = T/10^4 \text{ K}$ is the isothermal temperature of the wind. Given the uncertainties the computed bow-shock characteristics presented here can differ by a factor of a few in absolute terms, but their qualitative evolution is not affected.

We study the evolution of basic bow-shock characteristics, mainly the size, orientation, surface density, and emission measure, for different velocities of the isotropic ambient outflow, specifically for a negligible outflow velocity and a terminal outflow velocity of 500, 1000, and 2000 km s^{-1} . The last value is close to the one found from the analysis of X3 and X7 comet-shaped sources (Mužić et al. 2010). We assume an isotropic outflow, whose origin can be the ensemble of stars closer to the SMBH or an outflow from Sgr A* itself. The ambient density distribution is kept the same in all cases (see equation 2). So for increasing outflow velocities the ambient outflow rate \dot{M}_a needs to be changed accordingly to match the ambient density profile, for the hydrostatic equilibrium case $\dot{M}_a \propto \rho_a v_a$.

² We use *pericentre* and *peribothron* interchangeably.

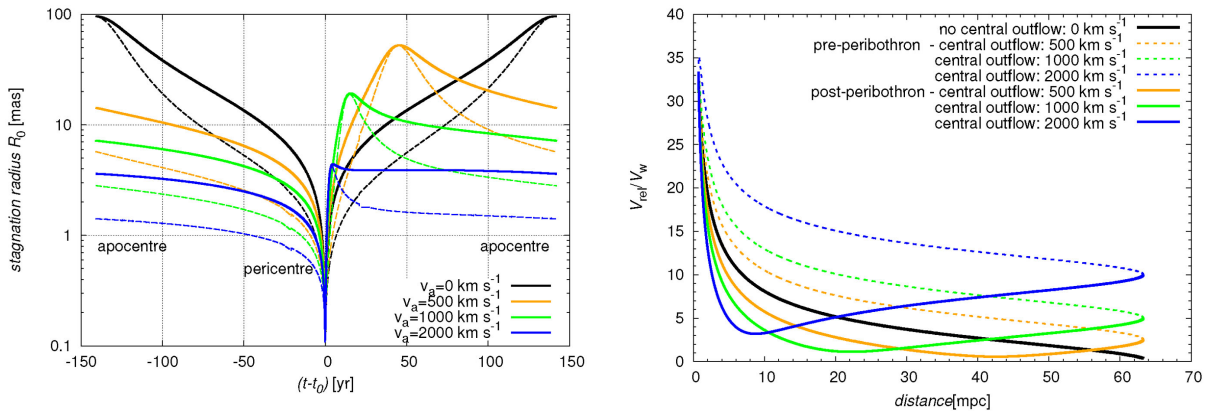


Figure 3. Left: temporal evolution of the stagnation radius R_0 , equation (16), for different velocities of the outflow (see the legend). The solid lines represent the stagnation radius as measured in the orbital plane, whereas the dashed lines stand for the projected angular scale of the stagnation radius based on the inferred inclination of 113° for the DSO source (Valencia-S. et al. 2015). Right: the ratio of relative velocity and stellar wind velocity, $\alpha = v_{\text{rel}}/v_w$, as a function of the distance from the SMBH (in milliparsecs). The black line denotes the case for negligible outflow; for non-zero cases an asymmetry develops between the pre-peribothron (dashed lines) and post-peribothron evolution (solid lines). The quantities in both panels were computed for the inferred highly elliptical orbit of the DSO source (Valencia-S. et al. 2015).

Whereas the spherically symmetric stationary inflow (Bondi 1952) represents one of the first detailed scenarios of SMBH accretion with zero angular momentum near the horizon (Melia 1992; Blandford & Begelman 1999; Melia & Coker 1999; Melia, Liu & Coker 2000), it has to be matched with an outflow at larger radii. Analytical estimates from the Bondi flow can be employed to relate the accretion rate to temperature and density measured near the Bondi capture radius, $r_B \simeq 4 \text{ arcsec } T_7^{-1}$, where T_7 is temperature in units of 10^7 K. Subsequently, these can be tested in the X-ray regime (e.g. Baganoff et al. 2003; Wang et al. 2013). An outflow prevails above the characteristic Bondi radius, where the material is supplied by hot-star winds present in the region (Quataert 2004; Martins et al. 2007). The outflow exceeds the amount of the inflowing material by orders of magnitude (Marrone et al. 2006). Substantial uncertainties still persist regarding the interpretation of the quiescent state of Sgr A*; nevertheless, many of them can be addressed within the radiatively inefficient scenario of RIAF models (Narayan & Yi 1994; Quataert & Gruzinov 2000; Das 2001).

3.1 Formation of temporal asymmetry of bow-shock properties due to central outflow

Even for the symmetric outflow from the Galactic Centre and an isotropic stellar wind, the star–SMBH system can behave asymmetrically along the trajectory of the source. This can be shown by the evaluation of the stagnation radius R_0 , equation (16), along the orbit, which is illustrated in the left-hand panel of Fig. 3. Unsurprisingly, for no outflow, the maximum of the stagnation radius, $R_0 \approx 100$ mas, occurs at the apobothron, where the ambient pressure is the smallest. The minimum of the stagnation radius, $R_0 \approx 0.1$ mas, is at the peribothron where the relative velocity as well as the ambient pressure are the highest.

For increasing outflow velocities, the asymmetry between pre-peribothron and post-peribothron phases develops: the minimum of the stagnation radius stays at the peribothron; however, the maximum shifts from the apobothron towards the peribothron and occurs during the post-peribothron phase; see Fig. 3 for comparison. The solid lines stand for the values in the orbital plane, the dashed lines

depict the projected values according to the current orbital solution of the DSO (Valencia-S. et al. 2015).

The evolution of the stagnation radius of the bow shock is determined by the value of the α -function, $\alpha = v_{\text{rel}}/v_w$. The plot of the function α for different outflow velocities as a function of distance from the SMBH is in Fig. 3 (right). It can be clearly seen that the case with zero outflow is symmetric (black solid line), whereas for the non-zero outflow the asymmetry is apparent between pre-peribothron phase (dashed lines) and post-peribothron (solid lines). At a fixed distance the difference becomes larger for stronger ambient wind; see Fig. 3 (right-hand panel).

3.2 Shell velocity profiles

The shocked gas layers – ambient and stellar wind shocks – are assumed to mix efficiently and quickly cool radiatively, which is typical of low-mass pre-main-sequence stars interacting with H II regions. Using equation (10) we evaluate the velocity profile of the shocked flow both as a function of the spherical angle θ ($\theta = 0$ rad corresponds to the vertex of the bow shock and θ close to π rad covers the bow-shock downstream region, further beyond the star) and the distance from the SMBH. The colour-coded profiles are plotted in Fig. 4: the left-hand column depicts the pre-peribothron profiles and the right-hand column the post-peribothron ones. These maps show the values of the ratio between the shell velocity v_t and the relative velocity v_{rel} , v_t/v_{rel} . The plots have two vertical axes: the left one shows the values of the spherical angle θ as measured along the bow shock and the right one depicts the values of the α -function, $\alpha = v_{\text{rel}}/v_w$, which is plotted as a grey curve. The absolute value of the shell velocity for a given distance can be determined from the α -function by knowing the stellar wind terminal velocity ($v_w = 200 \text{ km s}^{-1}$) in our model calculations.

The basic feature is that the velocity is close to zero near the vertex of the bow shock across all distances from the SMBH as well as different ambient velocity outflows. Furthermore, there is an increase downstream towards higher angles and at $\theta \approx 3$ rad the ratio α approaches unity, $v_t/v_{\text{rel}} \approx 1$.

The velocity profile along the bow shock, however, varies with the distance of the source from the SMBH, which is caused by

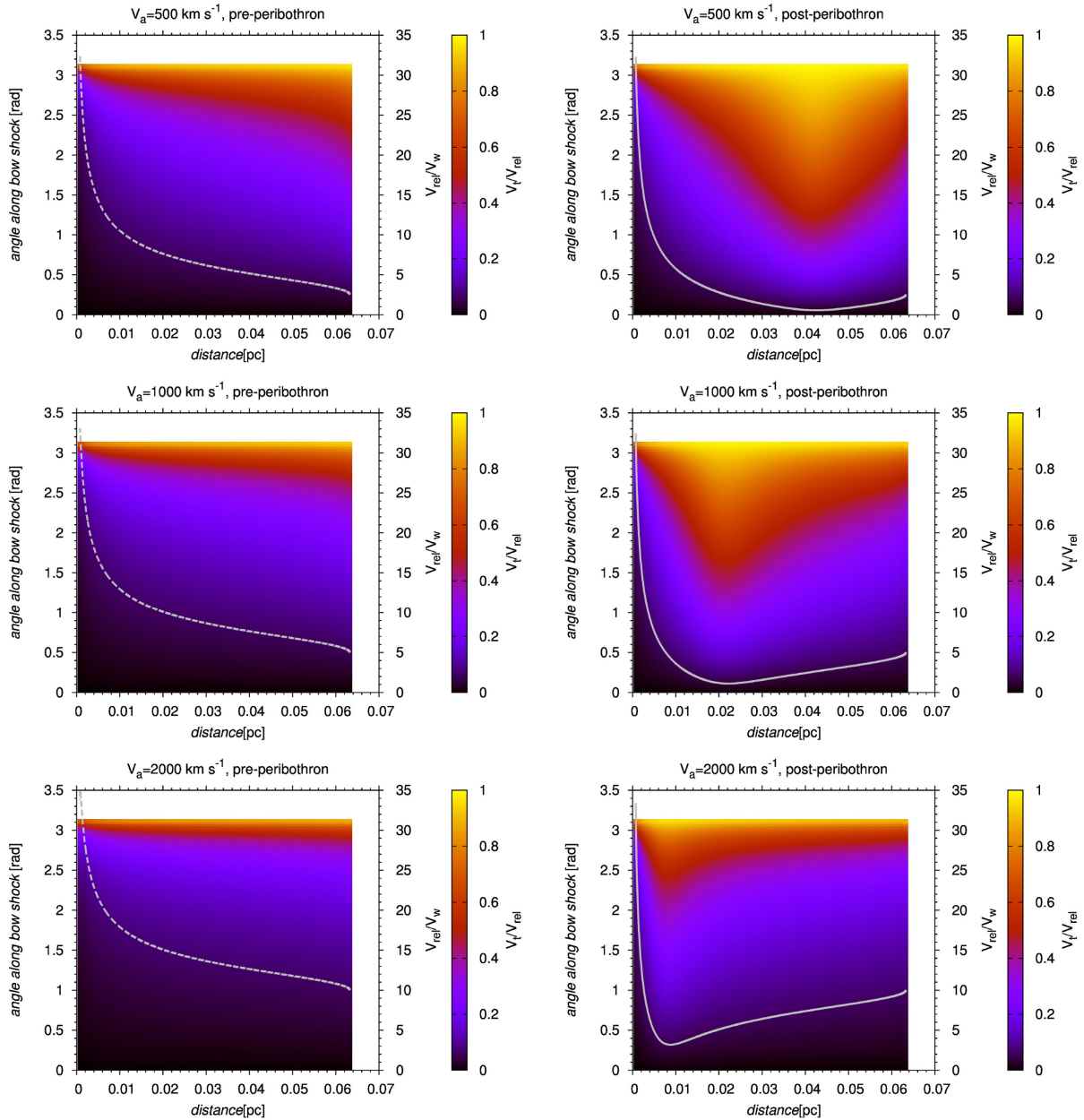


Figure 4. The colour-coded profiles of the velocity along the bow-shock shell (in units of the relative velocity of the star with respect to the ambient medium) as a function of the distance from the SMBH (horizontal axis, expressed in pc) and the spherical angle (left vertical axis, measured from the bow-shock symmetry axis in radians). The left-hand column contains pre-peribothron velocity profiles, the right-hand column depicts post-peribothron velocity profiles. The ratio of the relative velocity and the stellar wind velocity, v_{rel}/v_w , as a function of the distance is plotted as a grey line and its values are along the right vertical axis.

the change of the ratio $\alpha = v_{\text{rel}}/v_w$. Near the peribothron the ratio v_{rel}/v_w is largest and the shell velocity remains below $0.4v_{\text{rel}}$ up to $\theta \approx 3$ rad and then rises steeply. The ambient outflow leads to the minimum of the ratio v_{rel}/v_w in the post-peribothron phase. At this minimum the shell velocity reaches the values above $0.5v_{\text{rel}}$ closer to the vertex of the bow shock and the overall profile is flattened downstream. The asymmetry between the pre- and post-peribothron

phase is apparent: in the pre-pericentre part (left-hand side of Fig. 4), the region where $v_t \approx v_{\text{rel}}$ shrinks downstream towards the higher angle for stronger outflows. For comparison, in the post-peribothron part (right-hand panel in Fig. 4), the range of the distance from the SMBH, where the shell velocity v_t increases steeply close to the bow-shock vertex and then flattens out downstream, shifts from the apocentre closer to the SMBH. The stronger the

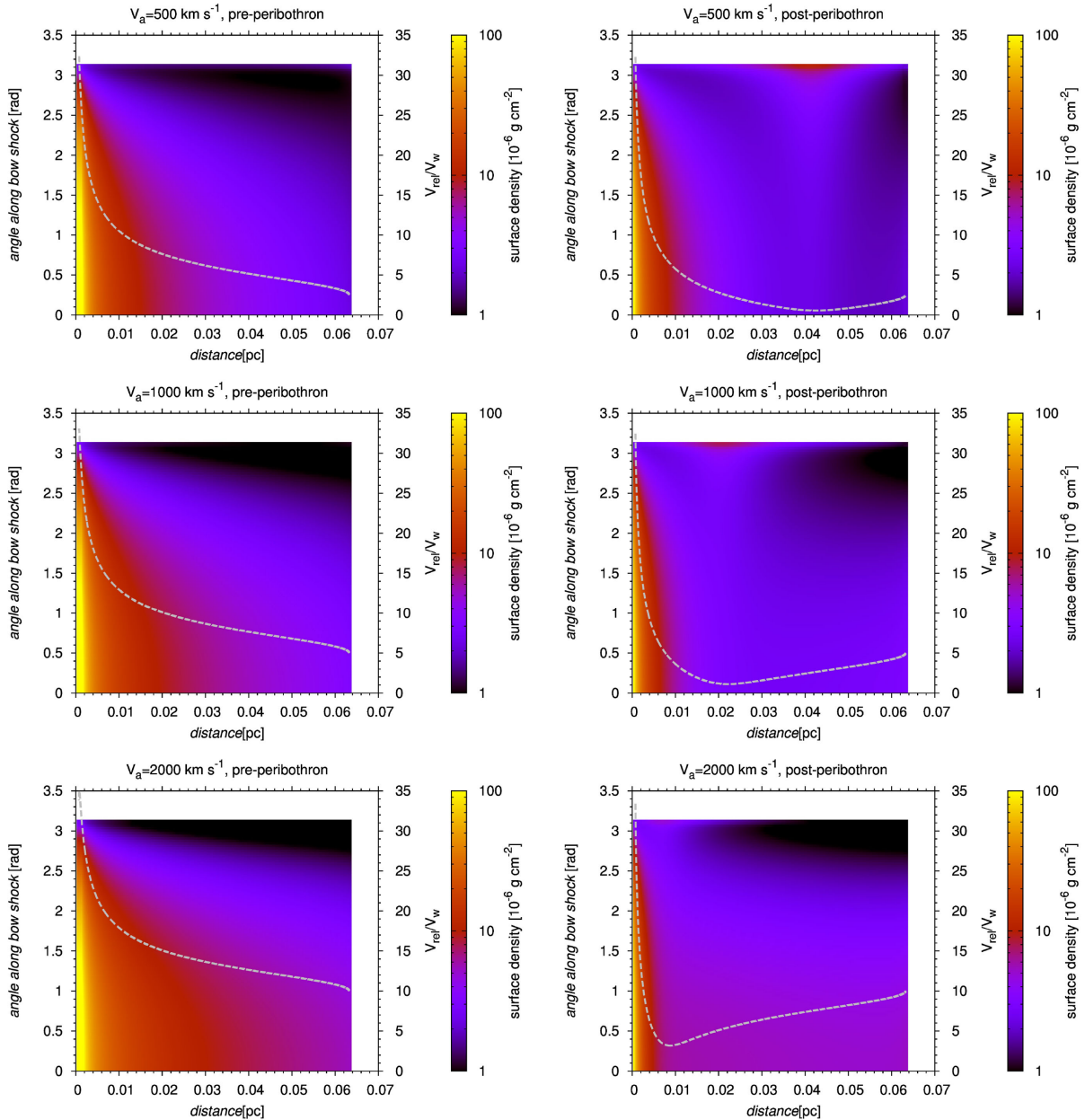


Figure 5. Colour-coded plots of the surface density of the stellar bow shock as a function of distance from the SMBH and the spherical angle measured from the symmetry axis of the bow shock. The surface density is expressed in $10^{-6} \text{ g cm}^{-2}$. The ratio of the relative velocity and the stellar wind velocity, $\alpha = v_{\text{rel}}/v_w$, is depicted as a grey line with the values along the right axis. The left-hand column corresponds to the pre-peribothron phase, while the right-hand column shows the post-peribothron part of the orbit.

outflow velocity is, the closer to the SMBH this flat profile (with the large shell velocity, $v_t \approx v_{\text{rel}}$) gets.

3.3 Surface density profiles

The surface density along the stellar bow shock can be computed from equation (4) combined with the shell velocity profile given by equation (10) for the thin axisymmetric bow-shock model. The

colour-coded plots of the surface density are shown in Fig. 5, which are divided into the pre-peribothron phase in the left-hand column and the post-peribothron phase in the right-hand column as in the case of the shell velocity (see Fig. 4).

The surface density is expressed in absolute units, specifically $10^{-6} \text{ g cm}^{-2}$, and is largest near the peribothron passage in all cases, where the bow shock shrinks in size significantly; see Fig. 3 (left-hand column). The analysis of the angular dependence for a fixed

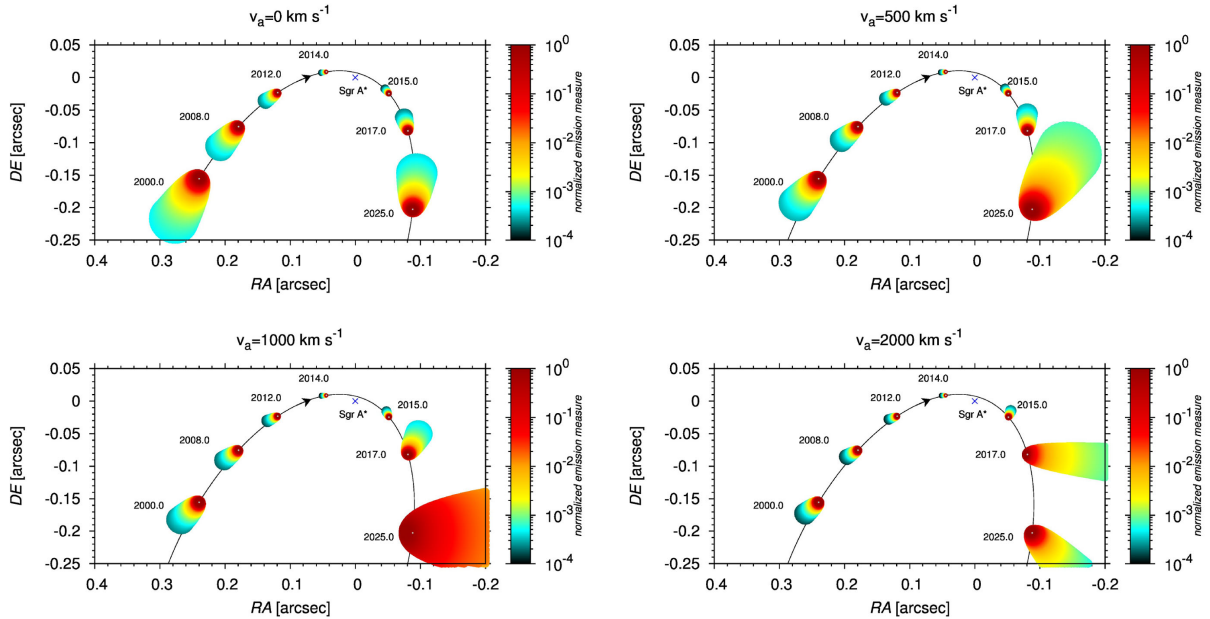


Figure 6. Emission measure maps of the DSO-like object normalized with respect to the maximum emission measure for each chosen epoch. The four cases correspond to four different outflow velocities: 0, 500, 1000, and 2000 km s⁻¹. The most apparent features are the change of the orientation and the size of the bow shock, and the differences in the emission measure distribution along the shocked shell in the post-pericentre part of the orbit.

distance during the pre-peribothron stage shows that the surface density drops for the downstream part, as expected. However, the post-pericentre profile is different from the pre-pericentre evolution – the decrease for larger angles is smaller and becomes apparent only for stronger outflows near the apocentre of the orbit. There is also a local maximum of the surface density at the distance where the minimum of the ratio v_{rel}/v_w occurs. This shallower profile shifts closer to the Galactic Centre for stronger outflows.

3.4 Relative change of emissivity along the shocked layer for different outflow velocities

We compute emission maps for the wind-blowing source on an eccentric trajectory around the SMBH, which is a plausible scenario for the DSO. Using equation (14) we obtain the angular dependence for the emission measure. These maps are transformed to the observer’s frame and normalized with respect to the maximum emission measure for each epoch (for the axisymmetric case the maximum is at the vertex of the bow shock). The results for different outflows are displayed in Fig. 6. The most notable features are the change of the bow-shock size, orientation, and the emission measure distribution along the bow shock in the post-pericentre part of the orbit for different outflow velocities. The bow-shock size scales with the stagnation radius R_0 whose evolution is in the left-hand part of Fig. 3. For a stronger ambient wind, the maximum bow-shock size shifts from the apocentre closer to the SMBH. For negligible outflow the maximum angular size of the stagnation radius is 96 mas, for 500 km s⁻¹ outflow the radius decreases to 53 mas, 1000 km s⁻¹ outflow yields 19 mas, and the stagnation radius shrinks to only 4 mas for an outflow of 2000 km s⁻¹.

When the layer of the shocked gas is externally ionized by the intense UV field and the shocked gas is approximately isothermal, the maps of the emission measure directly express the emissivity of

hydrogen recombination lines and that of the free-free continuum radiation. This is often the case in expanding H II regions, such as the Orion nebula (Bally et al. 2000; Bally & Reipurth 2001). The Galactic Centre mini-cavity may be considered to be such a photoionized H II region, where massive OB/Wolf–Rayet stars provide Lyman continuum photons with the production rate of $N_{\text{LyC}} \sim 10^{50} \text{ s}^{-1}$ (Serabyn & Lacy 1985).

The emission profiles as functions of the spherical angle change with the distance from the SMBH as well as with the velocity of the ambient flow; see Fig. 7 for 500 and 2000 km s⁻¹ outflow. For the pre-peribothron part of the orbital evolution the emission measure is largest near the axis of symmetry and then decreases to one-thousandth of the peak value downstream for angles of $\lesssim 3$ rad. The comparison with the post-peribothron part (see the right-hand column in Fig. 7) shows that there is a distance range where the emission measure profile is flatter and decreases to one-thousandth of the peak value for a larger angle, $\gtrsim 3$ rad. Again, this corresponds to the minimum of the ratio v_{rel}/v_w , which is plotted as a grey curve as in previous plots (Figs 4 and 5).

3.5 Evolution of bow-shock luminosity and comparison with other sources of emission

Furthermore, we compute the volumetric emission measure of the bow shock by multiplying the emission measure across the shocked layer, equation (14), by the infinitesimal area of the bow shock at angle θ , $\text{EM}_V = \text{EM} \times 2\pi w \sqrt{dz^2 + dw^2}$. By summing these contributions across the bow-shock layer we get the integrated emission measure that can be scaled to the luminosity for an optically thin case. In order to compare with the observations of Br γ emission line of the DSO source, we transform the volumetric emission measure

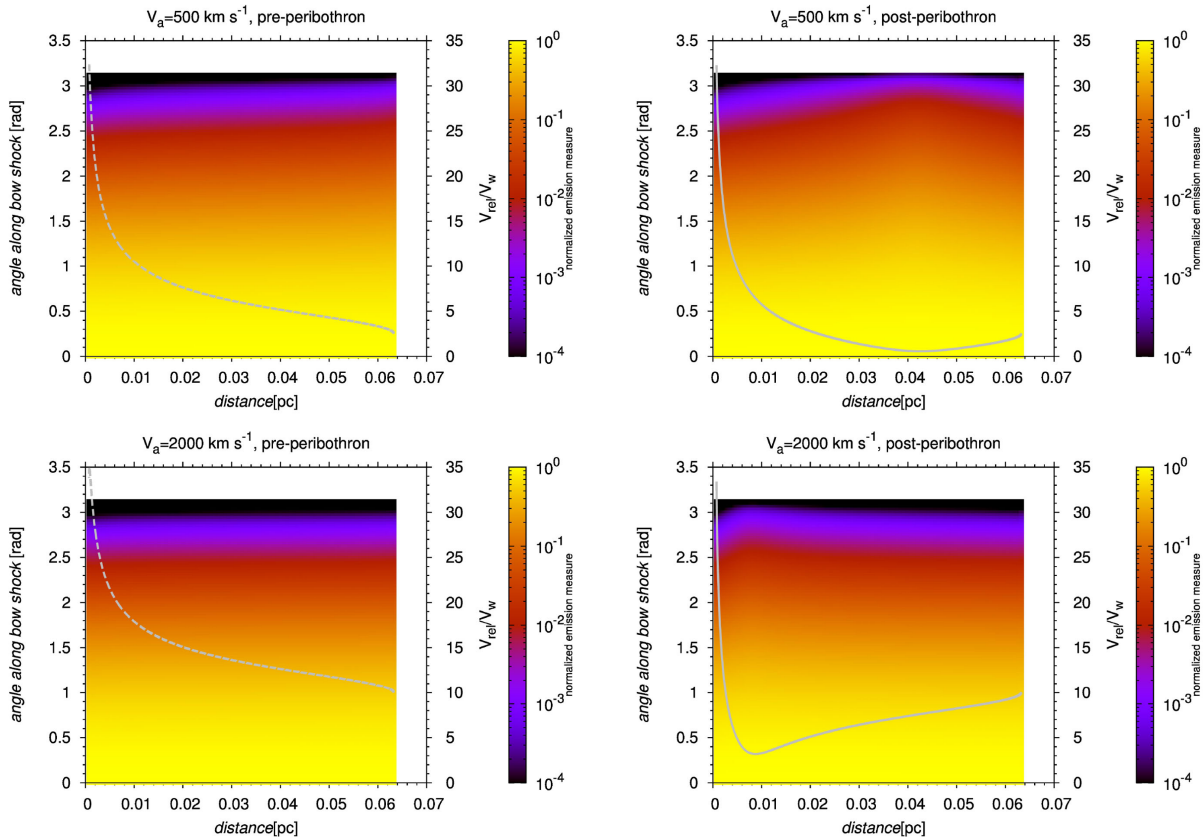


Figure 7. The colour-coded angular profile of the normalized emission measure as a function of the distance from the SMBH. Top panels: 500 km s^{-1} outflow; the left-hand panel corresponds to the pre-peribothron phase, the right-hand panel represents the post-peribothron evolution. Bottom panels: 2000 km s^{-1} outflow.

to $\text{Br}\gamma$ luminosity using the Case B recombination factor (Ballone et al. 2013, see also De Colle et al. 2014 for comparison):

$$L_{\text{Br}\gamma} \approx 3.44 \times 10^{-27} (T/10^4 \text{ K})^{-1.09} \text{EM}_V \text{ erg s}^{-1}, \quad (25)$$

where the temperature of the shocked layer is taken to be approximately constant, $T = 10^4 \text{ K}$, due to the heating rate of UV field of massive OB stars. We plot the temporal evolution of this luminosity for different outflow velocities from the Galactic Centre in the left-hand panel of Fig. 8. For all cases of the ambient outflow there is an increase of the bow-shock luminosity from the apobothron to the peribothron. For comparison, we compute the contribution from the isotropic stellar wind that is being launched at 0.01 au (in accordance with the analysis of stellar winds of young stars; Ferreira et al. 2006). This comparison shows that the circumstellar matter can dominate for the typical parameters of a young star adopted here and the contribution of the bow shock to the overall emission measure is of the order of 1 per cent at the pericentre and $\gtrsim 0.01$ per cent at the apocentre (see the contribution of the circumstellar matter and the overall luminosity in Fig. 8). The total luminosity of the wind and the bow shock is stable and our adopted parameters for the mass-loss rate, $\dot{m}_w = 10^{-8} M_\odot \text{ yr}^{-1}$, and the terminal wind velocity, $v_w = 200 \text{ km s}^{-1}$, approximately match the observed luminosity of the DSO source, as seen in the range of observed values in Fig. 8 according to Valencia-S. et al. (2015, grey band).

In general, the ratio of the bow-shock luminosity to the luminosity associated with the outflow (and also inflow) depends on the mass-loss rate and velocity field, as well as temperature and density of the circumstellar flow (see equation 25). Hence, the observability of bow shocks varies for different stages of stellar evolution (see Meyer et al. 2014, especially their table 3). As an exemplary case, we compute the temporal evolution of $\text{Br}\gamma$ luminosity for an order of magnitude larger mass-loss rate, $\dot{m}_w = 10^{-7} M_\odot \text{ yr}^{-1}$, and larger terminal wind velocity, $v_w = 600 \text{ km s}^{-1}$ (right-hand panel of Fig. 8). In this case the bow-shock luminosity is comparable to the stellar wind luminosity and is even greater at the pericentre of the orbit. The total $\text{Br}\gamma$ luminosity can then increase by a factor of a few during the pericentre passage. This is not detected by Valencia-S. et al. (2015) but Pfuhl et al. (2015) report an indication of a small increase.

An upper limit for the radiative bow-shock luminosity may be simply derived from the sum of kinetic terms of colliding ambient and stellar winds, since a fraction of the kinetic energy is thermalized (Wilkin, Canto & Raga 1997; Mohamed, Mackey & Langer 2012):

$$\dot{E}_{\text{tot}} \approx \dot{E}_{\text{amb}} + \dot{E}_{\text{wind}} = \frac{1}{2} \dot{m}_w (v_{\text{rel}}^2 + v_w^2). \quad (26)$$

The temporal evolution of \dot{E}_{tot} is shown in Fig. 8 (dashed lines). The maximum value for the case with the mass-loss rate of $\dot{m}_w = 10^{-8} M_\odot \text{ yr}^{-1}$ (left-hand panel of Fig. 8) is $\sim 10^{35} \text{ erg s}^{-1}$

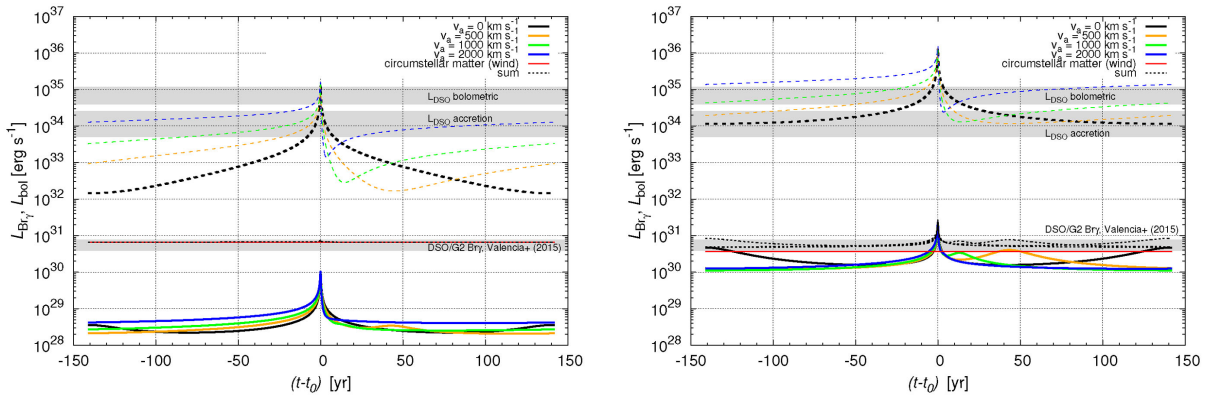


Figure 8. Left: temporal evolution of $\text{Br}\gamma$ luminosity for the following intrinsic stellar wind parameters: $\dot{m}_w = 10^{-8} M_\odot \text{ yr}^{-1}$, $v_w = 200 \text{ km s}^{-1}$. The bow-shock luminosity is computed for different outflow velocities (see the legend). The contribution of the circumstellar matter (wind) and the total luminosity are also plotted for comparison. The grey areas mark the ranges of the observed $\text{Br}\gamma$ luminosity, bolometric luminosity, and the inferred accretion luminosity of the DSO source around the peribothron passage; see also Eckart et al. (2013), Witzel et al. (2014), and Valencia-S. et al. (2015). Dashed lines represent an upper limit for total radiative luminosity for different outflow velocities. Right: the same as the left-hand panel for the following stellar wind parameters: $\dot{m}_w = 10^{-7} M_\odot \text{ yr}^{-1}$, $v_w = 600 \text{ km s}^{-1}$.

and the maximum for the case with $\dot{m}_w = 10^{-7} M_\odot \text{ yr}^{-1}$ (right-hand panel of Fig. 8) is one order of magnitude larger. One should take into account that this upper limit is associated with the bolometric luminosity of the bow shock (not only $\text{Br}\gamma$ luminosity) and only about 10 per cent of the kinetic energy is thermalized, as inferred from the comparison with hydrodynamic simulations (Mohamed et al. 2012). For completeness, the upper limit for the bolometric luminosity of the DSO is estimated to be $\sim 10\text{--}30 L_\odot$ (Eckart et al. 2013; Witzel et al. 2014; Valencia-S. et al. 2015), which means that the potential overall contribution of the bow-shock luminosity to the luminosity of the DSO is of the order of $\lesssim 10$ per cent, as inferred from the left-hand panel of Fig. 8, taking into account the conversion factor of 10 per cent between the kinetic energy and the radiative luminosity of the bow shock.

Another plausible contribution for the case of a young star is the accretion flow on to the stellar surface whose origin is an accretion disc surrounding the star; see Fig. 2 (left-hand panel) for illustration. The density and the emission measure of material flowing along accretion funnels was already computed and discussed in Valencia-S. et al. (2015) for an axisymmetric magnetospheric model of the accretion flow around the DSO. In the framework of the model of a pre-main-sequence star there is a known correlation between the line luminosity $L(\text{Br}\gamma)$ and the accretion luminosity L_{acc} (Alcalá et al. 2014):

$$\log(L_{\text{acc}}/L_\odot) = 1.16(0.07) \log[L(\text{Br}\gamma)/L_\odot] + 3.60(0.38). \quad (27)$$

For the DSO source, its measured $\text{Br}\gamma$ emission-line luminosity is of the order of $L(\text{Br}\gamma) = f_{\text{acc}} \times 10^{-3} L_\odot$ and stays approximately constant. The factor f_{acc} is of the order of unity. From equation (27) we get the following values for the accretion luminosity, (1.3, 2.9, 4.7, 6.6) L_\odot for $f_{\text{acc}} = \{1, 2, 3, 4\}$; see Fig. 8 for the comparison with the bolometric luminosity of the DSO source and the range of $\text{Br}\gamma$ luminosity.

The comparison of various contributions (bow shock, stellar wind, accretion flow) indicates that the circumstellar matter can dominate over the bow-shock emission. Hence, the overall luminosity from the stellar bow-shock source can remain constant within measurement uncertainties along its trajectory around the SMBH

unless the intrinsic properties of the star, i.e. inflow and outflow rates, change considerably. Significant changes in both the inflow and the outflow take place due to stellar evolution, which is expected on the time-scale of $10^3\text{--}10^4$ orbital periods ($P_{\text{orb}} \approx 100 \text{ yr}$ for the source closely bound to the SMBH in the S-cluster).

3.6 Contribution to the Doppler broadening of emission lines

The bow shocks of low-mass pre-main-sequence stars can be analysed using hydrogen recombination lines. It was shown (Scoville & Burkert 2013) that the dense shocked layer of colder gas in the bow shock could significantly contribute to the hydrogen line emission of the DSO if it is a compact stellar source. The DSO has been monitored using the $\text{Br}\gamma$ emission line and its line width is reported to increase upon approaching Sgr A* (Pfuhl et al. 2015; Valencia-S. et al. 2015).

The shell velocity increases from the stagnation point towards the rear part of the bow shock, as seen in the shell velocity maps in Fig. 4. The 3D velocity field along the shocked layer is displayed in the left-hand panel of Fig. 9 in the coordinate system centred on the stellar source. The shell velocity increases from 0 km s^{-1} at the vertex of the bow shock up to $\approx 1000 \text{ km s}^{-1}$ downstream (the right-hand panel of Fig. 9). The velocity along the bow shock decreases at stronger outflow velocities.

To illustrate the effect of the bow-shock flow on the width and the shape of emission lines, we calculate the Doppler contribution of the shell velocity field along the line of sight for pre-peribothron, peribothron, and immediate post-peribothron phases. As a specific example, we adopt the parameters of the DSO assuming it is a young star (Valencia-S. et al. 2015). Plots of the emission measure as a function of the line-of-sight shell velocity are depicted in Fig. 10 for two outflow models: no outflow (left-hand side) and a strong outflow of 2000 km s^{-1} (right-hand side). We assume an optically thin bow-shock flow, i.e. the whole shocked layer contributes to the observed line emission and there is no shielding effect included in the computation. In Fig. 10 the line-of-sight velocity of the shocked flow is corrected for the motion of the star around the SMBH.

We determine the size of the velocity span for an arbitrary value of the normalized emission measure, which we set to 0.5. The

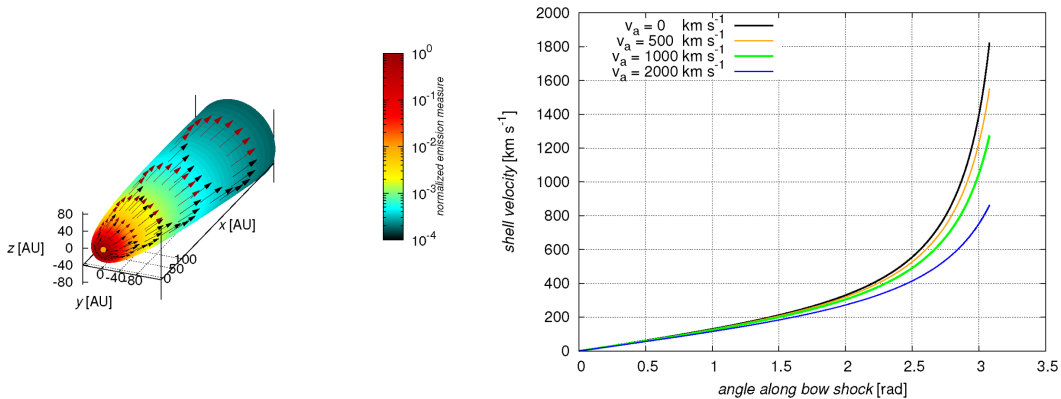


Figure 9. Left: 3D velocity field of the shocked gas in the stellar bow shock. The units along axes are in astronomical units with the origin at the position of the star (orange point). The colour wedge labels the normalized emission measure with respect to its maximum. Right: velocity profile along the shocked shell for different velocities of the outflow: 0, 500, 1000, and 2000 km s^{-1} , respectively (see the legend). The parameters used for computing both the emission map and the velocity field were adopted from the DSO model ($\dot{m}_w = 10^{-8} M_{\odot} \text{yr}^{-1}$, $v_w = 200 \text{ km s}^{-1}$) for the epoch of 2016.0.

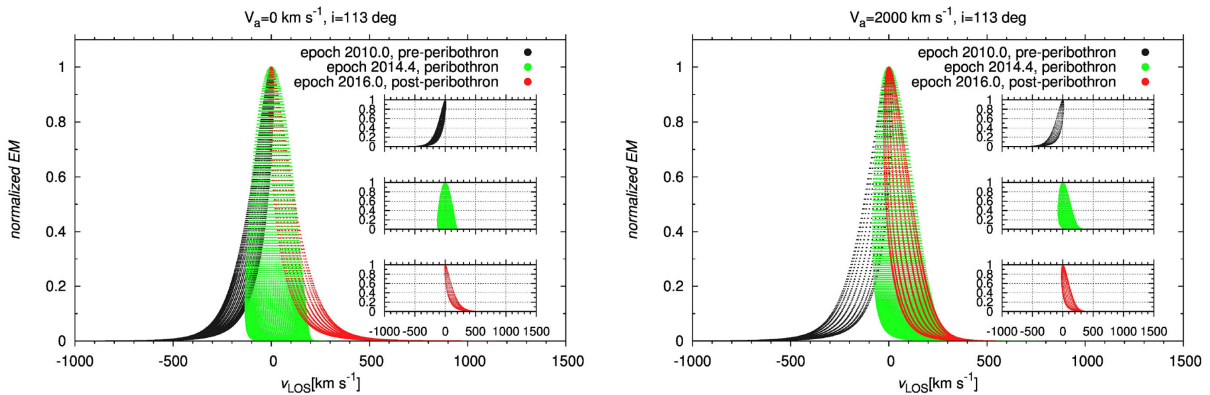


Figure 10. The plots of normalized emission measure versus the line-of-sight component of the velocity field of the shocked shell material. The depicted coloured regions show the Doppler contribution to the emission line width from the bow shock of a stellar source moving around the SMBH. The left-hand panel corresponds to the set-up with no outflow from the centre. The right-hand panel shows the model with a strong outflow of 2000 km s^{-1} from the Galactic Centre. The three bands of different colour correspond to the Doppler contributions for three different epochs: the black band indicates the pre-peribothron phase (~ 2010.0 for the DSO source), green points mark the peribothron passage (~ 2014.4 for the DSO), and the red points correspond to the immediate post-peribothron phase (~ 2016.0 for the DSO). These contributions are separately plotted in the figure insets. The orbital elements used for the calculation correspond to the inferred orbit of the DSO source with the orbital inclination of $i = 113^\circ$ (Valencia-S. et al. 2015).

Table 1. The size of the line-of-sight velocity span for two ambient outflow scenarios (no outflow and 2000 km s^{-1}) and several epochs in the pre-peribothron (2008.0, 2010.0, 2012.0), peribothron (2014.4), and post-peribothron phase (2016.0, 2018.0, 2020.0). The numbers in bold stand for the velocity span at the peribothron of the DSO source. The corresponding profiles of the normalized emission measure with respect to the line-of-sight velocity are plotted in Fig. 10 for three chosen epochs. The parameters for the calculation were adopted from the stellar scenario of the DSO.

Outflow velocity	Velocity span at EM = 0.5						
(km s^{-1})	2008.0	2010.0	2012.0	2014.4	2016.0	2018.0	2020.0
(km s^{-1})	(km s^{-1})	(km s^{-1})	(km s^{-1})	(km s^{-1})	(km s^{-1})	(km s^{-1})	(km s^{-1})
0	91	97	109	233	106	91	86
2000	116	123	138	218	137	182	162

comparison of the velocity span for the same value of the emission measure at all epochs can be considered as measure of the change of the line width of hydrogen recombination lines produced in the bow-shock layer. The values of the velocity span for a given outflow model and the epoch are summarized in Table 1.

The basic feature of the evolution of the velocity span is that in both cases of the outflow model the width increases by approximately a factor of 2 towards the pericentre and then decreases by the same factor. Qualitatively, a similar tendency is observed for the FWHM of $\text{Br}\gamma$ line for the DSO source: before

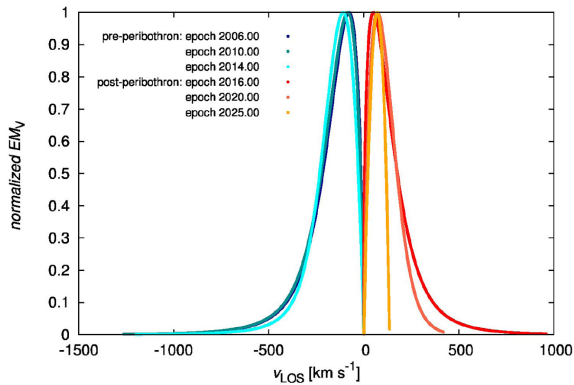


Figure 11. Computed emission line profiles for the outflow of 1000 km s^{-1} and different epochs in the pre-peribothron and post-peribothron part (see the legend).

pericentre the FWHM was $\sim 200 \text{ km s}^{-1}$, at the pericentre it increased up to $\sim 500 \text{ km s}^{-1}$, and the first observations after the pericentre indicate its decrease (Valencia-S. et al. 2015). Although the observed values of the line width seem to be larger in comparison with our model, the Doppler contribution of the bow shock is modulated by the terminal speed of the stellar wind, which is highly uncertain. For the young stellar sources the terminal wind speed could be also larger by a factor of a few than the value used in our calculation (we adopted $v_w = 200 \text{ km s}^{-1}$).

The outflow from the centre causes the line width to increase again in the post-peribothron phase at a certain epoch (see epoch 2018.0 in Table 1 for the case of 2000 km s^{-1} outflow). This is caused by the change of the orientation of the bow shock in the post-peribothron case; see the epoch 2017.0 in Fig. 6 for 2000 km s^{-1} outflow. The velocity span increases because of the contribution of both approaching and receding flows in the shell.

The plots in Fig. 10 also indicate that the pre-peribothron emission measure profile is blueshifted and the post-pericentre profile redshifted, which can skew the resulting line profile or at least make it asymmetric. We demonstrate this by constructing synthetic line profiles of bow-shock emission. First, we weigh the emission measure calculated using equation (14) by the area of infinitesimal bow-shock slices and these contributions are further normalized with respect to the maximum. Consequently, we plot the weighted normalized emission measure as a function of the line-of-sight velocity of the shocked gas corresponding to the given slice (see Fig. 11 for the outflow velocity of 1000 km s^{-1}). In the pre-peribothron part the flow is intrinsically blue-shifted, whereas in the post-pericentre part the emission is redshifted. The profile is highly asymmetric and variable in all cases. This is consistent with the observed spectra of bow-shock knots present in Herbig–Haro objects (see e.g. Grady et al. 2010).

3.7 Non-thermal emission of bow shocks near the Galactic Centre

The non-thermal emission of Sgr A* in the radio/sub-mm regime arises due to synchrotron radiation from relativistic electrons, and is highly variable on time-scales ranging from minutes to days and months. The pericentre passage of the DSO was predicted to lead to an increase in radio/sub-mm emission in two ways: by an increase

in accretion of matter into the central black hole, and by interactions with the hot plasma near the black hole leading to the formation of a bow shock. The bow-shock interaction with the accretion flow would lead to the acceleration of electrons to relativistic energies, producing synchrotron emission peaking at $\sim 1 \text{ GHz}$ (Narayan, Özel & Sironi 2012; Crumley & Kumar 2013; Sądowski et al. 2013). Depending on the models used, this excess flux density, which scales linearly with the size of the cloud, ranges from 0.02 to 22 Jy. For a pure cloud scenario, Sądowski et al. (2013) predict fluxes of 1.4–22 Jy at 1.4 GHz for a cross-section of 10^{30} cm^2 while Shcherbakov (2014) predict lower fluxes of $\sim 0.3 \text{ Jy}$ for a magnetically arrested cloud model of smaller cross-section ($\sim 10^{29} \text{ cm}^2$). For the case of a bow shock arising from the wind driven by a star, Crumley & Kumar (2013) predict a radio flux density of 0.02 Jy.

Here we revisit calculations of synchrotron emission to compare the scenarios of a star and a cloud for updated orbital elements (Valencia-S. et al. 2015) and our model set-up (ambient medium and parameters of a young star). Moreover, we assess scenarios with different outflows from the centre. Following the theory outlined in Crumley & Kumar (2013) and Sądowski et al. (2013, see also Rybicki & Lightman 1979) we compute the synchrotron flux around the peribothron passage at a fixed frequency of 1.4 GHz (light curve; see Fig. 12, left-hand panel) and subsequently we calculate the spectrum of the passage for the peribothron epoch taking into account synchrotron self-absorption (Fig. 12, right-hand panel). For the light curve we also compare two possible limits of synchrotron emission: *plowing model* (where all accelerated electrons are kept in the shocked region and radiate in the shocked magnetic field; solid lines) and *local model* (where accelerated electrons leave the shocked region and radiate in the unshocked magnetic field; dashed lines). For both scenarios, a star and a gas cloud, the flux peaks close to the peribothron, with the peak flux of $\sim 0.4 \text{ Jy}$ for the gas cloud with the fixed cross-section of $A_{\text{cloud}} = \pi \times 10^{30} \text{ cm}^2$ as in Crumley & Kumar (2013) and the maximum flux of $\sim 0.45 \text{ mJy}$ for the stellar model in this work. The difference is as much as three orders of magnitude, which is also apparent in the spectrum in Fig. 12 (right-hand panel), where the non-thermal flux associated with the star is below the intrinsic emission of Sgr A* across all frequencies for which reliable measurements were performed (observed flux denoted by green points for particular frequencies was collected from Davies, Walsh & Booth 1976; Falcke & Markoff 2000; Zhao et al. 2003; Marrone et al. 2008). This is also consistent with the findings of Crumley & Kumar (2013). We also find a small difference for different outflow velocities in the pre-peribothron phase, with the smaller flux for the stronger outflow. This difference is, however, negligible and in the post-peribothron phase the light curves have the same profile for all outflow velocities considered here.

Long-term observations of Sgr A* in the radio/sub-mm regime in 2013 and 2014 have not detected any significant increase in flux density beyond the intrinsic variability of Sgr A* (Bower, Brunthaler & Falcke 2013; Bower et al. 2015; Park et al. 2015). There was also no significant change in the spectral index reported, as would be expected by differences in spectra between intrinsic flux of Sgr A* and that of a bow shock; see the right-hand panel of Fig. 12 for comparison. Bower et al. (2015) estimate an upper size limit of $\sim 2 \times 10^{29} \text{ cm}^2$ to the DSO based on the absence of bow-shock emission at 1.4 GHz. Peri, Benaglia & Isequilla (2015) discuss the possibility of non-thermal radio emission by electrons accelerated in a bow shock of runaway/wind-blowing stars. Both the synchrotron and inverse-Compton mechanisms are viable candidates depending on the (largely uncertain) magnetic field intensity in the bow-shock region. The latter process is more likely to be relevant for the

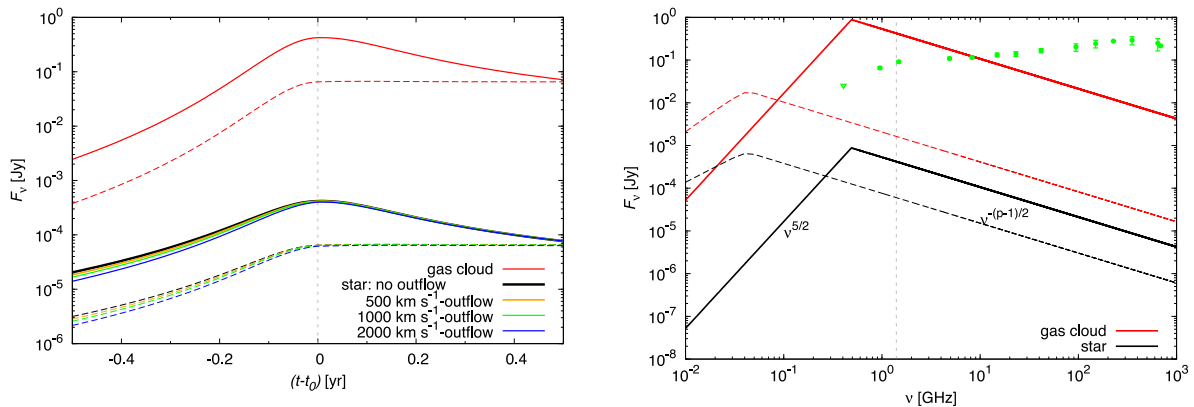


Figure 12. Left: light-curve profile at 1.4 GHz for the non-thermal emission of a bow shock formed by a star or a coreless gas cloud moving supersonically at low Mach numbers close to the Galactic Centre. In the calculation we considered both the plowing limit of synchrotron emission (solid lines) as well as the local model (dashed lines). Different outflow velocities were also taken into account for the passages of a star (see the legend). The vertical line denotes the peribothron passage. Right: spectrum profiles of synchrotron emission for a star and a cloud. The vertical line represents the frequency of 1.4 GHz considered in the calculation of the light curve. The high-energy power-law spectrum of accelerated electrons has a slope of $p = 2.4$ in our calculations, in accordance with the simulations of Sądowski et al. (2013). The green points represent the measurements of the intrinsic flux of Sgr A* (see the text for references). The bow-shock spectral profile and the spectrum of Sgr A* have a different spectral index for $\nu \gtrsim 1$ GHz. The distance to the Galactic Centre was taken to be 8 kpc.

production of high-energy photons. However in this case the expected signal is generally weak compared to the infrared band and many bow-shock stellar sources exhibit no detectable radio emission. In particular, observed peribothron passages of short-period stars S2 and S102 did not produce any flare (within uncertainties) above the quiescent emission of Sgr A* that would be typical of synchrotron emission associated with a stellar bow shock (with the power-law spectral distribution $S \propto \nu^\alpha$, where $\alpha < 0$; see light curves at 15 and 23 GHz in Herrnstein et al. 2004). However, Ginsburg et al. (2015) analyse the possibility of the detection of non-thermal bow-shock radiation and the synchrotron emission associated with the bow shock of S2 star should be detectable for larger stellar mass-loss rates of the order of $10^{-5} M_\odot \text{yr}^{-1}$ and faster stellar winds of the order of 10^3 km s^{-1} .

In conclusion, the lack of enhancement in the radio domain of the flaring activity during the 2014 DSO peribothron passage turns out to be consistent with the compact stellar scenario, where the bow-shock non-thermal emission associated with the moving body is expected to be weak, rather than a core-less gas cloud, where a more significant increase has been expected (see Fig. 12 for a comparison of both scenarios).

4 DISCUSSION

The basic feature studied in this paper is the formation of temporal asymmetry of the variation of bow-shock properties along the orbit of a star moving through a spherically symmetric outflow. Even if the ambient medium obeys perfect spherical symmetry of temperature and density profiles and the interaction of the star with its environment is approximately axially symmetric (Wilkin 1996), the coupled system of the star–Galactic Centre behaves highly asymmetrically when the post-pericentre and the pre-pericentre phases of the orbit are compared for different outflow velocities.

Although the presented toy model uses several assumptions (see Section 2) that may be violated to a certain extent in the complex Galactic Centre region, it enables one to carry out a fast calculation of the basic trends of bow-shock features, namely the size and

the orientation of the bow shock, change of its velocity profile, the Doppler contribution to its line emission, and the shocked layer density profile as functions of distance and time. The most important part of the analysis can be mainly performed by comparing the observed hydrogen line emission or free–free continuum maps with emission maps calculated from this model.

Since the first observations of the stellar proper motions in the S-cluster (Eckart & Genzel 1996, 1997), orbits of several stars have been well-constrained (Gillessen et al. 2009). Given the condition that the bow-shock emission is resolved, the observed signal could be studied and investigated for the basic signs of asymmetry. The upcoming interferometric observations with the 6-baseline interferometer GRAVITY in NIR *K* band (Eisenhauer et al. 2011) may provide the evidence for these trends of stellar bow-shock evolution, especially for the case of the post-peribothron evolution of the DSO and the pericentre passages of S2 and S102 stars, which have orbital periods of the order of 10 yr.

The current monitoring of the DSO infrared source is ideally suited for testing the properties of the ambient medium. The source size based on the analysis of the Br γ emission line maps (Valencia-S. et al. 2015) is limited to the region of $\lesssim 20$ mas, which is consistent with the outflow (see the temporal evolution of the stagnation radius in Fig. 3). However, the source has been monitored only close to its pericentre passage so far. If the bow shock contributes to the observed emission of the DSO and the ambient outflow is non-negligible, we expect the following trends during its post-peribothron evolution.

- (i) The bow-shock size increases and the source reaches the point along its orbit where the minimum of the ratio v_{rel}/v_w occurs.
- (ii) At this point the bow shock reaches its maximum size (see the stagnation radius evolution in Fig. 3); for the DSO source and an outflow velocity of 2000 km s^{-1} the maximum occurs at year ~ 2019 , for $v_a = 1000 \text{ km s}^{-1}$ at the epoch of ~ 2030 , and for $v_a = 500 \text{ km s}^{-1}$ at ~ 2060 .
- (iii) The stronger the spherical outflow, the sooner the source reaches this domain after the peribothron.

(iv) This phase is also characterized by a different velocity, density, and emission profiles (see Figs 4, 5, and 8, respectively). It is especially notable that at the maximum of the bow-shock size the emissivity drops downstream more slowly than before or after this phase.

(v) The broadening of the bow shock during the post-pericentre phase causes a drop in surface density, which can help to detect the central star, unless it is further shielded by the circumstellar dusty envelope and a disc with accretion streams.

It is not yet clear if a stable bow-shock structure has developed in the case of the DSO source. There can be different sources for its observed hydrogen emission lines, such as the accretion funnels from a circumstellar disc, as is discussed in Valencia-S. et al. (2015) in detail. However, even if the outlined trends corresponding to the stellar source–outflow interaction are not observed, it could have one or more of the following implications for the ambient medium and the source itself.

(i) There is no significant gas outflow from Sgr A*, which would be in contradiction with the analysis of X3/X7 comet-shaped sources and the mini-cavity formation theory,

(ii) or outflow from Sgr A* is not isotropic,

(iii) or the outflow is launched at larger distances due to the stellar winds of massive OB/WR stars.

(iv) DSO is a very compact source and/or it has no significant stellar wind (which has implications on the type of the central star), which would cause the density along the shocked layer to be low and the resulting emissivity of the bow shock below the detection limit. Consequently, the contribution of the shocked gas layer to the line width would be negligible as well.

(v) The ambient medium around the Galactic Centre is more diluted than assumed, see equation (2), which causes the ambient pressure to decrease. Hence, the bow-shock emission also drops; see equation (14).

(vi) If the ambient medium contains inhomogeneities of the length-scale H , which is of the order of $H/R_0 \approx 1$, it will lead to the degeneracy in the observed asymmetry, i.e. it will be difficult to disentangle the outflow and the inhomogeneity contribution. Moreover, these inhomogeneities would increase the density gradient locally, leading to the intrinsic asymmetry of the bow shock, for which the generalized solution of Wilkin (2000) applies.

A stellar bow shock is also susceptible to several hydrodynamic instabilities, namely

(i) Rayleigh–Taylor instability due to centrifugal acceleration of the flow,

(ii) Kelvin–Helmholtz instability due to relative velocity shear between the forward and the reverse shock layers,

(iii) radiatively cooled thin shells (with cooling parameter $\chi = t_{\text{cool}}/t_{\text{dyn}} \ll 1$), which are also susceptible to non-linear thin-shell instability (Vishniac 1994) and transverse acceleration instability (Dgani, Walder & Nussbaumer 1993).

Moreover, Dgani, van Buren & Noriega-Crespo (1996) investigate the stability of stellar bow shocks using linear stability analysis. They find that the bow-shock stability in the thin-shell limit depends on the single parameter α , which is the ratio of the relative velocity of a star with respect to the ambient medium and the stellar wind velocity, v_{rel}/v_w . Bow shocks with $v_{\text{rel}}/v_w \ll 1$ are more stable than those with $v_{\text{rel}}/v_w \gg 1$. Based on this result bow shocks associated with stellar sources around the SMBH are expected to be more stable near the apothron, where the ratio α is smaller in comparison

Bow-shock evolution along the orbit 1271

with the peribothron value, where the ratio reaches $v_{\text{rel}}/v_w \sim 35$ (right-hand panel of Fig. 3).

On the other hand, there are several mechanisms that inhibit the growth of hydrodynamic instabilities, namely,

(a) the presence of a warm interstellar medium (~ 8000 – 10000 K; Decin et al. 2012),

(b) ionizing radiation from an external source (Gvaramadze et al. 2014),

(c) interstellar magnetic field (van Marle, Decin & Meliani 2014).

All of these factors play a role in the Galactic Centre region and may contribute to the apparent stability of several observed bow-shock sources.

Taking into consideration the implications of the detection of the bow-shock asymmetrical evolution or its absence, it is worthwhile observing the DSO and the S-stars as well as prominent bow-shock sources along at least part of their orbits to search for the changes typical of a wind–wind bow-shock interaction and its evolution along the orbit.

The change of the line width of the DSO source, specifically related to Br γ emission lines, on its way towards the pericentre was attributed to the tidal stretching of the gas cloud. It has been claimed that this is proof of the unbound nature of the source (Pfuhl et al. 2015). However, the calculations presented in Section 3.6 show that qualitatively the same increase is caused by the line-of-sight component of the shell velocity field due to the projection of the elliptical orbit. Combined with the possible contribution of the winds and accretion funnels (Valencia-S. et al. 2015), the compact stellar model of the DSO can alternatively explain the observed characteristics.

It is also useful to compare the mass of the shell and that of the putative star associated with the DSO. Spectral decomposition puts an upper on the bolometric luminosity of the DSO, $L_{\text{DSO}} \lesssim 30L_{\odot}$ (Eckart et al. 2013; Valencia-S. et al. 2015), which automatically constrains the mass as well as the radius of the star, $M_{\text{DSO}} \lesssim 3M_{\odot}$ and $R_{\text{DSO}} \lesssim 10R_{\odot}$, respectively (see Zajacek et al. 2015 for the analysis and discussion). The mass of the shell M_{shell} may be simply estimated from the integral over 4π sr: $M_{\text{shell}} = \int_0^{R_0} \int_0^{4\pi} \rho_w R^2 d\Omega = \dot{M}_w R_0 / v_w$. For the stellar parameters, $\dot{m}_w = 10^{-8} M_{\odot} \text{ yr}^{-1}$ and $v_w = 200 \text{ km s}^{-1}$, the shell mass lies in the range $\sim 10^{-10} M_{\odot}$ up to $10^{-7} M_{\odot}$, being smaller at the peribothron. The mass estimate of the shell should be considered as a lower limit since it takes into account only the stellar wind contribution; see Mohamed et al. (2012) and Decin et al. (2012) for a more detailed discussion for α Ori – Betelgeuse. Finally, the total mass deposited along the orbit during one orbital period is of the order of $\dot{m}_w P_{\text{orb}} \approx 10^{-8} M_{\odot} \text{ yr}^{-1} \times 100 \text{ yr} = 10^{-6} M_{\odot}$.

Observations of several infrared-excess dusty objects provided the evidence for ongoing star-formation in the very central region of our Galaxy, as seen in the analysis of MIR sources in Eckart et al. (2004) and Moulataka et al. (2004, 2005), as well as the recent detection of proplyd-like bow-shock sources using radio continuum observations (Yusef-Zadeh et al. 2015a). Although the *in situ* star formation and the presence of young stars of T Tauri and LL Ori type was originally considered rather difficult due to the strong shearing tidal field in the central region (Morris 1993), it has been shown that the infall of low-angular-momentum clumps from the circumnuclear disc makes it possible due to the tidal compression at the peribothron (Jalali et al. 2014) or strong shocks provided by the collision of streams in tidally stretched filaments (Sanders 1998). These processes cause the gas to overcome the critical Jeans density and leads to the formation of a cluster of protostellar cores.

These pre-main-sequence stellar sources are characterized by continuing accretion of matter from a circumstellar envelope or disc that is accompanied by outflows, which is also indicated by recent radio and infrared observations of the inner $\sim 2\text{--}5$ pc from Sgr A* (Yusef-Zadeh et al. 2015b). These can drive shocks into the ambient medium and combined with the potential supersonic motion of a star, a bow shock is formed. Therefore a model of the DSO as a young star that is in the phase of both accretion and outflows is fully consistent with these findings.

5 CONCLUSIONS

We studied the effect of a quasi-spherical outflow from the Galactic Centre on moving stellar sources that develop bow-shock structures due to their supersonic motion with respect to the surrounding ambient medium. We showed that the density and the velocity of this outflow can be constrained through the change of bow-shock characteristics along the orbit. These include mainly the stagnation radius, shell velocity profile, density profile, emission measure maps, and the Doppler broadening of emission lines. We described the changes both qualitatively and quantitatively with respect to the distance of the source from the SMBH as well as along the bow-shock shell.

We demonstrated that the temporal evolution of the bow shock of a stellar source is fully symmetric with respect to the peribothron passage when the effect of the ambient outflow is negligible in comparison with the effect of the motion of the source. For stronger outflows the asymmetry develops between the pre-peribothron and post-peribothron orbital phases. We applied the model on the orbital configuration and parameters of the DSO source assuming to be a wind-blowing star rather than a coreless ionized cloud. The line-of-sight component of the shell velocity field can contribute to the observed increase of the emission line width. The calculations of the bow-shock evolution show that the observations of the DSO source during its post-pericentre phase are equally valuable as the pre-pericentre observations due to the potential asymmetry of both parts.

The results concerning the evolution of bow-shock characteristics along the orbit are relevant for all fast-moving stars closely bound to the Galactic Centre. They can also serve as a motivation for further, more detailed numerical studies.

ACKNOWLEDGEMENTS

We thank two anonymous referees for critical, constructive comments that helped to improve the manuscript. We are grateful to Rhys Taylor for helpful comments and discussion. The research leading to these results received funding from the European Union Seventh Framework Program (FP7/2007-2013) under grant agreement no. 312789 – Strong gravity: Probing Strong Gravity by Black Holes Across the Range of Masses. This work was supported in part by the Deutsche Forschungsgemeinschaft (DFG) via the Cologne Bonn Graduate School (BCGS), the Max Planck Society through the International Max Planck Research School (IMPRS) for Astronomy and Astrophysics, as well as special funds through the University of Cologne and SFB 956 – Conditions and Impact of Star Formation. Part of this work was supported by fruitful discussions with members of the Czech-DAAD collaboration programme ‘Effects of Albert Einstein’s Theory of General Relativity Revealed with the Instruments of European Southern Observatory’ and the Czech Science Foundation – DFG project no. 13-00070J.

REFERENCES

- Alcalá J. M. et al., 2014, *A&A*, 561, A2
 Baganoff F. K. et al., 2003, *ApJ*, 591, 891
 Ballone A. et al., 2013, *ApJ*, 776, 13
 Bally J., 2015, *Nature*, 524, 301
 Bally J., Reipurth B., 2001, *ApJ*, 546, 299
 Bally J., O’Dell C. R., McCaughrean M. J., 2000, *AJ*, 119, 2919
 Baranov V. B., Krasnobaev K. V., Kulikovskii A. G., 1971, *Sov. Phys. Dokl.*, 15, 791
 Blandford R. D., Begelman M. C., 1999, *MNRAS*, 303, L1
 Bondi H., 1952, *MNRAS*, 112, 195
 Bower G. C., Brunthaler A., Falcke H., 2013, *Astron. Telegram*, 5025, 1
 Bower G. C. et al., 2015, *ApJ*, 802, 69
 Broderick A. E., Loeb A., 2006, *ApJ*, 636, L109
 Broderick A. E., Fish V. L., Doeleman S. S., Loeb A., 2011, *ApJ*, 738, 38
 Buchholz R. M., Witzel G., Schödel R., Eckart A., 2013, *A&A*, 557, A82
 Burkert A., Schartmann M., Alig C., Gillessen S., Genzel R., Fritz T. K., Eisenhauer F., 2012, *ApJ*, 750, 58
 Cantó J., Raga A. C., González R., 2005, *Rev. Mex. Astron. Astrofis.*, 41, 101
 Crumley P., Kumar P., 2013, *MNRAS*, 436, 1955
 Cuadra J., Nayakshin S., Springel V., Di Matteo T., 2005, *MNRAS*, 360, L55
 Das T. K., 2001, *A&A*, 376, 697
 Davies R. D., Walsh D., Booth R. S., 1976, *MNRAS*, 177, 319
 De Colle F., Raga A. C., Contreras-Torres F. F., Toledo-Roy J. C., 2014, *ApJ*, 789, L33
 Decin L. et al., 2012, *A&A*, 548, A113
 Dexter J., Agol E., Fragile P. C., McKinney J. C., 2010, *ApJ*, 717, 1092
 Dgani R., Walder R., Nussbaumer H., 1993, *A&A*, 267, 155
 Dgani R., van Buren D., Noriega-Crespo A., 1996, *ApJ*, 461, 927
 Eckart A., Genzel R., 1996, *Nature*, 383, 415
 Eckart A., Genzel R., 1997, *MNRAS*, 284, 576
 Eckart A., Moutaka J., Viehmann T., Straubmeier C., Mouawad N., 2004, *ApJ*, 602, 760
 Eckart A., Schödel R., Straubmeier C., 2005, *The Black Hole at the Center of the Milky Way*. Imperial College Press, London
 Eckart A. et al., 2013, *A&A*, 551, A18
 Edwards S., Fischer W., Hillenbrand L., Kwan J., 2006, *ApJ*, 646, 319
 Eisenhauer F. et al., 2011, *The Messenger*, 143, 16
 Falcke H., Markoff S., 2000, *A&A*, 362, 113
 Ferreira J., Dougados C., Cabrit S., 2006, *A&A*, 453, 785
 Genzel R., Eisenhauer F., Gillessen S., 2010, *Rev. Mod. Phys.*, 82, 3121
 Ghez A. M. et al., 2003, *ApJ*, 586, L127
 Gillessen S., Eisenhauer F., Trippe S., Alexander T., Genzel R., Martins F., Ott T., 2009, *ApJ*, 692, 1075
 Gillessen S. et al., 2012, *Nature*, 481, 51
 Ginsburg I., Wang X., Loeb A., Cohen O., 2015, preprint ([arXiv:1509.06251](https://arxiv.org/abs/1509.06251))
 Grady C. A. et al., 2010, *ApJ*, 719, 1565
 Gvaramadze V. V., Menten K. M., Kniazev A. Y., Langer N., Mackey J., Kraus A., Meyer D. M.-A., Kamiński T., 2014, *MNRAS*, 437, 843
 Herrnstein R. M., Zhao J.-H., Bower G. C., Goss W. M., 2004, *AJ*, 127, 3399
 Jalali B. et al., 2014, *MNRAS*, 444, 1205
 Kunneriath D. et al., 2012, *A&A*, 538, A127
 Levin Y., Beloborodov A. M., 2003, *ApJ*, 590, L33
 Marrone D. P., Moran J. M., Zhao J.-H., Rao R., 2006, *ApJ*, 640, 308
 Marrone D. P. et al., 2008, *ApJ*, 682, 373
 Martins F., Genzel R., Hillier D. J., Eisenhauer F., Paumard T., Gillessen S., Ott T., Trippe S., 2007, *A&A*, 468, 233
 Melia F., 1992, *ApJ*, 387, L25
 Melia F., Coker R., 1999, *ApJ*, 511, 750

Melia F., Liu S., Coker R., 2000, *ApJ*, 545, L117
Merritt D., 2013, *Dynamics and Evolution of Galactic Nuclei*. Princeton Univ. Press, Princeton, NJ
Meyer D. M.-A., Mackey J., Langer N., Gvaramadze V. V., Mignone A., Izzard R. G., Kaper L., 2014, *MNRAS*, 444, 2754
Mohamed S., Mackey J., Langer N., 2012, *A&A*, 541, A1
Morris M., 1993, *ApJ*, 408, 496
Moultaka J., Eckart A., Viehmann T., Mouawad N., Straubmeier C., Ott T., Schödel R., 2004, *A&A*, 425, 529
Moultaka J., Eckart A., Schödel R., Viehmann T., Najarro F., 2005, *A&A*, 443, 163
Murray-Clay R. A., Loeb A., 2012, *Nature Commun.*, 3, 1049
Mužić K., Eckart A., Schödel R., Meyer L., Zensus A., 2007, *A&A*, 469, 993
Mužić K., Eckart A., Schödel R., Buchholz R., Zamaninasab M., Witzel G., 2010, *A&A*, 521, A13
Narayan R., Yi I., 1994, *ApJ*, 428, L13
Narayan R., Özel F., Sironi L., 2012, *ApJ*, 757, L20
Park J.-H., Trippe S., Krichbaum T. P., Kim J.-Y., Kino M., Bertarini A., Bremer M., de Vicente P., 2015, *A&A*, 576, L16
Perez K. et al., 2015, *Nature*, 4520, 646
Peri C. S., Benaglia P., Isequilla N. L., 2015, *A&A*, 578, A45
Pfuhl O. et al., 2015, *ApJ*, 798, 111
Psaltis D., 2012, *ApJ*, 759, 130
Quataert E., 2004, *ApJ*, 613, 322
Quataert E., Gruzinov A., 2000, *ApJ*, 545, 842
Rózańska A., Czerny B., Kunneriath D., Adhikari T. P., Karas V., Mościbrodzka M., 2014, *MNRAS*, 445, 4385
Rybicki B. G., Lightman P. A., 1979, *Radiative Processes in Astrophysics*. Wiley, New York
Sabha N. et al., 2012, *A&A*, 545, A70
Sabha N., Zamaninasab M., Eckart A., Moser L., 2014, in Sjouwerman L. O., Lang C. C., Ott J., eds, *Proc. IAU Symp. 303, The Galactic Center: Feeding and Feedback in a Normal Galactic Nucleus*. Cambridge Univ. Press, Cambridge, p. 150
Sądowski A., Sironi L., Abarca D., Guo X., Özel F., Narayan R., 2013, *MNRAS*, 432, 478
Sanchez-Bermudez J., Schödel R., Alberdi A., Mužić K., Hummel C. A., Pott J.-U., 2014, *A&A*, 567, A21
Sanders R. H., 1998, *MNRAS*, 294, 35
Scoville N., Burkert A., 2013, *ApJ*, 768, 108
Serabyn E., Lacy J. H., 1985, *ApJ*, 293, 445
Shcherbakov R. V., 2014, *ApJ*, 783, 31
Tanner A., Ghez A. M., Morris M., Becklin E. E., Cotera A., Ressler M., Werner M., Wizinowich P., 2002, *ApJ*, 575, 860
Tanner A., Ghez A. M., Morris M. R., Christou J. C., 2005, *ApJ*, 624, 742
Valencia-S M. et al., 2015, *ApJ*, 800, 125
van Marle A. J., Decin L., Meliani Z., 2014, *A&A*, 561, A152
Viehmann T., Eckart A., Schödel R., Moultaka J., Straubmeier C., Pott J.-U., 2005, *A&A*, 433, 117
Viehmann T., Eckart A., Schödel R., Pott J.-U., Moultaka J., 2006, *ApJ*, 642, 861
Vishniac E. T., 1994, *ApJ*, 428, 186
Wang Q. D. et al., 2013, *Science*, 341, 981
Wilkin F. P., 1996, *ApJ*, 459, L31
Wilkin F. P., 2000, *ApJ*, 532, 400
Wilkin F. P., Canto J., Raga A. C., 1997, in Reipurth B., Bertout C., eds, *Proc. IAU Symp. 182, Herbig-Haro Flows and the Birth of Low-Mass Stars*. Kluwer Academic Publishers, Dordrecht, p. 343
Witzel G. et al., 2014, *ApJ*, 796, L8
Yuan F., Bu D., Wu M., 2012, *ApJ*, 761, 130
Yuan F., Narayan R., 2014, *ARA&A*, 52, 529
Yusef-Zadeh F., Roberts D. A., Wardle M., Cotton W., Schödel R., Royster M. J., 2015a, *ApJ*, 801, L26
Yusef-Zadeh F. et al., 2015b, *ApJ*, 808, 97
Zajacek M., Karas V., Eckart A., 2014, *A&A*, 565, A17

Bow-shock evolution along the orbit 1273

Zajacek M., Eckart A., Peissker F., Karssen G. D., Karas V., 2015, preprint (arXiv:1507.00237)

Zhao J.-H., Young K. H., Herrnstein R. M., Ho P. T. P., Tsutsumi T., Lo K. Y., Goss W. M., Bower G. C., 2003, *ApJ*, 586, L29

APPENDIX A: EQUILIBRIUM OF A STELLAR BOW SHOCK ALONG THE ORBIT

An equilibrium, momentum-supported bow-shock model applied in this work clearly has its limitations. An equilibrium can be reached only when the crossing time-scale,

$$t_{\text{cross}} = R_0/v_{\text{rel}}, \quad (\text{A1})$$

which determines the ability of the ambient medium to shape the bow shock, and the wind-filling time-scale,

$$t_{\text{fill}} = R_0/v_w, \quad (\text{A2})$$

which is related to the ability of the stellar wind to fill the bow-shock cavity, are smaller than the orbital time-scale,

$$t_{\text{orb}} = D/v_{\text{orb}}, \quad (\text{A3})$$

where D is the distance of the star from the SMBH and v_{orb} is the stellar orbital velocity. We plot the ratio of these time-scales, $t_{\text{cross}}/t_{\text{orb}}$ (solid lines) and $t_{\text{fill}}/t_{\text{orb}}$ (dashed lines), for different velocities of the central outflow; see Fig. A1. For the terminal stellar wind velocity of $v_w = 200 \text{ km s}^{-1}$ and the mass-loss rate of $\dot{m}_w = 10^{-8} M_{\odot} \text{ yr}^{-1}$, the ratios are smaller than unity along the whole orbit, so the equilibrium bow-shock structure should be approximately reached and it may serve as a basis for our qualitative studies of temporal asymmetry.

APPENDIX B: VELOCITY DIVERGENCE AND DENSITY GRADIENT AT A FIXED POSITION OF THE BOW-SHOCK SOURCE FROM THE GALACTIC CENTRE

For the spherical central ambient outflow we have $\mathbf{v}_a = (v_r, v_{\theta}, v_{\phi}) = (v_r, 0, 0)$. The divergence of this flow in spherical

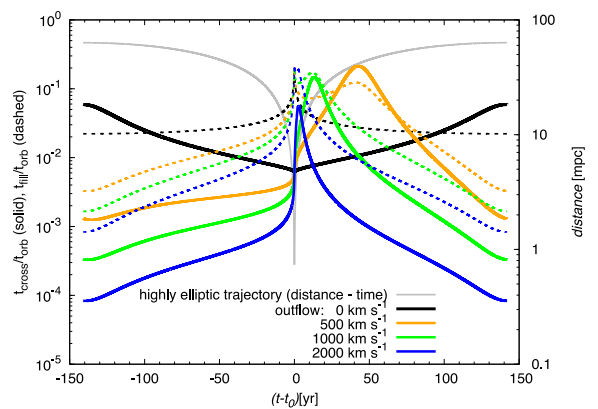


Figure A1. The evolution of ratios $t_{\text{cross}}/t_{\text{orb}}$ (solid lines; equations A1 and A3) and $t_{\text{fill}}/t_{\text{orb}}$ (dashed lines; equations A2 and A3) for different outflow velocities (see the legend) along the whole orbit (left vertical axis). The grey line represents the temporal evolution of the distance of the star from the SMBH for the assumed highly elliptical orbit (right vertical axis).

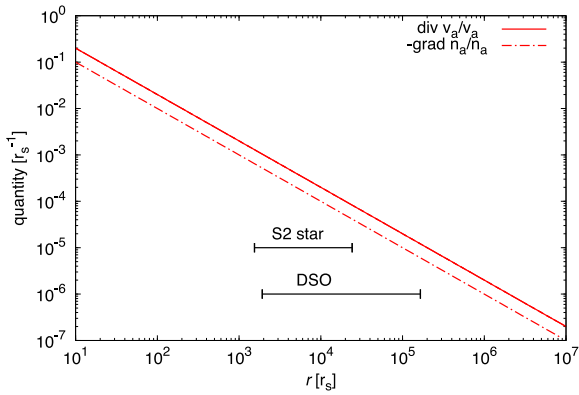


Figure B1. Profile of the divergence of the spherical central outflow divided by the velocity magnitude with respect to the distance from the Galactic Centre (solid line). The distance is expressed in Schwarzschild radii and the ratio of the divergence and the velocity magnitude is in r_s^{-1} . In the same plot we show the distance profile of the density gradient divided by the density at the given distance (dash-dotted line; we take its negative value for the plot). The horizontal lines in both panels mark the distance range for S2 star and the DSO source and are positioned at arbitrary values of the vertical axis.

coordinates yields,

$$\begin{aligned} \nabla \cdot \mathbf{v}_a &= \frac{1}{r^2} \frac{d}{dr} (r^2 v_r) \\ &= \frac{2v_r}{r_s} \left(\frac{r}{r_s} \right)^{-1}, \end{aligned}$$

where v_r is constant. The velocity divergence as a function of the distance from the Galactic Centre (expressed in Schwarzschild radii)

is plotted in Fig. B1 (solid line). The values along the vertical axis represent the velocity divergence divided by the velocity magnitude with respect to the distance of Schwarzschild radius. For the distance range of our interest (S-cluster) the values of the divergence are of the order of 10^{-3} up to $10^{-5} r_s^{-1}$.

Using the spherical density profile, equation (2), we compute the density gradient as a function of the distance,

$$\nabla n_a = -\frac{n_a^0}{r_s} \left(\frac{r}{r_s} \right)^{-2}.$$

The density gradient profile (divided by the density at the given distance) is plotted in Fig. B1 (dash-dotted line) and the corresponding values for the S-cluster distance range are of the order of 10^{-4} up to $10^{-5} r_s^{-1}$.

This paper has been typeset from a $\text{\TeX}/\text{\LaTeX}$ file prepared by the author.

A NIR source with a polarized emission

There has been a lot of discussion about the nature of NIR-excess sources in the innermost parsec of the Galactic centre. Especially the character of DSO/G2, which was approaching fast the pericentre of its orbit, remained unclear because it was not possible to resolve the brightness distribution of the source in a way that would enable us to study the geometry, in particular the asymmetry, of the source.

It was really quite a surprise when my colleague Banafsheh Shahzamanian detected DSO/G2 as a linearly polarized source in NIR K_s band with the polarization degree of $\sim 30\%$ and an alternating polarization angle. I constructed a radiative transfer model that could explain both the total as well as the polarized continuum emission of the source. Comparing the observed NIR flux densities with the synthetic flux densities based on the model, one can approximately constrain the geometry of the DSO/G2. The result was that it is a dust-enshrouded star with a non-spherical, optically thick dusty envelope with bipolar cavities, which develops a denser, dusty bow shock when approaching Sgr A*.

The model calculations are included in Section 4. “DSO model: a young, supersonic star” of the paper [Shahzamanian et al. \(2016\)](#), which was published in the peer-reviewed journal A&A.

Credit: Shahzamanian, Eckart, Zajaček et al., A&A 593, A131 (2016). Reproduced with permission ©ESO.

Polarized near-infrared light of the Dusty S-cluster Object (DSO/G2) at the Galactic center[★]

B. Shahzamanian^{1,2}, A. Eckart^{1,2}, M. Zajaček^{1,2}, M. Valencia-S.¹, N. Sabha¹,
 L. Moser^{1,2}, M. Parsa^{1,2}, F. Peissker¹, and C. Straubmeier¹

¹ I. Physikalisches Institut, Universität zu Köln, Zùlpicher Str.77, 50937 Köln, Germany
 e-mail: [shahzaman;eckart]@ph1.uni-koeln.de

² Max-Planck-Institut für Radioastronomie, Auf dem Hügel 69, 53121 Bonn, Germany

Received 25 May 2016 / Accepted 11 July 2016

ABSTRACT

We investigate an infrared-excess source called G2 or Dusty S-cluster Object (DSO), which moves on a highly eccentric orbit around the Galaxy's central black hole, Sgr A*. We use, for the first time, near-infrared polarimetric imaging data to determine the nature and properties of the DSO and obtain an improved K_s -band identification of this source in median polarimetry images of different observing years. The source started to deviate from the stellar confusion in 2008, and it does not show any flux density variability over the years we analyzed it. We measured the polarization degree and angle of the DSO between 2008 and 2012 and conclude, based on the significance analysis on polarization parameters, that it is an intrinsically polarized source (>20%) with a varying polarization angle as it approaches the position of Sgr A*. The DSO shows a near-infrared excess of $K_s - L' > 3$ that remains compact close to the pericenter of its orbit. Its observed parameters and the significant polarization obtained in this work show that the DSO might be a dust-enshrouded young star, forming a bow shock as it approaches the super massive black hole. The significantly high measured polarization degree indicates that it has a non-spherical geometry, and it can be modeled as a combination of a bow shock with a bipolar wind of the star. We used a 3D radiative transfer model that can reproduce the observed properties of the source such as the total flux density and the polarization degree. We obtain that the change of the polarization angle can be due to an intrinsic change in the source structure. Accretion disk precession of the young star in the gravitational field of the black hole can lead to the change of the bipolar outflow and therefore the polarization angle variation. It might also be the result of the source interaction with the ambient medium.

Key words. Galaxy: center – infrared: general – stars: pre-main sequence – stars: winds, outflows

1. Introduction

Since 2012, the focus of Galactic center (GC) observations has been set on investigating an infrared (IR) excess source detected by Gillessen et al. (2012) as a fast-moving object approaching the position of the central supermassive black hole (SMBH) of the Milky Way, Sagittarius A* (Sgr A*). It has been interpreted as a combination of dust and core-less gas cloud called G2 (Gillessen et al. 2012, 2013; Pfuhl et al. 2015) and also DSO, standing for Dusty S-cluster Object (Eckart et al. 2013). This source moves on a highly eccentric orbit and passed its closest approach to the SMBH in May 2014 (Meyer et al. 2014b; Valencia-S et al. 2015). Given the short distance of its periape, it has been suspected that it might produce extraordinary accretion events on to the Galaxy's central black hole (e.g. Shcherbakov 2014; Abarca et al. 2014; Scoville & Burkert 2013; Sądowski et al. 2013).

If the DSO is a pure gas cloud of a few Earth masses (Gillessen et al. 2012), it might have formed in the stellar cluster, possibly within the disk of young stars at a distance of few arcseconds from the GC. After forming there, it might

have moved on its current remarkably eccentric orbit by gravitational interaction with massive stars (Murray-Clay & Loeb 2012; Scoville & Burkert 2013). This scenario must have happened recently (1990–2000), therefore it should have been observed during the total time of its existence. As a consequence, the pure gas scenario seems unlikely, and several authors have proposed scenarios suggesting the presence of a central star for this source (e.g., Murray-Clay & Loeb 2012; Eckart et al. 2013; Scoville & Burkert 2013; Ballone et al. 2013; Phifer et al. 2013; Zajaček et al. 2014; Witzel et al. 2014; Valencia-S et al. 2015). Scoville & Burkert (2013) proposed that the DSO is a T Tauri star that was formed in the young stellar ring and then inserted into its current orbit. They suggested that a very dense bow shock is produced for the T Tauri star wind and modeled it numerically. Valencia-S et al. (2015) also discussed that the bright observed Bry emission of the DSO with a large line width might be the result of infalling material shaping a disk around the central star, which may be a T Tauri star with an age of $\sim 10^5$ yr. Considering the stellar nature, DSO would not be disrupted when reaching its closest point to the SMBH and did not need a recent formation. Using hydrodynamical simulations, Jalali et al. (2014) have shown that young stars could form very close to SMBHs within small molecular clumps on eccentric orbits around the black hole. They showed that for such orbital configurations,

[★] Based on NACO observations collected between 2004 and 2012 at the Very Large Telescope (VLT) of the European Organization for Astronomical Research in the Southern Hemisphere (ESO), Chile.

the gravitational potential of the SMBH and orbital (geometrical) compression increase the density of cold gas clumps to reach the threshold values suitable for star formation (see also [Mapelli & Trani \(2016\)](#) for a recent review).

The *L*-band observations of DSO/G2 close to the peribothron support the idea of the compactness of this source, which means that the source cannot be a pure gas cloud ([Ghez et al. 2014](#); [Witzel et al. 2014](#)). [Eckart et al. \(2013\)](#) revealed the first K_s -band identification of the DSO with a magnitude of ~ 18.9 from the ESO Very Large Telescope (VLT) continuum imaging data. Using the spectral decomposition of this source, they obtained an upper limit of $\sim 30 L_\odot$ for its luminosity. The *H*, K_s , and *L*-band continuum measurements can be matched either by an unusually warm dust component at a temperature of 550–650 K or by a stellar source enclosed in the dust at a temperature of ~ 450 K (see Fig. 15 in [Eckart et al. 2013](#)). The $H - K_s > 2.3$ color limit supports the scenario that the DSO is a dust-embedded star and not a core-less cloud of gas and dust ([Eckart et al. 2013](#)).

The mass of this object is higher than what was assumed for a pure gas source, but lower than the typical mass of S-cluster stars ($20 M_\odot$). [Valencia-S et al. \(2015\)](#) reported NIR observations of the DSO during its approach to the SMBH at the GC, which were carried out with SINFONI at the VLT from February to September 2014. They detected spatially compact Bry line emission from the DSO before and after its peribothron passage and also a Bry line width increase, which may indicate that the DSO is a young accreting star with a dust envelope. The observational data were used to obtain the orbital parameters of this object. Comparable to the previous estimates (e.g., [Meyer et al. 2014a](#)), [Valencia-S et al. \(2015\)](#) obtained a peribothron distance of about 163 ± 16 AU with a half-axis length of about 33 mpc and an ellipticity $e = 0.976$. When the DSO reaches the peribothron, tidal stretching and disruption of the envelope lead to a velocity dispersion enhancement in the accretion flow toward the central star ([Eckart et al. 2013](#); [Zajaček et al. 2014](#)). Based on a study by [Witzel et al. \(2014\)](#), the *L*-band emission of the DSO compared to the Bry emission measured by [Pfuhl et al. \(2015\)](#) is more compact. This shows that the *L*-band emission originates from an optically thick dust envelope around a central star, while the Bry emission is coming from the hot gas that is externally heated by ionized photons of the stars close to the DSO. However, [Valencia-S et al. \(2015\)](#) did not find evidence for significantly extended and tidally stretched Bry emission. The extra emission of Bry close to the DSO position is not connected to the DSO and is most likely emitted from other sources in the field ([Peissker et al.](#), in prep.). The DSO is not the only infrared excess source in the S-cluster of the GC, and there are more dusty sources in this region ([Eckart et al. 2013](#); [Meyer et al. 2014a](#)). These sources might be dust-enshrouded pre-main-sequence stars that form a bow shock ahead of their path when they move through the medium with a supersonic speed. Other candidates have also been observed in the radio continuum observations of the GC ([Yusef-Zadeh et al. 2015a](#)).

Imaging polarimetry is a powerful technique for studying dusty environments such as core-less dusty objects and/or circumstellar dusty regions. The analysis of polarization allows us to quantitatively evaluate the object geometries and the dust properties. Intrinsic polarization can be generated only if the system is not symmetric. The asymmetry can occur when the radiation field of the star is not isotropic as a result of a geometric distortion, for instance, when the star develops a bow shock ahead of its path, or when its photosphere surface brightness is not uniform, or in other words, is influenced by bright spots.

Therefore, supplementary to considering the continuum and line emissions from the DSO, studying the light polarization can be very helpful in determining the nature and properties of this source. If the DSO is a bow shock, the polarization is determined by the bow shock morphology. Subsequently, the E-vectors are predicted to be perpendicular to the direction of motion if the medium is homogeneous. If the dust shell surrounding the DSO is a disk, then the resulting polarization depends on the disk inclination.

In this paper we analyze the NIR polarimetric imaging data taken with NACO at the ESO VLT using its Wollaston prism to study the polarization properties of the DSO. In Sect. 2 we begin with the details about the observations, then describe the data reduction and determine the position of the DSO in the images. In Sect. 3 we present the results of the applied flux density calibration method: light curves, polarimetry measurements, and their statistical analysis. We present the performed radiative transfer model to describe the DSO polarization in Sect. 4. We discuss the implications of our results in Sect. 5 and finally summarize the main results of the NIR polarimetry of the DSO in Sect. 6.

2. Observations and data reduction

2.1. Data set and reduction process

The NIR observations have been carried out at the ESO VLT on Paranal, Chile. The data were obtained using the NAOS adaptive optics (AO) module and NIR camera CONICA (together NACO; [Lenzen et al. 2003](#); [Rousset et al. 2003](#); [Brandner et al. 2002](#)) at the VLT on Paranal, Chile. The AO loop was locked on IRS7, a supergiant with $K_s \sim 6.5$ – 7.0 mag and located $\sim 5.5''$ north of Sgr A*, using the NIR wavefront sensor. We collected all K_s -band ($2.2 \mu\text{m}$) data of the GC taken with S13 camera in 13 mas pixel scale polarimetry mode from 2004 to 2012. The Wollaston prism with the combination of a half-wave retarder plate in NACO provides the possibility of simultaneously measuring two orthogonal directions of the electric field vector. We used the reduced data sets as presented in [Shahzamanian et al. \(2015\)](#). Standard data reduction was applied with flat-fielding, sky subtraction, and bad-pixel correction. All the dithered exposures were aligned using a cross-correlation algorithm (ESO Eclipse Jitter; [Devillard 1999](#)). The sky background was measured on a dark cloud located at $713''$ east and $400''$ north of GC. The final sky background was obtained by getting the median of the dithered science epochs. During the observations, the PSF changed because the weather condition varied. Therefore, the quality of each epoch was determined based on the PSF measured from the stars in the field of view at the observing time. We created a data cube from the combination of the best-quality exposures (with seeing $< 2''$) of each observing night. To have a final image with longer integration time on the source and higher signal-to-noise-ratio (S/N), we obtained the median of the spatial pixels of the combined cube images. In this case, we cannot study the flux density and polarimetry variability on short times of minutes to months. For 2008, we combined all of the observing nights, since the position of the DSO does not change significantly within a few months. Table 1 shows observation dates, number of exposures, and integration times of the data sets used for the analysis here before the data were combined. We used the Lucy-Richardson deconvolution algorithm on the resulting image of the individual years created from the data cube for the aperture photometry. The PSF was extracted using the IDL-based StarFinder routine ([Diolaiti et al. 2000](#)) from isolated stars close to the DSO position.

B. Shahzamanian et al.: Polarized near-infrared light of the Dusty S-cluster Object (DSO/G2) at the Galactic center

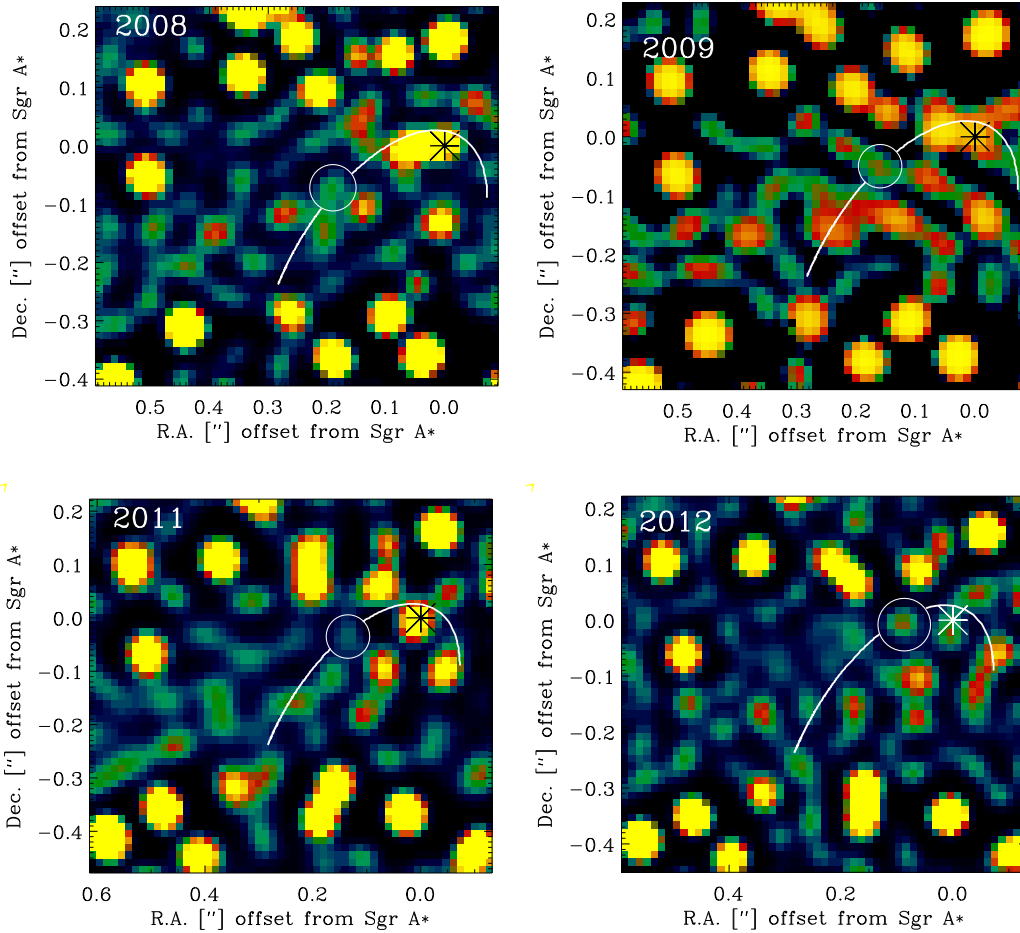


Fig. 1. Final K_s -band deconvolved median images of the central arcsecond at the GC in polarimetry mode (90° polarization channel) in 2008, 2009, 2011, and 2012 from top left to bottom right. The position of the DSO is shown by a circle on its orbit. The asterisk indicates the position of Sgr A*. In all the images north is up and east is to the left.

We aligned all the resulting median cubes of the four polarization channels of the individual observing years by using a cross-correlation algorithm. The image was restored by convolving the deconvolved image with a Gaussian beam of a FWHM of about 60 mas.

For the 90° -degree channel in 2008, 2009, 2011, and 2012 the resulting images are shown in Fig. 1. In all the years the DSO was clearly detected in its continuum emission in all channels taken with the NACO Wollaston prisms. To substantiate the detection of the DSO, we also show the results of a high-pass-filtered (smooth-subtracted) image analysis in Fig. A.1 for 2008 and 2012. In all these images the DSO flux density contribution can clearly be identified as an individual source component. While possible PSF contributions have not been cleaned in the high-pass filtered images, we have conducted our analysis of the DSO emission using the Lucy deconvolved images.

2.2. Position of the DSO

We obtained the position of the DSO in each year based on the Bry traced orbit from Meyer et al. (2014a) and Valencia-S et al. (2015). Between 2004 and 2007, this source was confused with S63 and could not be distinguished from the background. From

2008 on, it starts to be clear and resolved from stellar confusion. The crowded region of the S-cluster may be the reason of this confusion (Sabha et al. 2012). We used the data set presented in Table 1 to investigate the flux density and polarimetry of DSO.

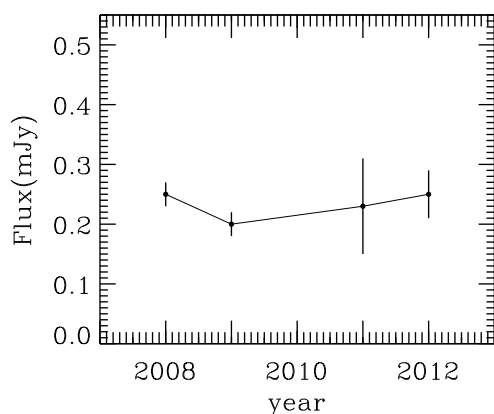
3. Analysis and results

3.1. Light curves

We measured the flux density of the DSO in each observing year by aperture photometry using a 30 mas radius circular aperture. Flux calibration was made by aperture photometry using circular apertures of 40 mas radius and based on the known flux values of 13 S-stars. Eight background apertures were placed on an area devoid of individual sources to measure the background flux in the deconvolved images. We placed two of these background apertures very close to the DSO position. We used the same stellar calibrators as were presented in Table 1 in Witzel et al. (2012) and Fig. 2 in Shahzamanian et al. (2015). We would like to note that considering the proper background apertures is critical for an accurate flux density estimation of the DSO, since it is a faint source in the K_s band and background emission can have a prominent effect on its flux density value estimation. We added

Table 1. Galactic center observations log.

Date (DD.MM.YYYY)	Start time (UT)	Stop time (UT)	Number of frames	Integration time (s)
25.05.2008	06:05:20.32	10:35:38.65	250	40
27.05.2008	04:52:04.92	08:29:38.07	184	40
30.05.2008	08:24:33.51	09:45:25.69	80	40
01.06.2008	06:04:51.56	10:10:26.78	240	40
03.06.2008	08:37:23.56	09:58:58.85	80	40
18.05.2009	04:37:55.08	10:19:54.10	286	40
27.05.2011	04:49:39.82	10:27:25.65	334	45
17.05.2012	04:49:20.72	09:52:57.08	256	45

**Fig. 2.** NIR K_s -band light curve of the DSO observed in polarimetry mode in 2008, 2009, 2011, and 2012.

the photon counts in each aperture and then added the resulting values of two orthogonal polarimetry channels to obtain the total flux densities. Then we corrected them for the background contribution. This was done for the DSO and the calibrators close to it. The obtained flux densities were corrected for the extinction, that is, the K_s -band extinction correction magnitude of 2.46 derived for the innermost arc-second by Schödel et al. (2010) was adopted. Subsequently, the light curve was obtained for 2008, 2009, 2011, and 2012, as presented in Fig. 2. The uncertainties of the measured DSO flux densities in the light curve were estimated by obtaining the observational noise by setting ten apertures in different positions of the background close to the DSO position.

The DSO does not show any intrinsic flux density variability in the K_s band based on our data set. The reason might be either a period of variability that does not match the time resolution of our data or an irregular variability. However, considering the limited data sample, any conclusion on the flux density variability and the effect of stellar contribution on the flux density estimation cannot be made at this point.

3.2. Polarimetry

We derived the polarization degree and angle by obtaining normalized Stokes parameters (I , Q , U , V) from the observed flux

Table 2. Polarimetry measurements of the DSO.

Observing year	p	ϕ
2008	30.14%	-62.87°
2009	32.6%	42.92°
2011	29.9%	18.125°
2012	37.64%	-9.67°

densities,

$$I = 1 \quad (1)$$

$$Q = \frac{f_0 - f_{90}}{f_0 + f_{90}} \quad (2)$$

$$U = \frac{f_{45} - f_{135}}{f_{45} + f_{135}} \quad (3)$$

$$V = 0, \quad (4)$$

where f_0 , f_{90} , and f_{45} , f_{135} are flux density pairs of orthogonally polarized channels. It is not possible to measure circular polarization in normalized Stokes V since NACO is not provided with a quarter-wave plate. The circular polarization of stellar sources in the GC is very small (Bailey et al. 1984), therefore we assumed that it can be ignored and set to 0. However, in the case of dusty sources that have a high dust density, circular polarization may be produced by multiple scattering. Polarization degree p and angle ϕ can be obtained as follows:

$$p = \sqrt{Q^2 + U^2} \quad (5)$$

$$\phi = \frac{1}{2} \arctan\left(\frac{U}{Q}\right), \quad (6)$$

where the polarization angle ϕ is measured from north to east and samples a range between 0° and 180° or -90° and 90° .

The instrumental polarization induced in the measured polarization can be corrected for by a model obtained from Witzel et al. (2011) that multiplies a combination of Mueller matrices for different elements of the telescope with the derived Stokes vectors. We applied their model to correct for the instrumental polarization effects, where the measured polarization parameters can be estimated with an accuracy of $\sim 1\%$ in polarization degree and $\sim 5^\circ$ in polarization angle (Witzel et al. 2011). We show the results of the polarimetry measurements for our data set in Table 2. Based on the calculated values of p and ϕ for different years, the DSO is polarized with a high polarization degree ($p > 20\%$) and a polarization angle that changes as the source moves on its orbit. Figure 3 presents a schematic illustration of the DSO polarization angle variation when the source

B. Shahzamanian et al.: Polarized near-infrared light of the Dusty S-cluster Object (DSO/G2) at the Galactic center



Fig. 3. Sketch of the DSO polarization angle variation when it moves on its eccentric orbit around the position of Sgr A* for three different years. The orange shaded areas show the range of possible values of the polarization angle based on our observation and the measurement uncertainties (see Table 3).

moves on an eccentric orbit around the position of Sgr A* before it reaches the peribothron. Standard error propagation for calculating the polarization uncertainties cannot be applied here since the errors on Q and U are not small compared to the measured values. Moreover, Q and U can be close to zero even if the flux density values in different polarimetry channels are large. In addition, the polarization degree and angle are mainly not Gaussian distributions.

In general, the effects that are responsible for producing NIR polarization in a GC source can be considered to be intrinsic to the source itself or to foreground effects caused by grain alignment along the line of sight, that is, dichroic extinction. Dichroic extinction can also play a significant role in polarization as a local effect for sources that are surrounded by an optically thick dust envelope (Whitney & Wolff 2002).

Figure 4 presents the polarization degree and angle of the DSO compared to those of several S-stars located close to the DSO position obtained in this work. It also shows the GC foreground polarization from Buchholz et al. (2013), which is $(6.1 \pm 1.3)\%$ at $20^\circ \pm 7^\circ$ in K_s band, widely parallel to the Galactic plane. Based on this figure, the measured polarization degree and angle of the DSO is not the foreground polarization and can be interpreted as intrinsic quantities.

In addition to the foreground polarization, some sources that are in the Northern Arm and the bow-shock sources have intrinsic polarization in K_s band as well as at longer wavelengths (Rauch et al. 2013). The intrinsic polarization of the stellar sources can be produced by the following processes: emission from aligned dust grains, dichroic extinction, and scattering on spherical grains and/or magnetically aligned dust grains. It is still an open question which of these processes is responsible for producing the observed intrinsic polarization of GC sources. We discuss two of these processes that may produce the DSO polarization in Sect. 4: scattering and dichroic extinction.

Buchholz et al. (2011) found that the K_s -band PSF shows a polarized structure. The authors found that for the core of the PSF (see their Fig. B.2) this effect is basically negligible. Here, the variations of the intrinsic PSF polarization amount to a value of only about 1–2%. The polarized nature of the PSF is of some importance for extended structures. We find that the continuum flux distribution of the DSO is unresolved. However, it is moving within the central stellar cluster. Buchholz et al. (2011) reported that on the first and second Airy ring (see their Fig. B.2) polarization degrees of up to 15% are possible. At this location

the flux density levels correspond to less than about 3% of the peak for a Strehl ratio of 50% in $0.5''$ seeing. In this case the polarized contributions of these neighboring sources are lower than 2% of the DSO peak flux. In 2009 and 2011 the DSO is at even larger distances from similarly bright sources, hence, the expected polarized flux contributions in these years is even lower than in 2008. In 2012 the distance of the DSO to two sources that are about 50 times brighter is close to the second Airy ring with flux contributions well below 1%. Hence, the polarized flux contribution from other sources is well below 15%. This implies that in all years the polarization estimates are to more than 85% (even more than 98% in 2008, 2009, and 2011) dominated by the DSO itself. Therefore, we did not consider PSF polarization variations in our present investigation.

Assuming the DSO has a bow-shock structure, a comprehensive model of bow shock polarization using observation results can enable us to analyze the influence of different polarization scenarios (emission, scattering, and dichroic extinction) that play a role in producing the intrinsic polarization of a bow shock.

3.3. Statistical significance of the measured values

The polarization degree is a positive defined quantity that becomes biased to higher values (than the intrinsic p of the source) at low S/N measurements. For this reason, it is possible to measure polarization degrees that are unphysically higher than 100% due to the observational uncertainties. Thus, it is important to keep in mind that the measured (or observed) polarization degree and angle of any astrophysical object are a good estimation of the source intrinsic properties only when the S/N is high. The DSO K_s -band emission from the yearly stacked images analyzed here have a medium S/N of ~ 6 –10 in 2008, 2009, and 2012 and a low S/N ~ 2.5 in 2011. In the first three cases, the distribution of the observed polarization degree can be described by a Rice function (Serkowski 1958; Vinokur 1965); while in the latter, even this function fails to properly model the high skewness of the polarization degree distribution (Simmons & Stewart 1985). In turn, the observed polarization-angle distribution depends on the flux-density S/N and on the intrinsic p of the source.

To estimate the significance of the measured DSO polarization, we assumed as null hypothesis that the source is intrinsically not polarized, meaning that the observed polarization angle ϕ_{obs} and degree p_{obs} are solely produced by the observational uncertainties. For this test, we therefore calculated f_0 , f_{90} , f_{45} , and f_{135} from the observed total flux density I_{obs} using $p = 0\%$ and $\phi = 0^\circ$ and assuming the intrinsic flux density to be the same as the observed $I = I_{\text{obs}}$. We simulated the effect of the noise in the polarization channels by adding a randomly selected amount to each channel that was drawn from a normal distribution with $\sigma(f_{\chi}) = 0.7 \sigma(I)$, where $\sigma(I)$ is the uncertainty of the observed total flux density. Using a Monte Carlo approach, we calculated 10 000 times the observed polarization degree and angle for such a setup using Eqs. (1)–(6). The normalized histograms of p_{obs} for the observations in 2008, 2009, 2011, and 2012 are shown in Fig. 5. These distributions represent the probability of measuring certain polarization degrees under the null hypothesis (i.e., the source is intrinsically not polarized) given the previously estimated I and their uncertainties. Figure 5 shows that in 2008, where $S/N \approx 10$, the most probable observed polarization degree is $\sim 9\%$ with 68/100 of the possible measurements within (4.3, 17.0)%. Under these conditions, measuring a DSO polarization degree higher than 30% when the source is intrinsically not polarized is only probable in less than 1/100 cases. In 2009

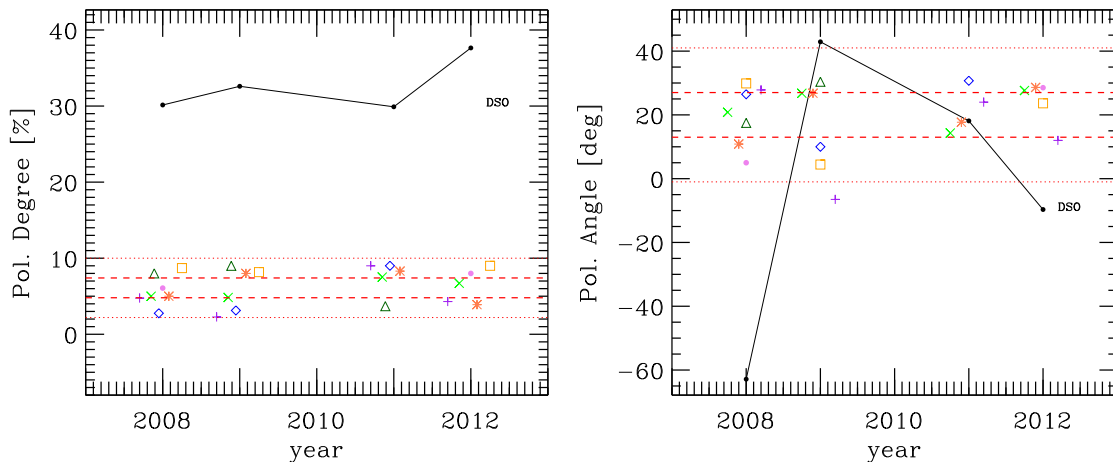


Fig. 4. *Left:* comparison of the polarization degree of the DSO (black dots) with those of GC S-stars located close to the DSO position (S7, S57, S19, S20, S40, S23, and S63; shown with X, asterisk, plus sign, diamond, triangle, violet point, and square, respectively). *Right:* comparison of the polarization angle of the DSO (black dots) with those of the S-stars similar to the left panel. In both panels, some of the considered stars are not isolated in some years in which it is difficult to calculate their polarization parameters, therefore we did not show them as data points. The regions between two dashed red lines and dotted lines present the 1 and 3σ confidence intervals of the K_s -band polarization degree and angle distributions of the stars reported in Buchholz et al. (2013), respectively. For the significance and uncertainties of the measured points see Sects. 3.3 and 3.4.

and 2012, where $S/N \approx 6$, the probability of finding an intrinsically unpolarized source of the same flux density as the DSO, and $p_{\text{obs}} \geq 35\%$ is $\sim 10/100$ cases. Only in 2011, the low S/N broadens the distribution of p_{obs} , implying that the intrinsic polarization degree cannot be estimated in this data set. In all tests of the null hypothesis, the observed polarization angle ϕ_{obs} can be any value between -90° and 90° because the intrinsic polarization degree was set to zero.

We conclude that three of the measurements of the DSO polarization degree are statistically significant at the confidence levels 0.99 in 2008, and 0.9 in 2009 and 2012¹. This means that intrinsic polarization of the DSO has been detected in 2008, 2009, and 2012.

3.4. Measurement uncertainties

After establishing the statistical significance of the polarization measurements of three observed epochs, our next goal is to estimate the uncertainty of the intrinsic parameters given the observed values. Several measurements of an intrinsically non-variable source would be ideal to assess the uncertainties in the polarization quantities. However, it is unknown whether the DSO is variable or not, and we can only rely on the stacked images of three years. Our alternative approach consists of using the Monte Carlo simulations presented before to estimate the range of most probable intrinsic values that would yield the observed DSO polarization.

We sampled the whole range of possible DSO intrinsic polarization degree and angle in a grid of $p \in [0.0, 0.7]$ in steps of 0.005, and $\phi \in [-90^\circ, 90^\circ]$ in steps of 2° , calculating each case 10 000 times. In this way, we constructed two data cubes. One of them has in the first axis the intrinsic polarization degree p , in the second axis the intrinsic polarization angle ϕ , and in the third

¹ Assuming as starting values for the simulation $p = 6\%$ and $\phi = 20^\circ$, i.e. an intrinsically unpolarized source located at the GC, which, therefore, will display p and ϕ values equal to that of the foreground polarization, the significance levels of the polarization measurements change to 0.98 for the 2008, and to 0.88 for 2009 and 2011.

the observed polarization degree p_{obs} . The value of i th cell corresponds to the probability of observing $p_{\text{obs},i}$ when the source has intrinsic p_i , ϕ_i , and the observed flux density (with its uncertainty). Similarly, the second cube has as axes p , ϕ , and ϕ_{obs} , and any i th cell equals the probability of observing $\phi_{\text{obs},i}$ given p_i , ϕ_i and $I \pm \sigma(I)$. From the sheets of (p, ϕ) at a constant p_{obs} in one cube, and at a constant ϕ_{obs} in the other, we can deduce the range of intrinsic polarization values that most probably yield the observed the polarization degree and angle.

Figure 6 shows the (p, ϕ) sheets for $p_{\text{obs}} = 30\%$ and $\phi_{\text{obs}} = -63^\circ$, as is the case for the DSO in 2008. As expected, the probability of measuring certain p_{obs} is independent of the intrinsic polarization angle of the source and peaks at the most probable intrinsic p_{best} – which does not necessarily equal p_{obs} . In contrast, the probability of observing a particular ϕ_{obs} depends on the intrinsic polarization degree and is symmetric with respect to ϕ . The most probable intrinsic polarization angle is the same as the observed value $\phi_{\text{best}} = \phi_{\text{obs}}$. The 68% ranges of intrinsic values that most probably produce the observed ones, $\sigma(p)$ and $\sigma(\phi)$ were calculated from the figures making transversal cuts at the positions of the most probable intrinsic p_{best} and ϕ_{best} , as shown in Fig. 6 (right). The results for all years are compiled in Table 3. Under the assumption that the DSO polarization degree is approximately constant over the studied years, the significance of the polarization degree measurement is larger than $1 - 1/100\,000$. The values for 2011 are reported in the table for completeness, but because of the low S/N of the flux-density measurement that year, they cannot be interpreted as intrinsic properties of the source.

4. DSO model: a young, supersonic star

Two mechanisms are responsible for the origin of the polarized flux density: Mie scattering, that is, photon scattering on spherical grains, and dichroic extinction, or selective extinction of photons due to the non-spherical shape of dust grains. Using the dust continuum radiative transfer modeling, we focused on the process of Mie scattering. The model of the DSO was required

B. Shahzamanian et al.: Polarized near-infrared light of the Dusty S-cluster Object (DSO/G2) at the Galactic center

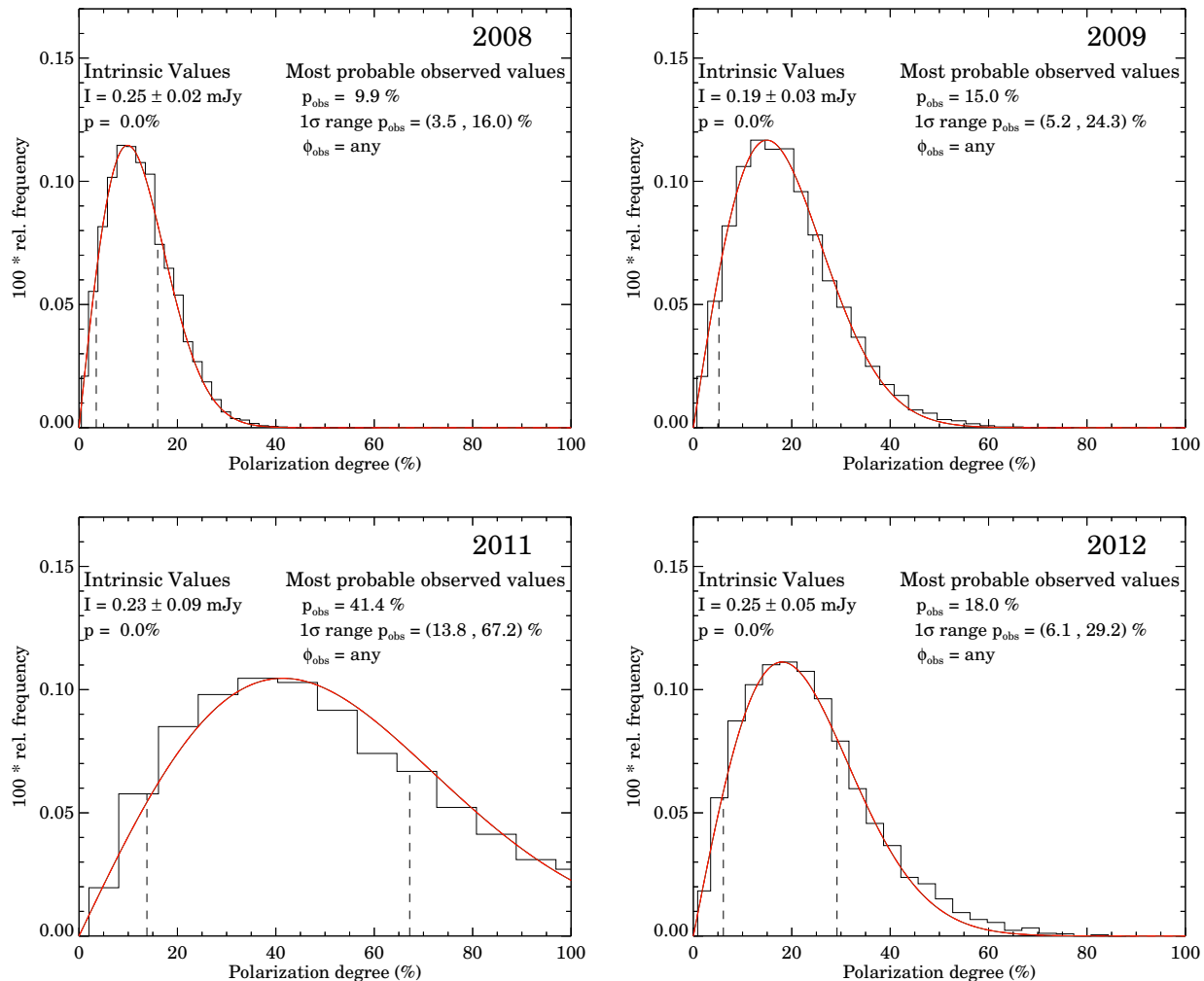


Fig. 5. Polarization degree distribution for the observations in 2008, 2009, 2011, and 2012 when considering the null hypothesis ($p = 0\%$, $\phi = 0^\circ$), the observed flux density I , and its uncertainty. The most probable observed polarization degree, p_{obs} in each case is the mode of the distributions. The range that contains 68% of the most probably observed values, $1\sigma p_{\text{obs}}$ is delineated with vertical dashed lines. The smooth line over the histograms corresponds to the best-fit Rice function.

Table 3. Most probable DSO intrinsic polarization values.

Year	$I \pm \sigma(I)$ /mJy	p_{obs}	ϕ_{obs}	$p_{\text{best}} \pm \sigma(p)$	$\sigma(\phi)$
2008	0.25 ± 0.02	30.1	117.1	28^{+10}_{-10}	9
2009	0.19 ± 0.03	32.6	42.9	28^{+16}_{-10}	15
2011 ^a	0.23 ± 0.09	29.9	18.1	$0.5^{+38}_{-0.5}$	58
2012	0.25 ± 0.05	37.6	170.3	32^{+18}_{-18}	15

Notes. ^(a) These values cannot be interpreted as intrinsic because of the low flux-density S/N obtained this year.

to meet the observed characteristics: total SED constraints—integrated flux densities in H , K_s , L' , and M bands, total polarization degree higher than $\sim 20^\circ$, and changes of polarization degree and angle along the orbit.

We considered different circumstellar geometries to assess whether they can explain the detected polarized signal and the

significant color excess in NIR bands. To test the properties of different constituents, we performed a series of dust continuum radiative transfer simulations using the Monte Carlo code Hyperion (Robitaille 2011). First, we considered only a stellar source and a bow shock layer in the calculation, which did not yield a significant polarized emission. Adding a spherical dusty shell around a stellar source provided enough extinction to match the NIR excess, but the total polarization degree remained below 10%. Finally, we added a flared disk with bipolar outflows into the density distribution, which caused the source to deviate more from the spherical geometry (see Fig. 7). The polarized emission in this composite model (star+flared disk+bipolar outflows+bow shock) is dominated by dust and stellar emission that is scattered on spherical dust grains. The largest contribution of polarized flux density originates in the region where the outflow intersects the dense bow-shock layer. An overview of different possible circumstellar geometries is provided in Table 4, where the values of the total linear polarization degree in K_s band and the color excess $K_s - L'$ are included. A high value of the total polarization degree in K_s band and an intrinsic NIR excess

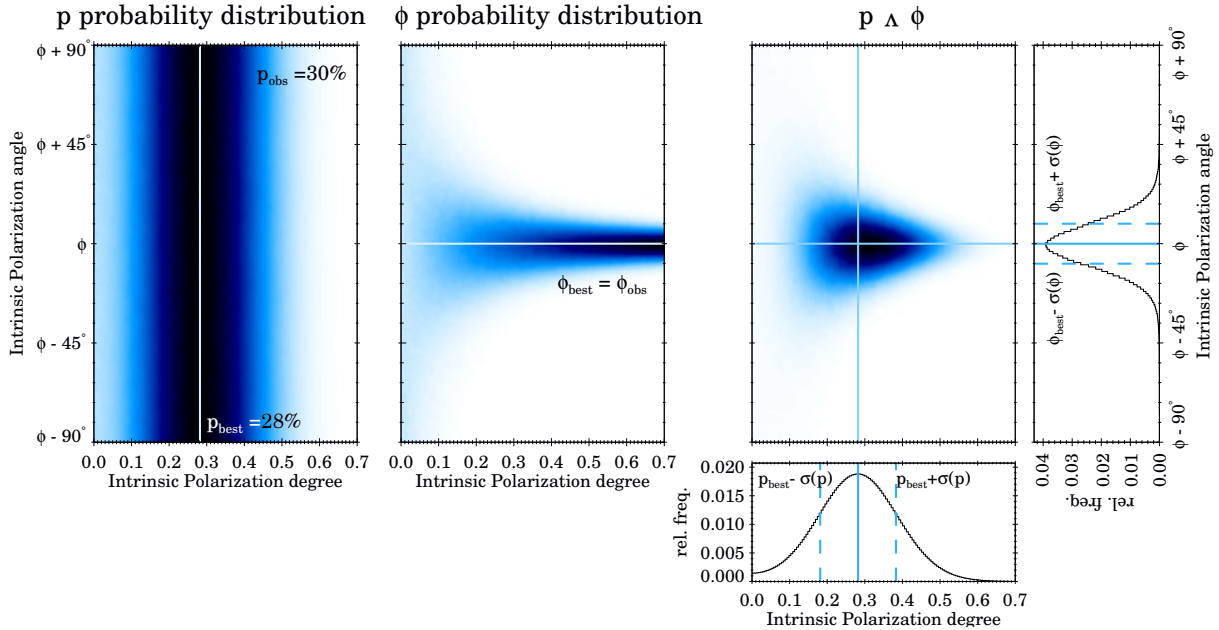


Fig. 6. *Left:* marginalized distributions of intrinsic polarization degree and angle, assuming that the observed values are the most probable ones. Here the case of 2008 data is shown. *Right:* combined probability obtained from the two distributions at the left. The *bottom and right panels* show transversal cuts to the combined distribution at the position of the marked lines.

between K_S and L' NIR bands are matched by the composite model star+disk+cavities+dense bow shock, whose properties are studied in more detail.

This scenario resembles proplyd-like objects, which seem to be present in the Sgr A West region (see Yusef-Zadeh et al. 2015b, for VLA continuum observations). Therefore, the DSO might be the first detected and monitored young stellar object in the vicinity of the SMBH that would manifest a very recent low-mass star-formation event close to the GC.

4.1. Monte Carlo radiative transfer simulations

We performed 3D Monte Carlo radiative transfer calculations using the code Hyperion (Robitaille 2011) to study under which conditions the model of a supersonic, young stellar object would yield the observed DSO properties. The advantage of the Monte Carlo approach is that it is suitable for arbitrary 3D geometry (stellar source surrounded by circumstellar envelope and bow shock), and we automatically obtain a full Stokes vector (I, Q, U, V), which allows us to easily calculate the total and the polarized flux density. In our simulation runs we set up a spherical polar grid containing $400 \times 200 \times 10$ grid points and subsequently added a density grid of gaseous-dusty mixture with a gas-to-dust ratio of 100:1. A power-law distribution with a slope of -3.5 (Kim et al. 1994) of spherical dust grains with a radius of between 0.01 and $10 \mu\text{m}$ was considered. The distance to the GC was taken to be 8 kpc.

The density of the circumstellar envelope was assumed to have a simple radial profile, $\rho_{\text{disc}} = \rho_0(r/1 \text{ AU})^{-1}$ with $\rho_0 = 10^{-14} \text{ g cm}^{-3}$, and the bipolar cavities were assumed to have an opening angle of 90° and a uniform density of $10^{-20} \text{ g cm}^{-3}$ (Sanchez-Bermudez et al. 2016). For the bow-shock component and its evolution, we considered the treatment of Zajaček et al. (2016) for the DSO based on the analytical axisymmetric model of Wilkin (1996), keeping the same density and temperature profiles for the hot corona around Sgr A*. A

DSO as a young, supersonic star - model components

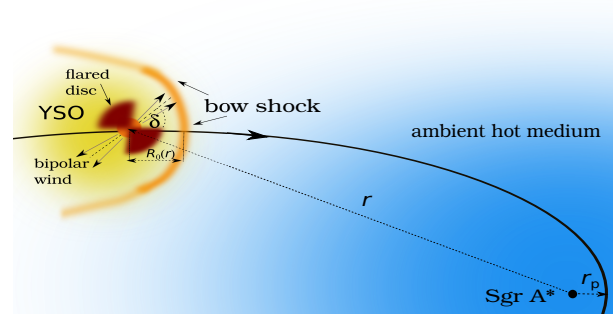


Fig. 7. Schematic view of the proplyd-like model of the DSO structure. See the text for a description of the model components.

two-dimensional bow-shock shape is obtained by the model of Wilkin (1996)

$$R(\theta) = R_0 \csc \theta \sqrt{3(1 - \theta \cot \theta)}, \quad (7)$$

where θ is the polar angle from the axis of symmetry, as seen by the star at the coordinate origin. R_0 is the so-called stand-off distance obtained by balancing the ram pressures of the stellar wind and ambient medium at $\theta = 0$, and it is given by

$$R_0 = \sqrt{\frac{\dot{m}_w v_w}{\Omega \rho_a v_*^2}}. \quad (8)$$

Here, \dot{m}_w is the stellar mass-loss rate, v_w the terminal velocity of the stellar wind, ρ_a the ambient medium mass density where $\rho_a = m_H n_H$ (with $n_H \approx n_e$), and m_H the mean molecular weight of hydrogen, and v_* is the velocity at which the star moves through the medium (i.e., the relative velocity of the star with respect to the ambient medium when the ambient medium is not stationary). The solid angle $\Omega = 2\pi(1 - \cos \theta_0)$, where θ_0 stands for

B. Shahzamanian et al.: Polarized near-infrared light of the Dusty S-cluster Object (DSO/G2) at the Galactic center

Table 4. Different circumstellar geometries with a list of constituents.

Geometry	K_s -band total linear polarization degree $\bar{p}_{K,L}$ [%]	$(K_s - L')_{\text{int}}$ (intrinsic)	$(K_s - L')_{\text{ext}}$ (with dust extinction)
Star	0 (~6% foreground pol. at the GC)	-0.9	0.4
Star+rotationally flattened envelope (50° inclination)	0.2	0.1	1.4
Star+flared disk	3.2	0.3	1.6
Star+dense bow shock (inclined)	4.1	1.9	3.2
Star+spherical dusty envelope+dense bow shock (inclined)	1.0	1.6	2.9
Star+flattened envelope+cavities (90% inclination)	10.1	1.2	2.4
Star+flared disk+flattened envelope+cavities (90% inclination)	10.5	-1.3	-0.03
Star+disk+cavities+dense bow shock	25.0	1.9	3.2

Notes. Important parameters are the total linear polarization degree in K_s band ($2.2\mu\text{m}$) and the color index $K_s - L'$. The observed values of the degree and the color index are matched by the composite model star+disk+cavities+dense bow shock that is used in the following analysis.

the half-opening angle of the bipolar outflow, represents the direction into which the stellar wind is blown, outside Ω there is no outflow (Zhang & Zheng 1997). For an isotropic stellar wind, $\theta_0 = \pi$, the solid angle is naturally $\Omega = 4\pi$, whereas for our non-spherical bipolar stellar outflow, $\theta_0 = \pi/4$, and the solid angle is then reduced to $\Omega = 2\pi(1 - \sqrt{2}/2) \approx 1.84$.

The bow shock consists of two layers: (a) a hot and sparse forward shock; and (b) a cold and denser reverse shock (Scoville & Burkert 2013). We considered only the colder and denser layer, whose density is about four orders of magnitude higher than for the hot shock (Scoville & Burkert 2013), and therefore it is more significant in terms of scattering on spherical dust particles. The initial value for the bow-shock density is set to $10^{-16} \text{ g cm}^{-3}$, in accordance with Scoville & Burkert (2013) for the distance of 10^{16} cm from Sgr A*.

For the typical parameters of a young star potentially associated with the DSO, which means a mass-loss rate of $\dot{m}_w = 10^{-8} M_\odot \text{ yr}^{-1}$ and a wind velocity of $v_w = 100 \text{ km s}^{-1}$, the stand-off distance is of about 10 AU (Zajaček et al. 2016), which sets the basic length-scale of the model. The typical angular scale of such an object is 1 mas at the distance of the GC, in accordance with the compactness of the DSO observed along the orbit (Valencia-S et al. 2015). The outer radius of the circumstellar envelope was set to 3 AU and the inner radius was set to the typical dust sublimation radius (Monnier & Millan-Gabet 2002),

$$R_{\text{sub}} = 1.1 \sqrt{Q_R} \left(\frac{L_\star}{1000 L_\odot} \right)^{1/2} \left(\frac{T_{\text{sub}}}{1500 \text{ K}} \right)^{-2} \text{ AU}, \quad (9)$$

which for the upper limit on the luminosity of the DSO $L_\star = 30 L_\odot$ and a ratio of dust absorption efficiencies $Q_R = 1$ leads to the estimate of $R_{\text{sub}} \approx 0.1 \text{ AU}$.

4.2. Comparison with observations

The described model of a supersonic, young stellar object with the adopted density distribution can reproduce the inferred flux densities in H , K_s , L' , and M NIR bands: $F_H \leq 0.14 \text{ mJy}$, $F_K \sim 0.3 \text{ mJy}$, $F_L \sim 1.9 \text{ mJy}$, and $F_M \sim 2.8 \text{ mJy}$, respectively (Eckart et al. 2013; Witzel et al. 2014; Gillessen et al. 2012). In Fig. 8 we compare the observed flux densities with the best-fit SED obtained from simulations.

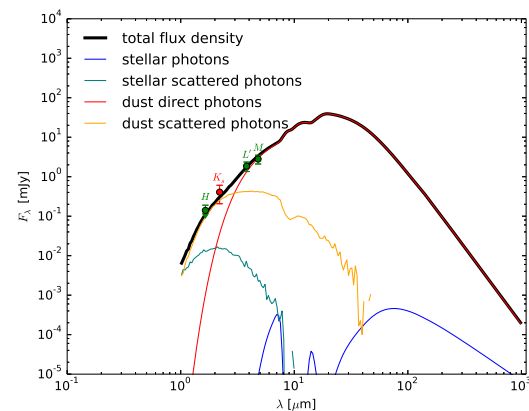


Fig. 8. SED for the young stellar object described in the text at the GC. The points label the flux densities inferred from the observations.

The obtained proper motion of the DSO between 2008 and 2009 is $v_\alpha = (-400) \text{ km s}^{-1}$, $v_\delta = (800) \text{ km s}^{-1}$ and between 2011 and 2012 it is $v_\alpha = (-2000) \text{ km s}^{-1}$, $v_\delta = (600) \text{ km s}^{-1}$. Therefore, v_\star changes from 894.42 km s^{-1} to $2088.06 \text{ km s}^{-1}$. The uncertainty of the proper motion is of about 1 mas yr^{-1} (Eckart et al. 2012). Using the relative velocity values from 2008 to 2012 in Eq. (8), the stand-off distance becomes about half of its value (see also Fig. 3 in Zajaček et al. 2016). Moreover, the density profile of the central region based on X-ray data derived in Shcherbakov & Baganoff (2010) indicates that the particle number density increases within the central arcseconds from the SMBH.

Owing to the increasing orbital velocity of the DSO and higher ambient pressure toward the pericenter, the bow shock shrinks and becomes denser. An increment by a factor of four and potentially even more in the bow-shock number density is expected between 2008 and 2012 under the assumption that the bow-shock mass stays approximately constant. This leads to the progressively higher scattering from the non-spherical bow shock for smaller distances from the SMBH. The increase in the density of the bow-shock layer leads to the progressive increase in polarization degree from an initial 30% in 2008 to almost 40% in 2012, which can be reproduced by radiative transfer simulations of the dust continuum.

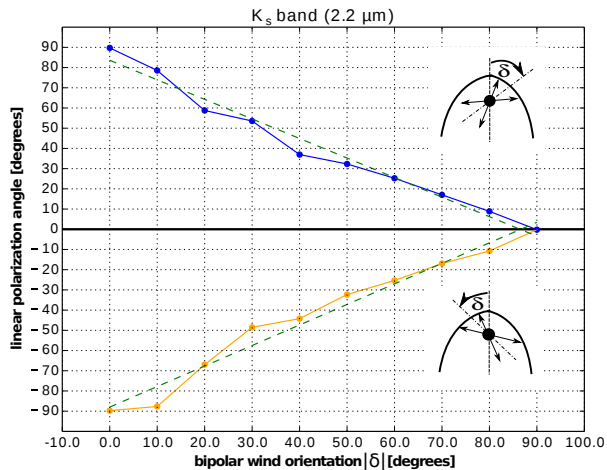


Fig. 9. Linear polarization angle as a function of bipolar wind orientation δ . The plot consists of two parts: the *upper panel* shows the dependence for the clockwise rotation of the bipolar wind; the *lower panel* is the same dependence for the counter-clockwise rotation of the bipolar wind. The lines correspond to the linear interpolation of the data; linear regression lines are depicted by green dashed lines.

The observed change in the polarization angle Φ is given by the combination of the external factors (i.e., motion of the DSO through the external accretion flow) and/or the internal factors (geometry of the circumstellar environment: disk, bipolar wind, and the bow shock).

Using the Monte Carlo radiative transfer calculations, we investigated the effect of the change in orientation of the bipolar wind with respect to the symmetry axis of the bow shock. The angle between the symmetry axis of the bow shock and the axis of the bipolar wind is denoted by δ . In our simulations, we gradually increased δ , starting at 0° (bipolar wind aligned with the bow-shock axis), and we stopped at 90° (bipolar wind perpendicular to the bow-shock axis). The increment is 10° , and we performed the simulations in both clockwise and counter-clockwise directions. In Fig. 9 we plot the dependency $\Phi = f(\delta)$ for the two directions (upper and lower part). In the calculations the bow shock lies in the orbital plane and we observe it from above. The calculated values are represented by points and the lines stand for linear interpolation (blue and orange lines) and the linear regression (green dashed lines).

The basic trend in Fig. 9 is the following: for the bipolar wind aligned with the bow-shock axis, $\delta = 0^\circ$, the polarization angle reaches values $\pm 90^\circ$; when the angle $|\delta|$ deviates from zero and approaches 90° , the polarization angle approaches zero. Therefore, the change of the orientation of the bipolar wind covers the whole range ($-90^\circ, +90^\circ$). The fitted linear relations are $\Phi_1 = -0.97(\pm 0.06)\delta + 84(\pm 3)$ (clockwise rotation) and $\Phi_2 = 1.02(\pm 0.07)\delta - 88(\pm 4)$ (counter-clockwise direction), which in principle may be approximated in the following way: $\Phi \approx -(+)\delta + (-)90$. The change in orientation of the bipolar wind takes place as a consequence of the torques induced by the supermassive black hole, which leads to its precession when the circumstellar disk is misaligned with the orbital plane. This naturally affects the inclination of the outflow that originates in the disk, and the precession takes place on the precession timescale, which is longer than the orbital timescale, $T_{\text{prec}} > T_{\text{orb}}$. The wobbling of the disk occurs on timescales shorter than one orbital period, approximately $T_{\text{wob}} \sim 1/2 T_{\text{orb}}$ (Bate et al. 2000).

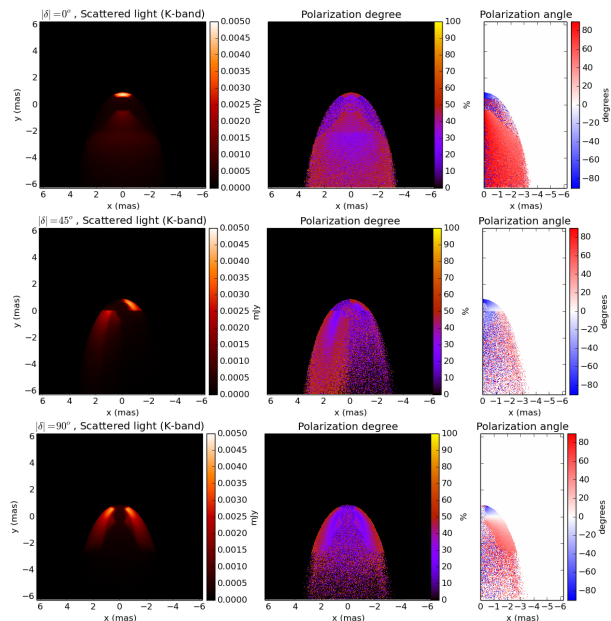


Fig. 10. Emission map of scattered light in K_s band, the distribution of the polarization degree, and the angle in the *left, middle, and right panels*, respectively, for three different configurations of the star-outflow system: $\delta = 0^\circ, 45^\circ, \text{ and } 90^\circ$ from top to bottom.

In addition, the change in polarization angle may be the combination of the change in internal geometry of the outflow and the external interaction of a supersonic star with an ambient wind with a certain velocity field. When the bipolar wind is aligned with the symmetry axis of the bow shock, the total polarization angle is perpendicular to the bow shock symmetry axis. Subsequently, when the supersonic star interacts with the external outflow or inflow, the bow-shock orientation changes because of the change in relative velocity. This would naturally lead to the corresponding alternation of the polarization angle.

For completeness, we also produce the images of scattered emission in K_s band, maps of linear polarization degree, and the distribution of the polarization angle for the configurations with $\delta = 0^\circ, \delta = 45^\circ, \text{ and } \delta = 90^\circ$ (see Fig. 10). Most of the polarized flux density originates in the bow-shock layer where the bipolar stellar wind intercepts the bow shock. The change in tilt of the bipolar cavity naturally leads to the modification of the polarization angle.

All in all, the main observed characteristics of the DSO, that is, compactness, the total flux density, the polarization degree and angle, and their corresponding changes, can be reproduced by the model of a supersonic YSO. A high polarization degree in K_s band is due to the scattering of stellar and dust photons, and the main contribution is due to the self-scattering of dust emission. The reconstructed RGB image of the DSO model from the radiative transfer is shown in Fig. 11, where blue stands for the K_s band, green for the L' band, and red for the M -band emission.

4.3. Effect of dichroic extinction

A fraction of the polarized flux density of the DSO may arise from dichroic extinction. Dust grains might not be necessarily spherical, but they might be cylindrical and aligned to a certain extent by a magnetic or radiation field. A significant

B. Shahzamanian et al.: Polarized near-infrared light of the Dusty S-cluster Object (DSO/G2) at the Galactic center

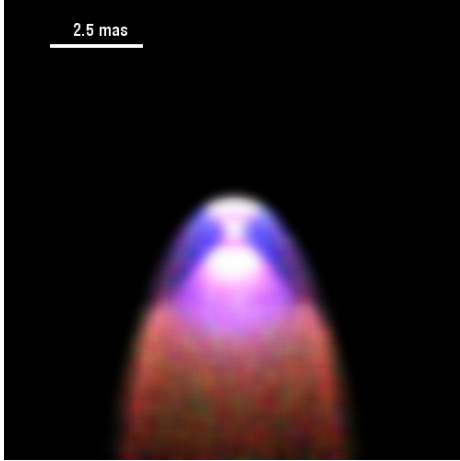


Fig. 11. RGB image of the DSO source model. Blue stands for the K_s band, green for the L' band, and red for the M -band emission.

polarized signal may then be created by dichroic extinction: photons with electric vectors that are parallel to the grain axis experience higher extinction than those with electric vectors that are perpendicular. Therefore, a polarized emission emerges with a polarization degree p that may be expressed in the following way (Krugel 2002):

$$p = \frac{e^{-\tau_{\min}} - e^{-\tau_{\max}}}{e^{-\tau_{\min}} + e^{-\tau_{\max}}}, \quad (10)$$

where τ_{\max} is the highest optical depth in the direction of the strongest attenuation and τ_{\min} is the lowest optical depth in the perpendicular direction. The difference is usually small, $\tau_{\max} - \tau_{\min} \rightarrow 0$, which then leads to

$$p = \frac{1}{2}(\tau_{\max} - \tau_{\min}) = \frac{1}{2}\sigma_{\text{gr}}(Q_{\text{ext}}^{\max} - Q_{\text{ext}}^{\min}) \int_0^l n(l)dl, \quad (11)$$

where σ_{gr} is the effective cross-section of the grain, Q_{ext}^{\max} and Q_{ext}^{\min} are the highest and lowest extinction efficiencies, and the integral $N = \int_0^l n(l)dl$ stands for the column density of dust along the line of sight.

Since the polarization degree p in Eq. (11) is proportional to the column density, which tends to increase toward the pericenter as a result of the increasing surface density of the bow-shock layer (see Zajaček et al. 2016, for detailed calculations), the slight increase in polarization degree toward the pericenter (2008–2012) might be partially caused by dichroic extinction.

5. Discussion

The obtained polarization degree of the DSO in different observing years is significantly higher than the foreground polarization (6.1% in K_s band), which shows that it is an intrinsically polarized source. Emission or absorption from elongated grains that are aligned magnetically and (Mie-) scattering on dust grains in the dusty stellar envelopes are the most probable processes to produce the intrinsic polarization. In the NIR, emission and absorption processes can take place at the same time and cancel each other out. When scattering on the spherical dust grains occurs, part of the light that is scattered forward is unpolarized, and the rest would be scattered perpendicular to the direction of incident light, which produces linear polarization. If a central star is

embedded in an isotropic envelope of spherical grains, the scattered light produces polarization with polarization vectors tangential to concentric circles about the central star that causes the overall polarization to be zero.

Polarization patterns can be more complex for more complex geometries such as YSOs that have dusty disks around the central source (see, e.g., Murakawa 2010), and bow-shock sources. In a system of a star that has a dusty disk around it, the polarization values of different regions around the source cancel each other out when the source is viewed face-on and no polarization would be detected, while when it is viewed edge-on, the source shows polarization (Buchholz et al. 2011). Scattering can also occur on elongated and non-spherical dust grains and has been modeled (see, e.g., Whitney & Wolff 2002), although in our radiative transfer model we assumed only spherical dust grains. All in all, polarization produced by light scattering depends on the source viewing angle and its geometry.

Since the measured polarization degree of the DSO that we obtain is high ($p > 20\%$), it might be caused by non-spherical geometry, for example, by a star with a bipolar wind and a bow shock.

In general, if the DSO is moving through the hot, X-ray emitting region of the interstellar medium with a supersonic velocity, a bow shock can form. Collisional ionization and high densities in the shocked layer of the stellar wind can generate its observed emission lines (Scoville & Burkert 2013). However, no increase in the Bry luminosity has been detected, which would be expected for the bow-shock dominated emission (Valencia-S et al. 2015).

The polarization angle varies during the years, that is to say, the direction of the polarization vector changes from its expected direction, which is perpendicular to the direction of motion. The modification of the polarization angle can be caused by the change in orientation of the bipolar wind of the star that occurs when the circumstellar disk is not aligned with the orbital plane. It can also be explained by a combination of the source motion and the interaction with the surrounding medium.

T Tauri stars generally exhibit an intrinsic polarization, and one of the main origins of their polarization is scattering by dust grains in circumstellar shells (see, e.g., Yudin & Evans 1998). In polarimetric images, they show variations in polarization degree and angle (Appenzeller & Mundt 1989). Many T Tauri stars have magnetospheric accretion flows since their circumstellar magnetic fields are powerful and globally ordered to maintain this type of large-scale accretion flows (Symington et al. 2005).

Some circumstellar disks of the low-mass stars have a bow-shock appearance like the proplyds (protoplanetary disks) of the Orion nebula cluster (O'dell & Wen 1994; Johnstone et al. 1998; Störzer & Hollenbach 1999). NIR polarimetry is a tool to constrain the disk parameters of the proplyds even if the disk structure itself is not resolvable (Rost et al. 2008). Based on our data set, we cannot spatially resolve a disk or a bow-shock structure because the source appears as a point source with the current angular resolution of 8 m class telescopes in K_s band. It might be similar to X3 and X7, the bow-shock sources within the inner $5''$ at the GC (Mužić et al. 2010). Moreover, as the source is not extended, it is not possible to measure the polarization in individual regions of the source, as was done in Rauch et al. (2013) for IRS 8.

6. Summary and conclusions

We have analyzed the NIR polarized observations of a Dusty S-cluster Object (DSO/G2) on an eccentric orbit around Sgr A*.

K_s -band polarization data were available for 2008, 2009, 2011, and 2012. In all these years we clearly detected K_s -band continuum emission in the different channels of the Wollaston prism. The data cover the polarization information of the DSO before its pericenter passage (May 2014). The source does not show significant variability in the overall K_s -band flux density during the observed years, and its polarization degree is mostly above 20%, which is higher than the foreground polarization measured on the surrounding stars. It appears that the polarization degree is approximately constant and the polarization angle varies as it approaches the position of Sgr A*. Based on our significance analysis, the polarization measurements of the DSO are significant in 2008, 2009, and 2012 and can be interpreted as source-intrinsic properties.

Since the total polarization degree is noticeably high, higher than 20% for all epochs, the DSO structure is expected to deviate from the spherical symmetry. Moreover, the analysis of Valencia-S et al. (2015) showed that the source remains compact, meaning that it is not effected by tidal forces close to the pericenter of its orbit. Gillessen et al. (2012) and Eckart et al. (2013) discussed a NIR excess of $K_s - L' > 3$, which implies the presence of a dense gaseous-dusty envelope. All of these basic observed parameters, the NIR excess, the compactness, and the significant polarization, may be reconciled within the model of a dust-enshrouded young star, to be precise, a pre-main-sequence star of class 1 (Zajaček et al. 2014; Zajacek et al. 2015), that forms a dense bow-shock layer by its supersonic motion upon approaching the supermassive black hole (Zajaček et al. 2016).

The obtained polarization properties of the DSO in this work can be caused by the non-spherical geometry of a bow shock and a bipolar wind of the star. We used the 3D radiative transfer model implementing the code Hyperion (Robitaille 2011) to compare the observed measurements to the model of the young stellar object forming a bow shock.

We conclude that the varying polarization angle is related to the intrinsic change of the circumstellar configuration. The change in bipolar outflow orientation may be due to the accretion disk wobbling or precession in the gravitational field of the SMBH. It can be also produced by external interaction of the DSO with the accretion flow. Although our model is simple, it can reproduce many observed properties of the DSO obtained in this work, such as the total flux density and the polarization degree. A more detailed analysis of the model will be provided in Zajaček et al. (in prep.).

Shahzamanian et al. (2015) showed that the Sgr A* system exhibits a stable geometry and accretion process that is consistent with the preferred jet or wind directions. The close fly-by of the DSO, or similar dusty sources (Peissker et al., in prep.), might have an effect on the stable accretion flow onto Sgr A* that depends on the nature of these objects. However, after the pericenter passage of the DSO, the object remained compact and its orbit Keplerian (Witzel et al. 2014; Valencia-S et al. 2015). Consequently, it did not lose a noticeable amount of energy and angular momentum during its closest approach to Sgr A*, and as a result experienced weak interactions with the central black hole (Park et al. 2015). However, based on hydrodynamical simulations, it may take several years for their interaction and to see a change in the activity of Sgr A* (Burkert et al. 2012; Schartmann et al. 2012), either as an increase in the accretion flow rate or in the appearance of jets (Yuan & Narayan 2014). Therefore, polarization and variability measurements of Sgr A* are needed to be continued as they are the ideal tool to probe any change in the apparently stable system as a function of the DSO fly-by. Moreover, future polarized observations of the DSO, that

is, after the pericenter passage, in the NIR can help us to better constrain the source polarization and structure.

Acknowledgements. The authors would like to thank the anonymous referee for the helpful comments on this paper. We would like to thank G. Witzel for fruitful discussions. This work was supported in part by the Deutsche Forschungsgemeinschaft (DFG) via the Cologne Bonn Graduate School (BCGS) and the Max Planck Society through the International Max Planck Research School (IMPRS) for Astronomy and Astrophysics. B. Shahzamanian has been supported by IMPRS and the BCGS. N. Sabha has been supported by BCGS. M. Zajacek and M. Parsa are members of the IMPRS. Part of this work was supported by fruitful discussions with members of the Czech Science Foundation DFG collaboration (No. 13-00070J). We also received funding from the European Union Seventh Framework Program (FP7/2007–2013) under grant agreement n312789; Strong gravity: Probing Strong Gravity by Black Holes Across the Range of Masses.

References

- Abarca, D., Sądowski, A., & Sironi, L. 2014, *MNRAS*, **440**, 1125
 Appenzeller, I., & Mundt, R. 1989, *A&ARv*, **1**, 291
 Bailey, J., Hough, J. H., & Axon, D. J. 1984, *MNRAS*, **208**, 661
 Ballone, A., Schartmann, M., Burkert, A., et al. 2013, *ApJ*, **776**, 13
 Bate, M. R., Bonnell, I. A., Clarke, C. J., et al. 2000, *MNRAS*, **317**, 773
 Brandner, W., Rousset, G., Lenzen, R., et al. 2002, *The Messenger*, **107**, 1
 Buchholz, R. M., Witzel, G., Schödel, R., et al. 2011, *A&A*, **534**, A117
 Buchholz, R. M., Witzel, G., Schödel, R., & Eckart, A. 2013, *A&A*, **557**, A82
 Burkert, A., Schartmann, M., Alig, C., et al. 2012, *ApJ*, **750**, 58
 Devillard, N. 1999, in *Astronomical Data Analysis Software and Systems VIII*, eds. D. M. Mehringer, R. L. Plante, & D. A. Roberts, *ASP Conf. Ser.*, **172**, 333
 Diolaiti, E., Bendinelli, O., Bonaccini, D., et al. 2000, *A&AS*, **147**, 335
 Eckart, A., Britzen, S., Horrobin, M., et al. 2012, in *Proc. Nuclei of Seyfert galaxies and QSOs – Central engine & conditions of star formation (Seyfert 2012)*, 6–8 November, Max-Planck-Institut für Radioastronomie (MPIfR), Bonn, Germany, 4
 Eckart, A., Mužić, K., Yazici, S., et al. 2013, *A&A*, **551**, A18
 Ghez, A. M., Witzel, G., Sitarski, B., et al. 2014, *ATel*, **6110**, 1
 Gillessen, S., Genzel, R., Fritz, T. K., et al. 2012, *Nature*, **481**, 51
 Gillessen, S., Genzel, R., Fritz, T. K., et al. 2013, *ApJ*, **763**, 78
 Jalali, B., Pelupessy, F. I., Eckart, A., et al. 2014, *MNRAS*, **444**, 1205
 Johnstone, D., Hollenbach, D., & Bally, J. 1998, *ApJ*, **499**, 758
 Kim, S.-H., Martin, P. G., & Hendry, P. D. 1994, *ApJ*, **422**, 164
 Krugel, E. 2002, *The Physics of Interstellar Dust*, Series in Astronomy and Astrophysics (Taylor & Francis)
 Lenzen, R., Hartung, M., Brandner, W., et al. 2003, in *Instrument Design and Performance for Optical/Infrared Ground-based Telescopes*, eds. M. Iye, & A. F. M. Moorwood, *SPIE Conf. Ser.*, **4841**, 944
 Mapelli, M., & Trani, A. A. 2016, *A&A*, **585**, A161
 Meyer, L., Ghez, A. M., Witzel, G., et al. 2014a, in *IAU Symp. 303*, eds. L. O. Sjouwerman, C. C. Lang, & J. Ott, 264
 Meyer, L., Witzel, G., Longstaff, F. A., & Ghez, A. M. 2014b, *ApJ*, **791**, 24
 Monnier, J. D., & Millan-Gabet, R. 2002, *ApJ*, **579**, 694
 Murakawa, K. 2010, *A&A*, **518**, A63
 Murray-Clay, R. A., & Loeb, A. 2012, *Nat. Comm.*, **3**, 1049
 Mužić, K., Eckart, A., Schödel, R., et al. 2010, *A&A*, **521**, A13
 O'dell, C. R., & Wen, Z. 1994, *ApJ*, **436**, 194
 Park, J.-H., Trippe, S., Krichbaum, T. P., et al. 2015, *A&A*, **576**, L16
 Pfühl, O., Gillessen, S., Eisenhauer, F., et al. 2015, *ApJ*, **798**, 111
 Pfiifer, K., Do, T., Meyer, L., et al. 2013, *ApJ*, **773**, L13
 Rauch, C., Mužić, K., Eckart, A., et al. 2013, *A&A*, **551**, A35
 Robitaille, T. P. 2011, *A&A*, **536**, A79
 Rost, S., Eckart, A., & Ott, T. 2008, *A&A*, **485**, 107
 Rousset, G., Lacombe, F., Puget, P., et al. 2003, in *Adaptive Optical System Technologies II*, eds. P. L. Wizinowich, & D. Bonaccini, *SPIE Conf. Ser.*, **4839**, 140
 Sabha, N., Eckart, A., Merritt, D., et al. 2012, *A&A*, **545**, A70
 Sanchez-Bermudez, J., Hummel, C. A., Tuthill, P., et al. 2016, *A&A*, **588**, A117
 Sądowski, A., Sironi, L., Abarca, D., et al. 2013, *MNRAS*, **432**, 478
 Schartmann, M., Burkert, A., Alig, C., et al. 2012, *ApJ*, **755**, 155
 Schödel, R., Najarro, F., Muzic, K., & Eckart, A. 2010, *A&A*, **511**, A18
 Scoville, N., & Burkert, A. 2013, *ApJ*, **768**, 108
 Serkowski, K. 1958, *Acta Astron.*, **8**, 135
 Shahzamanian, B., Eckart, A., Valencia-S., M., et al. 2015, *A&A*, **576**, A20
 Shcherbakov, R. V. 2014, *ApJ*, **783**, 31

B. Shahzamanian et al.: Polarized near-infrared light of the Dusty S-cluster Object (DSO/G2) at the Galactic center

Shcherbakov, R. V., & Baganoff, F. K. 2010, *ApJ*, 716, 504
 Simmons, J. F. L., & Stewart, B. G. 1985, *A&A*, 142, 100
 Störzer, H., & Hollenbach, D. 1999, *ApJ*, 515, 669
 Symington, N. H., Harries, T. J., & Kurosawa, R. 2005, *MNRAS*, 356, 1489
 Valencia-S., M., Eckart, A., Zajaček, M., et al. 2015, *ApJ*, 800, 125
 Vinokur, M. 1965, *Ann. d’Astrophys.*, 28, 412
 Whitney, B. A., & Wolff, M. J. 2002, *ApJ*, 574, 205
 Wilkin, F. P. 1996, *ApJ*, 459, L31
 Witzel, G., Eckart, A., Buchholz, R. M., et al. 2011, *A&A*, 525, A130
 Witzel, G., Eckart, A., Bremer, M., et al. 2012, *ApJS*, 203, 18
 Witzel, G., Ghez, A. M., Morris, M. R., et al. 2014, *ApJ*, 796, L8
 Yuan, F., & Narayan, R. 2014, *ARA&A*, 52, 529
 Yudin, R. V., & Evans, A. 1998, *A&AS*, 131, 401
 Yusef-Zadeh, F., Bushouse, H., Schödel, R., et al. 2015a, *ApJ*, 809, 10

Yusef-Zadeh, F., Roberts, D. A., Wardle, M., et al. 2015b, *ApJ*, 801, L26
 Zajaček, M., Eckart, A., Peissker, F., Karssen, G. D., & Karas, V. 2015, in Proc. 24th Annual Conference of Doctoral Students – WDS 2015 – Physics, eds. J. Safrankova, & J. Pavlu (Prague: Matfyzpress), 27
 Zajaček, M., Karas, V., & Eckart, A. 2014, *A&A*, 565, A17
 Zajaček, M., Eckart, A., Karas, V., et al. 2016, *MNRAS*, 455, 1257
 Zhang, Q., & Zheng, X. 1997, *ApJ*, 474, 719

Appendix A

We present the high-pass-filtered (smooth-subtracted) images of the central $0.65'' \times 0.65''$ for 2008 and 2012 in Fig. A.1. The DSO can be identified as a source component in the images.

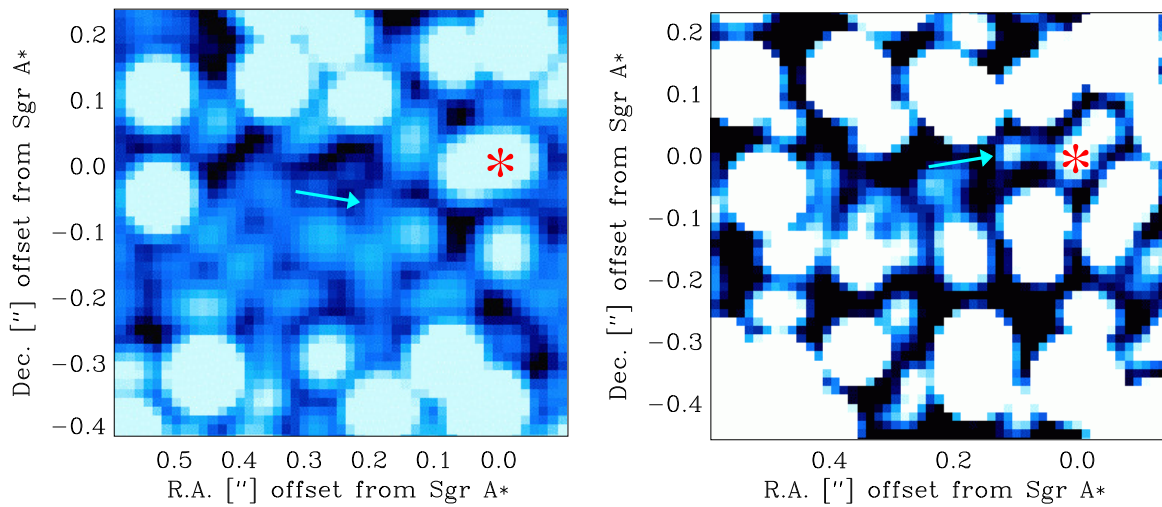


Fig. A.1. Color maps of high-pass-filtered (smooth-subtracted) adaptive optics images of the central $0.65'' \times 0.65''$. The arrow points at the contour line excursions that are due to the flux density contribution of the DSO. The red asterisk indicates the position of Sgr A*. *Left* is 90° position angle for 2008 and *right* is 90° position angle for 2012.

Nature of NIR-excess sources close to the Galactic centre

Based on the continuum observations in the NIR domains ([Eckart et al. 2013](#); [Witzel et al. 2014](#); [Shahzamanian et al. 2016](#)) it was needed to construct a model of the DSO/G2 source that includes both the total and polarized flux density. Given this motivation, I did a set of several Monte Carlo radiative transfer simulations with three-dimensional geometries of dusty circumstellar atmospheres, including a central star (with parameters of a pre-main-sequence star), a non-spherical dusty envelope, and a bow shock.

As we already discussed in [Shahzamanian et al. \(2016\)](#), a dust-enshrouded star can fully reproduce the total as well as polarized flux densities. It is also consistent with the non-detection of X-ray and radio counterparts. We also show that the overall scheme is consistent with a pre-main-sequence star that exhibits broad Br γ emission.

In principle, the continuum of the DSO/G2 source could be of a non-thermal nature. In that case, it can be fitted with a power-law distribution, like in synchrotron sources. Given the overall compactness of the continuum emission, it could be explained by a young neutron star and its wind nebula similar to the Crab pulsar. Such a pulsar wind nebula is also linearly polarized because of the synchrotron nature of its emission across a broad frequency range.

These results are included in the peer-reviewed paper, which is published in A&A.
Credit: Zajaček et al., A&A 602, A121 (2017). Reproduced with permission ©ESO.

Nature of the Galactic centre NIR-excess sources

I. What can we learn from the continuum observations of the DSO/G2 source?

Michal Zajaček^{1,2,3}, Silke Britzen², Andreas Eckart^{1,2}, Banafsheh Shahzamanian¹, Gerold Busch¹, Vladimír Karas³,
 Marzieh Parsa^{1,2}, Florian Peissker¹, Michal Dovčiak³, Matthias Subroweit¹,
 František Dinnbier^{1,3}, and J. Anton Zensus²

¹ I. Physikalisches Institut der Universität zu Köln, Zùlpicher Strasse 77, 50937 Köln, Germany
 e-mail: zajacek@ph1.uni-koeln.de

² Max-Planck-Institut für Radioastronomie (MPIfR), Auf dem Hügel 69, 53121 Bonn, Germany

³ Astronomical Institute, Academy of Sciences, Boční II 1401, 14131 Prague, Czech Republic

Received 31 January 2017 / Accepted 11 April 2017

ABSTRACT

Context. The Dusty S-cluster Object (DSO/G2) orbiting the supermassive black hole (Sgr A*) in the Galactic centre has been monitored in both near-infrared continuum and line emission. There has been a dispute about the character and the compactness of the object: it being interpreted as either a gas cloud or a dust-enshrouded star. A recent analysis of polarimetry data in K_s -band ($2.2\ \mu\text{m}$) allows us to put further constraints on the geometry of the DSO.

Aims. The purpose of this paper is to constrain the nature and the geometry of the DSO.

Methods. We compared 3D radiative transfer models of the DSO with the near-infrared (NIR) continuum data including polarimetry. In the analysis, we used basic dust continuum radiative transfer theory implemented in the 3D Monte Carlo code *Hyperion*. Moreover, we implemented analytical results of the two-body problem mechanics and the theory of non-thermal processes.

Results. We present a composite model of the DSO – a dust-enshrouded star that consists of a stellar source, dusty, optically thick envelope, bipolar cavities, and a bow shock. This scheme can match the NIR total as well as polarized properties of the observed spectral energy distribution (SED). The SED may be also explained in theory by a young pulsar wind nebula that typically exhibits a large linear polarization degree due to magnetospheric synchrotron emission.

Conclusions. The analysis of NIR polarimetry data combined with the radiative transfer modelling shows that the DSO is a peculiar source of compact nature in the S cluster ($r \lesssim 0.04\ \text{pc}$). It is most probably a young stellar object embedded in a non-spherical dusty envelope, whose components include optically thick dusty envelope, bipolar cavities, and a bow shock. Alternatively, the continuum emission could be of a non-thermal origin due to the presence of a young neutron star and its wind nebula. Although there has been so far no detection of X-ray and radio counterparts of the DSO, the analysis of the neutron star model shows that young, energetic neutron stars similar to the Crab pulsar could in principle be detected in the S cluster with current NIR facilities and they appear as apparent reddened, near-infrared-excess sources. The searches for pulsars in the NIR bands can thus complement standard radio searches, which can put further constraints on the unexplored pulsar population in the Galactic centre. Both thermal and non-thermal models are in accordance with the observed compactness, total as well polarized continuum emission of the DSO.

Key words. black hole physics – Galaxy: center – radiative transfer – polarization – stars: pre-main sequence – stars: neutron

1. Introduction

Since its discovery in 2012 (Gillessen et al. 2012) the near-infrared excess and recombination-line emitting source Dusty S-cluster Object also known as G2 (DSO/G2)¹ has caught a lot of attention because of its highly eccentric orbit around the supermassive black hole associated with the compact radio source Sgr A* at the Galactic centre. It has been intensively monitored, especially close to its pericentre passage in the spring of 2014 (Valencia-S. et al. 2015; Pfuhl et al. 2015), when it passed the black hole at the distance of about 160 AU. No enhanced activity of Sgr A* has been detected so far in the mm (Borkar et al. 2016), radio (Bower et al. 2015), and X-ray

¹ The name G2 first appeared in Burkert et al. (2012) to distinguish the source from the first object of a similar type – G1 (Clénet et al. 2004). The acronym DSO (Dusty S-cluster Object) was introduced by Eckart et al. (2013) to stress the dust emission of the source and the overall NIR excess.

domains (Mossoux et al. 2016); see however Ponti et al. (2015) for the discussion of a possible increase in the bright X-ray flaring rate.

Despite many monitoring programmes and detailed analyses, there has been a dispute about the significance of the detection of tidal stretching of the DSO, which has naturally led to a variety of interpretations. A careful treatment of the background emission by Valencia-S. et al. (2015) revealed the DSO as a compact, single-peak emission-line source at each epoch, both shortly before and after the pericentre passage (see however Pfuhl et al. 2015). Moreover, the DSO was detected as a compact continuum source in near-infrared (NIR) L -band by Witzel et al. (2014), and as a fainter, stable K_s -band source (Eckart et al. 2013; Shahzamanian et al. 2016).

Most of the scenarios that have been proposed so far to explain the DSO and related phenomena may be grouped into the three following categories:

Table 1. Overview of proposed scenarios concerning the nature and the formation of the DSO/G2 and a few corresponding papers.

Scenario	Papers
Star with dusty envelope/disc and outflow	Murray-Clay & Loeb (2012), Eckart et al. (2013), Scoville & Burkert (2013), Ballone et al. (2013) Zajaček et al. (2014), De Colle et al. (2014), Valencia-S. et al. (2015), Ballone et al. (2016), Shahzamanian et al. (2016)
Binary/binary dynamics	Zajaček et al. (2014), Prodan et al. (2015), Witzel et al. (2014), Stephan et al. (2016)
Core-less cloud/streamer	Gillessen et al. (2012), Burkert et al. (2012), Schartmann et al. (2012), Shcherbakov (2014) Pfuhl et al. (2015), Schartmann et al. (2015), McCourt et al. (2015), McCourt & Madigan (2016), Madigan et al. (2017)
Tidal disruption	Miralda-Escudé (2012), Guillochon et al. (2014)
Nova outburst	Meyer & Meyer-Hofmeister (2012)
Planet/protoplanet	Mapelli & Ripamonti (2015), Trani et al. (2016)

- (i) core-less cloud/streamer (Gillessen et al. 2012; Burkert et al. 2012; Schartmann et al. 2012, 2015; Pfuhl et al. 2015).
- (ii) a dust-enshrouded star. (Murray-Clay & Loeb 2012; Eckart et al. 2013; Scoville & Burkert 2013; Ballone et al. 2013, 2016; Zajaček et al. 2014; De Colle et al. 2014; Valencia-S. et al. 2015).
- (iii) binary/binary dynamics (Zajaček et al. 2014; Prodan et al. 2015; Witzel et al. 2014).

The scenarios (i); (ii); (iii), and a few more are summarized in Table 1 with corresponding references.

The apparent variety of studies may be explained by a lack of information about the intrinsic geometry of the DSO, which makes the problem of determining the DSO nature degenerate, which means that more interpretations of the source SED and line emission are plausible. Also, several observational studies denied the detection of K -band ($2.2\ \mu\text{m}$) counterpart of the object (Gillessen et al. 2012; Witzel et al. 2014), which led to very few constraints on the SED, making both scenarios – core-less cloud and dust-enshrouded star – theoretically possible (Eckart et al. 2013). On the other hand, Eckart et al. (2013) and Eckart et al. (2014) show the K -band detection of the DSO in both VLT and Keck data, which together with the overall compactness of the source in both line (Valencia-S. et al. 2015) and continuum emission (Witzel et al. 2014) strengthened the hypothesis of a dust-enshrouded star/binary.

New constraints on the intrinsic geometry of the source has recently been obtained by Shahzamanian et al. (2016) thanks to the detection of polarized continuum emission in NIR K_s band in the polarimetry mode of the NACO imager at the ESO VLT. In Shahzamanian et al. (2016) we also obtained an improved K_s -band identification of the source in median polarimetry images at different epochs 2008–2012 (before the pericentre passage). The main result is that the DSO is an intrinsically polarized source with a significant polarization degree of $\sim 30\%$, which is larger than the typical foreground polarization in the Galactic centre region at the level of $\sim 6\%$, with an alternating polarization angle as the source approaches the position of Sgr A*.

Apart from the DSO, Eckart et al. (2013) and Meyer et al. (2014) showed that the central arcsecond contains several (≤ 10) NIR-excess sources, some of which exhibit Bry emission line in their spectra. We show their approximate positions with respect to B-type S stars in Fig. 1. It is not yet clear whether these sources are related to each other, that is whether they have a common origin. However, they are definitely peculiar sources with respect to the prevailing population of main-sequence B-type S stars (Eckart & Genzel 1996, 1997; Ghez et al. 1998; Gillessen et al. 2009, 2017).

In this paper, we further elaborate on a model of the DSO (see previous models presented in Zajaček et al. 2014, 2016) taking into account the new K_s -band measurements and analysis as presented by Shahzamanian et al. (2016). By comparing

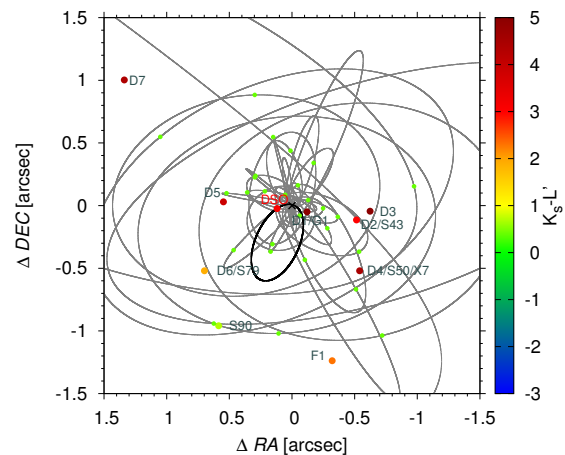


Fig. 1. Positions of S stars and infrared excess sources in the innermost ($3.0'' \times 3.0''$) of the Galactic centre according to Eckart et al. (2013). The colours denote the colour ($K_s - L'$) according to the colour scale to the right. A colour ($K_s - L'$) for ordinary, B-type S stars (e.g. S2 as a prototype) is expected to be ~ 0.4 (with line-of-sight extinction). The position of the DSO and S stars was calculated for 2012.0 epoch according to the orbital solutions in Valencia-S. et al. (2015) and Gillessen et al. (2009), respectively.

theoretical and numerical calculations with the NIR data, we can explain the peculiar characteristics of the DSO by using the model of a young embedded and accreting star surrounded by a non-spherical dusty envelope. This model can be also used for other NIR excess sources, although with a certain caution, since they may be of a different nature. The comparison of different formation scenarios for NIR-excess sources is studied in Zajaček et al. in prep. (hereafter Paper II).

In this study, we focus on the total as well as linearly polarized NIR continuum characteristics of the DSO. We do not include line radiative transfer in the modelling. We refer the reader to Valencia-S. et al. (2015) and Zajaček et al. (2015, 2016), where we studied the basics of the line emission mechanisms potentially responsible for generating broad Bry line. For a pre-main-sequence star, the large line width of the Bry emission line can be explained by the magnetospheric accretion mechanism, where the gas is channelled along the magnetic field lines from the inner parts of a circumstellar accretion disc, reaching nearly free-fall velocities of several $100\ \text{km s}^{-1}$, $v_{\text{infall}} \lesssim \sqrt{2GM_*/R_*}$. The line emission can thus be formed within a very compact region of a few stellar radii and the line luminosity is scaled by the accretion luminosity (Alcalá et al. 2014).

Furthermore, we also investigate whether the SED of the DSO and that of other excess sources could be of a non-thermal rather than a thermal origin by using the model of a PWN.

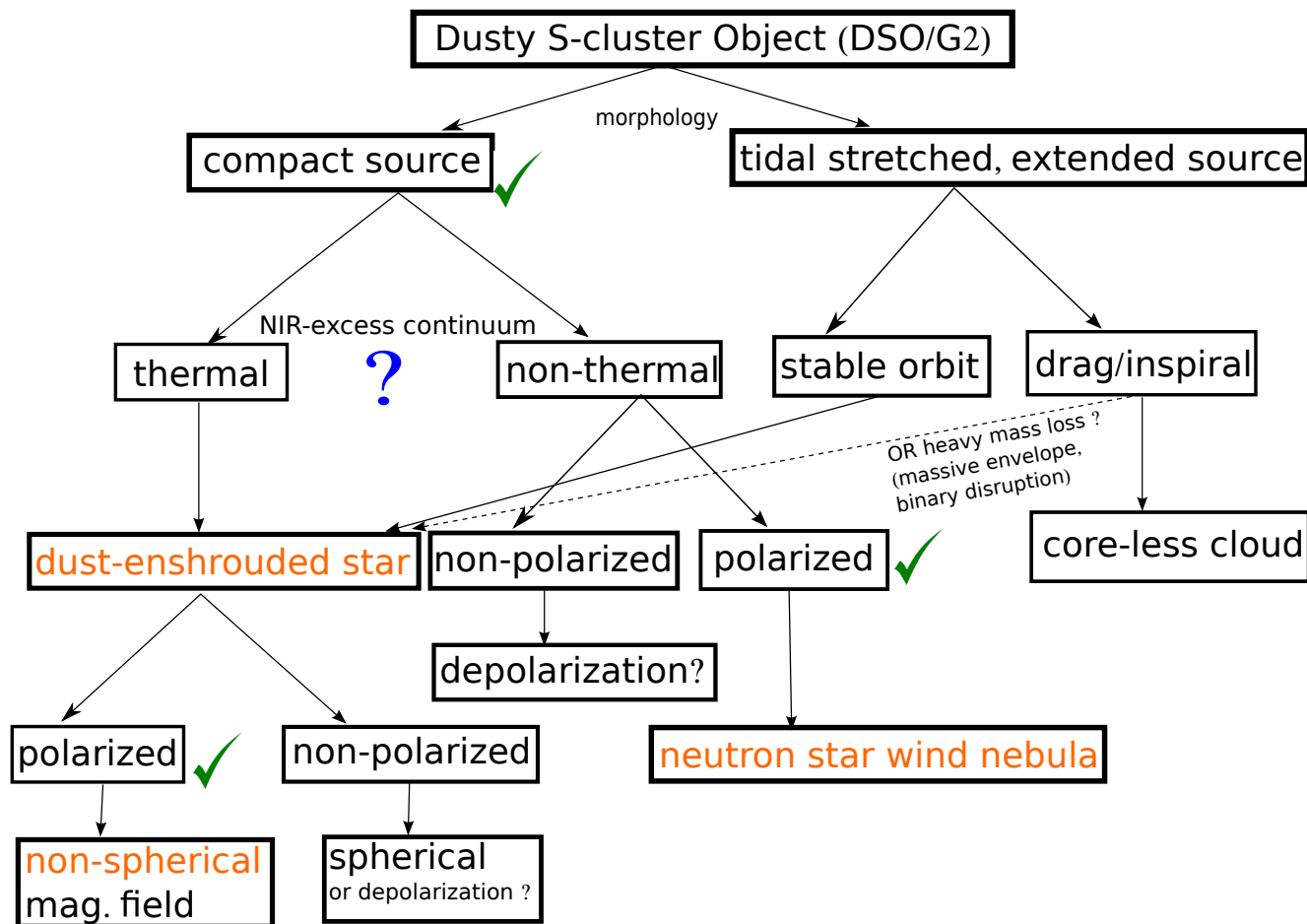


Fig. 2. Roadmap for solving the nature of the DSO/G2 source. The ticks (✓) label the implications of the analysis of observational data by Valencia-S. et al. (2015), Witzel et al. (2014), and Shahzamanian et al. (2016). The question-mark (?) on the left implies that the NIR continuum of the DSO can be either thermal (standard interpretation) or non-thermal. The orange colour marks the possible nature of the DSO that would explain the observed characteristics.

Although the PWN model has a smaller number of parameters and thus a certain elegance in comparison with the model of an embedded star, observationally we miss a clear X-ray or radio counterpart of the DSO, which would be expected for a young neutron star of a few 10^3 yr. On the other hand, our analysis shows that young PWNs resulting from SNII explosions, if present in the nuclear star cluster, could be detected by standard NIR imaging and would indeed manifest themselves as apparent NIR-excess, polarized sources.

The paper is structured as follows. In Sect. 2 we list important observational characteristics of the DSO. Subsequently, in Sect. 3, we briefly analyse the observational as well as theoretical evidence for the compactness of this peculiar source. The results of the modelling and the comparison with observations are presented in Sect. 4, where the main focus is on the pre-main-sequence star embedded in a non-spherical dusty envelope (Sect. 4.1). Moreover, we analyse the possibility that the SED could be of a non-thermal origin, which would open the way for interpreting the DSO as a young PWN (Sect. 4.2). In Sect. 5, we discuss several other characteristics of the DSO, mainly its association with a larger streamer and other dusty sources as well as further aspects of synchrotron, bremsstrahlung, and $\text{Br}\gamma$ luminosity as predicted by a dust-enshrouded star model. Finally, we summarize the main results of the Paper I in Sect. 6.

2. Summary of observational constraints

There are several important constraints that every model of the DSO must explain:

- near-infrared excess or reddening of $K_s - L' > 3$;
- broad emission lines, especially $\text{Br}\gamma$, with the FWHM of the order of 100 km s^{-1} ;
- a stable L' -band as well as K_s -band continuum emission;
- a polarized K_s -band continuum emission of $P_L \approx 30\%$.

Besides (a)–(d) characteristics, one should also consider the overall compactness or the diffuseness of the source (i.e. whether the object can be resolved given the PSF of the instrument used), and the overall orbital evolution (i.e. if one can detect significant drag/inspiral along the orbit as would be expected for a core-less cloud).

Since different aspects are involved, we set up the roadmap towards solving the DSO nature, which is illustrated in Fig. 2. In the further analysis, we consider the results of Valencia-S. et al. (2015) that show that the DSO exhibits a single-peak $\text{Br}\gamma$ emission line at each epoch, in other words they detect no significant stretching along the orbit as would be expected for a core-less cloud. A consistent result is presented by Witzel et al. (2014),

Table 2. Summary of NIR flux densities of the DSO.

Band	Wavelength [μm]	Frequency [Hz]	Flux density [mJy]	Refs.
<i>H</i>	1.65	1.82×10^{14}	$\lesssim 0.17$	1
<i>K_s</i>	2.2	1.36×10^{14}	0.23 ± 0.02	2
<i>L'</i>	3.8	7.89×10^{13}	1.2 ± 0.3	3
<i>M</i>	4.7	6.38×10^{13}	1.2 ± 0.4	4

References. (1) Eckart et al. (2013); (2) Eckart et al. (2013), Shahzamanian et al. (2016); (3) Gillessen et al. (2012), Eckart et al. (2013), Witzel et al. (2014); (4) Gillessen et al. (2012).

Table 3. Summary of observational constraints for the DSO nature.

Constraint	Note
SED	“red” source; $K_s - L' > 3$
broad emission lines	$FWHM_{\text{Br}\gamma} \sim 100 \text{ km s}^{-1}$
source of polarized <i>K_s</i> band emission	polarization degree $\sim 30\%$
stability and compactness	no significant tidal elongation

who detect a compact *L*-band emission of the DSO/G2 during the peribothron² passage in 2014.

Therefore, we are not going to consider the tidal stretching, which according to the roadmap in Fig. 2 would either indicate an extended circumstellar envelope that does not feel the gravitational field of the star, or a core-less cloud. These two scenarios will be further tested by the orbital evolution in the post-peribothron phase.

Concerning the spectral energy distribution of the DSO, we adopt the results of Gillessen et al. (2012), Eckart et al. (2013), and Shahzamanian et al. (2016); see also Shcherbakov (2014) for the first SED analysis of the DSO assuming a core-less cloud scenario. As analysed by Eckart et al. (2013) and confirmed by Shahzamanian et al. (2016), the source shows prominent reddening between NIR *K_s* and *L'* bands, $K_s - L' > 3$. Further measurements in *M* band were performed by Gillessen et al. (2012). The *H*-band flux density is an upper limit since there was no detection (Gillessen et al. 2012; Eckart et al. 2013).

In the NIR *H* band, Eckart et al. (2013) derive the minimum apparent magnitude of $m_H > 21.2$ based on the background level of the neighbouring stars. Using the extinction correction of $A_H = 4.21$, the upper limit on the flux density is $F_H \lesssim 0.17 \text{ mJy}$.

For the flux density in NIR *K_s*-band, we take a weighed mean of the measurements by Shahzamanian et al. (2016) (see our Table 3 for the summary of measurements). We obtain the mean flux density value of $\bar{F}_{2.2} = (0.23 \pm 0.02) \text{ mJy}$, both with and without considering the epoch 2011, when the ratio S/N was low.

For the *L'*-band magnitude, we consider the value of $m_{L'} = 14.4 \pm 0.3$ (Eckart et al. 2013). Using $A_{L'} = 1.09$, we obtain the flux density of $F_{3.8} = (1.2 \pm 0.3) \text{ mJy}$.

The absolute dereddened *M*-band magnitude obtained by Gillessen et al. (2012) is $M_M = -1.8 \pm 0.3$, which yields $F_{4.7} = (1.2 \pm 0.4) \text{ mJy}$. All of the inferred flux densities are summarized in Table 2. Based on the flux density measurements, the upper limit on the overall luminosity was set to $L_{\text{DSO}} < 30 L_\odot$ (Eckart et al. 2013; Witzel et al. 2014).

Another important constraint is the detection of polarized emission in NIR *K_s* band by Shahzamanian et al. (2016) with

² We use pericentre and peribothron interchangeably; peribothron is derived from Greek bothros, which means a hole dug in the ground, also a pit used for drink offerings for subterranean gods in the Greek mythology.

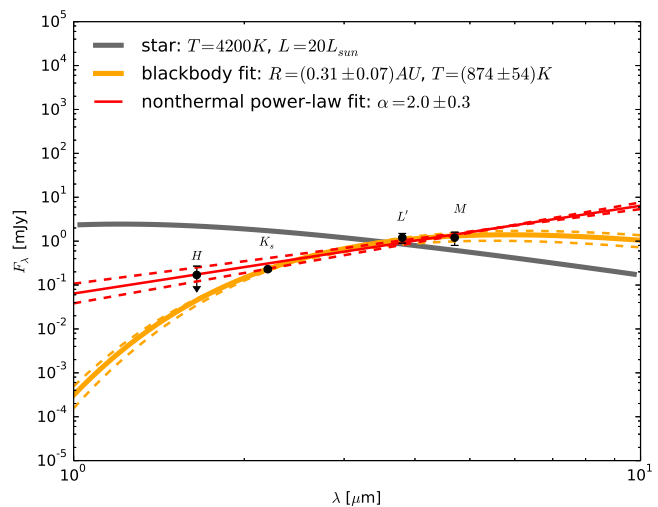


Fig. 3. Detected, dereddened flux densities of the DSO (black points) and the fitted continuum: thermal black-body fit curve corresponding to warm dust (orange solid and dashed lines) and non-thermal power-law emission fit $S_\nu \propto \nu^{-\alpha}$ with the index $\alpha = 2.0 \pm 0.3$ (red solid and dashed lines). For comparison, we also plot the black-body curve corresponding to the star of $T_\star = 4200 \text{ K}$ and $L_\star = 20 L_\odot$ (pre-main-sequence star without a dusty envelope; grey solid line).

the polarization degree of $\sim 30\%$ and a variable polarization angle for four consecutive epochs (2008, 2009, 2011, and 2012). The summary of all observational constraints is in Table 3.

The dereddened, continuum flux densities in the NIR domain were attributed to the warm dust emission in the temperature interval $T_{\text{dust}} = 400\text{--}600 \text{ K}$ (Gillessen et al. 2012; Eckart et al. 2013), which can reproduce the flux densities between *K_s* and *M* bands. In Fig. 3, we repeat the fit of the dereddened flux densities with a single-temperature black-body flux density profile $S_\nu(T, R) = (R/d)^2 \pi B_\nu(T)$, where $B_\nu(T)$ is a black-body specific intensity at temperature T , R is the characteristic radius of the object, and d is the distance to the Galactic centre, which we set to $d = 8 \text{ kpc}$ (Eckart et al. 2005, 2017; Genzel et al. 2010). The black-body fits gives the temperature of $T = (874 \pm 54) \text{ K}$, which corresponds to the warm dust component, and the characteristic radius of $R = (0.31 \pm 0.07) \text{ AU}$ for an optically thick black body. This corresponds to a rather compact source in comparison with the originally proposed mean length-scale of $R_c \approx 15 \text{ mas} \approx 120 \text{ AU}$ for a core-less gas cloud (Gillessen et al. 2012), in which case the emission would necessarily be optically thin. For comparison, we also plot the black-body curve corresponding to the star of $T_\star = 4200 \text{ K}$ and $L_\star = 20 L_\odot$ (without any circumstellar envelope), which naturally has a reversed slope than that of the DSO continuum (see Fig. 3).

On the other hand, an alternative model for the origin of the SED with increasing flux values towards longer wavelengths (smaller frequencies) is a nonthermal power law, $S_\nu = S_0(\nu/\nu_0)^{-\alpha}$. A naive fit of the power law model to the detected flux densities yields the profile,

$$S_\nu \approx 2.0 \left(\frac{\nu}{5.37 \times 10^{13} \text{ Hz}} \right)^{-2.0 \pm 0.3} \text{ mJy}, \quad (1)$$

with partial power-law slopes $\alpha_{ij} = -\log(S_{\nu_i}/S_{\nu_j})/\log(\nu_i/\nu_j)$ between bands i and j : $\alpha_{HK} \gtrsim 1.05$, $\alpha_{KL} = 3.02$, and $\alpha_{LM} \approx 0$. The qualitative behaviour of the continuum radiation of the DSO

M. Zajaček et al.: Galactic centre NIR-excess sources. Continuum of the DSO/G2

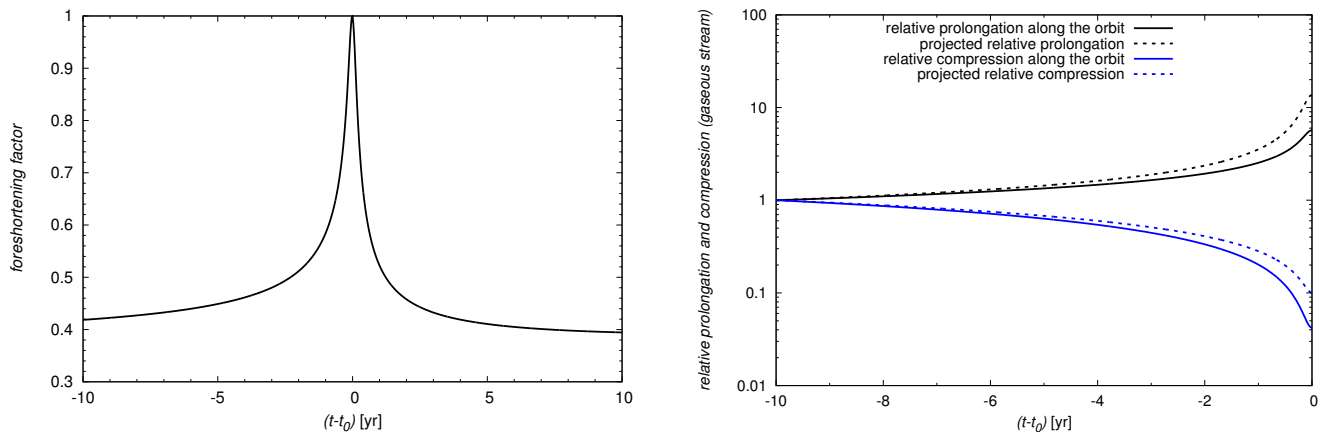


Fig. 4. *Left:* foreshortening factor for the size of any structure calculated for the DSO orbit with inclination $i = 113^\circ$. *Right:* relative tidal stretching and compression as function of time (in years with respect to the peribothron passage) in the orbital plane (solid lines) and with respect to the inclined orbit to the DSO (dashed lines).

is similar to the SED of few young pulsars detected in NIR domains (Mignani et al. 2012; Zharikov et al. 2013; Zyuzin et al. 2016) that are dominated by magnetospheric synchrotron radiation. Moreover, they exhibit a significant linear polarized emission with the polarization degree of a few 10% (Zajczyk et al. 2012). Thus, DSO-like sources could in principle be neutron stars and the detection of significant linearly polarized emission strengthens this hypothesis. The crucial point for the confirmation of this association is the detection of the counterparts in different domains, specifically radio and X-ray domains.

3. On the compactness of the DSO

In the literature, it is still debated whether the DSO/G2 source is of compact nature or not. In the further analysis we assume that the DSO has a compact nature, that is the source is not significantly stretched and elongated by tidal forces of the SMBH. This conclusion is based on the fact that both the line emission (Br γ) and the L' -band continuum emission did not show signs of tidal interaction during the closest passage (Valencia-S. et al. 2015; Witzel et al. 2014); see however Pfuhl et al. (2015) for a different view. In addition, K_s -band flux density was constant within uncertainties for four consecutive epochs (2008, 2009, 2011, and 2012, Shahzamanian et al. 2016). Since the DSO appears as a point-like source, it is only possible to infer an upper limit for its length-scale based on the minimum FWHM of the point spread function, $\theta_{\min} \approx 63(\lambda/2 \mu\text{m})$ mas.

A simple test of the compactness of the DSO is provided by the comparison of the observed evolution with that of a core-less gaseous stream approaching the black hole of $M_\bullet = 4 \times 10^6 M_\odot$. When the parts of the cloud move independently in the potential of the black hole, the cloud with initial radius R_{init} is stretched along the orbit and compressed in the perpendicular direction.

According to Shcherbakov (2014), we can express the relative prolongation as function of distance r from the SMBH in terms of the half-length L ,

$$\Lambda = \frac{L}{R_{\text{init}}} = \left(\frac{r_{\text{init}}}{r}\right)^{1/2} \left(\frac{r_A + r_P - r}{r_A + r_P - r_{\text{init}}}\right)^{1/2}, \quad (2)$$

where r_{init} is the initial distance at which the cloud was formed, having a spherical shape with the radius R_{init} , and r_P and r_A are pericentre and apocentre distances of the DSO, respectively. We

set r_{init} to the distance that corresponds to 10 yr before the peribothron passage (earlier date of formation would lead to larger prolongation). Similarly, the relative compression ρ in the direction perpendicular to the orbit may be expressed as,

$$\rho = H/R_{\text{init}} = \frac{r}{r_{\text{init}}}, \quad (3)$$

where H is the actual perpendicular cross-section of the cloud. For the orbital parameters of the DSO (Valencia-S. et al. 2015), both the relative prolongation $\Lambda(t)$ and compression $\rho(t)$ are plotted in Fig. 4 (right panel) as functions of time before the peribothron passage. For the observed dimensions of the object, the foreshortening due to the orbital inclination is important. The foreshortening factor as function of time is plotted in Fig. 4 (left panel). At the peribothron, the source should be viewed at full size and the relative prolongation is ~ 6 times that of the initial size (~ 10 times when foreshortening is taken into account). The compression in the perpendicular direction should lead to the general spaghettification of the cloud. The tidal elongation of this order was, however, not detected (Witzel et al. 2014; Valencia-S. et al. 2015).

Specifically, between the epoch 2011.39 (3 yr before the peribothron) and the peribothron passage, the prolongation factor is $\Lambda \approx 3.45$. If the DSO was a core-less cloud, it should have a pericentre length-scale $L_{\text{per}} = \Lambda R_{\text{init}}$. Gillessen et al. (2013b) infer the FWHM length-scale $R_{\text{FWHM}} = (42 \pm 10)$ mas from the Gaussian fit for epochs 2008.0, 2010.0, 2011.0, 2012.0, 2013.0. The pericentre size, with respect to 2011 epoch, should then be $L_{\text{per}} \approx 145$ mas $> \theta_{\min}$, which is more than a factor of two larger than PSF FWHM. Such a large size is inconsistent with a rather compact line emission detected by Valencia-S. et al. (2015) during the pericentre passage. In fact, the analysis of the L -band continuum emission of the DSO during the pericentre passage by Witzel et al. (2014) yields the diameter of 32 mas, which is fully consistent with the DSO being a point source.

On the other hand, since the DSO was detected as a point source at the pericentre, the upper limit on its length-scale is given by the diffraction limit $L_{\text{per}} \leq \theta_{\min} \approx 63$ mas. A core-less cloud or an extended envelope of a star that reached the size of L_{per} by tidal stretching must have been smaller by a factor of $\Lambda(-10 \text{ yr}) \approx 6$, that is 10 yr before the peribothron passage, yielding the characteristic size of $L(-10 \text{ yr}) \lesssim 10 \text{ mas} \approx 80 \text{ AU}$.

Based on this estimate, we set the characteristic radius of the potentially tidally perturbed part of the DSO to $R_c \lesssim 5$ mas.

Using the observationally inferred Bry luminosity of $L_{\text{Bry}} \approx 2 \times 10^{-3} L_\odot$ (Gillessen et al. 2012; Valencia-S. et al. 2015), we can estimate the electron density in the envelope assuming case B recombination (Gillessen et al. 2012),

$$n_e = 1.35 \times 10^6 f_V^{-1/2} \left(\frac{R_c}{5 \text{ mas}} \right)^{-3/2} \left(\frac{T_g}{10^4 \text{ K}} \right)^{0.54} \text{ cm}^{-3}, \quad (4)$$

where T_g is the expected gas temperature of the DSO and f_V is the volume filling factor, which we set to $f_V \leq 1$. For the mass of the DSO, in case it would be a gas cloud, we get

$$M_{\text{DSO,cloud}} \approx 2.2 \times 10^{27} f_V^{1/2} \left(\frac{R_c}{5 \text{ mas}} \right)^{3/2} \left(\frac{T_g}{10^4 \text{ K}} \right)^{0.54} \text{ g}, \quad (5)$$

which is about $M_{\text{DSO,cloud}} = 0.4 f_V^{1/2} M_{\text{Earth}}$. A smaller mass and a required higher density than originally estimated (Gillessen et al. 2012) shorten typical hydrodynamical time-scales that determine the lifetime of the cloud, specifically the cloud evaporation time-scale is (Burkert et al. 2012)

$$\tau_{\text{evap}} = 43 \left(\frac{r}{5.4 \times 10^{16}} \right)^{1/6} \left(\frac{M_{\text{DSO,cloud}}}{2.2 \times 10^{27} \text{ g}} \right)^{1/3} \text{ yr}, \quad (6)$$

where r is the distance from Sgr A* in units of 5.4×10^{16} cm, which corresponds approx. to the epoch of 2004. Such a short evaporation time-scale for a small, cold clump in the hot ambient plasma would necessarily lead to observable changes in the cloud line and continuum luminosities. However, the observations imply that the DSO is a rather compact, stable source in both line and continuum emission (Witzel et al. 2014; Valencia-S. et al. 2015; Shahzamanian et al. 2016).

Although a magnetically arrested cloud was suggested to explain the apparent stability (Shcherbakov 2014), it would still not prevent the cloud from the progressive evaporation and disruption (McCourt et al. 2015) as well as the loss of angular momentum when interacting with the ambient medium, leading to the inspiral and deviation from the original ellipse (Pfuhl et al. 2015; McCourt et al. 2015). Therefore, given the reasons above, a stellar nature of the DSO is more consistent with its observed line and continuum characteristics.

The basic estimate of the distance r_t where an object with a characteristic radius R_{DSO} and mass M_{DSO} is tidally disrupted is given by $r_t = R_{\text{DSO}}(3M_\star/M_{\text{DSO}})^{1/3}$. For a stellar source, we get an estimate $r_t \approx 1.07(R_{\text{DSO}}/1 R_\odot)(M_{\text{DSO}}/1 M_\odot)^{-1/3}$ AU. Since the peribothron distance of the DSO is $r_p = a(1 - e) = 0.033 \text{ pc} \times (1 - 0.976) \approx 163 \text{ AU}$ (Valencia-S. et al. 2015) and no visible tidal interaction was observed, the upper limit on the length-scale of the stellar system that stays stable is $R_{\text{DSO}} \approx 0.7 (M_{\text{DSO}}/1 M_\odot)^{1/3}$ AU. On the other hand, for the cloud of $R_{\text{DSO}} = 15 \text{ mas} \approx 2.7 \times 10^4 R_\odot$ and the mass of three Earth mass, $M_{\text{DSO}} \approx 10^{-5} M_\odot$ (Gillessen et al. 2012), the tidal radius is $r_t \approx 1.3 \times 10^6 \text{ AU}$. Hence, the cloud should be strongly perturbed not only at the pericentre, but during the whole phase of infall, since the apocentre distance is $r_A = a(1 + e) \approx 1.3 \times 10^4 \text{ AU}$. In summary, to explain the compact behaviour of the object, the emitting material (gas+dust) should be located in the inner astronomical unit from the star.

On the other hand, since the NIR-continuum is dominated by thermal dust emission (for a dust-enshrouded star), one can estimate the lower distance limit where the dust is located from the

dust sublimation radius r_{sub} (Monnier & Millan-Gabet 2002),

$$r_{\text{sub}} = 1.1 \sqrt{Q_R} \left(\frac{L_{\text{DSO}}}{1000 L_\odot} \right)^{1/2} \left(\frac{T_{\text{sub}}}{1500 \text{ K}} \right)^{-2} \text{ AU}, \quad (7)$$

where Q_R is the ratio of absorption efficiencies, which we consider to be of the order of unity, and T_{sub} is the dust sublimation temperature, for which we take 1500 K. The inferred luminosity of the DSO is of the order of $L_{\text{DSO}} \approx 10 L_\odot$ (Eckart et al. 2013; Witzel et al. 2014), and so the expected sublimation radius is $r_{\text{sub}} \approx 0.1 \text{ AU}$. Hence, since the continuum emission seems to be compact and no clear evidence of tidal interaction was detected during the peribothron passage (Witzel et al. 2014), the distance range, where the dust emitting the NIR-continuum is located and stays gravitationally unperturbed, is quite narrow, $r_{\text{sub}} \lesssim r \lesssim r_t$, that is $0.1 \text{ AU} \lesssim r \lesssim 1 \text{ AU}$.

4. Modelling the total and polarized continuum emission of the DSO

In this section, we focus on the modelling of the total as well as polarized flux density in corresponding NIR bands. The main aim is the continuum radiative transfer in the dense dusty envelope surrounding a star with the emphasis on the linearly polarized emission (Sect. 4.1). The continuum profile is shaped by reprocessing the stellar emission by the surrounding dusty envelope. Linear polarization may arise due to (i) photon scattering on spherical dust grains (Mie scattering); (ii) dichroic extinction caused by selective absorption of photons in the medium where non-spherical grains are aligned due to radiation or magnetic field. The overall linear polarization degree for young stars may vary from the fraction of a percent up to a few 10%, depending on the geometry as well as the extinction of the dusty envelope (see Kolokolova et al. 2015, for a review).

In case of a hypothetical non-thermal origin of the DSO continuum (Sect. 4.2, one expects a slope of the flux density $S_\nu \propto \nu^{-n}$, where $n > 0$. Typically, young neutron stars exhibit a multiwavelength non-thermal continuum, which arises due to the synchrotron process in the magnetosphere of young neutron stars. Another contribution is the thermal emission of the cooling surface. However, for young ($\lesssim 10$ kyr) and middle-aged ($\gtrsim 100$ kyr) neutron stars, the non-thermal component dominates in NIR bands. Since neutron stars typically possess a highly-ordered strong magnetic field, the non-thermal component is expected to be partially linearly polarized. Using the homogeneous magnetic field approximation, the linear polarization degree for the synchrotron emission can be determined as (Rybicki & Lightman 1979),

$$P_L \lesssim \frac{n+1}{n+5/3}, \quad (8)$$

where for $n \approx 0.7$ one gets $P_L \lesssim 0.72$, whereas the measured value in K_s band (VLT/ISAAC) is $P_L^{\text{avg}} \approx 0.47$ (Zajczyk et al. 2012) for the surrounding PWN.

4.1. Thermal origin of the SED: DSO as a dust-enshrouded star

To find the model of a dust-enshrouded star that reproduces the observed characteristics (SED, broad emission lines, linear polarization, and overall stability and compactness; see also Table 3 for the summary) we perform a set of 3D dust continuum radiative transfer simulations with different components and morphologies of dusty envelopes. For solving the radiative transfer

equation, we choose a Monte Carlo technique suitable for arbitrary three-dimensional dusty envelopes (Whitney 2011). For all our simulations of a dust-enshrouded star, we used an open-source parallelized code *Hyperion* (Robitaille 2011), which enables to create SEDs as well as images for a required wavelength range as well as different inclinations of the source. Since in the random walk of photons the scattering process is also included, we obtain a full Stokes vector (I, Q, U, V) , which enables us to calculate the linear polarization degree as well as the angle according to standard definitions,

$$P_L = \frac{\sqrt{Q^2 + U^2}}{I},$$

$$\phi = \frac{1}{2} \arctan\left(\frac{U}{Q}\right). \quad (9)$$

Since the extinction is expected to be high in the innermost parts of the envelope, we make use of a modified random walk (MRW) implemented in the code in the thickest regions.

An important part of the modelling is the generation of the dust distribution, for which we use the code *bhmie* by C.F. Bohren and D. Huffman (improved by B. Draine; Bohren et al. 1998), which provides solutions to the Mie scattering and absorption of light by spherical dust particles. We generate dust grains with a power-law distribution $n(a) \propto a^{-3.5}$ with the smallest and the largest grain size of $(a_{\min}, a_{\max}) = (0.01, 10.0) \mu\text{m}$. The gas-to-dust mass ratio in the dusty circumstellar envelope for all geometries is assumed to be 100. The distance to the Galactic centre is set to 8 kpc for flux density calculations.

For most of the simulations, we set up a 3D spherical grid that contains $400 \times 200 \times 10$ grid points, and add a density grid of gaseous-dusty mixture with the dust properties as explained above. For all synthetic SEDs and images, the total flux density was determined via the integration over the whole source and then compared to observationally determined values in Table 2.

4.1.1. Different morphologies: source components

At first, we performed radiative transfer calculations for different geometries of circumstellar envelopes to assess whether they can reproduce the detected high polarization degree in K_s -band and the NIR-excess. First, we started with the simplest models with a star at the centre and flattened envelope and/or bow shock. For all these cases, the polarization degree remains below 10%. Breaking the spherical symmetry by introducing the cavities, having half-opening angle of 45° , increases the polarization degree to $\sim 10\%$ (without a bow shock layer). Adding a dense bow shock layer, the linear polarization fraction typically reaches $>20\%$, depending on the density of the envelope and the inclination. Qualitatively, the dependence of the linear polarization degree on the envelope geometry is sketched in Fig. 9.

The density grid in the radiative transfer models has different morphological and density components, whose characteristics are explained below:

- *Star*: based on the upper luminosity limit of $L_{\text{DSO}} \lesssim 30 L_\odot$ (Eckart et al. 2013; Witzel et al. 2014), the central star of the DSO should belong to the category of pre-main-sequence stars with the mass constraint $M_\star \lesssim 3 M_\odot$ (Zajaček et al. 2015). Given the NIR-excess, that is the rising SED longward of 2 microns, it should belong to the category of class I objects – protostars (Lada 1987)³ with an age of 10^5 yr up

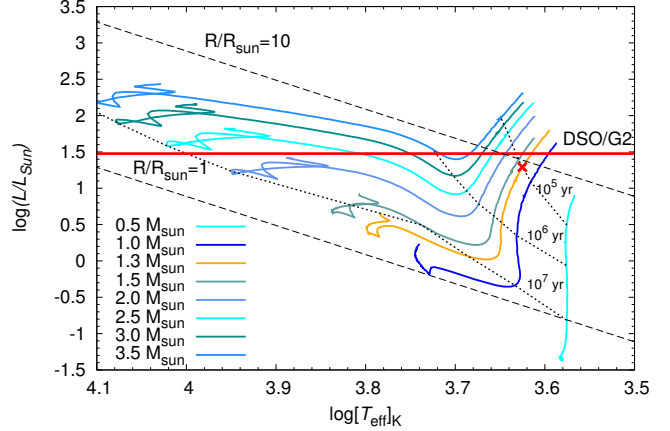


Fig. 5. A set of the evolutionary tracks of pre-main-sequence stars based on Siess et al. (2000). The red line marks the upper limit for the bolometric luminosity of the DSO, $L_{\text{DSO}} \lesssim 30 L_\odot$. The orange solid line depicts the mass of $1.3 M_\odot$, which we used for choosing the input parameters for radiative transfer calculations (red point).

to 10^6 yr. The comparison of stellar evolutionary tracks for different masses is in Fig. 5 for the metallicity fraction of $Z = 0.02$, which was constructed based on the computed tables by Siess et al. (2000). In the set of Monte Carlo simulations, we vary the luminosity and the temperature of stars to fit the observed flux density values and we get reasonable match for $M_\star = 1.3 M_\odot$, $L_\star = 19.6 L_\odot$ and $T_{\text{eff}} = 4220$ K – labelled as the red cross in Fig. 5. These stellar parameters were used in all the simulations presented in this paper, unless indicated otherwise.

- *Flattened envelope*: to the first approximation, the dust-enshrouded star may be modelled as a star surrounded by a rotationally flattened, infalling dusty envelope that forms a disc at the corotation radius r_c . The density profile is given by (Ulrich 1976),

$$\rho(r, \theta) = \frac{\dot{M}_{\text{acc}}}{4\pi(GM_{\text{DSO}}r_c^3)^{1/2}} \left(\frac{r}{r_c}\right)^{-3/2} \left(1 + \frac{\mu}{\mu_0}\right)^{-1/2} \times \left(\frac{\mu}{\mu_0} + \frac{2\mu_0^2 r_c}{r}\right)^{-1}, \quad (10)$$

where \dot{M}_{acc} is the infall rate. The quantities μ and μ_0 are related by an equation of the streamline, $\mu_0^3 + \mu_0(r/r_c - 1) - \mu(r/r_c) = 0$.

The model of Ulrich envelope can match the SED of the DSO for stellar parameters $M_\star = 1.3 M_\odot$, $L_\star = 4.3 L_\odot$, $T_{\text{eff}} = 4400$ K, $R_\star = 3.3 R_\odot$ (age $\sim 760\,000$ yr). The suitable parameters of the envelope are $\dot{M}_{\text{acc}} = 5 \times 10^{-7} M_\odot \text{yr}^{-1}$, $r_{\min} = 10 R_\star$, and $r_c = 20 R_\star$, where r_{\min} is the minimal distance of the envelope from the star. We vary the maximum distance of the envelope r_{\max} from 0.5 AU up to 50 AU, which affects the SED due to a different dust temperature distribution. For the SEDs of the flattened envelope at different inclinations ($0^\circ, 30^\circ, 60^\circ, 90^\circ$) and three different maximum radii $r_{\max} = [0.5, 5, 50]$ AU, see Fig. 6. Because of observational uncertainties, more suitable configurations are possible, for example $r_{\max} = 5$ AU and the inclination of 90° or $r_{\max} = 50$ AU and the inclination in the range of

³ The Lada-Wilking morphological classification of young stellar objects based on the spectral slope of their SEDs, $\alpha =$

$d \log(\lambda F_\lambda) / d \log(\lambda)$: class I sources ($0 < \alpha \leq 3$), class II sources ($-2 \leq \alpha \leq 0$), and class III sources ($-3 < \alpha \leq -2$).

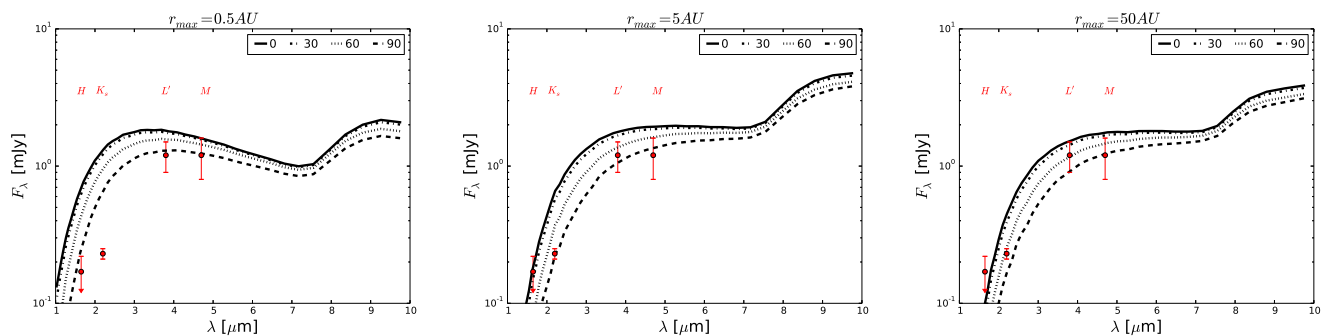


Fig. 6. Model SEDs of a star surrounded by rotationally flattened envelope for different inclinations in the range (0° , 90°) with an increment of 30° , see the key for different linestyles representing different inclinations. The points with error bars correspond to observationally inferred values, see Table 2. *Left panel:* maximum radius of the envelope is set to $r_{\max} = 0.5$ AU. *Middle panel:* $r_{\max} = 5$ AU. *Right panel:* $r_{\max} = 50$ AU.

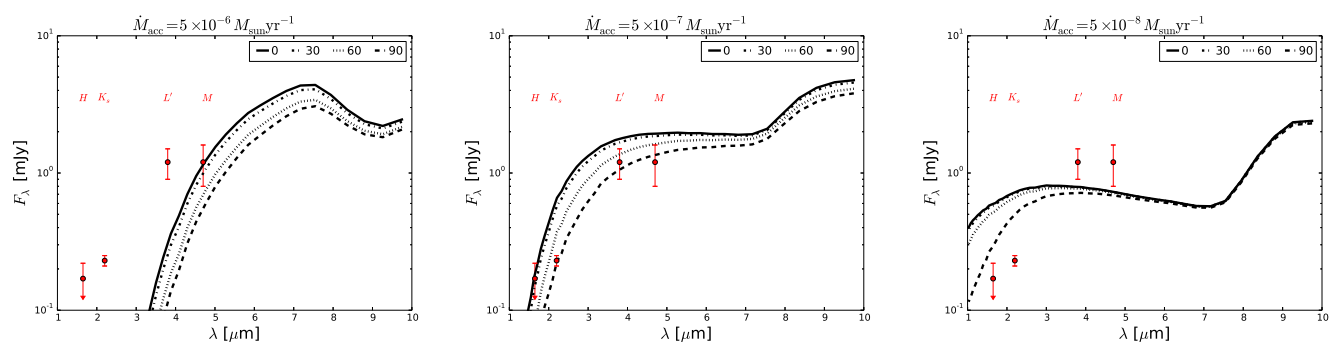


Fig. 7. Model SEDs of a star surrounded by rotationally flattened envelope with the fixed maximum radius of $r_{\max} = 5$ AU for different inclinations in the range (0° , 90°) with an increment of 30° , see the key for different linestyles representing different inclinations. The points with error bars correspond to observationally inferred values, see Table 2. *Left panel:* accretion rate is set to $\dot{M}_{\text{acc}} = 5 \times 10^{-6} M_\odot \text{yr}^{-1}$. *Middle panel:* $\dot{M}_{\text{acc}} = 5 \times 10^{-7} M_\odot \text{yr}^{-1}$. *Right panel:* $\dot{M}_{\text{acc}} = 5 \times 10^{-8} M_\odot \text{yr}^{-1}$.

$i = (60^\circ, 90^\circ)$. The lower value of $r_{\max} = 0.5$ AU is not suitable because of the large flux in K_s band, which can be explained by a lower extinction and a more prominent stellar emission. In the range $r_{\max} = (5, 50)$ AU, the SED does not depend much on this parameter because of the decreasing gas and dust density according to Eq. (10). On the other hand, the SED depends strongly on the accretion rate \dot{M}_{acc} . We vary the accretion rate between $\dot{M}_{\text{acc}} = (5 \times 10^{-6}, 5 \times 10^{-8}) M_\odot \text{yr}^{-1}$ for the fixed maximum radius of $r_{\max} = 5$ AU, see Fig. 7. Clearly, the best match of SED values is for an intermediate value of $\dot{M}_{\text{acc}} = 5 \times 10^{-7} M_\odot \text{yr}^{-1}$ (middle panel), increasing or decreasing the accretion rate by an order of magnitude significantly changes calculated fluxes, which is caused by large changes in the dust density, $\rho \propto \dot{M}_{\text{acc}}$, see Eq. (10). Although a star surrounded by a flattened envelope can satisfactorily explain the SED of the DSO, the calculated polarized emission in K_s band from radiative transfer models yields the maximum total polarization degree of $\bar{p}_{K_s, L} = 2.7\%$ for $i = 90^\circ$, which is well below the detected value of $\sim 30\%$ (Shahzamanian et al. 2016). This implies that the simple geometry of the flattened envelope cannot alone explain the properties of the DSO.

– *Spherically concentrated dusty envelope/flared disc:* for more complex models, we set up a stratified spherical dusty envelope that was intersected by bipolar cavities in some models with smaller number densities (see below). In the final set of models, the spectral slope could be reproduced by the following mean mass densities of the gas+dust mixture: $1 \times 10^{-13} \text{ g cm}^{-3}$ for $r = 0.1\text{--}1.0$ AU, $1 \times 10^{-14} \text{ g cm}^{-3}$ for $r = 1.0\text{--}2.0$ AU, and $1 \times 10^{-15} \text{ g cm}^{-3}$ for $r = 2.0\text{--}3.0$ AU.

– *Bipolar cavity:* the bipolar cavities were introduced in the model to increase the non-spherical nature of the DSO, which is naturally needed to obtain a non-zero total polarization degree in the model, see Fig. 9. Furthermore, the walls of cavities also provide effective space for single scattering events of stellar and dust photons that escape from the star and the envelope, respectively. The density inside cavities is set to be uniform and smaller than in the envelope by several orders of magnitude: $1 \times 10^{-20} \text{ g cm}^{-3}$, which is a typical order of magnitude (see e.g. Sanchez-Bermudez et al. 2016). The half-opening angle of the cavity is initially varied to investigate the impact of the parameter space on the SED and the polarization, then set to $\theta_0 = 45^\circ$.

– *Bow shock:* the DSO and other objects in the S-cluster are expected to move supersonically through the ambient medium, especially close to the pericentre of their orbits (see Fig. 1 in Zajaček et al. 2016), see also De Colle et al. (2014), Ballone et al. (2013, 2016), Christie et al. (2016). The expected Mach number of the DSO is $M = v_{\text{rel}}/c_s \lesssim 10$ (Zajaček et al. 2016), where v_{rel} is the relative velocity of the DSO with respect to the medium and c_s is the local sound speed. This necessarily leads to the formation of the bow shock layer whose densest part lies ahead of the star close to the stagnation point. It was shown that the bow shock of the DSO can contribute to the continuum as well as line emission of the source (Scoville & Burkert 2013). The contribution of the bow-shock NIR continuum emission depends on the dust content and dust size distribution in the bow shock layer, which by itself is not a trivial hydrodynamical problem (van Marle et al. 2011). However, the existence of a bow

M. Zajaček et al.: Galactic centre NIR-excess sources. Continuum of the DSO/G2

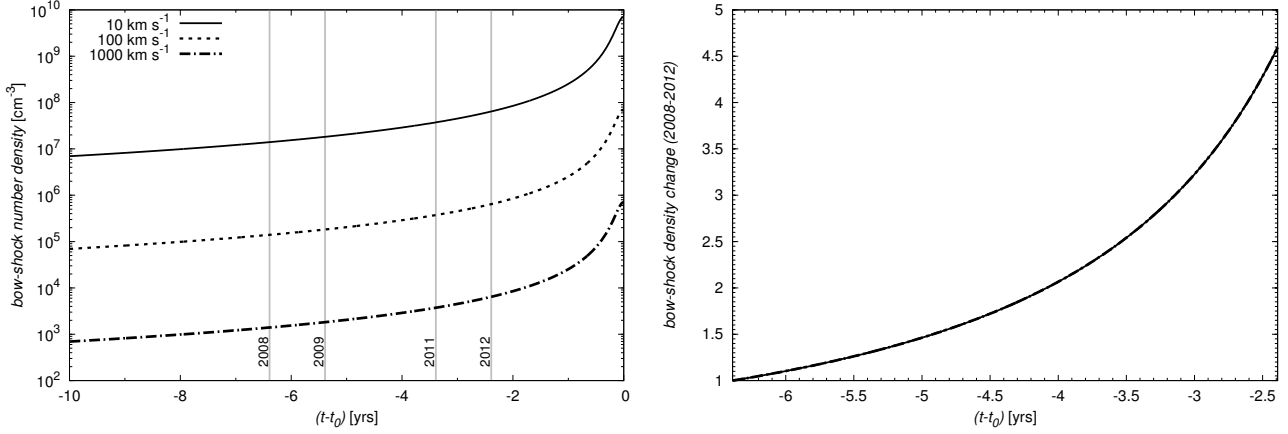


Fig. 8. *Left:* the number density of the shocked layer for different wind velocities (see the key) and the stellar mass-loss rate of $\dot{m}_w = 10^{-8} M_\odot \text{ yr}^{-1}$. *Right:* the relative change in the bow-shock density between the epochs 2008–2012.

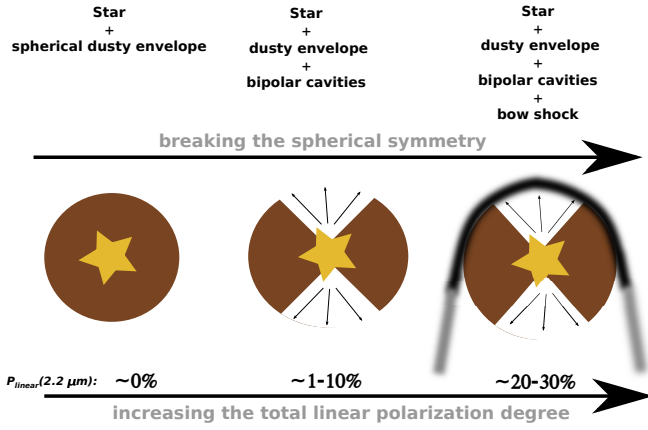


Fig. 9. Sketch of how the geometry of circumstellar envelope affects the total linear polarization degree in K_s band.

shock would further increase the overall asymmetry of the source and hence make the total linear polarization degree larger, see Fig. 9.

For modelling the stellar bow shock associated with the supersonic motion of the DSO, we apply the analytical model of Wilkin (1996) for the shape of the axisymmetric layer,

$$R(\theta) = R_0 \csc \theta \sqrt{3(1 - \theta \cot \theta)}, \quad (11)$$

where θ is a polar angle from the axis of symmetry as seen from the star that lies at the coordinate origin. The standoff distance R_0 depends on two intrinsic stellar parameters – the mass-loss rate \dot{m}_w and the terminal wind velocity v_w – as well as the density profile of the ambient medium $\rho_a(r)$ and the relative velocity of the star with respect to the ambient medium v_{rel} . The general form for the standoff distance is (Wilkin 1996; Zhang & Zheng 1997; Christie et al. 2016),

$$R_0 = \left(\frac{\dot{m}_w v_w}{\Omega(1 + \beta)\rho_a v_{\text{rel}}^2} \right)^{1/2}, \quad (12)$$

where β is the ratio of the thermal and the ram pressure of the ambient medium, $\beta = P_{\text{th}}/P_{\text{ram}}$. When a star moves supersonically, its Mach number is larger than one, $M = v_{\text{rel}}/c_s = 1/\sqrt{\kappa\beta} > 1$, where κ is an adiabatic index. When the thermal pressure is low, that is the ram pressure is much higher

than the thermal pressure of the medium, the term $\beta \rightarrow 0$. For the ambient medium, we assume the radial profile as in Zajaček et al. (2016),

$$n_a \approx n_a^0 \left(\frac{r}{r_0} \right)^{-\gamma_n}, \quad (13)$$

$$T_a \approx T_a^0 \left(\frac{r}{r_0} \right)^{-\gamma_T}, \quad (14)$$

where we set r_0 to the Schwarzschild radius r_s ($r_s \equiv 2GM_\star/c^2 \doteq 2.95 \times 10^5 M_\star/M_\odot \text{ cm}$). The normalisation parameters are $n_a^0 = 1.3 \times 10^7 \text{ cm}^{-3}$ and $T_a^0 = 9.5 \times 10^{10} \text{ K}$ and the power-law indices are $\gamma_n \approx \gamma_T = 1$. At the pericentre, the estimated distance of the DSO according to Valencia-S. et al. (2015) is $r_p = a(1 - e) \approx 1925 r_s$ and the corresponding orbital velocity is $v_p \approx 6600 \text{ km s}^{-1}$. If we assume $v_{\text{rel}} \approx v_p$ and $\kappa \approx 1$, then the factor $\beta \approx 0.01$, so the thermal pressure may be neglected at the pericentre⁴.

The factor Ω is the solid angle, into which the stellar wind/outflow is blown. For a general case, the factor $\Omega = 2\pi(1 - \cos \theta_0)$, where θ_0 is a half-opening angle of the outflow. For an isotropic stellar wind, we have $\theta_0 = \pi$, and so we naturally get $\Omega = 4\pi$. For bipolar cavities with $\theta_0 = \pi/4$, we get $\Omega = 2\pi(1 - \sqrt{2}/2) \approx 1.84$.

The density of the shocked wind layer ρ_{bs} may be estimated from the Rankine-Hugoniot jump conditions (Christie et al. 2016),

$$\rho_{\text{bs}} = \rho_a \frac{\kappa + 1}{\kappa - 1} \left(\frac{v_{\text{rel}}}{v_w} \right)^2 (1 + \beta). \quad (15)$$

In case the motion of the ambient medium may be neglected, $v_{\text{rel}} = v_\star$, and the thermal pressure is negligible (close to the pericentre), $\beta \rightarrow 0$, then the relative change in density of the shocked layer between the years 2008–2012 (or any two points at the distance of r_0 and r' along the orbit) may be expressed as,

$$\frac{\rho'}{\rho_0} = \left(\frac{r_0}{r'} \right)^{(\gamma_n+1)} \left(\frac{2a - r'}{2a - r_0} \right), \quad (16)$$

⁴ However, at the apocentre of the DSO orbit, the factor $\beta \approx 0.9$, since the ratio of the thermal factors at the apocentre and the pericentre may be expressed as $\beta_A/\beta_P = (1 + e)/(1 - e)$.

Table 4. Circumstellar geometries with a different set of components.

Geometry	K_s -band total linear polarization degree $\overline{p}_{K,L}$ [%]	$(K_s - L)_{\text{int}}$ (intrinsic)	$(K_s - L)_{\text{ext}} = (K_s - L)_{\text{int}} + (A_K - A_L)$ (with extinction)
Star	0 (~6% foreground pol. at Gal. Ctr.)	-0.9	0.4
Star+rotationally flattened envelope (90° inclination)	2.7	1.6	2.9
Star+flared disc	3.2	0.3	1.6
Star+dense bow shock (inclined)	4.1	1.9	3.2
Star+spherical dusty envelope+dense bow shock (inclined)	1.0	1.6	2.9
Star+flattened envelope+cavities (90° inclination)	10.1	1.2	2.4
Star+flared disc+flattened envelope+cavities (90° inclination)	10.5	-1.3	-0.03
Star+envelope+cavities+dense bow shock	23.0	1.6	2.9
Observations (Shahzamanian et al. 2016)	~30	1.8	3.1

Notes. Important parameters are the total linear polarization degree in K_s band ($2.2\mu\text{m}$) and the colour index $K_s - L'$ (with and without line-of-sight extinction). The observed values for the polarization degree and the colour index are also included. The observed values of the polarization degree and the colour index are matched best by the composite model star+disc+cavities+dense bow shock.

which for $\gamma_n = 1$ and the orbital elements according to Valencia-S. et al. (2015) yields $\rho_{2012}/\rho_{2008} \approx 4.35$. The number density of the shocked layer as function of time as well as the relative change between the years (2008-2012) are plotted in Fig. 8 in left and right panels, respectively. For these calculations, the thermal term was included according to Eq. (15), which explains a small difference with respect to the estimate of the relative density increase above. The stellar parameters were adopted from the previous analysis of Scoville & Burkert (2013) and Zajaček et al. (2016): the mass-loss rate $\dot{m}_w = 10^{-8} M_\odot \text{yr}^{-1}$ and variable wind velocities in the range $10\text{--}1000 \text{ km s}^{-1}$. For the radiative transfer simulations, we tried different values of the bow-shock density and the best match to the observed SED and the polarized emission was reached for $v_w = 10 \text{ km s}^{-1}$, which is a rather slow outflow.

The summary of the polarization degree and the source colour ($K_s - L'$) (with and without line-of-sight extinction) for all the circumstellar geometries, which were tested, is summarized in Table 4. In total, there are eight radiative transfer models presented as well as corresponding, observationally inferred values.

4.1.2. Final model: supersonic, dust-enshrouded star with non-spherical envelope

From the set of radiative transfer simulations with different circumstellar geometries (see Table 4), the model that can meet all constraints listed in Table 3 consists of the following components:

- a pre-main-sequence star;
- spherically concentrated dusty envelope/geometrically thick disc;
- bipolar cavity with a half-opening angle $\theta_0 = 45^\circ$;
- bow shock.

The detailed discussion of the adopted parameters and densities of the gas/dust envelope is in the previous subsection. The illustration of the model is in Fig. 10 (left panel). An important parameter in terms of the intrinsic geometry is the angle δ that determines the orientation of the bipolar outflow with respect to the axis of symmetry of the bow shock. Unless otherwise indicated, we set $\delta = 0^\circ$, that is the bipolar cavities are aligned with the symmetry axis of the bow shock.

An exemplary model SED is in Fig. 10 (right panel) calculated for the viewing angle of 90° . Here we use the same convention for the viewing angle as Mužić et al. (2010, see their Fig. 3) – 0° corresponds to the front view of the bow shock (circular shape in projection), 90° corresponds to the side view (bow-shock shape), and 180° corresponds to the view from the

tail part (also circular shape in projection). The thick black solid line represents the total continuum flux density and thinner, grey lines stand for individual components: stellar emission, scattered stellar emission, dust emission, and scattered dust emission. It is clearly visible that L' -band flux density is dominated by the thermal dust emission (direct photons), whereas K_s -band emission is dominated by scattered emission, mainly scattered dust photons and to a smaller extent, scattered stellar photons. The stellar photospheric emission is negligible across the whole NIR- and MIR-spectrum.

We also check the dependence of the SED on the viewing angle, see Fig. 11 (left panel). Quantitatively, the best match is for viewing angles larger than 50° and less than 130° . The dependence of the SED on the viewing angle implies a possible source of continuum variability as the DSO source orbits Sgr A*. For K_s and L' bands, the variability is a few 0.1 mJy within an expected viewing angle $\sim 80^\circ\text{--}150^\circ$, see Appendix A for estimates, which depend mainly on the relative velocity of the star with respect to the medium, which is in general uncertain. However, close to the pericentre, the relative velocity should approach the orbital velocity.

The linear polarization degree as function of wavelength is depicted in Fig. 11 (right panel). The largest total polarization degree, $P_L \gtrsim 20\%$, is for the viewing angles close to 90° when the source is highly non-spherical. On the other hand, for the viewing angle either close to 0° or 180° , the total linear polarization degree is $\lesssim 10\%$, since the source appears rather circular.

The dependence of the total linear polarization degree in K_s band on the inclination is in Fig. 12 (right panel). For radiative transfer calculations, we set the position angle of the bipolar cavities to $\delta = 0^\circ$, that is aligned with the symmetry axis of the bow shock. The plot in Fig. 12 shows that a gradual increase in the bow-shock density (see also Fig. 8) over the interval 2008–2012 leads to an increase in the total linear polarization degree over certain inclination ranges. A potential increase in the polarization degree is also discussed in Shahzamanian et al. (2016). It is, however, detected only for one epoch, 2012.0 (see their Fig. 4 and Table 3), when the polarization degree reaches $p_L \approx 37.6\%$, so a progressive increase cannot be considered significant at this point. In addition, Fig. 12 implies that the polarization degree can change when the inclination of the source geometry (bow shock), that is the viewing angle with respect to the observer, changes for different epochs. Indeed, this is the case for the DSO due to its fast motion along the elliptical orbit around Sgr A*, see also the calculation of the viewing angle variation close to the pericentre passage presented in Appendix A. Furthermore, we perform the simulations for a bipolar outflow that is misaligned with the bow-shock symmetry axis. In Fig. 12, two additional dependencies for $\delta = 45^\circ$ and $\delta = 90^\circ$ are calculated

M. Zajaček et al.: Galactic centre NIR-excess sources. Continuum of the DSO/G2

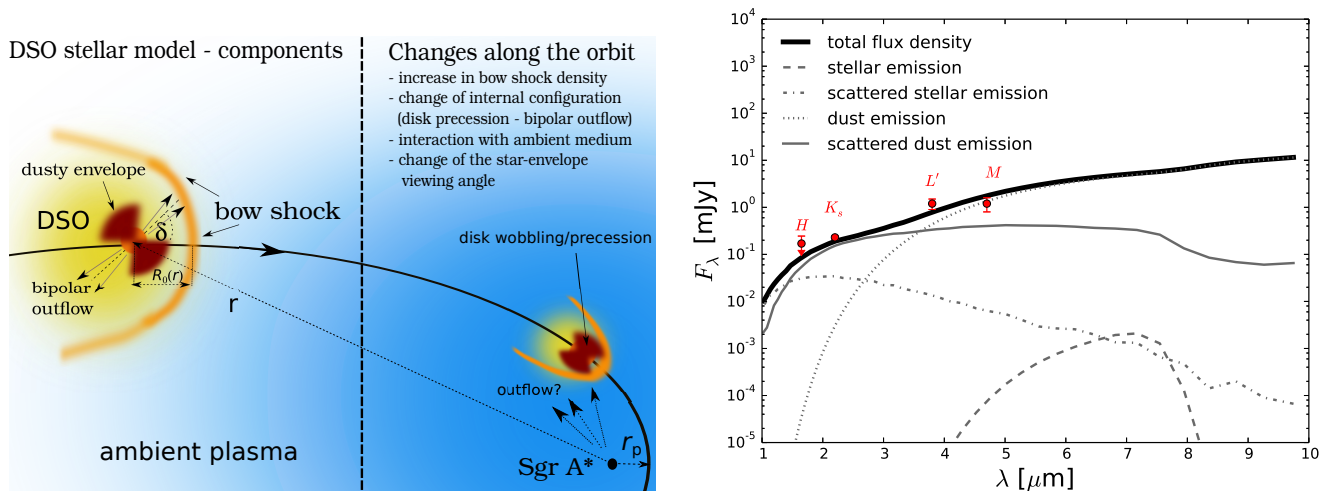


Fig. 10. *Left:* illustration of the components of the DSO model explained as a pre-main-sequence star. The right side explains possible sources of the changes in the continuum emission of the DSO/G2 (polarization degree and angle). *Right:* calculated SED for the composite model of the DSO (star, dusty envelope, bipolar cavities, bow shock) for the viewing angle of 90° . The thick solid line stands for the total continuum flux density, whereas grey lines represent individual source contributions (see the key). The points represent observationally inferred flux densities/limits for H , K_s , L' , and M bands.

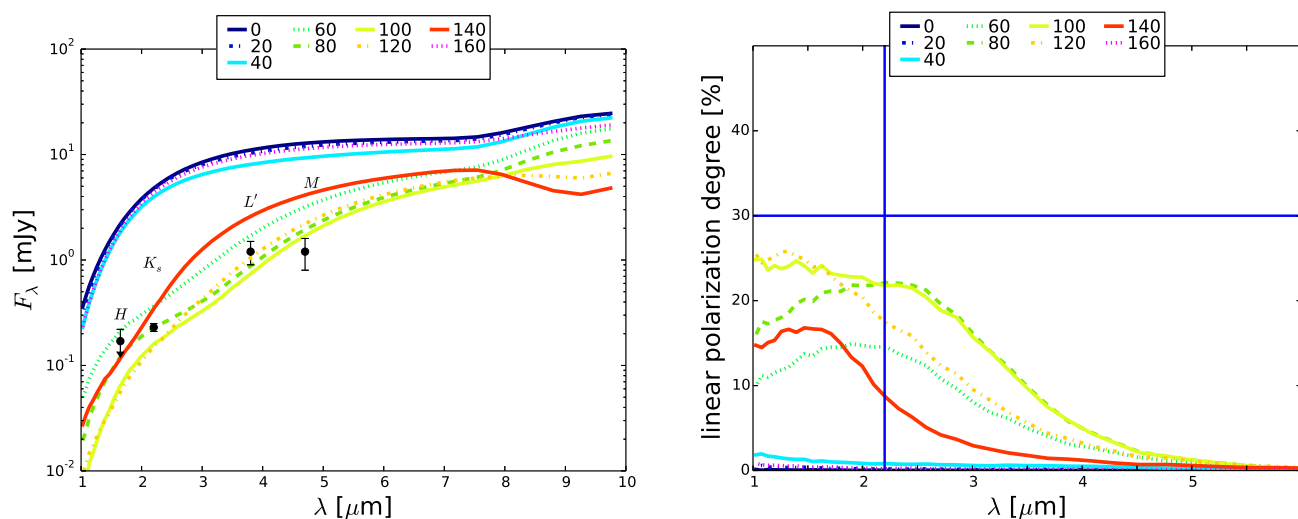


Fig. 11. *Left:* spectral energy distribution of the composite stellar model of the DSO as function of the viewing angle. The points represent observationally inferred values. Different viewing angles from 0° up to 180° are labelled by different colours according to the key. *Right:* linear polarization degree as function of wavelength for different viewing angles (see the key). The vertical thick line marks the values along the K_s band ($2.2\mu\text{m}$), the horizontal line denotes the value of $p_L = 30\%$, which is close to observationally inferred values for four consecutive epochs (2008, 2009, 2011, 2012; Shahzamanian et al., 2016).

for the largest density (epoch 2012.0). Given our model set-up and an expected range of viewing angles (see the shaded area in Fig. 12), the polarization degree of $\sim 30\%$ is better reproduced by the configuration, in which the position angle δ of the bipolar outflow is between 0° – 45° , that is more aligned towards the bow-shock symmetry axis. When the orientation of the bipolar outflow is perpendicular to the symmetry axis, $\delta = 90^\circ$, the dependence of the polarization degree on the inclination is rather flat and stays below or around 20%.

Qualitatively, all the polarization curves in Fig. 11 (right panel) have a peak that is close to $2.2\mu\text{m}$ for the viewing angles around 90° , and the peak shifts towards shorter wavelengths for both smaller and larger viewing angles than 90° . The curves resemble the empirical Serkowski law, $p_L = p_{\text{max}} \exp\{-K \ln^2(\lambda_{\text{max}}/\lambda)\}$ (Kolokolova et al. 2015), where λ_{max}

is the wavelength at which the polarization curve reaches the maximum $p_L = p_{\text{max}}$ and the coefficient K determines the width of the curve. However, the Serkowski law is used to fit the linear polarization degree in the ISM that arises due to dichroic extinction, whereas the simulations presented here are performed for spherical grains, and without the implementation of the magnetic field, whose configuration at the studied distances from Sgr A* is still highly uncertain and beyond the scope of this paper.

The variation of the position angle δ of the bipolar cavity leads to the change of the brightness distribution in the total as well as the linearly polarized light, and hence the change of the polarization angle Φ . In Shahzamanian et al. (2016) we fitted the dependency of the polarization angle on the position angle with the relation that is approximately equal to $\Phi \approx -(+)\delta + (-)90^\circ$ (see Fig. 9 in Shahzamanian et al. 2016). This relation is also

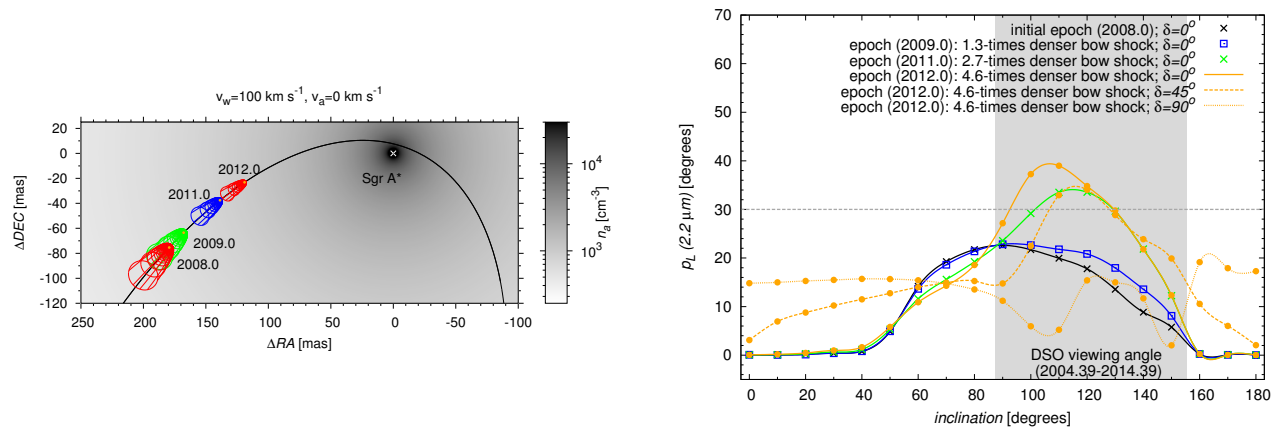


Fig. 12. *Left:* schematic plot of the bow-shock evolution of the DSO along the orbit. The mass-loss rate was taken to be $\dot{m}_w = 10^{-8} M_\odot \text{yr}^{-1}$ and the terminal wind velocity is $v_w = 100 \text{ km s}^{-1}$. The ambient density was colour-coded according to the distribution expressed by Eq. (13). *Right:* total linear polarization degree in K_s band for different inclinations (0–180 degrees) of the DSO composite model. According to the key, the solid lines represent different epochs, 2008–2012, with a gradually increasing bow-shock density (see also Fig. 8). The three orange lines associated with the largest bow-shock density represent the set-ups for three different position angles of the bipolar outflow, $\delta = 0^\circ$, 45° , and 90° . The shaded rectangular region represents different angles of the bow-shock axis with respect to the line of sight for the period of 10 yr before the pericentre passage of the DSO, assuming a negligible motion of the ambient medium in comparison with the orbital velocity of the DSO. The horizontal dashed line marks the polarization degree value of $p_L = 30\%$, which is approximately the observationally inferred degree for the DSO (Shahzamanian et al. 2016).

evident in the simulated images of the linear polarized light in Fig. 13, where we change the position angle in 45° steps from 0° up to 90° (from the top to the bottom panels in Fig. 13). Most of the scattered, polarized light comes from the region where the bipolar cavities intersect the bow-shock shell. On the other hand, the minimum of the polarized emission is overlapping naturally with the optically thick dusty envelope that also hides the star at the centre.

Shahzamanian et al. (2016) measured a variable polarization angle for four epochs, see their Fig. 4 (right panel). There are two possible mechanisms that can be employed to explain a variable polarization angle – see also the left panel of Fig. 10 for the illustration:

- (i) intrinsic changes in the star-envelope orientation: these changes would be due to the torques induced by the massive black hole, which would lead to the precession of the circumstellar disc/bipolar outflows in case the disc is misaligned with respect to the orbital plane. The precession time-scale is longer than the orbital time-scale, $T_{\text{prec}} > T_{\text{orb}}$. On the other hand, the wobbling of the disc takes place on the time-scale shorter than one orbital period, approx. $T_{\text{wobble}} \approx 1/2 T_{\text{orb}}$ (Bate et al. 2000);
- (ii) external interaction of the star with the nuclear outflow/inflow: such an interaction could change the viewing angle on the star-bow shock-bipolar outflow system, especially for the case when the outflow/inflow velocity is comparable to the orbital velocity of the star, which would significantly affect the relative velocity, $v_{\text{rel}} = v_{\text{star}} - v_a$, and hence also the orientation of the bow shock with respect to the observer, see the modelling by Zajaček et al. (2016).

The simulated RGB image (Red colour – L' band, Green colour – M band, Blue colour – K_s band) of the source model of the DSO is in Fig. 14 with the labels of the components. For the simulated image, we set the position angle δ to 90° , that is perpendicular to the symmetry axis of the bow shock (compare with the simulated image in Fig. 11 in Shahzamanian et al. 2016, which was computed for $\delta = 0^\circ$). The inset in Fig. 14 illustrates

the magnetospheric accretion that was used to explain the origin of the broad Bry line of the DSO (Valencia-S. et al. 2015; Zajaček et al. 2015).

Independently of the previous analysis, where the K_s -band flux density is linearly polarized mainly due to dust photons scattering off spherical dust grains, a correlation was found between the linear polarization degree in K_s towards luminous stars embedded in molecular clouds and the optical depth τ_K , which can be fitted by a power law (Kolokolova et al. 2015),

$$P_{L,K} = 2.2\tau_K^{0.75} (\%). \quad (17)$$

Jones et al. (1992) explain this correlation by a 50/50 mixture of the constant, that is a perfectly aligned component to the magnetic field, with random components.

When applied to the DSO with $P_{\text{DSO}} \approx 30\%$, we get $\tau_{\text{DSO}} \approx 33$ as an estimate for the optical depth to the object along the line of sight, most of which can be attributed to the locally dense, optically thick envelope surrounding the stellar core. Similar values for the polarization degree and the optical depth in K_s band were found for the Becklin-Neugebauer object and OMC1-25 in the Orion star-forming region (Kolokolova et al. 2015), which are both deeply embedded objects detected as prominent infrared excess sources.

4.1.3. Effect of surrounding stars on the polarized emission

In the previous analysis, we assumed that the main source of photons that are absorbed and scattered off dust grains in the surrounding envelope is the star at the centre. The question arises to what extent other stars in the S cluster contribute to the detected polarized emission. There are about $N_S = 30$ stars of mostly spectral type B in the innermost arcsecond, $r_S \approx 1'' \approx 0.04 \text{ pc}$ (Eckart et al. 2005). Under the assumption of an approximately uniform distribution of stars in the sphere of radius r_S , this gives the stellar number density in the S cluster $n_S = N/(4/3\pi r_S^3)^{-1} \approx 10^5 \text{ pc}^{-3}$. The average distance of any star from the DSO then is $\overline{D}_S = (n_S)^{-1/3} \approx 0.02 \text{ pc} = 4.4 \times 10^3 \text{ AU}$.

M. Zajačec et al.: Galactic centre NIR-excess sources. Continuum of the DSO/G2

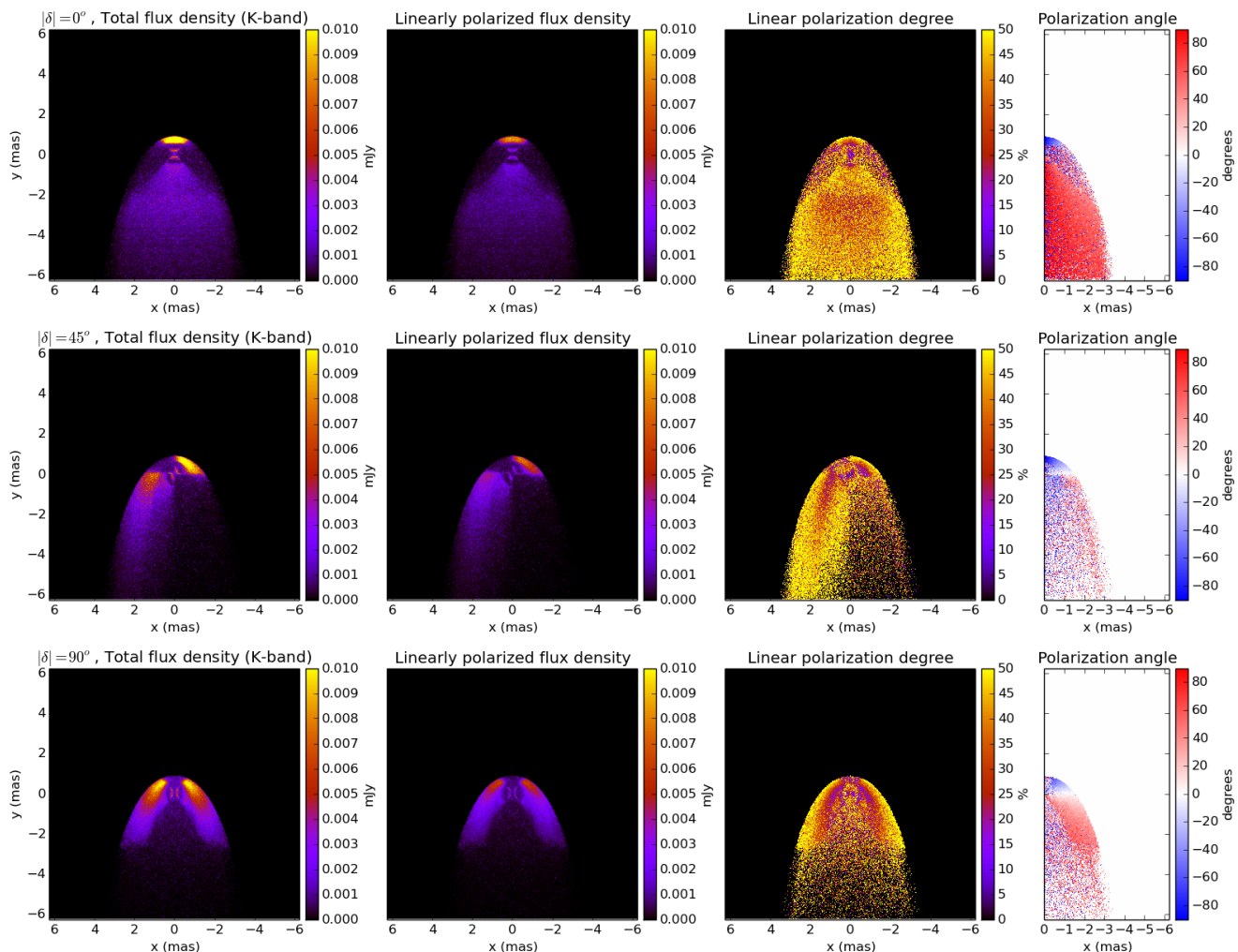


Fig. 13. Simulated images of the total flux density in K_s band (first panels from the left side), linearly polarized flux density (second panels from the left side), the distribution of the polarization degree (second panels from the right side), and the distribution of the polarization angle (first panels from the right side) for the different position angle of the bipolar outflow; $\delta = 0^\circ$, 45° , and 90° from the top to the bottom panels.

The ratio of total fluxes at the position where photons are scattered off grains is,

$$\frac{F_{\text{DSO}}}{F_S} = \left(\frac{T_{\text{DSO}}}{T_S} \right)^4 \left(\frac{R_{\text{DSO}}}{R_S} \right)^2 \left(\frac{D_S}{D_{\text{DSO}}} \right)^2, \quad (18)$$

where T_{DSO} and T_S are effective temperatures of the DSO and a typical S star, respectively. For the DSO, assuming it is a pre-main-sequence star, we take the previous value $T_{\text{DSO}} \approx 4200$ K. For a typical B0 star, the effective temperature is $T_S \approx 25\,000$ K. In terms of stellar radii, both the pre-main-sequence star and the B0 star have similar stellar radii of the order of $R_{\text{DSO}} \approx R_S = 10R_\odot$. Finally, distances of stellar sources from the scattering material are approximately $D_S \approx \overline{D_S} \approx 4.4 \times 10^3$ AU and for the DSO star, $D_{\text{DSO}} \approx 1$ AU. Plugging these estimated values into Eq. (18), we get $F_{\text{DSO}}/F_S \approx 1.5 \times 10^4$, hence the contribution of other S stars is on average negligible in comparison with the central source.

An occasional close approach of an S star could contribute more. However, if these events were frequent, they should be reflected in a larger degree of variability of both the total and the polarized continuum emission. So far the DSO has appeared to be a rather stable source (Shahzamanian et al. 2016).

4.2. Possible non-thermal origin of the SED: NIR-“excess” sources as young neutron stars?

In this subsection, we discuss the possibility that young neutron stars can in principle be detected in the central arcsecond of the Galactic centre and, under certain conditions, their characteristics would be similar to the Dusty S-cluster Object and other infrared excess sources, namely the positive spectral slope (larger flux density for longer wavelengths) and a significant polarized emission in NIR wavebands. As the first step, we check the energetics that would be required to produce flux densities comparable to the DSO. The flux density in K_s band is $F_\nu = 0.23 \pm 0.02$ mJy (see Table 2). This leads to the overall K_s band luminosity of $L_K = \nu F_\nu 4\pi r^2 = 0.23 \times 10^{-3} \times 10^{-23} \times 1.36 \times 10^{14} \times 4\pi (8000 \text{ pc})^2 \text{ erg s}^{-1} = 2.4 \times 10^{33} \text{ erg s}^{-1}$. This luminosity is of the same order of magnitude as the one found for PSR B0540-69 in the Large Magellanic Cloud (Mignani et al. 2012). Mignani et al. (2012) also show that the K_s band luminosity and the spin-down energy \dot{E} are correlated, $L_K \propto \dot{E}^{1.72 \pm 0.03}$, which implies that NIR emission is rotation-powered and associated with the magnetospheric origin and/or the neutron star wind termination shock. Using the correlation, $L_K \approx 6.1 \times 10^{-33} \dot{E}^{1.72}$,

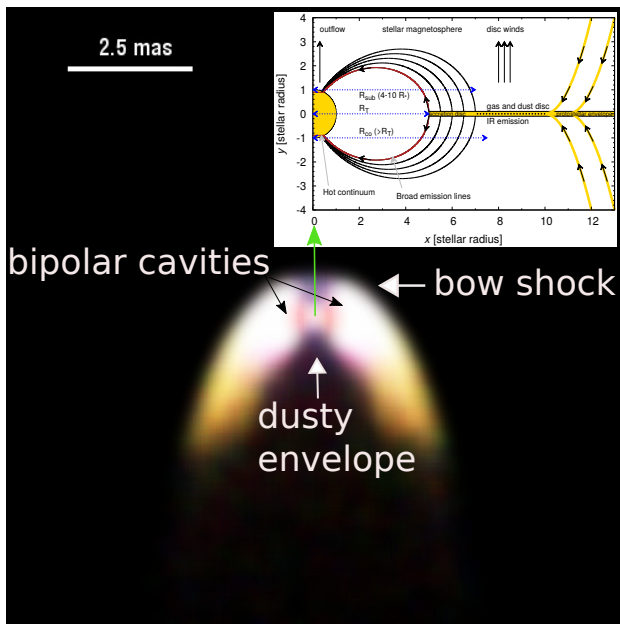


Fig. 14. A simulated three-colour image of the source model of the Dusty S-cluster object (DSO/G2) for the position angle of the bipolar outflow $\delta = 90^\circ$. Blue colour stands for K_s band, green colour for L' band, and the red one for M band emission. See Shahzamanian et al. (2016) for an analogous composite image, but for the position angle $\delta = 0^\circ$. The figure inset was adopted from Zajaček et al. (2015) and illustrates the magnetospheric accretion that takes place on the scale of several stellar radii and is possibly responsible for broad emission lines of the DSO.

we can estimate a spin-down power of the pulsar potentially associated with the DSO, $\dot{E}_{\text{DSO}} \approx 1.4 \times 10^{38} \text{ erg s}^{-1}$, which is of the same order of magnitude as the Crab pulsar, J0534+2200 (Manchester et al. 2005).

Hence, the neutron star associated with the DSO and other NIR-excess sources would have to be a rather young, Crab-like PWN with the characteristic age of $\tau = P/2\dot{P} \approx 10^3 \text{ yr}$, where P is a pulsar period and \dot{P} is the period derivative or spin-down rate. The origin would be young, massive OB stars having an age of a few millions observed in the central parsec (Buchholz et al. 2009). The power-law slope inferred for the DSO, see Eq. (1), is qualitatively consistent with the observations of neutron stars in near-infrared bands (Mignani et al. 2012; Zharikov et al. 2013; Zyuzin et al. 2016), however, it appears to be steeper than for observed pulsars (Mignani et al. 2012), which have the mean spectral index $\alpha \approx 0.7$.

The SED alone does not give any convincing argument for the neutron star hypothesis and the dust-enshrouded star is thought to be a more natural scenario. On the other hand, the detection of linearly polarized emission in K_s band and a high polarization degree of $\sim 30\%$ (Shahzamanian et al. 2016) imply that the DSO may indeed be a peculiar source in the S cluster and the neutron star model can naturally explain the polarized emission via the synchrotron mechanism in the dipole magnetic field, see Eq. (8). For instance, the infrared imaging and polarimetric observations of the PWN SNR G21.5-0.9 (Zajczyk et al. 2012) indeed show a high degree of linear polarization in K_s band, $P_L \approx 0.47$ and a comparably high polarization degree is expected for other PWNe.

Young, rotation-powered neutron stars are expected to have radio and X-ray counterparts whose luminosities are proportional to the $\dot{E}_{\text{rad}} = -\dot{E}_{\text{spin-down}} = 4\pi^2 I \dot{P} / P^3$, where I is the

moment of inertia of the neutron star, $I \approx 10^{45} \text{ g cm}^2$. In general, there seems to be a trend of increasing radiative efficiency η_f towards shorter wavelengths, $\eta_f \equiv L_f / \dot{E}_{\text{rad}}$, where f is the spectral domain (Lorimer & Kramer 2012).

In the X-ray domain, the scatter of efficiencies is relatively small, and approximately equal to $\eta_X \approx 10^{-4}$ (Kargaltsev & Pavlov 2007). In case of the pulsar and its wind nebula associated with the DSO, this gives an estimate of the X-ray luminosity $L_X = \eta_X \dot{E}_{\text{DSO}} \approx 10^{34} \text{ erg s}^{-1}$, which is, given the uncertainties, comparable to the quiescent X-ray emission of Sgr A*, $L_{X,\text{Sgr A}^*} \approx 10^{33} \text{ erg s}^{-1}$ (Yuan & Narayan 2014), associated with the thermal bremsstrahlung process in the hot plasma surrounding Sgr A*.

Towards the radio domain, the radiative efficiency for rotation-powered pulsars becomes smaller and the scatter is larger, $\eta_R = 10^{-8} - 10^{-5}$, which leads to the values for the pulsar associated with the DSO, $L_R = \eta_R \dot{E}_{\text{DSO}} \approx 10^{30} - 10^{33} \text{ erg s}^{-1}$, which is smaller or comparable to the luminosity of Sgr A* in this domain (Yuan & Narayan 2014). In some cases, pulsars are only detected at higher energies and appear to be radio-quiet (e.g. Geminga pulsar; Camilo 2003) under the sensitivity constraints of radio surveys, which either implies that the radio beam is narrow and not directed at the Earth or that radiative efficiencies in the radio domain for some young pulsars are smaller in comparison with X-ray and γ -ray domains.

So far no clear X-ray and radio counterparts of the DSO were detected (Bower et al. 2015; Mossoux et al. 2016; Borkar et al. 2016). However, given the rough estimates above, a high background flux towards Sgr A*, and low angular resolution in the X-ray domain, even young pulsars of a Crab type can be beyond the sensitivity limits of current X-ray and radio instruments. Therefore, weak, infrared excess sources similar to the DSO could be candidates for pulsars and deserve follow-up monitoring with upcoming, high-sensitivity facilities (E-ELT, Square Kilometer Array – SKA).

Given the large orbital velocities of stars and potential stellar remnants in the S cluster with respect to the ambient medium, PWN are expected to be non-spherical and elongated in the direction of the motion. The length-scale of the termination-shock of the pulsar wind is given by the pressure balance as expressed by Eq. (12), where the wind pressure term $p_w = \dot{m}_w v_w / (4\pi r^2)$ is replaced by $p_{\text{pwn}} = \dot{E}_{\text{rad}} / (4\pi r^2)$, which leads to the stand-off distance

$$R_{\text{PWN}} = \left(\frac{\dot{E}_{\text{rad}}}{4\pi c \rho_a v_{\text{rel}}^2} \right)^{1/2}, \quad (19)$$

where we neglected the thermal term. The relative velocity with respect to the ambient medium may be approximated by the orbital velocity close to the pericentre of the orbit, $v_{\text{rel}} \approx v_\star$. Taking $\dot{E}_{\text{rad}} = 1.4 \times 10^{38} \text{ erg s}^{-1}$ as estimated for the pulsar potentially associated with the DSO, we calculate the evolution of the stand-off distance according to Eq. (19) during the period of 10 yr before the pericentre passage, see Fig. 15. We see that even for a relatively young PWN with the spin-down energy of the same order as the Crab pulsar, the stand-off distance is comparable or smaller than the diffraction limit of 63 mas, $R_{\text{PWN}} \leq \theta_{\text{min}}$, that is the PWN would effectively appear as a point source, mainly due to a large relative velocity close to Sgr A*.

A detailed analysis of the generation of Bry line in the PWN is beyond the scope of this paper. We just note that the source of Bry could be the collisional excitation of hydrogen atoms prior to their ionization in the bow-shock layer, as was similarly suggested by Scoville & Burkert (2013) for a bow shock

M. Zajaček et al.: Galactic centre NIR-excess sources. Continuum of the DSO/G2

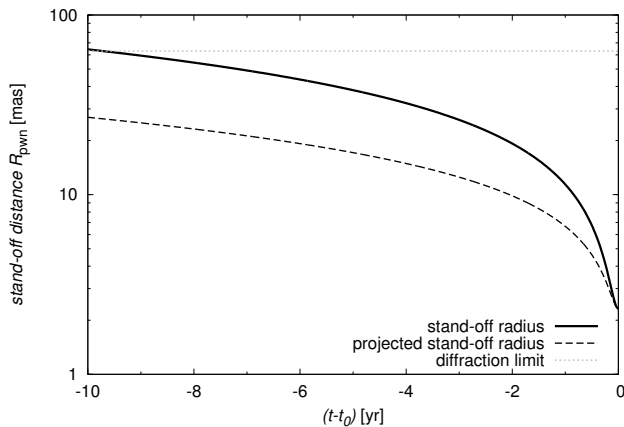


Fig. 15. Evolution of the stand-off distance (in mas) of the PWN as a function of time (in years before the pericentre). The total luminosity is set to $\dot{E}_{\text{rad}} = 1.4 \times 10^{38} \text{ erg s}^{-1}$, the density of the ambient medium is computed according to Eq. (13), and the orbital velocity is calculated using the orbital elements of the DSO as inferred by Valencia-S. et al. (2015) using Bry emission of the DSO.

associated with a T Tauri star. Specifically, there are several pulsar bow shocks that exhibit H α emission (Cordes 1996; Brownsberger & Romani 2014), and hence Bry line could be produced by the same process. Quantitatively, for three pulsars at kiloparsec distances – B0740-28, B1957+20, B2224+65 (see Table 2 in Chatterjee & Cordes, 2002) – the corresponding H α luminosities are in the range of $L_{\text{H}\alpha} \approx 6.5 \times 10^{28} - 1.6 \times 10^{30} \text{ erg s}^{-1}$, that is $L_{\text{H}\alpha} \approx 2 \times 10^{-5} - 4 \times 10^{-4} L_{\odot}$, which is at least an order of magnitude less than the Bry luminosity of the DSO (Gillessen et al. 2012; Valencia-S. et al. 2015). In general, Chatterjee & Cordes (2002) derive a scaling relation for H α luminosity of pulsars, $L_{\text{H}\alpha} \propto 4\pi X \dot{E}_{\text{rad}} v_{*}$, where X is a fraction of neutral hydrogen. Analogous dependencies are expected for Bry luminosity, under the assumption that the line is produced by the collisional excitation in the pulsar bow shock.

In addition, natal kick velocities during supernova explosions in the clockwise stellar disc could, under a certain configuration, lead to the formation of highly-eccentric orbits similar to that of the DSO; see the analysis of dynamics presented in Paper II. In summary, given the properties of the DSO and that of other NIR-excess sources, one cannot a priori exclude the PWN hypothesis as an explanation of the phenomenon.

5. Discussion

The focus of this paper was on the detailed analysis of the total and polarized continuum emission of the DSO in the NIR domain as explained by an enshrouded pre-main-sequence star model. A detailed analysis of other phenomena associated with the DSO, for example a tentative association with a larger tail/streamer, emission in other domains, and the analysis of the line emission are beyond the scope of this study. However, let us briefly comment on some of these aspects to put the continuum analysis in a larger context. These and other aspects of NIR-excess sources in the Galactic centre will also be examined in detail in upcoming papers of this series.

5.1. DSO/G2 and G1 as parts of a larger gaseous streamer?

It was claimed previously that DSO/G2 is accompanied by an elongated, low-surface-brightness tail that is clearly visible in

the position-velocity diagrams (Gillessen et al. 2012, 2013a,b; Pfuhl et al. 2015). A dynamical connection of the DSO/G2 to the tail would favour the “gas-stream-like” scheme: according to this scenario, DSO would be a clump of a more extended filamentary structure. However, this clump could still be compact and associated with a star; see also Ballone et al. (2016) for the hydrodynamical model of the “G2+G2t” complex. Indeed, the numerical models of the formation of young stars close to the supermassive black hole suggest that the star formation takes place in infalling gaseous clumps that undergo fragmentation and stretching (Jalali et al. 2014). The occurrence of denser clumps – protostars – embedded in a larger streamer is therefore expected in the earliest stages of the star formation in the strong gravity regime, where tidal forces cannot be neglected.

However, apart from the arguments above, the connection of the DSO to a larger filamentary structure is still disputed observationally, mainly because of a spatial and kinematical offset from the DSO (Eckart et al. 2014; Meyer et al. 2014; Phifer et al. 2013); see also Peissker et al. (in prep.). It is plausible that the tail is rather a back/foreground feature associated with the minispiral (Eckart et al. 2014). The denser filament in the south-east direction could be a result of the interaction of the northern and the eastern minispiral arms whose dynamics is consistent with two Keplerian bundles (see Fig. 21 in Zhao et al. 2009; and Fig. 10 in Vollmer & Duschl 2000). Meyer et al. (2014) also claim that while the DSO and the filament have similar radial velocities, there is a significant spatial offset, which is not visible in position-velocity plots of Gillessen et al. (2012, 2013a,b) and Pfuhl et al. (2015), who use an artificial curved slit of a finite width to extract radial velocities, which masks spatial offsets. This also means that the filament can be an artefact as the result of the masking process in the data reduction procedure, which implies that an apparent association of small line-emitting sources that have a spatial offset are grouped together in the position-velocity diagram.

The association of the PWN to a larger filament is also plausible, since it could be a remnant of the material from the supernova explosion, for example in the clockwise disc of massive OB stars. In this sense, the fast-moving pulsar can “catch up” with the expanding shell, as also seems to be the case of Sgr A East remnant and the “Cannonball” pulsar (Zhao et al. 2013).

Pfuhl et al. (2015) also propose a possible dynamical connection between the DSO/G2 object and G1 clump, that is both features could be parts of the same streamer and dynamically related. If this was the case, it could be used for constraining the properties of the accretion flow around Sgr A* (McCourt & Madigan 2016; Madigan et al. 2017), based on the amount of dragging, which is only prominent for core-less clumps. However, the association of these two, reddened sources is still under investigation and should be confirmed/excluded based on continuing monitoring – even if the inclination of both orbits is comparable, the orientation of the orbits in space can be different. Also, G1 object survived the pericentre passage, so it also seems less likely that it is a pure gas cloud (Sitariski et al. 2015). In summary, even if the DSO was associated with or moving through a larger gaseous structure, it would not rule out a young-star or PWN hypothesis presented in this study.

5.2. Core-less cloud models vs. stellar models of the DSO

Following the roadmap in Fig. 2, we will look at a few observables that distinguish the core-less cloud and stellar interpretation of the DSO. A dynamical comparison of the evolution of a

core-less cloud and a stellar model using a simplified test particle model was done in Zajaček et al. (2014). The basic result for an assumed density profile of the ambient medium was that a core-less cloud starts progressively deviating from the Keplerian orbit soon after the pericentre, where the velocity of the cloud as well as the density of the medium are the highest and therefore the non-gravitational acceleration due to a hydrodynamical drag is the largest as well; see also McCourt & Madigan (2016) and Madigan et al. (2017). The star is naturally much less sensitive to the ambient medium because of the smaller ratio of the cross-section to the mass, and follows the original trajectory. Up to now, the DSO does not deviate within uncertainties from the inferred highly-eccentric orbit (Peisker et al., in prep.), which may indicate a stellar nature. However, it could also be argued that the hydrodynamical drag is smaller due to a smaller ambient density than usually assumed in the models of RIAFs.

A stronger argument in favour of a stellar model is the compactness of the source as discussed in detail in Sect. 3. In K_s and L' band continuum, the DSO is fully consistent with a point source (Eckart et al. 2014; Witzel et al. 2014; Shahzamanian et al. 2016). Concerning the analysis of Bry line emission, there are contradictory observational results. While Valencia-S. et al. (2015) detect a single-peak Bry emission at each epoch, both shortly before and after the peribothron passage (see their Fig. 8), which is consistent with a stellar model, Pfuhl et al. (2015), on the other hand, detect both a red-shifted peak and a blue-shifted peak for the same epoch (see their Fig. 15), which indicates the effect of stretching of the gas along the orbit. Despite this observational contradiction, it is difficult to reconcile an apparent compact continuum emission (tracing dust) and a stretched Bry emission (tracing gas) with the gas cloud model, since such a cloud would be expected to consist of a well-mixed gas-dust components. This was interpreted by Witzel et al. (2014) in terms of a binary merger model, which is accompanied by an expanding dusty outflow forming an optically thick photosphere (Pejcha 2014). Since binary mergers contract on a Kelvin-Helmholtz time-scale and are surrounded by a dusty envelope, they share several characteristics with pre-main-sequence stars. Therefore, our dust-enshrouded star model is applicable to this scheme.

In Schartmann et al. (2015), a compact cloud model is presented, where the authors claim that the cloud follows the Keplerian orbit and stays rather compact. However, for the epochs 2005–2015 the full width at half maximum of the normalized Bry emission in their model is clearly above the diffraction limit of 63 mas and reaches as much as 115 mas at the pericentre. Therefore, the cloud should have been clearly resolved at all epochs of the monitoring. In their model, the cloud also undergoes tidal stretching and disruption, with an expected enhancement in accretion as early as 2014.6 (see their Fig. 1), which is not consistent with the monitoring of Sgr A* (Borkar et al. 2016; Bower et al. 2015; Mossoux et al. 2016). This indicates a rather unchanged luminosity of the quiescent state as well as the overall flare statistics.

5.3. Contribution of the DSO passage to the variability of Sgr A*?

Concerning the passage of the DSO close to the Galactic centre, there are two possibilities of how the source could have affected the radiative properties of Sgr A*:

- (i) non-thermal emission associated with the shock front;
- (ii) increase in the flaring activity of Sgr A* due to the changing accretion-flow properties close to Sgr A*.

There have been several multi-wavelength observational campaigns that aimed at capturing the signs of the DSO/Sgr A* interaction. The X-ray flux density of Sgr A* was monitored by Chandra X-ray satellite and no increase in the quiescent X-ray emission was detected during 2013–2014 campaign (Haggard et al. 2014), which collected ~ 900 ks of data. Also, no change in the radio quiescent emission was detected (Bower et al. 2015; Borkar et al. 2016). This implies that the shock associated with the supersonic motion of the DSO was far less strong and bright than the predicted values (Narayan et al. 2012) that exceeded the quiescent level of Sgr A*. It means that either the actual source has a smaller cross-section than the one assumed for synchrotron calculations, $\sigma \lesssim 2 \times 10^{29}$ cm² that corresponds to the diameter of $D \lesssim 34$ AU (Bower et al. 2015), or that the ambient medium is rather rarefied even in comparison with the original RIAF models.

Concerning the flaring activity of Sgr A*, there is no statistically significant enhancement detected in both X-ray and infrared bands (Valencia-S. et al. 2015; Mossoux et al. 2016). Based on the analysis of ~ 15 yr of XMM, Chandra, and Swift data, Ponti et al. (2015) discuss an increase in the rate of bright X-ray flares. However, an alternative and plausible explanation is an effect of the X-ray flare clustering (Haggard 2017) rather than the actual increase in the flaring rate, so the overall statistics does not seem to be affected by the DSO passage (Mossoux et al. 2016).

Nevertheless, it is of interest to estimate the non-thermal synchrotron or potential X-ray bremsstrahlung flux for the stellar model of the DSO. These estimates may also be scaled for different stellar parameters when other stars will pass in the vicinity of Sgr A* and future facilities with the larger sensitivity may detect the corresponding emission.

5.3.1. Bow-shock synchrotron emission

The source of the non-thermal synchrotron emission of the DSO are the electrons accelerated in the bow shock. We apply the theory and the model of Crumley & Kumar (2013) and Sądowski et al. (2013) (based on Rybicki & Lightman 1979) to calculate synchrotron spectra and the light curve of the source. In the left panel of Fig. 16, the spectra are calculated for the epoch of the pericentre passage, when the flux density is the largest across all frequencies. The right panel of Fig. 16 displays the light curve computed for the frequency of 1.4 GHz. For both the spectrum and the light curve, two limiting cases are taken into account:

- (i) “plowing” model that assumes that all electrons accelerated in the bow shock radiate in the shock-enhanced magnetic field;
- (ii) “local” model that assumes that the electrons accelerated in the shock leave it and radiate in the local, ambient magnetic field.

Two sets of stellar parameters were considered: the mass-loss rate of $\dot{m}_w = 5 \times 10^{-9} M_\odot \text{ yr}^{-1}$ and the wind velocity of $v_w = 10 \text{ km s}^{-1}$ and $\dot{m}_w = 10^{-8} M_\odot \text{ yr}^{-1}$, $v_w = 10 \text{ km s}^{-1}$, which are expected for a class 1 pre-main-sequence source (Edwards et al. 2006) with the empirical relation $\dot{M}_w \approx 0.001\text{--}0.1 \dot{M}_{\text{acc}}$ between the accretion rate and the outflow rate. For both parameter sets, the peak flux densities are at least two orders of magnitude smaller than the quiescent radio flux density of Sgr A*, that is the stellar model can naturally explain the non-detection of any enhancement in the flux density due to an expected small bow-shock size at the pericentre. In addition, the values are

M. Zajaček et al.: Galactic centre NIR-excess sources. Continuum of the DSO/G2

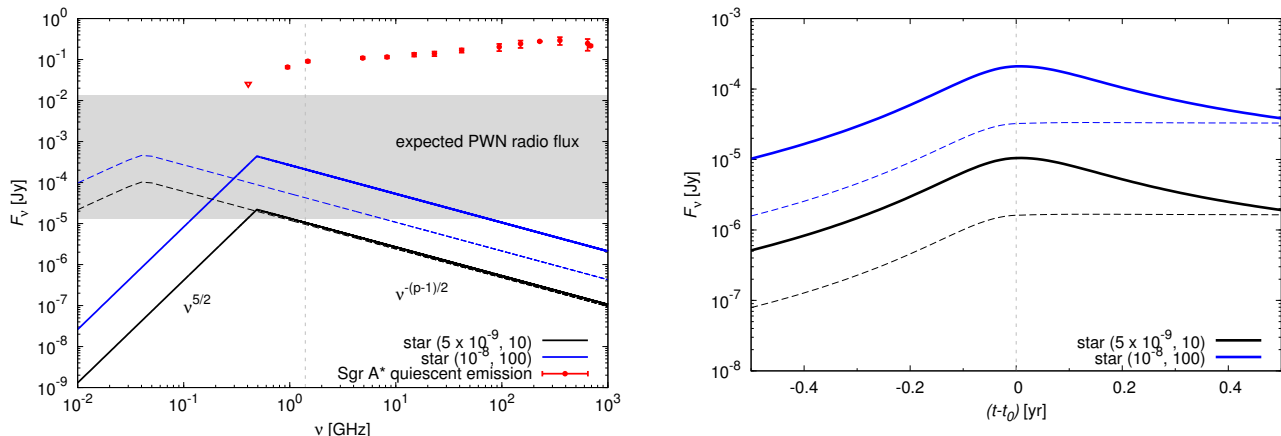


Fig. 16. *Left panel:* calculated synchrotron spectrum for electrons accelerated in the bow shock. Spectra were calculated for two sets of the mass-loss rate and the terminal wind velocity that are within the range of values expected from the stellar model: $\dot{m}_w = 5 \times 10^{-9} M_\odot \text{ yr}^{-1}$, $v_w = 10 \text{ km s}^{-1}$ and $\dot{m}_w = 10^{-8} M_\odot \text{ yr}^{-1}$, $v_w = 100 \text{ km s}^{-1}$. Solid lines correspond to the plowing synchrotron model and the dashed lines to the local model. The energy spectrum of accelerated electrons has a power-law index of $p = 2.4$ in accordance with particle-in-cell simulations of Sądowski et al. (2013). The red points are observationally determined values adopted from Davies et al. (1976), Falcke & Markoff (2000), Zhao et al. (2003), and Marrone et al. (2008). The shaded region represents an estimate of the radio flux density of the PWN. *Right panel:* a synthetic light curve calculated at 1.4 GHz considering for both the plowing (solid lines) and the local model (dashed lines). Two sets of stellar parameters were considered as in the left panel.

comparable to the radio flux density of the PWN, taking into account the radio efficiencies of $\eta_R \approx 10^{-8} - 10^{-5}$ and the spin-down luminosity of $\dot{E}_{\text{rad}} = 1.4 \times 10^{38} \text{ erg s}^{-1}$. In summary, both stellar models – a dust-enshrouded pre-main-sequence star and a PWN – are expected to have radio flux densities below the quiescent level of Sgr A*, implying only a marginal possibility of detection of any change in the radio flux of Sgr A* and its close vicinity.

5.3.2. X-ray bremsstrahlung

Due to an expected supersonic motion of the DSO close to the pericentre (Zajaček et al. 2016), two layers of shocked stellar wind and ambient gas should form and subsequently mix. The shocked gas is expected to cool down by the thermal bremsstrahlung process (Christie et al. 2016). Here we use order-of-magnitude estimates to calculate the bremsstrahlung luminosity.

First, the ionized medium in the central parsec of the Galactic centre can in principle cause losses to the bremsstrahlung due to the Thomson scattering. We can estimate the optical depth of the scattering using $\tau_T \sim \sigma_T n_e L$, where $\sigma_T = 6.65 \times 10^{-25} \text{ cm}^2$ is the cross-section for the Thomson scattering, n_e is the electron number density, and L is the length of the part of the line of sight that crosses the hot gas. For an estimate, we take the number density of electrons at the Bondi radius, $R_B \approx 0.16 (T_a / 10^7 \text{ K})^{-1} \text{ pc}$, $n_e(R_B) = 130 \text{ cm}^{-3}$ (Baganoff et al. 2003) and the line-of-sight length is set to the Bondi radius, $L \approx R_B$. Finally, the estimate gives $\tau_T \sim 4.3 \times 10^{-5} \ll 1$ and therefore the Thomson scattering losses can be neglected.

We take the volume emission coefficient per unit frequency band and integrate it over the frequency interval of the X-ray band, $(\nu_1, \nu_2) = (0.04, 0.8) \times 10^{18} \text{ Hz}$. For the volume emission coefficient ϵ_ν , holds (Lang 1978; Rybicki & Lightman 1979),

$$\epsilon_\nu d\nu \approx 5.4 \times 10^{-39} Z^2 T_{\text{sh}}^{-1/2} n_i n_e g(\nu, T_{\text{sh}}) \times \exp(-h\nu/kT_{\text{sh}}) d\nu \text{ erg s}^{-1} \text{ cm}^{-3} \text{ Hz}^{-1}, \quad (20)$$

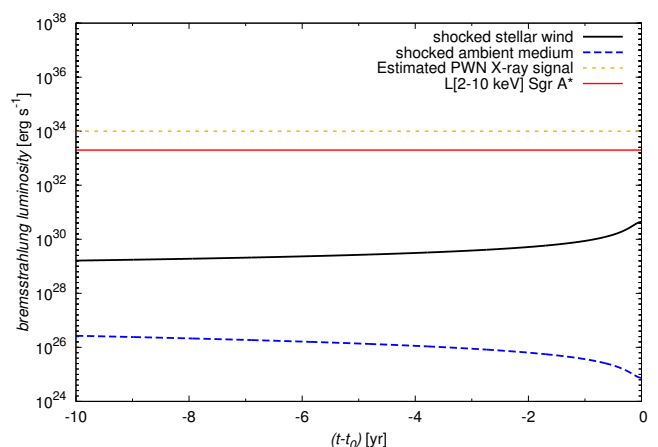


Fig. 17. Temporal evolution of the X-ray bremsstrahlung signal from two components: shocked wind (black solid line) and shocked ambient medium (blue dashed line). Two vertical lines represent the quiescent emission of Sgr A*, $L[2 - 10 \text{ keV}] \sim 2 \times 10^{33} \text{ erg s}^{-1}$ (Haggard 2017), and the estimated PWN signal, assuming the conversion factor of $\eta_X = 10^{-4}$ between the spin-down luminosity and the X-ray luminosity. The stellar parameters were set to $\dot{m}_w = 10^{-8} M_\odot \text{ yr}^{-1}$ and $v_w = 100 \text{ km s}^{-1}$.

where Z is the proton number of participating ions, n_i and n_e are number densities of ions and electrons, respectively, and T_{sh} is the temperature of the shocked gas. The temperature of the shocked ambient medium for the supersonic motion of the DSO may be estimated as $T_{\text{sh}} = 1.38 \times 10^5 (v_\star / 100 \text{ km s}^{-1})^2 \text{ K}$ for an ionized medium (McKee & Hollenbach 1980), which yields $T_{\text{sh}} \sim 10^8 - 10^9 \text{ K}$ for relative velocities of $v_\star \sim 10^3 \text{ km s}^{-1}$ close to the pericentre. The shocked stellar wind is colder by about three orders of magnitude (Scoville & Burkert 2013), but denser, so it is likely to contribute more to the overall bremsstrahlung.

The Gaunt factor $g(\nu, T_{\text{sh}})$ may be approximated in the given range ($T_{\text{sh}} = 10^5 - 10^8 \text{ K}$, $\nu = 10^{18} \text{ Hz}$) via (Lang 1978)

$$g(\nu, T_{\text{sh}}) \sim \sqrt{3}/\pi \log(4.7 \times 10^{10} T_{\text{sh}}/\nu), \quad (21)$$

which varies only a little for the considered frequency range. According to Eckart (1983), we set $g(\nu, T_{\text{sh}}) = 1.5$. Using Eq. (20), the bremsstrahlung luminosity can be expressed as,

$$L_{\text{brems}} \sim 5.4 \times 10^{-39} \times 4\pi \times 1.5 V_{\text{sh}} Z^2 T_{\text{sh}}^{-1/2} n_i n_e \times \int_{\nu_1}^{\nu_2} \exp(-h\nu/kT_{\text{sh}}) d\nu \text{ erg s}^{-1}. \quad (22)$$

The integral $\int \exp(-h\nu/kT_{\text{sh}}) d\nu$ yields $\sim 0.63 \times 10^{10} T_{\text{sh}}$ (Eckart 1983). Furthermore, we express the temperature of shocked gas in $T_8 \equiv (T_{\text{sh}}/10^8 \text{ K})$ and assume that the shocked gas consists fully of ionized hydrogen and helium, so one can replace the term $Z^2 n_i n_e = 1.55 n_e^2$. We approximate the volume of the shocked gas by a spherical half-shell with the volume of $V_{\text{sh}} \sim 2\pi R_0^3 f_{\text{HR}}$, where f_{HR} is the ratio of the bow-shock thickness to the stand-off radius, Eq. (12). Finally, the bremsstrahlung luminosity becomes

$$L_{\text{brems}} \approx 6.2 \times 10^{-23} R_0^3(t) f_{\text{HR}}(t) n_e^2 T_8^{1/2} \text{ erg s}^{-1}, \quad (23)$$

where both the stand-off radius $R_0(t)$ and the ratio $f_{\text{HR}}(t)$ depend on the orbital phase (time) of the DSO (Zajaček et al. 2016; Christie et al. 2016).

We calculate the bremsstrahlung luminosity using Eq. (23) for both shocked layers, ambient and stellar wind layer. The density of the shocked stellar wind is computed using Eq. (15) and we take the temperature of $T_{\text{sh}} \approx 10^5 \text{ K}$. The shocked ambient medium is denser than the ambient profile, Eq. (13), by about a factor of four and its temperature reaches $T_{\text{sh}} \approx 10^8 \text{ K}$. For both cases, the stellar mass-loss rate is set to $\dot{m}_w = 10^{-8} M_{\odot} \text{ yr}^{-1}$ and the wind velocity to $v_w = 100 \text{ km s}^{-1}$. In Fig. 17, we plot the bremsstrahlung light curves for both layers. In case of the shocked wind, the luminosity increases because of the dominant density term – the density in the shocked layer increases towards the pericentre. For the shocked ambient medium, the overall luminosity decreases because of the dominant size term, that is the size of the bow shock decreases. The bremsstrahlung signal from the shocked wind should dominate, but its luminosity is at least three orders of magnitude smaller than the quiescent luminosity of Sgr A*, $L[2-10 \text{ keV}] \sim 2 \times 10^{33} \text{ erg s}^{-1}$ (Haggard 2017). The X-ray flux from the hypothetical PWN is expected to be stronger, at least at the level of the quiescent emission of Sgr A*.

The low level of the X-ray bremsstrahlung emission for a stellar bow shock is not surprising. During the passage of S2 star through the pericentre in 2002, there was no significant increase in the emission of Sgr A* detected (Yuan & Wang 2016). It is worth monitoring the flaring rate during the next passage in early 2018, since some theoretical calculations predict the emission at the level of the quiescent state (Christie et al. 2016).

5.4. Bry emission model for a young star

One of the prominent features of the DSO are the recombination emission lines, mainly Bry line that is used for monitoring. So far and quite surprisingly, the luminosity of Bry line has remained constant within uncertainties (Gillissen et al. 2013a,b; Valencia-S. et al. 2015). It is not straightforward to explain the plateau of the light curve within the stellar model. In the framework of a photoevaporating and tidally disrupted protoplanetary disc, Murray-Clay & Loeb (2012) predict that the total Bry luminosity at the peribothron should be larger by a factor of five with respect to 2011 epoch. In case Bry recombination line originates due to the collisional ionization in the bow shock, the luminosity should also increase by a factor of a few (Scoville & Burkert 2013; Zajaček et al. 2016).

One of the simplest solutions to the plateau of Bry line is to look for processes that are independent of the distance from Sgr A* and of the velocity of the DSO. Circumstellar outflows and inflows that originate within the tidal radius of the DSO r_t (see Sect. 3) belong to such processes as was suggested by Valencia-S. et al. (2015). A likely process contributing to Bry emission in class I objects is the accretion of gas from the inner rim of an accretion disc that is truncated by a dipole magnetic field. The inferred large line width of Bry line of the order of $FWHM_{\text{Bry}} \approx 100 \text{ km s}^{-1}$ (Phifer et al. 2013; Valencia-S. et al. 2015) is consistent with the magnetospheric accretion model (Hartmann et al. 1994; Edwards et al. 1994; Muzerolle et al. 1998), where the disc gas is channeled along magnetic field lines from the truncation radius R_T onto the stellar surface. The poloidal velocities are close to a free-fall velocity,

$$v_{\text{pol}} = 618 \left(\frac{M_{\star}}{1 M_{\odot}} \right)^{1/2} \left(\frac{R_{\star}}{1 R_{\odot}} \right)^{-1/2} f_T \text{ km s}^{-1}, \quad (24)$$

where $f_T = \sqrt{1 - R_{\star}/R_T}$ is the truncation factor, correcting the free-fall velocity for the finite truncation radius. Pre-main-sequence stars exhibit a considerable magnetic field with an intensity of $\sim 1 \text{ kG}$, which truncates an accretion disc at several stellar radii,

$$\frac{R_T}{R_{\star}} \approx 6.5 B_3^{4/7} R_2^{5/7} \dot{M}_{-8}^{-2/7} M_1^{-1/7}, \quad (25)$$

where the strength of the dipole magnetic field at the equator of the star B_3 is in kG, the stellar radius R_2 is in units of $2 R_{\odot}$, the accretion rate \dot{M}_{-8} is in $10^{-8} M_{\odot} \text{ yr}^{-1}$, and the stellar mass M_1 is expressed in $1 M_{\odot}$. Using an estimate in Eq. (25), the truncation factor in Eq. (24) is $f_T \approx 0.9$, which leads to $v_{\text{pol}} \approx 560 \text{ km s}^{-1}$. The line-of-sight velocity of the accreting gas that determines the Doppler broadening of an emerging line depends on the viewing angle of the star-disc system, which is itself variable for any structure bound to the star, for example a bow shock or a disc (see Appendix A for the calculation of the viewing angle).

A stationary accretion can only proceed when the disc truncation radius is inside the corotation radius, which is defined as the distance from the star where the Keplerian angular velocity equals to the rotational angular velocity of the star,

$$R_{\text{co}} \approx 4.2 M_1^{1/3} P_1^{2/3} R_{\odot}, \quad (26)$$

where P_1 is the stellar rotational period in units of one day.

For pre-main-sequence stars, a correlation was found between the accretion luminosity L_{acc} and the luminosity of Bry emission. The correlation does not have to necessarily imply that Bry is a tracer of accretion (Mendigutía et al. 2015) or that the emission originates within a few stellar radii from the star. We can, however, use the $L_{\text{acc}}-L_{\text{Bry}}$ correlation to show that a realistic accretion rate can reproduce the observed, approximately constant Bry luminosity of $L_{\text{Bry}} \approx (1-4) \times 10^{-3} L_{\odot}$ for the DSO (Gillissen et al. 2013a,b; Pfuhl et al. 2015; Valencia-S. et al. 2015). Applying the correlation inferred from a recent fit to several low-mass stars (Alcalá et al. 2014),

$$\log(L_{\text{acc}}/L_{\odot}) = 1.16(0.07) \log(L_{\text{Bry}}/L_{\odot}) + 3.60(0.38), \quad (27)$$

⁵ The relation for the truncation radius, Eq. (25), gives an upper limit, since the ram gas pressure is larger in the disc geometry than in a spherical approximation that was used for this derivation.

M. Zajaček et al.: Galactic centre NIR-excess sources. Continuum of the DSO/G2

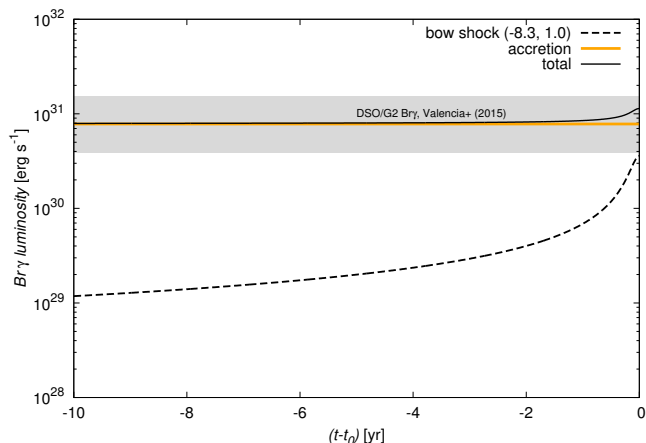


Fig. 18. A temporal, synthetic evolution of the luminosity of Br γ line for the bow shock contribution, the accretion contribution, and the total light curve. The wind parameters of the star were set to $\dot{m}_w = 5 \times 10^{-9} M_\odot \text{ yr}^{-1}$ and $v_w = 10 \text{ km s}^{-1}$ (logarithms of these values are in the parentheses). The shaded region corresponds to the constant, observationally inferred luminosity of Br γ line (Valencia-S. et al. 2015).

we get the accretion luminosities $L_{\text{acc}} \approx 1.3\text{--}6.6 L_\odot$. Hence, the accretion luminosity may be in principle a significant fraction of the continuum emission of the DSO.

Having calculated an order of magnitude of the accretion luminosity allows us to estimate the accretion rate \dot{M}_{acc} , assuming a certain value for the truncation radius $R_T \approx 5 R_\star$,

$$\begin{aligned} \dot{M}_{\text{acc}} &\approx \frac{L_{\text{acc}} R_\star}{GM_\star} \left(1 - \frac{R_\star}{R_T}\right)^{-1} \\ &\approx 4.1 \times 10^{-8} \left(\frac{L_{\text{acc}}}{L_\odot}\right) \left(\frac{R_\star}{R_\odot}\right) \left(\frac{M_\star}{M_\odot}\right)^{-1} M_\odot \text{ yr}^{-1}. \end{aligned} \quad (28)$$

Given the constraints on the mass and the radius of the DSO based on the bolometric luminosity of $30 L_\odot$ (see Fig. 5), $M_{\text{DSO}} \lesssim 3 M_\odot$ and $R_{\text{DSO}} \lesssim 10 R_\odot$, respectively, the upper limit of the accretion rate is $\dot{M}_{\text{acc}} \leq 10^{-7} M_\odot \text{ yr}^{-1}$. The gas accretion in young stellar systems seems to be linked to stellar and circumstellar outflows with the rate of $\dot{M}_w \approx 0.001\text{--}0.1 \dot{M}_{\text{acc}}$ (Edwards et al. 2006).

Hence, the simple model of the accretion described above complements the previous components of the DSO model analysed in Sect. 4, see also Fig. 14 for an illustration. The accretion of gas onto the star and associated outflows can in principle stabilise the light curve of Br γ emission of the DSO, see Fig. 18. While the emission associated with the bow shock is expected to increase towards the pericentre, the accretion luminosity may stay rather constant since accretion flows are located well inside the circumstellar tidal radius. For a certain set of parameters, the total luminosity can be constant within uncertainties. In Fig. 18, the outflow rate of the star is set to $5 \times 10^{-9} M_\odot \text{ yr}^{-1}$ and the terminal wind velocity is 10 km s^{-1} .

6. Summary

The previous analysis of NIR observational data has shown that the NIR-excess source DSO/G2 is a peculiar object in the S-cluster, which was further supported by the detection of a high linear polarization degree of 30% in the NIR K_s band. Taking into account the compact behaviour during the closest

passage around the SMBH, we focused on possible compact, stellar models of the fast-moving source. It appears that the SED characteristics of the DSO are reproduced best by either a young, embedded stellar object with a non-spherical dusty envelope (consisting of a dusty envelope, bipolar cavities, and a bow shock) or, on the other hand, a compact remnant, specifically a PWN. In both cases, the objects are expected to move supersonically close to Sgr A*.

Given the star-formation potential of the Galactic centre region, we first investigated the scenario of a pre-main-sequence star of class I that is still embedded in dense, optically thick dusty envelope. We found a composite stellar model surrounded by a non-spherical envelope (a star-dusty envelope-bipolar cavities-bow shock) that could reproduce the main characteristics of the continuum emission, including the linear polarization. In the framework of this model, bipolar cavities and the bow shock serve as sites for scattering stellar and dust photons. Furthermore, they increase the overall deviation of the source from the spherical symmetry. The K_s band continuum emission is dominated by scattered dust photons, which explains the significant polarized emission in this band. The polarization degree of $\sim 30\%$ is consistent with an optically thick dusty envelope and is comparable to other observed embedded young stellar objects in molecular cloud regions.

Moreover, we also looked at the neutron star model that could explain the SED as well as a high linear polarization degree – more specifically, the DSO would exhibit similar characteristics as a young, Crab-like PWN. Although energetically it would be possible to reproduce the NIR flux densities and the spectral slope, given the non-detection of X-ray or radio counterparts makes this model speculative. On the other hand, our estimates demonstrated that even current NIR facilities could be used to search for candidates of young PWN in the innermost parsec of the Galactic centre in the NIR domain. Such sources would actually manifest themselves as highly polarized, apparent NIR-excess sources, with flux densities comparable to the DSO. Some of the NIR-excess sources observed in the S cluster region could thus be suitable candidates for PWN. The imaging with the current and future NIR instruments can thus complement standard radio searches for young neutron stars in the Galactic centre region, which will allow us to put more constraints on the neutron star population in the innermost parsec. Future monitoring of the DSO and other NIR-excess sources, mainly with the focus on the radiative properties (both continuum and line emission) and the dynamics, will further narrow down the scenarios to explain these intriguing sources in the central arcsecond of the Galactic centre.

Acknowledgements. We thank an anonymous referee for very useful suggestions that improved the paper. Michal Zajaček (M.Z.) is grateful for the hospitality of the Astronomical Institute of the Academy of Sciences of the Czech Republic where a part of this paper was written. M.Z. thanks all the participants of the Cologne-Prague-Kiel meeting 2016 (CPK16) for the discussion and the input. M.Z. would like to give special thanks to Mónica Valencia-S. for initiating the project and useful discussions. M.Z. and M.P. are members of the International Max Planck Research School for Astronomy and Astrophysics at the Universities of Bonn and Cologne. This project received the support of the Czech Science Foundation grant “Albert Einstein Centre for Gravitation and Astrophysics” (No. 14-37086G). A part of the project was supported by the collaboration within SFB956-A2 (“Conditions for Star Formation in Nearby AGN and QSO Hosts”) at the Universities of Cologne and Bonn.

References

- Alcalá, J. M., Natta, A., Manara, C. F., et al. 2014, *A&A*, **561**, A2
 Baganoff, F. K., Maeda, Y., Morris, M., et al. 2003, *ApJ*, **591**, 891
 Ballone, A., Schartmann, M., Burkert, A., et al. 2013, *ApJ*, **776**, L3

- Ballone, A., Schartmann, M., Burkert, A., et al. 2016, *ApJ*, 819, L28
- Bate, M. R., Bonnell, I. A., Clarke, C. J., et al. 2000, *MNRAS*, 317, 773
- Bohren, C., Clothiaux, E., & Huffman, D. 1998, *Absorption and Scattering of Light by Small Particles* (Wiley-VCH)
- Borkar, A., Eckart, A., Straubmeier, C., et al. 2016, *MNRAS*, 458, 2336
- Bower, G. C., Markoff, S., Dexter, J., et al. 2015, *ApJ*, 802, 69
- Brownsberger, S., & Romani, R. W. 2014, *ApJ*, 784, 154
- Buchholz, R. M., Schödel, R., & Eckart, A. 2009, *A&A*, 499, 483
- Burkert, A., Schartmann, M., Alig, C., et al. 2012, *ApJ*, 750, 58
- Camilo, F. 2003, in *Radio Pulsars*, ed. M. Bailes, D. J. Nice, & S. E. Thorsett, *ASP Conf. Ser.*, 302, 145
- Chatterjee, S., & Cordes, J. M. 2002, *ApJ*, 575, 407
- Christie, I. M., Petropoulou, M., Mimica, P., & Giannios, D. 2016, *MNRAS*, 459, 2420
- Clénet, Y., Rouan, D., Gendron, E., et al. 2004, *A&A*, 417, L15
- Cordes, J. M. 1996, in *IAU Colloq. 160: Pulsars: Problems and Progress*, eds. S. Johnston, M. A. Walker, & M. Bailes, *ASP Conf. Ser.*, 105, 393
- Crumley, P., & Kumar, P. 2013, *MNRAS*, 436, 1955
- Davies, R. D., Walsh, D., & Booth, R. S. 1976, *MNRAS*, 177, 319
- De Colle, F., Raga, A. C., Contreras-Torres, F. F., & Toledo-Roy, J. C. 2014, *ApJ*, 789, L33
- Eckart, A. 1983, Ph.D. Thesis, Westfälische Wilhelms Universität Münster, Germany
- Eckart, A., & Genzel, R. 1996, *Nature*, 383, 415
- Eckart, A., & Genzel, R. 1997, *MNRAS*, 284, 576
- Eckart, A., Schödel, R., & Straubmeier, C. 2005, *The black hole at the center of the Milky Way*, eds. Eckart, A., Schödel, R., & Straubmeier, C. (London: Imperial College Press)
- Eckart, A., Mužić, K., Yazici, S., et al. 2013, *A&A*, 551, A18
- Eckart, A., Horrobin, M., Britzen, S., et al. 2014, in *IAU Symp.*, 303, eds. L. O. Sjouwerman, C. C. Lang, & J. Ott, 269
- Eckart, A., Hüttemann, A., Kiefer, C., et al. 2017, *Foundations of Physics*, 47, 553
- Edwards, S., Hartigan, P., Ghandour, L., & Andrulis, C. 1994, *AJ*, 108, 1056
- Edwards, S., Fischer, W., Hillenbrand, L., & Kwan, J. 2006, *ApJ*, 646, 319
- Falcke, H., & Markoff, S. 2000, *A&A*, 362, 113
- Genzel, R., Eisenhauer, F., & Gillessen, S. 2010, *Rev. Mod. Phys.*, 82, 3121
- Ghez, A. M., Klein, B. L., Morris, M., & Becklin, E. E. 1998, *ApJ*, 509, 678
- Gillessen, S., Eisenhauer, F., Trippe, S., et al. 2009, *ApJ*, 692, 1075
- Gillessen, S., Genzel, R., Fritz, T. K., et al. 2012, *Nature*, 481, 51
- Gillessen, S., Genzel, R., Fritz, T. K., et al. 2013a, *ApJ*, 763, 78
- Gillessen, S., Genzel, R., Fritz, T. K., et al. 2013b, *ApJ*, 774, 44
- Gillessen, S., Plewa, P., Eisenhauer, F., et al. 2017, *ApJ*, 837, 30
- Guillochon, J., Loeb, A., MacLeod, M., & Ramirez-Ruiz, E. 2014, *ApJ*, 786, L12
- Haggard, D. 2017, in *IAU Symp.* 322, eds. R. M. Crocker, S. N. Longmore, & G. V. Bicknell, 1
- Haggard, D., Baganoff, F. K., Rea, N., et al. 2014, *ATel*, 6242, 1
- Hartmann, L., Hewett, R., & Calvet, N. 1994, *ApJ*, 426, 669
- Jalali, B., Pelupessy, F. I., Eckart, A., et al. 2014, *MNRAS*, 444, 1205
- Jones, T. J., Klebe, D., & Dickey, J. M. 1992, *ApJ*, 389, 602
- Kargaltsev, O., & Pavlov, G. G. 2007, *ApJ*, 670, 655
- Kokololova, L., Hough, J., & Levasseur-Regourd, A.-C. 2015, *Polarimetry of Stars and Planetary Systems* (Cambridge University Press)
- Lada, C. J. 1987, in *Star Forming Regions*, eds. M. Peimbert, & J. Jugaku, *IAU Symp.*, 115, 1
- Lang, K. R. 1978, *Astrophysical formulae. A compendium for the physicist and astrophysicist* (Berlin: Springer)
- Lorimer, D. R., & Kramer, M. 2012, *Handbook of Pulsar Astronomy* (Cambridge University Press)
- Madigan, A.-M., McCourt, M., & O'Leary, R. M. 2017, *MNRAS*, 465, 2310
- Manchester, R. N., Hobbs, G. B., Teoh, A., & Hobbs, M. 2005, *AJ*, 129, 1993
- Mapelli, M., & Ripamonti, E. 2015, *ApJ*, 806, 197
- Marrone, D. P., Baganoff, F. K., Morris, M. R., et al. 2008, *ApJ*, 682, 373
- McCourt, M., & Madigan, A.-M. 2016, *MNRAS*, 455, 2187
- McCourt, M., O'Leary, R. M., Madigan, A.-M., & Quataert, E. 2015, *MNRAS*, 449, 2
- McKee, C. F., & Hollenbach, D. J. 1980, *ARA&A*, 18, 219
- Mendigutía, I., Oudmaijer, R. D., Rigliaco, E., et al. 2015, *MNRAS*, 452, 2837
- Meyer, F., & Meyer-Hofmeister, E. 2012, *A&A*, 546, L2
- Meyer, L., Ghez, A. M., Witzel, G., et al. 2014, in *IAU Symp.*, 303, eds. L. O. Sjouwerman, C. C. Lang, & J. Ott, 264
- Mignani, R. P., De Luca, A., Hummel, W., et al. 2012, *A&A*, 544, A100
- Miralda-Escudé, J. 2012, *ApJ*, 756, 86
- Monnier, J. D., & Millan-Gabet, R. 2002, *ApJ*, 579, 694
- Mossoux, E., Grosso, N., Bushouse, H., et al. 2016, *A&A*, 589, A116
- Murray-Clay, R. A., & Loeb, A. 2012, *Nat. Commun.*, 3, 1049
- Mužić, K., Eckart, A., Schödel, R., et al. 2010, *A&A*, 521, A13
- Muzerolle, J., Calvet, N., & Hartmann, L. 1998, *ApJ*, 492, 743
- Narayan, R., Özel, F., & Sironi, L. 2012, *ApJ*, 757, L20
- Pejcha, O. 2014, *ApJ*, 788, 22
- Pfuhl, O., Gillessen, S., Eisenhauer, F., et al. 2015, *ApJ*, 798, 111
- Phifer, K., Do, T., Meyer, L., et al. 2013, *ApJ*, 773, L13
- Ponti, G., De Marco, B., Morris, M. R., et al. 2015, *MNRAS*, 454, 1525
- Prodan, S., Antonini, F., & Perets, H. B. 2015, *ApJ*, 799, 118
- Robitaille, T. P. 2011, *A&A*, 536, A79
- Rybicki, G. B., & Lightman, A. P. 1979, *Radiative Processes in Astrophysics* (Wiley)
- Sanchez-Bermudez, J., Hummel, C. A., Tuthill, P., et al. 2016, *A&A*, 588, A117
- Sądowski, A., Sironi, L., Abarca, D., et al. 2013, *MNRAS*, 432, 478
- Schartmann, M., Burkert, A., Alig, C., et al. 2012, *ApJ*, 755, 155
- Schartmann, M., Ballone, A., Burkert, A., et al. 2015, *ApJ*, 811, 155
- Scoville, N., & Burkert, A. 2013, *ApJ*, 768, 108
- Shahzamanian, B., Eckart, A., Zajaček, M., et al. 2016, *A&A*, 593, A131
- Shcherbakov, R. V. 2014, *ApJ*, 783, 31
- Siess, L., Dufour, E., & Forestini, M. 2000, *A&A*, 358, 593
- Sitariski, B., Ghez, A. M., Morris, M., et al. 2015, in *AAS Meeting Abstracts*, 225, 102.07
- Stephan, A. P., Naoz, S., Ghez, A. M., et al. 2016, *MNRAS*, 460, 3494
- Trani, A. A., Mapelli, M., Spera, M., & Bressan, A. 2016, *ApJ*, 831, 61
- Ulrich, R. K. 1976, *ApJ*, 210, 377
- Valencia-S., M., Eckart, A., Zajaček, M., et al. 2015, *ApJ*, 800, 125
- van Marle, A. J., Meliani, Z., Keppens, R., & Decin, L. 2011, *ApJ*, 734, L26
- Vollmer, B., & Duschl, W. J. 2000, *New Astron.*, 4, 581
- Whitney, B. A. 2011, in *Fluid Flows to Black Hole: A Tribute to S. Chandrasekhar on His Birth Centenary*, eds. D. J. Saikia, & V. Trimble (World Scientific Publishing Co), 151
- Wilkin, F. P. 1996, *ApJ*, 459, L31
- Witzel, G., Ghez, A. M., Morris, M. R., et al. 2014, *ApJ*, 796, L8
- Yuan, F., & Narayan, R. 2014, *ARA&A*, 52, 529
- Yuan, Q., & Wang, Q. D. 2016, *MNRAS*, 456, 1438
- Zajczyk, A., Gallant, Y. A., Slane, P., et al. 2012, *A&A*, 542, A12
- Zajaček, M., Karas, V., & Eckart, A. 2014, *A&A*, 565, A17
- Zajaček, M., Eckart, A., Peissker, F., Karssen, G. D., & Karas, V. 2015, in *Proc. 24th Annual Conf. Doctoral Students – WDS 2015 – Physics*, eds. J. Safrankova, & J. Pavlu (Prague, Matfyzpress), 27
- Zajaček, M., Eckart, A., Karas, V., et al. 2016, *MNRAS*, 455, 1257
- Zhang, Q., & Zheng, X. 1997, *ApJ*, 474, 719
- Zhao, J.-H., Young, K. H., Herrnstein, R. M., et al. 2003, *ApJ*, 586, L29
- Zhao, J.-H., Morris, M. R., Goss, W. M., & An, T. 2009, *ApJ*, 699, 186
- Zhao, J.-H., Morris, M. R., & Goss, W. M. 2013, *ApJ*, 777, 146
- Zharikov, S. V., Zyuzin, D. A., Shibanov, Y. A., & Mennickent, R. E. 2013, *A&A*, 554, A120
- Zyuzin, D., Zharikov, S., Shibanov, Y., et al. 2016, *MNRAS*, 455, 1746

Appendix A: Viewing angle of the bow shock

We present the calculation of an expected angle between the symmetry axis of the bow shock structure and the line of sight as a function of time (with respect to the peribothron). In the calculation, we use the orbital elements as derived by Valencia-S. et al. (2015). We use the convention, in which 0 degrees corresponds to the front view of the bow shock, 180 degrees is the view from the tail portion, and 90 degrees corresponds to the side view. We include three possible cases: a negligible motion of the medium, an outflow of 1000 km s^{-1} , and an inflow of 1000 km s^{-1} , see Fig. A.1.

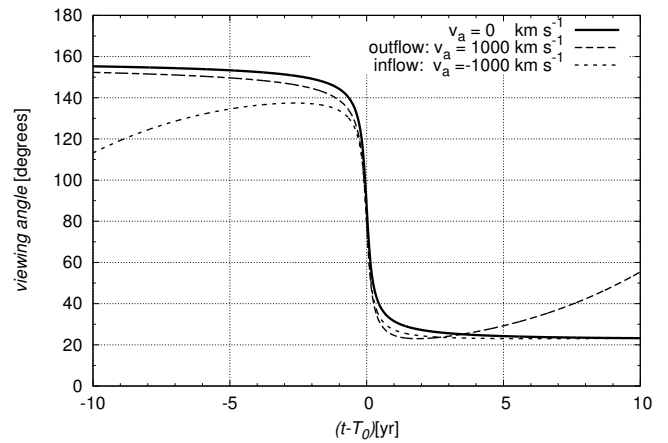


Fig. A.1. Viewing angle of the bow shock as a function of time for a negligible motion of the medium, an outflow of 1000 km s^{-1} , and an inflow of 1000 km s^{-1} (see the key).

A short review on the DSO

Given the amount of continuum and line-emission data of the Dusty S-cluster Object (DSO/G2), we give an overview of proposed interpretations of the phenomenon. We briefly discuss basic proposed scenarios – from the core-less cloud/streamer, through the dust-enshrouded (young) star, to binary models. The focus is given on the detection of linearly polarized emission in K_s band ($2.2\ \mu\text{m}$) as analysed by [Shahzamanian et al. \(2016\)](#). Subsequently, we provide the description of the model of a dust-enshrouded star with a non-spherical dusty envelope, which can match the total as well as the polarized flux density of the source. Towards the end, we give an overview of *in-situ* star-formation scenarios in the Galactic centre region: disc-based and infall-based.

The review was peer-reviewed and published in the Observatory (A Review of Astronomy).

Credit: Zajaček, Eckart, and Shahzamanian, The Observatory 137, 112 (2017). Reproduced with the permission of ©the Editors of the Observatory.

gravitational-wave emission, at least to low orders we can compete or be more precise than *LIGO*, and I think that's the beauty of combining these methods. By completely different methods, completely different régimes if the theory is correct, it has to fit all across the parameter space and that's where the power lies in the combination of the two methods.

Professor P. G. Murdin. How close are you to being in a position of not having accurate enough terrestrial clocks to do this?

Professor Kramer. Fortunately, we're still on the safe side. First of all, our clock colleagues are making superb progress: they now have precisions of down to 10^{-21} . But as those clocks are only stable for weeks to months, they hand over from clock to clock, while our pulsar time-scales are accurate over years and decades. So for the instantaneous measurement, we don't run into problems and that's the real measurement we do. When we do the instantaneous measurement, we refer it to an atomic clock in the observatory, do the GPS transfer, correct it to atomic time and international time. We can, however, — and this is a nice experiment — show by just looking at pulsars, that our colleagues in Paris at the BIPM tune their atomic clocks from time to time. We see this in our signal because suddenly, we see some deviation that is common to all the pulsars. Nothing is secret. [Laughter.] So I think again, we're feeding off each other and helping each other.

The President. Michael, thank you very much indeed, and thanks for a wonderful George Darwin Lecture. [Applause.] So that concludes today's programme. May I invite you to a seasonal drinks reception in the RAS library immediately following this meeting, and I give notice that the next Open Meeting of the Society will be on Friday, 13th of January 2017. Finally, a happy Christmas to Fellows and visitors. [Applause.]

POLARIMETRY NARROWS DOWN THE POSSIBILITIES FOR THE
DUSTY S-CLUSTER OBJECT (DSO/G2) IN THE GALACTIC CENTRE

*By Michal Zajaček, Andreas Eckart & Banafsheh Shahzamanian
University of Cologne*

There have been many speculations about the character of the dusty object moving fast in the vicinity of the Galactic-centre black hole. The recent detection of polarized continuum emission provides new constraints for the models. The fact that the object is intrinsically polarized implies that it is non-spherical. The authors propose that a young star developing a bow shock can explain the main characteristics. However, more observations in the future are needed for the final confirmation of the nature of the source.

Discussion

The object known as the Dusty S-cluster Object (DSO; where S-cluster is the name of the innermost stellar cluster in the Galactic centre), often also denoted as G2, was considered shortly after its discovery¹ as a small gas and dust cloud of only three Earth masses. However, subsequent monitoring by the *Very Large Telescope* of the European Southern Observatory as well as the *Keck* telescopes has shown that the object does not tidally stretch in a way we would expect for a simple core-less gas cloud. Instead, the dusty source has stayed more compact than expected and survived intact the close passage to the black hole in the spring of 2014^{2,3}.

Despite the compactness, the dispute about the character of the object has continued, mainly because it has not been possible to resolve directly the internal structure of the enigmatic object, as is possible, for example, for nearby young stars in the Orion star-forming region. To make things more complicated, some experts claim^{1,4} that they do detect the tidal stretching of the source. As a result, many scenarios for the nature of the DSO have been proposed. They can be mostly grouped into three categories: a core-less cloud¹ or streamer^{4,5}, a dust-enshrouded star^{6,7}, and a binary scenario — either binary merger^{3,8} or disruption⁷ of both components, where one of them can escape the Milky Way entirely as a so-called hypervelocity star.

However, there is a way to go partially around the angular-resolution problem. One can try to study the polarization properties of the incoming electromagnetic signal to see if the source as a whole is polarized or not. Polarized sources have a preferred plane in which the electric-field vectors are oscillating, which gives hints about their internal geometry as well as radiative processes.

It was quite a surprise when it was discovered⁹ that the DSO is an intrinsically polarized source in the near-infrared K_s -band (2.2 micrometres). Whereas surrounding stars close to its position have a degree of polarization close to zero, the DSO exhibits a polarization degree of around 30 percent for four consecutive epochs (2008, 2009, 2011, and 2012). This implies that the source must deviate from spherical symmetry, otherwise the individual polarization contributions would cancel out.

The detection of polarized emission puts a new constraint on the character of the object. In general, the DSO is a very faint source in an extremely crowded stellar field: the number density of stars in the central few light years is about 10 million times that in the Sun's neighbourhood. Therefore disentangling the emission of the DSO from that of the surrounding sources is often challenging. In addition, it is not possible to resolve the brightness distribution as it is for nearby objects. As a consequence, it is necessary to combine carefully orbital dynamics, spectral properties, and, at last, the polarimetry, to see the full picture of the mosaic.

In the polarization-detection paper, the authors⁹ also construct a numerical radiative-transfer model of the DSO. The model consists of typical ingredients of young stars: a star at the centre of the DSO is the source of thermal photons, and is surrounded by a dusty envelope and bipolar cavities due to outflows, which together re-process the emission of the star — UV and optical photons are absorbed by dust particles and re-emitted at longer wavelengths, mostly in the near- and mid-infrared domains. Furthermore, the photons emitted by the star and the dust are scattered by dust particles, which is the source of polarized emission in the model.

Moreover, since the DSO is expected to move supersonically close to the black hole, a bow shock is formed ahead of the star¹⁰. All of these components, which one would expect for a supersonic young star in the Galactic-centre region, lead to a significantly non-spherical nature of the source, which gives rise to the overall polarized near-infrared emission. Not only is the model successful in explaining the polarization properties, it can also match other observed characteristics of the DSO, namely a significant near-infrared excess or ‘reddening’ due to dust emission and broad hydrogen-emission lines, which arise due to the Doppler broadening either because of the material flowing towards the star (accretion) or by gas outflows or winds, which are both typical features of young stars².

It could be argued that the overall non-spherical shape is caused by the gradual prolongation of the gaseous component by tidal forces rather than the model described. However, the DSO/G2 source does not show convincing signs of tidal interaction in either line or continuum emission^{2,3}. Tidal stretching would be expected for a core-less cloud or a star with an extended envelope with a length-scale of about 100 AU. In that case the source would be tidally stretched along the orbit by a factor of a few², which was not detected during the peribothron passage^{2,3}, when the effects of the orbital foreshortening are minimized. In fact, the DSO is fully consistent with being a point source³.

Therefore, based on the compactness and a prominent IR excess, a pre-main-sequence star surrounded by a non-spherical dusty envelope (envelope with bipolar cavities) seems to be a more natural scheme to explain the continuum and line-emission characteristics. In the framework of this scenario, a bow shock forms due to an expected supersonic motion close to the pericentre, which further breaks the spherical symmetry.

Further monitoring of the source will help us to test the proposed model, mainly by the means of orbital dynamics. If the motion of the source does not deviate from a simple Keplerian ellipse, it must be a compact object, not a cloud. On the other hand, the core-less cloud would sooner or later start spiralling in towards the black hole because of the interaction with the surrounding ambient medium.

It remains a small puzzle, though, how such a young star as proposed to explain the DSO phenomenon can be formed and subsequently orbit so close to the black hole for such a long period of time — possibly several-hundred-thousand years, which is the estimated age of class 0 and class I protostellar objects². Thanks to the computer modelling, this problem can be partially tested by means of numerical experiments. It was already confirmed¹¹ that *in-situ* star formation close to the black hole can take place when a cold molecular cloud of about 100 solar masses falls in towards the black hole from the region where there is a molecular circum-nuclear disc that contains clumps of a similar mass (approximately 1.5–6 parsecs from Sgr A*). In this model, the critical density for the onset of the collapse is reached by the tidal focussing because of the black hole’s gravity — one can talk about so-called ‘black-hole-assisted’ star formation. Another proposed scenario is the gravitational instability and the fragmentation of a massive accretion disc encircling the black hole¹², which is supported by the observed stellar disc containing massive young stars with an age of only a few million years. On-going star formation in the central 2 parsecs was also supported by recent radio and infrared observations¹³ in terms of finding localized water and SiO masers and identifying infrared-excess sources whose spectral energy distribution is consistent with massive young stellar objects.

Since the star formation close to the massive black hole has many intricacies, several important details of how stars are formed at the Galactic centre remain still blurred. New, powerful instruments in the near future, such as the *James Webb Space Telescope* or *European Extremely Large Telescope*, will certainly shed new light on the problem. Regardless of some remaining theoretical problems, the observations seem to show that star formation can proceed in different environments throughout the Galaxy — from the close vicinity of the supermassive black hole at the Galactic centre all the way to the Galaxy outskirts.

References

- (1) S. Gillessen *et al.*, *Nature*, **481**, 51, 2012.
- (2) M. Valencia *et al.*, *ApJ*, **800**, 125, 2015.
- (3) G. Witzel *et al.*, *ApJ*, **796**, L8, 2014.
- (4) O. Pfuhl *et al.*, *ApJ*, **798**, 111, 2015.
- (5) M. McCourt & A.-M. Madigan, *MNRAS*, **455**, 2, 2016.
- (6) A. Eckart *et al.*, *A&A*, **551**, A18, 2013.
- (7) M. Zajaček, V. Karas & A. Eckart, *A&A*, **565**, A17, 2014.
- (8) A. P. Stephan *et al.*, *MNRAS*, **460**, 4, 2016.
- (9) B. Shahzamanian *et al.*, *A&A*, **593**, A131, 2016.
- (10) M. Zajaček *et al.*, *MNRAS*, **455**, 2, 2016.
- (11) B. Jalali *et al.*, *MNRAS*, **444**, 2, 2014.
- (12) Y. Levin & A. M. Beloborodov, *ApJ*, **590**, L33, 2003.
- (13) F. Yusef-Zadeh *et al.*, *ApJ*, **808**, 97, 2015.

SPECTROSCOPIC BINARY ORBITS FROM PHOTOELECTRIC RADIAL VELOCITIES

PAPER 254: HD 155878, HD 156613, HD 159027, AND HD 162054

*By R. F. Griffin
Cambridge Observatories*

The stars mainly discussed in this paper are all between about the eighth and ninth magnitudes and are located in the constellation Hercules. They came to attention as binaries in the course of the writer's 'Clube Selected Areas' programme¹ of radial-velocity observations (recent succinct descriptions of which may be found in the *Introductions* to Papers 251 and 253^{2,3}). HD 159027 and HD 162054 are in Area 1, and so is HD 155878 although it was not actually on the Clube programme, while HD 156613, which is at a somewhat higher declination, is in Area 2. All except for HD 162054 are *Hipparcos* stars, and they all have good magnitudes and colour indices determined by the satellite's *Tycho* programme. In no case has the companion star been apparent in the radial-velocity traces.

Interaction modes of neutron stars

Currently we observe many young, massive stars as well as older late-type stars in the Galactic centre. Based on this it is possible to approximately reconstruct the recent star-formation history of the Galactic centre. Because of several episodes of star formation, neutron stars should be present in the Nuclear star cluster as end-products of massive star evolution, in a similar way as they occur in globular clusters ([Freire et al. 2003](#)).

Isolated neutron stars of different ages have a characteristic distribution of periods and magnetic field intensities. Even older isolated neutron stars have still magnetic fields large enough to effectively interact with the plasma environment in the Galactic centre region. Since the environment has significant density gradients, especially in the minispiral region, I dedicated some time to study the distribution of interaction modes of neutron stars as a function of the temperature and the density of the ambient medium, and different distributions of periods and magnetic field intensities of neutron stars.

These results are included in the peer-reviewed paper published in *Acta Polytechnica*, which is a part of IBWS 2014 proceedings.

Credit: Zajaček, Karas, & Kunneriath, *Acta Polytechnica* 55, 203 (2015). Reproduced with permission ©Czech Technical University in Prague.

GALACTIC CENTER MINISPIRAL: INTERACTION MODES OF NEUTRON STARS

MICHAL ZAJAČEK^{a,b,c,d,*}, VLADIMÍR KARAS^c, DEVAKY KUNNERIATH^c^a *I. Physikalisches Institut der Universität zu Köln, Zùlpicher Strasse 77, D-50937 Köln, Germany*^b *Max-Planck-Institut für Radioastronomie (MPIfR), Auf dem Hügel 69, D-53121 Bonn, Germany*^c *Astronomical Institute, Academy of Sciences, Boční II 1401, CZ-14131 Prague, Czech Republic*^d *Charles University in Prague, Faculty of Mathematics and Physics, V Holešovičkách 2, CZ-18000 Prague, Czech Republic** corresponding author: michal.zajacek31@gmail.com

ABSTRACT. Streams of gas and dust in the inner parsec of the Galactic center form a distinct feature known as the Minispiral, which has been studied in radio waveband as well as in the infrared wavebands. A large fraction of the Minispiral gas is ionized by radiation of OB stars present in the Nuclear Star Cluster (NSC). Based on the inferred mass in the innermost parsec ($\sim 10^6$ solar masses), over $\sim 10^3$ – 10^4 neutron stars should move in the sphere of gravitational influence of the SMBH. We estimate that a fraction of them propagate through the denser, ionized medium concentrated mainly along the three arms of the Minispiral. Based on the properties of the gaseous medium, we discuss different interaction regimes of magnetised neutron stars passing through this region. Moreover, we sketch expected observational effects of these regimes. The simulation results may be applied to other galactic nuclei hosting NSC, where the expected distribution of the interaction regimes is different across different galaxy types.

KEYWORDS: galaxy center; individual objects; Sagittarius A; neutron stars.

1. INTRODUCTION

The Galactic center hosts the supermassive black hole (SMBH) observed as the compact radio source Sgr A* which is surrounded by the Nuclear star cluster (NSC) and gaseous-dusty structures, such as HII Minispiral arms of Sgr A West, supernova remnant Sgr A East, molecular clouds, and the Circumnuclear disk [1, 2]. It is the closest SMBH and hence its environment can be studied with the highest resolution among galactic nuclei in the radio-, mm-, submm-, infrared, and X-ray wavebands [2]. However, despite high-resolution multiwavelength studies several processes are still not satisfactorily explained, such as the star-formation near the SMBH, the feeding and feedback of Sgr A*, and the distribution of the magnetic field and its interaction with other stellar and non-stellar components.

The observations of the Galactic center region revealed a large population of young massive stars orbiting the SMBH as close as ~ 0.1 pc [3]. In fact, the NSC seems to be one of the densest concentrations of young massive stars in the Galaxy [1]. On the other hand, there is an observable flat distribution of late-type stars with a radius of as much as $10''$ [4, 5]. Thus, a steep relaxed Bahcall-Wolf cusp of stars with a slope of $7/4$ or $3/2$ [6, 7] is probably absent [5, 8].

The estimates of the number of stellar remnants that use the power-law initial mass function (IMF) (standard Salpeter or top-heavy) combined with the mass segregation over the age of the bulge (~ 10 Gyr)

lead to a considerable population of stellar black holes of the order of $\sim 10^4$ [9, 10]. The same order is expected for neutron stars based on multiwavelength statistical studies [11]. Based on the total X-ray luminosity of the innermost parsec, [12] set an upper limit on the number of compact remnants ($\lesssim 40000$).

Such an abundant population of neutron stars exhibiting strong magnetic fields could be utilized to further extend our knowledge about the processes in the Galactic center. The observations of neutron stars (pulsars as well as X-ray sources) near the SMBH would contribute to:

- our understanding of the star formation processes near the Galactic center using the number and the age distribution of observed sources,
- mapping the gravitational potential near the SMBH using their period derivatives,
- constraining the electron density profile in the Galactic center using their dispersion measures.

Despite continued efforts only very few pulsars have been detected in the broader Galactic center region. It is thought that the lack of detections is due to profound interstellar dispersion and scattering. However, there are observational hints that such a population is present. [13] report the discovery of two highly dispersed pulsars with angular separation $\lesssim 0.3^\circ$ from the Galactic center. [14] confirm the detection of three pulsars with large dispersion measures with an offset of $\sim 10'$ – $15'$ from Sgr A*. There is an indication of the

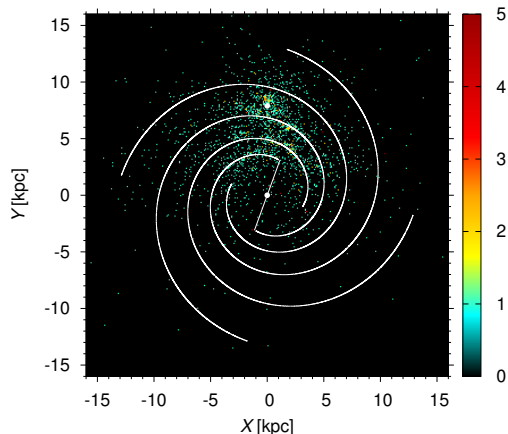


FIGURE 1. The distribution of 2302 pulsars in the XY Galactic plane. Four logarithmic spiral arms are marked by white lines. Sgr A* and the Sun are labelled as white points at position (0,0) kpc and (0, 7.9) kpc, respectively. The data are taken from the ATNF Pulsar Catalogue <http://www.atnf.csiro.au/research/pulsar/psrcat> [16].

relation between the Sgr A East SNR and the “Cannonball” source, which was detected in both the X-ray and radio wavebands and appears to be a pulsar wind nebula (PWN) [15]. This shows that neutron stars can form directly in the Galactic center environment.

In the innermost parsec only one magnetar PSR J1745-2900 was affirmed by independent detections [17–19] at a projected distance of $\sim 2.4 \pm 0.3''$ from Sgr A*, having a period of 3.7635537(2) [20]. The consequence of the lack of sensitivity to detect more neutron stars in the Bulge and the Galactic center is shown in Figure 1, where most of the detected sources are concentrated relatively close to the Sun.

In this contribution we aim to clarify the distribution of the interaction modes of neutron stars in the Galactic center. Based on the results we discuss the possibility of detecting neutron stars in the innermost parsec indirectly, specifically by looking for bow-shock structures similar to that of the “Cannonball” [15].

The structure of the paper is as follows. In Section 2 we explain the set-up of the model and the methods that are employed, including the introduction to a simple, analytical theory of interaction modes of neutron stars that is, however, sufficient for our purposes. Subsequently, in Section 3 we study the distribution of interaction modes in the innermost parsec of the Galaxy. In Section 4 we discuss the consequences of this distribution and the possibilities of detecting a fraction of the population indirectly. Finally, we summarize our conclusions in Section 5.

2. SET-UP OF THE MODEL AND METHODS

In our model we concentrate on the innermost parsec of the Galactic center, which lies within the sphere

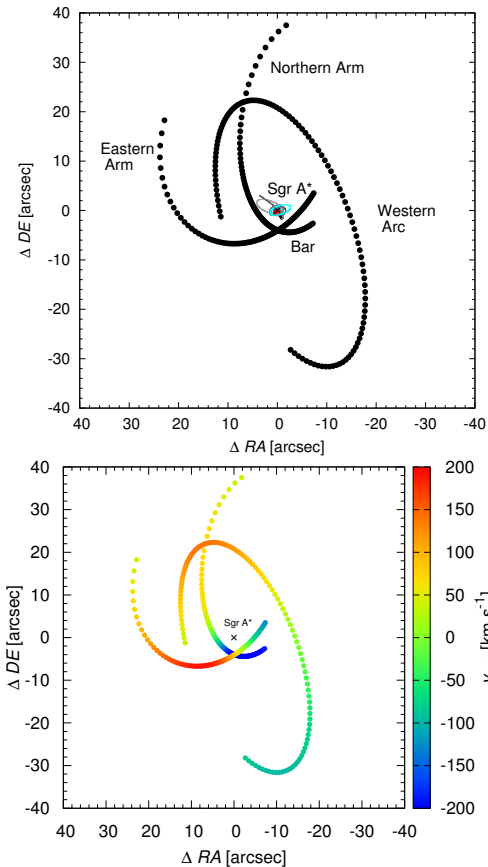


FIGURE 2. The Minispiral model. Top panel: the nomenclature of the main components. Bottom panel: Keplerian velocity profile of the gaseous material according to [21, 22].

of influence of the supermassive black hole (Sgr A*) with the radius r_{SI} :

$$r_{SI} \approx 1.7 \left(\frac{M_{\bullet}}{4.0 \times 10^6 M_{\odot}} \right) \left(\frac{\sigma}{100 \text{ km s}^{-1}} \right)^{-2}, \quad (1)$$

where M_{\bullet} is the central black hole mass and σ is the stellar velocity dispersion.

Since we are studying processes that occur at a distance of $\gtrsim 1000$ gravitational radii from the SMBH we approximate the gravitational field by a Newtonian point mass of $M_{\bullet} = 4.0 \times 10^6 M_{\odot}$ [1, 2]. We employ a Monte Carlo approach for studying the rate of interactions between neutron stars and gaseous-dusty structures. Initially, we generate the orbits of neutron stars that do not interact with each other and with other stellar and non-stellar components of the NSC except for the SMBH. Hence, the orbital elements of individual stars do not change in the course of the simulation. Although this may seem an oversimplification, it is sufficient for statistical studies of the distribution of interaction modes.

The thermal HII region of Sgr A West known as the Minispiral has been studied in the radio-, mm-, and

infrared wavelengths [21–23]. It consists of four main components: the Northern Arm, the Western Arc, the Eastern Arm, and the Bar (see Figure 2) [21–23]. The Minispiral consists of a mixture of ionised and neutral gas and dust, with temperature ranging from ~ 100 K for dust up to 10^4 K for the hot ionised gas phase. The inferred electron densities are $\sim 10^4$ – 10^5 cm^{-3} [21, 22].

In our simplified model the Minispiral is represented as a system of spherical clumps along the three arms (~ 20 for each arm) with the length-scale of each clump 1–2 arcsec. The density and temperature profiles are taken from [21–23], but we also analyse the interaction modes for values outside this range. The velocity profile is assumed to be roughly Keplerian, consisting of three streams as inferred from observations by [21, 22] (see Figure 2). We note that deviations from Keplerian motion were also detected, probably due to magnetohydrodynamic effects [21, 22].

2.1. INTERACTION MODES OF MAGNETIZED NEUTRON STARS

Many observed neutron stars exhibit considerable magnetic fields, in the case of pulsars most frequently of the order of 10^{12} Gauss. The warm ionized gas that is also detected close to the Galactic centre, specifically in the Sgr A West region (see, e.g., [23] and references therein) has high electric conductivity that is proportional to its temperature, $\lambda_e \approx 10^7 T_e^{3/2} \text{ cm}^{-1}$. Therefore, this plasma must interact effectively with the large magnetic field of neutron stars. Consequently, we need magnetohydrodynamic (MHD) equations describing the gas dynamics in the potential of a neutron star. In fact, if we are close to the neutron star surface, we have to solve a system of relativistic magnetohydrodynamic equations (RMHD), which is often difficult for real systems.

In our analysis, we focus on the fundamental characteristics of the interaction of a rotating magnetized neutron star with the plasma in the surroundings. This interaction consists of two parts: *gravitational interaction* characterized by an accretion rate \dot{M} of the captured medium; and *electromagnetic interaction* which is described by a magnetic dipolar moment μ and by a rotational period of a neutron star P . These three basic parameters, \dot{M} , μ , and P , are further complemented by the mass of neutron star M_{NS} and the relative velocity with respect to the medium v_∞ . In fact, neutron stars are a part of the broader class of *gravimagnetic rotators* characterized by mass M , angular momentum $\mathbf{J} = I\boldsymbol{\Omega}$, and the magnetic field, which is as the first approximation characterized by the dipole moment $\boldsymbol{\mu}$.

In order to simplify the problem, we consider the following assumptions:

(a) the interaction takes place far from the neutron star surface, so relativistic approach is not necessary,

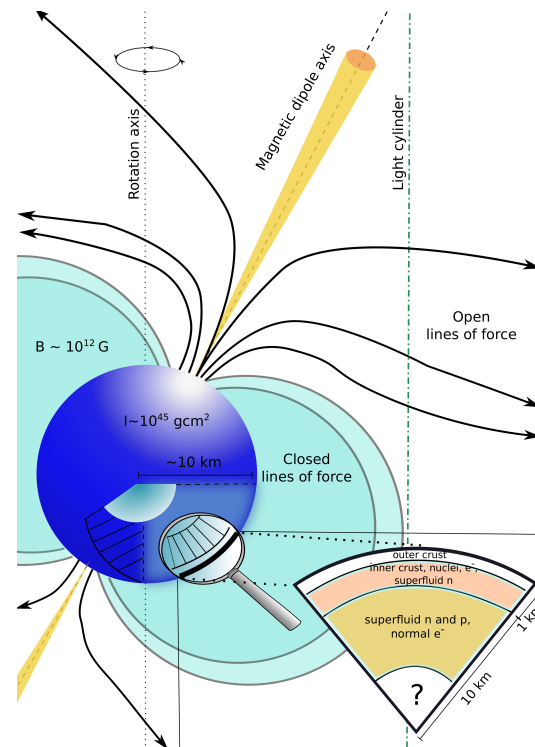


FIGURE 3. Sketch of a canonical pulsar. In the lower right corner, a cross-section of the neutron star is depicted with two basic components: the crust and the superfluid neutron interior. Magnetic field lines are closed up to the light cylinder. Closer to the magnetic pole, field lines open and relativistic particles escape.

(b) the electromagnetic part of the interaction is independent of the accretion flux parameters,

(c) the intrinsic magnetic field of neutron stars is a dipole field.

Let us make a few notes concerning the the assumptions (a), (b), and (c). Point (a) means that the interaction of interstellar plasma with the magnetic field or a relativistic particle wind of the neutron star takes place at $r \gg GM_{\text{NS}}/c^2$, which is often the case. Assumption (b) means that infalling plasma does not distort the intrinsic magnetic field of the neutron star significantly. Point (c) is approximately valid due to the conservation of the magnetic flux. The ratio of the quadrupole q and dipole μ components of the field scales with the stellar radius as $q/\mu \propto R$ during the core-collapse, so the field is effectively cleansed of higher multipole components. The dipole field is the most representative component far away from the surface, where the interaction with the ambient medium takes place. The closer to the surface the matter gets, the more important the quadrupole and the higher multipole components become.

Given assumptions (a), (b), (c), the problem becomes much simpler and many effects of the interaction are thus neglected. However, one still gets basic

information about the character and the scale of the interaction if fundamental parameters of the neutron star and those of the ambient medium are given.

For a non-rotating neutron star, the harmonic surface current $j \approx \sin \theta$ induces a dipole field outside the sphere having the following form:

$$\mathbf{B}_d = \frac{2\mu \sin \theta}{r^3} \mathbf{e}_r - \frac{\mu \cos \theta}{r^3} \mathbf{e}_\theta, \quad (2)$$

where \mathbf{e}_r and \mathbf{e}_θ are unit vectors, μ denotes the dipole moment. The angle θ is measured from the axis perpendicular to the dipole field axis (see the sketch in Figure 3). The magnetic field magnitude B_0 at the poles is twice as big as at the equator, which follows from the magnitude relation $B_d = \mu/r^3(1+3 \sin^2 \theta)^{1/2}$. The magnetic dipole moment is given by the field magnitude at the poles B_0 and the neutron star radius R_{NS} , $\mu = 1/2 B_0 R_{\text{NS}}^3$, yielding typical values $\mu \approx 1/2(2 \times 10^{12} \text{ Oe}) \times 10^{18} \text{ cm}^3 = 10^{30} \text{ Oe cm}^3$.¹

In the case of a rotating dipole, the electric component of the electromagnetic field also has to be considered. If the rotational axis of a neutron star is inclined with respect to the dipole axis by angle α , the neutron star emits electromagnetic dipole radiation at rotational frequency Ω . In the frame of this model, there exists the distance $R_l = c/\Omega$, below which the electromagnetic field is static and the electric component is given by $E \approx v/c B = (\Omega r/c) B = (r/R_l) B$. While approaching the radius of the light cylinder, R_l , the electric component becomes comparable to the magnetic component. On the crossing of the light cylinder, the electromagnetic field is no longer static and it becomes a propagating electromagnetic wave. The magnetic dipole radiation carries away energy that may be written in terms of the magnetic dipole μ ,

$$\frac{dE_{\text{rad}}}{dt} = \frac{2}{3c^3} \mu^2 \Omega^4 \sin^2 \alpha. \quad (3)$$

Gaseous environment and possible modes of accretion. A neutron star is assumed to pass through an ideally conducting plasma of density ρ_∞ , temperature T_∞ , and the sound speed c_∞ at infinity. We also consider the relative motion of a star with respect to the surrounding medium, $v = v_*$. The plasma starts falling onto the neutron star, due to its attraction. In the case of neutron stars with a negligible magnetic field, the stationary flow of matter, or the capture rate, is given by the Bondi-Hoyle-Lyttleton relation (cf., e.g., [24]):

$$\dot{M}_c = \delta \frac{(2GM_{\text{NS}})^2}{(v_*^2 + c_\infty^2)^{3/2}} \rho_\infty, \quad (4)$$

where δ is a dimensionless factor of the order of unity. Defining the capture cross-section $\sigma_G = \delta \pi R_G^2$, with R_G denoting the capture radius,

$$R_G = \frac{2GM_{\text{NS}}}{v_*^2 + c_\infty^2}, \quad (5)$$

¹1 Oe is a unit of \mathbf{H} field in cgs units. The equivalent in SI units is 1 A/m, 1 A/m = $(4\pi \cdot 10^{-3})$ Oe.

we may use a convenient form of the capture rate:

$$\dot{M}_c = \sigma_G \rho_\infty v_*. \quad (6)$$

In realistic astrophysical problems, quantities T_∞ , ρ_∞ , and c_∞ are taken at finite distances, $R \gg R_G$.

Possible accretion modes may be divided into three distinct groups:

- $v_* \ll c_\infty$; spherical accretion, without angular momentum in accreting matter,
- $v_* \gg c_\infty$; cylindrical accretion – axially-symmetric accretion, without angular momentum in the accreting matter,
- the disk accretion, infalling matter has a considerable angular momentum.

The following critical radii can be distinguished in agreement with the terminology of [25].

Stopping radius. Neutron stars as gravimagnetic rotators attract ionized matter due to gravitational forces on the one hand, and they prevent accretion due to electromagnetic forces on the other. In the rotating dipole model, the electromagnetic field is stationary inside the light cylinder, $R_l = c/\Omega$, and changes into a freely propagating electromagnetic wave beyond it.

The luminosity L_m of the magnetic dipole radiation may be estimated by (3), $L_m = dE_{\text{rad}}/dt$. Goldreich and Julian [26] found out that near the magnetic axis of the neutron star, which is inclined by a small angle with respect to the rotational axis, the electric component is directed along the magnetic field, $E \approx (\Omega r/c) B_0$, and it accelerates charged particles beyond the light cylinder up to relativistic energies, which effectively forms a *pulsar wind*. It is assumed that this wind becomes frozen in the surrounding medium and passes its impulse to it.

The pressure of the wind may be estimated as $P_{\text{ej}} = L_m/(4\pi r^2 v_{\text{ej}})$. However, it may happen that the accreted plasma penetrates into the region surrounded by the light cylinder. It is prevented from accretion onto the surface by the pressure of the static magnetic field, $P_m = B^2/(8\pi) = \mu^2/(8\pi r^6)$. To sum up, the pressure of electromagnetic forces is of a different character inside and outside the light cylinder, and may be approximated by the following relations:

$$P_m = \begin{cases} \frac{\mu^2}{8\pi r^6} & \text{if } r \leq R_l, \\ \frac{L_m}{4\pi r^2 c} & \text{if } r > R_l. \end{cases} \quad (7)$$

Using the light cylinder radius, R_l , we may rewrite the dipole radiation luminosity of the neutron star L_m , (3), into the form:

$$L_m = \kappa_t \frac{\mu^2}{R_l^3} \Omega, \quad (8)$$

where $\kappa_t = 2/3 \sin^2 \alpha$ is a dimensionless factor. Using (8), the electromagnetic pressure acting on the surrounding gas expressed by (7) may be rewritten into

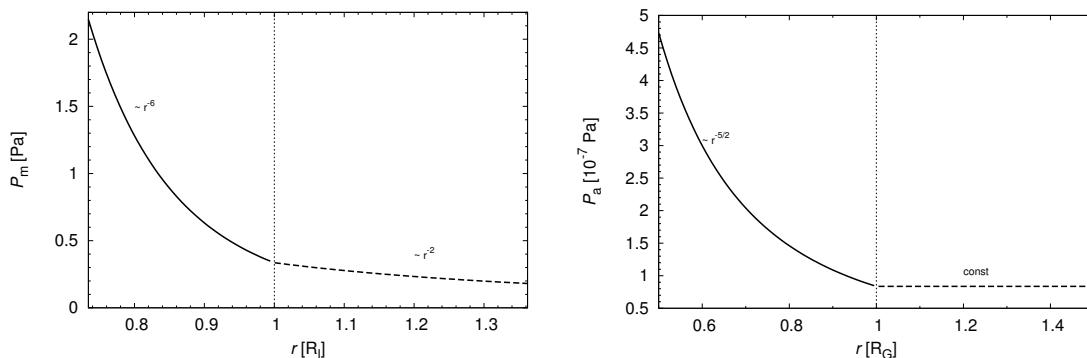


FIGURE 4. Left panel: the pressure exerted by a stationary magnetic field varies as $\sim r^{-6}$, whereas outside the light cylinder the pressure of relativistic particles that act on infalling plasma falls off with distance as $\sim r^{-2}$. The distance is expressed in light radii (R_l). Right panel: the pressure caused by accreted plasma is approximately constant beyond the gravitational capture radius, whereas for smaller radii gas falls freely and the pressure increases as $\sim r^{-5/2}$ while approaching the star. The units are expressed in gravitational capture radii (R_G).

the following relations:

$$P_m = \begin{cases} \frac{\mu^2}{8\pi r^6} & \text{if } r \leq R_l, \\ \frac{\kappa_t \mu^2}{4\pi R_l^4 r^2} & \text{if } r > R_l. \end{cases} \quad (9)$$

Electromagnetic pressure P_m is continuous for $\kappa_t = 1/2$ at $r = R_l$.

Matter being accreted onto the neutron star exerts pressure, which is approximately constant beyond the gravitational capture radius R_G and is equal to $1/2\rho_\infty v_\star^2$. For radii smaller than capture radius R_G , matter falls almost freely and exerts dynamic pressure $1/2\rho(r)v(r)^2$. Under the assumption of spherical accretion, $\dot{M}_c = 4\pi r^2 \rho(r)v(r)$, which becomes $\dot{M}_c = 4\pi R_G^2 \rho_\infty v_\star$ beyond the capture radius, the accretion pressure P_a can be estimated as follows:

$$P_a = \begin{cases} \frac{\dot{M}_c v_\star}{8\pi R_G^2} & \text{if } r > R_G, \\ \frac{\dot{M}_c v_\star}{8\pi r^2} \left(\frac{R_G}{r}\right)^{1/2} & \text{if } r \leq R_G. \end{cases} \quad (10)$$

The accretion pressure is a continuous function according to (10).

Both the electromagnetic pressure P_m and the accretion pressure P_a as functions of distance are plotted in Figure 4 for the following set of parameters: $P = 1$ s, $B_0 = 2 \times 10^{12}$ G, $R_0 = 10^6$ cm, $n_H = 10^4$ cm $^{-3}$, $T_e = 6 \times 10^3$ K, $M_{NS} = 1.4 M_\odot$, $v_\star = 100$ km s $^{-1}$.

The plasma being accreted by a neutron star is halted at the *stopping radius* where the pressure of the electromagnetic forces is in balance with the pressure of the accreted matter. The stopping radius may be derived from the following condition:

$$P_m = P_a. \quad (11)$$

If the pressure of electromagnetic forces is represented by the pressure of a static dipole field, then (11) yields the Alfvén radius, R_A . If the electromagnetic pressure P_m is related to the outflow of relativistic particles (pulsar wind), then the corresponding radius

is the so-called Shvartsman radius, R_{Sh} . The stopping radius may therefore be expressed as [25]:

$$R_{st} = \begin{cases} R_A & \text{if } R_{st} \leq R_l, \\ R_{Sh} & \text{if } R_{st} > R_l. \end{cases} \quad (12)$$

For the case when $R_{st} \leq R_l$, the Alfvén radius is given by the corresponding relations in (9) and (10), so again we get two cases for distances larger or smaller than the capture radius R_G :

$$R_A = \begin{cases} \left(\frac{4\mu^2 G^2 M_{NS}^2}{M_c v_\star^5}\right)^{1/6} & \text{if } R_A > R_G, \\ \left(\frac{\mu^2}{M_c (2GM_{NS})^{1/2}}\right)^{2/7} & \text{if } R_A \leq R_G. \end{cases} \quad (13)$$

For $R_{st} > R_l$, the relativistic pulsar wind interacts with the accreted matter. By comparing the dependencies in Figure 4, we see that the accretion pressure increases as $\sim r^{-5/2}$ for $R_{st} \leq R_G$ and thus more rapidly than the pressure of the pulsar wind, which decreases as $\sim r^{-2}$. Hence, for $R_{st} \leq R_G$, no stable cavern can be maintained by the ejection of matter. However, using (9) for $r > R_l$ and (10) for $r > R_G$, we may find the stopping radius for distances $R_{st} > R_G$. This radius is also known as the Shvartsman radius and may be expressed in the following way:

$$R_{Sh} = \left(\frac{2L_{ej}}{\dot{M}_c v_\star v_{ej}}\right)^{1/2} R_G, \\ R_{Sh} = \left(\frac{8\kappa_t \mu^2 (GM_{NS})^2 \Omega^4}{\dot{M}_c v_\star^5 c^4}\right)^{1/2} \quad \text{if } v_{ej} = c. \quad (14)$$

Let us note that the relations (13) and (14) are valid for accretion rates below the Eddington limit for accretion, $G\dot{M}_c M_{NS}/R_{st} < L_{Edd}$. The supercritical regime occurs in disk accretion modes that do not develop when neutron stars are just passing through an ionized plasma medium that has low angular momentum.

Corotation radius. The corotation radius of a rotating neutron star is another important distance scale.

Name	Notation	Relation between distances	Observational effects
Ejector	E	$R_{\text{st}} > \max\{R_G, R_l\}$	radiopulsars
Propeller	P	$R_c < R_{\text{st}} \leq \max\{R_G, R_l\}$	spinning-down more efficient, transient sources
Accretor	A	$R_{\text{st}} \leq R_G$ and $R_{\text{st}} \leq R_c$	X-ray pulsars, X-ray bursters

TABLE 1. Summary of the interaction modes and the types of neutron stars that appear to be relevant in different regimes within the environment of the Minispiral.

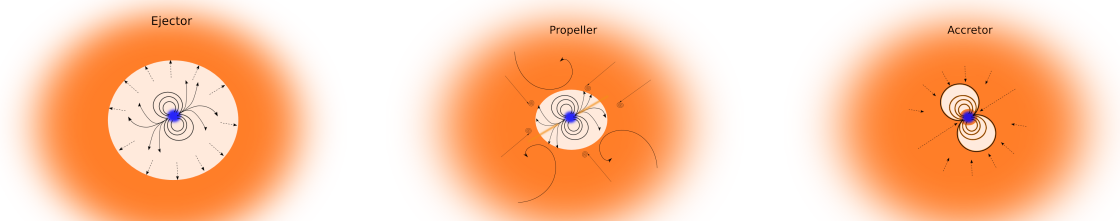


FIGURE 5. Illustrations of basic interaction modes of magnetized neutron stars with the surrounding environment: ejector, propeller, accretor.

If accreting plasma penetrates beyond the light cylinder, it is stopped at the Alfvén radius, $R_{\text{st}} \approx R_A$, where the plasma pressure and the pressure of the static magnetic field are in balance. Further evolution of stopped plasma is given by the rotational velocity of the neutron star. Let us assume that the plasma becomes frozen at R_{st} in the magnetic field and corotates with it at the angular velocity of the neutron star, Ω . The plasma clump will eventually reach the surface of the neutron star if the rotational velocity at the stopping radius R_{st} is smaller than the Keplerian velocity at the same distance:

$$\Omega R_{\text{st}} < \left(\frac{GM_{\text{NS}}}{R_{\text{st}}} \right)^{1/2}. \quad (15)$$

However, if the condition (15) is not met, a centrifugal barrier develops that prevents plasma from accreting further. The critical, corotation radius R_c that separates the two modes is given by the equality in (15):

$$R_c = \left(\frac{GM_{\text{NS}}}{\Omega^2} \right)^{1/3}. \quad (16)$$

If $R_{\text{st}} < R_c$, rotation does not considerably effect the accretion flux. If $R_{\text{st}} \geq R_c$, stationary accretion is not allowed.

Interaction modes. The mode of interaction of magnetized rotating neutron stars and also other gravimagnetic rotators is given by the relations between four fundamental distance scales: stopping radius R_{st} , light cylinder radius R_l , gravitational capture radius R_G and corotation radius R_c . Elementary combinatorics yields $4! = 24$ possible relations between these

Quantity	μ	σ
$\log P$	-0.2188	0.3488
$\log B$	12.0900	0.4711

TABLE 2. Parameters of the synthetic distribution of the period (in seconds) and the synthetic distribution of the surface magnetic field (in Gauss).

radii. However, when taking astrophysics into consideration, we get just a few modes. For example, R_l is always greater than R_c . We do not take supercritical regimes into account in our analysis, since they occur in systems with disk accretion, and binary systems are also not considered. The classification of three main interaction modes — ejector (E), propeller (P), and accretor (A) — and thus types of neutron stars according to [25] is summarized in Table 1. The sketches of these basic regimes are shown in Figure 5.

3. RESULTS: DISTRIBUTION OF INTERACTION MODES IN THE GALACTIC CENTER

In our Monte Carlo simulations we produce a sufficiently large synthetic population of neutron stars. The number of members of this population is of the order of 10^4 – 10^6 . As a nominal distribution of period $\log P$ and surface dipole magnetic field $\log B$ we take the Gaussian fit of the main peak of the observed distributions in the catalogue by [16]

$$N(\log P) \propto \exp\left(-\frac{(\log P - \mu_P)^2}{2\sigma_P^2}\right),$$

$$N(\log B) \propto \exp\left(-\frac{(\log B - \mu_B)^2}{2\sigma_B^2}\right), \quad (17)$$

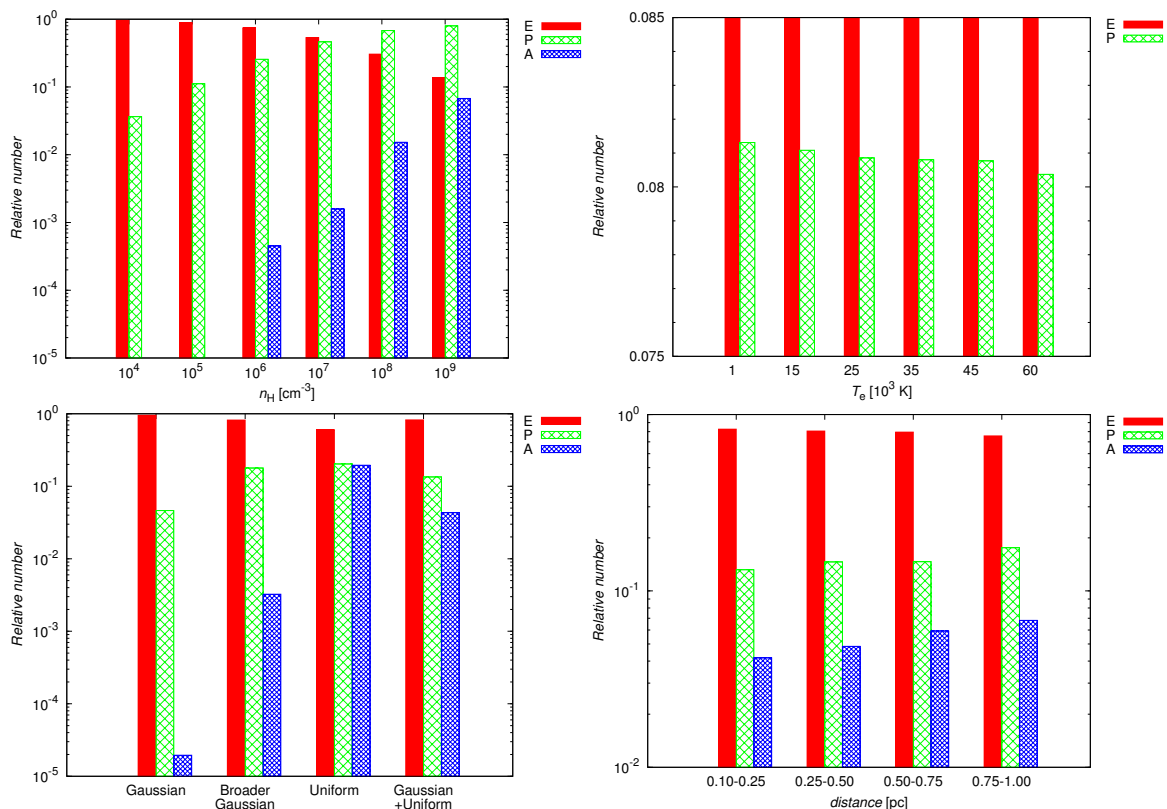


FIGURE 6. Histograms of the relative distribution of interaction modes of neutron stars in the Galactic center. The relative number is in the logarithmic scale. Top left panel: the distribution of interaction modes of the neutron stars that interact with the ionized gas in the Minispiral region. Three basic modes are monitored: ejector (E), propeller (P), and accretor (A). The distribution alters significantly as the density increases. The temperature is fixed at $\bar{T}_e = 6 \times 10^3$ K. Top right panel: the distribution of interaction modes for the fixed density of $\bar{n}_e = 5 \times 10^4$ cm $^{-3}$. We vary the temperature according to the description in the plot. Only two modes, ejector and propeller, are present. The relative number of ejector modes increases (0.9187, 0.9189, 0.9191, 0.9192, 0.9192, 0.9196) with the increasing temperature. Bottom left panel: distribution of interaction modes of neutron stars passing through the Minispiral for four different distributions: (1) Gaussian, (2) broader Gaussian, (3) uniform distribution, and (4) combined distribution: Gaussian + uniform. Parameters of individual distributions are summarized in Table 3. Bottom right panel: distribution of interaction modes of neutron stars for an increasing distance from the Galactic center. The magnetic field and period of neutron stars are distributed according to the combined distribution (4) in Table 3.

where μ_P and μ_B are mean values of the Gaussian distribution and σ_P^2 and σ_B^2 are the corresponding variances. The values of the period and surface magnetic field are independently attributed to each neutron star according to the distribution with the parameters in Table 2.

First, we fix the mean temperature of the ionized gas, $\bar{T}_e = 6 \times 10^3$ K. The density is continually increased by an order of magnitude, starting with 10^4 cm $^{-3}$; we consider densities up to 10^9 cm $^{-3}$.

Neutron stars are distributed uniformly in the space of orbital elements, having a uniform distribution of the logarithm of semi-major axis, (0.05, 1.00) pc, eccentricity, (0.0, 1.0), and the cosine of inclination, (-1, 1). The number of interactions with the Minispiral arms per unit of time is ~ 1 –10 %, depending on the length-scale of individual clumps, 1–2 arcsec, respectively. Thus, for an expected size of the population $\sim 10^4$,

about 100 to 1000 members may interact with the ionized gas of the Minispiral.

Furthermore, the occurrence of interaction modes (E, P, A) is investigated according to the classification in Table 1. We summarize the results via a series of histograms in Figure 6 (Top left panel). It is obvious that for typical densities in the Sgr A West region inferred from observations (10^4 – 10^5 cm $^{-3}$, see [22, 23]) ejector mode is predominant ($\gtrsim 90$ %); for larger densities the fraction of propeller neutron stars increases and at $\sim 10^7$ cm $^{-3}$ it is approximately the same as the fraction of ejectors and starts to prevail for higher densities, at which the accretor regime also becomes more prominent. This behaviour can be explained by the dependence of the stopping radius, see (13) and (14), on the accretion rate: for higher densities, \dot{M}_c increases and the stopping radius decreases. Thus, we naturally obtain a larger fraction of propellers and

Number	Distribution type	Parameters
1	Gaussian	$\mu_P = -0.2188, \sigma_P = 0.3488$ $\mu_B = 12.0900, \sigma_B = 0.4711$
2	Gaussian	$\mu_P = -0.2178, \sigma_P = 0.7019$ $\mu_B = 12.0888, \sigma_B = 0.85098$
3	Uniform	$\log P_{\min} = -3, \log P_{\max} = 2$ $\log B_{\min} = 7, \log B_{\max} = 15$
4	Combined	$\mu_P = -0.2189, \sigma_P = 0.3478$ $\mu_B = 12.09, \sigma_B = 0.47$ $\log P_{\min} = -3, \log P_{\max} = 2$ $\log B_{\min} = 7, \log B_{\max} = 15$

TABLE 3. Distributions of the period and the maximum surface intensity of the dipole magnetic field of neutron stars considered in our work.

accretors for higher densities. Such densities may hypothetically be found in cold, obscured regions of the Minispiral [27], in the Circumnuclear disk [1, 2], and in dense gaseous-dusty tori and disks of AGN.

Second, we perform the simulation run with fixed density $\bar{n}_e = 5 \times 10^4 \text{ cm}^{-3}$. The parameters related to the magnetic field and period distributions are kept as before. The electron temperature is varied from 1000 K to 60000 K. We just make a note that the motivation for these density and temperature variations comes from the fact that the Minispiral consists of several streams and clumps of different properties that coexist [23]. After several runs we find that the distribution of the interaction regimes does not vary significantly: ejectors constitute $\gtrsim 92\%$ and propellers $\lesssim 8\%$ of those neutron stars that collide with the streams, see Figure 6 (Top right panel). For higher temperature the accretion rate \dot{M}_c drops and the stopping radius increases, see (13) and (14). Hence, the number of propellers decreases whereas ejectors are more abundant. However, the dependence of distribution on temperature is rather weak. No accretors appear since we keep the density at $5 \times 10^3 \text{ cm}^{-3}$ (compare also with Figure 6 – Top left panel).

Moreover, we study the distribution of the interaction regimes of neutron stars for stratified Minispiral clumps and different distributions. To this end, we implement clumps with a variable density profile. They consist of four concentric shells with the corresponding outer radii $r_N = (1/2)^{N-1} \times 0.08 \text{ pc}$, $N \in [1, 2, 3, 4]$. The number density increases towards the center, starting with 10^4 cm^{-3} up to 10^7 cm^{-3} , increasing inwards by one order of magnitude for each concentric shell. The temperature is set at the mean value of $\bar{T}_e = 6000 \text{ K}$. This scheme ensures that most of the gaseous medium has number densities in the range $(10^4, 10^5) \text{ cm}^{-3}$, which in agreement with radio and infrared observations.

We analyse the interaction modes for four different distributions whose types and parameters are summarized in Table 3. Distribution (1) is inferred from the Gaussian fit of the main peak of both the period and

the magnetic field distributions of observed neutron stars [16]. Distribution (2) is a broader Gaussian distribution, (3) is a uniform distribution across a large span of values: $B \in (10^7, 10^{15}) \text{ G}$ and $P \in (10^{-3}, 10^2) \text{ s}$. Distribution (4) is a combined distribution of (1) and (3), where (3) uniformly fills an ellipse in PB plane that satisfies the following condition,

$$\frac{(\log P - \mu_P)^2}{s_P^2} + \frac{(\log B - \mu_B)^2}{s_B^2} \leq 1,$$

where s_P and s_B are the corresponding semi-major axes:

$$s_P = (\log P_{\max} - \log P_{\min})/2,$$

$$s_B = (\log B_{\max} - \log B_{\min})/2.$$

We perform Monte Carlo simulations with the distribution of the orbital elements of neutron stars as described before. The results of the study of the modes of neutron stars that interact with the Minispiral are presented in Figure 6 (Bottom left panel). In the case of distribution (1), the ejector mode dominates, whereas the propeller and the accretor modes are represented by small amounts, $(E; P; A) \approx (95.4; 4.6; 2 \times 10^{-3}) \%$. For the broader Gaussian distribution (2), the ejector mode decreases, whereas the propeller and the accretor modes increase in comparison with the distribution (1), $(E; P; A) \approx (81.9; 17.8; 0.3) \%$. This trend continues in the case of uniform distribution (3), for which the accretor mode rises considerably, $(E; P; A) \approx (60.2; 20.3; 19.5) \%$. Finally, the combined distribution (4) with a Gaussian peak results in the dominant ejector mode again, $(E; P; A) \approx (82.3; 13.4; 4.3) \%$. In all studied cases the ejector mode dominates ($\gtrsim 60\%$). However, the distribution of the interaction modes is very sensitive to the internal properties of neutron stars (surface magnetic field and period), which evolve with time. The purpose of the four discussed distributions of the period and magnetic field is to show general trends; more detailed studies based on the age distribution of stars in the Galactic center are required to constrain the distribution further.

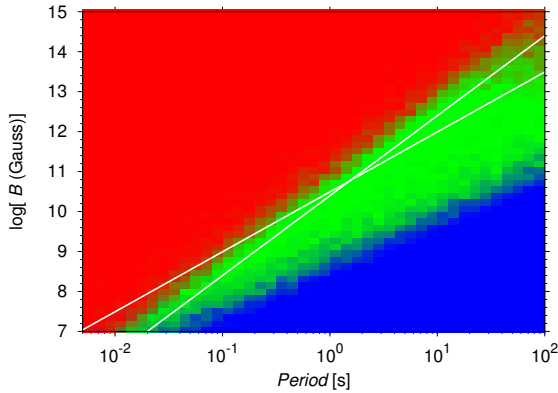


FIGURE 7. The uniform distribution of interacting neutron stars in the PB plane. Interaction modes are color-coded: ejector–red, propeller–green, and accretor–blue. Two white lines mark the *death lines*, below which pulsating neutron stars turn off.

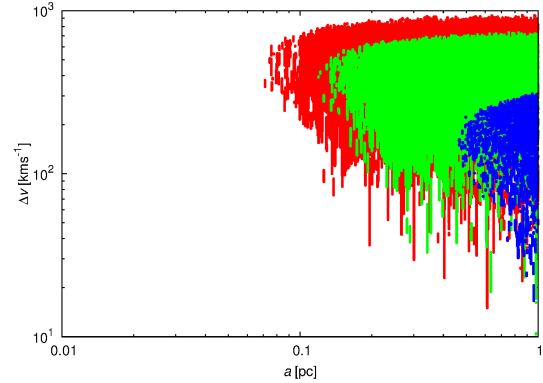


FIGURE 8. The relative velocity of interacting neutron stars with respect to the Minispiral streams versus the semi-major axes of neutron stars. Red points label the interactions with the Northern Arm, green points stand for the Eastern Arm, and blue points represent passages through the Western Arc.

Finally, we study the change in the distribution of interaction regimes with increasing distance from the Galactic center. We use the combined distribution (4) of the period and magnetic field to analyse the general behaviour, see Figure 6 (bottom right panel). The greater the distance, the smaller the abundance of ejectors is, whereas the number of propellers and accretors increases. This is due to the fact that the relative velocity between stars and gaseous clumps decreases for a larger distance, which implies an increase in the capture rate \dot{M}_c , see (4). This is translated into shrinkage of the stopping sphere, according to (13) and (14). Hence, there is a higher probability that the gravitational capture radius and also the light radius become larger than the stopping radius, which favours the onset of the propeller and accretor stage, see Table 1.

Distribution of interaction modes in the PB plane. It is useful to plot the interaction modes of neutron stars passing through the ionized Minispiral region in the PB plane (period-magnetic field). We plot such a map for a uniform distribution (3; see Table 3) and distinguish individual regimes by colour: ejector – red, propeller – green, and accretor – blue. The points in the PB plane where multiple modes occur are marked by shades of these colours according to the probability of occurrence of particular regimes.

The PB plane is divided by a pair of *death lines*, $B \approx 2.5 \times 10^{10} P^2$ (G) and $B \approx 3.1 \times 10^{10} P^{3/2}$ (G). Above these lines, electron-positron pairs can be produced in strong magnetic fields, and the pulsars are active, whereas below these lines pair production no longer proceeds and pulsars are turned off [28]. The ejector mode dominates the region above these lines, the accretor stage prevails below them, and the propeller mode occurs in the vicinity of these lines, see Figure 7.

4. DISCUSSION

Let us briefly discuss plausible observable consequences of the results presented here.

Ejectors manifest themselves mainly as radiopulsars. The predicted number of neutron stars in the central parsec of the Galactic centre is $\sim 10^4$; the expected fraction of ejectors is $\sim 90\%$ (see Figure 6) assuming that the dominant population of neutron stars is the same as is observed in the disk population. This fraction could be decreased if the population of old, isolated accreting neutron stars is more prominent. One should be aware of the fact that pulsars stay active for a certain amount of time, which can be approximated as $\tau \approx 100$ Myr, when they reach the death lines and turn off, see Fig. 7. Around the death lines they become propellers and with further spin-down and magnetic field decay they start to accrete interstellar matter.

We take the beaming fraction of the ejectors $f_b = 0.2$ [29], i.e. pulsars that are expected to beam towards us, so potentially ~ 1800 pulsars could be detectable with sufficient sensitivity. However, there is an apparent lack of pulsar detections in the Galactic centre region. The pulsar searches in the Galactic disk are generally affected by high background temperature, which increases the minimum detectable flux. Moreover, all observations pointed toward the Galactic centre region suffer from interstellar scattering resulting from turbulent plasma, which causes temporal broadening of the pulses to $\sim 2000 \nu_{\text{GHz}}^{-4}$ s [30] (ν_{GHz} is the observing frequency in GHz). At usual observing frequencies ~ 1 GHz it is not possible to detect even long-period pulsars and the surveys have to increase the frequency to ~ 10 GHz. However, since pulsars have spectral energy distribution in the power-law form $S_\nu \propto \nu^\alpha$, where $\alpha < 0$, the flux decreases for higher frequencies. To sum up, the lack of observed radiopulsars in the Galactic centre may be explained by the

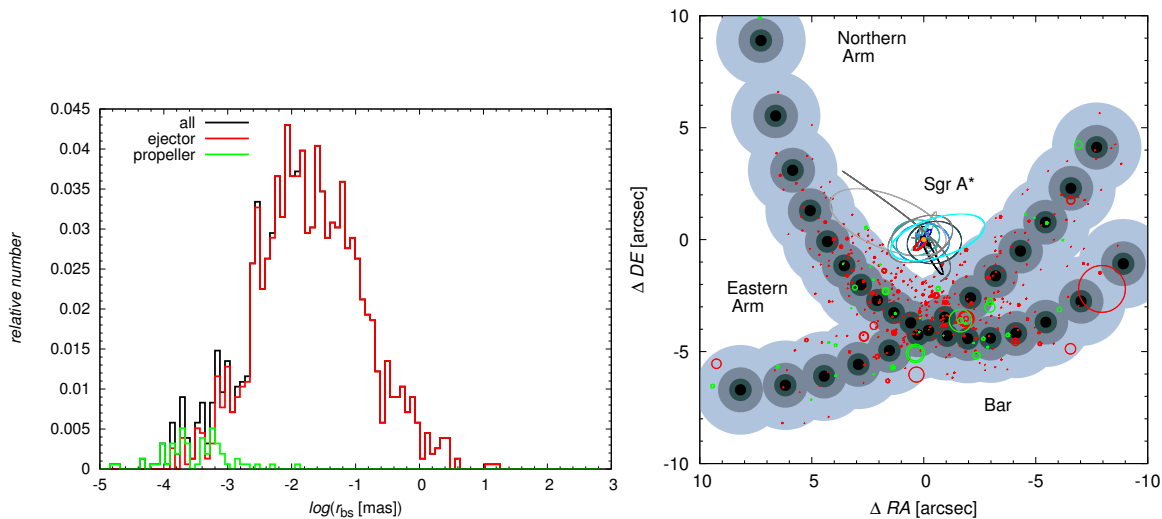


FIGURE 9. Exemplary simulated distribution of bow-shock sizes associated with neutron stars according to Gaussian distribution (1) in Table 3. Left panel: histogram of bow-shock sizes. The green histogram represents propeller bow-shocks with rather small characteristic length-scales that are beyond the detection limit. Right panel: comparison of bow-shock sizes in the simulated $20'' \times 20''$ image of the Minispiral. The ejector bow-shocks (red circles) are artificially enlarged by a factor of 100 and propeller bow-shocks are enlarged 10^5 -times for clarity. The elliptical orbits of selected S-stars are also plotted for illustration.

low sensitivity of current observing facilities. A major breakthrough is expected to come with *Square Kilometer Array-SKA* project [31], which will provide much higher sensitivity than current instruments. Mapping the close vicinity of Sgr A* will be the task of the *Event Horizon Telescope-EHT* [32], which may detect pulsars strongly bound to the supermassive black hole and the data could be used to put the theory of general relativity to very precise tests.

Another way to detect ejectors—pulsars is to look for the cavities, pulsar wind nebulae (PWN), and bow-shock structures formed when supersonic ejecting neutron stars emitting relativistic wind propagate through the denser medium of the Minispiral. For the average electron temperature of the plasma in the Minispiral region, $\bar{T}_e \approx 6 \times 10^3$ K [22], the speed of sound is $c_s \approx (k\bar{T}_e/m_H)^{1/2} \approx 7 \text{ km s}^{-1}$. According to Fig. 8 of the semi-major axis—relative velocity plot, typical relative velocities of neutron stars that encounter the high-density gas of the Minispiral are greater than the speed of sound of the interstellar medium by one–two orders of magnitude. Hence, the motion is generally supersonic and bow-shock structures associated with neutron stars potentially form in the Minispiral arms. The size of such a cavity is determined by the energy input, $\dot{E} \approx -\dot{E}_{\text{rot}} = -I\Omega\dot{\Omega}$, from the central ejector, and also by the structure and the properties of the surrounding medium. The velocity of the pulsar \mathbf{v}_{rel} with respect to the ambient medium also influences the size and the orientation of the bow-shock structure. Along the relative velocity \mathbf{v}_{rel} , the pressure of the wind of the ejector and the ram pressure of the ISM are in balance at the contact discontinuity.

The distance of the contact discontinuity from the central ejector is given by the *stand-off* distance (see, e.g., [33]):

$$r_{\text{bs}} = \left(\frac{\dot{E}}{4\pi c \rho_a v_{\text{rel}}^2} \right)^{1/2}, \quad (18)$$

where the density of the ambient medium (the Minispiral) is $\rho_a \approx m_H n_H$, and we adopt the values from [22, 23]; the major part of the Minispiral gaseous clumps has $n_H \approx 10^4$ – 10^5 cm^{-3} , with the core of each clump of 10^7 cm^{-3} . Equation (18) describes the characteristic size of both the bow-shock associated with a fast neutron star and the pulsar wind nebula, i.e. the distance of the contact discontinuity from the central pulsar. In the case of PWN, the termination shock is characterized by concentric tori and jets, as is observed in the Crab nebula, for example.

We compute the typical sizes of bow shocks and/or PWN for an ensemble of 10^4 neutron stars using (18) and the assumption that the Gaussian distribution in Table 3, 1st line, is approximately valid for the Galactic center population. Assuming that $\gtrsim 90\%$ of interacting pulsars are ejectors, about one thousand (in our exemplary runs ~ 1500) bow-shock structures could be present along the Minispiral arms. However, most of them are rather small ($< 1 \text{ mas}$) and are therefore below the detection limit. Propeller bow shocks are all below $\sim 0.01 \text{ mas}$, whereas the bow-shock structures of ejectors have sizes above this value and up to $\sim 10 \text{ mas}$, see Fig. 9 (Left panel) for comparison; the values along the horizontal axis are decadic logarithms of stand-off radii in milliarcseconds.

The number of larger bow-shock structures ($\gtrsim 1 \text{ mas}$) is ~ 30 for ~ 1500 neutron stars that interact

with the Minispiral out of $\sim 10^4$ neutron stars that occupy the innermost parsec. However, ~ 10 of them are greater than 10 mas. Fig. 9 (Right panel) compares of their sizes with the whole Minispiral structure as seen from the Earth for an exemplary simulation.

In addition, neutron stars are expected to occur closer to the SMBH where relativistic effects could be detected. They may be members of the S-cluster, where they were originally locked in binary systems with hot stars. Close pericenter passages can, however, disrupt such binary systems due to triple scattering. The components become separated, and for a certain set of orbital parameters, one component can escape the system on a hyperbolic orbit (see [34] for details). These hypervelocity neutron stars could potentially be seen to interact with the gaseous environment of Sgr A West and further away.

The HII region of Sgr A West, especially the dense Minispiral arms and the bar, seem to be a promising target to search for the effects of interaction with passing compact objects both for the number of encounters and for the observable effects. Due to its large size, the Minispiral appears to be a more favourable target for detecting the manifestation of the neutron star population than an isolated clump, such as G2/DSO currently observed in the Galactic center [35].

5. CONCLUSIONS

We have studied the distribution of interaction modes of the neutron star population in the Galactic center. We have explained that the established mode of interaction depends on the intrinsic properties of a neutron star (the rotational period and the magnetic dipole surface intensity) and the external conditions (parameters of the gaseous medium: density and temperature).

We focused on the distribution of three main interaction regimes of neutron stars: ejector (E), propeller (P), and accretor (A). We found that the distribution of the modes is strongly dependent on the plasma density, where it is only weakly dependent on temperature in the range $\sim (10^3, 10^4)$ K. This further implies that the distribution varies across different galaxy types.

We went on propose an alternative way to look for ejecting neutron stars in the Galactic center. One can look for the signatures of the interaction of neutron stars with the dense Minispiral arms. Common structures associated with the supersonic motion of pulsars are bow-shocks. Our analysis shows that the number of relatively large structures in this region, $\gtrsim 10$ mas, can be of the order of ~ 10 . However, we stress that the results depend on the assumed distribution of the rotational periods and the surface magnetic fields. The comparison of different synthetic distributions of bow-shock sizes with the observed structures will help to constrain the parameters of the Galactic center population of young neutron stars.

These bow-shocks are expected to be sources of polarized non-thermal radiation, possibly detectable in the X-ray, infrared, and radio wavelengths. Several cases of such comet-shaped sources are indeed observed in this region [15, 36]. Further analysis is required to strengthen or reject their association with propagating neutron stars. In our upcoming paper we will further explore the observability of these features (Zajaček et al., in preparation).

ACKNOWLEDGEMENTS

The authors acknowledge support from the Grant Agency of Charles University in Prague (grant # 879113, "The study of neutron stars in the galactic center") and also funding from an ongoing grant GAČR-DFG No. 14-37086G.

REFERENCES

- [1] R. Genzel, F. Eisenhauer, S. Gillessen. The Galactic Center massive black hole and nuclear star cluster. *Reviews of Modern Physics* **82**:3121–3195, 2010. 1006.0064 DOI:10.1103/RevModPhys.82.3121.
- [2] A. Eckart, R. Schödel, C. Straubmeier. *The Black Hole at the Center of the Milky Way* (London: Imperial College Press). 2005.
- [3] H. Bartko, F. Martins, S. Trippe, et al. An Extremely Top-Heavy Initial Mass Function in the Galactic Center Stellar Disks. *ApJ* **708**:834–840, 2010. 0908.2177 DOI:10.1088/0004-637X/708/1/834.
- [4] R. M. Buchholz, R. Schödel, A. Eckart. Composition of the galactic center star cluster. Population analysis from adaptive optics narrow band spectral energy distributions. *A&A* **499**:483–501, 2009. 0903.2135 DOI:10.1051/0004-6361/200811497.
- [5] T. Do, A. M. Ghez, M. R. Morris, et al. High Angular Resolution Integral-Field Spectroscopy of the Galaxy's Nuclear Cluster: A Missing Stellar Cusp? *ApJ* **703**:1323–1337, 2009. 0908.0311 DOI:10.1088/0004-637X/703/2/1323.
- [6] J. N. Bahcall, R. A. Wolf. Star distribution around a massive black hole in a globular cluster. *ApJ* **209**:214–232, 1976. DOI:10.1086/154711.
- [7] J. N. Bahcall, R. A. Wolf. The star distribution around a massive black hole in a globular cluster. II Unequal star masses. *ApJ* **216**:883–907, 1977. DOI:10.1086/155534.
- [8] R. Schödel, A. Feldmeier, D. Kunneriath, et al. Surface brightness profile of the Milky Way's nuclear star cluster. *A&A* **566**:A47, 2014. 1403.6657 DOI:10.1051/0004-6361/201423481.
- [9] M. Morris. Massive star formation near the Galactic center and the fate of the stellar remnants. *ApJ* **408**:496–506, 1993. DOI:10.1086/172607.
- [10] J. Miralda-Escudé, A. Gould. A Cluster of Black Holes at the Galactic Center. *ApJ* **545**:847–853, 2000. astro-ph/0003269 DOI:10.1086/317837.
- [11] R. S. Wharton, S. Chatterjee, J. M. Cordes, et al. Multiwavelength Constraints on Pulsar Populations in the Galactic Center. *ApJ* **753**:108, 2012. 1111.4216 DOI:10.1088/0004-637X/753/2/108.

- [12] P. Deegan, S. Nayakshin. Constraining the number of compact remnants near Sgr A*. *MNRAS* **377**:897–904, 2007. [arXiv:astro-ph/0611524](https://arxiv.org/abs/astro-ph/0611524)
doi:10.1111/j.1365-2966.2007.11659.x.
- [13] S. Johnston, M. Kramer, D. R. Lorimer, et al. Discovery of two pulsars towards the Galactic Centre. *MNRAS* **373**:L6–L10, 2006. [astro-ph/0606465](https://arxiv.org/abs/astro-ph/0606465)
doi:10.1111/j.1745-3933.2006.00232.x.
- [14] J. S. Deneva, J. M. Cordes, T. J. W. Lazio. Discovery of Three Pulsars from a Galactic Center Pulsar Population. *ApJL* **702**:L177–L181, 2009. 0908.1331 doi:10.1088/0004-637X/702/2/L177.
- [15] J.-H. Zhao, M. R. Morris, W. M. Goss. Radio Detection of a Candidate Neutron Star Associated with Galactic Center Supernova Remnant Sagittarius A East. *ApJ* **777**:146, 2013. 1309.7020
doi:10.1088/0004-637X/777/2/146.
- [16] R. N. Manchester, G. B. Hobbs, A. Teoh, M. Hobbs. The Australia Telescope National Facility Pulsar Catalogue. <http://www.atnf.csiro.au/research/pulsar/psrcat/>, 2005.
- [17] J. A. Kennea, D. N. Burrows, C. Kouveliotou, et al. Swift Discovery of a New Soft Gamma Repeater, SGR J1745-29, near Sagittarius A*. *ApJL* **770**:L24, 2013. 1305.2128 doi:10.1088/2041-8205/770/2/L24.
- [18] K. Mori, E. V. Gotthelf, S. Zhang, et al. NuSTAR Discovery of a 3.76 s Transient Magnetar Near Sagittarius A*. *ApJL* **770**:L23, 2013. 1305.1945
doi:10.1088/2041-8205/770/2/L23.
- [19] R. Eatough, R. Karuppusamy, M. Kramer, et al. Detection of radio pulsations from the direction of the NuSTAR 3.76 second X-ray pulsar at 8.35 GHz. *The Astronomer's Telegram* **5040**:1, 2013.
- [20] N. Rea, P. Esposito, J. A. Pons, et al. A Strongly Magnetized Pulsar within the Grasp of the Milky Way's Supermassive Black Hole. *ApJL* **775**:L34, 2013. 1307.6331 doi:10.1088/2041-8205/775/2/L34.
- [21] J.-H. Zhao, M. R. Morris, W. M. Goss, T. An. Dynamics of Ionized Gas at the Galactic Center: Very Large Array Observations of the Three-dimensional Velocity Field and Location of the Ionized Streams in Sagittarius A West. *ApJ* **699**:186–214, 2009. 0904.3133 doi:10.1088/0004-637X/699/1/186.
- [22] J.-H. Zhao, R. Blundell, J. M. Moran, et al. The High-density Ionized Gas in the Central Parsec of the Galaxy. *ApJ* **723**:1097–1109, 2010. 1009.1401
doi:10.1088/0004-637X/723/2/1097.
- [23] D. Kunneriath, A. Eckart, S. N. Vogel, et al. The Galactic centre mini-spiral in the mm-regime. *A&A* **538**:A127, 2012. 1201.2362
doi:10.1051/0004-6361/201117676.
- [24] I. Zel'dovich, I. Novikov. *Relativistic Astrophysics [by] Ya.B. Zeldovich and I.D. Novikov: Rev. and Enl. from the Original Russian Ed. by the Authors. Translated by Eli Arlock. Edited by Kip S. Thorne and W. David Arnett.* University of Chicago Press, 1971.
- [25] V. M. Lipunov. *Astrophysics of Neutron Stars.* Berlin/Heidelberg: Springer-Verlag, 1992.
- [26] P. Goldreich, W. H. Julian. Pulsar Electrodynamics. *ApJ* **157**:869, 1969. doi:10.1086/150119.
- [27] J. Moutkaka, A. Eckart, K. Mužić. Ices in the Galactic Center? *Journal of Physics Conference Series* **372**(1):012019, 2012. doi:10.1088/1742-6596/372/1/012019.
- [28] T. Padmanabhan. *Theoretical Astrophysics: Volume 2, Stars and Stellar Systems.* Theoretical Astrophysics. Cambridge University Press, 2000.
- [29] R. T. Emmering, R. A. Chevalier. The intrinsic luminosity and initial period of pulsars. *ApJ* **345**:931–938, 1989. doi:10.1086/167963.
- [30] D. R. Lorimer, M. Kramer. *Handbook of Pulsar Astronomy.* 2004.
- [31] M. Kramer, D. C. Backer, J. M. Cordes, et al. Strong-field tests of gravity using pulsars and black holes. *NewAR* **48**:993–1002, 2004. [astro-ph/0409379](https://arxiv.org/abs/astro-ph/0409379)
doi:10.1016/j.newar.2004.09.020.
- [32] V. L. Fish, S. S. Doeleman, C. Beaudoin, et al. 1.3 mm Wavelength VLBI of Sagittarius A*: Detection of Time-variable Emission on Event Horizon Scales. *ApJL* **727**:L36, 2011. 1011.2472
doi:10.1088/2041-8205/727/2/L36.
- [33] S. Brownsberger, R. W. Romani. A Survey for H α Pulsar Bow Shocks. *ApJ* **784**:154, 2014. 1402.5465
doi:10.1088/0004-637X/784/2/154.
- [34] M. Zajaček, V. Karas, A. Eckart. Dust-enshrouded star near supermassive black hole: predictions for high-eccentricity passages near low-luminosity galactic nuclei. *A&A* **565**:A17, 2014. 1403.5792
doi:10.1051/0004-6361/201322713.
- [35] R. de la Fuente Marcos, C. de la Fuente Marcos. Colliding with G2 near the Galactic Centre: a geometrical approach. *MNRAS* **435**:L19–L23, 2013. 1306.4921 doi:10.1093/mnras/slt085.
- [36] K. Mužić, A. Eckart, R. Schödel, et al. Comet-shaped sources at the Galactic center. Evidence of a wind from the central 0.2 pc. *A&A* **521**:A13, 2010. 1006.0909 doi:10.1051/0004-6361/200913087.

Charge of the Galactic centre black hole

The Galactic centre black hole associated with the compact radio source Sgr A* is fully characterized by three classical, externally observable parameters: mass M_{\bullet} , the angular momentum or dimensionless spin parameter a_{\bullet} , and the electric charge Q_{\bullet} , according to the *no-hair* theorem for stationary Kerr-Newman black holes (Heusler 1996).

The mass of the black hole is constrained well based on the motion of S stars in the innermost arcsecond. The current value is $M_{\bullet} = (4.3 \pm 0.3) \times 10^6 M_{\odot}$ (Eckart et al. 2017). The spin parameter is constrained to be rather large, $a_{\bullet} \gtrsim 0.4$, based on the modelling of the total and polarized NIR variable emission (Eckart et al. 2006; Meyer et al. 2006a).

The third parameter – the electric charge of the black hole Q_{\bullet} – is not constrained at all, but is usually set to zero due to neutralization by the surrounding plasma, $Q_{\bullet} = 0$. In our study, we revisit the question of the electric charge of the Galactic centre black hole and we put constraints on the realistic values of the charge based on the properties of the ambient medium. We also analyse the typical timescales for charging/discharging. Finally, we look at the potential observable effects of the charged SMBH at the Galactic centre. These can be used in the future to constrain the values of the charge of Sgr A*.

This analysis and the main results are included in the peer-reviewed paper, which was published in the Monthly Notices of the Royal Astronomical Society.

Credit: Zajaček, Tursunov, Eckart & Britzen, MNRAS 480, 4408 (2018). Reproduced with permission ©Oxford University Press.



On the charge of the Galactic centre black hole

Michal Zajaček,^{1,2,3*} Arman Tursunov,⁴ Andreas Eckart^{1,2} and Silke Britzen¹

¹Max-Planck-Institut für Radioastronomie (MPIfR), Auf dem Hügel 69, D-53121 Bonn, Germany

²I. Physikalisches Institut der Universität zu Köln, Zùlpicher Strasse 77, D-50937 Köln, Germany

³Astronomical Institute, Academy of Sciences, Boční II 1401, CZ-14131 Prague, Czech Republic

⁴Institute of Physics and Research Centre of Theoretical Physics and Astrophysics, Faculty of Philosophy and Science, Silesian University in Opava, Bezručovo nám.13, CZ-74601 Opava, Czech Republic

Accepted 2018 August 5. Received 2018 May 29; in original form 2017 September 29

ABSTRACT

The Galactic centre supermassive black hole (SMBH), in sharp contrast with its complex environment, is characterized by only three classical parameters – mass, spin, and electric charge. Its charge is poorly constrained. It is, however, usually assumed to be zero because of neutralization due to the presence of plasma. We revisit the question of the SMBH charge and put realistic limits on its value, time-scales of charging and discharging, and observable consequences of the potential, small charge associated with the Galactic centre black hole. The electric charge due to classical arguments based on the mass difference between protons and electrons is $\lesssim 10^9$ C and is of a transient nature on the viscous time-scale. However, the rotation of a black hole in magnetic field generates electric field due to the twisting of magnetic field lines. This electric field can be associated with induced charge, for which we estimate an upper limit of $\lesssim 10^{15}$ C. Moreover, this charge is most likely positive due to an expected alignment between the magnetic field and the black hole spin. Even a small charge of this order significantly shifts the position of the innermost stable circular orbit (ISCO) of charged particles. In addition, we propose a novel observational test based on the presence of the bremsstrahlung surface brightness decrease, which is more sensitive for smaller unshielded electric charges than the black hole shadow size. Based on this test, the current upper observational limit on the charge of Sgr A* is $\lesssim 3 \times 10^8$ C.

Key words: black hole physics – radiation mechanisms: general – Galaxy: centre.

1 INTRODUCTION

The observations of the Galactic centre across the electromagnetic spectrum, ranging from radio to gamma wavelengths, revealed the complex structure of the Nuclear Star Cluster (NSC) as well as that of the gaseous-dusty medium of the central parsec (Eckart, Schödel & Straubmeier 2005; Melia 2007; Genzel, Eisenhauer & Gillessen 2010; Eckart et al. 2017). The presence of the concentrated, dark mass at the dynamical centre of the NSC was revealed by the near-infrared (NIR) observations of stars using adaptive optics. The first proof for the compact dark single object in the Galactic centre came with the detection and the analysis of the first proper motion of stars orbiting Sgr A* inside 1 arcsec ~ 0.04 pc, so-called S stars (Eckart & Genzel 1996, 1997; Ghez et al. 1998; Zajaček & Tursunov 2018). Based on these and follow-up observations (Gillessen et al. 2009, 2017; Boehle et al. 2016; Parsa et al. 2017; Gravity Collaboration 2018), the large mass of the dark object has been confirmed and a more pre-

cise value has been determined – $\sim (4.15 \pm 0.13 \pm 0.57) \times 10^6 M_{\odot}$ (Parsa et al. 2017). If we associate this dark mass with a non-rotating black hole for simplicity, this yields a Schwarzschild radius of $R_{\text{Schw}} = 1.2 \times 10^{12}$ cm ($M_{\bullet}/4 \times 10^6 M_{\odot}$) and the expected mean density is

$$\rho_{\bullet} = 1.7 \times 10^{25} \left(\frac{M_{\bullet}}{4 \times 10^6 M_{\odot}} \right) \times \left(\frac{R_{\text{Schw}}}{3.9 \times 10^{-7} \text{ pc}} \right)^{-3} M_{\odot} \text{ pc}^{-3}. \quad (1)$$

In case of stellar orbits, the tightest constraint for the density of the dark mass comes from the monitoring of B-type star S2 with the pericentre distance of $r_p \simeq 5.8 \times 10^{-4}$ pc (Schödel et al. 2002; Gillessen et al. 2009, 2017; Parsa et al. 2017; Gravity Collaboration 2018):

$$\rho_{\text{S2}} = 5.2 \times 10^{15} \left(\frac{M_{\bullet}}{4.3 \times 10^6 M_{\odot}} \right) \times \left(\frac{r_p}{5.8 \times 10^{-4} \text{ pc}} \right)^{-3} M_{\odot} \text{ pc}^{-3}. \quad (2)$$

*E-mail: zajacek@ph1.uni-koeln.de

The most stringent density constraint was given by 3σ very-long-baseline interferometry (VLBI) source size of $\sim 37 \mu\text{as}$ (Doeleman et al. 2008; Lu et al. 2018). When combined with the lower limit on the mass $M_{\text{SgrA}^*} \gtrsim 4 \times 10^5 M_{\odot}$ based on the proper motion measurements (Reid & Brunthaler 2004), VLBI yields the lower limit of $\rho_{\text{SgrA}^*} \geq 9.3 \times 10^{22} M_{\odot} \text{pc}^{-3}$. This is about two orders of magnitude less than the density expected for a black hole of $\sim 4 \times 10^6 M_{\odot}$, see equation (1). The most plausible stable configuration that can explain such a large concentration of mass emerges within the framework of general relativity: a singularity surrounded by an event horizon – a black hole, ruling out most of the alternatives (Eckart et al. 2017).

According to the uniqueness or the general relativistic ‘no-hair’ theorem (Heusler 1996), any stationary black hole is fully characterized by only three classical and externally observable quantities: mass M_{\bullet} , angular momentum J_{\bullet} (often the quantity $a_{\bullet} = J_{\bullet}/M_{\bullet}c$ is used that has a dimension of length), and the electric charge Q_{\bullet} .¹ Because of the high-precision observations of stars in the NSC, including the innermost S cluster, the current value for the SMBH mass is $M_{\bullet} = (4.3 \pm 0.3) \times 10^6 M_{\odot}$ (Eckart et al. 2017), which is based on different methods, primarily the orbits of S stars (Parsa et al. 2017), the Jeans modelling of the properties of the NSC (Do et al. 2013), and the general relativistic fits to the double-peaked X-ray flares that show signs of gravitational lensing (Karssen et al. 2017). The constraints for the spin J_{\bullet} were inferred indirectly based on the variable total and polarized NIR emission (Eckart et al. 2006). The spin can be determined based on the modelling of spin-dependent quantities, mainly the light curves of a hot spot or a jet base. In this way, Meyer et al. (2006) obtained constraints for the spin – which are rather weak – and the spin parameter is $a_{\bullet} \gtrsim 0.4$ as well as the inclination, which is inferred based on the stable polarization angle of the flares and tends to be rather large $i \gtrsim 35^{\circ}$. The value of the spin parameter determined based on quasi-periodic oscillations for Sgr A* reaches a unique value of ≈ 0.44 (Kato et al. 2010), which is consistent with the value inferred from the fitting of the NIR flares.

In general, the charge of the black hole Q_{\bullet} is often set equal to zero due to the presence of plasma around astrophysical black holes. However, a black hole can acquire primordial charge because it was formed by a collapse of a charged (compact) star (Ray et al. 2003). It is not clear on which time-scales such a charged black hole discharges or alternatively, can increase its charge. Also, from an astrophysical point of view, it is of a general interest if a charged black hole can be observationally distinguished from a non-charged case, clearly depending on the value of the charge.

In addition, electric charge can be loaded or induced by black hole due to its rotation in external magnetic field within the mechanism similar to the Faraday unipolar generator. Such a mechanism is more relevant for supermassive black holes (SMBHs) in the local Universe, since the primordial charge information is expected to be lost. The induction mechanism works in such a way that the rotation of a black hole generates electric potential between horizon and infinity that leads to the process of selective accretion of charged particles of plasma surrounding the black hole. In particular, a rotating black hole embedded in a uniform, aligned magnetic field will acquire an electric charge until an equilibrium value is reached $Q_{\bullet, w} = 2B_0 J_{\bullet}$, a so-called Wald charge (Wald 1974), where B_0 is an asymptotic magnetic field strength. There is an evidence that significant and highly aligned magnetic field must be present in the

Galactic centre with equipartition strength of 10 G in the vicinity of the event horizon of the SMBH (Eckart et al. 2012; Eatough et al. 2013; Morris 2015).

The twisting of magnetic field lines threading the horizon of rotating black hole produces an electric field that accelerates the charged particles along the magnetic field lines. Moreover, magnetic field plays the role of a catalysing element that allows the extraction of rotational energy from rotating black hole through interaction of charged particles with an induced electric field in such processes as the Blandford–Znajek mechanism (Blandford & Znajek 1977) and the magnetic Penrose process (Wagh, Dhurandhar & Dadhich 1985). Both of these processes that allow the energy extraction from rotating black holes require the presence of an induced electric field (Dadhich et al. 2018).

Even a small charge associated with the black hole can have considerable effects on the electromagnetic processes in its vicinity, such as the bremsstrahlung emission and the motion of charged particles as we will show. The value of this small electric charge for black holes embedded in plasma will be necessarily temporary and fluctuating, mainly due to the attraction of oppositely charged particles and/or the variability of the magnetic field in which the black hole is immersed. Even for an extreme case of a charged black hole in vacuum, a spontaneous loss of charge would occur due to pair production with an exponential time-dependence (Gibbons 1975).

In this paper, we revisit the question of a charge, mainly of an electric origin, associated with the Galactic centre SMBH. Previously, several theoretical studies have focused on the space–time structure of charged black holes (Karas & Vokrouhlický 1991a,b; Kovář et al. 2011; Pugliese, Quevedo & Ruffini 2011). Here, we are aiming at the connection between the current theoretical knowledge with a real astrophysical case – Sgr A* SMBH, for which we gathered most constraints on its nearby plasma environment (Eckart et al. 2017) – in order to put realistic constraints on electric charge of our nearest SMBH.

The study is structured as follows. In Section 2, we analyse the potential for charging given the plasma properties in the surroundings of Sgr A*. Subsequently, we put constraints on the charge of the Galactic centre black hole in Section 3, including different processes that can induce charge and change its value, namely accretion of charged matter and the induction mechanism based on the black hole rotation in the magnetic field. In Section 4, we focus on possible observational consequences of the charged SMBH, specifically the effect of charge on the black hole shadow size, the bremsstrahlung brightness profile, and the position of the innermost stable orbits of charged particles. We summarize the charge constraints in Section 5, where we discuss additional effects of the black hole rotation and a potential non-electric origin of the charge. Finally, we conclude with Section 6.

2 PROSPECTS FOR CHARGING

Based on the analysis of surface brightness profiles in soft X-ray bands, there is an evidence for hot extended plasma, which surrounds the compact radio source Sgr A* (Shcherbakov & Baganoff 2010; Wang et al. 2013; Różańska et al. 2015). In addition, observations of polarized emission show that a relatively strong magnetic field is present in the Central Molecular Zone, which exhibits a highly ordered configuration (Morris 2015). The large-scale ordered magnetic field as well as the ionized, extended gas surrounding Sgr A* in the central region can be used to put constraints on the charge of the SMBH at the Galactic Centre, which has not been done properly before for any black hole candidate. The de-

¹In case a magnetic monopole could exist, it could be the fourth parameter.

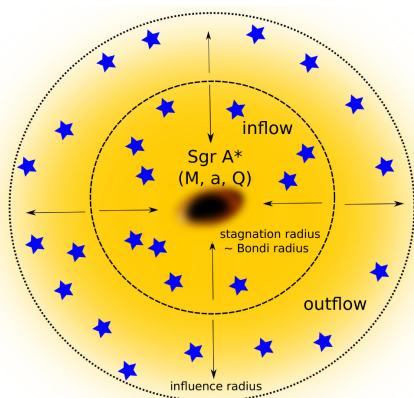
4410 *M. Zajaček et al.*

Figure 1. Illustration of the basic set-up at the Galactic centre: an SMBH characterized by mass M_* , spin a_* , and an electric charge Q_* surrounded by an NSC and hot plasma emitting thermal bremsstrahlung. The dark area at the centre illustrates the shadow the black hole casts, which can be non-spherical due to the black hole rotation and the viewing angle. The inner circle denotes the stagnation radius, which is approximately equal to the Bondi radius, inside which the gas inflow towards the black hole takes place. The outer circle represents the sphere of gravitational influence of the SMBH, inside which its potential prevails over the stellar cluster potential.

creasing surface brightness profile is satisfactorily fitted by thermal bremsstrahlung (see Róžańska et al. 2015, for an analysis). The plasma is dynamically modelled in the framework of hot accretion flows, obtaining the temperature of $k_B T_e = 1, 2,$ and 3.5 keV ($T_e = (11.6 - 40.6) \times 10^6$ K) at the outer radius of the flow, using either the radiatively inefficient accretion flow (RIAF) model (Wang et al. 2013), outflows of stars (Shcherbakov & Baganoff 2010), or the classical Bondi accretion flow (Róžańska et al. 2015), respectively. Although several models are consistent with the observed surface brightness of plasma, both the RIAF and the Bondi accretion, which occur within the NSC, are expected to have a stagnation radius R_{stag} that divides the matter flowing in towards the SMBH and the outflowing gas (Yalinewich et al. 2018). In Fig. 1, we illustrate the basic set-up, including the inflow, outflow region, and the stagnation radius.

2.1 Magnetic field properties

There is an observational evidence for the highly ordered structure of the magnetic field in the central regions of the Galaxy (Morris 2015). Two configurations were inferred from the observations of the polarized emission: a toroidal magnetic field associated with denser molecular clouds that is parallel with the Galactic plane and a poloidal field in the diluted intercloud region approximately perpendicular to the Galactic plane, which is also manifested by non-thermal radio filaments. The poloidal field in the intercloud region has magnitudes of ~ 10 μG (close to the equipartition value with cosmic rays), and it reaches ~ 1 mG in thin non-thermal filaments. The magnetic field in dense clouds has a toroidal geometry, and it reaches the value of ~ 1 mG (Ferrière 2009).

Closer to Sgr A*, Eatough et al. (2013) inferred the lower limit of magnetic field strength along the line of sight, $B \gtrsim 8$ mG, based on the Faraday rotation of the polarized emission of magnetar PSR J1745-2900, which is located at the deprojected distance of $r \gtrsim 0.12$ pc. In addition, they confirmed an ordered configuration of

the magnetic field threading the hot plasma. Inside the stagnation radius, hot and magnetized plasma descends towards Sgr A* and in this direction, an increase in the plasma density as well as in the magnetic field intensity is necessary. To explain the synchrotron emission of flares on the event-horizon scales, a magnetic field of the order of ~ 10 – 100 G is required (Falcke & Markoff 2000; Mościbrodzka et al. 2009; Dexter et al. 2010; Eckart et al. 2012). A simple scaling $B \propto r^{-1}$ is generally consistent with the increase from the Bondi-radius scales up to the event horizon.

2.2 Plasma properties

The inflow of plasma effectively takes place inside the Bondi radius, which gives the range of influence of the SMBH on the hot plasma

$$R_B \approx 0.125 \left(\frac{M_*}{4 \times 10^6 M_\odot} \right) \left(\frac{T_e}{10^7 \text{ K}} \right)^{-1} \left(\frac{\mu_{\text{HII}}}{0.5} \right) \text{ pc}, \quad (3)$$

where we assumed a fully ionized hydrogen plasma with the mean molecular weight of $\mu_{\text{HII}} = 0.5$ (Lang 1978). This assumption is supported by the observation of hot, ionized gas in the central arc-second (Róžańska et al. 2015). In addition, at the inferred temperature of several keV and the number density of the order of 10 cm^{-3} at the Bondi radius (Baganoff et al. 2003), the ionization fraction of hydrogen atoms is basically unity according to the Saha equation, $(1 - \chi)/\chi^2 \simeq 4.14 \times 10^{-16} n_{\text{tot}} T_g^{-3/2} \exp(1.58 \times 10^3 \text{ K}/T_g)$, where $\chi \equiv n_i/n_{\text{tot}}$ is the ionization fraction of the gas with the total gas number density of n_{tot} and temperature of T_g . However, during the past high-luminosity states of Sgr A*, thermal instability could have operated in the inner parsec, creating the multiphase environment where hot and cold phases could coexist (Róžańska et al. 2014). In addition, observations at millimetre wavelengths show the presence of both ionized and neutral/molecular medium in this region (the denser and colder region is referred to as the minispiral, Moser et al. 2017). In the following, we will focus on the hot ionized phase, which is expected to dominate inside the Bondi radius.

Plasma in the Galactic centre region is so hot inside the Bondi radius that it may be considered weakly coupled. This is easily shown by the coupling ratio R_c of the mean potential energy of particles and their kinetic energy:

$$R_c = \frac{E_p}{E_k} \sim \frac{e^2 (L_i 4\pi \epsilon_0)^{-1}}{k_B T_e} = \frac{e^2 n_p^{1/3} (4\pi \epsilon_0)^{-1}}{k_B T_e}, \quad (4)$$

where L_i is the mean interparticle distance, $L_i = n_p^{-1/3}$, where n_p is the particle density. For the typical (electron) particle density at the Bondi radius $n_p \approx n_e \approx 10 \text{ cm}^{-3}$ and the electron temperature of $k_B T_e \sim 1$ keV (Baganoff et al. 2003; Wang et al. 2013) as inferred from *Chandra* observations, we get $R_c \approx 3 \times 10^{-10}$, i.e. the Galactic centre plasma is very weakly coupled.

The Bondi radius of the accretion flow in the Galactic centre is thus well inside the sphere of influence of the SMBH, which represents the length-scale on which the potential of the SMBH prevails over the stellar cluster potential. For the Galactic centre SMBH and the averaged 1D stellar velocity dispersion of $\sigma_* \approx 100 \text{ km s}^{-1}$, we get (see e.g. Merritt 2013; Genozov, Stone & Metzger 2015)

$$R_{\text{inf}} \simeq GM_*/\sigma_*^2 = 1.7 \left(\frac{M_*}{4 \times 10^6 M_\odot} \right) \times \left(\frac{\sigma_*}{100 \text{ km s}^{-1}} \right)^{-2} \text{ pc}. \quad (5)$$

When considering a 1D steady-state inflow–outflow structure of the gas in the vicinity of a galactic nucleus, a characteristic feature is the existence of the stagnation radius R_{stag} , where the radial velocity

passes through zero (Generozov et al. 2015). Stellar winds inside the stagnation radius flow towards the black hole and a fraction of the matter is accreted, while the matter outside it forms an outflow, which is illustrated in Fig. 1. For the case when the heating rate due to fast outflows v_w is larger than the stellar velocity dispersion σ_* , $v_w \gg \sigma_*$, the stagnation radius can be approximately expressed as (Generozov et al. 2015)

$$R_{\text{stag}} \approx \left(\frac{13 + 8\Gamma}{4 + 2\Gamma} - \frac{3\nu}{2 + \Gamma} \right) \frac{GM_\bullet}{\nu v_w^2} \approx \begin{cases} 0.30 \left(\frac{M_\bullet}{4 \times 10^6 M_\odot} \right) \left(\frac{v_w}{500 \text{ km s}^{-1}} \right)^{-2} \text{ pc,} & \text{core } (\Gamma = 0.1), \\ 0.16 \left(\frac{M_\bullet}{4 \times 10^6 M_\odot} \right) \left(\frac{v_w}{500 \text{ km s}^{-1}} \right)^{-2} \text{ pc,} & \text{cusp } (\Gamma = 0.8), \end{cases} \quad (6)$$

where Γ is the inner power-law slope of the stellar brightness profile, where we consider two limiting cases, the core profile with $\Gamma = 0.1$ and the cusp profile with $\Gamma = 0.8$. The quantity $\nu = -d\rho/dr|_{R_{\text{stag}}}$ is the gas density power-law slope at R_{stag} , which according to the numerical analysis of Generozov et al. (2015) is $\nu \approx 1/6[(4\Gamma + 3)]$. According to the estimates in equation (6), the stagnation radius is expected to be nearly coincident with the Bondi radius with an offset given by the factor (Generozov et al. 2015)

$$\frac{R_{\text{stag}}}{R_B} \approx \frac{13 + 8\Gamma}{(2 + \Gamma)(3 + 4\Gamma)}, \quad (7)$$

which is of the order of unity.

In the further analysis and estimates, we consider the dynamical model of Rózańska et al. (2015), who fitted the thermal bremsstrahlung emission of the hot plasma with the classical Bondi solution. They found that the Bondi solution can reproduce well the surface brightness profile up to the outer radius of $r_{\text{out}} \sim 3 \text{ arcsec} \approx R_B$ (where $1 \text{ arcsec} \approx 0.04 \text{ pc}$), which is consistent with the Bondi radius expressed in equation (3).

Considering the surface brightness profile of the hot flow inferred from 134 ks *Chandra* ACIS-I observations, the best-fitting model of the spherical Bondi flow gives the asymptotic values of the electron density of $n_{e,0}^{\text{out}} = 18.3 \pm 0.1 \text{ cm}^{-3}$, the electron temperature of $T_{e,0}^{\text{out}} = 3.5 \pm 0.3 \text{ keV}$, and the sound speed of $c_s^{\text{out}} = 7.4 \times 10^7 \text{ cm s}^{-1}$. The steady spherical Bondi solution gives power-law profiles for the electron density and the electron temperature inside the Bondi radius

$$n_e \approx n_{e,0} \left(\frac{r}{r_0} \right)^{-3/2}, \quad T_e \approx T_{e,0} \left(\frac{r}{r_0} \right)^{-1}, \quad (8)$$

where $n_{e,0} = 70 \text{ cm}^{-3}$ and $T_{e,0} = 9 \text{ keV}$ at $r_0 = 0.4 \text{ arcsec}$ (Rózańska et al. 2015). The temperature has a virial profile for the adiabatic index of $\gamma_{\text{ad}} = 5/3$.

The importance of collisional processes between plasma constituents – mainly protons and electrons – can be evaluated by comparing the collisional time-scales of electron–electron and electron–proton interactions with the typical dynamical time-scale (free-fall time-scale) and the viscous time-scale. The electron–electron collisional frequency approximately is $\nu_{ee} \simeq 3.75 n_e T_e^{-3/2} \log \Lambda_{ee} \text{ Hz}$, where $\log \Lambda_{ee}$ is the Coulomb logarithm, while the frequency of electrons colliding with protons may be estimated as $\nu_{ep} \simeq 5.26 n_i T_e^{-3/2} \log \Lambda_{ei} \text{ Hz}$. Assuming that the electron and proton number densities are approximately the same, $n_i \approx n_e$, the corresponding collisional time-scales of electrons with themselves and protons are approximately constant with radius, given the Bondi profiles in equations (8). The electron–electron collisional time-scale is $\tau_{ee} \approx (\nu_{ee})^{-1} \approx 13 \text{ yr}$ for $\log \Lambda_{ee} = 10$. In a similar way, the

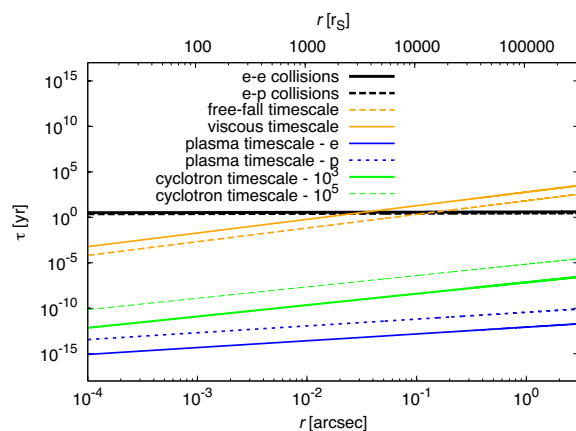


Figure 2. Radial profiles of electron–electron and electron–proton collisional time-scales estimated based on density and temperature radial profiles expressed by equation (8). Inside the innermost 1000 Schwarzschild radii, the electron–electron and electron–proton collisions occur on longer time-scales than the dynamical and accretion processes governed by Sgr A*. On the other hand, the density and velocity plasma oscillations take place on significantly shorter scales throughout the GC region. The same applies to the range of cyclotron time-scales.

electron–proton collisional time-scale is $\tau_{ep} \approx 9 \text{ yr}$. The free-fall (dynamical) time-scale evaluated for the initial infall distance of $r_0 = 1000 r_s$ is

$$t_{\text{dyn}} \approx t_{\text{ff}} \simeq 0.062 \left(\frac{r_0}{1000 r_s} \right)^{3/2} \left(\frac{M_\bullet}{4 \times 10^6 M_\odot} \right)^{-1/2}. \quad (9)$$

The viscous time-scale t_{vis} may be in general expressed as (Lasota 2016)

$$t_{\text{vis}} \approx \alpha^{-1} (H/r_0)^{-2} t_{\text{dyn}}, \quad (10)$$

where the ratio of the thickness of the accretion flow to the radial length-scale is expected to be of the order of unity since the accretion flow around Sgr A* is generally considered to be optically thin and geometrically thick as for hot accretion flows in general (Yuan & Narayan 2014). When the viscosity parameter α is of the order of 0.1 (King, Pringle & Livio 2007; Lasota 2016), the viscous time-scale is $t_{\text{vis}} \approx 10 t_{\text{dyn}}$.

When compared to the free-fall and viscous time-scales, see Fig. 2, the electron–electron and electron–proton interactions take place on longer time-scales than the dynamical and accretion processes inside the inner 1000 Schwarzschild radii. This implies that particle collisions are irrelevant for the dynamical processes in the immediate vicinity of Sgr A*.

On the other hand, the ordered plasma oscillations with the characteristic plasma frequency ν_p are relevant on all spatial scales. The presence of plasma close to the SMBH at the Galactic centre means that the immediate vicinity of Sgr A* cannot be observed at frequencies smaller than the plasma frequency, $\nu < \nu_p$, because of charge oscillations in the plasma. The Bondi-flow model of Rózańska et al. (2015) predicts the number densities of electrons at the scale of $r = 10 r_s$ to be $n_e \approx 10^7 \text{ cm}^{-3}$ and that yields the plasma frequency of

$$\nu_p = 28.4 \left(\frac{n_e}{10^7 \text{ cm}^{-3}} \right)^{1/2} \text{ MHz}, \quad (11)$$

which would effectively block electromagnetic radiation with wavelengths longer than $\lambda_p \simeq 11 \text{ m}$ from the innermost region. By coin-

4412 *M. Zajaček et al.*

idence, the plasma frequency close to the Galactic centre expressed by equation (11), which depends on the electron density, is close to the cyclotron frequency for electrons gyrating in the magnetic field with the intensity of $B \sim 10$ G:

$$v_{\text{cyc}} = \frac{B}{2\pi\gamma_L} \frac{e}{m_e} \simeq 28 \left(\frac{B}{10\text{ G}} \right) \gamma_L^{-1} \text{ MHz}, \quad (12)$$

where γ_L is a Lorentz factor. The approximate profile of the cyclotron time-scale can be evaluated using the assumption that the magnetic field pressure is a fraction of the gas pressure, $P_{\text{gas}} = n_e k_B T_e$. Then, the magnetic field is $B = \sqrt{8\pi P_{\text{gas}}/\beta}$, where we take $\beta = 100$ to reproduce the magnetic field strengths as determined based on the magnetar observations at larger distances and the flare observations on the ISCO scales (Eckart et al. 2012; Eatough et al. 2013). The Lorentz factor is taken in the range $\gamma_L = 10^3 - 10^5$ as inferred from the flare observations in the X-ray and infrared domains (Eckart et al. 2012). Based on Fig. 2, both the plasma time-scale and the cyclotron time-scales for electrons are shorter than the dynamical, viscous, and collisional time-scales in the whole considered region.

Although particle collisions can be neglected for dynamical processes in the vicinity of Sgr A*, this does not apply to radiative processes in the same region, namely for the detected thermal X-ray bremsstrahlung (Baganoff et al. 2003; Mossoux & Eckart 2018). By definition, the bremsstrahlung requires the Coulomb interaction of particles, with the dominant contribution of unlike particles, electrons and protons. This is not in contradiction with the low estimated rate of collisions in the central region since the interactions over the whole region contribute to the observed surface brightness.

The average electron and proton (ion) density can be estimated from the emissivity of thermal bremsstrahlung and the quiescent X-ray luminosity of Sgr A*. In principle, the thermal bremsstrahlung can experience losses due to Thomson scattering. The optical depth along the line of sight may be estimated as $\tau_T = \int_0^{R_B} \sigma_T n_e(l) dl$, where l is the line-of-sight coordinate. Given the cross-section of Thomson scattering, $\sigma_T = 6.65 \times 10^{-25} \text{ cm}^2$, the electron density profile given by equation (8), and the typical length-scale given by the Bondi radius, R_B , the optical depth is given by

$$\tau_{\text{Brems}} = \int_0^{R_B} \sigma_T n_e(l) dl = \frac{\sigma_T n_{e,0} r_0^{3/2}}{R_B^{1/2}} \approx 2 \times 10^{-7}, \quad (13)$$

and hence the losses due to Thomson scattering are negligible. Given the average quiescent X-ray luminosity of Sgr A* in the range of 2–10 keV, $L_{2-10} = 2 \times 10^{33} \text{ erg s}^{-1}$ (Haggard 2017), one can estimate the electron density from the thermal bremsstrahlung luminosity

$$L_{\text{brems}} \approx 6.8 \times 10^{-38} Z^2 n_i n_e T_g^{-1/2} V(R_B) g_{\text{ff}}(v, T_g) \times \int_{v_1}^{v_2} \exp(-hv/kT_g) dv \text{ erg s}^{-1}, \quad (14)$$

where n_i is the ion number density, Z is the proton number of participating ions, T_g is the temperature of the gas, $V(R_B) \approx 4/3\pi R_B^3$ is the volume inside the Bondi radius, $g_{\text{ff}}(v, T_g)$ is a Gaunt factor used for the quantum corrections to classical formulas, which we set to $g_{\text{ff}} = 1.5$ in the given temperature range of ($10^7, 10^8$) K and the frequency range of (2, 10) keV (v_1, v_2) = (0.5, 2.4) $\times 10^{18}$ Hz. The integral in equation (14) can be approximated as $\int_{v_1}^{v_2} \exp(-hv/kT_g) dv \sim 0.98 \times 10^{10} T_g$. For fully ionized hydrogen and helium plasma, the term $Z^2 n_i n_e$ becomes $1.55 n_e^2$. Putting the numerical factors all to-

gether into equation (14) yields

$$L_{\text{brems}} \approx 3.725 \times 10^{30} \bar{n}_e^2 \left(\frac{T_g}{10^8 \text{ K}} \right)^{1/2} \left(\frac{R_B}{0.125 \text{ pc}} \right)^3 \text{ erg s}^{-1}. \quad (15)$$

Given the measured X-ray luminosity of $L_{2-10} \approx 2 \times 10^{33} \text{ erg s}^{-1}$, the mean electron density using equation (15) is $\bar{n}_e \approx 23 \text{ cm}^{-3}$, which is very close to the asymptotic value of $n_e^{\text{out}} = 18.3 \pm 0.1 \text{ cm}^{-3}$ derived by Różańska et al. (2015) from the Bondi solution.

2.3 Classical estimates of charging

The fundamental mechanism, which can lead to charging of the black hole, are different thermal speeds for electrons and protons in the fully ionized plasma, $v_{\text{th,e}} = (k_B T_e/m_e)^{1/2}$ and $v_{\text{th,p}} = (k_B T_p/m_p)^{1/2}$, following from the fact that the Galactic centre plasma is collisionless. Given a considerable mass difference between electrons and protons, $m_p = 1837 m_e$, it is expected that the ratio of thermal speeds is

$$\frac{v_{\text{th,e}}}{v_{\text{th,p}}} = \left(\frac{T_e m_p}{T_p m_e} \right)^{1/2} \approx 43, \quad (16)$$

under the assumption that $T_e \approx T_p$. This leads to the ratio of the corresponding Bondi radii for protons and electrons

$$\frac{R_{\text{B,p}}}{R_{\text{B,e}}} = \frac{T_e m_p}{T_p m_e}. \quad (17)$$

Next, we can estimate the total charge by integrating across the corresponding Bondi radius. In the spherical symmetry, the total charge inside the Bondi radius can be calculated as $|Q| = \int_0^{R_B} \rho_Q 4\pi r^2 dr$, where ρ_Q is the charge density. Under the assumption of a power-law density profile for both electrons and protons, $n_{e,p} = n_0 (r/r_0)^{-\gamma_n}$ ($\gamma_n = 3/2$ for the spherical Bondi flow), the ratio of positive and negative charge in the range of influence of the SMBH can be calculated as follows:

$$\left| \frac{Q_+}{Q_-} \right| = \frac{\int_0^{R_{\text{B,p}}} e n_p 4\pi r^2 dr}{\int_0^{R_{\text{B,e}}} e n_e 4\pi r^2 dr} = \left(\frac{R_{\text{B,p}}}{R_{\text{B,e}}} \right)^{3-\gamma_n} = \left(\frac{T_e m_p}{T_p m_e} \right)^{3-\gamma_n} \approx 8 \times 10^4, \quad (18)$$

where the last estimate is valid for $T_e \approx T_p$, which, however, does not have to be quite valid in the hot accretion flows that surround quiescent black holes, such as Sgr A* or M87, where a two-temperature flow is expected to exist (Yuan & Narayan 2014). At large distances from the black hole, close to the stagnation radius, the electron and proton temperatures are expected to be almost same. Closer to the black hole, in the free-fall regime of the Bondi flow, the electron and the proton (ion) temperatures differ, the proton temperature is larger than the electron temperature by about a factor of $\simeq 1-5$, $T_e/T_p \geq 1/5$ (Mościbrodzka et al. 2009; Dexter et al. 2010), which gives the lower limit to the excess of the positive charge in the range of influence of the SMBH, $\left| \frac{Q_+}{Q_-} \right| \gtrsim 7000$.

A similar analysis as above was discussed and performed for stationary plasma atmospheres of stars (see Neslušan 2001, and references therein) and in general, for gravitationally bound systems of plasma (Bally & Harrison 1978). In the hot atmosphere, where the plasma may be considered collisionless, lighter electrons tend to separate from heavier protons. The separation is stopped by an induced electrostatic field $\psi = (1/4\pi\epsilon_0) Q_{\text{eq}}/r$. In the gravitational

field of an approximately spherical mass of M_\bullet , $\phi = GM_\bullet/r$, the potential energy of protons can be expressed as $E_p = -m_p\phi + e\psi$, and for electrons with negative charge in a similar way, $E_e = -m_e\phi - e\psi$. Given the assumption of the stationary equilibrium plasma densities, the number densities of protons and electrons are proportional to $\exp(-E_p/k_B T_p)$ and $\exp(-E_e/k_B T_p)$, respectively. Given the quasineutrality of plasma around stars and Sgr A*, the difference between the densities of protons and electrons is expected to be small, which implies $E_p \approx E_e$. The induced equilibrium charge of the central body surrounded by plasma then is

$$Q_{\text{eq}} = \frac{2\pi\epsilon_0 G(m_p - m_e)}{e} M_\bullet \approx 3.1 \times 10^8 \left(\frac{M_\bullet}{4 \times 10^6 M_\odot} \right) C. \quad (19)$$

Equation (19) was derived under the assumption of spherical stationary plasma around a point mass, which is certainly not met in the environment of dynamical plasma around Sgr A*. The real charge of Sgr A* will therefore deviate from the stationary value of Q_{eq} . The mechanism of charging will, however, still tend to operate and a rough approximation of charge expressed by equation (19) is still more precise than the assumption of a neutral black hole. The equilibrium value Q_{eq} also expresses the upper limit of an electric charge associated with Sgr A*, for which the stationary number densities of protons and electrons in plasma remain approximately constant. For charges $Q \gg Q_{\text{eq}}$, a significant difference in the number densities is expected that would decrease with the distance, unless the charge of the black hole would be Debye shielded, as we will discuss later in this paper.

Given the simple calculations above, it is expected that the black hole at the Galactic centre can acquire a small positive charge, given the fact that more positive charge is in the range of its gravitational influence than negative charge. In the following, we will look at more realistic scenarios of how the black hole charge could be induced in the accretion flow, given the fact that black holes are expected to have a non-zero spin and should be immersed in a magnetic field.

3 LIMITS ON THE BLACK HOLE CHARGE

3.1 Maximum theoretical values of the charge of Sgr A*

The uppermost limit on the charge of Sgr A* may be derived using the space-time of the black hole that is characterized by its mass M_\bullet , electric charge Q_\bullet , and rotation parameter a_\bullet . In the most general case, the Kerr–Newman (KN) solution (Newman et al. 1965) fully describes such a black hole in vacuum. The KN metric can be expressed in Boyer–Lindquist coordinates in the following way (Misner, Thorne & Wheeler 1973):

$$ds^2 = - \left(\frac{dr^2}{\Delta} + d\theta^2 \right) \rho^2 + (c dt - a_\bullet \sin^2 \theta d\Phi)^2 \frac{\Delta}{\rho^2} - [(r^2 + a_\bullet^2) d\Phi - a_\bullet c dt]^2 \frac{\sin^2 \theta}{\rho^2}, \quad (20)$$

where $\rho^2 = r^2 + a_\bullet^2 \cos^2 \theta$ and $\Delta = r^2 - r_S r + a_\bullet^2 + r_Q^2$. The length-scales r_S and r_Q^2 correspond to the Schwarzschild radius $r_S = 2GM_\bullet/c^2 = 1.2 \times 10^{12} (M_\bullet/4 \times 10^6 M_\odot) \text{ cm}$ and $r_Q^2 = GQ_\bullet^2/(4\pi\epsilon_0 c^4)$, respectively. The position of the event horizons is obtained with the condition $\Delta = 0$, which leads to the quadratic equation, $r^2 - r_S r + a_\bullet^2 + r_Q^2 = 0$, with two possible horizons $r_{1,2} = 1/2(r_S \pm \sqrt{r_S^2 - 4(a_\bullet^2 + r_Q^2)})$ for $r_S > 2\sqrt{a_\bullet^2 + r_Q^2}$. For

$r_S < 2\sqrt{a_\bullet^2 + r_Q^2}$, no horizons exist, so the object is a naked singularity. The condition $r_S = 2\sqrt{a_\bullet^2 + r_Q^2}$ leads to a single event horizon located at $r = 1/2 r_S$, which represents an extremal black hole, and it also gives an upper limit for an electric charge of the SMBH at the Galactic centre:

$$Q_{\text{max}}^{\text{rot}} = 2c^2 \sqrt{\frac{\pi\epsilon_0}{G} \left(\frac{G^2 M_\bullet^2}{c^4} - a_\bullet^2 \right)}, \quad (21)$$

which can be rewritten using a dimensionless parameter $a_\bullet = \tilde{a}_\bullet GM_\bullet/c^2$ into the form

$$Q_{\text{max}}^{\text{rot}} = 2M_\bullet \sqrt{\pi\epsilon_0 G(1 - \tilde{a}_\bullet^2)}. \quad (22)$$

Relation (21) represents a theoretical limit for the maximum charge of a rotating black hole. Above this limit, the massive object at the Galactic centre would be not a black hole anymore, but a naked singularity, which can be ruled out based on observational and causal arguments (Eckart et al. 2017). In addition, a direct transition between a non-extremal black hole and an extremal one due to the accretion of charged matter (test particles or shells) is not possible as was shown in Wang et al. (1998, see also references therein).

For a non-rotating black hole ($a_\bullet = 0$), the maximum charge is proportional to the black hole mass. Evaluating for Sgr A* gives

$$Q_{\text{max}}^{\text{nonrot}} = 2\sqrt{\pi\epsilon_0 G} M_\bullet = 6.86 \times 10^{26} \left(\frac{M_\bullet}{4 \times 10^6 M_\odot} \right) C. \quad (23)$$

In Fig. 3, we plot the effect of the rotation of the black hole on its maximum electric charge. Close to the maximum rotation, the maximum charge is close to zero.

In the following, we discuss limits on the electric charge of the Galactic centre black hole based on induced electric field of a rotating black hole immersed in the circumnuclear magnetic field.

3.2 Charge induced by rotating SMBH

There are indications that a considerable magnetic field must be present in the vicinity of SMBH at the Galactic centre (Eckart et al. 2012; Eatough et al. 2013; Różańska et al. 2015), which suggests the value of 10 G in the vicinity of the event horizon. The exact solution for the electromagnetic fields in the vicinity of Sgr A* is far from being properly defined, however, it is natural to assume that the magnetic field shares the symmetries of the background space–time metric, such as the axial symmetry and stationarity. The central SMBH is assumed to be a standard Kerr black hole whose gravitational potential dominates the system. Moreover, the small density of the plasma around Sgr A* implies that the magnetosphere of SMBH can be described within the test field approximation. This assumption implies that the four-vector potential can be written in the form $A^\alpha = k_1 \xi_{(t)}^\alpha + k_2 \xi_{(\phi)}^\alpha$, where k_1 and k_2 are the arbitrary parameters and $\xi_{(t)}^\alpha$ and $\xi_{(\phi)}^\alpha$ are a unit time-like and space-like Killing vectors, respectively, which are related to the symmetries of the black hole space–time. For estimation purposes, one can assume that the magnetic field is homogeneous and aligned along the axis of rotation of black hole with the strength B . Then, the solution of Maxwell equations for corresponding four-vector potential in rotating black hole space–time can be written in the following form (Wald 1974):

$$A_t = \frac{B}{2} (g_{t\phi} + 2ag_{tt}), \quad A_\phi = \frac{B}{2} (g_{\phi\phi} + 2ag_{t\phi}). \quad (24)$$

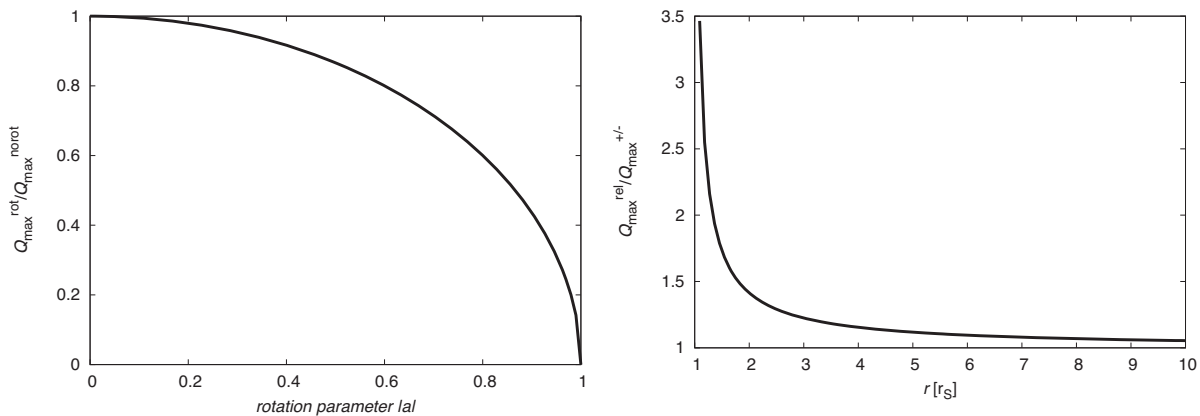
4414 *M. Zajaček et al.*

Figure 3. *Left:* Effect of the rotation of the black hole on its maximum electric charge. *Right:* The dependence of the relativistic correction to both the maximum positive and negative charge of the SMBH. In the relativistic regime, the electrostatic force increases towards the event horizon, which becomes apparent inside the innermost stable orbit.

The rotation of a black hole gives the contribution to the Faraday induction that generates the electric potential A_t and thus produces an induced electric field, just in the same manner as if the field would be induced in magnetic field by a rotating ring. This is how the black hole obtains non-zero induced charge. The potential difference between the horizon of a black hole and infinity takes the form

$$\Delta\phi = \phi_H - \phi_\infty = \frac{Q - 2aMB}{2M}. \quad (25)$$

The potential difference leads to the process of selective accretion, which implies that a rotating black hole in external homogeneous magnetic field can obtain maximum net electric charge $Q = 2aMB$.

The statement of selective accretion by rotating black hole in the presence of magnetic field is quite general and independent of the exact shape of the field and the type of accreting charged matter, which can, however, put restrictions on the time-scales of selective accretion due to charge separation in a plasma. In general, the energy of charged particle in stationary field and space–time is $E = -P_\mu \xi_{(t)}^\mu$, where $P_\mu = mu_\mu - qA_\mu$ is generalized four-momentum. The difference of electrostatic energy of a particle at infinity and at the horizon is $E_H - E_\infty = qA_t|_{r \rightarrow r_H} - qA_t|_{r \rightarrow \infty} = \delta$. When $\delta > 0$, the black hole accretes the particles with q charges, while when $\delta < 0$, it is energetically more favourable to accrete the particles with $-q$ charge. In both cases, the black hole will accrete a net charge until the difference δ is reduced to zero. The sign of induced charge depends on the relative orientation of magnetic field lines and black hole spin (Tursunov, Stuchlík & Kološ 2016). If one assumes that the magnetic field is created by the dynamics of the surrounding conducting plasma that co-rotates with the black hole, then the sign of induced charge is more likely positive.

This analysis can also put a limit on the maximum induced charge of SMBH. If magnetic field is oriented along the rotation axis of a black hole, the black hole induces electric charge given by $Q_{\bullet\text{ind}} = 2aM_\bullet B_{\text{ext}}$. Given an upper boundary for the spin parameter $a_\bullet \leq M_\bullet$, one can estimate the upper boundary for the induced charge as follows:

$$Q_{\bullet\text{ind}}^{\text{max}} = 2.32 \times 10^{15} \left(\frac{M_\bullet}{4 \times 10^6 M_\odot} \right)^2 \left(\frac{B_{\text{ext}}}{10\text{G}} \right) \text{C}, \quad (26)$$

where the external magnetic field is expressed in units of 10 G, which is the estimated magnetic field strength associated with the flaring activity of Sgr A* (Eckart et al. 2012). Independently from the precise configuration of magnetic field in the Galactic centre, the order of magnitude of estimated induced charge is about $10^{15} \pm 1$ C, if the assumptions of the axial symmetry and stationarity is preserved. In the case of Sgr A*, there is a convincing evidence that the magnetic field in the Galactic centre is indeed highly oriented and ordered (Morris 2015), which supports our assumptions.

We would like to stress that the induced charge plays a role of a driving force in the processes of energy extraction from rotating black holes. Two leading processes by which the rotational energy can be extracted out are the Blandford–Znajek mechanism (Blandford & Znajek 1977) and the magnetic version of Penrose process (Penrose 1969; Wagh et al. 1985), both of which use the existence of negative energy states of particles with respect to observer at infinity. In both of these processes, the rotation of a black hole in magnetic field generates quadrupole electric field by twisting of magnetic field lines (Dadhich et al. 2018). An infall of oppositely charged particles (relative to the sign of induced charge) leads to the discharge of the induced field and therefore the extraction of rotational energy of a black hole. In Blandford–Znajek mechanisms, the presence of induced field completes current circuit for infalling oppositely charged negative energy flux. This field is responsible for acceleration of charged particles that can be launched as black hole jets. Similarly, e.g. in the case of a uniform magnetic field considered above, the discharge of induced electric field $Q_{\bullet\text{ind}} = 2aM_\bullet B$ would lead to the decrease of black hole spin a and resulting extraction of rotational energy of a black hole, while B is constant by its definition.

Multiple numerical simulations of two processes for general relativistic magnetohydrodynamic flow showing the efficient extraction of energy from rotating black holes imply that the induced electric field is not screened at least in the close vicinity of black holes. The problem of screening of induced electric field by surrounding plasma for Sgr A* is discussed in Section 4.2.

The value of $Q_{\bullet\text{ind}}^{\text{max}}$ is small in comparison with Q_{max} implying that its effect on the space–time geometry can be neglected. The upper boundary for the charge-to-mass ratio for the Galactic centre

SMBH (Kim, Lee & Lee 2001) is

$$\begin{aligned} \frac{Q_{\bullet}^{\text{ind}}}{M_{\bullet}} &= 2B_0 \frac{J_{\bullet}}{M_{\bullet}} \leq 2B_0 M_{\bullet} \\ &= 8 \times 10^{-13} \left(\frac{B_0}{10\text{G}} \right) \left(\frac{M_{\bullet}}{4 \times 10^6 M_{\odot}} \right) \ll 1. \end{aligned} \quad (27)$$

Relation (27) implies that the induced black hole charge is weak in a sense that its effect on the dynamics of neutral matter can be neglected and Kerr metric approximation can be used. However, induced charge can have considerable effect on the dynamics of charged matter and consequently on some of the observables of Sgr A*, which we specifically discuss in Section 4.

3.3 Charge fluctuation due to accretion

The electric charge of $Q_{\text{max}}^{\text{horot}}$ is a theoretical upper limit. In reality, the accretion of positively charged particles (protons) will stop to proceed when the Coulomb force between the SMBH and the proton is of the same value and opposite orientation as the gravitational force, giving the condition for the maximum positive charge in a non-relativistic case:

$$Q_{\text{max}}^+ = 4\pi\epsilon_0 GM_{\bullet} \left(\frac{m_p}{e} \right) = 6.16 \times 10^8 \left(\frac{M_{\bullet}}{4 \times 10^6 M_{\odot}} \right) C, \quad (28)$$

which is much smaller than the maximum charge, $Q_{\text{max}}^+/Q_{\text{max}} = 2\sqrt{\pi\epsilon_0 GM_p/e} \approx 9 \times 10^{-19}$.

In a similar way, the maximum negative charge derived for accreting electrons is

$$Q_{\text{max}}^- = 4\pi\epsilon_0 GM_{\bullet} \left(\frac{m_e}{e} \right) = 3.36 \times 10^5 \left(\frac{M_{\bullet}}{4 \times 10^6 M_{\odot}} \right) C, \quad (29)$$

which leads to an even smaller ratio $Q_{\text{max}}^-/Q_{\text{max}} = 2\sqrt{\pi\epsilon_0 GM_e/e} \approx 4.9 \times 10^{-22}$. The ratios of maximum positive and negative charges to the maximum charge allowed for the SMBH imply that the space-time metric is not affected by an electric charge in a significant way.

Equations (28) and (29) are applicable only far from the black hole. In the relativistic regime, the motion of charged particles in the simplest regime without rotation can be studied within the Reissner–Nordström solution, which can be acquired from the KN metric by setting $a_{\bullet} = 0$ in equation (20). The line element in the geometrized units with $c = 1 = G$ can be written as

$$ds^2 = -f(r)dt^2 + f(r)^{-1}dr^2 + r^2 d\theta^2 + r^2 \sin^2 \theta d\phi^2, \quad (30)$$

where the lapse function is defined as

$$f(r) = 1 - \frac{r_S}{r} + \frac{r_Q^2}{r^2}. \quad (31)$$

The four-vector potential A_{α} of electromagnetic field generated by the charge Q_{\bullet} of the Reissner–Nordström black hole takes the form

$$A_{\mu} = \frac{Q_{\bullet}}{r} \delta_{\mu}^{(t)}. \quad (32)$$

The dynamics of charged particle in curved space–time in presence of electromagnetic fields is governed by the equation

$$\frac{du^{\mu}}{d\tau} + \Gamma_{\alpha\beta}^{\mu} u^{\alpha} u^{\beta} = \frac{q}{m} F_{\nu}^{\mu} u^{\nu}, \quad (33)$$

where $u^{\mu} = dx^{\mu}/d\tau$ is the four-velocity of the particle with mass m and charge q , normalized by the condition $u^{\mu} u_{\mu} = -1$, τ is the

proper time of the particle, $F_{\mu\nu} = A_{\nu,\mu} - A_{\mu,\nu}$ is an antisymmetric tensor of the electromagnetic field and components of $\Gamma_{\alpha\beta}^{\mu}$ are the Christoffel symbols.

One of the interesting features of the motion of charged particles in the vicinity of Reissner–Nordström black hole is the existence of trapped equilibrium state of a particle where the electrostatic forces between two charges compensate the gravitational attraction of a black hole. The four-velocity of a particle at this state is $u^{\alpha} = (1/\sqrt{-g_{tt}}, 0, 0, 0)$. Thus, the time component of equation (33) takes the form

$$r_S - 2\frac{r_Q^2}{r} + 2\frac{Qq}{m} \left(1 - \frac{r_S}{r} - \frac{r_Q^2}{r^2} \right)^{1/2} = 0. \quad (34)$$

Since the gravitational effect of the charge Q_{\bullet} is small in comparison with those of the mass of the black hole (corresponding to $r_Q \ll r_S$), one can neglect the higher order terms in Q_{\bullet} (equation 34). Thus, for the charge Q we get

$$Q_{\bullet} = \frac{mr_S}{2q} \left(1 - \frac{r_S}{r} \right)^{-1/2}. \quad (35)$$

The charge (35) can be interpreted as the maximum net charge that can be accreted into the black hole from the given position r before the electrostatic force will prevail and the accretion of same-charge particles stops. Restoring the constant in (35), we get charge in SI units as

$$Q_{\text{max}}^{\text{rel}} = 4\pi\epsilon_0 GM_{\bullet} \frac{m_{\text{par}}}{q_{\text{par}}} \left(1 - \frac{r_S}{r} \right)^{-1/2}. \quad (36)$$

The factor $\left(1 - \frac{r_S}{r} \right)^{-1/2}$ is the general relativistic correction to the corresponding Newtonian equation. This implies that the electrostatic force increases while approaching black hole. Close to the horizon, the divergence of (36) means that the black hole requires infinite charge in order to keep the equilibrium position of the particle. We plot the ratio $Q_{\text{max}}^{\text{rel}}/Q_{\text{max}}^{\pm}$, i.e. the relativistic correction in Fig. 3.

3.4 Charge and dynamical time-scales

The electric charge of the SMBH is expected to fluctuate due to discharging by particles of an opposite charge. This is especially efficient when the free-fall time-scale of particles with the opposite charge is significantly shorter than the free-fall time-scale of the particles with the same charge as that of the black hole. The free-fall time-scale for a charged black hole is modified due to the presence of an additional Coulomb term in the equation of the motion for a radial infall (neglecting the gas pressure):

$$\frac{dv}{dt} = -\frac{GM_{\bullet}}{r^2} + \frac{1}{4\pi\epsilon_0} \frac{Q_{\bullet} q_{\text{par}}}{r^2 m_{\text{par}}}, \quad (37)$$

where q_{par} and m_{par} are the charge and the mass of the particle, respectively. The signs in the equation are the following: for the positive charge of the black hole $Q_{\bullet} = +Q^+$, the particle charge is $q_{\text{par}} = +e$ for the proton ($m_{\text{par}} = m_p$) and $q_{\text{par}} = -e$ for the electron ($m_{\text{par}} = m_e$). For the negative charge of the black hole $Q_{\bullet} = -Q^-$, the signs of particle charges are kept as before.

The Newtonian free-fall time-scale derived from equation (37) for a particle falling in from the initial distance of r_0 is

$$t_{\text{ff},Q} = \frac{\pi r_0^{3/2}}{\sqrt{8(GM_{\bullet} - \frac{1}{4\pi\epsilon_0} \frac{Q_{\bullet} q_{\text{par}}}{m_{\text{par}}})}}, \quad (38)$$

4416 *M. Zajaček et al.*

which becomes $t_{\text{ff}}(Q_\bullet = 0) = \pi r_0^{3/2}/\sqrt{8GM_\bullet}$ for zero charge of the SMBH. The direct outcome of equation (38) is the difference of free-fall time-scales for protons and electrons for a given charge of the SMBH.

In Fig. 4, we plot the free-fall time-scales for protons and electrons for a positive charge of the SMBH (left-hand panel) and for its negative charge (right-hand panel). The time-scales are comparable up to $Q^+ \lesssim 10^{-5} Q_{\text{max}}^+$ for the positively charged black hole and up to $Q^- \lesssim 10^{-2} Q_{\text{max}}^-$, which further limits a charge of the SMBH since for larger charges the infall of opposite charges is progressively faster than the infall of the same charges. For the maximum positive charge of Sgr A*, the free-fall time-scale for electrons is $t_{\text{ff}, Q_{\text{max}}^+} = 8.5$ yr for an initial distance at the Bondi radius. This is a much shorter time-scale than the free-fall time-scale of protons for the maximum negative charge, which is close to the free-fall time-scale for a non-charged black hole with an initial distance at the Bondi radius, $t_{\text{ff}} = 366$ yr.

The free-fall time-scale from the Bondi radius is the basic dynamical time-scale in the accretion flow. Any disturbance in the accretion flow develops on the viscous time-scale given by equation (10), which for the assumption of the thick flow $H \approx r_0$ and $\alpha \approx 0.1$ is approximately $t_{\text{vis}} \approx 10 t_{\text{ff}}(r_0, Q_\bullet)$.

In the following, we define a specific charge of accreted matter ϵ , which relates the accretion rate of the charged matter to the total accretion rate as $\dot{M}_{\text{acc}}^{\text{charge}} = \epsilon \dot{M}_{\text{acc}}$. From this relation, the charging rate of the black hole, \dot{Q}_\bullet , may be expressed as

$$\dot{Q}_\bullet = \epsilon \frac{q_{\text{par}}}{m_{\text{par}}} \dot{M}_{\text{acc}}, \quad (39)$$

where \dot{M}_{acc} is the total accretion rate. The total accretion rate was inferred from the observations via the Faraday rotation by Marone et al. (2007), who obtain $\dot{M}_{\text{acc}} = 2 \times 10^{-9} M_\odot \text{yr}^{-1}$ up to $2 \times 10^{-7} M_\odot \text{yr}^{-1}$, depending on the configuration of the magnetic field. For the induced positive charge Q_{ind}^+ , the charging (induction) time-scale follows from equation (39):

$$\tau_{\text{charge}}^+ = \frac{m_{\text{p}} Q_{\text{ind}}^+}{e \epsilon_{\text{pos}} \dot{M}_{\text{acc}}}, \quad (40)$$

while for the induced negative charge we get

$$\tau_{\text{charge}}^- = \frac{m_{\text{e}} Q_{\text{ind}}^-}{e \epsilon_{\text{neg}} \dot{M}_{\text{acc}}}. \quad (41)$$

To charge the black hole positively, mainly by the induction process described in Section 3.2, the charging time-scale expressed by equation (40) needs to be smaller than the discharge time-scale, which can be estimated by the viscous time-scale of electrons on the scale of the gravitational radius. On the other hand, the charging time-scale must be larger than the time-scale given by the plasma frequency for protons, $\tau_{\text{p}} = 2\pi(\epsilon_0 m_{\text{e}}/(n_{\text{e}} e^2))^{1/2}$, which expresses the charged density fluctuations on scales larger than the Debye length. For the exemplary values of $Q_{\text{ind}} = Q_{\bullet,10} 10^{10} C$ and $\dot{M}_{\text{acc}} = \dot{M}_{-8} = 10^{-8} M_\odot \text{yr}^{-1}$, we obtain the limits

$$1.3 \times 10^{-13} Q_{\bullet,10} \dot{M}_{-8}^{-1} \lesssim \epsilon_{\text{pos}} \lesssim 1.4 \times 10^{-6} Q_{\bullet,10} \dot{M}_{-8}^{-1}. \quad (42)$$

In an analogous way, the negative charged fraction of the accretion rate is

$$1.7 \times 10^{-18} Q_{\bullet,10} \dot{M}_{-8}^{-1} \lesssim \epsilon_{\text{neg}} \lesssim 3.3 \times 10^{-8} Q_{\bullet,10} \dot{M}_{-8}^{-1}, \quad (43)$$

as inferred by comparing (41) to the viscous time-scale of protons (upper time-scale limit for discharging) and to the time-scale of electron plasma oscillations (both evaluated at the ISCO scale of $r_{\text{ISCO}} \approx GM_\bullet/c^2$).

The charging of Sgr A* can thus effectively proceed when a rather small fraction of accreted matter (ϵ_{pos} or ϵ_{neg}) is charged. The charging process of the accreted fluid may proceed at a larger distance from the SMBH horizon plausibly due to strong irradiation or the external (Galactic) magnetic field (Kovář et al. 2011).

The process of the black hole charging can proceed efficiently when the gravitational and electrostatic forces acting on a particle are greater than the thermal pressure forces inside a region of radius R_{charge} , which is equivalent to the condition that the viscous time-scale of the inward motion must be smaller than the thermal time-scale, $t_{\text{vis}, Q} < t_{\text{th}}$ inside R_{charge} . The thermal time-scale is simply, $t_{\text{th}} = R_{\text{charge}}/v_{\text{th}}$, where the thermal speed v_{th} is related to either electrons or protons. The condition of the smaller viscous time-scale is met inside the sphere of radius R_{charge} , whose radius progressively gets smaller and it reaches zero at either the maximum positive or negative charge, see equations (28) and (29). Under the assumption that the accretion flow is thick in a sense ($H/r_0 \approx 1$), it can be simply derived that

$$R_{\text{charge}} \lesssim (\alpha/\pi)^2 \frac{m_{\text{par}}}{k_{\text{B}} T_{\text{g}}} \left(8GM_\bullet - \frac{2}{\pi \epsilon_0} Q_\bullet \frac{q_{\text{par}}}{m_{\text{par}}} \right), \quad (44)$$

with the sign convention as in equation (38). For the zero charge of the black hole, the relation (44) is similar to the definition of the Bondi radius, equation (3), $R_{\text{charge}} \lesssim 8(\alpha/\pi)^2 GM_\bullet/v_{\text{th}}^2$.

In Fig. 5, we plot equation (44) for both positive charging (protons falling into the positively charged black hole; see left-hand panel) and negative charging (electrons falling into negatively charged black hole; right-hand panel). Inside the radius R_{charge} , basic condition for charging is met – particles with the same sign of the charge are not prevented from descending towards the black hole by thermal pressure. However, the particles of the opposite charge also fall in progressively faster inside the discharging sphere with the radius of $R_{\text{discharge}}$ defined analogously to equation (44), which effectively limits the realistic values of the electrostatic charge of the black hole.

The necessary condition for an increasing charge of the SMBH is that $R_{\text{charge}} \gtrsim R_{\text{discharge}}$, which is only met for the positive charging, see the left-hand panel of Fig. 5. For negative charging, the discharging length-scale of protons is always larger than the charging length-scale of electrons purely because of the mass difference. Therefore, the negative charging of black holes is rather inefficient.

Hence, the Galactic centre black hole and black holes in general are prone to have a small positive charge. This is also supported by the analysis in Section 3.2, where it is shown that black holes whose spin is oriented parallel to the magnetic field intensity preferentially accrete positively charged particles, while those with antiparallel spin are being negatively charged. Since we expect a certain degree of alignment in a relaxed system of a black hole and its associated accretion flow, the induced charge is expected to be positive.

For the positive charging in Fig. 5 (left-hand panel), the charging length-scale for protons is larger than the discharging radius of electrons up to a certain charge Q_{eq} , which for the general case of different electron and proton temperatures is

$$Q_{\text{eq}} = \frac{4\pi \epsilon_0 GM_\bullet [(T_{\text{e}}/T_{\text{p}})m_{\text{p}} - m_{\text{e}}]}{e (1 + T_{\text{e}}/T_{\text{p}})}. \quad (45)$$

For the case of the same temperature $T_{\text{e}} \approx T_{\text{p}}$, equation (45) becomes identical to the equilibrium charge in equation (19), $Q_{\text{eq}} = 3.1 \times 10^8 (M_\bullet/4 \times 10^6 M_\odot) C$. This charge is associated with the charging/discharging length-scale of $R_{\text{charge}} = 0.2$ arcsec for the free-fall accretion and $R_{\text{charge}} = 2.1$ mas for the accretion with the viscosity parameter of $\alpha = 0.1$, which is one

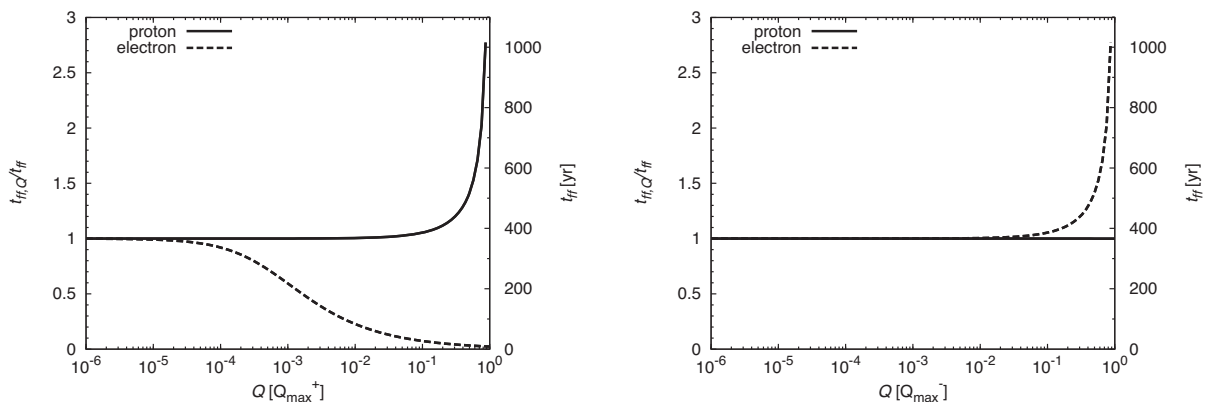


Figure 4. *Left-hand panel:* The free-fall time-scales for protons and electrons calculated for a positive charge of the SMBH at the Galactic centre expressed in units of the maximum positive charge (Q_{\max}^+ , see equation 28). The scale on the left vertical axis expresses the ratio $t_{\text{ff}, Q}/t_{\text{ff}}$, whereas the scale along the right vertical axis is the free-fall time-scale for an initial distance equal to Bondi radius (equation (3)) expressed in years. *Right-hand panel:* The same as in the left-hand panel, calculated for a negative charge of the SMBH expressed in units of the maximum negative charge (Q_{\max}^- , see equation 29).

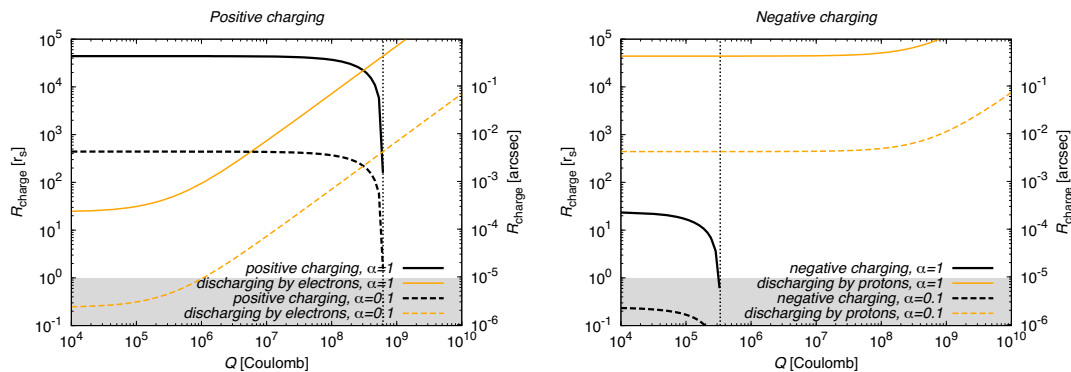


Figure 5. The dependence of the radius of the sphere, where the basic condition for the charging or the discharging, $t_{\text{vis}, Q} < t_{\text{th}}$, is met for both the positive charging (left-hand panel) and the negative charging (right-hand panel). The solid lines mark the charging/discharging length-scale for the purely free-fall accretion, while the dashed lines represent the viscous inflow for $\alpha = 0.1$. The charging can effectively proceed when the charging length-scale R_{charge} is larger than the discharging length-scale. The shaded region marks the region below the event horizon.

and three orders of magnitude smaller than the Bondi radius, respectively.

4 OBSERVABLE EFFECTS ASSOCIATED WITH A CHARGED BLACK HOLE

Although the simple analysis based on the first principles showed that the charge associated with the Galactic centre black hole is at least 10 orders of magnitude smaller than the charge corresponding to an extremal black hole, it is useful to list observational signatures that a charged black hole could have. The electric charge, if present, most likely does not reach values significant for the space–time metric. However, despite its expected small value, it is useful to design observational tests of its presence. It is therefore of astrophysical interest to name several potential observables that can be employed to test the presence of the charged SMBH at the Galactic centre.

4.1 Effect on the black hole shadow

For shorter wavelengths in the radio domain than λ_p , plasma does not block the emission, however, it causes significant scatter broadening of any structure up to 1.4 mm (Lo et al. 1998). At wavelengths $\lambda < 1.4$ mm, it is possible to resolve the structure using the VLBI since the size of Sgr A* starts to be source-dominated (Krichbaum et al. 1998; Doeleman et al. 2008). Of a particular interest is a well-defined curve on the sky plane that divides the region, where photon geodesics intersect the event horizon from the region where photons can escape to the observer – the so-called black hole shadow (Falcke, Melia & Agol 2000).

It was previously claimed by Zakharov (2014) that the charge associated with the Galactic centre black hole could be detected via the VLBI imaging of Sgr A*, based on the detection of the shadow. They report that a Reissner–Nordström black hole with a significant charge close to $Q_* = Q_{\max}^{\text{norot}}$ is more consistent with the VLBI detection of Sgr A* by Doeleman et al. (2008) with the core diameter of 37_{-10}^{+16} μas . This argument is based on the theoretical calculations of the shadow diameter, namely the shadow diameter for the Schwarzschild black hole is $6\sqrt{3}GM_{\bullet}/c^2$, which

4418 *M. Zajaček et al.*

is $\sim 51.2 \mu\text{s}$ at the distance of 8 kpc at the Galactic centre. For an extremal Reissner–Nordström black hole, one gets the shadow diameter $4GM_{\bullet}/c^2$, i.e. by about 38 per cent smaller than for the Schwarzschild black hole, which corresponds to $\sim 39.4 \mu\text{s}$. The shadow diameter for the nearly extremal charged black hole is thus closer to the core size found by Doeleman et al. (2008).

However, the core size found by Doeleman et al. (2008) does not correspond in a straightforward way to the black hole shadow size. It can be either a Doppler beamed accretion flow or the footpoint of the jet (Doeleman et al. 2008; Dexter, McKinney & Agol 2012; Eckart et al. 2017) and in these cases, it is difficult to make a connection to the charge of the black hole. In general, the black hole shadow is not a clean observable. Not only does the charge influence its size but also the spin, see Fig. 6 for comparison. In addition, the charge starts significantly influencing the size of the shadow for fractions of the maximum charge, $Q_{\bullet} \gtrsim 0.1 Q_{\text{max}}^{\text{norot}}$. For the maximum positive charge value of $Q_{\text{max}}^{+} \approx 6 \times 10^8 \text{ C}$, see equation (28), there is practically no difference in the size of the shadow.

Next, we show that the bremsstrahlung surface brightness profile on the scales of 100–1000 r_S can be used to test the presence of a much smaller charge associated with Sgr A* than by using the shadow size.

4.2 Testing the presence of a black hole Debye shield – does a charged black hole have an impact on the bremsstrahlung profile?

The charge associated with Sgr A* can have a considerable impact on the motion and the distribution of charged particles, electrons, protons, and ions, in its vicinity. However, this only applies to the charged black hole that is not shielded. In the classical plasma theory, any charged body immersed in stationary plasma with the electron density n_e and temperature T_e is shielded beyond the characteristic Debye length-scale, $\lambda_D = \sqrt{\epsilon_0 k_B T_e / (n_e e^2)}$, which results in the exponential potential decrease, $\phi = \phi_0 \exp(-r/\lambda_D)$, where ϕ_0 is the potential of a point charge in vacuum.

The plasma around Sgr A* is, however, certainly not stationary but rather dynamic, given the large velocity of accretion flow in the potential of Sgr A* and turbulence. Therefore, the standard Debye theory is not applicable to this environment.

Even if the Debye shield around Sgr A* were created, it would have such a small length-scale that it would completely lie inside the ISCO, where it would be dynamically sheared and it would be therefore highly unstable. When evaluated on the scale of the ISCO, using the extrapolated density and temperature profiles in equation (8), the Debye length is

$$\lambda_{\text{ISCO}} = 5 \left(\frac{T_e}{8.7 \times 10^{12} \text{ K}} \right)^{1/2} \left(\frac{n_e}{1.7 \times 10^9 \text{ cm}^{-3}} \right)^{-1/2} \text{ m}, \quad (46)$$

while at the Bondi radius it would be only one order of magnitude larger, $\lambda_{\text{Bondi}} \approx 141 \text{ m}$.

Moreover, using the classical estimates, the Debye sphere would not be formed based purely on viscous time-scales if the charged fraction of accreted matter is large enough. If we imagine that the positively charged black hole is surrounded by a negatively charged Debye shell, its mass can be estimated simple as $M_{\text{Debye}} \approx (Q_{\text{ind}}^{+}/e)m_e$, where Q_{ind}^{+} is the induced positive black hole charge. Since the Debye shell lies inside the ISCO, it is being depleted as well as refilled all the time. If the depletion rate of electrons $\dot{M}_{\text{acc}}^{-} = \epsilon_{\text{neg}} \dot{M}_{\text{acc}}$ is larger than the filling rate \dot{M}_{Debye} , then the Debye shell is highly transient and does not screen out the charge of the black hole. The filling rate of the Debye shell is assumed to take place

on the viscous time-scale of electrons, taking into account the positive charge of the black hole, $t_{\text{vis}}^{-} = \alpha^{-1} (H/r_{\text{ISCO}})^{-2} t_{\text{fit}}(r_{\text{ISCO}}, Q_{\text{ind}}^{+})$. Then, the Debye filling rate can be expressed as

$$\dot{M}_{\text{Debye}} \sim \frac{Q_{\text{ind}}^{+} m_e}{e t_{\text{vis}}^{-}}. \quad (47)$$

The Debye shell will not form if $\dot{M}_{\text{acc}}^{-} > \dot{M}_{\text{Debye}}$, which puts the lower limit on the negatively charged fraction of the accreted matter, $\epsilon_{\text{neg}} > Q_{\text{ind}}^{+} m_e / (e \dot{M}_{\text{acc}} t_{\text{vis}}^{-}) \approx 7 \times 10^{-17}$. It implies that if the accreted matter contains a negatively charged fraction of the order of ϵ_{neg} , then the Debye shell is expected not to form at all. Even if the Debye shell forms temporarily, it would be strongly perturbed by the turbulence and outflows. In addition, a more general analysis done by Bally & Harrison (1978) showed that all self-gravitating systems with length-scales L larger than the Debye length, $L \gg \lambda_D$, are positively charged in order to hold in the electron gas, i.e. these objects are not Debye screened.

An unshielded charged black hole would lead to the charge separation that directly influences the emissivity of the thermal bremsstrahlung, because the emission efficiency drops significantly for like particles, proton–proton and electron–electron interactions, as there is no dipole component in the collisions. The bremsstrahlung is dominantly produced by radiating electrons that move in the Coulomb field of protons (or positively charged ions), and the corresponding emissivity is given by equation (14), $\epsilon_{\text{Brems}} \propto Z^2 n_i n_e$. Therefore, inside the sphere of the electrostatic influence of the black hole, the drop in bremsstrahlung emissivity is expected, creating a drop or ‘hole’ in the surface density of the thermal bremsstrahlung, which is centred at Sgr A*.

Let us assume that Sgr A* is positively charged with the charge of Q_{\bullet} . The electrostatic potential further from the unscreened charged black hole is $\phi \approx Q_{\bullet} / (4\pi \epsilon_0 r)$. Under the assumption of the equilibrium Maxwell–Boltzmann distribution, it would yield to the charge separation and the corresponding charge particle density would vary as $n_i \propto \exp(-q\phi/k_B T_p)$ on top of the power-law (Bondi) dependence $n_i \propto r^{-3/2}$. In Fig. 7 (left-hand panel), several number density profiles are plotted for electrons (solid lines) and protons (dashed lines) for increasing positive charge of the black hole, $Q_{\bullet} = 10^7 - 10^9 \text{ C}$, including the zero charge.

To simulate the effect of an unscreened SMBH with the positive charge of Q_{\bullet} , we use the Abel integral to obtain the projected luminosity profile $J(R_{\text{proj}})$ from the deprojected one $L_{\text{brems}}(r)$, see equation (14):

$$J(R_{\text{proj}}) = 2 \int_{R_{\text{proj}}}^{R_t} \frac{L_{\text{brems}}(r) r \, dr}{\sqrt{r^2 - R_{\text{proj}}^2}}, \quad (48)$$

where the truncation radius R_t represents the length-scale where the thermal bremsstrahlung in the Galactic centre becomes negligible. We set the truncation radius to the Bondi radius (or approximately the stagnation radius), $R_t \approx R_B \approx R_{\text{stag}}$, see also equations (3) and (7).

The projected luminosity profile calculated using equation (48) is plotted in Fig. 7 (right-hand panel). The solid line represents the case of the non-charged black hole, or a completely Debye-shielded black hole, and the dashed lines depict the cases of the SMBH with the positive charge of $Q_{\bullet} = 10^7 - 10^9 \text{ C}$, which have progressively smaller luminosity profile than the non-charged case. A special case is the equilibrium charge Q_{eq} , see equation (19), up to which the electron and proton number densities are comparable within a factor of a few, $n_e \approx n_p$, see also Fig. 7 (left-hand panel) for $Q_{\bullet} = 10^7 - 10^8 \text{ C}$. For larger black hole charges, the drop in

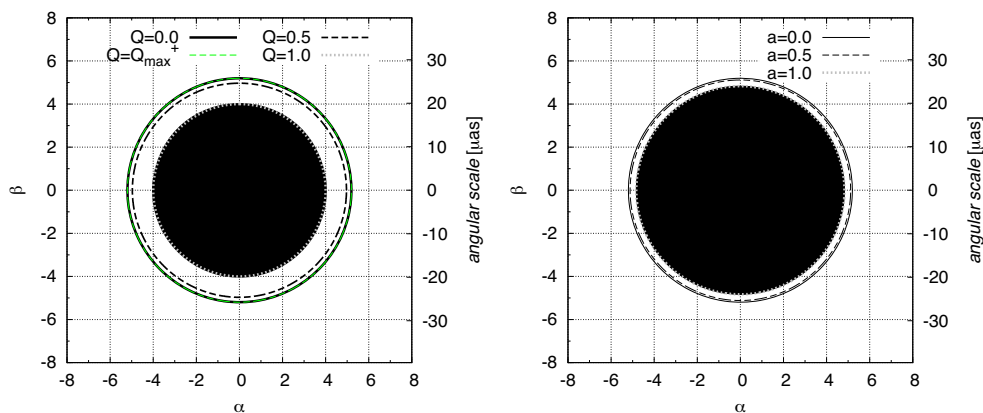


Figure 6. *Left:* The black hole shadow size in gravitational units for a non-rotating, Reissner–Nordström black hole for an increasing value of the charge according to the legend. The right vertical axis is expressed in microarcseconds for the distance of the Galactic centre – 8 kpc. *Right:* The same as the left figure but for the rotating black hole (Kerr). The calculations are performed for the top view, in the direction of the spin axis, for increasing values of the spin parameter according to the legend.

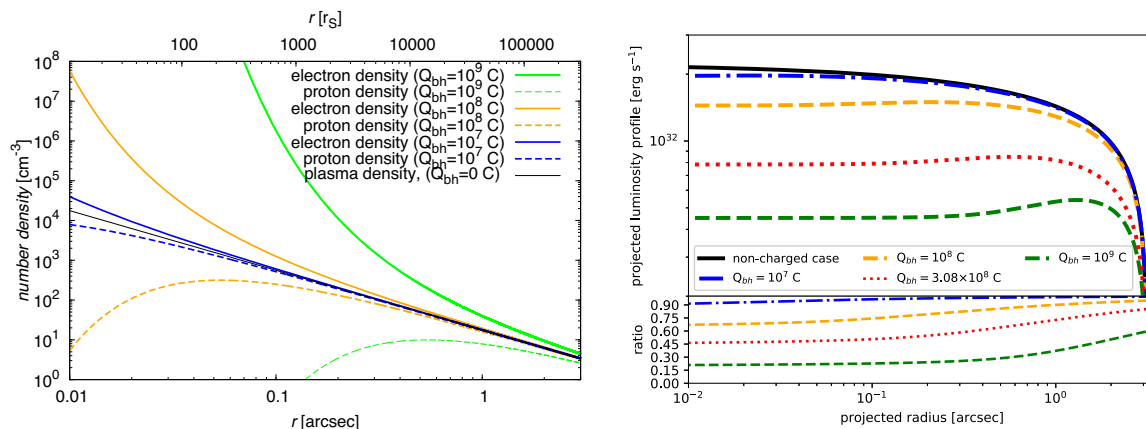


Figure 7. *Left:* Density profiles of electrons and protons in the Galactic centre as affected by a potential charged SMBH. The black solid line represents the non-charged power law. The coloured lines (blue, orange, green) manifest the changed profiles due to the presence of a positive point charge at the centre: the blue solid and dashed lines represent the case for $Q_{\bullet} = 10^7$ C, the orange lines stand for $Q_{\bullet} = 10^8$ C, and the green lines represent $Q_{\bullet} = 10^9$ C. *Right:* The *bremsstrahlung* surface brightness profile for the case of a non-charged black hole (solid black line) and for the case of a charged black hole in the Galactic centre with the charge of 10^7 C, 10^8 C, and 10^9 C, represented by the dashed blue, orange, and green lines, respectively. The drops in the brightness profile with respect to the non-charged case are depicted by a sub-plot that shows the ratio of the brightness profile for the charged case with respect to the non-charged case.

the *bremsstrahlung* profile is more prominent, specifically reaching ~ 37 per cent of the luminosity for non-charged case at the projected radius of $R \sim 1$ arcsec for $Q_{\bullet} = +10^9$ C. In general, the difference in the electron and proton number densities by factor f_n , $n_e = f_n n_p$, corresponds to the black hole charge of

$$Q_{\bullet}(f_n) = \frac{2\pi\epsilon_0 G(m_p - m_e)}{e} M_{\bullet} + \frac{2\pi\epsilon_0 k_B T_{e,0} r_0}{e} \log f_n, \quad (49)$$

where $T_{e,0}$ is the electron (\sim proton) temperature at radius r_0 . Relation (49) holds under the assumption of the equilibrium Maxwell–Boltzmann distribution of electrons and protons.

The calculated surface brightness in Fig. 7 corresponds to the quiescent state of Sgr A*, i.e. this profile is expected if one can remove the non-thermal variable source at the very centre. In order to satisfactorily do that, the angular resolution of X-ray instruments should be better than ~ 0.1 arcsec. The effect of the *bremsstrahlung*

flattening or drop is just at (or rather beyond) the limit of what can be measured right now. Therefore, this experiment and the analysis speaks for next generation X-ray telescopes that have a half and the full order of magnitude better resolving powers compared to the current situation.

Rózańska et al. (2015) construct a projected *bremsstrahlung* profile in their Fig. 6. At the 1σ level, the profile shows a decrease in the brightness at radii $\lesssim 0.4$ arcsec. This is, however, still consistent within uncertainties with the flat and the slightly rising profile at the 3σ level. Flat to slightly decreasing luminosity profile allows us to put the upper limit on the black hole charge if we assume that the charge is not screened. The projected profile inferred from *Chandra* observations by Rózańska et al. (2015) is consistent within the uncertainty with all profiles up to the equilibrium value of $Q \lesssim Q_{\text{eq}} \approx 3.1 \times 10^8$ C, see Fig. 7 (right-hand panel).

4420 *M. Zajaček et al.*

For larger charge values, the projected profile is expected to decrease below $R = 2$ arcsec, see the green dashed curve in Fig. 7, which corresponds to $Q_{\bullet} = 10^9$ C. The equilibrium value of the black hole charge $Q_{\text{eq}} \approx 3.1 \times 10^8$ C, which was derived based on the classical mass segregation arguments, see equation (19), corresponds to the charging/discharging length-scale of $R_{\text{charge}} \approx 0.21$ arcsec according to equation (44), assuming the free-fall flow. This scale is comparable to the projected radius, where the observed bremsstrahlung profile is consistent with the flat to decreasing flux density (Różańska et al. 2015).

Within uncertainties, this is consistent with the constraints given by induction mechanism presented in subsection 3.2, which gives an upper limit of the order of 10^{15} C. In the future, if the angular resolution of X-ray instruments is one half to one order of magnitude better, one can distinguish the unresolved central component from the surroundings and it will be possible to model it away without assuming intrinsic physics. One could, in particular, take multiple images of the flares and model a variable point source and an extended quiescent component. Hence, this procedure should yield a well-constrained background with a more precise brightness profile, based on which the decrease could be confirmed or excluded.

In case the drop in the bremsstrahlung profile is confirmed on sub-arcsecond scales from Sgr A*, one should naturally consider also other possibilities for the decrease, in particular the lower temperature due to plasma cooling and/or the decrease in the ambient gas density. However, the presence of small electric charge associated with Sgr A* remains as an interesting possibility for both explaining the bremsstrahlung flattening as well as for testing the presence of the Debye-shell effect around SMBHs immersed in plasma.

4.3 Effect of charge on ISCO of Sgr A*

One of the important characteristics of black holes in accretion theory playing crucial role in observational constraints of black hole parameters is the location of the innermost stable circular orbit (ISCO). For a non-rotating neutral black hole, the ISCO is located at $r = 3r_S$. Rotation of black hole shifts the position of ISCO of co-rotating particles towards the horizon matching with it in the extremely rotating case $a_{\bullet} = J_{\bullet}/M_{\bullet} = 1$. The presence of the black hole charge acts in a similar way to the ISCO, shifting it towards the horizon for both neutral and charged particles (Pugliese et al. 2011). Motion of charged particle with mass m_{par} and charge q_{par} moving around non-rotating black hole with charge Q_{\bullet} is restricted by the energy boundary function or the effective potential

$$\frac{E_{\text{par}}}{m_{\text{par}}c^2} = \frac{k_1 q_{\text{par}} Q_{\bullet}}{r} + \left[\left(1 - \frac{1}{r} + \frac{k_2 Q_{\bullet}^2}{r^2} \right) \times \left(1 + \frac{L_{\text{par}}^2}{m_{\text{par}}c^2 r^2} \right) \right]^{1/2}, \quad (50)$$

where E_{par} and L_{par} are the energy and angular momentum of charged particle and r is the radius given in the units of gravitational radius r_S . At infinity or in the absence of the fields $E_{\text{par}}/(m_{\text{par}}c^2) = 1$. For neutral particles at ISCO of neutral black hole $E_{\text{par}}/(m_{\text{par}}c^2) = \sqrt{8/9}$. The constants k_1 and k_2 are the coupling constants responsible for the interaction between charges and the gravity. For an electron around Sgr A*, the constants can be

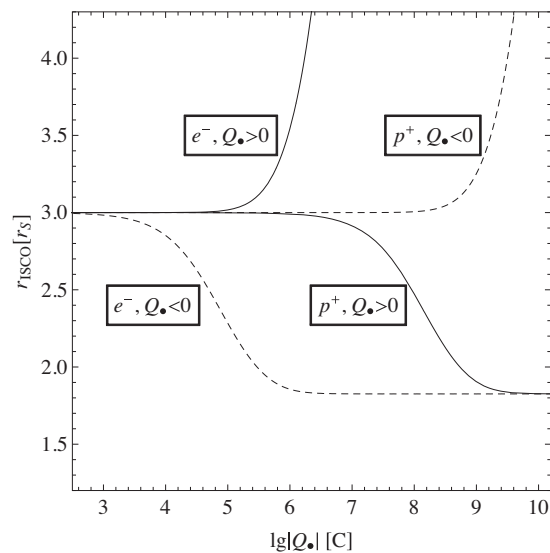


Figure 8. Location of the ISCO of electrons e^- and protons p^+ around Sgr A* for positive and negative configurations of the SMBH charge Q_{\bullet} . The radii on vertical axis are given in the units of gravitational radii of Sgr A*.

estimated as

$$k_1 = \frac{1}{m_e c^2 r_S^*} \approx 1.03 \times 10^{-6} \frac{\text{s}^2}{\text{g cm}^3}, \quad (51)$$

$$k_2 = \frac{G}{c^4 r_S^{2*}} \approx 5.92 \times 10^{-74} \frac{\text{s}^2}{\text{g cm}^3}. \quad (52)$$

Smallness of the constant k_2 representing the gravitational effect of the black hole charge imply that the effect of the black hole charge on the space-time curvature can be neglected in most of the physically relevant cases. Indeed, the possible charge of the SMBH at the Galactic centre restricted by the upper limits (see Section 3) is not able to provide sufficient curvature of the background black hole geometry, and thus, does not influence the motion of neutral particles. However, for the motion of charged particles, the effect of even small black hole charge can sufficiently shift the location of orbits due to large values of the charge to mass ratio for elementary particles.

The location of the ISCO of charged particles around Sgr A* as a function of the black hole charge Q_{\bullet} is plotted in Fig. 8. As one can see from the plot, the position of the ISCO for electrons shifts from $r = 3r_S$ (corresponding to the ISCO of neutral particles) towards or outwards from black hole starting already from relatively small charges of the order of 10^3 – 10^5 C. Thus, even a small black hole charge that does not affect the background geometry can sufficiently shift the ISCO of free electrons and protons orbiting around Sgr A*. In case of like-charges (e^- , $Q_{\bullet} < 0$ or p^+ , $Q_{\bullet} > 0$), the ISCO can be shifted from the distance $r = 3r_S$ up to $r = 1.83 r_S$, which can mimic the black hole spin with the value of $a_{\bullet} = 0.64$. This should be taken into account in the spin determination of Sgr A* since previous estimates are close to this value, in general above ~ 0.4 (Meyer et al. 2006; Kato et al. 2010; Zamaninasab et al. 2010).

Particles at the ISCO can have ultrarelativistic velocities, which leads to the emission of electromagnetic radiation from the inner parts of the accretion flow. The shift of the ISCO towards the event horizon increases the gamma-factor of charges and the gravitational

redshift $z = (\lambda_0 - \lambda)/\lambda_0$ of emitted photons, where λ and λ_0 are the wavelengths of a photon measured by local and detached observers. The shift of the ISCO radius from $r = 3r_S$ (neutral) to $r = 1.83 r_S$ (charged) increases the gravitational redshift of emitted electromagnetic radiation from $z = 0.225$ to $z = 0.485$.

5 SUMMARY AND DISCUSSION

In this section, we summarize the constraints on the electric charge of the Galactic centre black hole. Subsequently, we look at the potential effects of the rotation on the maximum electric charge. In addition, we discuss potential non-electric origins of the black hole charge.

5.1 Charge values associated with the Galactic centre black hole

In Section 3, we studied limits on the electric charge of Sgr A* based on different mechanisms, namely the accretion of charged constituents of plasma and the induction mechanism based on a rotating SMBH in the external magnetic field. We summarize these constraints in Table 1. The charging based on accretion of protons or electrons is not stable and leads to the discharging on the discharging time-scale. However, the rotation of the SMBH within the external magnetic field is a plausible process that can result in a stable charge of the SMBH not only in the Galactic centre but in galactic nuclei in general.

All the upper limits on the electric charge in Table 1 are at least 10 orders of magnitude below the maximum charge (see equation 23), and hence the space-time metric is not affected. However, the dynamics of charged particles is significantly affected by even these small values and can be observationally tested via the change in the bremsstrahlung brightness profile.

5.2 Effect of rotation

As was already indicated by equation (22), the rotation of the SMBH does effect the value of the maximum allowed charge for a black hole. For the maximum rotation, $\tilde{a}_* = 1$, the maximum charge vanishes completely. However, the dependence of Q_{\max}^{rot} on a_* is only prominent for large spins, see also the left-hand panel of Fig. 3. In astrophysical relevant systems, the maximum rotation parameter is $a_*^{\text{max}} = 0.998$ (Thorne 1974), which results in $Q_{\max}^{\text{rot}} \approx 0.06 Q_{\max}^{\text{norot}} = 4.3 \times 10^{25} \text{ C}$. This is still about 10 orders of magnitude larger than the constraints analysed in Section 3. For Sgr A*, the spin is estimated to be even smaller, $a_* \sim 0.5$ (Meyer et al. 2006; Zamaninasab et al. 2010). Therefore, the previous analysis is valid also for the case when Sgr A* has a significant spin.

5.3 Non-electric origin of the black hole charge

The black hole charge can also be of a non-electric origin (Zakharov 2014), namely a tidal charge induced by an extra dimension in the Randall–Sundrum (RS) braneworld solutions or 5D warped geometry theory (Randall & Sundrum 1999; Bin-Nun 2010, 2011), in which the observable Universe is a (3 + 1)-brane (domain wall) that includes the standard matter fields and the gravity field propagates further to higher dimensions. The RS solution yields the 4D Einstein gravity in the low-energy regime. However, in the high-energy regime deviations from the Einstein solution appear, in particular in the early universe and the vicinity of compact objects (Stuchlík & Kotrlóvá 2009). Both the high-energy (local) and the bulk stress

(non-local) affects the matching problem on the brane in comparison with Einstein solutions. In particular, the matching does not result in the exterior Schwarzschild metric for spherical bodies in general (Kotrlóvá, Stuchlík & Török 2008).

A class of the RS brane black hole solutions is obtained by solving the effective gravitational field equations given the spherically symmetric metric on the (3 + 1)-brane (see Maartens 2004, for a review). These black holes are characterized by Reissner–Nordström-like static metric that has the non-electric charge b instead of the standard Q^2 . This charge characterizes the stresses induced by the Weyl curvature tensor of the bulk space, i.e. 5D graviton stresses that effectively act like tides. Thus, the parameter b is often referred to as the tidal charge and can be both negative and positive. Detailed studies of the optical phenomena associated with brany black holes, in particular quasiperiodic oscillations that are of an astrophysical relevance, were performed in several studies (Schee & Stuchlík 2009; Stuchlík & Kotrlóvá 2009).

As pointed by Zakharov (2014), the tidal charge could be tested by detecting the black hole shadow. While the electric charge causes the shadow to shrink, which is only noticeable for nearly extremal charges (see subsection 4.1), the tidal charge could act in the opposite sense – enlarging the shadow size. Thus, if a noticeable change in the shadow size is detected, it would most likely be caused by non-electric tidal charge since the electric charge is expected to have negligible effects on the metric as we showed in Section 3 and summarized in subsection 5.1.

5.4 Comparison with previous studies

Zakharov (2014) uses an argument that the measured core size of Sgr A* of $\sim 40 \mu\text{as}$ (Doeleman et al. 2008; Fish et al. 2011) is more consistent with the Reissner–Nordström black hole with the charge close to the extremal value of Q_{\max}^{norot} than with the Schwarzschild black hole whose shadow is expected to be $\sim 53 \mu\text{as}$. However, one needs to stress that the core size does not directly express the shadow size at all since it does not have to be centred at the black hole – it can, for instance, be caused by a Doppler-boosted accretion flow or the jet-launching site (Dexter et al. 2012; Eckart et al. 2017). Hence, the charge constraint given by Zakharov (2014) is uncertain at this point and should be further tested when the analysis of the observations by the Event Horizon Telescope² is available.

Iorio (2012) gives the following estimate on the charge of Sgr A* based on the geodesic trajectories of the orbital motion (Chaliasos 2001), in particular using S2 star orbit, $Q_* \lesssim 3.6 \times 10^{27} \text{ C}$, leaving space for the charge larger than an extremal value.

In comparison with Iorio (2012) and Zakharov (2014), we take into account the presence of plasma and the magnetic field in the vicinity of Sgr A*, which leads to tighter constraints and significantly smaller values, see Table 1. Moreover, our suggested test based on the bremsstrahlung brightness profile, see subsection 4.2, is significantly more sensitive to smaller charge than the shadow size or stellar trajectories.

6 CONCLUSIONS

We performed analytical calculations to find out if the SMBH at the Galactic centre can get charged and what the realistic values of its charge are. Based on the classical estimates and total amount of the charge in the sphere of influence of the black hole, we expect

²<http://eventhorizontelescope.org/>

4422 *M. Zajaček et al.***Table 1.** Summary of the constraints on the electric charge of the SMBH at the Galactic centre presented in Section 3.

Process	Limit	Notes	Subsection
Mass difference between p and e	$Q_{\text{eq}} = 3.1 \times 10^8 \left(\frac{M_{\bullet}}{4 \times 10^6 M_{\odot}} \right) \text{ C}$	stable charge	Subsection 2.3
Accretion of protons	$Q_{\text{max}}^+ = 6.16 \times 10^8 \left(\frac{M_{\bullet}}{4 \times 10^6 M_{\odot}} \right) \text{ C}$	unstable charge	Subsection 3.3
Accretion of electrons	$Q_{\text{max}}^- = 3.36 \times 10^5 \left(\frac{M_{\bullet}}{4 \times 10^6 M_{\odot}} \right) \text{ C}$	unstable charge	Subsection 3.3
Magnetic field & SMBH rotation	$Q_{\bullet \text{ind}}^{\text{max}} \lesssim 10^{15} \left(\frac{M_{\bullet}}{4 \times 10^6 M_{\odot}} \right)^2 \left(\frac{B_{\text{ext}}}{10 \text{ G}} \right) \text{ C}$	stable charge	Subsection 3.2
Extremal SMBH	$Q_{\text{max}} = 6.86 \times 10^{26} \left(\frac{M_{\bullet}}{4 \times 10^6 M_{\odot}} \right) \sqrt{1 - a_{\bullet}^2} \text{ C}$	uppermost limit	Subsection 3

that the black hole can acquire a small, transient positive charge of $\lesssim 10^9 \text{ C}$, which does not have an influence on the space–time metric. Based on the general relativistic calculations, we further explore the induced charge based on the rotating black hole that is immersed in the external magnetic field. Such a configuration is in general expected in almost all galactic nuclei. If the black hole spin axis is approximately aligned with the external magnetic field, we again expect that the induced charge is positive, with the uppermost limit of $Q_{\bullet} \lesssim 10^{15} \text{ C}$. Although the space–time metric is not influenced significantly by electric charge within the limits we found, even such a small charge can significantly influence the typical viscous time-scales for protons and electrons as well as an infall of small charged particles (dust particles). Most importantly, for like charges of test particles and Sgr A*, the ISCO shifts significantly in comparison with the no-charge case even for a small charge of the order of 10^6 – 10^{10} C , which effectively mimics the black hole spin of $a_{\bullet} \sim 0.6$. This effect should be taken into account in the future numerical calculations as well as the analysis of observation data.

We also revisited observational tests of the presence of the charge for the Galactic centre black hole. The black shadow size, which was proposed previously, is only sensitive for large values of the charge, close to an extremal value, which are unrealistic as we showed. We propose a new test based on the observed surface brightness profile of the thermal bremsstrahlung inside the innermost 10^5 Schwarzschild radii, which is the region that coincides with the S cluster. Within this range, a flattening and a decrease in the bremsstrahlung surface brightness is expected to occur due to the presence of the charged, unshielded black hole starting with about 20 orders of magnitude smaller values than the extremal case. Since the *Chandra* X-ray observations with the angular resolution of 0.5 arcsec did detect a weak indication of the drop in the brightness profile at $R_{\text{proj}} \lesssim 0.4$ arcsec, it puts an observational upper limit on the charge $Q_{\text{Sgr A}^*} \lesssim 3 \times 10^8 \text{ C}$.

ACKNOWLEDGEMENTS

We thank Vladimír Karas and Zdeněk Stuchlík for very useful comments on the manuscript. We are especially grateful to Elahé Hosseini for checking the calculations. We received funding from the European Union Seventh Framework Program (FP7/2013–2017) under grant agreement no 312789 - Strong gravity: Probing Strong Gravity by Black Holes Across the Range of Masses. This work was supported in part by the Deutsche Forschungsgemeinschaft (DFG) via the Cologne Bonn Graduate School (BCGS), the Max Planck Society through the International Max Planck Research School (IMPRS) for Astronomy and Astrophysics as well as special funds through the University of Cologne and SFB 956 Conditions and Impact of Star Formation. M. Zajaček is a member of the Inter-

national Max Planck Research School at the Universities of Cologne and Bonn. Arman Tursunov acknowledges the Czech Science Foundation Grant No. 16-03564Y and the Silesian University in Opava Grant No. SGS/14/2016.

REFERENCES

- Baganoff F. K. et al., 2003, *ApJ*, 591, 891
 Bally J., Harrison E. R., 1978, *ApJ*, 220, 743
 Bin-Nun A. Y., 2010, *Phys. Rev. D*, 81, 123011
 Bin-Nun A. Y., 2011, *Class. Quantum Gravity*, 28, 114003
 Blandford R. D., Znajek R. L., 1977, *MNRAS*, 179, 433
 Boehle A. et al., 2016, *ApJ*, 830, 17
 Chaliasos E., 2001, *Celest. Mech. Dyn. Astron.*, 79, 135
 Dadhich N., Tursunov A., Ahmedov B., Stuchlík Z., 2018, *MNRAS*, 478, L89
 Dexter J., Agol E., Fragile P. C., McKinney J. C., 2010, *ApJ*, 717, 1092
 Dexter J., McKinney J. C., Agol E., 2012, *MNRAS*, 421, 1517
 Do T. et al., 2013, *ApJ*, 779, L6
 Doeleman S. S. et al., 2008, *Nature*, 455, 78
 Eatough R. P. et al., 2013, *Nature*, 501, 391
 Eckart A., Genzel R., 1996, *Nature*, 383, 415
 Eckart A., Genzel R., 1997, *MNRAS*, 284, 576
 Eckart A., Schödel R., Straubmeier C., 2005, *The Black Hole at the Center of the Milky Way*. Imperial College Press, London
 Eckart A., Schödel R., Meyer L., Trippe S., Ott T., Genzel R., 2006, *A&A*, 455, 1
 Eckart A. et al., 2012, *A&A*, 537, A52
 Eckart A. et al., 2017, *Found. Phys.*, 47, 553
 Falcke H., Markoff S., 2000, *A&A*, 362, 113
 Falcke H., Melia F., Agol E., 2000, *ApJ*, 528, L13
 Ferrière K., 2009, *A&A*, 505, 1183
 Fish V. L. et al., 2011, *ApJ*, 727, L36
 Generozov A., Stone N. C., Metzger B. D., 2015, *MNRAS*, 453, 775
 Genzel R., Eisenhauer F., Gillessen S., 2010, *Rev. Mod. Phys.*, 82, 3121
 Ghez A. M., Klein B. L., Morris M., Becklin E. E., 1998, *ApJ*, 509, 678
 Gibbons G. W., 1975, *Commun. Math. Phys.*, 44, 245
 Gillessen S., Eisenhauer F., Trippe S., Alexander T., Genzel R., Martins F., Ott T., 2009, *ApJ*, 692, 1075
 Gillessen S. et al., 2017, *ApJ*, 837, 30
 Gravity Collaboration, 2018, *A&A*, 615, L15
 Haggard D., 2017, in Crocker R. M., Longmore S. N., Bicknell G. V., eds, *Proc. IAU Symp. 322, The Multi-Messenger Astrophysics of the Galactic Centre*, Cambridge Univ. Press, Cambridge. p. 1
 Heusler M., 1996, *Black Hole Uniqueness Theorems*. Cambridge Univ. Press, Cambridge
 Iorio L., 2012, *Gen. Relativ. Gravit.*, 44, 1753
 Karas V., Vokrouhlický D., 1991a, *J. Physique I*, 1, 1005
 Karas V., Vokrouhlický D., 1991b, *J. Math. Phys.*, 32, 714
 Karssen G. D., Bursa M., Eckart A., Valencia-S M., Dovčiak M., Karas V., Horák J., 2017, *MNRAS*, 472, 4422
 Kato Y., Miyoshi M., Takahashi R., Negoro H., Matsumoto R., 2010, *MNRAS*, 403, L74

- Kim H., Lee C. H., Lee H. K., 2001, *Phys. Rev. D*, 63, 064037
- King A. R., Pringle J. E., Livio M., 2007, *MNRAS*, 376, 1740
- Kotrlová A., Stuchlík Z., Török G., 2008, *Class. Quantum Gravity*, 25, 225016
- Kovář J., Slaný P., Stuchlík Z., Karas V., Cremaschini C., Miller J. C., 2011, *Phys. Rev. D*, 84, 084002
- Krichbaum T. P. et al., 1998, *A&A*, 335, L106
- Lang K. R., 1978, *Astrophysical Formulae. A Compendium For The Physicist And Astrophysicist*. Springer, Berlin
- Lasota J.-P., 2016, in Bambi C., ed., *Astrophysics and Space Science Library*, Vol. 440, *Astrophysics of Black Holes: From Fundamental Aspects to Latest Developments*, Springer-Verlag, Berlin, Heidelberg, p. 1
- Lo K. Y., Shen Z.-Q., Zhao J.-H., Ho P. T. P., 1998, *ApJ*, 508, L61
- Lu R.-S. et al., 2018, *ApJ*, 859, 60
- Maartens R., 2004, *Living Rev. Relativ.*, 7, 7
- Marrone D. P., Moran J. M., Zhao J.-H., Rao R., 2007, *ApJ*, 654, L57
- Melia F., 2007, *The Galactic Supermassive Black Hole*. Princeton Univ. Press, Princeton
- Merritt D., 2013, *Dynamics and Evolution of Galactic Nuclei*. Princeton Univ. Press, Princeton
- Meyer L., Eckart A., Schödel R., Duschl W. J., Mužić K., Dovčiak M., Karas V., 2006, *A&A*, 460, 15
- Misner C. W., Thorne K. S., Wheeler J. A., 1973, *Gravitation*. W.H. Freeman and Co., San Francisco
- Morris M. R., 2015, *Manifestations of the Galactic Center Magnetic Field*, Springer International Publishing, Switzerland, p. 391
- Mościbrodzka M., Gammie C. F., Dolence J. C., Shiokawa H., Leung P. K., 2009, *ApJ*, 706, 497
- Moser L. et al., 2017, *A&A*, 603, A68
- Mossoux E., Eckart A., 2018, *MNRAS*, 474, 3787
- Neslušan L., 2001, *A&A*, 372, 913
- Newman E. T., Couch E., Chinnappared K., Exton A., Prakash A., Torrence R., 1965, *J. Math. Phys.*, 6, 918
- Parsa M., Eckart A., Shahzamanian B., Karas V., Zajaček M., Zensus J. A., Straubmeier C., 2017, *ApJ*, 845, 22
- Penrose R., 1969, *Nuovo Cimento Riv.*, 1, 252
- Pugliese D., Quevedo H., Ruffini R., 2011, *Phys. Rev. D*, 83, 104052
- Randall L., Sundrum R., 1999, *Phys. Rev. Lett.*, 83, 3370
- Ray S., Espíndola A. L., Malheiro M., Lemos J. P., Zanchin V. T., 2003, *Phys. Rev. D*, 68, 084004
- Reid M. J., Brunthaler A., 2004, *ApJ*, 616, 872
- Róžańska A., Czerny B., Kunneriath D., Adhikari T. P., Karas V., Mościbrodzka M., 2014, *MNRAS*, 445, 4385
- Róžańska A., Mróz P., Mościbrodzka M., Sobolewska M., Adhikari T. P., 2015, *A&A*, 581, A64
- Schee J., Stuchlík Z., 2009, *Int. J. Mod. Phys. D*, 18, 983
- Schödel R. et al., 2002, *Nature*, 419, 694
- Shcherbakov R. V., Baganoff F. K., 2010, *ApJ*, 716, 504
- Stuchlík Z., Kotrlová A., 2009, *Gen. Relativ. Gravit.*, 41, 1305
- Thorne K. S., 1974, *ApJ*, 191, 507
- Tursunov A., Stuchlík Z., Kološ M., 2016, *Phys. Rev. D*, 93, 084012
- Wagh S. M., Dhurandhar S. V., Dadhich N., 1985, *ApJ*, 290, 12
- Wald R. M., 1974, *Phys. Rev. D*, 10, 1680
- Wang B., Su R.-K., Yu P. K. N., Young E. C. M., 1998, *Phys. Rev. D*, 57, 5284
- Wang Q. D. et al., 2013, *Science*, 341, 981
- Yalinewich A., Sari R., Generozov A., Stone N. C., Metzger B. D., 2018, *MNRAS*, 479, 4778
- Yuan F., Narayan R., 2014, *ARA&A*, 52, 529
- Zajaček M., Tursunov A., 2018, preprint ([arXiv:1804.11014](https://arxiv.org/abs/1804.11014))
- Zakharov A. F., 2014, *Phys. Rev. D*, 90, 062007
- Zamaninasab M. et al., 2010, *A&A*, 510, A3

This paper has been typeset from a $\text{\TeX}/\text{\LaTeX}$ file prepared by the author.

Conclusions and Outlook

10.1 Summary and discussion

In this thesis, we studied the interplay between the black hole environment and the interstellar medium, with the focus on the Galactic centre, which can be studied in the greatest detail among galactic nuclei. It is possible to resolve both the stellar content and gaseous structures in the sphere of influence of the supermassive black hole. In particular, I focused with my colleagues on the properties of rather extreme stellar populations that had not been studied before in detail. Among these, there are localized sources with NIR-excess, which can be attributed to the dusty material, and these appear to be pre-main-sequence stars. Moreover, there are end-products of massive star formation – neutron stars – which can effectively interact with the ionized medium in the central Cavity due to their large magnetic fields of the order of $B_{\text{dip}} \sim 10^{12}$ G. Finally, we were interested in the parameters of Sgr A*, which are expected to be only three classical, externally observable parameters – mass, spin, and electric charge – with the charge being only weakly constrained and not tested at all in the observational studies.

Below we summarize the main results of the thesis with the focus on the NIR-excess sources, interaction modes of neutron stars, and the charge of Sgr A*.

10.1.1 NIR-excess sources: Nature of Dusty S-cluster Object (G2)

When the Dusty S-cluster Object (DSO/G2) was discovered ([Gillessen et al. 2012b,b](#); [Phifer et al. 2013](#)), its nature was not clear and many favoured the core-less cloud hypothesis due to a reported tidal interaction of the source with the SMBH. Subsequently, many models appeared that could capture some of the characteristics of the source. We summarize these models and a few corresponding papers in Table 10.1:

Observationally, the DSO appears to be a rather stable source in both continuum and line emission, with the bolometric luminosity of $L_{\text{DSO}} \lesssim 30 L_{\odot}$ and the luminosity of Bry line emission of $L_{\text{Bry}} \approx 10^{-3} L_{\odot}$. Although the detection of tidal stretching in the line emission remains to be controversial, the continuum emission in L' -band is consistent with being a point source ([Witzel et al. 2014](#)). The Bry line emission is likely Doppler broadened to the line width of several 100 km s^{-1} ([Valencia-S. et al. 2015](#)). In terms of linearly polarized continuum emission, [Shahzamanian et al. \(2016\)](#) detected a polarized K_s -band emission ($2.2 \mu\text{m}$) with

Table 10.1: Summary of proposed scenarios of the DSO/G2 source with several corresponding papers.

Scenario	Papers
star with dusty envelope/disc and outflow	Murray-Clay & Loeb (2012); Eckart et al. (2013); Scoville & Burkert (2013); Ballone et al. (2013) Zajaček et al. (2014); De Colle et al. (2014); Valencia-S. et al. (2015); Ballone et al. (2016); Shahzamanian et al. (2016); Morsony et al. (2017)
binary/binary dynamics	Zajaček et al. (2014); Prodan et al. (2015); Witzel et al. (2014); Stephan et al. (2016)
core-less cloud/streamer	Gillessen et al. (2012a); Burkert et al. (2012); Schartmann et al. (2012); Shcherbakov (2014) Pfuhl et al. (2015); Schartmann et al. (2015); McCourt et al. (2015); McCourt & Madigan (2016); Madigan et al. (2017)
tidal disruption nova outburst	Miralda-Escudé (2012); Guillochon et al. (2014) Meyer & Meyer-Hofmeister (2012)
planet/protoplanet	Mapelli & Ripamonti (2015); Trani et al. (2016)
neutron star dynamics	Zajaček et al. (2017); Bortolas et al. (2017)

the polarization degree of $p_L \approx 30\%$ and a variable polarization angle before the periaipse of the source. The main observational constraints are summarized in Table 10.2.

Table 10.2: Observational constraints for the modelling of DSO.

Constraint	Note
SED, reddening	$K_s - L' > 3$
broad emission lines	$FWHM_{\text{Br}\gamma} \sim 100 \text{ km s}^{-1}$
source of polarized K_s band emission	polarization degree $\sim 30\%$
stability and compactness	no significant tidal elongation

Given the observational constraints, we concluded in Zajaček et al. (2017) that depending on the character of the spectral energy distribution, i.e. whether it is of thermal nature or non-thermal, two basic scenarios are possible: a *dust-enshrouded* star/binary or a young neutron star formed after a recent supernova explosion in the Clockwise Disc (CWD) outside the S-cluster. The roadmap towards solving the problem of the nature of the DSO is sketched in Figure 10.1.

Given the fact that no localized radio and X-ray counterparts of the DSO were detected, the observational constraints imply a dusty stellar source, plausibly a young dust-enshrouded star or a binary merger product. Using Monte Carlo code *Hyperion* (an open-source parallelized three-dimensional dust continuum radiative transfer code; Robitaille 2011), we performed a series of 3D Monte Carlo simulations of various set-ups to look for the model that can reproduce the constraints in Table 10.2 best.

We obtained a composite stellar model that consists of a pre-main-sequence star surrounded by a dense, optically thick dusty envelope dissected by bipolar cavities and a bow shock layer, whose density changes depending on the distance of the source from Sgr A*. Such a set-up can match both the total and polarized continuum emission of the source. Given an assumed young age of the star corresponding to Class I Young Stellar Object (having an age of 10^6 yr), the star is still accreting material from an inner rim of a circumstellar accretion disc, which can explain the broad emission recombination lines, mainly Br γ . The formation of a bow shock is expected due to a supersonic motion of the DSO/G2 close to the pericentre and its evolution along the orbit becomes asymmetric when an outflow from the direction of Sgr A* is present (Zajaček et al. 2016). The asymmetry between the pre-pericentre and the post-pericentre parts is profound for an expected outflow speed of $\lesssim 2000 \text{ km s}^{-1}$ (Mužić et al. 2010).

The spectral energy distribution and the simulated RGB image of the final model is in Fig. 10.2

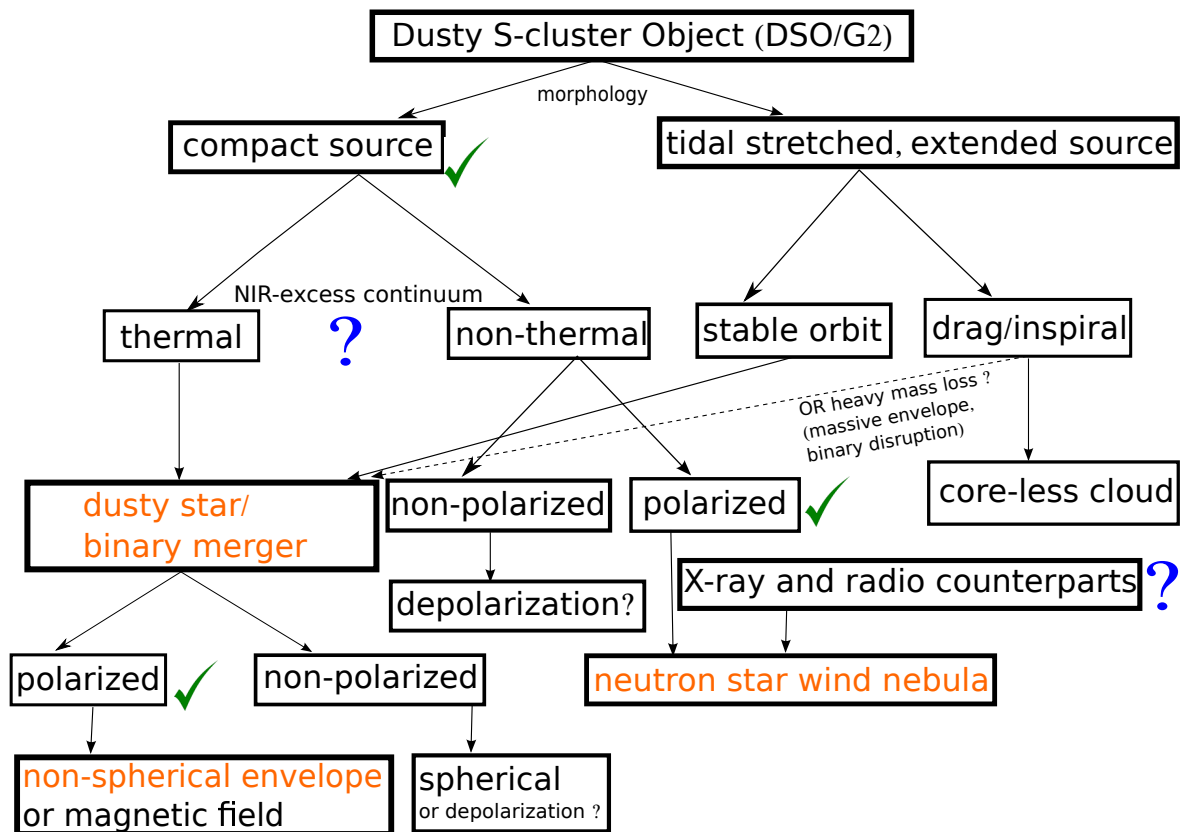


Figure 10.1: Roadmap towards solving the nature of the DSO/G2 source. So far the most plausible scenario is the dust-enshrouded star/binary merger surrounded by a non-spherical dusty envelope. In case a radio and X-ray counterpart are detected in the future, the roadmap would switch be towards a pulsar wind nebula scenario. With modifications adopted from Zajaček et al. (2017).

10.1.2 Interaction modes of neutron stars

We studied the distribution of interaction modes of neutron stars, focusing on the basic regimes, namely the ejector, accretor, propeller, and georotator. The mode is determined by the intrinsic characteristics of neutron stars (rotational period and magnetic field surface intensity) as well as by the properties of the ambient medium (density and temperature). Finally, the relative velocity of the neutron star with respect to the ambient medium also influences the type of interaction.

In our analysis, we focused on the interaction of neutron stars with the gas in the central Cavity, which is located in the innermost 1.5 pc. In particular, the fraction of neutron stars that interact with the denser Minispiral arms is in the range $\sim 0.3 - 10\%$, depending on the spatial distribution of neutron stars (steep profile, declining density towards the centre, flat density profile towards the centre). The interaction fraction is depicted in Fig. 10.3 for different orbital distributions.

We found out that the distribution of interaction modes is strongly dependent on the density of the ambient medium and only weakly dependent on the ambient temperature in the range $10^3 - 10^4$ K. The interaction modes in the 2D parameter space of the relative velocity–dipole magnetic field are depicted in Fig. 10.4. The dividing lines between individual modes

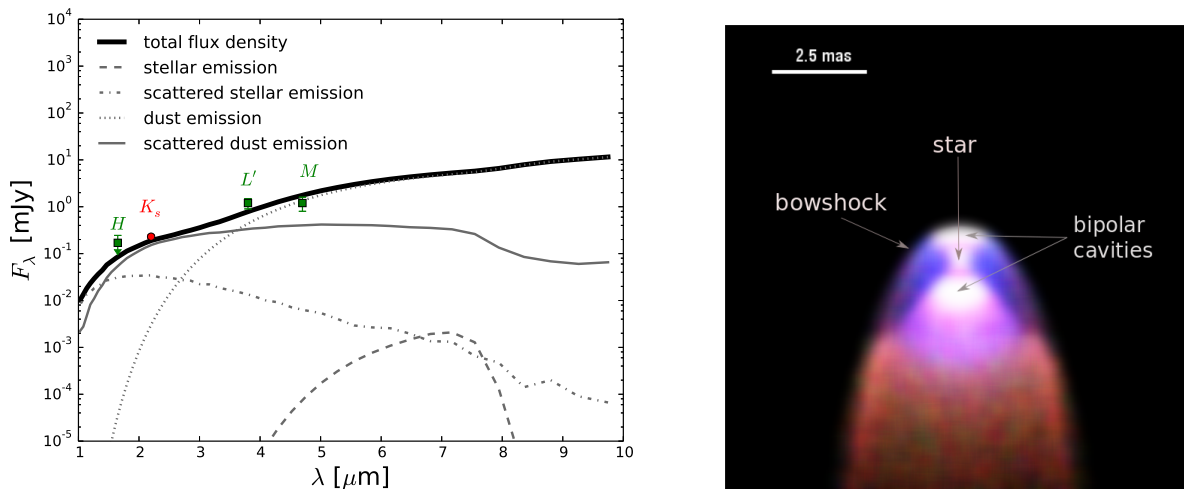


Figure 10.2: **Left:** Spectral energy distribution of a composite stellar model of the DSO source. Individual components are represented by lines according to the legend. The points with errorbars mark the observationally inferred continuum flux densities according to Eckart et al. (2013) and Shahzamanian et al. (2016). For the flux density at NIR K_s band, a significant linearly polarized signal was detected by Shahzamanian et al. (2016). Adopted from Zajaček et al. (2017) with modifications. **Right:** A simulated RGB image of the source model; the red colour represents M -band flux density, the green colour stands for L' -band flux density, and the blue colour corresponds to K_s -band flux density. Adopted from Shahzamanian et al. (2016) with modifications.

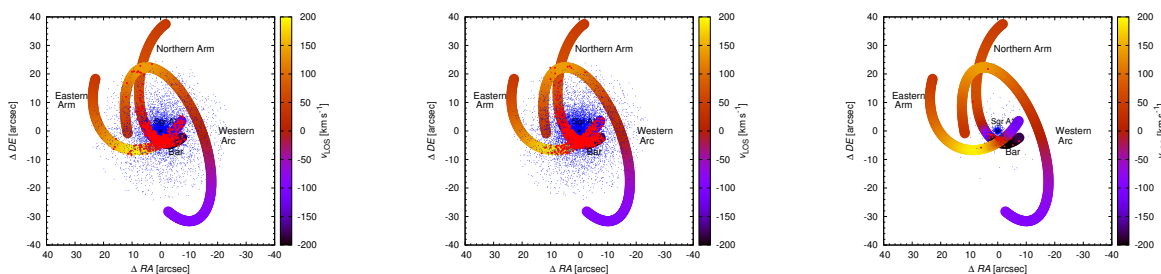


Figure 10.3: Interaction of the population of neutron stars with the denser Minispiral streamers in the central Cavity of the Galactic centre. Blue dots represent the whole population of 10000 neutron stars around Sgr A*, while red dots stand for the neutron stars that interact with the Minispiral. Left: a broken power-law density profile (a); Middle: a broken power-law profile with a declining density (b); Right: a density cusp of neutron stars (c).

were obtained using the theory presented in Lipunov (1992).

Furthermore, we looked for alternative ways to search for neutron stars, besides standard radio timing measurements of pulsars. One of the alternative ways is to look for the interaction between supersonic neutron stars and the denser ambient medium concentrated along the Minispiral arms, which can be detected in the form of bow shocks emitting non-thermal synchrotron emission that should be linearly polarized. In Zajaček et al. (2015), we found that the number of bow shocks larger than $\gtrsim 10$ mas should be of the order of 10. This number is, however, dependent on the assumed distribution of rotational periods and surface

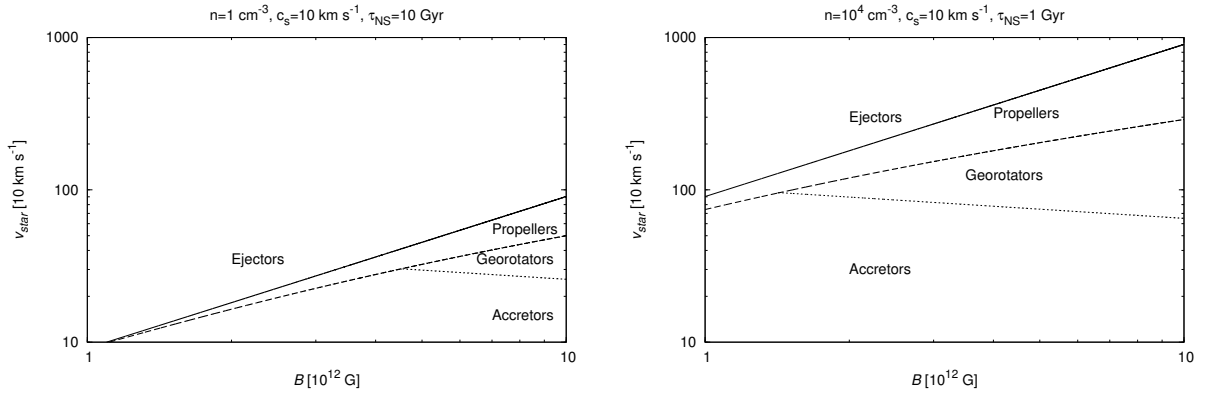


Figure 10.4: **Left:** Interaction modes of neutron stars in the relative velocity–dipole magnetic field space for a number density of 1 cm^{-3} of the ambient medium. **Right:** The same as in the left figure calculated for the ambient number density 10^4 cm^{-3} , approximately corresponding to the Minispiral arms.

magnetic fields – in our case we considered the distribution based on the observed pulsar population (Manchester et al. 2005), which is naturally biased towards ejecting neutron stars that have powerful pulsar winds. In principle, comparing the synthetic distribution of bow shocks associated with neutron stars with the observed one can be used to constrain the basic parameters of the Galactic centre neutron star population.

Another alternative way to look for neutron stars, especially recently created in supernova explosions, is to use current and future IR facilities (VLT, ELT), which can obtain spectral energy distribution of faint sources in the Nuclear Star Cluster. Sources that will have positive spectral indices (rising flux densities towards longer wavelengths) in combination with a polarization degree of the order of 10% will be suitable candidates for young neutron stars (Zajaček et al. 2017).

10.1.3 Charge of Sgr A*

Among three externally observable, classical parameters of the Galactic centre black hole (Sgr A*), only its mass is constrained well through the monitoring of S stars bound to it. The spin is only weakly constrained to be $a_{\bullet} \gtrsim 0.5$ based on the fitting of variable NIR emission (Eckart et al. 2017). The electric charge of the black hole is usually set to zero due to neutralization by plasma environment in the vicinity.

However, we showed that there is a potential for obtaining a small positive charge due to the fact that more positive charge is in the sphere of influence of the SMBH than a negative charge. This prevalence of the positively charged protons over electrons is estimated based on the relation we derived,

$$\left| \frac{Q_+}{Q_-} \right| = \left(\frac{T_e m_p}{T_p m_e} \right)^{3-\gamma_n} \approx 8 \times 10^4, \quad (10.1)$$

where γ_n is the power-law index of the plasma density distribution, which is $\gamma_n = 3/2$ for the spherical Bondi flow. Subsequently, we estimated that the maximum positive and negative charge that the Galactic centre black hole can obtain is at least ten orders of magnitude smaller than the charge corresponding to an extremal black hole,

$$Q_{\max} = 2 \sqrt{\pi \epsilon_0 G M_{\bullet}} = 6.86 \times 10^{26} \left(\frac{M_{\bullet}}{4 \times 10^6 M_{\odot}} \right) C. \quad (10.2)$$

Such a small charge does not have naturally any effect on the spacetime metric of the black hole solution, i.e. it does not, for instance, influence the size of the black hole shadow. However, even such a small electric charge can significantly influence the free-fall timescale and dynamics of charged particles (protons, electrons, and dust particles depending on the charge-to-mass ratio q/m).

From an astrophysical point of view, it is useful to design observational tests of the presence of the black hole charge associated with Sgr A* source. As we mentioned, the black hole shadow test is only sensitive to the charge starting at $\sim 10\%$ of the extremal value. A much more sensitive test that we propose is based on the flattening/decline of the surface brightness profile of the thermal bremsstrahlung observed in the X-ray domain. This bremsstrahlung “hole” can occur for the radius of $100 r_s$ for the electric charge $Q_{\bullet} \approx 10^{13} C$, i.e. about thirteen orders of magnitude smaller than the extremal charge, Eq. (10.2). For a detailed analysis, see [Zajaček et al. \(2018\)](#).

10.2 Future prospects

The research presented in the previous chapters was not only relevant for the time when it was published, but it has a potential for the further development in the future. Below we list several projects I have been working on at the time this PhD thesis was finished.

10.2.1 More dusty sources: DSO/G2, G1 and their friends

DSO/G2 source is not the only source with a NIR-excess emission in the S-cluster ($r \lesssim 1'' = 0.04$ pc). Other sources were previously detected. The first NIR-excess source close to Sgr A* was detected by [Clénet et al. \(2004\)](#), see also [Genzel et al. \(2003\)](#); [Ghez et al. \(2005\)](#), which is called now as G1 ([Pfuhl et al. 2015](#); [Witzel et al. 2017](#)). The comprehensive study of NIR-excess sources in continuum and the comparison of their colour indices was presented in [Eckart et al. \(2013\)](#). The first spectra of some of them were published in [Meyer et al. \(2014\)](#). Some of their characteristics are summarized in Table 10.3.

The spectral indices calculated in Table 10.3 show that some of the characteristics are qualitatively similar, namely the positive slopes α_{HK} and α_{KL} , except for S90 and D3–1. Also, for most of the sources, $\alpha_{\text{KL}} > \alpha_{\text{HK}}$, which points towards the dust emission that is more dominant towards longer wavelengths. As noted by [Meyer et al. \(2014\)](#), the sources do not exhibit absorption features in their spectra which are typical for late-type stars. Some sources have Bry emission line in their spectra, but not all of them. Two sources have an extended structure, at least D4/S50/X7 and D1/G1, while others appear point-like.

For the future, it will be of interest to consider the model of a dust-enshrouded star presented in [Zajaček et al. \(2017\)](#) to other sources. In particular, [Witzel et al. \(2017\)](#) claim that G1 shows signs of tidal interaction with Sgr A*, so in principle we can apply the model of a dust-enshrouded star and see if the changes in L'-band magnitude of G1 can be reproduced.

Table 10.3: Summary of detected, localized NIR-excess sources, including their continuum and line emission characteristics; α_{HK} and α_{KL} express the slopes between the corresponding NIR bands with the convention, $F_\lambda \propto \lambda^\alpha$. References: (1) Eckart et al. (2013); (2) Meyer et al. (2014); (3) Pfuhl et al. (2015); (4) Ghez et al. (2005); (5) Clénet et al. (2004); (6) Mužić et al. (2010).

Source	H	K_s	L'	$H - K_s$	$K_s - L'$	α_{HK}	α_{KL}	Bry line emission	References	Notes
D2/S43-3	18.7	16.5	13.5	2.2	3.0	0.8	2.9	yes	(1), (2)	–
D6/S79	17.6	15.4	13.5	2.2	1.9	0.8	1.1	–	(1)	–
S90	17.4	15.3	14.6	2.1	0.7	0.5	-1.0	–	(1)	–
F1	18.3	16.0	13.7	2.3	2.3	1.2	1.7	–	(1)	–
F2	18.0	15.8	12.9	2.2	2.9	0.8	2.7	–	(1)	–
D3-1	21.3	19.8	13.8	1.5	6.0	-1.4	8.0	yes	(1),(2)	–
D5-2	19.8	17.3	13.4	2.5	3.9	1.8	4.4	no	(1), (2)	–
D4/S50/X7	19.3	17.1	12.6	2.2	4.5	0.8	5.4	–	(1), (6)	bow-shock shape
D7	23.4	18.5	14.1	4.9	4.4	9.5	5.3	–	(1)	–
D1/G1	–	≥ 17.3	14.4	–	2.9	–	2.7	yes	(3),(4),(5)	extended cloudy structure
DSO/G2	≥ 21.2	18.7	14.4	2.5	4.3	1.8	5.1	yes	(1), (2)	high eccentricity

10.2.2 Neutron star dynamics

In the Clockwise Disc of massive and bright OB stars, which has a radius span of 0.04 pc to 0.5 pc (Genzel et al. 2010), it is expected that supernova explosions will result in the formation of neutron stars with an initial kick velocity of $\Delta v_{\text{kick}} = 380 \text{ km s}^{-1}$ (Faucher-Giguère & Kaspi 2006) that is similar to the Keplerian circular velocity at the distance range of the Disc,

$$v_{\text{circ}} = 415 \left(\frac{M_\bullet}{4 \times 10^6 M_\odot} \right)^{1/2} \left(\frac{r}{0.1 \text{ pc}} \right)^{-1/2}, \quad (10.3)$$

which implies that the kick velocity can significantly affect the angular momentum of a newborn neutron star. If the kick velocity is in opposite direction to that of an original orbital velocity, the loss of an angular momentum leads to an increase in eccentricity and the final plunging orbit is similar to that of the DSO/G2 NIR-excess source. We illustrate this effect in Fig. 10.5.

In the simplified case of a natal kick that would occur in the Clockwise Disc at the distance corresponding to the apocentre distance of the DSO, $r_A = a(1 + e) \sim 0.06 \text{ pc}$, in the direction opposite to the orbital motion, we can obtain a sufficient angular momentum change, as it is illustrated in Fig. 10.5. The required change in the angular momentum ΔJ between a nearly circular orbit of the object at r_A and the angular momentum corresponding to the current highly-eccentric orbit of the DSO can be evaluated as $\Delta J_{\text{orbit}} = J_c(r_A) - J_{\text{DSO}} = \sqrt{GM_\bullet r_A} (1 - \sqrt{1 - e})$, which for the eccentricity of $e = 0.98$ and the semi-major axis of $a = 0.033 \text{ pc}$ gives $\Delta J_{\text{orbit}} = 0.85 J_c(r_A) \approx 8.5 \times 10^{24} \text{ cm}^2 \text{ s}^{-1}$. If we assume, for simplicity, that the kick velocity vector is anti-parallel to the original circular velocity at r_A , the change of the angular momentum per unit mass is $\Delta J_{\text{kick}} = r_A \Delta v_{\text{kick}}$, which for the mean kick velocity of $\Delta v_{\text{kick}} = 380 \text{ km s}^{-1}$ (Faucher-Giguère & Kaspi 2006), leads to $\Delta J_{\text{kick}} = 0.74 J_c(r_A) \approx 7.6 \times 10^{24} \text{ cm}^2 \text{ s}^{-1}$, which is comparable to ΔJ_{orbit} . Natal kicks during supernova explosions in the Clockwise Disc can thus lead to the formation of infalling pulsars towards Sgr A*, with similar orbital characteristics as those of the DSO.

Further work in this project may be focused on the statistical distribution of the neutron star population that originates in a single starburst population, such as in the case of the Clockwise Disc. In particular, one can calculate numerically the distribution of orbital elements for such

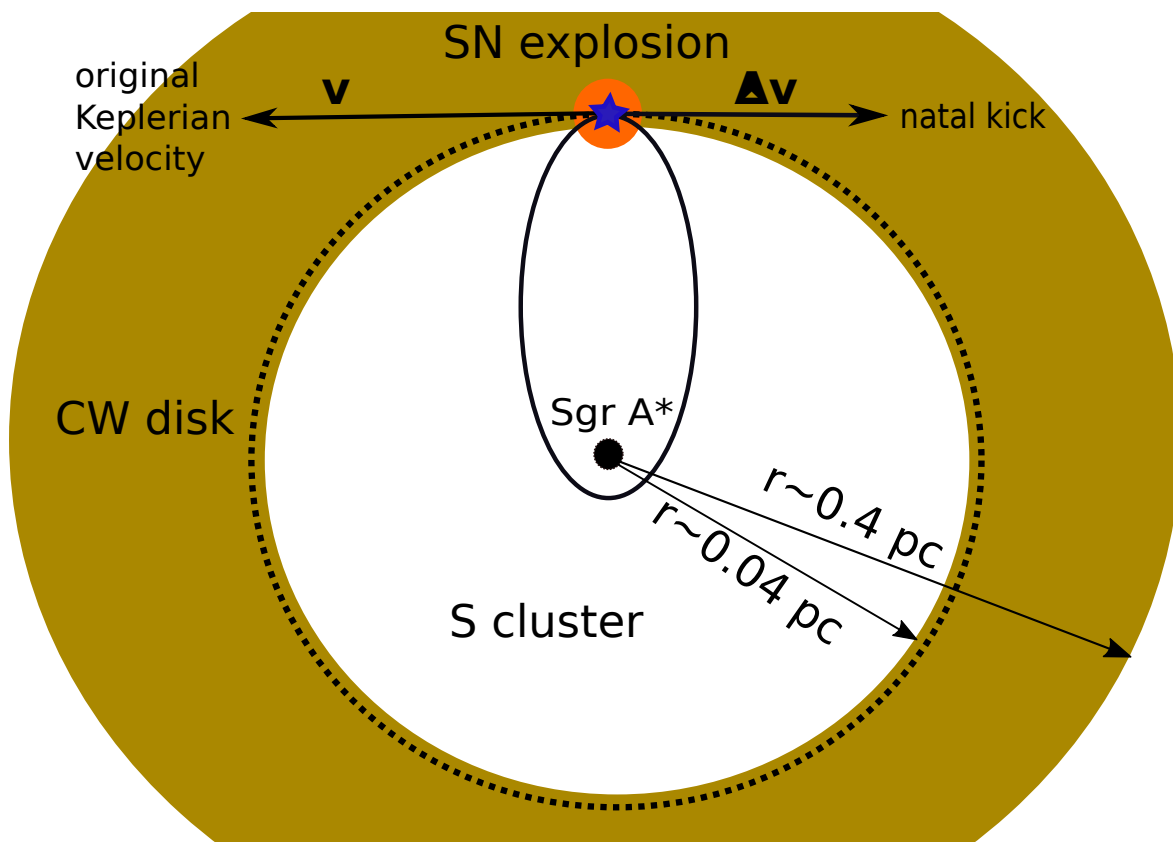


Figure 10.5: The illustration of how a supernova kick in the Clockwise Disc can influence the orbital parameters of its end-product – the result is a neutron star on a highly eccentric orbit, approaching Sgr A* as close as the inner parts of the S-cluster. Courtesy of M. Zajaček.

a population. The fractions of neutron stars that are kept in the Nuclear Star Cluster and of those that escape are of special interest for further calculations of gravitational-wave emission from neutron stars ($M_{\text{NS}} \approx 1.4 M_{\odot}$) infalling towards Sgr A* black hole (so-called Extreme Mass Ratio Inspirals - EMRIs, see [Eckart et al. 2017](#), for more details).

10.2.3 Dynamics of binary black hole systems: OJ287 as a special case

OJ287 is one of the best candidates among Active Galactic Nuclei (AGN) to host a supermassive black hole binary. This was motivated by thermal optical flares that occur every ~ 12 years. These optical flares, which have been observed since 1890, are fully predictable under the assumption that they occur at constant phase angles of a quasi-Keplerian orbit of a binary black hole system ([Valtonen et al. 2016](#)).

With the luminosity distance of 1.592 Mpc (redshift of 0.306) and the mass of the primary of the order of $10^{10} M_{\odot}$, OJ287 is one of few AGNs that can be resolved at event horizon scales with the Event Horizon Telescope (EHT). The system was also observed in April 2017, which will help to confirm or exclude the binary nature of the AGN.

A new light on this enigmatic source was shed by the study of [Britzen et al. \(2018\)](#), who reanalyzed 120 Very Long Baseline Array (VLBA) observations at 15 GHz with the time coverage between April 1995 and January 2017. We found that the jet of OJ287 is both rotating and precessing. Also, the analysis of components revealed, for the first time, the

detailed kinematics of the jet, namely the spine of the jet (originating in the ergosphere of a rotating black hole) and the sheath of the jet, which originates rather in an accretion disc. Half of the precessing period of the jet coincides with the main periodicity of optical flares. We suggest that the whole variability of the source may be fully explained by the geometry – the rotating and precessing jet, which leads to the variable viewing angle and the Doppler boosting. In this framework, the optical emission can be of a non-thermal, synchrotron nature. The longer periodicity of ~ 24 years that is attributed to the jet precession may be explained by the binary black hole model, in which the disc-jet precession is driven by a secondary black hole. Alternatively, the Lense-Thirring precession of a misaligned disc with respect to the black hole angular momentum (Caproni et al. 2004) can also explain the jet precession, namely for the steeper density profile of an accretion disc. The geometry of the model of OJ287 is illustrated in Fig. 10.6, including both the binary black hole model and the Lense-Thirring precession. Note that the previous model involving a binary black hole, in which the secondary component plunges through an accretion disc surrounding the primary black hole, is not necessary.

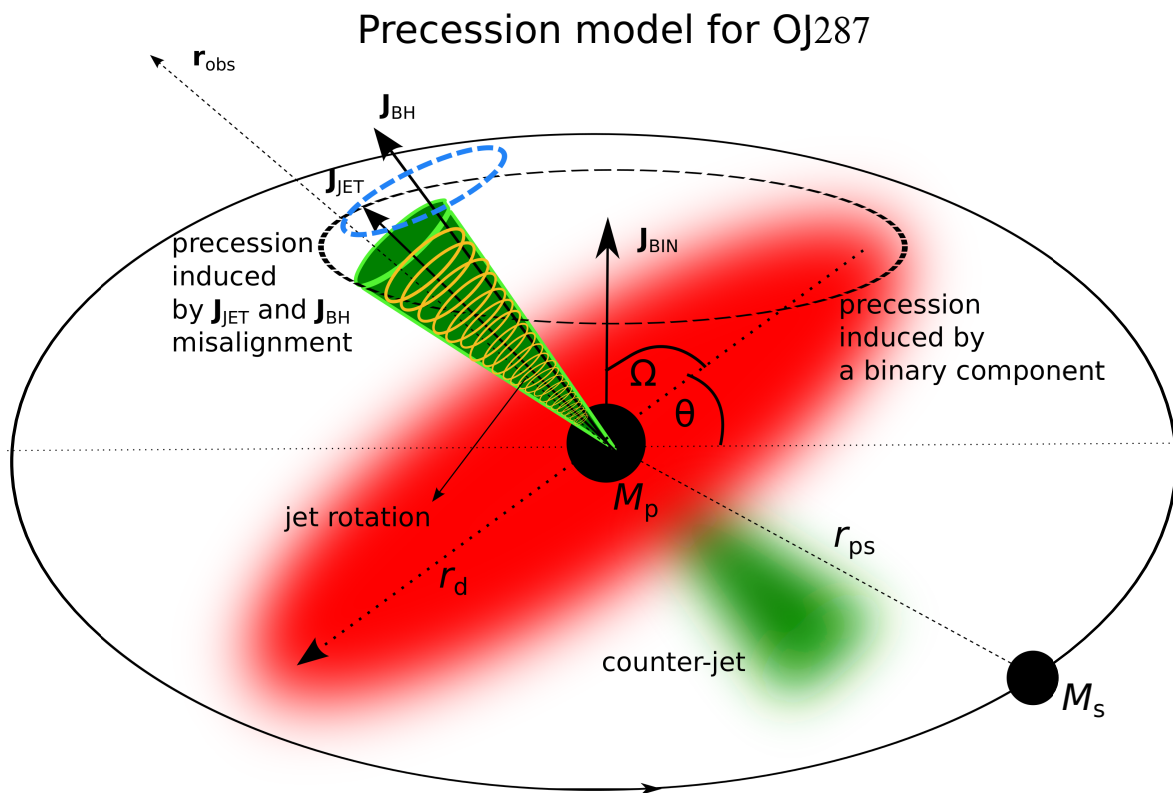


Figure 10.6: The figure illustrates the geometry of the model representing the blazar OJ287. The longer periodicity of ~ 24 years may be explained either by the disc/jet precession driven by a secondary black hole or by a Lense-Thirring precession of an accretion disc surrounding only a single black hole. The shorter period of 1 year is explained by the jet rotation. Courtesy of M. Zajaček. For details, see Britzen et al. (2018).

In the future, we are planning to use the Very Long Baseline Array (VLBA) radio maps to constrain the parameters of a precessing jet model, in a similar way as was previously

done by [Abraham \(2000\)](#). One can use the simple precessing model to fit the kinematics of superluminal as well as stationary components. This way one can obtain the limits on the Lorentz factor γ and on the bulk motion of the jet.

10.2.4 Analysis of JWST observations

James Webb Space Telescope (JWST) is the successor to the Hubble Space Telescope (HST) that is going to be launched in 2018. Its primary aperture is 6.5 meters and it will be operate in the infrared wavelength range of $0.6\ \mu\text{m} - 28\ \mu\text{m}$. It will observe the surrounding Universe from the Lagrange point L2, in the direction opposite to the Sun with respect to the Earth. It is ideally suited for observing high-redshift (early) galaxies and cold objects such as protoplanetary discs and exoplanets.

Concerning the Galactic centre, JWST will be able to detect clouds and clumps of dust (the Minispiral) and the dust-enshrouded stars. One of the sources of interest is the association of young, dusty stars IRS13N ([Mužić et al. 2008](#)). The telescope can obtain images and spectra and do the Integral Field Spectroscopy. An exemplary, simulated image is given in Fig. 10.7 as modelled by MIRIsim, which shows Field of Views (FOVs) pointed at S-cluster and IRS13N sources.

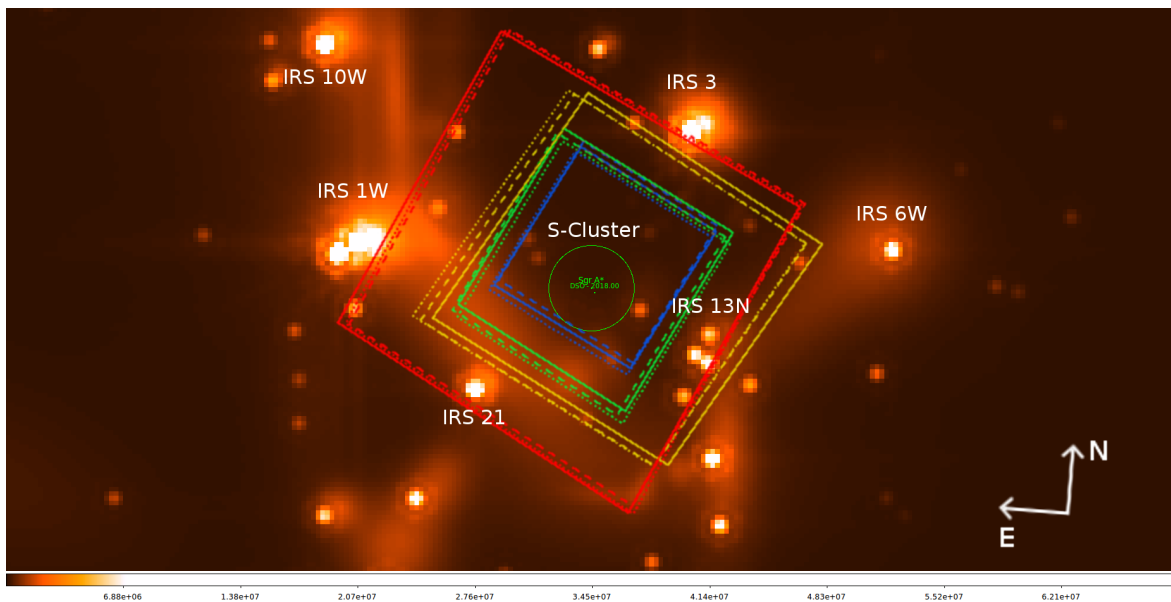


Figure 10.7: A simulated image depicting fields of view (FOVs) of 12 Medium Resolution Spectrometer (MRS) channels pointed at S-cluster and IRS13N sources. The green circle marks the region where the DSO/G2 orbits Sgr A*. Taken from [Vider \(2017\)](#).

When the data from JWST will be reduced and analysed, one can compare the observed spectra of dusty sources with the simulated ones, e.g. obtained using Monte Carlo Radiative Transfer codes, which should further constrain the fundamental parameters of these sources. JWST observations will thus shed new light on young stars and their formation in the extreme environment of the Galactic centre in particular.



Bibliography

- Abraham, Z. 2000, *A&A*, 355, 915
- Adams, W. S. 1914, *PASP*, 26, 198
- Adams, W. S. 1915, *PASP*, 27, 236
- Alpher, R. A., Bethe, H., & Gamow, G. 1948, *Physical Review*, 73, 803
- Angélil, R., Saha, P., & Merritt, D. 2010, *ApJ*, 720, 1303
- Baade, W. & Zwicky, F. 1934, *Contributions from the Mount Wilson Observatory*, vol. 3, pp.79-83, 3, 79
- Balick, B. & Brown, R. L. 1974, *ApJ*, 194, 265
- Ballone, A., Schartmann, M., Burkert, A., et al. 2013, *ApJ*, 776, 13
- Ballone, A., Schartmann, M., Burkert, A., et al. 2016, *ApJ*, 819, L28
- Bartko, H., Martins, F., Trippe, S., et al. 2010, *ApJ*, 708, 834
- Bartusiak, M. 2015, *Black hole* (Yale University Press, New Haven & London)
- Becklin, E. E. & Neugebauer, G. 1968, *ApJ*, 151, 145
- Bessel, F. W. 1844, *MNRAS*, 6, 136
- Bethe, H. A. 1939, *Physical Review*, 55, 434
- Birkhoff, G. D. & Langer, R. E. 1923, *Relativity and modern physics*
- Blum, R. D., Ramírez, S. V., Sellgren, K., & Olsen, K. 2003, *ApJ*, 597, 323
- Bond, G. 1862, *Astronomische Nachrichten*, 57, 131
- Borkar, A., Eckart, A., Straubmeier, C., et al. 2016, *MNRAS*, 458, 2336
- Bortolas, E., Mapelli, M., & Spera, M. 2017, *MNRAS*, 469, 1510

- Bower, G. C., Deller, A., Demorest, P., et al. 2014, *ApJ*, 780, L2
- Britzen, S., Fendt, C., Witzel, G., et al. 2018, *MNRAS*, 478, 3199
- Brown, R. L. 1982, *ApJ*, 262, 110
- Brown, R. L., Johnston, K. J., & Lo, K. Y. 1981, *ApJ*, 250, 155
- Brown, R. L. & Lo, K. Y. 1982, *ApJ*, 253, 108
- Buchholz, R. M., Schödel, R., & Eckart, A. 2009, *A&A*, 499, 483
- Burbidge, E. M., Burbidge, G. R., Fowler, W. A., & Hoyle, F. 1957, *Reviews of Modern Physics*, 29, 547
- Burbidge, G. R. 1958, *ApJ*, 128, 1
- Burbidge, G. R. 1959, in *IAU Symposium, Vol. 9, URSI Symp. 1: Paris Symposium on Radio Astronomy*, ed. R. N. Bracewell, 541
- Burkert, A., Scharfmann, M., Alig, C., et al. 2012, *ApJ*, 750, 58
- Caproni, A., Mosquera Cuesta, H. J., & Abraham, Z. 2004, *ApJ*, 616, L99
- Chandrasekhar, S. 1931a, *MNRAS*, 91, 456
- Chandrasekhar, S. 1931b, *ApJ*, 74, 81
- Christopher, M. H., Scoville, N. Z., Stolovy, S. R., & Yun, M. S. 2005, *ApJ*, 622, 346
- Clark, B. G. & Hogg, D. E. 1966, *ApJ*, 145, 21
- Clénet, Y., Rouan, D., Gendron, E., et al. 2004, *A&A*, 417, L15
- Colgate, S. A. & White, R. H. 1966, *ApJ*, 143, 626
- Davidson, J. A., Werner, M. W., Wu, X., et al. 1992, *ApJ*, 387, 189
- De Colle, F., Raga, A. C., Contreras-Torres, F. F., & Toledo-Roy, J. C. 2014, *ApJ*, 789, L33
- Dexter, J. & O’Leary, R. M. 2014, *ApJ*, 783, L7
- Do, T., Ghez, A. M., Morris, M. R., et al. 2009, *ApJ*, 703, 1323
- Dovčiak, M., Karas, V., Matt, G., & Goosmann, R. W. 2008, *MNRAS*, 384, 361
- Dyson, J. E. 1968, *Ap&SS*, 1, 388
- Eatough, R., Karuppusamy, R., Kramer, M., & et al.,. 2013a, *The Astronomer’s Telegram*, 5040, 1
- Eatough, R. P., Falcke, H., Karuppusamy, R., et al. 2013b, *Nature*, 501, 391
- Eckart, A., Baganoff, F. K., Morris, M., et al. 2004a, *A&A*, 427, 1
- Eckart, A., Baganoff, F. K., Morris, M. R., et al. 2009, *A&A*, 500, 935

- Eckart, A., Baganoff, F. K., Zamaninasab, M., et al. 2008a, *A&A*, 479, 625
- Eckart, A. & Genzel, R. 1996, *Nature*, 383, 415
- Eckart, A. & Genzel, R. 1997, *MNRAS*, 284, 576
- Eckart, A., Hüttemann, A., Kiefer, C., et al. 2017, *Foundations of Physics*, 47, 553, ArXiv: 1703.09118
- Eckart, A., Moultaqa, J., Viehmann, T., Straubmeier, C., & Mouawad, N. 2004b, *ApJ*, 602, 760
- Eckart, A., Mužić, K., Yazici, S., et al. 2013, *A&A*, 551, A18
- Eckart, A., Schödel, R., García-Marín, M., et al. 2008b, *A&A*, 492, 337
- Eckart, A., Schödel, R., Meyer, L., et al. 2006, *A&A*, 455, 1
- Eckart, A., Schödel, R., & Straubmeier, C. 2005, *The Black Hole at the Center of the Milky Way* (London: Imperial College Press)
- Eddington, A. S. 1926, *The Internal Constitution of the Stars*
- Edge, D. O., Shakeshaft, J. R., McAdam, W. B., Baldwin, J. E., & Archer, S. 1959, *MmRAS*, 68, 37
- Einstein, A. 1915, *Sitzungsberichte der Königlich Preußischen Akademie der Wissenschaften* (Berlin), Seite 778-786.
- Einstein, A. 1939, *Annals of Mathematics*, 40, 922
- Ewing, E. A. 1964, *Science News Letters*, 39
- Faucher-Giguère, C.-A. & Kaspi, V. M. 2006, *ApJ*, 643, 332
- Fowler, R. H. 1926, *MNRAS*, 87, 114
- Freire, P. C., Camilo, F., Kramer, M., et al. 2003, *MNRAS*, 340, 1359
- Fritz, T. K., Gillessen, S., Dodds-Eden, K., et al. 2010, *ApJ*, 721, 395
- Genzel, R., Eisenhauer, F., & Gillessen, S. 2010, *Reviews of Modern Physics*, 82, 3121
- Genzel, R., Schödel, R., Ott, T., et al. 2003, *ApJ*, 594, 812
- Genzel, R., Watson, D. M., Townes, C. H., et al. 1984, *ApJ*, 276, 551
- Gerhard, O. 2001, *ApJ*, 546, L39
- Ghez, A. M., Duchêne, G., Matthews, K., et al. 2003, *ApJ*, 586, L127
- Ghez, A. M., Hornstein, S. D., Lu, J. R., et al. 2005, *ApJ*, 635, 1087
- Ghez, A. M., Klein, B. L., Morris, M., & Becklin, E. E. 1998, *ApJ*, 509, 678

- Gillessen, S., Eisenhauer, F., Trippe, S., et al. 2009a, *ApJ*, 692, 1075
- Gillessen, S., Eisenhauer, F., Trippe, S., et al. 2009b, *ApJ*, 692, 1075
- Gillessen, S., Genzel, R., Fritz, T. K., et al. 2013a, *ApJ*, 763, 78
- Gillessen, S., Genzel, R., Fritz, T. K., et al. 2013b, *ApJ*, 774, 44
- Gillessen, S., Genzel, R., Fritz, T. K., et al. 2012a, *Nature*, 481, 51
- Gillessen, S., Genzel, R., Fritz, T. K., et al. 2012b, *Nature*, 481, 51
- Gillessen, S., Plewa, P. M., Eisenhauer, F., et al. 2017, *ApJ*, 837, 30
- Ginzburg, V. L. 1961, *Soviet Ast.*, 5, 282
- Guillochon, J., Loeb, A., MacLeod, M., & Ramirez-Ruiz, E. 2014, *ApJ*, 786, L12
- Harrison, B. K., Thorne, K. S., Wakano, M., & Wheeler, J. A. 1965, *Gravitation Theory and Gravitational Collapse*
- Hartmann, M., Debattista, V. P., Seth, A., Cappellari, M., & Quinn, T. R. 2011, *MNRAS*, 418, 2697
- Hazard, C., Mackey, M. B., & Shimmins, A. J. 1963, *Nature*, 197, 1037
- Heusler, M. 1996, *Black hole uniqueness theorems* (Cambridge ; New York : Cambridge University Press)
- Hewish, A., Bell, S. J., Pilkington, J. D. H., Scott, P. F., & Collins, R. A. 1968, *Nature*, 217, 709
- Hey, J. S. 1975, *The radio universe*
- Hoyle, F. & Fowler, W. A. 1963, *Nature*, 197, 533
- Hubble, E. 1929, *Proceedings of the National Academy of Science*, 15, 168
- Israel, W. 1987, *Dark stars: the evolution of an idea.*, ed. S. W. Hawking & W. Israel, 199–276
- Jackson, J. M., Geis, N., Genzel, R., et al. 1993, *ApJ*, 402, 173
- Jalali, B., Pelupessy, F. I., Eckart, A., et al. 2014, *MNRAS*, 444, 1205
- Jansky, K. G. 1933, *Nature*, 132, 66
- Jog, C. J. 2013, *MNRAS*, 434, L56
- Kennea, J. A., Burrows, D. N., Kouveliotou, C., et al. 2013, *ApJ*, 770, L24
- Kerr, R. P. 1963, *Physical Review Letters*, 11, 237
- Kim, S. S. & Morris, M. 2003, *ApJ*, 597, 312
- Kopal, Z. 1959, *Close binary systems* (London: Chapman & Hall)

- Krabbe, A., Genzel, R., Eckart, A., et al. 1995, *ApJ*, 447, L95
- Kunneriath, D., Eckart, A., Vogel, S. N., et al. 2012, *A&A*, 538, A127
- Kunneriath, D., Witzel, G., Eckart, A., et al. 2010, *A&A*, 517, A46+
- Lacy, J. H., Baas, F., Townes, C. H., & Geballe, T. R. 1979, *ApJ*, 227, L17
- Lacy, J. H., Townes, C. H., Geballe, T. R., & Hollenbach, D. J. 1980, *ApJ*, 241, 132
- Lacy, J. H., Townes, C. H., & Hollenbach, D. J. 1982, *ApJ*, 262, 120
- Landau, L. 1938, *Nature*, 141, 333
- Levin, Y. & Beloborodov, A. M. 2003, *ApJ*, 590, L33
- Lipunov, V. M. 1992, *Astrophysics of Neutron Stars* (Berlin/Heidelberg: Springer-Verlag)
- Lo, K. Y., Schilizzi, R. T., Cohen, M. H., & Ross, H. N. 1975, *ApJ*, 202, L63
- Lynden-Bell, D. 1969, *Nature*, 223, 690
- Lynden-Bell, D. & Rees, M. J. 1971, *MNRAS*, 152, 461
- Madigan, A.-M., McCourt, M., & O’Leary, R. M. 2017, *MNRAS*, 465, 2310
- Manchester, R. N., Hobbs, G. B., Teoh, A., & Hobbs, M. 2005, *AJ*, 129, 1993
- Mapelli, M. & Ripamonti, E. 2015, *ApJ*, 806, 197
- Matthews, T. A. & Sandage, A. R. 1963, *ApJ*, 138, 30
- McCourt, M. & Madigan, A.-M. 2016, *MNRAS*, 455, 2187
- McCourt, M., O’Leary, R. M., Madigan, A.-M., & Quataert, E. 2015, *MNRAS*, 449, 2
- McNamara, D. H., Madsen, J. B., Barnes, J., & Ericksen, B. F. 2000, *PASP*, 112, 202
- Merritt, D. 2013, *Dynamics and Evolution of Galactic Nuclei*
- Meyer, F. & Meyer-Hofmeister, E. 2012, *A&A*, 546, L2
- Meyer, L., Do, T., Ghez, A., et al. 2009, *ApJ*, 694, L87
- Meyer, L., Eckart, A., Schödel, R., et al. 2006a, *A&A*, 460, 15
- Meyer, L., Ghez, A. M., Witzel, G., et al. 2014, in *IAU Symposium*, Vol. 303, *IAU Symposium*, ed. L. O. Sjouwerman, C. C. Lang, & J. Ott, 264–268
- Meyer, L., Schödel, R., Eckart, A., et al. 2007, *A&A*, 473, 707
- Meyer, L., Schödel, R., Eckart, A., et al. 2006b, *A&A*, 458, L25
- Miller, A. I. 2005, *Empire of the Stars: Obsession, Friendship, and Betrayal in the Quest for Black Holes* (Houghton Mifflin Company: Boston, New York)

- Milosavljević, M. & Loeb, A. 2004, *ApJ*, 604, L45
- Miralda-Escudé, J. 2012, *ApJ*, 756, 86
- Misner, C. W., Thorne, K. S., & Wheeler, J. A. 1973, *Gravitation*
- Mori, K., Gotthelf, E. V., Zhang, S., et al. 2013, *ApJ*, 770, L23
- Moroz, V. I. 1961, *AZh*, 38, 487
- Morris, M. 1993, *ApJ*, 408, 496
- Morsony, B. J., Gracey, B. T., Workman, J. C., & Yoon, D. 2017, *ApJ*, 843, 29
- Moser, L., Sánchez-Monge, Á., Eckart, A., et al. 2017, *A&A*, 603, A68
- Muno, M. P., Baganoff, F. K., Brandt, W. N., Morris, M. R., & Starck, J.-L. 2008, *ApJ*, 673, 251
- Murray-Clay, R. A. & Loeb, A. 2012, *Nature Communications*, 3, 1049
- Mužić, K., Eckart, A., Schödel, R., et al. 2010, *A&A*, 521, A13
- Mužić, K., Schödel, R., Eckart, A., Meyer, L., & Zensus, A. 2008, *A&A*, 482, 173
- Neumayer, N., Walcher, C. J., Andersen, D., et al. 2011, *MNRAS*, 413, 1875
- Newman, E. T., Couch, E., Chinnapared, K., et al. 1965, *Journal of Mathematical Physics*, 6, 918
- Nordström, G. 1918, *Koninklijke Nederlandse Akademie van Wetenschappen Proceedings Series B Physical Sciences*, 20, 1076
- Olczak, C., Pfalzner, S., & Spurzem, R. 2006, *ApJ*, 642, 1140
- Oppenheimer, J. R. & Snyder, H. 1939, *Physical Review*, 56, 455
- Oppenheimer, J. R. & Volkoff, G. M. 1939, *Physical Review*, 55, 374
- Paczynski, B. & Trimble, V. 1979, in *IAU Symposium, Vol. 84, The Large-Scale Characteristics of the Galaxy*, ed. W. B. Burton, 401–403
- Parsa, M., Eckart, A., Shahzamanian, B., et al. 2017, *The Astrophysical Journal*, 845, 22
- Paumard, T., Genzel, R., Martins, F., et al. 2006, *ApJ*, 643, 1011
- Penrose, R. 1969, *Nuovo Cimento Rivista Serie*, 1
- Pfahl, E. & Loeb, A. 2004, *ApJ*, 615, 253
- Pfuhl, O., Fritz, T. K., Zilka, M., et al. 2011, *ApJ*, 741, 108
- Pfuhl, O., Gillessen, S., Eisenhauer, F., et al. 2015, *ApJ*, 798, 111
- Phifer, K., Do, T., Meyer, L., et al. 2013, *ApJ*, 773, L13

- Piddington, J. H. & Minnett, H. C. 1951, Australian Journal of Scientific Research A Physical Sciences, 4, 459
- Portegies Zwart, S. F., McMillan, S. L. W., & Gerhard, O. 2003, ApJ, 593, 352
- Prodan, S., Antonini, F., & Perets, H. B. 2015, ApJ, 799, 118
- Rauch, C., Mužić, K., Eckart, A., et al. 2013, A&A, 551, A35
- Rea, N., Esposito, P., Pons, J. A., & et al.,. 2013, ApJ, 775, L34
- Reber, G. 1944, ApJ, 100, 279
- Reissner, H. 1916, Annalen der Physik, 355, 106
- Rindler, W. 1956, MNRAS, 116, 662
- Roberts, D. A. & Goss, W. M. 1993, ApJS, 86, 133
- Roberts, M. S. E. 2005, The Pulsar Wind Nebula Catalog (March 2005 version; McGill University, Montreal; available on the World-Wide-Web at <http://www.physics.mcgill.ca/~pulsar/pwncat.html>)
- Robitaille, T. P. 2011, A&A, 536, A79
- Sabha, N., Witzel, G., Eckart, A., et al. 2010, A&A, 512, A2
- Salpeter, E. E. 1964, ApJ, 140, 796
- Sanchez-Bermudez, J., Schödel, R., Alberdi, A., et al. 2014, A&A, 567, A21
- Schartmann, M., Ballone, A., Burkert, A., et al. 2015, ApJ, 811, 155
- Schartmann, M., Burkert, A., Alig, C., et al. 2012, ApJ, 755, 155
- Schmidt, M. 1963, Nature, 197, 1040
- Schödel, R., Feldmeier, A., Neumayer, N., Meyer, L., & Yelda, S. 2014, Classical and Quantum Gravity, 31, 244007
- Schödel, R., Merritt, D., & Eckart, A. 2009a, A&A, 502, 91
- Schödel, R., Merritt, D., & Eckart, A. 2009b, A&A, 502, 91
- Schödel, R., Ott, T., Genzel, R., et al. 2002, Nature, 419, 694
- Schwarzschild, K. 1916, Sitzungsberichte der Königlich Preußischen Akademie der Wissenschaften (Berlin), 1916, Seite 189-196
- Scoville, N. & Burkert, A. 2013, ApJ, 768, 108
- Serabyn, E. & Lacy, J. H. 1985, ApJ, 293, 445
- Shahzamanian, B., Eckart, A., Zajaček, M., et al. 2016, A&A, 593, A131

- Shakura, N. I. & Sunyaev, R. A. 1973, *A&A*, 24, 337
- Shapiro, S. L. & Teukolsky, S. A. 1983, *Black holes, white dwarfs, and neutron stars: The physics of compact objects*
- Shapley, H. 1918, *ApJ*, 48
- Shapley, H. & Curtis, H. D. 1921, *Bulletin of the National Research Council*, Vol. 2, Part 3, No. 11, p. 171-217, 2, 171
- Shcherbakov, R. V. 2014, *ApJ*, 783, 31
- Southworth, G. C. 1982, 1945, *Microwave Radiation from the Sun (with Erratum)*, ed. W. T. Sullivan, III, 168
- Spitler, L. G., Lee, K. J., Eatough, R. P., et al. 2014, *ApJ*, 780, L3
- Stebbins, J. & Whitford, A. E. 1947, *ApJ*, 106, 235
- Stephan, A. P., Naoz, S., Ghez, A. M., et al. 2016, *MNRAS*, 460, 3494
- Tanner, A., Ghez, A. M., Morris, M. R., & Christou, J. C. 2005, *ApJ*, 624, 742
- Thorne, K. 1994, *Black Holes and Time Warps: Einstein's Outrageous Legacy*, Commonwealth Fund Book Program (W.W. Norton)
- Tolman, R. C. 1939, *Physical Review*, 55, 364
- Toomre, A. 1964, *ApJ*, 139, 1217
- Townes, C. H., Lacy, J. H., Geballe, T. R., & Hollenbach, D. J. 1983, *Nature*, 301, 661
- Trani, A. A., Mapelli, M., Spera, M., & Bressan, A. 2016, *ApJ*, 831, 61
- Trumpler, R. J. 1930, *Lick Observatory Bulletin*, 14, 154
- Valencia-S., M., Eckart, A., Zajaček, M., et al. 2015, *ApJ*, 800, 125
- Vallée, J. P. 2005, *AJ*, 130, 569
- Valtonen, M. J., Zola, S., Ciprini, S., et al. 2016, *ApJ*, 819, L37
- Vider, S. 2017, *Planning Mid-Infrared Observations of the Galactic Center with the James Webb Space Telescope* (BSc. Thesis, Universität zu Köln 2017)
- Viehmann, T., Eckart, A., Schödel, R., Pott, J.-U., & Moutaka, J. 2006, *ApJ*, 642, 861
- Vollmer, B. & Duschl, W. J. 2001a, *A&A*, 367, 72
- Vollmer, B. & Duschl, W. J. 2001b, *A&A*, 377, 1016
- Wex, N. & Kopeikin, S. M. 1999, *ApJ*, 514, 388
- Wharton, R. S., Chatterjee, S., Cordes, J. M., Deneva, J. S., & Lazio, T. J. W. 2012, *ApJ*, 753, 108

- Witzel, G., Eckart, A., Bremer, M., et al. 2012, *ApJS*, 203, 18
- Witzel, G., Ghez, A. M., Morris, M. R., et al. 2014, *ApJ*, 796, L8
- Witzel, G., Sitarski, B. N., Ghez, A. M., et al. 2017, *ApJ*, 847, 80
- Wollman, E. R., Geballe, T. R., Lacy, J. H., Townes, C. H., & Rank, D. M. 1976, *ApJ*, 205, L5
- Wollman, E. R., Geballe, T. R., Lacy, J. H., Townes, C. H., & Rank, D. M. 1977, *ApJ*, 218, L103
- Yusef-Zadeh, F., Roberts, D. A., Wardle, M., et al. 2015, *ApJ*, 801, L26
- Yusef-Zadeh, F., Royster, M., Wardle, M., et al. 2013, *ApJ*, 767, L32
- Zajacek, M. 2014, Master Thesis, Charles University in Prague, 150 pp. (2014)
- Zajacek, M., Eckart, A., & Shahzamanian, B. 2017, *The Observatory*, 137, 112
- Zajacek, M., Karas, V., & Kunneriath, D. 2015, *Acta Polytechnica*, 55, 203
- Zajaček, M., Britzen, S., Eckart, A., et al. 2017, *A&A*, 602, A121
- Zajaček, M., Eckart, A., Karas, V., et al. 2016, *MNRAS*, 455, 1257
- Zajaček, M., Karas, V., & Eckart, A. 2014, *A&A*, 565, A17
- Zajaček, M., Tursunov, A., Eckart, A., & Britzen, S. 2018, *MNRAS*, 480, 4408
- Zamaninasab, M., Eckart, A., Meyer, L., et al. 2008, *Journal of Physics Conference Series*, 131, 012008
- Zamaninasab, M., Eckart, A., Witzel, G., et al. 2010, *A&A*, 510, A3
- Zel'dovich, Y. B. 1964, *Soviet Physics Doklady*, 9, 195
- Zeldovich, Y. B. & Guseynov, O. H. 1966, *ApJ*, 144, 840
- Zel'dovich, Y. B. & Novikov, I. D. 1972, *General Relativity and Gravitation*, 3, 119
- Zhao, J.-H., Morris, M. R., Goss, W. M., & An, T. 2009, *ApJ*, 699, 186
- Zubovas, K., Nayakshin, S., & Markoff, S. 2012, *MNRAS*, 421, 1315



Acknowledgements

At this place one is supposed to thank the people that helped them to complete the PhD studies or one should say PhD research. In my case it should be another “thesis” by itself, but I will try to list people that helped me the most. First of all, I would like to thank my supervisor Prof. Dr. Andreas Eckart for accepting me to his group and for enabling me to perform the research in the field of galactic nuclei, with the focus on the Galactic centre, in which I had some background from master studies in Prague. I really appreciate that Andreas gave me a lot of freedom to perform my own, independent research, with some of the ideas not being exactly at the “mainstream”, but that is what exactly attracted me. It was also nice that I could contribute to his interdisciplinary philosophical/astrophysical paper on the Galactic centre black hole, which by itself is a great and original piece of work with historical, philosophical, as well as astrophysical considerations. Next I would like to thank the whole IMPRS team, including the speaker, Prof. Dr. Anton Zensus, the current coordinator, Dr. R. Mauersberger, the previous coordinator, Dr. E. Angelakis, and the secretary, Dr. Simone Pott, for all the help and the support, when something concerning the administration was needed. In particular, I am grateful to Mrs. Tuyet-Le Tran and Mrs. Barbara Menten from MPIfR for all the help with the health insurance papers and other administration. I shall also thank all the administration as well as technical staff at the University of Cologne for being always ready to help.

I am also very grateful to my previous supervisor Prof. Dr. Vladimír Karas (now director at the Astronomical Institute of the Academy of Sciences of the Czech Republic), who is willing to continually give me useful advice, support, and encouragement to continue in research in astrophysics. I am glad that together with Vladimír and Andreas we could further develop a very fruitful and successful Cologne-Prague collaboration. It was a very nice experience to help organise Cologne-Prague-Kiel meetings 2016 and 2017 at the Castle Wahn in Porz-Wahn. I am also very grateful to my very first supervisor Doc. Dr. Miroslav Brož for guiding my small research project at the end of my bachelor studies. Since these times I am indeed in love with celestial mechanics and astrodynamics, which is present basically everywhere, from our very close cosmic vicinity in the Solar System, all the way to the Galactic centre.

In addition, I would like to thank Dr. Silke Britzen for many useful discussions and input at MPIfR. Silke is one of the most optimistic and curious scientists I have ever met and her “drive” to both begin and, perhaps more importantly, finish projects has been very inspirational

for me.

Scientifically, I would like to thank many people for a lot of input and constructive criticism. In particular, I spent a lot of time working and discussing with Banafsheh (about the nature and the polarization of the DSO), Gerold (many things of Galactic and extragalactic origin), Monica (DSO and extragalactic stuff), Florian (DSO), Marzieh (S-star orbits and DSO), Lars Fuhrmann (radio observations and Effelsberg), Silke (DSO, OJ287, and arts), Andreas (DSO, star-formation, black hole charge, bremsstrahlung, stellar dynamics, philosophy of science, Stargate, Star Trek, Riddick, Ringworld...), Vladimir (relativistic astrophysics, DSO, neutron stars, Prague, CPK meetings...), Alvaro (VLA observations), Arman (general relativity, motion of charged particles), Franta (DSO, neutron stars, dynamics), Elaheh (S2, bow shocks, DSO, G1...), Behrang (star formation) and many others.

The whole AEGROUP is an amazing place to be. It feels more like a family and several members helped me a lot when some of my small “catastrophes” happened (stolen backpack, broken arm, fainting...). For all the encouragement and the help I would like to thank Gerold, Nastaran, Nadeen, Banafsheh, Monica, Marzieh, Matthias, Munawwar, Yasir, Abhijeet, Elaheh, Florian, Behrang, Christian, Matthew, Steffen, Michael, Lukas, Sebastian (in a random order) and others (I am sorry in case I forgot someone). It was always nice to hang out with you somewhere – especially the Christmas dinners are unforgettable! In particular, I would like to thank Gerold for being my colleague “mentor”, who helped me many times, for example with my bad German (translating this thesis abstract).

It was also nice to work at Ph1, whose building was sometimes shaking a bit, but the atmosphere was always comfortable and very friendly. I really enjoyed the INTERGROUP meetings with Alvaro, Daniel, Sebastian, Sumeyee, Gerold, Nastaran, Pavol, Elaheh, Andres, Balaji, Jan, and other amazing people.

Special thanks also goes to Arman Tursunov, who joined my research activities during the last phase of my PhD, specifically during the Bad Honnef conference. In a few months we finished a draft of the paper on the charge of the Galactic centre black hole, which is included in this thesis. This paper, now published in MNRAS, was also featured as a highlight in October issue (2018) of Nature Astronomy. I am glad that Arman liked this collaboration so much that he came to Cologne for a sabbatical research stay (2018-2019).

Although I spent doing PhD three years, I have had an opportunity to be involved in amateur and professional astronomy for more than 10 years now. The path from my small hometown Malacky in western Slovakia, through Bratislava and Prague, and ending up in Cologne/Bonn area was not always straightforward, but has certainly been worth taking. At this place, I would like to thank all Slovak astronomers who despite the small financial contribution from the state were willing to organize astronomical competitions (“What do you know about stars?” and the Astronomical Olympiad), camps, and clubs for young people. This was a very important start for my career since I was motivated to spend my free time during elementary and high-school studies to calculate small problems and do observations. I would like to especially thank to Tomáš Dobrovodský (now director at the Observatory and Planetarium in Žiar nad Hronom), who organized a very useful astronomy club in Malacky, where I learned a lot about basics of practical astronomical observations.

In addition, I am grateful to the Slovak Association for Youth, Science, and Technology (AMAVET) for supporting my travel to student conferences, ESI 2009 in Tunisia and MOSTRATEC 2010 in Brazil, where I presented my first scientific project on the measurement of the solar flux density. I have continued the cooperation with AMAVET up to the present time and I have managed to launch some of my own ideas for the popularization of science

and technology (LaBaK and others). I have to say that it has been always very inspirational to see enthusiastic young people doing research on an international level, which is supported in a large extent by the MILSET organization (International Movement for Leisure Activities in Science and Technology; MILSET - Mouvement International pour le Loisir Scientifique et Technique).

Last but not the least, I would like to thank my great parents, Viera and Marian, and my sister Barbora with her family for supporting me all the time in many ways. I would also like to thank the whole Zajaček, Zajíček, and Krajčír families for all the help, support, and love. Without you, it would not be possible to be at this stage: *Ďakujem za všetko!*



Selbständigkeitserklärung

Ich versichere, dass ich die von mir vorgelegte Dissertation selbständig angefertigt, die benutzten Quellen und Hilfsmittel vollständig angegeben und die Stellen der Arbeit – einschließlich Tabellen, Karten und Abbildungen –, die anderen Werken im Wortlaut oder dem Sinn nach entnommen sind, in jedem Einzelfall als Entlehnung kenntlich gemacht habe; dass diese Dissertation noch keiner anderen Fakultät oder Universität zur Prüfung vorgelegen hat; dass sie – abgesehen von unten angegebenen Teilpublikationen – noch nicht veröffentlicht worden ist, sowie, dass ich eine solche Veröffentlichung vor Abschluss des Promotionsverfahrens nicht vornehmen werde. Die Bestimmungen der Promotionsordnung sind mir bekannt. Die von mir vorgelegte Dissertation ist von Prof. Dr. Andreas Eckart betreut worden.

Köln, den 10.08.2017

(Michal Zajaček)

Teilpublikationen

- *A stellar flyby close to the Galactic center: Can we detect stars on highly relativistic orbits?*; **M. Zajaček** and A. A. Tursunov; *Astronomische Nachrichten* 339 (5), 324 (2018).
- *On the charge of the Galactic centre black hole*; **M. Zajaček**, A. A. Tursunov, A. Eckart, S. Britzen; *MNRAS* 480, 4408 (2018).
- *Nature of the Galactic centre NIR-excess sources. I. What can we learn from the continuum observations of the DSO/G2 source?*; **M. Zajaček**, S. Britzen, A. Eckart, B. Shahzamanian, G. Busch, V. Karas, M. Parsa, F. Peissker, M. Dovčiak, M. Subroweit, F. Dinnbier, J. Anton Zensus; *A&A* 602, A121 (2017).
- *Polarimetry narrows down the possibilities for the Dusty S-cluster Object (DSO/G2) in the Galactic centre*; **M. Zajaček**, A. Eckart, B. Shahzamanian; *The Observatory Magazine* 137 (2017).

- *Effect of an isotropic outflow from the Galactic Centre on the bow-shock evolution along the orbit*; **M. Zajaček**, A. Eckart, V. Karas, D. Kunneriath, B. Shahzamanian, N. Sabha, K. Mužić, M. Valencia-S.; MNRAS 455 (2016).
- *Infrared-excess Source DSO/G2 Near the Galactic Center: Theory vs. Observations*; **M. Zajaček**, A. Eckart, F. Peissker, G. D. Karssen, V. Karas; Proceedings of the 24th Annual Conference of Doctoral Students - WDS 2015 - Physics (eds. J. Safrankova and J. Pavlu), Prague, Matfyzpress (2015).
- *Galactic Center Minispiral: Interaction Modes of Neutron Stars*; **M. Zajaček**, V. Karas, D. Kunneriath; Acta Polytechnica 55 (2015).
- *Dust-enshrouded star near supermassive black hole: predictions for high-eccentricity passages near low-luminosity galactic nuclei*; **M. Zajaček**, V. Karas, A. Eckart; A&A 565, A17 (2014).

Weitere Publikationen

- *OJ287: deciphering the ‘Rosetta stone’ of blazars*; S. Britzen, C. Fendt, G. Witzel, S.-J. Qian, I. N. Pashchenko, O. Kurtanidze, **M. Zajaček**, G. Martinez, V. Karas, M. Aller, H. Aller, A. Eckart, K. Nilsson, P. Arévalo, J. Cuadra, M. Subroweit, A. Witzel; MNRAS 478, 3199 (2018).
- *From accretion to star formation in galactic nuclei*; **M. Zajaček**; The Observatory, Vol. 137, p. 267-272 (2017).
- *OJ287 taken to pieces: the origin of a precessing and rotating jet*; S. Britzen, C. Fendt, G. Witzel, S.-J. Qian, I. N. Pashchenko, O. Kurtanidze, **M. Zajaček**, G. Martinez, V. Karas, M. Aller, H. Aller, A. Eckart, K. Nilsson, P. Arévalo, J. Cuadra, A. Witzel; Journal of Physics: Conference Series 942, Issue 1, article id. 012005 (2017).
- *Polarization properties of bow shock sources close to the Galactic centre*; **M. Zajaček**, V. Karas, E. Hosseini, A. Eckart, B. Shahzamanian, M. Valencia-S., F. Peissker, G. Busch, S. Britzen, J. A. Zensus; Proceedings of RAGtime 17-19: Workshops on black holes and neutron stars, 17-19 (2017).
- *Modelling the bow-shock evolution along the DSO/G2 orbit in the Galactic centre*; L. Štofanová, **M. Zajaček**, D. Kunneriath, A. Eckart, V. Karas; Proceedings of RAGtime 17-19: Workshops on black holes and neutron stars, 17-19 (2017).
- *Bow shocks as tracers of the environment and stellar outflows near the supermassive black hole*; L. Štofanová, **M. Zajaček**, V. Karas; The X-ray Universe 2017, Proceedings of the conference held 6-9 June, 2017 in Rome, Italy. Edited by J.-U. Ness and S. Migliari (2017).
- *Investigating the Relativistic Motion of the Stars Near the Supermassive Black Hole in the Galactic Center*; M. Parsa, A. Eckart, B. Shahzamanian, V. Karas, **M. Zajaček**, J. A. Zensus, C. Straubmeier; ApJ 845 (2017).

- *The Milky Way's Supermassive Black Hole: How Good a Case Is It?*; A. Eckart, A. Hüttemann, C. Kiefer, S. Britzen, **M. Zajaček**, C. Lämmerzahl, M. Stöckler, M. Valencia-S., V. Karas, M. García-Marín; *Foundations of Physics* 47, Issue 5 (2017).
- *Plunging neutron stars as origin of organised magnetic field in galactic nuclei*; V. Karas, O. Kopáček, D. Kunneriath, **M. Zajaček**, A. Araudo, A. Eckart, J. Kovář; *Contrib. Astron. Obs. Skalnaté Pleso* 47, 124-132 (2017).
- *Detection of polarized continuum emission of the Dusty S-cluster Object (DSO/G2)*; B. Shahzamanian, **M. Zajaček**, M. Valencia-S., F. Peissker, A. Eckart, N. Sabha, M. Parsa; *IAU Symposium* 322 (2017).
- *Nature of the Dusty S-cluster Object (DSO/G2): Pre-main-sequence star with non-spherical dusty envelope*; **M. Zajaček**, B. Shahzamanian, M. Valencia-S., F. Peissker, A. Eckart, N. Sabha, M. Parsa; *IAU Symposium* 322 (2017).
- *Polarized near-infrared light of the Dusty S-cluster Object (DSO/G2) at the Galactic center*; B. Shahzamanian, A. Eckart, **M. Zajaček**, M. Valencia-S., N. Sabha, L. Moser, M. Parsa, F. Peissker, C. Straubmeier; *A&A* 593, A131 (2016).
- *Monitoring the Dusty S-cluster Object (DSO/G2) on its Orbit toward the Galactic Center Black Hole*; M. Valencia-S., A. Eckart, **M. Zajaček**; F. Peissker, M. Parsa, N. Grosso, E. Mossoux, D. Porquet, B. Jalali, V. Karas, S. Yazici, B. Shahzamanian, N. Sabha, R. Saalfeld, S. Smajic, R. Grellmann, L. Moser, M. Horrobin, A. Borkar, M. García-Marín, M. Dovciak, D. Kunneriath, G. D. Karssen, M. Bursa, C. Straubmeier, H. Bushouse; *ApJ* 800, 125 (2015).
- *Variable and Polarised Near-infrared Emission from the Galactic Centre*; B. Shahzamanian, A. Eckart, M. Valencia-S., G. Witzel, M. Zamaninasab, **M. Zajaček**, N. Sabha, M. García-Marín, V. Karas, F. Peissker, G. D. Karssen, M. Parsa, N. Grosso, E. Mossoux, D. Porquet, B. Jalali, M. Horrobin, R. Buchholz, M. Dovčiak, D. Kunneriath, M. Bursa, A. Zensus, R. Schödel, J. Moulataka, C. Straubmeier; *The Messenger* 159 (2015).
- *Monitoring the Dusty S-cluster object (DSO/G2) near the Galactic center black hole: model predictions for Br-gamma energy shift during the passage*; V. Karas, **M. Zajaček**, D. Kunneriath, M. Valencia-S., A. Eckart; *The Extremes of Black Hole Accretion, Proceedings of the conference held 8-10 June, 2015 in Madrid, Spain* (2015).
- *Infrared-excess Source DSO/G2 Near the Galactic Center: Theory vs. Observations*; **M. Zajaček**, A. Eckart, F. Peissker, G. D. Karssen, V. Karas; *Proceedings of the 24th Annual Conference of Doctoral Students - WDS 2015 - Physics* (eds. J. Safrankova and J. Pavlu), Prague, Matfyzpress, pp. 27-35 (2015).
- *Gaseous environment in LLAGN: modes of interaction with compact star nuclear population*; **M. Zajaček**, V. Karas, L. Šubr, D. Kunneriath, A. Eckart; *Galaxies in 3D across the Universe, Proceedings of the International Astronomical Union, IAU Symposium* 309 (2015).
- *Effects of environmental drag onto a fast-moving magnetic compact star near a supermassive black hole*; V. Karas, L. Šubr, D. Kunneriath, **M. Zajaček**; *Proceedings of RAGtime 14/16: Workshops on black holes and neutron stars* (2014).

- *The infrared K-band identification of the DSO/G2 source from VLT and Keck data; A. Eckart, M. Horrobin, S. Britzen, M. Zamaninasab, K. Mužić, N. Sabha, B. Shahzamanian, S. Yazici, L. Moser, M. García-Marin, M. Valencia-S., A. Borkar, M. Bursa, G. Karssen, V. Karas, **M. Zajaček**, L. Bronfman, R. Finger, B. Jalali, M. Vitale, C. Rauch, D. Kunneriath, J. Moulataka, C. Straubmeier, Y. E. Rashed, K. Markakis, J. Anton Zensus; Proceedings of the International Astronomical Union 303 (2014).*

Astronomy and Astrophysics

Editor in Chief: T. Forveille

T. Forveille

Astronomy & Astrophysics
Observatoire de Paris
61, avenue de l'Observatoire
75014 Paris, France

Tel.: 33 0(1) 43 29 05 41
Fax: 33 0(1) 43 29 05 57
e-mail: aanda.paris@obspm.fr
Web: <http://www.aanda.org>

merging
Annales d'Astrophysique
Arkiv for Astronomi
Bulletin of the Astronomical Institutes
of the Netherlands
Bulletin Astronomique
Journal des Observateurs
Zeitschrift fur Astrophysik
Bulletin of the Astronomical Institutes
of Czechoslovakia

Paris, July 3, 2017

Reprint Permission

Material:

Zajacek et al., 2014, A&A 565, A17
Shahzamanian et al., 2016, A&A 593, A131
Zajacek et al., 2017, A&A, 602, A121

To be used in:

PhD thesis, University of Cologne

Permission granted to:

Michal Zajacek
University of Cologne & MPIfR Bonn
zajacek@ph1.uni-koeln.de

I hold copyright on the material referred to above, and hereby grant permission for its use as requested herewith.

The article should be reproduced in the same format as that published in A&A (for example, in an appendix). In particular, the present permission rules do not allow copy-and-pasting parts of the article into the main text of the thesis.

Credit should be given as follows:

Credit: Author, A&A, vol, page, year, reproduced with permission © ESO.



Thierry Forveille
A&A Editor-in-Chief

Sponsored by Argentina, Austria, Belgium, Brazil, Chile, Czech Republic, Denmark, Estonia, Finland, France, Germany, Greece, Hungary, Italy, Netherlands, Poland, Portugal, Slovak Republic, Spain, Sweden, and Switzerland.
Produced and distributed by EDP Sciences for ESO.

Dear Michal Zajacek,

Thank you for your enquiry.

Regarding:

M. Valencia-S. et al 2015 ApJ 800 125

AAS grants back to authors the non-exclusive right of republication, subject only to giving appropriate credit to the journal in which the article was published. This non-exclusive right of republication gives authors the right to approve or deny reproduction of all or part of the article and to post the final published version online.

Therefore, please go ahead with the inclusion of this material in your new work - no permission is required from AAS.

This permission does not apply to any material/figure which is credited to another source in the AAS publication or has been obtained from a third party. Express permission for such materials/figures must be obtained from the copyright owner.

If you have any questions, please contact the Permissions team.

Kind regards,

Kathryn Shaw

Copyright & Permissions Team
Gemma Alaway - Senior Rights & Permissions Adviser
Kathryn Shaw - Rights & Permissions Assistant

Contact Details

E-mail: permissions@iop.org

For further information about copyright and how to request permission:

<http://iopscience.iop.org/page/copyright>

Please see our Author Rights Policy

<http://iopublishing.org/author-rights/>

Please note: Any statements made by IOP Publishing to the effect that authors do not need to get permission to use any content where IOP Publishing is not the publisher is not intended to constitute any sort of legal advice. Authors must make their own decisions as to the suitability of the content they are using and whether they require permission for it to be published within their article.

Self-Archiving Policy P

Dear Michal Zajaček,

RE. M. Zajaček et al. Effect of an isotropic outflow from the Galactic Centre on the bow-shock evolution along the orbit. *MNRAS* (2016) 455 (2): 1257-1274

My apologies for the delay in responding to you and thank you for your email requesting permission to reuse all or part of your article in a thesis/dissertation.

As part of your copyright agreement with Oxford University Press you have retained the right, after publication, to use all or part of the article and abstract, in the preparation of derivative works, extension of the article into a booklength work, in a thesis/dissertation, or in another works collection, provided that a full acknowledgement is made to the original publication in the journal. As a result, you should not require direct permission from Oxford University Press to reuse your article.

Authors may upload a PDF of the accepted manuscript to institutional and/or centrally organized repositories and/or in free public servers, upon acceptance for publication in the journal. Authors may upload the version of record to institutional and/or centrally organized repositories and/or in free public servers, upon publication in the journal.

Please Note: Inclusion under a Creative Commons License or any other Open-Access License allowing onward reuse is prohibited.

For full details of our publication and rights policy, including **credit-lines**, please see the attached link to our website:

https://academic.oup.com/journals/pages/access_purchase/rights_and_permissions/self_archiving_policy_p

If you have any other queries, please feel free to contact us.

Kind regards,

Louise

Miss Louise Eyre | Permissions Assistant | Rights Department

Academic and Journals Divisions | Global Business Development

Oxford University Press | Great Clarendon Street | Oxford | OX2 6DP

Tel: +44(0)1865 354454 | Email: louise.eyre@oup.com | www.oxfordjournals.org



Acta Polytechnica
Editorial Office
Central Library
Czech Technical University in Prague
Czech Republic
<https://ojs.cvut.cz/ojs/ap>

26. 6. 2017

We certify, that the article

Michal Zajacek, Vladimir Karas, Devaky Kunneriath
**GALACTIC CENTER MINISPIRAL:
INTERACTION MODES OF NEUTRON STARS**
<https://doi.org/10.14311/AP.2015.55.0203>

published in Acta Polytechnica 55(3) 2015,
ISSN 1210-2709 (print) ISSN 1805-2363(online).
under [Creative Commons Attribution 4.0 International License](#)

can be used by authors for the PhD dissertation of Michal Zajaček
at the University of Cologne, Germany
with appropriate citation.

Iva Adlerová



THE OBSERVATORY MAGAZINE

Telephone 01235 767509

16 Swan Close
Grove
Wantage
Oxfordshire
OX12 0QE

e-mail: manager@obsmag.org

21 June 2017

Michal Zajacek
University of Cologne
I. Physikalisches Institut
Zùlpicher Strasse 77
50937 Cologne
Germany

Dear Michal,

The Editors of *The Observatory* give you permission to include the paper published in the *Magazine* (Volume 137, page 112, 2017) in any other work, including your PhD Thesis.

Best wishes,



David Stickland
Managing Editor



Lebenslauf

Persönliche Angaben

Name:	RNDR. Michal Zajaček
Anschrift:	L. Novomeského 4 901 01 Malacky Slowakei
Email:	zajacek@ph1.uni-koeln.de
Geburtsdatum und -ort:	31.12.1988 in Malacky, Slowakei
Staatsangehörigkeit:	slowakisch

Ausbildung und Berufserfahrung

1995 - 2004	Katholische Grundschule in Malacky, Slowakei
2004 - 2009	Evangelisches Lyceum A. C. zu Pressburg (Bratislava), Slowakei
2009 - 2012	Bachelor of Science (Allgemeine Physik), Karlsuniversität zu Prag, Tschechien
2012 - 2014	Master of Science (Astronomie und Astrophysik), Karlsuniversität zu Prag, Tschechien
2014 - 2017	Promotionsstudium (Experimentalphysik), Universität zu Köln Max-Planck Institut für Radioastronomie, Bonn, Deutschland International Max Planck Research School for A&A

Stipendien und Auszeichnungen

2018	Forschungshighlight "Ladung im Schwarzen Loch" in <i>Nature Astronomy</i>
2014 - 2017	Stipendium der Max Planck Gesellschaft
2011 - 2014	Stipendium der Math.-Phys. Fakultät, Karlsuniversität zu Prag, für ausgezeichnete Studium Ergebnisse
2013 - 2014	Forschungsstipendium (# 879113, Neutronsterne im Galaktischen Zentrum) der Karlsuniversität zu Prag
2013	MILSET "Regards and Gratitude award" (Abu Dhabi, Vereinigte Arabische Emirate)

